

# Earthquake Engineering

## New Research



Takumi Miura & Yuuki Ikeda

Editors

NOVA



# **EARTHQUAKE ENGINEERING: NEW RESEARCH**

No part of this digital document may be reproduced, stored in a retrieval system or transmitted in any form or by any means. The publisher has taken reasonable care in the preparation of this digital document, but makes no expressed or implied warranty of any kind and assumes no responsibility for any errors or omissions. No liability is assumed for incidental or consequential damages in connection with or arising out of information contained herein. This digital document is sold with the clear understanding that the publisher is not engaged in rendering legal, medical or any other professional services.



**EARTHQUAKE ENGINEERING:  
NEW RESEARCH**

**TAKUMI MIURA  
AND  
YUUKI IKEDA  
EDITORS**

**Nova Science Publishers, Inc.**  
*New York*

Copyright © 2009 by Nova Science Publishers, Inc.

**All rights reserved.** No part of this book may be reproduced, stored in a retrieval system or transmitted in any form or by any means: electronic, electrostatic, magnetic, tape, mechanical photocopying, recording or otherwise without the written permission of the Publisher.

For permission to use material from this book please contact us:

Telephone 631-231-7269; Fax 631-231-8175

Web Site: <http://www.novapublishers.com>

#### **NOTICE TO THE READER**

The Publisher has taken reasonable care in the preparation of this book, but makes no expressed or implied warranty of any kind and assumes no responsibility for any errors or omissions. No liability is assumed for incidental or consequential damages in connection with or arising out of information contained in this book. The Publisher shall not be liable for any special, consequential, or exemplary damages resulting, in whole or in part, from the readers' use of, or reliance upon, this material. Any parts of this book based on government reports are so indicated and copyright is claimed for those parts to the extent applicable to compilations of such works.

Independent verification should be sought for any data, advice or recommendations contained in this book. In addition, no responsibility is assumed by the publisher for any injury and/or damage to persons or property arising from any methods, products, instructions, ideas or otherwise contained in this publication.

This publication is designed to provide accurate and authoritative information with regard to the subject matter covered herein. It is sold with the clear understanding that the Publisher is not engaged in rendering legal or any other professional services. If legal or any other expert assistance is required, the services of a competent person should be sought. FROM A DECLARATION OF PARTICIPANTS JOINTLY ADOPTED BY A COMMITTEE OF THE AMERICAN BAR ASSOCIATION AND A COMMITTEE OF PUBLISHERS.

#### **LIBRARY OF CONGRESS CATALOGING-IN-PUBLICATION DATA**

ISBN 978-1-60876-556-0 (E-Book)

*Published by Nova Science Publishers, Inc. ✦ New York*

# CONTENTS

<b>Preface</b>		<b>vii</b>
<b>Research and Review Studies</b>		<b>1</b>
<b>Chapter 1</b>	Multi-scale Analysis for Estimating Strong Ground Motion and Structure Responses <i>Tsuyoshi Ichimura and Muneo Hori</i>	<b>3</b>
<b>Chapter 2</b>	Prediction of the Seismic Displacement of Landslides and Gravity Walls Using a Multi-block Model <i>Constantine A. Stamatopoulos</i>	<b>17</b>
<b>Chapter 3</b>	Geotechnical Seismic Isolation <i>Hing-Ho Tsang</i>	<b>55</b>
<b>Chapter 4</b>	Dynamic Responses of High-Speed Railway Bridges under Earthquakes and Their Influences on Running Safety of Train Vehicles <i>Weiwei Guo, He Xia and Chaoyi Xia</i>	<b>89</b>
<b>Chapter 5</b>	On the Seismic Attenuation with Consideration of the Prediction Model Complexity <i>Ka-Veng Yuen and He-Qing Mu</i>	<b>135</b>
<b>Chapter 6</b>	Using Ambient Noise Measurements in the Process of Assessing Earthquake Hazards in Urban Areas: Examples from Israel <i>Y. Zaslavsky, A. Shapira, G. Ataev, M. Gorstein, T. Aksinenko, M. Kalmanovich, N. Perelman and R. Hofstetter</i>	<b>155</b>
<b>Chapter 7</b>	Seismic Resistant Braced Frame Structures with Shape Memory Alloy-Based Self-centering Damping Device <i>Yunfeng Zhang and Songye Zhu</i>	<b>219</b>
<b>Chapter 8</b>	Application of Numerical Tools for the Modelling of Granular Soil Behaviour under Earthquakes: The State-of-the-Art <i>S. López-Querol</i>	<b>255</b>

<b>Chapter 9</b>	The Use of Dissipated Energy at Modeling of Cyclic Loaded Saturated Soils <i>S. Lenart</i>	<b>295</b>
<b>Chapter 10</b>	Simplified Modal Response History Analysis for Asymmetric-Plan Structures <i>Jui-Liang Lin and Keh-Chyuan Tsai</i>	<b>323</b>
<b>Index</b>		<b>363</b>

## PREFACE

This new book deals with earthquake engineering including seismology, tsunamis, ground motion characteristics, soil and foundation dynamics, wave propagation, probabilistic and deterministic methods of dynamic analysis, experimental behaviour of structures, and methods for earthquake resistant design and retrofit of structures that are germane to practicing engineers. It includes seismic code requirements and system identification, as well as supplemental energy dissipation, base isolation, and structural control emphasizing earthquake engineering.

While full three-dimensional (3D) numerical simulation is a solution to estimate strong ground motion and a seismic structure response for a given earthquake, it is difficult to carry out numerical computation because of its huge computational cost; the order of a target domain size is  $10^{4-5}$  m and the target resolution required is  $10^{-2-0}$  m. In Chapter 1, we present an efficient approach which is based upon multi-scale analysis to make a 3D simulation of wave propagation and amplification as well as seismic responses of an infrastructure. The formulation of the multi-scale analysis is presented, and it is validated by comparing a strong ground motion and a seismic structure response which is obtained by directly analyzing the whole system. The usefulness and applicability of this multiscale approach are also discussed.

Newmark's sliding-block model is usually employed to predict the seismic displacement of slopes. Yet, when displacement is large, the conventional sliding-block model predicts displacements that are larger than expected for the given input motion and soil strength. Alternatively, to simulate slope movement when the displacement is large, a multi-block sliding model has been proposed. Similarly to the Sarma (1979) stability method, a general mass sliding on a slip surface that consists of  $n$  linear segments is considered. In order for the mass to move, interfaces where resisting forces are exerted must be formed between nodes of the slip surface. Thus, the mass is divided into  $n$  blocks sliding in  $n$  different inclinations. For landslides, the masses and lengths of each block entering the calculation are updated in terms of the distance moved. In addition, constitutive equations that simulate strength degradation along the slip surface coupled with the multi-block model are proposed in order to simulate the triggering of the slides. On the other hand, gravity walls, as a result of the applied shaking, move outwards, away from the retained soil. Simplified analyses predicting the seismic displacement of gravity walls are based on the Mononobe-Okabe method combined with Newmark's sliding-block model. The wall-backfill system is modeled, according to the multi-block methodology, using two bodies: (a) the wall that slides outward along the wall-foundation soil and (b) the wedge that slides along the plane of least resistance in the retained

soil. The new method, unlike the previous, is kinematically compatible and generally predicts different seismic wall displacement for the given input motion and soil strength. Chapter 2 first describes the multi-block model and its extensions for the prediction of the seismic displacement of landslides and gravity walls outlined above. Then, it validates the above methodologies by predicting the response of a well-documented earthquake-induced landslide and of a gravity walls (a) measured in shaking-table tests and (b) computed by elaborate numerical analyses.

Traditionally, seismic isolation is a flexible or sliding interface positioned between a structure and its foundation for the purpose of decoupling the motions of the ground from that of the structure. In recent years, novel seismic isolation methods have been proposed, in which the flexible or sliding interface is in direct contact with geological sediments and the isolation mechanism primarily involves geotechnics.

Smooth synthetic liners have been proposed beneath foundations or between soil layers for dissipating seismic energy through sliding. Rubber-soil mixtures have also been proposed around foundations for absorbing seismic energy with a function similar to that of a cushion. The low cost of these proposed seismic isolation methods can greatly benefit developing countries where resources and technology are not adequate for earthquake mitigation using well-developed, yet expensive, techniques.

In Chapter 3, the background and principles of these new methods will be introduced, followed by the latest research findings. Potential problems and further research directions will be identified and discussed.

In Chapter 4, the current situation, problems to be studied and further research trend in the field of dynamic interaction of vehicles and bridges under seismic excitations are summarized. A seismic analysis model of a simply-supported beam subjected to movable wheel with sprung mass is presented and the solution is deduced. A dynamic model of coupled train-bridge system subjected to earthquakes is then established, in which the bridge is modeled with the modal comprehension analysis technique, and each vehicle is modeled with 31 degrees of freedom. The seismic loads are imposed on the bridge by using the influence matrix and exerted on the vehicles through the dynamic wheel-rail interaction relationships. The normal wheel-rail interaction is tackled by using the Hertzian contact theory, and the tangent wheel-rail interaction by the Kalker linear theory and the Shen-Hedrick-Elkins theory. Case studies are performed to several actual bridges in China, including the simply-supported bridges with different span-lengths on the Qinghuangdao-Shenyang Special Passenger railway, and the continuous PC girder bridges on the planned Beijing-Shanghai high-speed railway. Through input of typical seismic waves with different propagation velocities to the train-bridge system, the histories of the train running through the bridge are simulated and the dynamic responses of the bridge and the vehicles are calculated. The influences of different train speeds and earthquake wave propagation velocities in non-uniform seismic excitations on the dynamic responses of the train-bridge system are studied. The critical train speeds are proposed for running safety on high-speed railway bridges under earthquakes of various intensities.

Estimation of peak ground acceleration is one of the main issues in civil and earthquake engineering practice. The Boore-Joyner-Fumal empirical formula is well known for this purpose by estimating the peak ground acceleration using information such as the magnitude of earthquake, the site-to-fault distance and the site foundation properties. The complexity of this prediction formula is investigated in this study. For example, should we use a first-order

or a second-order polynomial for the earthquake magnitude? It is obvious that a more complicated prediction model class (i.e., a formula with more free parameters) possesses smaller fitting error for a set of data. However, this does not imply that the complicated predictive formula is more realistic since over-fitting may occur if there are too many free parameters. In Chapter 5 we propose to use the Bayesian probabilistic model class selection approach to obtain the most suitable prediction model class for the seismic attenuation formula. In this approach, each prediction model class is evaluated by the plausibility given the dataset. A complicated model class is penalized by the “Ockham factor”, which is a natural consequence of the aforementioned plausibility, instead of any ad-hoc penalty terms. The optimal model class is robust in the sense that there is balance between the data fitting capability and the sensitivity to noise. A database of strong-motion records, obtained from the China Earthquake Data Center, is utilized for the analysis. The optimal prediction model class and its most plausible model parameters are determined. Quantification of the uncertainty of the parameters is allowed by the Bayesian probabilistic methodology and this can be used for uncertainty analysis of the predicted peak ground acceleration. It turns out that the optimal model class is simpler than the full order attenuation model suggested by Boore, Joyner and Fumal (1993).

As explained in Chapter 6, ground motion amplifications due to soft soils, common in urban areas, are a major contributor to increasing damage and number of casualties. The great variability in the subsurface conditions across a town/city and the relatively high costs associated with obtaining the appropriate information about the subsurface, strongly limit proper hazard assessments. Direct information from strong motion recordings in urban areas is usually unavailable. Such is the situation in Israel which is small and its population centers are in close proximity to the seismically active Dead Sea Fault system, capable of generating earthquakes with magnitude as high as 7.5.

Heavily limited with relevant local recordings of strong ground motions, we adhere to the use of simplified modelling of the earthquake processes. More precisely, we generate synthetic spectra of the expected ground motions by implementing the so called Stochastic Approach (e.g. Boore, 2000), in which we integrate analytical models to determine the nonlinear response of the site under investigation that requires modelling of subsurface. Then, Monte-Carlo simulations are used to obtain the uniform hazard, site-specific acceleration spectrum.

Over the years, we have conducted site investigations in several thousands of sites across Israel. These investigations demonstrate the usefulness of using horizontal-to-vertical (H/V) spectra of ambient noise measurements to identify sites with high potential for being vulnerable to amplification effects and characterize the sites with respect to their expected resonance frequencies and the corresponding H/V levels. This information, together with any available geological, geotechnical and geophysical information, helps building a reliable model of the subsurface, which is then integrated in the processes of the seismic hazard assessment.

Modeling the subsurface and assessing the earthquake hazards in urban areas involves systematic ambient noise measurements on a grid with spacing of 500 m. At instances where high variations are observed, the spatial density of measurements is significantly increased. In doing so, we are able to develop a regional subsurface model, which is systematic with all additional information we compile, i.e., geological maps, borehole information, seismic refraction surveys etc.

In order to reduce the scatter in H/V observations, the processing scheme involves continuous recording of ambient noise for about 1-2 hours and careful selection of time windows from which H/V functions are calculated. To assure stability in H/V observations, measurements are repeated in different times and dates. At several occasions, while measuring the ambient noise or when we deliberately aimed at recording seismic events, it is possible to support ambient noise spectral ratios with spectral H/V observations from earthquakes (often considered transfer functions) and explosions recorded by accelerometers and seismometers. In all cases, we obtained similar H/V spectral ratios from the different data sets.

At the final stage of the hazard assessment process, we divide the study region into zones of similar hazard characteristics, which are used for earthquake scenarios and better represent the design acceleration spectra for safer buildings.

Chapter 7 deals with seismic resistant braced frame structures with a special type of bracing element termed self-centering friction damping brace (SFDB). The SFDB provides a passive form of energy dissipation with its core re-centering component made of stranded superelastic shape memory alloy (SMA) wires while enhanced energy dissipation mechanism is provided through friction. Superelastic Nitinol is selected as the SMA material for SFDB because of its superb superelastic property and excellent fatigue life. The mechanical property of superelastic Nitinol wires was experimentally investigated through a series of uniaxial cyclic tests. The fatigue life and the effect of loading rate and ambient temperature are studied as a part of the experimental program. Three types of constitutive models for superelastic SMAs with increasing complexity and modeling details are discussed. Based on the calibrated constitutive model for superelastic Nitinol wires, analytical model for SFDB has been developed to simulate the unique flag-shaped hysteresis of SFDB. The seismic performance of SFDB frames is evaluated through nonlinear pushover and time history analysis of two prototype buildings—a 3-story and a 6-story concentrically braced frames, at different seismic intensity levels. A displacement-based design procedure for SFDB frame is also presented, in which SFDBs are proportioned based on the target performance level under design basis earthquakes. The simulation results demonstrate that SFDB frame has a few desirable performance characteristics such as minimal residual drift after frequent and design basis earthquakes due to its self-centering capability. SFDB frame has the potential to withstand several design basis earthquakes without the need for repair or replacement of SFDB if properly designed.

Granular soils suffer changes in their mechanical properties when they are subjected to seismic loadings. There are two extreme situations related to the soil saturation conditions, i.e. dry and saturated soil, for which densification and liquefaction phenomena, respectively, may happen. Densification is due to the solid skeleton rearrangement as the shaking goes on, which produces a reduction of the initial soil volume to occur and, typically, the soil stiffness to increase. Conversely, liquefaction may be found in saturated sandy soils not enough drained or totally undrained; the same trend of the solid particles to rearrange during vibrations causes the accumulation of excess pore water pressure to develop, and consequently, a reduction of both initial effective stress and soil stiffness, until the soil does not behave like a solid any more but like a fluid. Both phenomena may result in important negative effects on natural and man made geo-structures (like dams, road and railway embankments or foundations). Therefore, numerical codes capable to model them may constitute useful tools for diminishing possible casualties and excessive material resources to

be spent at seismic sites. Constitutive laws for soils specifically developed for dynamic loadings are needed for accurately reproduce the physics of these processes. In Chapter 8, several examples of densification and liquefaction cases in the history are provided, after which a state-of-the-art on the most important and used constitutive laws, coupled formulations, and examples of applications are given.

As presented in Chapter 9, the energy concept for the analysis of densification and liquefaction of cohesionless soils was first introduced by Nemat-Nasser and Shokoh (1979). It is based on the idea that during deformation of these soils under dynamic loads, part of the energy is dissipated into the soil. This dissipated energy per unit volume is represented by the area of the hysteric strain-stress loop and could be determined experimentally. It considers both the amplitude of shear strain and the number of cycles, combining both the effects of stress and strain. Using the Palmgren-Miner cumulative damage hypothesis, the effect of random motions of an earthquake or other random dynamic load can be taken into account by dissipated energy use.

The main advantage of using the dissipated energy was found in the case of saturated soils. The relation between dissipated energy and the residual excess pore water pressure generated in saturated soils during dynamic loading is already well known. Recent studies have shown that similar relations exist also in the case of temporary excess pore pressures.

Besides relations between dissipated energy and pore pressure changes in saturated cyclic loaded soils, the paper highlights also the relation between dissipated energy and softening of soil during cyclic loading. Softening of soil during cyclic loading, so-called short-term flow, makes a perceivable impact on strain progression. After a few cycles of loading, soil starts to exhibit very low stiffness at the beginning of a load cycle and it strengthens later. It is obvious that strain developed during this short-term flow presents the main share of a total strain developed during cyclic loading, and it leads therefore to the deformation behavior of a soil. The duration of this phenomenon and stiffness of soil during this phase is in question.

It has been found that the duration of the softening phase, as well as shear modulus of soil during this phase are both related to residual pore pressure ratio. A simple constitutive model, especially suitable for a cyclic mobility modeling, was developed based on an energy approach. Its main part presents a new pore pressure generation model and findings related to short-term flow and dissipated energy.

The modal equation of motion is the foundation of structural dynamics, which plays a key role in earthquake engineering computations. Each modal equation of motion has a corresponding single-degree-of-freedom (SDOF) modal system. Thus, the modal equation of motion and the corresponding SDOF modal system are regarded as the most basic elements synthesizing the motion of the original multiple-degree-of-freedom (MDOF) structure. Modal response history analyses are widely used in structural dynamic analyses due to the efficiency in calculation and the clarity in conception. Although the vibration modes are only meaningful for elastic structures, the inelastic SDOF modal systems have also been developed based on the pushover curve representing the relationship of roof translation versus base shear for the original MDOF structure. The stated inelastic SDOF modal systems are widely applied to earthquake engineering. One of such applications is using inelastic response spectra to estimate the seismic demands of original MDOF structures. In recent years, the modal response history analyses considering the effects of higher vibration modes were proposed to approximately estimate the seismic responses of inelastic MDOF structures. However, there are three relationships of two roof translations versus two base shears and one

roof rotation versus one base torque simultaneously available for two-way asymmetric-plan buildings subjected to seismic loads. Moreover, the pushover curves representing the stated three relationships in acceleration-displacement response spectra (ADRS) format are bifurcated after the original MDOF structure becomes inelastic. Thus, it is unable to use the conventional SDOF modal system to simultaneously simulate the stated three force-deformation relationships for inelastic asymmetric-plan structures. The research in Chapter 10 decomposed the SDOF modal equation of motion into a set of three coupled equations of motion for two-way asymmetric-plan structures. The mentioned set of three coupled equations of motion is called as three-degree-of-freedom (3DOF) modal equation of motion. The 3DOF modal system corresponding to each 3DOF modal equation of motion was constructed. The elastic properties of the 3DOF modal system are exactly obtained from the corresponding 3DOF modal equation of motion. The inelastic properties of the 3DOF modal system are determined from the properties of the mentioned three pushover curves of the original MDOF structure. It is verified that the modal response history analyses by using the proposed 3DOF modal systems for two-way asymmetric-plan inelastic building systems are more satisfactory than those by using conventional SDOF modal systems. It is also validated that the proposed 3DOF modal equations of motion are advantageous to the modal response history analyses for non-proportionally damped two-way asymmetric-plan elastic building systems.

## **RESEARCH AND REVIEW STUDIES**



*Chapter 1*

# MULTI-SCALE ANALYSIS FOR ESTIMATING STRONG GROUND MOTION AND STRUCTURE RESPONSES

*Tsuyoshi Ichimura<sup>1</sup> and Muneo Hori<sup>2</sup>*

<sup>1</sup> Dept. Civil and Environmental Eng., Tokyo Institute of Technology

<sup>2</sup> Earthquake Research Institute, University of Tokyo

## Abstract

While full three-dimensional (3D) numerical simulation is a solution to estimate strong ground motion and a seismic structure response for a given earthquake, it is difficult to carry out numerical computation because of its huge computational cost; the order of a target domain size is  $10^4\sim 5$  m and the target resolution required is  $10^{-2}\sim 0$  m. In this article, we present an efficient approach which is based upon multi-scale analysis to make a 3D simulation of wave propagation and amplification as well as seismic responses of an infrastructure. The formulation of the multi-scale analysis is presented, and it is validated by comparing a strong ground motion and a seismic structure response which is obtained by directly analyzing the whole system. The usefulness and applicability of this multiscale approach are also discussed.

## 1. Introduction

It is necessary to increase spatial resolution in predicting strong ground motion and seismic structure response for a given earthquake, in order to advance design and construction of large structures such as long-span bridges and underground tunnels. Seismic responses of such structures are influenced considerably by local differences in the amplitude and phase of input strong ground motion, in particular when the structures are of complicated configuration or located in several non-flattened ground layers. A full three-dimensional (3D) numerical simulation will be a useful tool to estimate the strong ground motion and structure response in higher spatial resolution; the simulation is made for earthquake wave propagation from fault to infrastructure, as depicted in Fig. 1-a). Advancement of computational seismology and earthquake engineering accelerates research into developing such a tool.

However, it is difficult to carry out such 3D simulation since it requires its huge computational cost; the spatial resolution required for the structure analysis is in the engineering length-scale, say,  $10^{-2\sim 0}$  m, while the target domain size is in the geological length scale, say,  $10^{2\sim 5}$  m. In most cases, an approximate simulation is made which computes wave propagation in the geological length scale neglecting soft surface layers and then input resulting waves into the surface layers to analyze structure responses. This approximation is rather crude, and hence the analysis of soil-structure interaction is often simplified; a simple parallel layer model is used for surface layers, and two-dimensional state of plane strain is assumed. By its own nature, the approximate simulation is not applicable to a large-scale structure as mentioned above.

Recently, studies of earthquake motion prediction are conducted for practical engineering purposes (e.g., [1]), and remarkable progress of 3D seismic wave propagation simulation is being achieved (e.g., [2, 3, 4, 5, 6, 7, 8]). Also, in the field of computational mechanics, 3D numerical simulation with finer spatial discretization is being studied to analyze dynamic response of structures (e.g., [9, 10, 11]). Therefore, it can be expected that an efficient approach to carry out 3D numerical simulation of strong ground motion and structure response can be made by combining these two advanced simulations.

In this article, we present a multi-scale analysis for the 3D numerical simulation. The key idea of this analysis is to rationally link numerical simulation in the geological length-scale to that in the engineering length-scale; see Fig. 1-b). The rationality of the link is due to the mathematical theory that takes advantages of the singular perturbation expansion; this theory is established for analysis of general heterogeneous media [8, 12, 13]. Separately carrying out two numerical computations, the multi-scale analysis drastically reduces computational cost for the 3D simulation of strong ground motion and seismic structure responses.

The contents of this article are as follows: First, in section 2., multi-scale analysis is formulated for the 3D simulation of strong ground motion and seismic structure response. Next, we present an example of applying the multi-scale analysis in section 3.. The target problem is an underground shaft which connects a large-scale tunnel to the ground; the shaft runs through soft soil deposit. The results of the multi-scale analysis are compared with the *direct* analysis that is obtained by the huge-scale numerical computation, and it is shown that the agreement of the multi-scale analysis with the direct analysis is more than satisfactory. Some discussions are made for the potential usefulness of the multi-scale analysis in order to estimate strong ground motion and seismic structure responses of large infrastructures.

## 2. Formulation of Multi-Scale Analysis

In this section, we present the multi-scale analysis for the 3D numerical simulation of strong ground motion and seismic structure responses. The target problem is a fault-infrastructure system, denoted by  $D$ , as shown in Fig. 1-a). Since the formulation is used for the numerical computation, we start from a discretized wave equation by a finite element method (FEM) in spatial domain, i.e.,

$$[M][\ddot{u}] + [C][\dot{u}] + [K][u] = [0] \quad (\text{for } D). \quad (1)$$

where  $[M]$ ,  $[C]$  and  $[K]$  are mass, damping and stiffness matrices, respectively, and  $[u]$  is displacement vectors. Since  $[u]$  include displacement of both ground and the infrastructure, the spatial length-scale of Eq. (1) is in the engineering length scale and hence the dimension of the matrices and vector is huge.

Now, we formulate the multi-scale analysis proposed by the authors[8, 12, 13]. If viewed in the geological length-scale, local stiffness (which is determined in the engineering length-scale) is *averaged* so that it represents *effective* stiffness. In this manner, a stiffness matrix in the geological length-scale, denoted by  $[\bar{K}]$ , is constructed. Similarly,  $[\bar{C}]$  and  $[\bar{M}]$  are constructed using  $[M]$  and  $[C]$ , respectively. The dimension of  $[\bar{K}]$  is much smaller than that of  $[K]$ , and hence displacement viewed in the geological length-scale,  $[u^{(0)}]$ , is obtained by numerically solving

$$[\bar{M}][\ddot{u}^{(0)}] + [\bar{C}][\dot{u}^{(0)}] + [\bar{K}][u^{(0)}] = [0] \quad (\text{for } D). \quad (2)$$

The boundary conditions for  $[u^{(0)}]$  are easily derived from those of  $[u]$ . We should mention that the construction of  $[\bar{K}]$  is not trivial. Several averaging schemes which estimate effective properties are proposed, and we make use the scheme that is based on stochastic modeling[12].

We refine  $[u^{(0)}]$  so that displacement in the engineering length-scale is obtained. By suitably interpolating  $[u^{(0)}]$  (which is discretized in the geological length-scale), we can make a new displacement vector (which is discretized in the engineering length scale). This displacement, denoted by  $[u^{(0)*}]$ , is of the same dimension as  $[u]$ , but its spatial variation is in the geological length-scale. Thus, we need correction which changes in the engineering length-scale. The correction is needed only for a sub-domain of  $D$  which includes an infrastructure in it, in order to estimate the strong ground motion and seismic structure response. We choose a sub-domain, denoted by  $D_s$ , and determine the correction  $[u^{(1)}]$  by solving Eq. (1), as follows:

$$[M_s](\ddot{[u_s^{(0)*}]}) + [C_s](\dot{[u_s^{(0)*}]} + [\dot{u}^{(1)}]) + [K_s]([u_s^{(0)*}] + [u^{(1)}]) = [0] \quad (\text{for } D_s), \quad (3)$$

where  $[M_s]$ ,  $[C_s]$ ,  $[K_s]$  and  $[u_s^{(0)*}]$  are obtained by extracting  $[M]$ ,  $[C]$ ,  $[K]$  and  $[u^{(0)*}]$  for  $D_s$ , respectively. The dimension of  $[K_s]$  and others is much smaller than  $[K]$ , and hence Eq. (3) is numerically solved. Dispersion boundary conditions (or absorbing boundary conditions) must be posed for  $[u^{(1)}]$  since it is the correction of  $[u^{(0)}]$ .

The analysis of solving Eqs. (2) and (3) for  $[u^{(0)}]$  and  $[u^{(1)}]$  is respectively called the macro-analysis and the micro-analysis, and the multi-scale analysis combines the macro-analysis and the micro-analysis. This is called the macro-micro analysis. Denoting  $[u_s^{(0)*}] + [u^{(1)}]$  by  $[u_s]$ , we can rewrite Eq. (3) as

$$[M_s][\ddot{u}_s] + [C_s][\dot{u}_s] + [K_s][u_s] = [0] \quad (\text{for } D_s).$$

Thus, the macro-micro analysis is similar to the sub-structure method that solves Eq. (1) separating  $D$  into a set of sub-domains. The boundary conditions of the above differential equation are determined by connecting the solution of each neighboring sub-domains so that Eq. (1) is solved. The macro-micro analysis method, however, obtains the solution  $[u_s]$  only for  $D_s$ , since it uses  $[u_s^{(0)*}]$ , displacement which is discretized in the engineering length scale but changes in the geological length-scale, as an approximation of the boundary conditions on  $\partial D_s$ .

### 3. Numerical Experiments

In this section, we solve an example problem using the multi-scale analysis. The results of the 3D simulation of strong ground motion and structure responses are compared with those of the 3D simulation of analyzing the whole domain in the engineering length-scale by using huge numerical computation; from now on, the analysis that directly solves the whole domain is called direct analysis. As mentioned in the preceding section, the multi-scale analysis approximates the boundary conditions for the sub-domain, and hence the validity of this approximation is verified from the comparison.

First, we explain the example problem. The target domain is located above a basin; see Fig. 2-a). The dimension of the domain is  $9000 \times 9000 \times 2000$  m. This domain is of the largest size that can be numerically solved in the authors' computational environment with the accuracy being ensured up to 2 Hz. A fault is not included in this underground structure model. The domain consists of two layers, namely, bedrock and basement; the thickness of the both layers is 1000 m. Soft soil deposit of slightly complicated geometry is put at the center on the top surface; see Fig. 2-b). The material properties of the two layers and soil deposits are summarized in Table 1.

A large-scale structure is located in the basement at the center of the domain, as shown in Fig. 2. The structure is an underground tunnel which is connected to a vertical shaft; there is a small duct which connects the main tunnel and the shaft. Our major concern is the vertical shaft, since it goes through the basement and the soft soil deposit; the wave amplification characteristics is considerably different in these two layers and the seismic response of the shaft is complicated near the interface between them. The shaft is modeled as a cylinder of the radius 22.4 m and the height 99 m, and the connecting duct as smoothly curved tube. The main tunnel is modeled as a cylinder with the radius 5.2 m and length 170 m. The configuration of the shaft and the connecting ducts is shown in Fig. 2-b). For simplicity, we assume that all structures are made of reinforced concrete (RC) and its material property is linear elasticity; see Table 1.

While the macro-micro analysis is developed for a fault-infrastructure system, the domain of the present example problem is not so large as to be called a fault-infrastructure system; the domain size is reduced so that displacement in the engineering length-scale is obtained by the direct analysis. Instead of emitting earthquake waves from the fault, we assume that an ideal Ricker wave of the center time and frequency being 2.0 s and 1.0 Hz is input to the bottom surface; see Fig. 3 for the waveform of the input Ricker wave. The direction of the wave is vertical to the main tunnel so that it is shaken transversely. We should mention that the use of the Ricker wave is a standard practice in computational seismology, in order to examine the performance of a numerical analysis method of solving wave propagation problems.

Now, we explain the multi-scale analysis for the 3D simulation of the target problem. Models made for the macro-analysis and micro-analysis are shown in Fig. 4. The macro-analysis model is of the same configuration as the original domain, although the structures and the soil deposits are excluded since they are negligible if viewed in the geological length-scale. The micro-analysis model is a surface sub-domain of  $1000 \times 1000 \times 300$  m; this depth is needed in order to make the multi-scale analysis results coincide with those of the direct analysis. As mentioned, we seek to ensure the accuracy of numerical computation

up to 2 Hz. Since a FEM is applied to numerically solve Eqs. (2) and (3) for the multi-scale analysis, an ordinary criterion that the description of one wavelength requires 15 elements is used. Thus, the macro-analysis uses elements of 40 m and 20 m for the bedrock and the basement layers, respectively. The micro-analysis uses elements of 0.5 ~ 20 m.

Newmark  $\beta$  method ( $\delta = 1/2$ ,  $\beta = 1/4$ ) is applied for time integration of solving Eqs. (2) and (3) for the multi-scale analysis or Eq. (1) for the direct analysis. Simple explicit time integrations cannot be used since Courant's condition of the present example is too severe; fine meshes are used around the main tunnel and the impedance contrast between the tunnel and the basement is high. For instance, the direct analysis solves

$$([K] + \frac{2}{\delta t}[C] + \frac{4}{\delta t^2}[M])[u_{n+1}] = (\frac{2}{\delta t}[C] + \frac{4}{\delta t^2}[M])[u_n] + ([C] + \frac{4}{\delta t}[M])[v_n] + [M][a_n]. \quad (4)$$

Here,  $[v]$  and  $[a]$  are velocity and acceleration vectors, suffix indicates the time increment number, and  $\delta t$  is the time increment. Note that this discretized equation is rewritten as

$$[M](2[a^{ap}] - [a_n]) + [C]([v_n] + [a^{ap}]\delta t) + [K][u_{n+1}] = [0],$$

where  $[a^{ap}] = 2(([u_{n+1}] - [u_n])/\delta t - [v_n])/\delta t$ ; the vectors for  $[M]$  and  $[C]$  correspond to  $[\ddot{u}]$  and  $[\dot{u}]$ , respectively, measured at  $t = n\delta t$ .

We use the Rayleigh damping matrix,  $[C] = a[K] + b[M]$ . The parameters  $a$  and  $b$  are determined so that the material damping characteristics is reproduced. The values of  $a$  and  $b$  used in the numerical computation as well as the damping constant are presented in Table 1; these values are determined by minimum error fitting to the damping constant.

Now, we present the results of the 3D simulation. First, we study the 3D simulation of strong ground motion. The distribution of the maximum norm for surface displacement is plotted in Fig. 5; a) is for the direct analysis (or  $[u]$ ), which is regarded to provide a numerically exact solution, and b) and c) are for the macro-analysis and the multi-scale analyses (or  $[u^{(0)}]$  and  $[u_s]$ , respectively). The direct analysis shows larger amplification of strong ground motion in the soil deposit. This amplification is fully neglected in  $[u^{(0)}]$ , but  $[u^{(1)}]$  succeeds to correct  $[u^{(0)}]$  and the distribution of  $[u_s]$  is quite similar to  $[u]$ ; see Figs. 5-a) and 5-c).

In order to study the detail of the synthesized strong ground motion, we choose 12 observation points on the top surface and compare the waveform; these points, denoted by a-m, are set at equal intervals and cross the soft soil deposit, as shown in Fig. 6-a). A displacement component parallel to the input Ricker wave is analyzed. For the response displacement waveform and Fourier amplitude spectrum of these 12 points, the comparison of the macro-analysis and the multi-scale analysis with the direct analysis is presented in Figs. 7 and 8, respectively; solid lines are for the direct analysis and dotted lines are for the macro-analysis and the multi-scale analysis. Like Fig. 5-a), the direct analysis shows larger amplification of strong ground motion in the soil deposit (points j-c), and the multi-scale analysis succeeds to produce waveform and Fourier spectrum obtained from the direct analysis for all 12 points. It is transparent that  $[u^{(1)}]$  corrects the geological length-scale solution  $[u^{(0)}]$ . As mentioned, this  $[u^{(0)}]$  is regarded as the boundary conditions for the sub-domain to obtain  $[u_s]$ . The thickness of the sub-domain is 300 m. Thus, it is remarkable that this thickness is needed to use the geological length-scale solution as artificial boundary conditions at the bottom surface of the sub-domain.

Next, we study the 3D simulation of the seismic structure response. The target structure is the vertical shaft which runs in the basement and the soft soil deposit. Fig. 9 shows the maximum deformation of the shaft, together with a contour map of the displacement norm; a) and b) are for the direct analysis ( $[u]$ ) and the multi-scale analysis ( $[u_S]$ ). As is seen, an upper part of the shaft has larger deformation, which is caused by the soil-structure interaction effect. The multi-scale analysis is able to produce this deformation concentration. This is not surprising since the waves synthesized by the multi-scale analysis are in almost perfect agreement with those synthesized by the direct analysis, as shown in Fig. 8. In Fig. 10, the mode of deformation at the primary natural frequency of the structure (0.98 Hz) is plotted, together with a contour map of the frequency component norm. The result of the multi-scale analysis agrees with that of the direct analysis.

We choose 12 observation points, n–z, at an equal interval along a vertical line on the surface of the shaft, to examine the waveform of the structure response; see Fig. 6-b) for the location of the observation points. The points n–p are located in the soft soil deposit. Like Fig. 8, we compare the response wave profiles and Fourier spectra computed by the 3D simulation of the direct analysis and the multi-scale analysis. The results are shown in Fig. 11. While the structure response is drastically amplified near the surface, the multi-scale analysis succeeds to compute the structure response obtained by the direct analysis.

For the present example problem, it is clearly shown that the multi-scale analysis is able to make a full 3D simulation of strong ground motion and seismic response, as accurately as the direct analysis. The multi-scale analysis requires much smaller computational environment since Eqs. (2) and (3) are for a vector of smaller dimension. We should mention that the computation cost of solving Eq. (4) by a conjugate gradient method is  $O(N \log N)$  where  $N$  is the vector dimension. Thus, reducing the vector size is essential to increase the numerical efficiency. Similar efficiency is expected even for the case when non-linear materials are used for structures.

As mentioned, the sub-domain used for the micro-analysis is deeper than usual; the clearance of the main tunnel to the bottom model surface is more than 100 m. This implies that the strong ground motion of the engineering length-scale does not vanish at the depth of 100 m for the present example. Thus, the use of the geological length-scale solution produces non-negligible errors, when the clearance is smaller. While further investigation is surely needed, we need to clarify the requirement for the strong ground motion input to a shallow underground structure model.

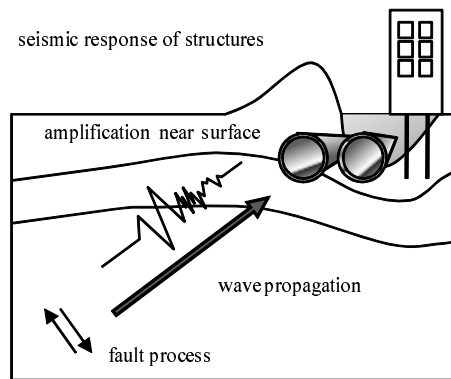
## 4. Conclusion

In this article, we present the multi-scale analysis for the 3D simulation of strong ground motion and seismic response. While the present analysis solves two problems, the required computational cost is much reduced. The comparison with the direct analysis shows that the accuracy of the multi-scale analysis is satisfactory.

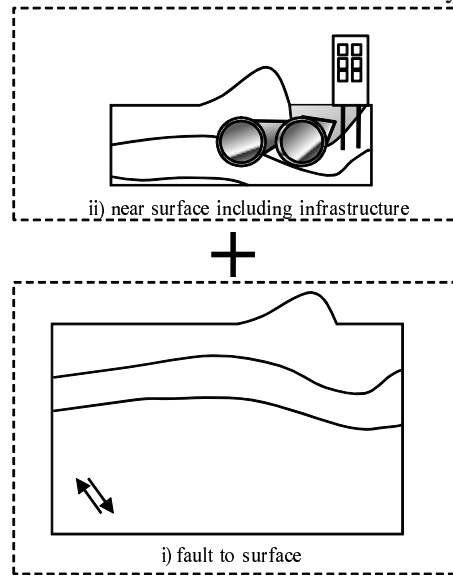
In closing this article, we should mention that the determination of the effective matrices ( $[\bar{K}]$ ,  $[\bar{C}]$  or  $[\bar{M}]$ ) is essential in order to determine a solution in the geological length-scale ( $[u^{(0)}]$ ). A well-established mathematical theory and advanced averaging schemes have been proposed; see [8, 12, 13].

**Table 1. Material properties.**

	primary wave (m/sec)	secondary wave (m/sec)	unit weight (tf/m <sup>3</sup> )	damping constant $h$	damping coefficient $a$	damping coefficient $b$
soil	300	100	1.7	0.15	0.3642	0.029
basement	1260	600	1.8	0.04	0.0971	0.008
bedrock	2950	1700	2.0	0.005	0.0121	0.001
RC	3373	2127	2.5	0.005	0.0121	0.001

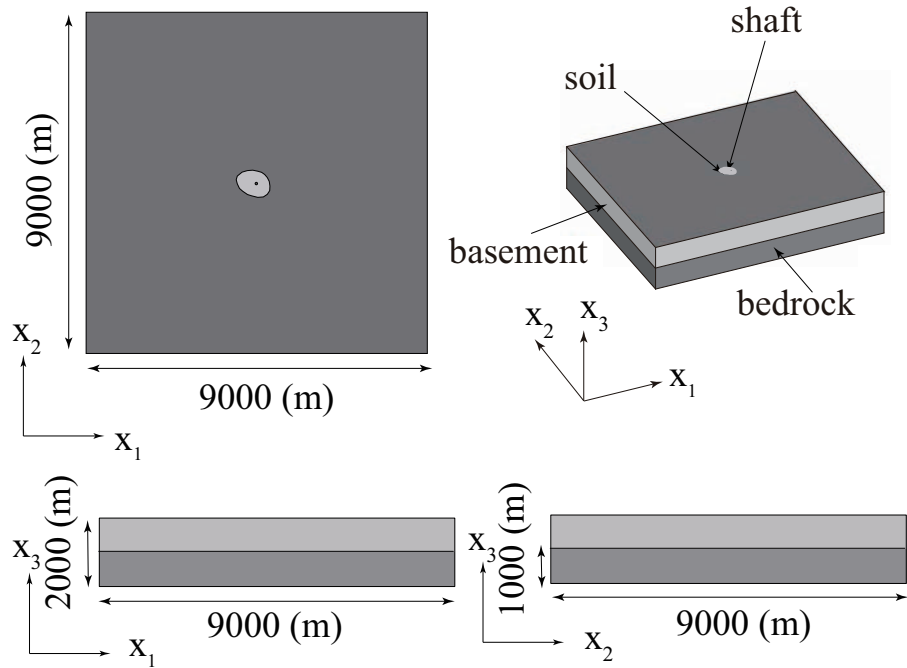


a) fault-infrastructure model for direct analysis

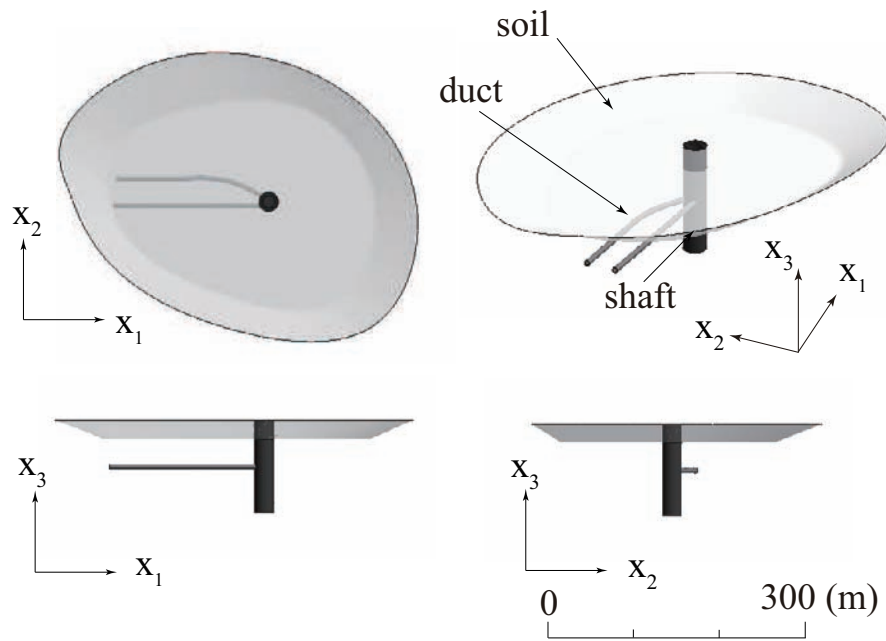


b) decomposed problems for multi-scale analysis

Figure 1. Schematic view of direct analysis and multi-scale analysis.



a) whole model



b) shaft model and soil layer model

Figure 2. Target problem.

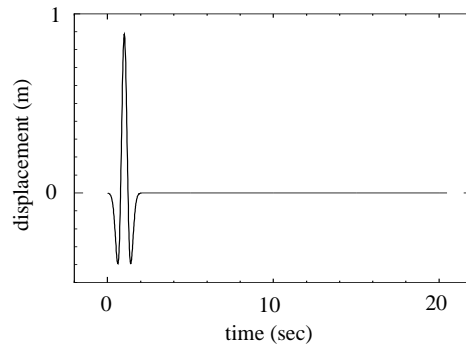


Figure 3. Waveform of input Ricker wave.

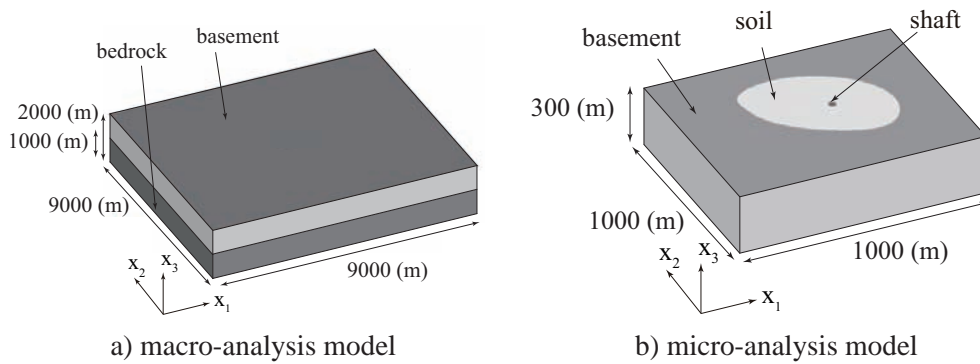


Figure 4. 3D models for multi-scale analysis; a) is a 3D model from fault to surface for macro-analysis, and b) is a 3D model around target infrastructure for micro-analysis.

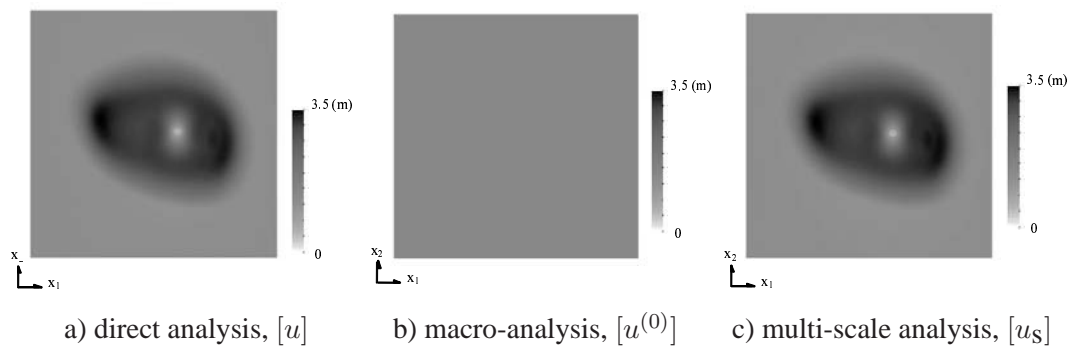


Figure 5. Distribution of maximum displacement norm on top surface.

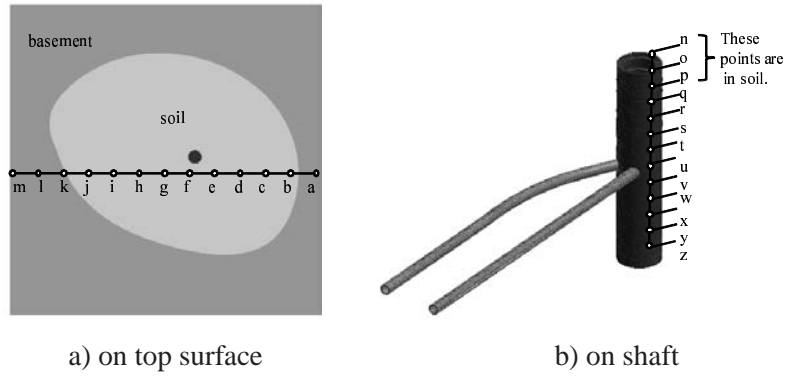


Figure 6. Locations of observation points.

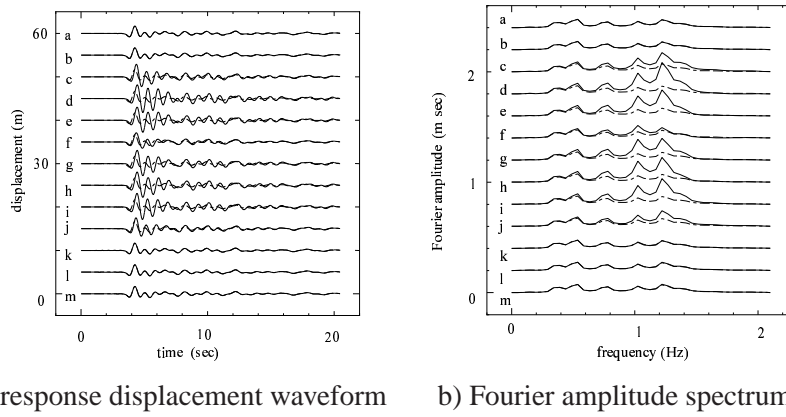


Figure 7. Comparison of wave component in the  $x_2$  direction at points a–m shown in Fig. 6-a); macro-analysis,  $[u^{(0)}]$ , (dotted) and direct analysis,  $[u]$ , (solid).

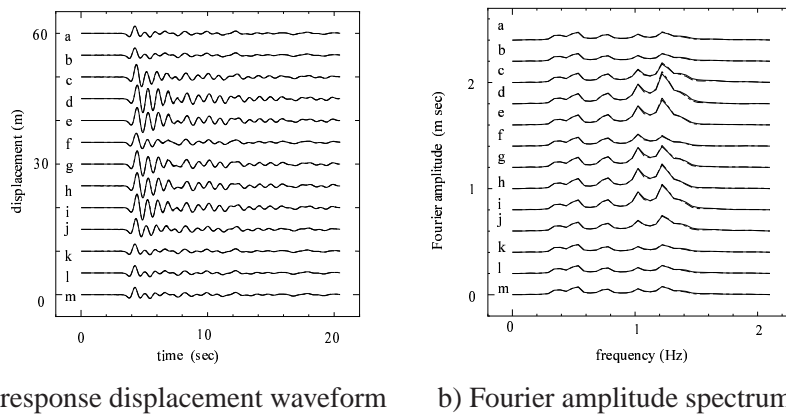


Figure 8. Comparison of wave component in the  $x_2$  direction at point a–m shown in Fig. 6-a): multi-scale analysis,  $[u_S]$ , (dotted) and direct analysis,  $[u]$ , (solid).

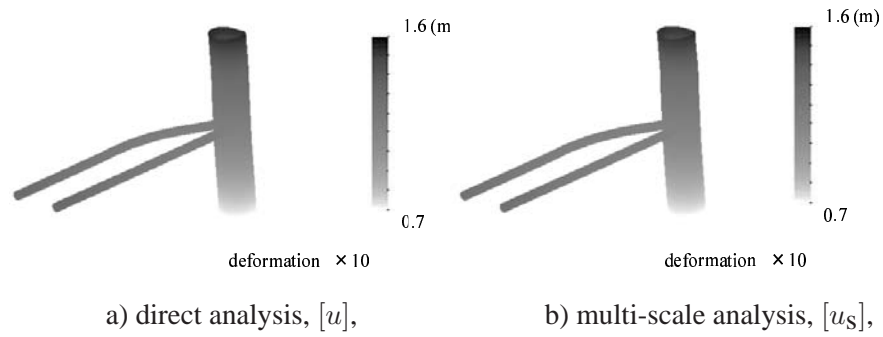


Figure 9. Distribution of maximum displacement norm with deformation on shaft.

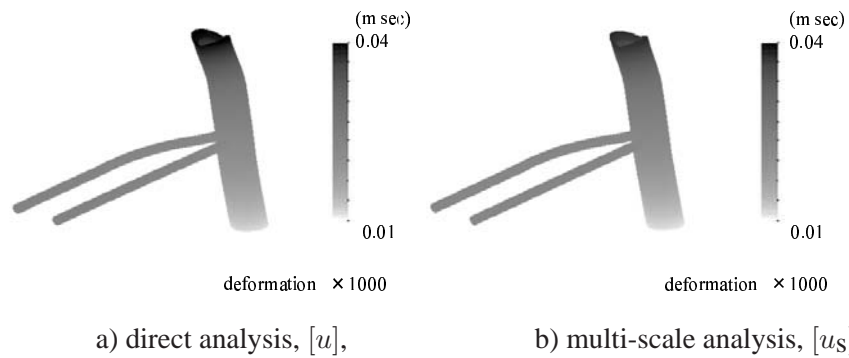
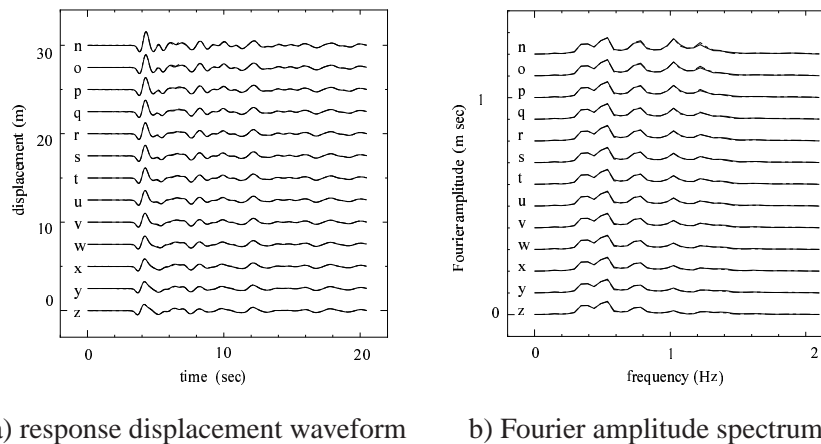


Figure 10. Distribution of frequency component norm on shaft on 0.98 Hz.

Figure 11. Comparison of structure response in the  $x_2$  direction at points n-z shown in Fig. 6-b); multi-scale analysis,  $[u_S]$ , (dotted) and direct analysis,  $[u]$ , (solid).

## Acknowledgement

The authors would like to express appreciation to Mr. Yohei Yamaki for his helpful support.

## References

- [1] Irikura K, Miyake H, Iwata T, Kamae K, Kawabe H, Dalguer LA. Recipe for predicting strong ground motion from future large earthquake. *Proc. of the 13th World Conference on Earthquake Engineering* 2004; 1371.
- [2] Koketsu K, Fujiwara H, Ikegami Y. Finite-element simulation of seismic ground motion with a voxel mesh. *Pure Appl. Geophys.* 2004; 161: 2463-2478.
- [3] Komatitsch D, Liu Q, Tromp J, Suss P, Stidham C, Shaw JH. Simulations of ground motion in the Los Angeles Basin based upon the spectral element method. *Bulletin of the Seismological Society of America* 2004; 94: 187-206.
- [4] Bielak J, Ghattas O, Kim EJ. Parallel octree-based finite element method for large-scale earthquake ground motion simulation. *Computer Modeling in Engineering and Sciences* 2005; 10: 99-112.
- [5] Furumura T. Large-scale parallel simulation of seismic wave propagation and strong ground motions for the past and future earthquakes in Japan. *Journal of the Earth Simulator* 2005; 3: 29-38.
- [6] Kaeser M, Dumbser M. An arbitrary high-order discontinuous Galerkin method for elastic waves on unstructured meshes – I. The two-dimensional isotropic case with external source terms. *Geophys. J. Int.* 2006; 166: 855-877.
- [7] Ma S, Liu P. Modeling of the perfectly matched layer absorbing boundaries and intrinsic attenuation in explicit finite-element methods. *Bulletin of the Seismological Society of America* 2006; 96:1779-1794.
- [8] Ichimura T, Hori M, Kuwamoto H. Earthquake Motion Simulation with Multiscale Finite Element Analysis on Hybrid Grid. *Bulletin of the Seismological Society of America* 2007; 97: 1133-1143.
- [9] Ogino M, Shioya R, Kawai H, Yoshimura S. Seismic Response Analysis of Nuclear Pressure Vessel Model with ADVENTURE System on the Earth Simulator. *Journal of the Earth Simulator* 2005; 2: 41-54.
- [10] Elgamal A, Lu J, He L, Law K, Yang Z. Techniques for Simulation of Large-Scale Nonlinear Soil-Structure Systems. *International Workshop on Constitutive Modelling, Development, Implementation, Evaluation, and Application* 2007.
- [11] Dobashi H, Ochiai E, Ichimura T, Yamaki Y, Hori M, Yamada T, Ohbo N, Moriguchi M. 3D FE Analysis for Seismic Response of Complicated Large-Scale Ramp Tunnel Structure. *ECCOMAS Thematic Conference on Computational Methods in Structural Dynamics and Earthquake Engineering* 2007.

- 
- [12] Ichimura T, Hori M. Macro-Micro Analysis Method for Wave Propagation in Stochastic Media. *Earthquake Engineering & Structural Dynamics* 2006; 35: 419-432.
- [13] Ichimura T, Hori M. Strong Ground Motion Prediction using Macro-Micro Analysis Method, *Earthquake Engineering & Structural Dynamics* 2006, 35: 395-417.



*Chapter 2*

**PREDICTION OF THE SEISMIC DISPLACEMENT  
OF LANDSLIDES AND GRAVITY WALLS  
USING A MULTI-BLOCK MODEL**

*Constantine A. Stamatopoulos*

Athens, Greece

**Abstract**

Newmark's sliding-block model is usually employed to predict the seismic displacement of slopes. Yet, when displacement is large, the conventional sliding-block model predicts displacements that are larger than expected for the given input motion and soil strength. Alternatively, to simulate slope movement when the displacement is large, a multi-block sliding model has been proposed. Similarly to the Sarma (1979) stability method, a general mass sliding on a slip surface that consists of  $n$  linear segments is considered. In order for the mass to move, interfaces where resisting forces are exerted must be formed between nodes of the slip surface. Thus, the mass is divided into  $n$  blocks sliding in  $n$  different inclinations. For landslides, the masses and lengths of each block entering the calculation are updated in terms of the distance moved. In addition, constitutive equations that simulate strength degradation along the slip surface coupled with the multi-block model are proposed in order to simulate the triggering of the slides. On the other hand, gravity walls, as a result of the applied shaking, move outwards, away from the retained soil. Simplified analyses predicting the seismic displacement of gravity walls are based on the Mononobe-Okabe method combined with Newmark's sliding-block model. The wall-backfill system is modeled, according to the multi-block methodology, using two bodies: (a) the wall that slides outward along the wall-foundation soil and (b) the wedge that slides along the plane of least resistance in the retained soil. The new method, unlike the previous, is kinematically compatible and generally predicts different seismic wall displacement for the given input motion and soil strength. The chapter first describes the multi-block model and its extensions for the prediction of the seismic displacement of landslides and gravity walls outlined above. Then, it validates the above methodologies by predicting the response of a well-documented earthquake-induced landslide and of a gravity walls (a) measured in shaking-table tests and (b) computed by elaborate numerical analyses.

## 1. Introduction

Newmark's sliding-block model (Newmark, 1965), shown in Fig. 1, is usually employed to predict the seismic displacement of slopes (Kramer, 1996, Modaressi et al., 1995, Stark and Contreras, 1998). Newmark's model consists of a block on an inclined plane. Critical acceleration factor,  $k_{c-sl}$ , is the minimum factor that when multiplied by the acceleration of gravity,  $g$ , gives the horizontal acceleration which is just sufficient to cause movement of the block. Every time during the earthquake that the applied horizontal acceleration is larger than the critical acceleration ( $k_{c-sl} g$ ), the block slides downwards. The total displacement of the block is equal to the sum of these partial displacements that are caused by the momentary slides. The seismic displacement of slopes is estimated using the sliding-block model with similar critical and applied seismic acceleration.

When the displacement of slopes is large, the conventional sliding-block model has shortcomings. It predicts displacements that are larger than expected for similar input motion and soil strength (Stamatopoulos, 1996). The reason is that it does not model the change of geometry of the sliding mass with displacement towards a gentler configuration. In addition, ordinary computer codes based on the Finite Element Method cannot be applied when displacement is very large. To overcome the problem, mesh-free techniques have been proposed (Foester and Modaressi, 2001). Yet, such approaches are still in a developing stage.

Alternatively, to simulate slope movement when the displacement is large, a multi-block sliding model has been proposed (Stamatopoulos, 1992, Ambraseys and Srbulov, 1995, Stamatopoulos et al. 2000, Sarma and Chlimintzas, 2001a, b). Similarly to the Sarma (1979) stability method (Fig. 2), a general mass sliding on a slip surface that consists of  $n$  linear segments is considered. In order for the mass to move, at the nodes of the slip surface, interfaces where resisting forces are exerted must be formed (Fig. 2). Thus, the mass is divided into  $n$  blocks sliding in  $n$  different inclinations. At the interface between two consecutive blocks, the velocity must be continuous. This principle gives that the relative displacement of the  $n$  blocks is related to each other and the governing equation of motion is reduced to have only one displacement as variable. For large displacement, the masses and lengths of each block are updated during calculation in terms of the distance moved. Furthermore, constitutive equations that simulate strength degradation along the slip surface coupled with the multi-block model are needed in order to simulate the triggering of the slides. A constitutive model that predicts the continuous change of resistance along the slip surface due to build-up of pore pressures has been developed and implemented in the multi-block model.

On the other hand, gravity walls (Fig. 3a), as a result of the applied shaking, move outwards, away from the retained soil. Simplified analyses predicting the seismic displacement of gravity walls are based on the Mononobe-Okabe method combined with Newmark's sliding-block model. The Mononobe-Okabe (MO) method (Mononobe and Matsuo, 1924, Okabe, 1926) estimates the lateral force,  $P_{a-MO}$ , on gravity walls retaining dry soil by using frictional resistance and inertia forces. The force  $P_{a-MO}$  acts on the wall from the wedge of the soil behind the wall with inclination that corresponds to the maximum pressure applied on the wall. Richards and Elms (RE, 1979) estimate the force acting on the wall by the retained soil by the MO method, as a function of the seismic acceleration applied on the retained soil. The critical horizontal acceleration factor for relative motion of the wall-backfill

system, denoted as  $\{k_{c-RE}\}$ , is estimated by considering the equilibrium of forces acting on the wall. As in the condition of limiting equilibrium the seismic acceleration acting on the retained soil equals (by definition) the critical acceleration,  $k_{c-RE}$  must be obtained by iteration (Iai, 2001). The seismic displacement of the wall is estimated using the critical acceleration factor  $k_{c-RE}$ , and the applied acceleration history using Newmark's sliding block.

Consistently with the RE method mentioned above, the wall-backfill system is modeled, according to the multi-block methodology, using two bodies (Fig. 3b): (a) the wall that slides outward along the wall-foundation soil and (b) the wedge that slides downward along the plane of least resistance in the retained soil. In typical walls, the resistance on the wall-backfill interface is less than on any other internal sub-planes in the retained soil. It is inferred that, according to the law of limit equilibrium, the internal slip sub-plane between the two bodies should remain in the wall-backfill interface. This implies that the first body of the two-body system is always the wall, while the second body, that is part of the soil behind the wall, changes its shape with displacement.

The new method, unlike the previous, is kinematically compatible. It generally produces an interface force between the wall and the retained soil which is different from the Mononobe-Okabe force. Yet, just prior to relative movement, the two methods predict similar interface forces. The reason is that the MO solution was obtained using the equilibrium of only the critical wedge in the retained soil, while the new method considers the equilibrium of a two-body system that includes both the wall and the critical soil wedge. Only just prior to relative movement, the dynamic effects of the wall do not affect the solution. As a consequence, the new method predicts similar critical acceleration, but different seismic wall displacement than the RE approach.

The chapter first describes the multi-block model and its extensions for the prediction of the seismic displacement of landslides and gravity walls outlined above. Then, it validates the above methodologies by predicting the response of a well-documented earthquake-induced landslide and of gravity walls (a) measured in shaking-table tests and (b) computed by elaborate numerical analyses.

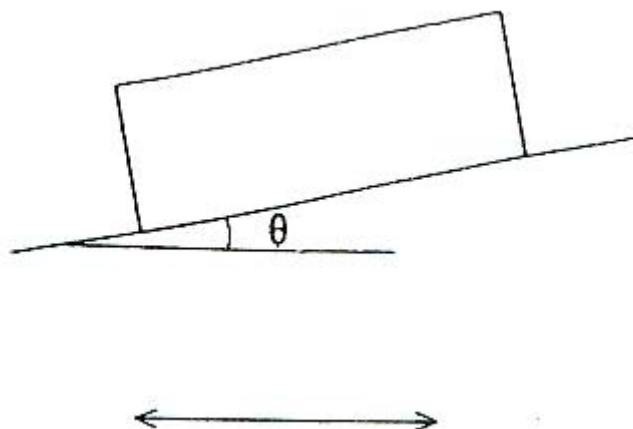


Figure 1. Newmark's sliding-block model.

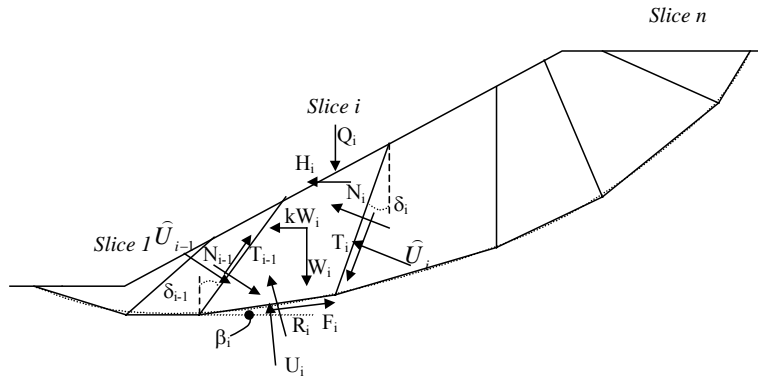


Figure 2. The multi-block stability method proposed by Sarma (1979).

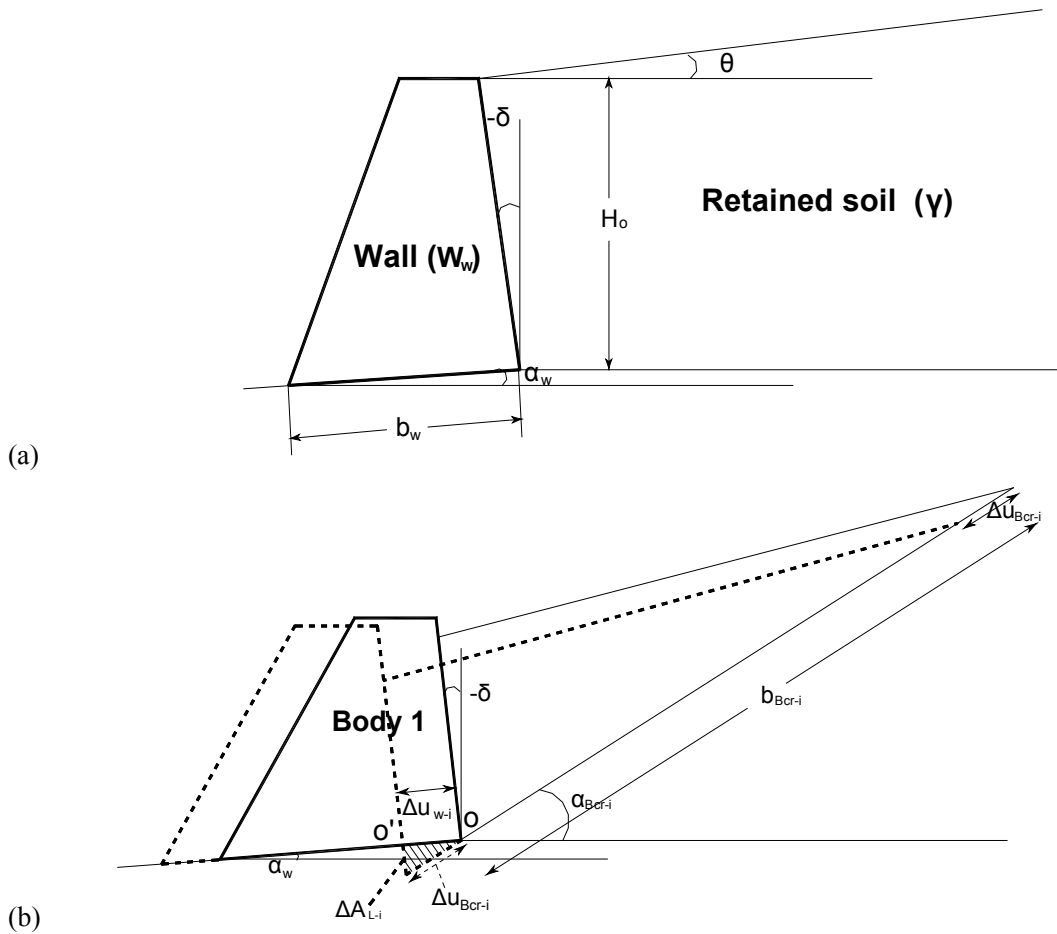


Figure 3. (a). Gravity wall and retained soil geometry considered in the present study. (b). The modeling of gravity walls using 2 blocks. The deformation of the wall-backfill system with displacement at increment "i". The solid and dotted lines give the initial and final configurations of the increment respectively. The increment  $\Delta u_{w-i}$  is shown large for clarity. Points O and O' are the points where the slip sub-planes in the backfill start of increments "i" and "i+1" respectively.

## 2. The Multi-block Model

Similarly to the Sarma (1979) stability method, shown in Fig. 2, a general mass sliding on a slip surface that consists of  $n$  linear segments is considered. In order for the mass to move, interfaces where resisting forces are exerted must be formed between the nodes of the slip surface (Fig. 2). Thus, the mass is divided into  $n$  blocks sliding in different inclinations. At the interface between two consecutive blocks, the velocity must be continuous. This principle gives that the relative displacement of the  $n$  blocks is related to each other as:

$$u_i/u_{i+1} = du_i/du_{i+1} = \cos(\delta_i + \beta_{i+1}) / \cos(\delta_i + \beta_i) \quad (1)$$

where  $u$  is the displacement moved along a segment of the slip surface, the subscripts  $i$  and  $i+1$  refer to blocks  $i$  and  $i+1$  counting uphill,  $d$  refers to increment and  $\beta_i$  and  $(90 - \delta_i)$  are the inclinations of the segment and interface  $i$  respectively, shown in Fig. 2.

The forces that are exerted in block "i" are given in Fig. 2. Soil is assumed to behave as a Mohr-Coulomb material. As the body moves, the Mohr Coulomb failure criterion applies at both the slip surface and the interfaces. The equation of motion of block (i) along the direction of motion, when a horizontal component of acceleration  $a(t)$ , is applied, is :

$$\begin{aligned} m_i ( d^2 u_n / dt^2 ) q_i \cos \varphi_i = & -U_i l_i \sin \varphi_i + (m_i g Q_i) v_i - (m_i a(t) + H_i) x_i + c_i l_i \cos \varphi_i \\ & + (1 / \cos \varphi_{i-1}) N_{i-1} d_i - (1 / \cos \varphi_i) N_i f_i \\ & + s a_i (c_{i-1} b_{i-1} - \tan \varphi_{i-1} U_{i-1} b_{i-1}) - s b_i (c_i b_i - \tan \varphi_i U_i b_i) \end{aligned} \quad (2)$$

where

$$\begin{aligned} v_i &= \sin(\varphi_i - \beta_i), & x_i &= \cos(\varphi_i - \beta_i), \\ d_i &= \cos(\delta_{i-1} + \beta_i - \varphi_i - \varphi_{i-1}), & f_i &= \cos(\delta_{i-1} + \beta_i - \varphi_i - \varphi_{i-1}), \\ s a_i &= \sin(\delta_{i-1} + \beta_i - \varphi_i), & s b_i &= \sin(\delta_i + \beta_i - \varphi_i), \\ q_i &= \prod_{j=i}^{n-1} [ \cos(\delta_j + \beta_{j+1}) / \cos(\delta_j + \beta_j) ] \end{aligned}$$

and  $m_i$  is the mass of block  $i$ ,  $\varphi_i$ ,  $c_i$ ,  $\varphi_{i-1}$ ,  $c_{i-1}$  are the frictional and cohesive components of resistance at the  $i$  slip segment and interface respectively,  $l_i$  and  $d_i$  are the lengths of the  $i$  slip segment and interface respectively,  $U_i$ ,  $U_{i-1}$  are the pore pressures at the  $i$  slip segment and interface respectively and  $Q_i$  and  $H_i$  are the vertical and horizontal external loads of block  $i$  respectively. To eliminate the interslice forces,  $N_i$ , the (i) equation is multiplied by a factor. Summing all equations and expressing displacement of all blocks in terms of the displacement of the upper block,  $u_n$ , the equation of motion is obtained. It is a single second-order differential equation in terms of time. As it is very long, it is not presented here. It is given by Sarma and Chlimitzas (2001 a and b). When a horizontal component of acceleration  $a(t)$  is applied, it has the general form

$$du_n^2/dt^2 = A (a(t) - a_c) \text{ for } du_n/dt > 0 \quad (3)$$

where  $A$  is a factor and  $a_c$  is the critical acceleration, defined as the horizontal acceleration which is just sufficient to start movement of the mass. The factors  $A$  and  $a_c$  depend of the geometry, the pore pressure and the strength of the  $n$  blocks of the sliding mass. The factor  $a_c$  is positive and negative when the sliding mass is stable and unstable respectively. According to the principle of limit equilibrium, the inclinations of the interfaces  $\delta_i$  correspond to the inclinations that produce failure at a minimum value of  $a_c$ .

### 3. Extension of the Multi-block Model to Predict the Response of Landslides

#### Sliding System Model for Large Displacement

When slide displacement is large, to solve accurately equation (3), the masses and lengths of each block  $i$  are updated during calculations in terms of the distance moved. The location of the interfaces does not change. The transformation rule, that states that when each block is displaced by  $d\bar{u}_i$ , each point of the block including the ground surface at the top of the block is also displaced by  $d\bar{u}_i$ , is applied. Incremental application is needed because a point may move from one block to the previous, and thus its incremental displacement for given  $d\bar{u}_n$  will change from  $d\bar{u}_i$  to  $d\bar{u}_{i-1}$ . The deformation that this rule predicts in a two-block system is illustrated in Fig. 4a.

Separation of blocks occurs when an interslice force,  $N_i$ , is negative. Fig. 4b illustrates a typical case where this occurs: when the angle  $\beta_{m,1}$  representing the initial inclination of the first block of the system, is less than the angle  $\beta_{m,0}$  representing the slope of the free ground surface immediately preceding the first block. In this case, the increased soil mass of the first block cannot maintain contact with the rest of the material and is detached from the system. For frictional materials, the angle of the internal sub-plane at the node of separation can be obtained from the resistance of the material inside block  $i$ ,  $\phi_{in_i}$ , according to what stability predicts as:

$$\delta_{i-separ} = 90^\circ - \phi_{in_i} \quad (4)$$

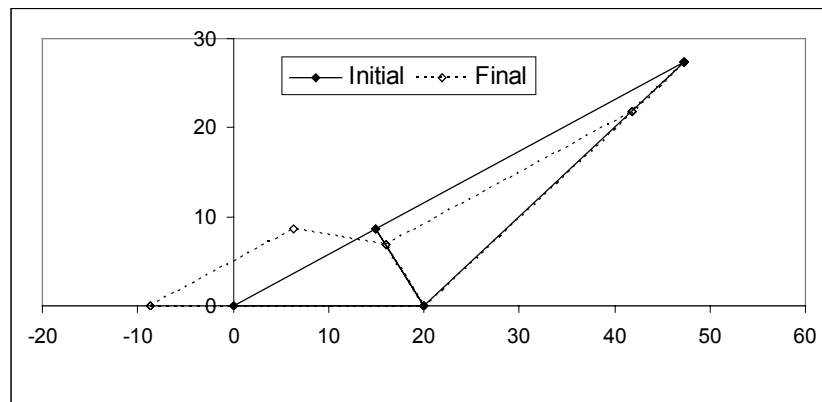
In addition, earthquake-induced slides usually occur due to generation of large excess pore pressures (Sassa et al., 1996, Stark and Contreras, 1998). With constant strength, the multi-block model can be applied in back analyses of slides to approximately estimate the residual soil strength (Stamatopoulos et al., 2000). Yet, constitutive equations that simulate strength degradation along the slip surface coupled with the multi-block model are needed in order to simulate the triggering of the slides and predict accurately the seismic displacement. Such models should predict the continuous change of resistance along the slip surface from its initial value to the peak strength and then at the large displacement residual value.

Constitutive models of various complexities simulating the response of localized discontinuities in saturated soils have been proposed and are used in both finite element codes and sliding-block models. In the context of numerical approaches using finite elements, if the interface is to represent strain at localized or failure zones in a soil medium, the constitutive model of the interface should be compatible and derived from the constitutive model of the

surrounding materials. Based on this concept, Aubry et al. (1990) and Modaressi et al. (1998) relate stresses to displacement along and normal to the slip surface. In association with the sliding-block model, Sarma (1975) proposed a simplified model predicting pore pressures build-up based on Skempton's A and B parameters. A more elaborate model predicting the continuous change of resistance along a slip surface has been developed by Modaressi H. et al. (1995). The model is based on the elasto-plastic model by Aubry et al. (1993), relates shear stress to shear displacement, and requires only five parameters. The model has not been calibrated with soil response measured along slip surfaces for different soils. Recently, Gerolymos and Gazetas (2007) have proposed a constitutive model for grain-crushing-induced pore-water pressures. The model extends Hardin's theory for crushing of soil particles and has 12 parameters.

The purpose of the sections below are (a) to propose and validate a constitutive model simulating the change of resistance along a slip surface due to generation of excess pore pressures, (b) to implement it at the multi-block sliding system model and (c) based on this improved model to propose a methodology predicting the triggering and the final displacement of earthquake-induced slides. The best testing device to simulate soil response along slip surfaces is the ring shear test. In this test, similarly to field conditions, relative displacement at the slip surface can be very large, larger than a few centimeters, or even meters. The first objective is to propose a general model that simulates the soil response due to pore pressures build-up in these tests with a small number of model parameters.

(a)



(b)

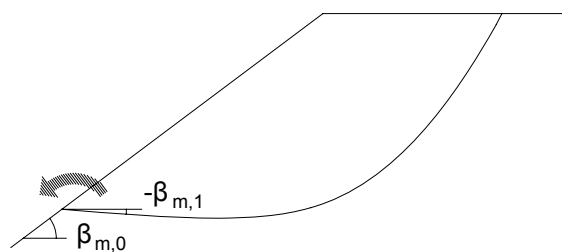


Figure 4. The case of landslides. (a) Deformation assumed in the multi-block model. A case of two blocks is given. (b) Typical case where separation of blocks occurs (Sarma and Chlimintzas, 2001).

## Constitutive Model Predicting the Response along Slip Surfaces due to Pore Pressure Build-Up

### Soil Response

Extensive ring shear testing of soils from (a) the 4th Avenue – Alasca slide (Stark and Contreras, 1998), (b) the Nikawa slide (Sassa et al., 1996) and (c) the Vaiont slide (Tika and Hutchinson, 1999) are reported in the bibliography. Table 1 gives the main classification characteristics of the soils of the three slides. Typical results of the ring shear tests are given in Figs 5 to 7. In the cases of the 4th Avenue – Alasca and Nikawa slides, both the shear stress and the excess pore pressure versus shear displacement relationships exist. In the case of the Vaiont slide only the shear stress versus shear displacement relationship exists. Table 1 presents the main characteristics of the shear stress-shear displacement relationships. In addition, the main characteristics of the shear stress-shear displacement relationship from ring shear tests on other soils together with the main classification characteristics of these soils are given in table form by Stark and Contreras (1998). They are presented in table 2.

All test results indicate that as shear displacement increases, the shear stress increases, reaches a peak and then progressively decreases towards a limit value. At large displacement, as displacement increases further, soil shear strength remains more-or-less constant. Accordingly, as shear displacement increases, the excess pore pressure increases at a steadily decreasing rate towards a limit value. An exception is only one test, where negative excess pore pressure is measured at the initial stages of loading of an overconsolidated sample from Nikawa slope.

Quantitatively, large differences in the values of the measured maximum ( $\tau_m$ ) and residual ( $\tau_r$ ) soil strengths are observed:  $\tau_m$  varies from 11 to 392kPa, while  $\tau_r$  from 7 to 98kPa. The corresponding ratios (a)  $\tau_m/\sigma'_o$  and (b)  $\tau_r/\sigma'_o$ , where  $\sigma'_o$  is the initial effective normal stress, vary (a) from 0.20 to 0.61 and (b) from 0.05 to 0.17, respectively. Also, the ratio  $\tau_m/\tau_r$  varies from 1.4 to 5.4. In addition, differences in the shear displacement at peak and residual strength are observed: At  $\tau_m$  shear displacement varies from 0.3mm to 10mm, while at  $\tau_r$  from 19mm to 24m.

Yet, results of tables 1 and 2 illustrate that for given soil layer and speed of shearing,  $\tau_r$  is more-or-less proportional to the vertical consolidation stress. Additional data illustrating this for the soil of the Vaiont slide is given in Fig. 7b by Tika and Hutchinson (1999). It is inferred that the total residual friction angle,  $\phi_r$ , is a parameter more-or-less-independent of the applied stress. It should be noted that  $\phi_r$  is related to the final generated excess pore pressure,  $P_f$ , as

$$\tan\phi_r = \tan\phi_{CS} ( 1 - P_f/\sigma'_o ) \quad (5)$$

where  $\phi_{CS}$  is the final effective friction angle. Equation (5) is relevant especially for sands, where, according to discussion above, a small  $\phi_r$  value may be a result of excess pore pressure generation due to grain crushing.

## Proposed Model

As discussed previously, ring shear tests illustrate that at large displacement, as displacement increases further, soil strength and excess pore pressure remain more-or-less constant. Consistently, a steady-state (or critical state) model is proposed. The steady-state is that measured in constant-volume ring shear tests, that may be different to that measured in triaxial tests.

The model uses the following equations

$$\tau = \sigma' r f \quad (6)$$

$$dP = -d\sigma' = du K (\tan\phi_{cs} - \tau/\sigma') \quad (7)$$

where

$$f = 1 - b \ln [ \tan\phi_{cs} \sigma' / (\sigma'_o \tan\phi_{res}) ] \quad (8)$$

$$r = \tan\phi_{cs} u / ( a + u ) \quad (9)$$

$$K = k_1 (\sigma'/Pa)^{k_2} \quad (10)$$

In the above equations  $\tau$  is the shear stress,  $\sigma'$  is the effective normal stress, compressive positive,  $\sigma'_o$  is the initial effective normal stress,  $P$  is the excess pore pressure,  $K$  is the elastic normal stiffness coefficient,  $u$  is the shear displacement along the slip surface,  $Pa$  is the atmospheric pressure (equals about 100kPa),  $\phi_{cs}$  is the final (critical-state) effective friction angle,  $\phi_{res}$  is the final (critical-state) total friction angle and  $a$ ,  $k_1$ ,  $k_2$ ,  $b$  are fitting parameters. Displacement is in m and stresses and pressures in kPa. Unloading is not modelled, as it is assumed that relative motion of slides is only downslope.

## Discussion of the Model and Its Parameters

The model is based on (a) the critical state theory that predicts that (i) as shear strain increases soil gradually reaches a steady-state and (ii) the response is affected by the distance from the critical state (The factor  $f$  gives the effect of the distance from the critical state), (b) the fact that plastic shear strain depends on the  $\tau/\sigma'$  ratio, (c) a Roscoe type dilation equation and (d) the proposition that the constitutive model of displacement and stress of an interface should be of the same form as the constitutive model of shear strain and shear stress of soils.

The model structure is similar with the previous model by Modaressi H. et al. (1995). It differs from this previous model in (a) the form of the factors  $f$  and  $K$  and (b) taking the dilation angle equal to  $\phi_{cs}$ . The form of the factor  $f$  in terms of  $\tan\phi_{res}$  is critical for the ability of the model to predict the measured response, because, as discussed above, for given soil deposit and speed of shearing, laboratory tests have shown that the residual soil strength is more-or-less proportional to the vertical consolidation stress. Taking  $K$  as  $[k_1 (\sigma'/Pa)^{k_2}]$  is consistent with the assumption often used in soil models (e.g. Papadimitriou et al, 2001) that the elastic moduli of soils may be affected by the confining stress. Taking the dilation angle equal to  $\phi_{cs}$  is consistent with sophisticated critical state models (e.g. Papadimitriou et al,

2001) for samples with final shear stress less than that at the critical state ( $\varphi_{\text{res}} < \varphi_{\text{cs}}$ ). This condition clearly exists in the cases considered in the present study.

The model has six parameters:  $\varphi_{\text{cs}}$ ,  $\varphi_{\text{res}}$ ,  $b$ ,  $a$ ,  $k_1$ ,  $k_2$ . These parameters can be estimated from constant-volume ring shear tests. In particular, the parameters  $\varphi_{\text{res}}$  and  $\varphi_{\text{cs}}$  can be estimated from the final (residual) shear stress and effective vertical stress: The parameter  $\varphi_{\text{res}}$  equals  $\arctan(\tau_r/\sigma'_o)$  where  $\tau_r$  is the residual shear stress and  $\sigma'_o$  is the initial effective normal stress. The angle  $\varphi_{\text{cs}}$  equals  $\arctan(\tau_r/\sigma'_r)$  where  $\sigma'_r$  is the final effective normal stress. The angle  $\varphi_{\text{cs}}$  for sands typically equals  $30^\circ$  and for clays  $26^\circ$  (Modaressi and Lopez-Caballero, 2001). The remaining parameters  $k_1$ ,  $k_2$ ,  $b$ ,  $a$  are fitting parameters. The parameter  $k_1$  affects primarily the displacement where the residual value of strength is reached. It decreases as the displacement where the residual strength is reached increases. The parameter  $k_2$  describes the effect of the confining stress on the displacement where the residual value of strength is reached. It can be obtained when for a given soil, ring shear tests with different confining stresses exist. The parameter  $b$  indicates the manner that the distance from the critical state affects the shear stress. The parameter  $a$  affects mainly the shape of the stress-displacement curve.

### **Calibration of the Model Parameters, Comparison between Measurements and Predictions and Discussion**

As in the multi-block model the shear stress - displacement relationship is of primary importance, the focus is the prediction of this relationship. Prediction of the excess pore pressure generation versus displacement validates the model assumptions. Model parameters were varied for each soil type, and not for each individual test.

First the ring shear tests of table 1, where the shear stress-shear displacement relationships are available, were considered. The obtained model parameters that better fit the shear stress - shear displacement curves are given in table 3. Fig. 8 gives typical predictions of tests from the soil from (a) the 4th Avenue – Alasca, (b) the Nikawa and (c) the Vaiont slides. Table 4 compares the measured with the predicted response. The ratio of predicted to measured values for shear stress at different shear displacements is between 0.7 and 1.5 in all cases. It is inferred that the accuracy of the predictions is satisfactory.

Regarding pore pressures, such data exist only for the soil from (a) the 4th Avenue – Alasca and (b) the Nikawa slides (cases 1.1 and 1.2 of table 1). Fig. 8 gives typical predictions of pore pressure response from these two slides. Table 4 compares the measured with the predicted response. The model qualitatively does not predict the dilation that occurs at the initial stages of test No1.2b and underpredicts or overpredicts the pore pressure that develops at the initial stages of tests No 1.1b, 1.1d, 1.1e, 1.2a. Beyond the initial stage, the ratio of predicted to measured values of pore pressure at different shear displacements of all samples is between 0.8 and 1.1. It is inferred that the accuracy of the predictions is reasonable.

Finally, the cases of table 2, where only the values of peak and residual shear stress with the corresponding displacements were found, were considered. As soils are fine-grained, according to the previous discussion, the friction angle  $\varphi_{\text{cs}}$  is assumed  $26^\circ$ . The model parameters obtained that better predict the measured response are given in table 3. Table 5 compares the measured with the predicted response. The ratio of predicted to measured values of the peak and residual shear stress is between 0.7 and 1.5 in all cases. The ratio of predicted

to measured values of the shear stress when the displacement takes the measured peak and residual shear stress is between 0.8 and 1.5. It is inferred that the accuracy of the predictions is satisfactory.

Table 3 indicates that for all cases the model parameter  $a$  equals  $10^{-4}$ , the parameter  $\phi_{cs}$  varies between  $26$  and  $31^\circ$ , the parameter  $\phi_{res}$  takes values between  $4$  and  $10^\circ$ , the parameter  $k_1$  takes values between  $4 \times 10^2$  and  $15 \times 10^4 \text{ kPa/m}$ , the parameter  $k_2$  equals to  $1$  except for two cases and the parameter  $b$  varies between  $0.01$  and  $0.24$ . Statistical analyses, shown in Fig. 9, indicate that as clay size fraction increases,  $\phi_{res}$  decreases,  $k_1$  increases and  $b$  increases. Yet, the coefficient of correlation of these relationships is small. Statistical analysis in terms of the Plasticity Index produces even smaller correlation.

The value of the model parameter  $a$  used ( $10^{-4}$ ) is within the range of the values  $10^{-5}$  to  $10^{-3}$  suggested by the previous similar model by Modaressi H et al. (1995). The typical value of  $k_1$  given for clays in the previous model by Modaressi H et al. (1995) of  $61(10^4) \text{ kPa} \cdot \text{m}$  is somewhat larger than the range of values of the present model. According to Modaressi and Lopez-Caballero (2001) under conventional triaxial loading the parameter  $b$  typically equals  $0.1$  for sands and  $1$  for clays. Consistently, the obtained values of the parameter  $b$  increase with fines content. The obtained values are smaller than those proposed by Modaressi and Lopez-Caballero (2001). The difference can be attributed to the fact that soil response of the current model is of a lower value of residual strength mobilized in ring-shear tests as compared to triaxial tests. For example, in clays in triaxial tests  $\tau_r/\sigma'_o$  typically equals  $0.2$  (Modaressi and Lopez-Caballero, 2001), while as previously discussed, in ring-shear tests it can be as low as  $0.07$ .

Concluding, the proposed model simulates the excess pore pressure generation and subsequently the small value of residual shear strength measured in constant-volume ring shear tests. In particular, it simulates well the shear stress - displacement curves and the middle and final stages of the pore pressure - displacements curves of ring shear tests. From the six parameters of the proposed model, the parameter  $a$  does not change, the parameter  $\phi_{cs}$  can be approximately obtained according to the sand/clay differentiation and the parameter  $k_2$  equals  $1$  for most cases. It is inferred that in the proposed model the parameters that vary considerably are only three:  $\phi_{res}$ ,  $k_1$  and  $b$ . The constitutive model does not simulate the effect of strain rate on the residual soil strength that has been measured in ring shear tests (e.g. Tika and Hutchinson, 1999). Thus, when estimating the residual soil strength, the laboratory tests should have similar strain rate to that at the field during the landslides.

**Table 1. Summary of constant volume ring shear tests found in the bibliography (Sassa et al., 1996, Stark and Contreras, 1998, Tika and Hutchinson, 1999) where much data is available, and partial results.**

No	Soil deposit	Liquid limit (%)	Plastic limit (%)	Clay size fraction (% < 0.002m)	$\sigma'_o$ (kPa)	$\tau_m/\sigma'_o$	u at $\tau_m$ (mm)	$\tau_r/\sigma'_o$	u at $\tau_r$ (mm)
1.1a	4th Avenue – Alasca	40	20	59	100	0.28	1.2	0.07	55
1.1b	"	34	19	57	230	0.28	1.1	0.07	75
1.1c	"	36	21	56	300	0.24	1.3	0.06	75
1.1d	"	38	21	55	400	0.23	1.8	0.06	120
1.1e	"	39	20	62	500	0.23	1.8	0.06	130

**Table 1. Continued**

No	Soil deposit	Liquid limit (%)	Plastic limit (%)	Clay size fraction (% < 0.002m)	$\sigma'_o$ (kPa)	$\tau_m/\sigma'_o$	u at $\tau_m$ (mm)	$\tau_r/\sigma'_o$	u at $\tau_r$ (mm)
1.2a	Nikawa - (OCR=1)	-	-	0	300	0.47	4.0	0.17	24300
1.2b	Nikawa - (OCR=1.9)	-	-	0	230	0.61	1.0	0.15	28400
1.3a	Vaiont - sample 4 - slow	49	30	20	500	0.48	5	0.22	600
1.3b	Vaiont - sample 3 - slow	50	28	20	500	0.47	5	0.20	600
1.4a	Vaiont - sample 4 - fast	49	30	20	505	0.42	5	0.15	600
<b>1.4b</b>	Vaiont - sample 4 - fast	49	30	20	980	0.38	5	0.10	600
<b>1.4c</b>	Vaiont - sample 3 - fast	50	28	20	505	0.43	10	0.15	700
<b>1.4d</b>	Vaiont - sample 3 - fast	50	28	20	980	0.40	5	0.10	900

slow= speed 0.0145 mm/s

fast= speed 2600 mm/s

**Table 2. Summary of other constant volume ring shear tests and partial results (Stark and Contreras, 1998).**

No	Soil deposit and location	Liquid limit (%)	Plastic limit (%)	Clay size fraction (% < 0.002m)	Vertical consolidation stress $\sigma'_o$ (kPa)	$\tau_m/\sigma'_o$	Shear displ. at $\tau_m$ (mm)	Undrained residual strength ratio $\tau_r/\sigma'_{v-o}$	Shear displ. at $\tau_r$ (mm)
2.1a	Drammen clay,	47	23	70	95	0.27	1.1	0.09	19
2.1b	Danvik-gate,	48	24	72	255	0.22	1.3	0.11	16
2.1c	Drammen, Norway	47	25	65	400	0.20	1.1	0.11	60
2.2a	Bootlegger Cove clay,	42	23	47	150	0.31	1.5	0.11	95
2.2b	outside Fourth Ave.	40	21	42	225	0.32	1.6	0.10	110
2.2c	landslide, Anchorage,	42	23	49	400	0.31	1.7	0.11	125
2.2d	Alaska	41	22	45	500	0.30	1.7	0.11	140
2.3a	Cohesive alluvium,	30	22	19	95.8	0.19	2.2	0.10	52
2.3b	Enid Dam,	28	22	20	147	0.27	1.1	0.05	77
2.3c	Enid, Mississippi	23	19	17	191	0.24	1.1	0.07	70
2.3d		25	22	20	287	0.23	1.2	0.07	72
2.3e		30	22	20	383	0.23	1.2	0.06	75

Table 2. Continued

No	Soil deposit and location	Liquid limit (%)	Plastic limit (%)	Clay size fraction (% < 0.002m)	Vertical consolidation stress $\sigma'_{v0}$ (kPa)	$\tau_m/\sigma'_{v0}$	Shear displ. at $\tau_m$ (mm)	Undrained residual strength ratio $\tau_r/\sigma'_{v-0}$	Shear displ. at $\tau_r$ (mm)
2.4a	Cohesive alluvium, Jackson, Alabama	59	31	51	51.8	0.21	0.50	0.13	36
2.4b		59	31	51	79.4	0.23	0.35	0.16	50
2.4c		59	31	51	100	0.23	0.37	0.14	38
2.5a	Upper Bonneville clay, Salt Lake City, Utah	46	23	33	47.9	0.32	0.30	0.11	39
2.5b		46	23	33	95.8	0.36	0.60	0.15	25
2.5c		46	23	33	191.5	0.31	1.2	0.12	29
2.5d		46	23	33	383	0.34	2.0	0.14	36

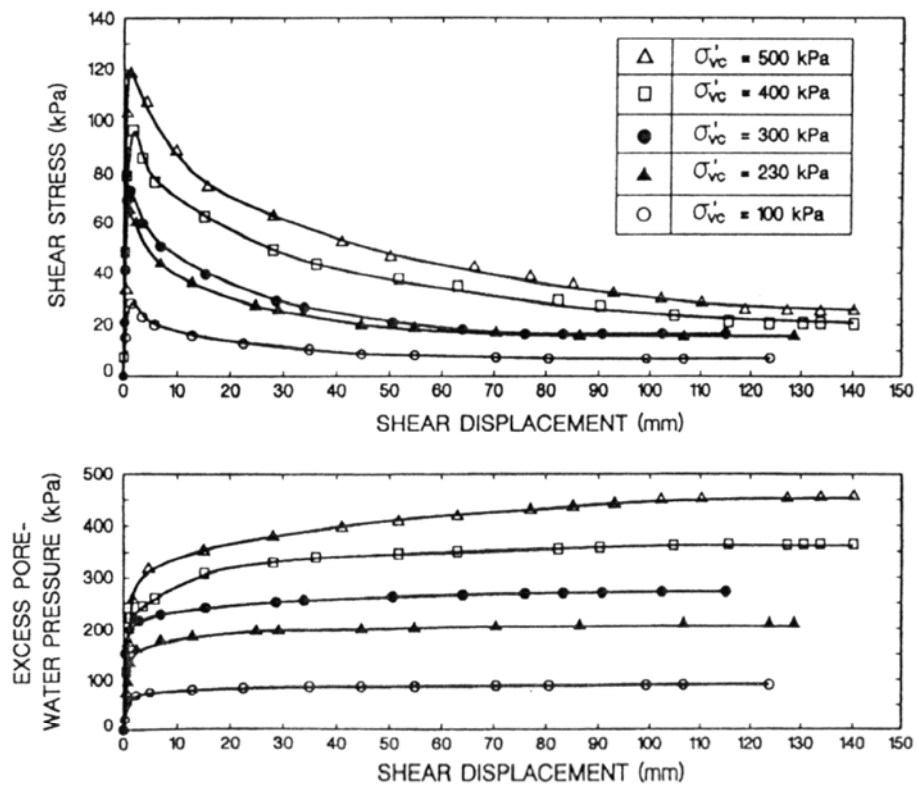


Figure 5. Measured response of ring shear tests on a sample from the 4th Avenue – Alasca slide (Stark and Contreras, 1998).

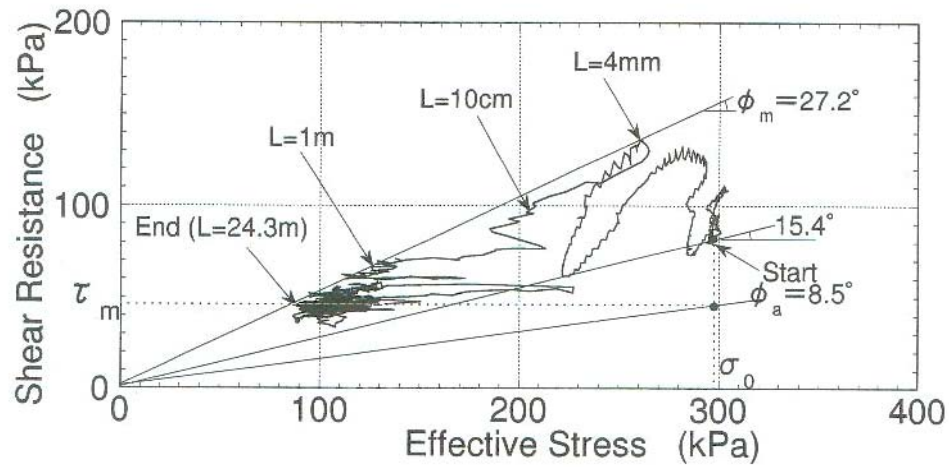


Figure 6 . Measured response of ring shear tests on a normally-consolidated sample from the Nikawa slide (Sassa et al, 1995).

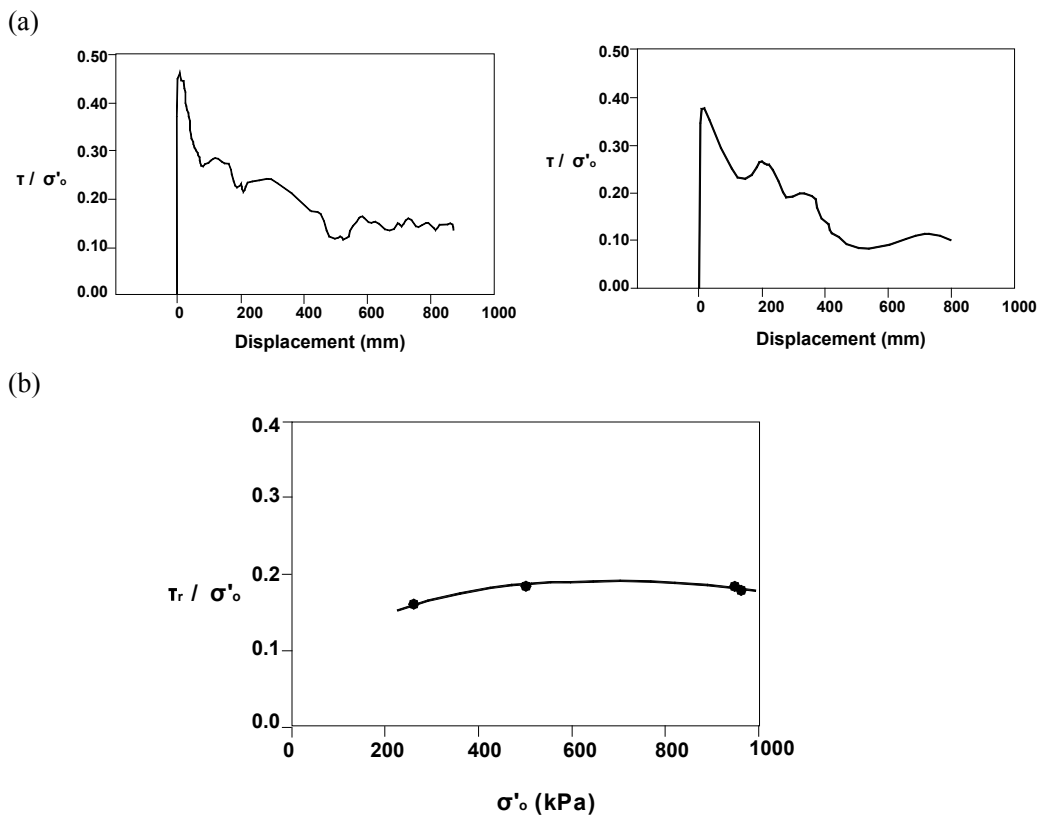


Figure 7. (a) Measured response of ring shear tests on sample 4 from the Vaiont slide. (b) Measured effect of vertical consolidation stress on the residual shear strength ratio ( $\tau_r/\sigma'_0$ ) on sample 3 from Vaiont slide (Tika and Hutchinson, 1999).

**Table 3. Model parameters predicting the response of the tests of tables 1 and 2.**

Case	$\varphi_{cs}$ ( $^{\circ}$ )	$\varphi_{res}$ ( $^{\circ}$ )	b	a ( $10^{-4}$ m)	$k_1$ kPa/m	$k_2$
1.1	26	4	0.12	1	100000	1
1.2	31	8.5	0.07	1	400	4
1.3	28	10	0.03	1	90000	1
1.4	28	8.5	0.01	1	70000	1
2.1	26	6	0.22	1	130000	1
2.2	26	6	0.2	1	25000	1
2.3	26	4	0.24	1	30000	1
2.4	26	8	0.3	1	150000	1
2.5	26	8	0.15	1	130000	0.7

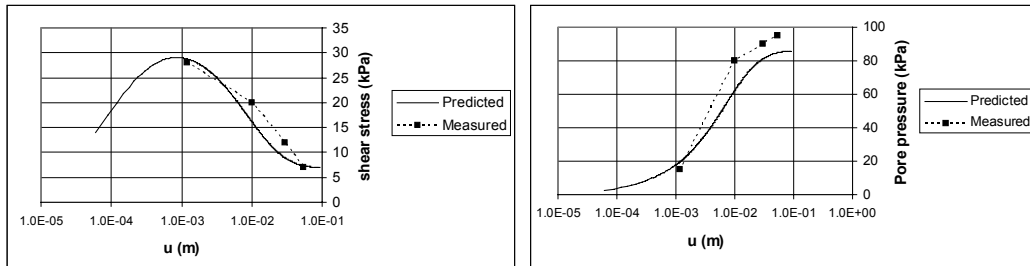
**Table 4. The accuracy of the model predictions. Cases of table 1. The ratio of predicted to measured values for shear stress and pore pressures at different shear displacements.**

No	u (m)	Predicted / Measured		No	u (m)	Predicted / Measured	
		$\tau$	P			$\tau$	
1.1a	0.0012	1.03	1.33	1.3a	0.005	0.85	
	0.01	0.81	0.78		0.05	1.12	
	0.03	0.74	0.90		0.2	0.86	
	0.055	1.04	0.89		0.6	0.87	
1.1b	0.0011	1.04	2.19	1.3b	0.002	0.89	
	0.01	0.93	0.84		0.05	1.16	
	0.03	0.68	1.04		0.6	0.87	
1.1c	0.075	1.01	0.98	1.4a	0.01	1.02	
	0.0013	1.19	2.09		0.1	0.87	
	0.01	0.97	0.89		0.2	0.88	
	0.03	0.67	0.97		0.4	0.92	
1.1d	0.075	1.17	0.99	1.4b	0.7	1.14	
	0.0018	1.20	2.05		0.005	1.15	
	0.01	0.86	0.92		0.2	0.95	
	0.03	0.76	1.01		0.4	1.22	
	0.075	0.88	0.98		0.6	1.43	
1.1e	0.12	1.16	0.98	1.4c	0.01	0.99	
	0.0018	1.20	0.51		0.2	0.95	
	0.01	0.95	0.89		0.4	0.92	
	0.03	0.74	1.10		0.6	1.14	
	0.075	1.00	0.99		0.4	0.92	
1.2a	0.13	1.16	0.95	1.4d	0.005	1.10	
	0.004	1.09	0.25		0.2	0.95	
	0.1	1.19	0.95		0.4	0.92	
	1	1.09	1.05		0.8	1.14	
1.2b	24.3	1.50	0.89				
	0.001	0.80	0.99				
	0.1	0.80					
	1	1.38	1.09				
	28.4	1.37	0.87				

**Table 5. The accuracy of the model predictions. Cases of table 2. The ratio of predicted to measured values of (a) the peak and residual shear stress and (b) the shear stress when the displacement takes the measured peak and residual shear stress.**

Predicted / Measured					Predicted / Measured				
No	$\tau_{max}$	$\tau_r$	$\tau$ at u of $\tau_{m-MEAS}$	$\tau$ at u of $\tau_{r-MEAS}$	No	$\tau_{max}$	$\tau_r$	$\tau$ at u of $\tau_{m-MEAS}$	$\tau$ at u of $\tau_{r-MEAS}$
2.1a	0.89	1.11	0.87	1.16	2.4a	1.09	1.03	1.07	1.03
2.1b	1.11	0.95	1.07	1.04	2.4b	1.03	0.85	0.97	0.85
2.1c	1.21	0.95	1.19	0.95	2.4c	1.01	0.99	0.96	0.99
2.2a	0.98	1.38	0.98	1.38	2.5a	0.92	1.32	0.86	1.32
2.2b	0.94	1.10	0.94	1.16	2.5b	0.84	0.95	0.83	0.96
2.2c	0.97	1.08	0.97	1.11	2.5c	1.00	1.16	1.00	1.19
2.2d	1.00	0.98	1.00	0.99	2.5d	0.94	0.99	0.91	1.02
2.3a	1.22	0.68	1.21	0.84					
2.3b	0.84	1.50	0.83	1.51					
2.3c	0.84	1.35	0.83	1.50					
2.3d	0.99	1.01	0.99	1.12					
2.3e	0.99	1.20	0.99	1.28					

(a)



(b)

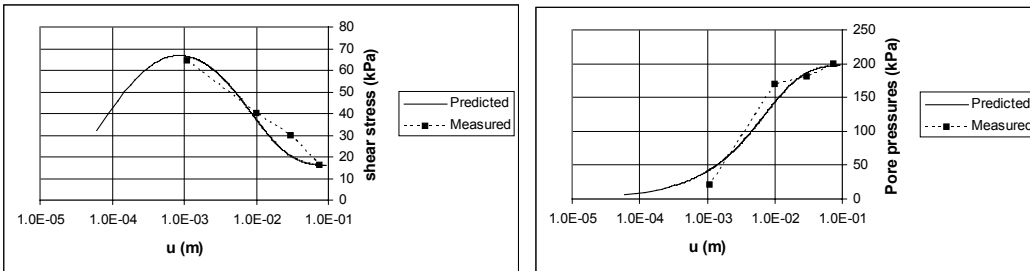


Figure 8. Continued on next page.

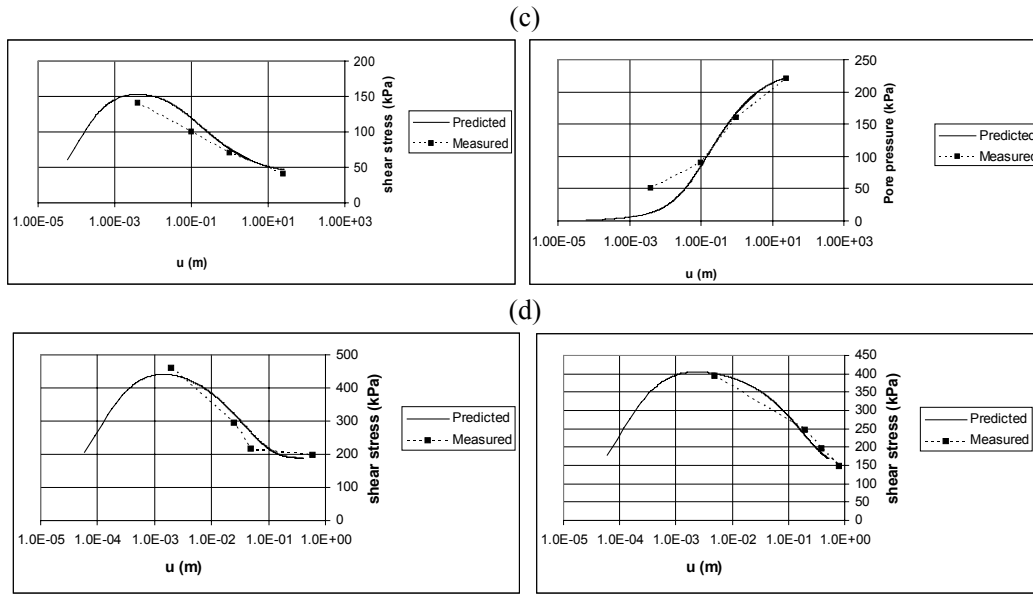


Figure 8. Predicted by the proposed model versus measured response of ring shear tests.. Tests (a) 1.1a, (b) 1.1b, (c) 1.2a and (d) 1.3b and 1.4d of table 1.

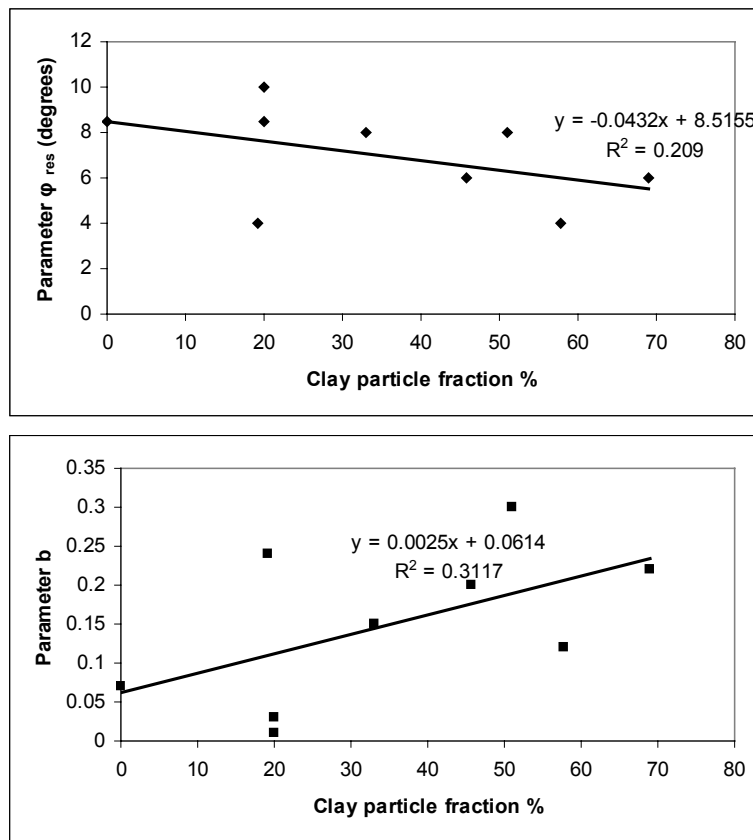


Figure 9. Continued on next page.

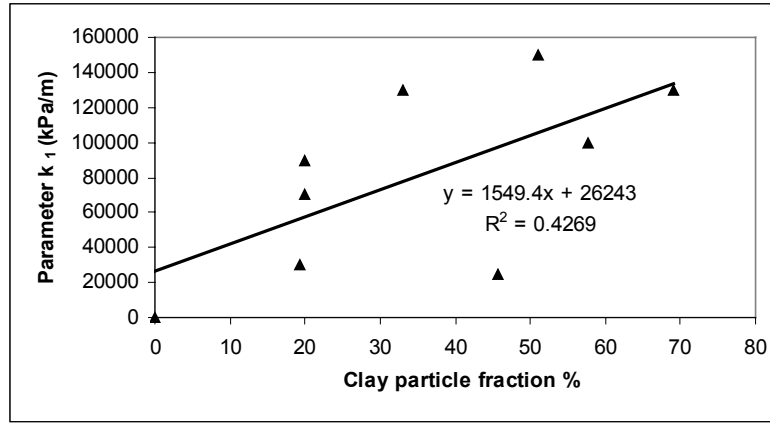


Figure 9. Variation of the estimated model parameters  $\varphi_{res}$ ,  $b$  and  $k_1$  in terms of clay particle fraction.

### Implementation

In equation (2), the multi-block sliding system model was based on both the frictional and cohesive resistance of the Mohr-Coulomb model. The proposed constitutive model is coupled with the multi-block sliding system by varying only the friction angle at the base of each block 'i' as

$$\varphi_i = \arctan(\tau_i / \sigma'_{o-i}) \quad (11)$$

In equation (11)  $\sigma'_{o-i}$  is the effective normal stress at the base block i without considering the excess pore pressures. At each increment,  $\tau_i$  is predicted from equations (6) to (10) (by taking  $u$  and  $\sigma'_o$  of these equations equal to  $u_i$  and  $\sigma'_{o-i}$  respectively).

Furthermore, when the proposed constitutive model is applied, it is needed first to estimate (a)  $\sigma'_{o-i}$  and (b) the initial equilibrium shear stress along the slip surface, or equivalently the equilibrium friction angle at zero displacement. The stresses  $\sigma'_{o-i}$  equal  $(R_i / l_i - U_i)$  where  $R_i$  and  $l_i$  are the normal force at the base of block i and the length of the base of block i, respectively and  $U_i$  is the initial pore pressure at the base of block i. The forces  $R_i$  are estimated from the equilibrium equations of the multi-block model. The initial equilibrium friction angle is estimated by finding the friction angle consistent with a critical acceleration value equal to zero (or equivalently a factor of safety equal to unity) at the initial slide configuration, using iterations. It may be noted that this implies uniform stress ratio along the slip surface. This is reasonable, as the slip surface is initially stable with more-or less uniform strength. Generation of excess pore pressures that may cause failure and may be non-uniform, will develop at a later stage, when the earthquake is applied.

A computer program that solves equations (2) and (6) to (11) has been developed by the author. Equation (2) is a second order differential equation. It is solved numerically by the Euler method (e.g. Dahlquist and Bjorck, 1974). At each time step, the masses and lengths are updated according to the transformation rule described above. Parametric analyses using different time steps illustrated that a time step of 0.01s, typically used in earthquake records found in the literature, produces adequate accuracy. The input geometry is specified as the nodes of the linear segments defining the slip, ground and water table surfaces. The inclinations of the internal slip surfaces must also be specified. The parameters of the

constitutive soil model are specified in each segment of the slip surface. The computer program includes graphics that illustrate (a) the initial and final deformed configurations of the slope, (b) the applied acceleration, the critical acceleration and the mass of each block of the slide, all versus time and (c) the excess pore pressure, the equivalent resistance (specified as the friction angle of equation (11)) and the acceleration, velocity and displacement of each block versus time.

### **Steps Needed to Apply the Model**

The steps required to apply the multi-block model to investigate if triggering will occur and to predict the final displacement of earthquake-induced slides are:

- (a) The soil strength and a representative seismic motion of the problem under consideration are established. For the Mohr-Coulomb model, both the peak and residual strength values of the soil layers of the problem must be specified. In addition, along the potential slip surface the parameters of the proposed constitutive model must be specified.
- (b) The potential slip surface of maximum displacement is located by stability analyses using the Mohr-Coulomb model for strength of the soil layers of the problem considering also the inertia seismic forces. Stability analysis that locates a slip surface consisting of linear segments can be performed by the procedure developed recently by Sarma and Tan (2006) in terms of the minimum critical acceleration value. In addition, it can be performed by the procedure described by Dawson et al. (1999) and implemented in the code FLAC (Itasca Consultants, 2005). The method performs a full solution of the coupled stress/displacement equilibrium and constitutive equations. For a given set of properties, the system is determined to be stable or unstable. By automatically performing simulations for different strength properties, the critical slip surface can be located.
- (c) The slip surface is simulated as a series of linear segments according to (b). Then, a first estimate of the inclination of the internal linear segments is obtained according to the condition of minimum critical acceleration value of the initial slide configuration using the Mohr-Coulomb model. For this first estimate, along the slip surface the residual value of soil strength should be used. At the interfaces the peak value of soil strength should be used. The reason is that at the interfaces different material is sheared at each time increment, and thus the residual strength value is not relevant.
- (d) The slide triggering is investigated and the potential slide deformation is estimated using the multi-block model. The representative seismic motion is applied. At the slip surface the proposed constitutive model is used. At the interfaces, similarly to (c), the Mohr-Coulomb model with peak values of strength is used. Model parameters are specified. If the displacement is large compared to the length of the slip surface, a better estimate of the interslice angle is obtained according to criterion of maximum displacement using iterations.

## 4. Extension of the Multi-block Model: Prediction of the Displacement of Gravity Walls Retaining Dry Soil

### General

As was discussed in the introduction, the seismic movement of the wall-backfill system of Fig. 3a is modeled using the multi-block sliding system of Fig. 2 considering two bodies. Total contact is assumed between the two bodies. At the initial configuration, the first body corresponds to the gravity wall and the second to the critical wedge in the soil behind the wall (Fig. 3b). According to the limiting equilibrium method (e.g. Sama, 1999), the inclination of this wedge in the soil behind the wall is the inclination that produces instability with the minimum possible applied horizontal acceleration. As a result of the applied shaking, gravity walls move outwards, away from the retained soil. Assuming that contact always exists between the wall and the retained soil, the outward wall movement causes deformation of the retained soil near the wall. In typical walls, the resistance on the wall-backfill interface is less than on any other internal sub-planes in the retained soil. It is inferred that, according to the law of limit equilibrium (where the slip surface develops at the location where relative motion occurs for the least value of applied acceleration), the internal slip sub-plane between the two bodies should remain in the wall-backfill interface. This implies that the first body of the two-body system is always the wall, while the second body is always part of the soil behind the wall. Unlike the first body, the second body changes its shape with displacement. The analysis is performed incrementally with applied excitation  $a(t)$  applied in small time increments. The change in shape of the second body can be determined by applying the limit equilibrium condition at each time step.

### Analytical Solution Algorithm

At each increment 'i', the seismic excitation is  $(k_i g)$  where  $g$  is the acceleration of gravity and the parameters that define (a) the inclination of the base, the weight, the contact length of (i) the first body and (ii) the second body of Fig. 3b and (b) the interface angle and length between the two bodies, are (a) (i)  $\alpha_w$ ,  $W_w$ ,  $b_w$ , (ii)  $\alpha_{Bcr-i}$ ,  $W_{Bcr-i}$ ,  $b_{Bcr-i}$  and (b)  $\delta$  and  $d_i$  respectively. The parameters  $\alpha_{Bcr-i}$ ,  $W_{Bcr-i}$ ,  $b_{Bcr-i}$  and  $d_i$  are not known a priori, and depend on the distance moved. The algorithm estimating them is given later. In addition, the strengths below both bodies and at the interface are (a)  $\phi_w$  and  $c_w$ , (b)  $\phi_B$  and  $c_B$  and (c)  $\phi_I$  and  $c_I$  respectively.

At each time increment, the first body (or the wall) is displaced by  $\Delta \bar{u}_{W-i}$  along the wall-foundation soil interface (Fig. 3b). The second body (or the critical wedge behind the wall) is displaced by  $\Delta \bar{u}_{Bcr-i}$  along the slip surface of the backfill. Unlike  $\Delta \bar{u}_{Bcr-i}$ , the direction of  $\Delta \bar{u}_{W-i}$  does not change in the analysis. Thus, the absolute value of the distance moved by the wall,  $u_w$ , equals the sum of all the absolute values of  $\Delta \bar{u}_{W-i}$ 's. It is assumed that at each time increment the total contact between the two bodies is retained along the shearing surface. The governing equation of the sliding system is obtained from equations (1) and (2) as

$$d^2u_W / dt^2 = Z_{W-i} g (k_i - k_{c-i}) \quad (12a)$$

where

$$Z_{W-i} = \frac{W_W \cos(\alpha_W - \phi_W) \cos(\phi_I - \alpha_{Bcr-i} - \delta + \phi_B) + W_{Bcr-i} \cos(\alpha_{Bcr-i} - \phi_B) \cos(\phi_I - \alpha_W - \delta + \phi_W)}{W_W \cos \phi_W \cos(\phi_I - \alpha_{Bcr-i} - \delta + \phi_B) \lambda_i + W_{Bcr-i} \cos \phi_B \cos(\phi_I - \alpha_W - \delta + \phi_W)} \lambda_i \quad (12b)$$

and

$$k_{c-i} = AA / BB \quad (12c)$$

where

$$\begin{aligned} AA &= [W_W \sin(\phi_W - \alpha_W) + c_W b_W \cos \phi_W] \cos(\phi_I + \phi_B - \alpha_{Bcr-i} - \delta) + \\ &+ [W_{Bcr-i} \sin(\phi_B - \alpha_{Bcr-i}) + c_B b_{Bcr-i} \cos \phi_B] \cos(\phi_I + \phi_W - \alpha_W - \delta) + \\ &+ c_I d_i \cos \phi_I \cos(\phi_W - \phi_B + \alpha_W - \alpha_{Bcr-i}) \\ BB &= W_W \cos(\phi_W - \alpha_W) \cos(\phi_I + \phi_B - \alpha_{Bcr-i} - \delta) + W_{Bcr-i} \cos(\phi_B - \alpha_{Bcr-i}) \cos(\phi_I + \phi_W - \alpha_W - \delta) \end{aligned}$$

### Definition of the Critical Soil Wedge

As will be illustrated later, the only shape factor in the parameters of Fig. 3a defining the geometry of the backfill that changes as the wall is displaced is the backfill height. At increment "i", this height is denoted as  $H_i$ . The interface length of the two bodies can be expressed in terms of  $H_i$  and  $\delta$  as

$$d_i = H_i / \cos(-\delta) \quad (13)$$

Also, at increment "i" the length of a potential slip surface and the weight of a soil wedge behind the wall with inclination not necessarily equal to the critical, denoted as  $b_{B-i}$  and  $W_{B-i}$  respectively, can be expressed in terms of the corresponding inclination of the soil wedge behind the wall,  $\alpha_{B-i}$ , as:

$$b_{B-i} = H_i \frac{1 - \tan \delta \tan \theta}{\cos \alpha_{B-i} (\tan \alpha_{B-i} - \tan \theta)} \quad (14a)$$

$$W_{B-i} = 0.5 \gamma H_i^2 \frac{(1 - \tan \alpha_{B-i} \tan \delta)(1 - \tan \delta \tan \theta)}{\tan \alpha_{B-i} - \tan \theta} \quad (14b)$$

In addition, the following dimensionless symbols are introduced:

$$X_i = 2 W_W / (\gamma H_i^2) \quad (15a)$$

$$S_{W-i} = 2c_W b_W / (\gamma H_i^2), S_{B-i} = 2c_B / (\gamma H_i), S_{I-i} = 2c_I / (\gamma H_i) \quad (15b)$$

Then, according to equation (14c), the horizontal acceleration factor for relative motion of the two-body system of Fig. 3 when the angle of inclination of the soil wedge is  $\alpha_{B-i}$  equals

$$k_{cB-i} = AA_B / BB_B \quad (16a)$$

where:

$$\begin{aligned} AA_B = & \left\{ X(G-M) + S_{W-i} \sqrt{1+M^2} + S_{I-i} [G-M - (1+GM)D] \right\} \cdot [(1+AB)(1+FD) - (B-A)(F-D)] \\ & + \left\{ (DA_i - 1) \frac{(DK-1)}{A_i - K} \cdot (B-A_i) + S_{B-i} \cdot (1+A_i^2) \cdot \frac{(1-DK)}{A_i - K} - S_{I-i} [B-A_i - (1+A_i B)D] \right\} \\ & \cdot [(1+GM)(1+FD) - (G-M)(F-D)] \end{aligned} \quad (16b)$$

and

$$\begin{aligned} BB_B = & X \cdot (1+MG) \cdot [(1+FD)(1+A_i B) - (F-D)(B-A_i)] + \\ & \frac{(DK-1)(DA_i-1)}{A_i-K} \cdot (1+A_i B) \cdot [(1+FD)(1+GM) - (F-D)(G-M)] \end{aligned} \quad (16c)$$

where

$$M = \tan \alpha_W, D = \tan \delta, K = \tan \theta, B = \tan \phi_B, G = \tan \phi_W, F = \tan \phi_I, A_i = \tan \alpha_{B-i}$$

The critical rupture angle  $\alpha_{Bcr-i}$  corresponds to the value of  $\alpha_{B-i}$  that minimizes  $k_{cB-i}$  in equation (18). An analytical solution estimating  $\alpha_{Bcr-i}$  is given by Stamatopoulos et al (2001). Alternatively,  $\alpha_{Bcr-i}$  can be obtained numerically by searching the factor  $\alpha_{B-i}$  that minimizes  $k_{cB-i}$  in equation (16). As illustrated by Stamatopoulos et al (2001),  $k_{cB-i}$  is a parabola in terms of  $(\tan \alpha_{B-i})$ , having a single well-defined minimum. It is inferred that estimating numerically  $(\tan \alpha_{Bcr-i})$ , and thus  $\alpha_{Bcr-i}$  also, is a simple matter using for example the bisection method (e.g. Dahlquist and Bjorck, 1974). Once the inclination  $\alpha_{Bcr-i}$  has been obtained,  $W_{Bcr-i}$  and  $b_{Bcr-i}$  can also be obtained from  $H_i, \delta, \theta, \alpha_{Bcr-i}$  and  $\gamma$ , using equations (14) by replacing  $\alpha_{B-i}$  with  $\alpha_{Bcr-i}$ .

## Changes of Geometry with Outward Wall Displacement

It was stated above that the wall at each time increment "i" is displaced outwards by  $\Delta \bar{u}_{W-i}$ , while the critical soil wedge is displaced by  $\Delta \bar{u}_{Bcr-i}$ . Fig. 3b gives, in enlarged scale of incremental displacement, the induced deformation. It can be observed that the only shape factor in the parameters of Fig. 3a defining the backfill that changes as the wall is displaced is the backfill height. In particular, the height of the backfill at increment "i" equals

$$H_i = H_0 - \sum_{k=1}^{i-1} [ \Delta u_{w-k} ( \sin \alpha_{Bcr-k} / \lambda_k - \sin \alpha_w ) ] \quad (17)$$

Fig. 3b also shows that a part of the cross-sectional area of the backfill, denoted as  $\Delta A_{L-i}$ , is lost in the analysis. Yet, when the increment  $\Delta u_{W-i}$  is sufficiently small, the effect of the lost part can be neglected. The reason is that this area is proportional to the square of (the small increment)  $\Delta u_{W-i}$ . Once the deformed shape is estimated, the new inclination of the critical soil wedge from the new point at the base of the wall-backfill interface (point O' of Fig. 3b), must be estimated with the procedure described above.

## Computer Program

A computer program was written by the author, that predicts the seismic displacement of gravity walls retaining dry soil, according to the model given above. The input required by the computer program includes (a) the nodes defining the wall geometry, (b) the parameters  $W_w$ ,  $\theta$ ,  $\gamma$ ,  $H_0$ ,  $\phi_B$ ,  $c_B$ ,  $\phi_w$ ,  $c_w$ ,  $\phi_I$  and  $c_I$  and (c) the applied horizontal excitation. Numerical integration is performed after every time increment "i" of the earthquake record using the Euler's method (e.g. Dahlquist and Bjorck, 1974). At each increment,  $H_i$  is updated and iteration is performed to estimate the new inclination of the slip surface,  $\alpha_{Bcr-i}$ . Graphics illustrating the final geometry of the wall-retaining soil system are included in the computer program. Parametric analyses using different time steps illustrated that a time step of 0.01s, typically used in earthquake records found in the literature, produces adequate accuracy of both the numerical integration and the simulation of retained soil deformation, at least for wall displacement less than 2m.

## Discussion

As was indicated in the introduction, sliding-block methods usually estimate the seismic displacement  $u_{sl}$  by the Newmark model. The corresponding equation that is solved (e.g. Ambraseys and Menu, 1988) is usually:

$$d^2 u_{sl} / dt^2 = g ( k(t) - k_{c-o} ) \text{ for } du_{sl} / dt > 0 \quad (18)$$

where  $k(t)$  and  $k_{c-o}$  are the dimensionless applied acceleration and critical acceleration factors. From equation (14) it can be inferred that the governing equations of motion for the wall of the proposed model at the initial configuration is:

$$d^2 u_w / dt^2 = Z_{W-o} g (k(t) - k_{c-o}) \quad (19)$$

where  $Z_{W-o}$  is the factor given by equation (12b) when the subscript "i" is replaced by the subscript "o". Comparison of equations (18) and (19) illustrates that they differ by the factor  $Z_{W-o}$ . Thus, for the case of small displacement, the factor  $Z_{W-o}$  relates the seismic displacement of the previous commonly-used method to the displacement of the wall of the present model, for equal critical acceleration and applied excitation. For the case of large displacement, the difference of the two methods increases, as the new model considers, additionally, the deformation of the backfill.

### **Procedure Application and Limitations**

The proposed model is intended for the prediction of the seismic displacement of gravity walls retaining dry soil of the general geometry given in Fig. 3a. By "dry" soil it is meant that there is no water table and no pore water pressures. It is not implied that the water content is necessarily zero. Similarly to the analysis of Kotta et al (1988), it is recommended to accept performing one-dimensional equivalent-linear dynamic analyses to obtain the required acceleration time history. In these analyses, the soil profile including the soil retained by the wall should be considered. The input motion should be typical of the region and should be applied at the underlying bedrock. The effect of the shear strain on the shear modulus and the damping of soils should be considered. The acceleration time history required for the prediction of wall displacement should be obtained at a depth  $2H_o/3$ , where the height  $H_o$  is defined in Fig. 3a. This depth is the "representative" depth of the slip surface of the wall-backfill system.

The proposed model cannot be applied for backfill soils that exhibit considerable strain softening. In this case, the situation is more complex, as the shear resistance varies with displacement. In addition, both the location of the slip line in the soil behind the wall at the initial configuration and the change of the geometry with displacement are affected by both the peak and residual values of strength.

## **5. Validation of the Multi-block Model for the Prediction of the Triggerring and Deformation of Landslides**

### **The Nikawa Slide**

One the most well-documented slides directly related to an earthquake is the Nikawa slide. Knowledge of (a) the initial and final slide configurations, (b) the soil response along the slip surface, and (c) the applied seismic motion exists. In this section the multi-block model for landslides is validated by the prediction of this slide.

The slide was triggered by the 1995 Hyogoken-nambu earthquake with magnitude  $M_w$  equal to 7. With a landslide volume in the order of  $110,000 \text{ m}^3$ , moving rapidly over a distance of about 100 m, it destroyed 11 residential buildings causing 34 fatalities (Sassa et al. 1995, 1996). Fig. 10a shows the plan of the slope before the landslide and the outline of the

landslide area (Sassa et al., 1996). A cross-section of the landslide is given in Fig. 10b (Sassa et al., 1996). The water table level at the region (measured about a month after the earthquake) is also given. Seismic records do not exist at the site. However, accelerations have been recorded on nearby sites. Kallou and Gazetas (2001) indicate that the accelerogram of Skinkobe, given in Fig. 11a, is possibly the most representative of the site. In addition the seismic shaking at the Nikawa slope was perhaps accentuated by topographic amplification (Kallou and Gazetas, 2001).

The region has two formations: the soil and the underlying rock at a depth of about 35m from the crest of the slope (Sassa et al., 1995). Geotechnical data of the soil formation includes cyclic ring shear tests. About one third of the slip surface was below the water table at time of landslide. Sassa et al. (1996) performed two fast cyclic ring shear tests on samples with a degree of saturation of 0.35, to simulate average field conditions. The results are given in Fig. 4 and table 1. They illustrate that as a result of cyclic loading, the sand resistance first increases and then drastically decreases. The peak total friction angle is 25 and 31° in the two tests and the residual total friction angle is only 8.5°. The residual strength value occurs at very large shear displacement, about 25m. Yet, at 1m displacement most of the soil strength has already been lost.

### **Establishment of the Soil Strength and Density**

As described above, the region has two formations: the soil and the underlying rock at a depth of about 35m from the crest of the slope. For the soil, for the Mohr-Coulomb model the two ring shear tests gave average total peak strength parameters  $c=0$ ,  $\phi=28^\circ$  and average residual total strength parameters  $c=0$ ,  $\phi=8.5^\circ$ . For the proposed soil model, the parameters that better fit the two ring shear tests and should be used are those given in table 3 (case 1.2). Finally, the total unit density of the soil was taken as  $1.8\text{T/m}^3$ , a typical value for sands

### **Prediction of the Location of the Slip Surface**

Rigorous stability analysis to obtain the slip surface consisting of linear segments cannot be performed in the present case study. The reason is that only the "average" value of residual soil strength along the slip surface is known. It is expected that the residual soil strength decreases as the degree of saturation increases (Gerolymos and Gazetas, 2007). The variation of the residual soil strength with degree of saturation, and thus versus depth is not known. Yet, it should be noted that stability analyses using the code FLAC (Itasca consultants, 2005) were performed. These analyses illustrated that the location of the observed slip surface can be predicted when non-uniform soil conditions, with a considerably smaller friction angle below the water table, are assumed.

### **Multi-block Predictions**

The slide is represented by a five-block system, where the front two blocks (left of the node B of Fig. 12) are dummy with zero area and their purpose is to define the trajectory of the slide outside the original slip surface (Fig. 12a). The water table of Fig. 10b was applied. First, an

estimate of the inclination of the critical interfaces at the initial configuration is made. According to the previous discussion, along the slip surface, the strength is simulated as  $\varphi=8.5^\circ$  and at the interfaces  $\varphi' = 28^\circ$  was used. Figure 13a shows the obtained variation of the critical acceleration versus each of the interface angles  $\delta_C$  and  $\delta_D$ , shown in Fig. 12. Any of these two graphs is produced by holding constant the critical value of the other angle. It is inferred that an initial estimate of the critical values of  $\delta_C$  and  $\delta_D$  are  $-20$  and  $-25^\circ$  respectively.

Once an initial estimate of the critical values of the angles  $\delta$  is established, the multi-block model is applied. At the slip surface the proposed constitutive model is used. At the interfaces, again a frictional resistance of  $\varphi' = 28^\circ$  was used. The angle  $\delta_A$  is obtained according to equation (4). The reason is that the inclination of the slip surface at the left of node A is greater than the inclination at the right. Thus, the mass to the left of node A cannot maintain contact with the rest of the slide and was subsequently detached from the system. According to the previous discussion, the acceleration history of Fig. 11a, was applied. The seismic shaking was perhaps accentuated by topographic amplification (Kallou and Gazetas, 2001). Yet, to demonstrate conservatively that the proposed model predicts the triggering mechanism, this effect is not considered. To estimate the angle  $\delta_B$  (see Fig. 12) and establish a better estimate of  $\delta_C$  and  $\delta_d$  the criterion of maximum displacement is applied, using iterations. Fig. 11b gives the displacement of block 2 (from bottom to top, defined by nodes B and C of Fig. 12) in terms of the interface angles. Any of these graphs is produced by holding constant the critical value of the other angle. It is noted that the critical value of angles  $\delta_B$ ,  $\delta_C$  and  $\delta_d$  are  $-38$ ,  $-45$  and  $-48^\circ$  respectively.

For these values of  $\delta$ , Fig. 11b gives the computed excess pore pressure and equivalent friction angle (given by equation (11)) of block 2, in terms of time. Fig. 11c gives the computed slide acceleration, velocity and distance moved of the same block, as well as the critical acceleration of the slide, in terms of time. From Fig. 11 it can be observed that as the earthquake is applied, some shear displacement accumulates. This causes excess pore pressure to be generated and the friction angle to increase. Once the peak friction angle is reached, due to material softening, the friction angle decreases drastically, at about  $t=12s$ , to its residual value. At this point, the critical acceleration of the sliding system is negative (this means that the slide is unstable) and the slide velocity starts to increase and displacement to accumulate rapidly. As the slide moves, the mass slides at a progressively smaller average inclination. The critical acceleration of the system gradually increases and at  $t=17s$  becomes positive. Then, the slide velocity starts to decrease, and becomes zero, at  $t=32s$ . According to the above discussion, when the slide reached node A (Fig. 12), the model predicts that some mass is lost. The obtained deformed geometry is given in Fig. 12. As separation occurs, only the final top part of the slide is given. In the same figure, a comparison is made between the computed deformation and the measured deformation at the top part of the slide.

From the above it is inferred that the proposed multi-block model predicted the triggering of Nikawa slide. In addition, the computed deformed geometry agrees reasonably with that measured. Furthermore, the computed time duration of motion (about 20s) agrees with the observed rapid occurrence of the slide.

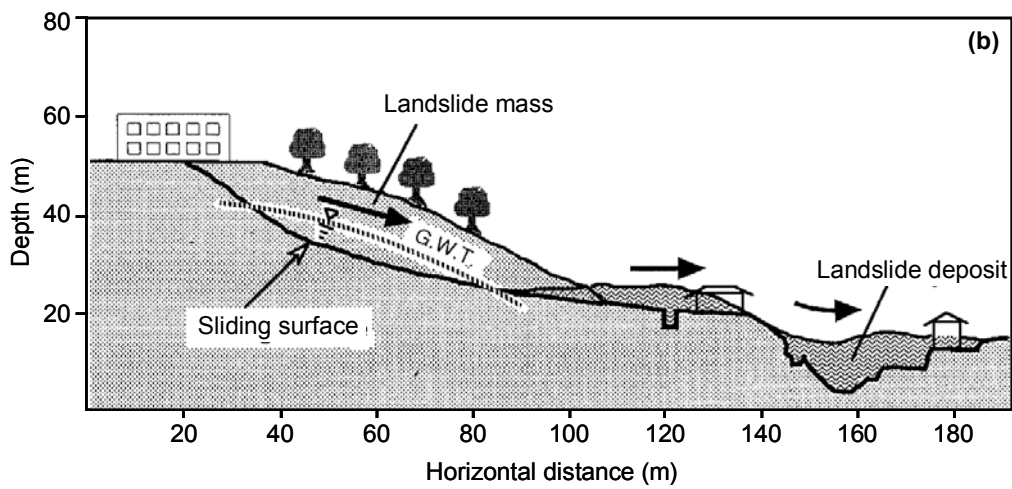
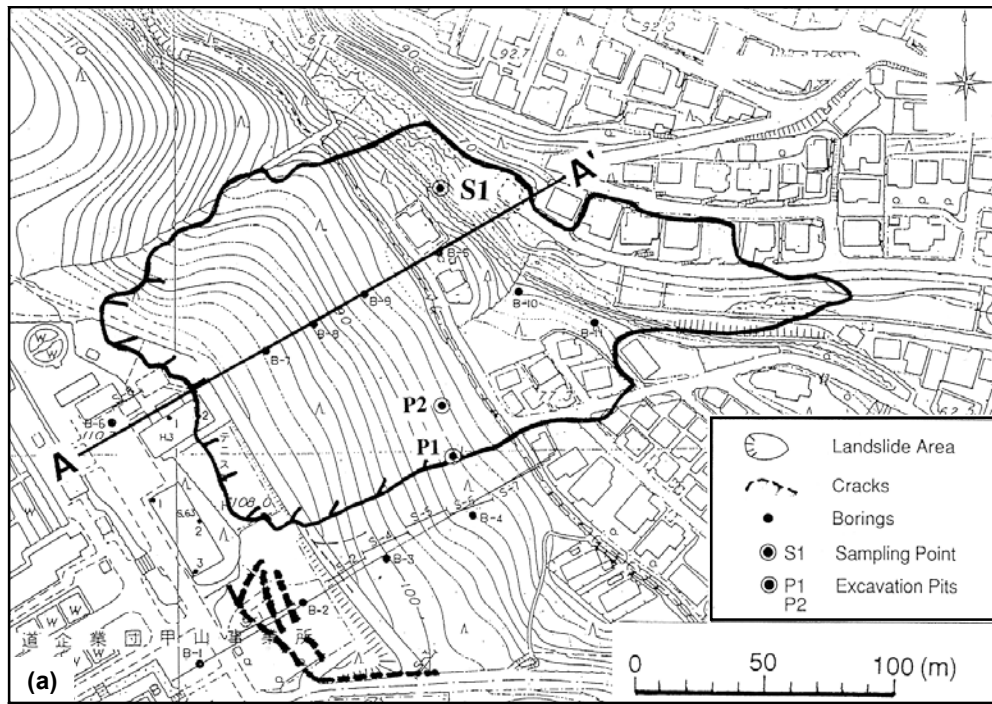


Figure 10. The Nikawa landslide: (a) plan view, and (b) cross section (Sassa et al, 1996)

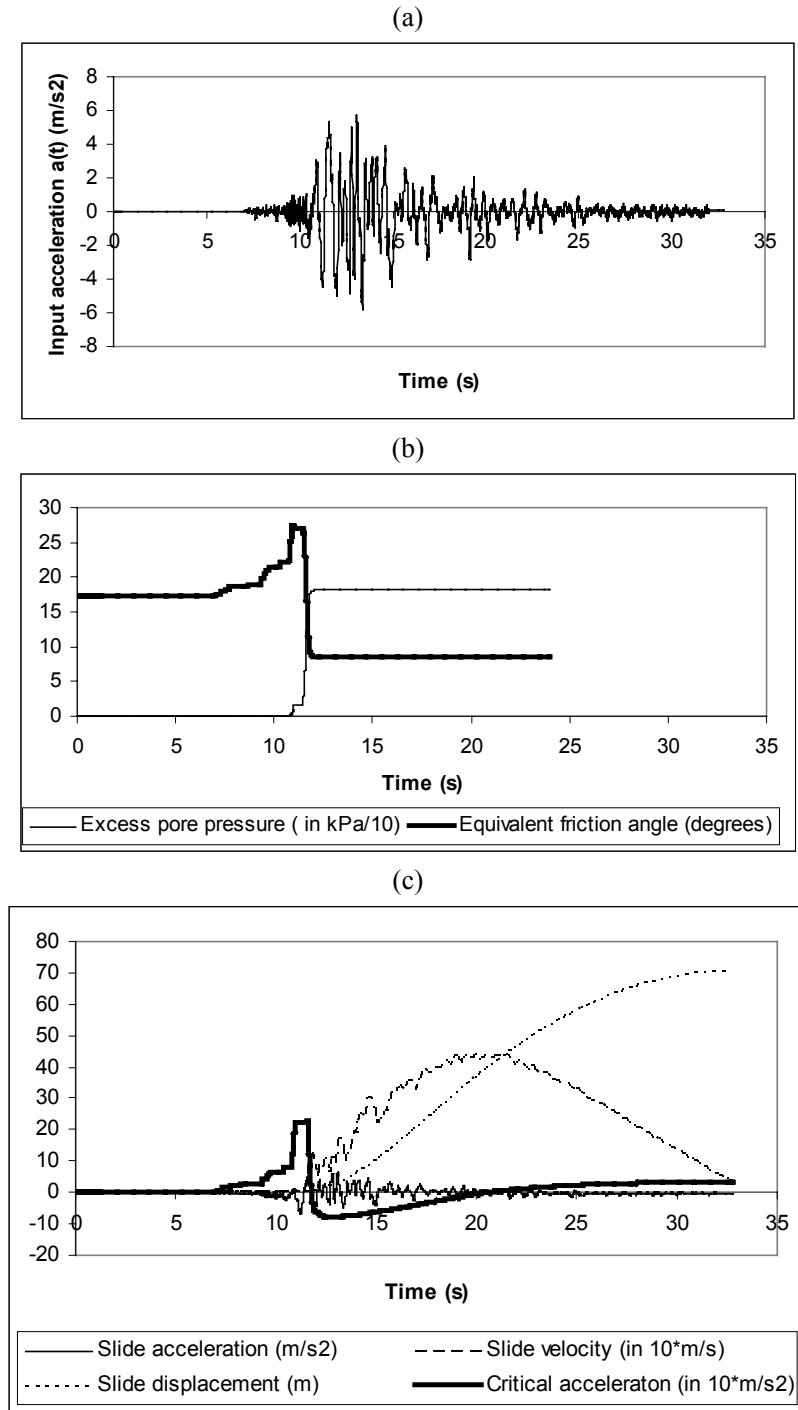


Figure 11. Nikawa slide predictions: (a) Applied acceleration, (b) computed excess pore pressure and equivalent friction angle (given by equation (11)) of block 2 and (c) computed slide acceleration, velocity, distance moved, as well as critical acceleration, of block 2 block, in terms of time.

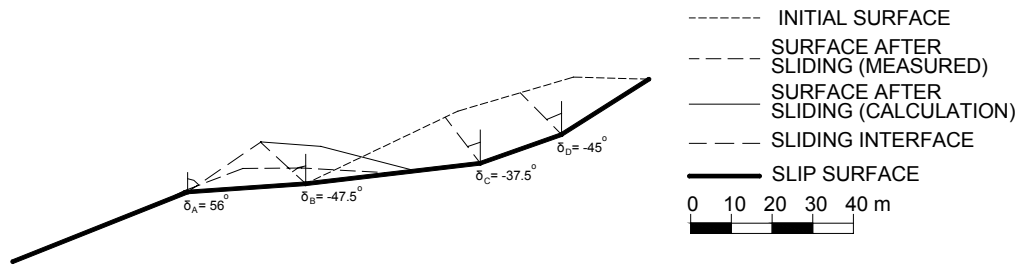
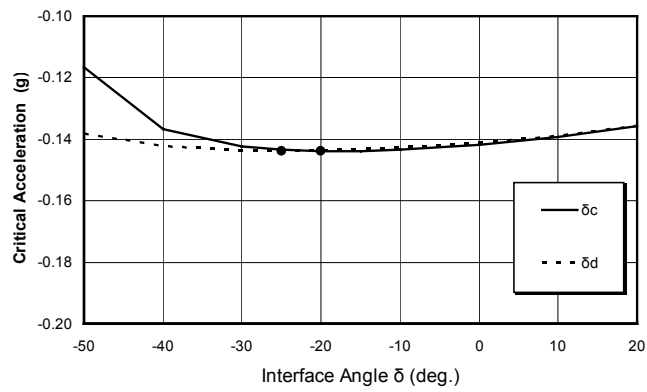


Figure 12. Nikawa slide predictions: Initial slide configuration assumed and computed and measured final configuration.

(a)



(b)

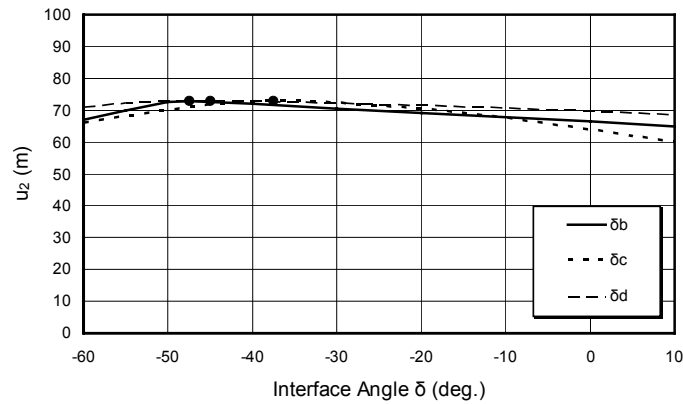


Figure 13. Nikawa slide predictions: (a) Critical acceleration coefficient for relative motion at the initial configuration and (b) the displacement of block 2 in terms of the interface angles.

## 6. Validation of the Multi-block Model for the Case of Gravity Walls

### Comparison with Shaking-Table Tests by Nishimura et al (1995)

The shaking-table test results of a model gravity wall by Nishimura et al. (1995) are first used to evaluate the proposed model for gravity walls. The configuration of the shaking-table tests is given in Fig. 14a. The geometrical and strength properties of the wall-backfill system (Fig. 8) of the configuration tested were measured:  $W_w=3.54\text{kN/m}$ ,  $H_o=0.36\text{m}$ ,  $b_w=0.45\text{m}$ ,  $\alpha_w=\delta=\theta=0^\circ$ ,  $\gamma=16\text{kN/m}^3$ ,  $\phi_B=30^\circ$ ,  $\phi_w=15^\circ$ ,  $\phi_I=20^\circ$  and  $c_B=c_w=c_I=0^\circ$ . The applied horizontal acceleration at the base of the configuration is given in Fig. 15a. The measured wall displacement versus time is given in Fig. 15b. The observed final configuration of the wall-backfill system is given in Fig. 14a.

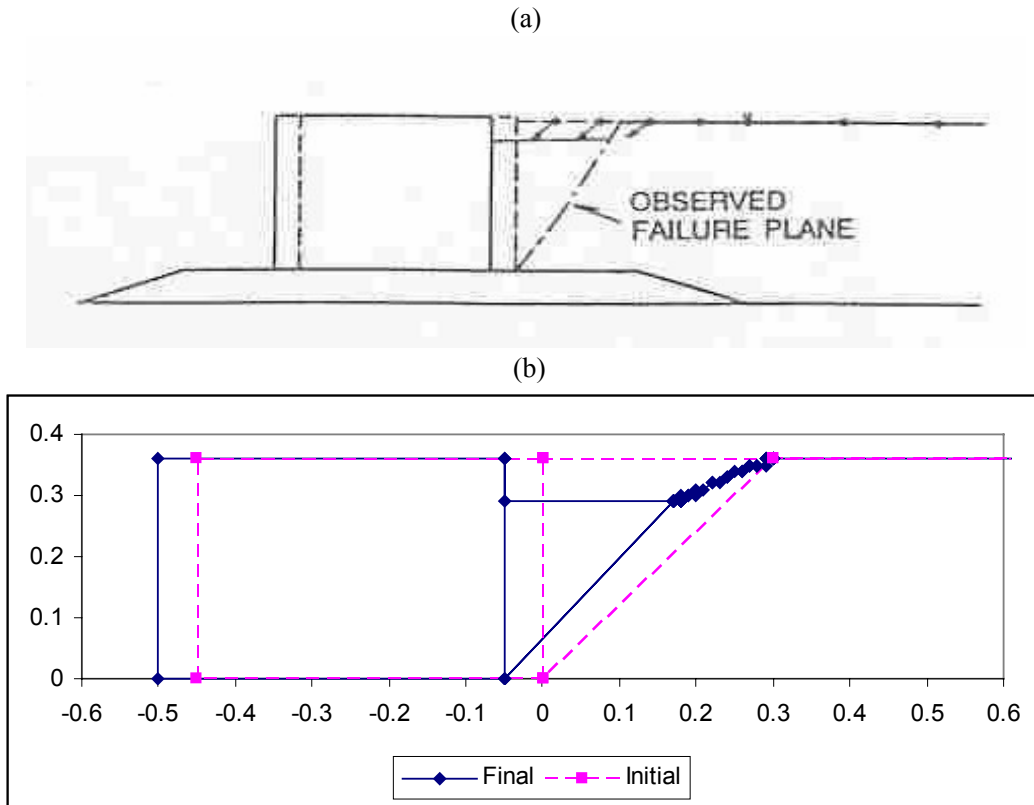


Figure 14. The shaking-table tests by Mishimura et al (1995). (a) Configuration of the tests and measured final deformation. (b) Predicted final deformation by the proposed model.

The proposed model predicts that  $\alpha_{Bcr-0}=49^\circ$  and  $k_{c-0}=0.12$ . As the horizontal acceleration was applied at the base of the backfill and the backfill has very small height, dynamic analysis was not performed. The acceleration history of Fig. 15a was applied to estimate the wall displacement. The computed accumulation of wall displacement with time with both the proposed model and equation (18) is given in Fig. 15c. When the proposed model was used,

the computed final deformation of the wall-backfill system is given in Fig. 14b, the computed final wall displacement is 5.6 cm and the computed slip surface inclination at the final configuration is  $47^\circ$ . When equation (18), which does not take into account changes in soil wedge geometry, was used, the final wall seismic displacement increased to 6.5 cm.

When the proposed model was used, as illustrated in Fig. 15, the computed displacement accumulation response agrees with the one measured. In addition, as illustrated in Fig. 14, the computed final deformation of the backfill agrees with the one measured. Furthermore, the ratio of computed by measured (a) wall displacement and (b) initial and final slip surface inclination is (a) 1.04 and (b) 0.98 and 0.94 respectively. When the previous commonly-used method (equation (18)) was used, predictions are less accurate.

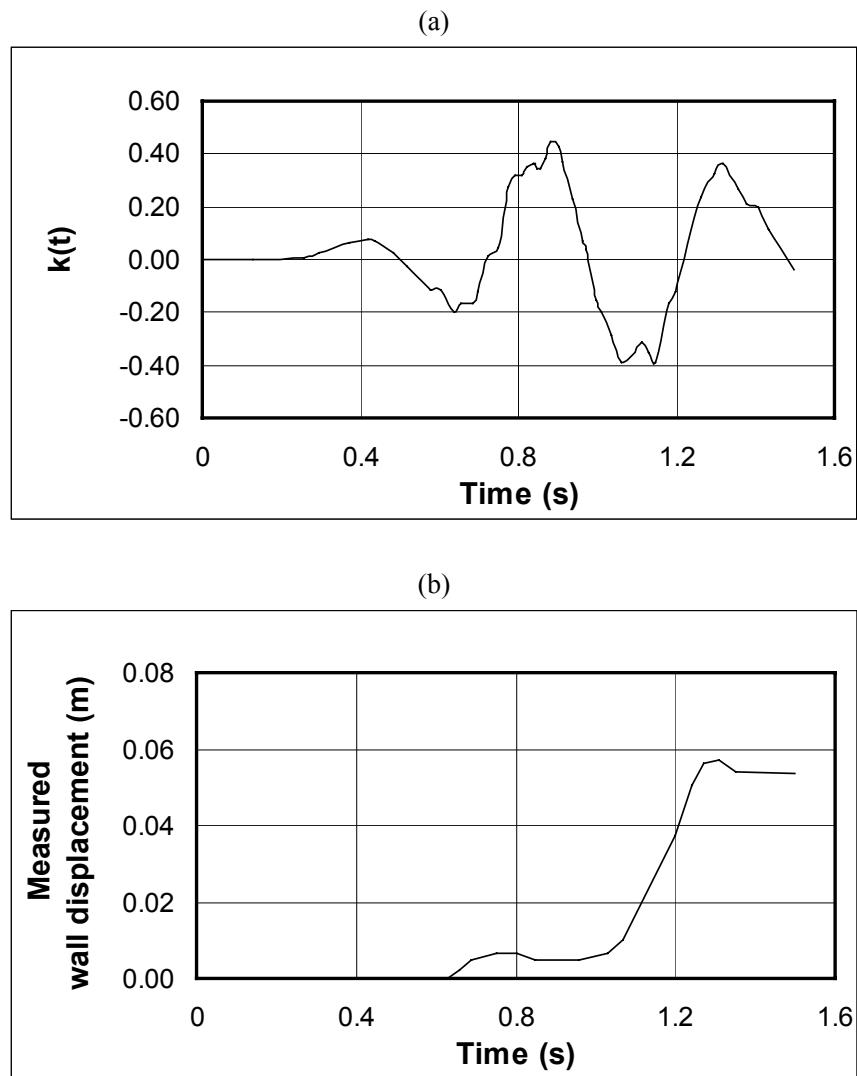


Figure 15. Continued on next page.

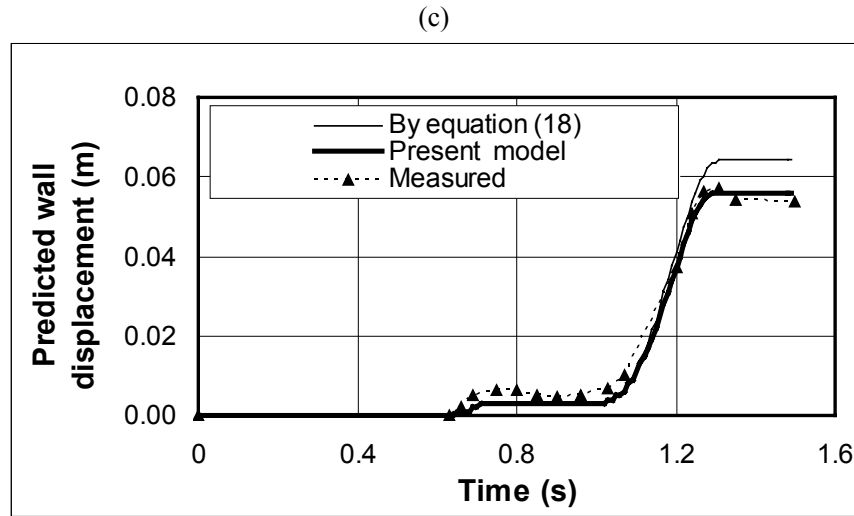


Figure 15. The shaking-table tests by Mishimura et al (1995). (a) Applied acceleration at the base and (b) measured and (c) predicted accumulation of wall displacement.

### Prediction of Response Computed by Elasto-plastic Dynamic Analysis

A full dynamic elasto-plastic analysis of a model concrete gravity wall 8m high with  $W_w$  equal to 634kN/m resting on a soil 30m deep, shown in Fig. 16, was recently performed (Modaressi and Lopez-Caballero, 2001, Lopez-Caballero and Modaressi, 2002). Both the retained and the foundation soil are normally-consolidated clay above the water table. The retained soil has a plasticity index of 30% and uniform shear wave velocity,  $V_s$ , of 123m/s. Below the wall, the plasticity index of the soil is 15% and  $V_s$  increases with depth: (a) From zero to 6m below the base of the wall  $V_s$  equals 123m/s, (b) from 6 to 12m below the base of the wall  $V_s$  equals 200m/s, (c) from 12 to 20m below the base of the wall  $V_s$  equals 260m/s and (d) from 20 to 30m below the base of the wall  $V_s$  equals 325m/s. The large-strain strength parameters of the soil and the wall-soil boundaries are  $\phi_B=26^\circ$ ,  $c_B=0$ ,  $\phi_w=18^\circ$ ,  $c_w=0$  and  $\phi_I=11^\circ$ ,  $c_I=0$ . The dynamic numerical analyses were performed using the GEFDYN Finite-Elements software. The Hujeux elastoplastic model was used to model the soil behavior. The parameters of the Hujeux model were such that when the shear strain increases, the stiffness degradation and the hysteretic damping computed are similar to those predicted by Vucevic and Dobry (1995) in terms of the plasticity index. The Irpinia NS (Italy) Cairano 16/1/1981 earthquake record, scaled to different values of maximum acceleration, was applied at the base of the mesh, where it is assumed that is the bedrock. This earthquake record has a fundamental period  $T_f$  of 0.3s. The fundamental period of the soil stratum, including the backfill, corresponding to the small-strain moduli is 1.2s. Table 6 gives the computed wall final horizontal displacement for the different values of maximum applied acceleration.

The parameters for the proposed simplified model (Fig. 8) of this problem are  $W_w=634\text{kN/m}$ ,  $H_o=8\text{m}$ ,  $b_w=5\text{m}$ ,  $\alpha_w=\delta=\theta=0^\circ$ ,  $\gamma=18\text{kN/m}^3$ ,  $\phi_B=26^\circ$ ,  $\phi_w=18^\circ$ ,  $\phi_I=11^\circ$  and  $c_B=c_w=c_I=0^\circ$ . With these values, the model predicts  $\alpha_{Bcr-0}=54.2^\circ$  and  $k_{c-0}=0.016$ . In order to predict the seismic wall displacement, one-dimensional equivalent linear elastic analyses were performed using the code Cyberquake (BRGM Software, 1998) to obtain the representative

earthquake motion. According to the problem considered, a clay with plasticity and variation of shear velocity as described previously is assumed. The same (i) applied accelerations at the base of the foundation soil and (ii) equivalent shear modulus degradation and damping versus shear strain relations for the two types of clay (i.e. as predicted by the relationships of Vucetic and Dobry, 1991) were used as in the elaborate elasto-plastic analysis. Table 6 gives the wall displacement predicted by the proposed simplified method in terms of the applied acceleration. Predictions are given for both (a) the bedrock record and (b) the record computed by the equivalent linear dynamic analyses at a depth of 5.3m. Predictions using equation (20) are also given.

From table 6 it can be observed that the values of seismic wall displacement predicted with the proposed simplified method compare well with the values computed by the dynamic elasto-plastic method. The wall displacement estimated by the proposed simplified model using the acceleration deduced by the linear dynamic analyses, divided by the wall displacement computed by the elasto-plastic dynamic method, for all five cases, varies between 1.00 and 1.10. In addition, from table 6 it can be observed that the predictions by the proposed model are closer to the wall displacement computed in the elasto-plastic dynamic method than the predictions of the previous commonly-used method (equation (20)), especially when the wall displacement is large. This is presumably because changes in the geometry of the retained soil as the wall moves outwards are not considered by equation (20).

**Table 6. Wall displacement ( $u_w$ ) computed by the elasto-plastic dynamic Finite Element Method (FEM) and predicted by the simplified proposed model when (a) the bedrock record is applied and (b) the record computed by the linear dynamic analyses at a depth of 5.3m is applied. Input motions of different magnitude are applied in the underlying rock. The estimated wall displacement by equation (20) is also given.**

$a_{m\text{-bedrock}}$ (g)	$u_{w\text{-FEM}}$ (cm)	$u_w$ predicted by the simplified models (cm)				$(u_{w\text{-predicted}}) / u_{w\text{-FEM}}$			
		The bedrock record is applied		The record computed by the linear dynamic analyses is applied		The bedrock record is applied		The record computed by the linear dynamic analyses is applied	
		I (b)	II (c)	I (d)	II (e)	(b)/(a)	(c)/(a)	(d)/(a)	(e)/(a)
0.11	15	2.0	2.5	15	27	0.13	0.17	1.00	1.77
0.28	33	10	14	36	73	0.30	0.33	1.09	2.22
0.33	38	13	19	41	86	0.34	0.39	1.08	2.27
0.39	45	16	25	48	101	0.36	0.44	1.07	2.25
0.56	63	26	44	69	147	0.41	0.56	1.10	2.33

I: Predicted by the proposed model

II: Predicted by equation (20)

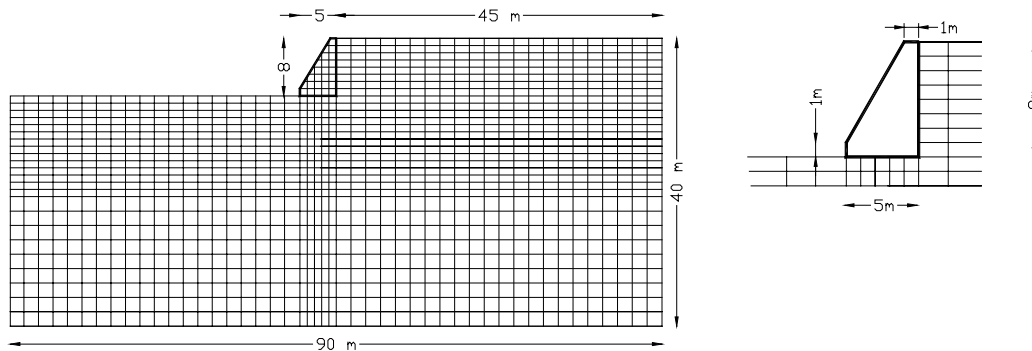


Figure 16. The configuration considered in the FEM elasto-plastic dynamic analyses by Modaressi and Lopez-Coballero (1998).

## 7. Conclusions

A multi-block sliding system model has been developed. Similarly to the Sarma (1979) stability method, a general mass sliding on a slip surface that consists of  $n$  linear segments is considered. In order for the mass to move, interfaces where resisting forces are exerted must be formed at the nodes of the slip surface. Thus, the mass is divided into  $n$  blocks sliding in  $n$  different inclinations.

To simulate slope movement when the displacement is large, the masses and lengths of each block are updated during calculations in terms of the distance moved. Furthermore, constitutive equations that simulate strength degradation along the slip surface coupled with the multi-block model are needed in order to simulate the triggering of the slides and predict accurately the seismic displacement. A constitutive model that predicts the continuous change of resistance along the slip surface due to build-up of pore pressures has been developed and implemented in the multi-block model.

On the other hand, gravity walls, as a result of the applied shaking, move outwards, away from the retained soil. Simplified analyses predicting the seismic displacement of gravity walls are based on the Mononobe-Okabe method and Newmark's sliding-block model. The configuration of the wall-backfill system is modeled, according to the multi-block methodology, using two bodies: (a) the wall that slides outward along the wall-foundation soil and (b) the wedge that slides downward along the plane of least resistance in the retained soil. The new method, unlike the previous, is kinematically compatible. It generally predicts similar critical acceleration for relative motion, but different seismic wall displacement.

The chapter first describes the multi-block model and its extensions for the prediction of the seismic displacement of landslides and gravity walls, outlined above. Then, it validates these methodologies by predicting the response of a well-documented earthquake-induced landslide and of gravity walls (a) measured in shaking-table tests and (b) computed by elaborate numerical analyses.

## Acknowledgements

This work was supported by (a) the European Commission, DG XII for Science, Research and Development (projects ENV4-CT97-0392 and GOCE-CT-2003-505448) and (b) the Hellenic Organization of Seismic Protection (OASP). The author wishes to thank Prof. S. Sarma, Prof. A. Modaressi, Mr Aris Stamatopoulos, Mr Stavros Aneroussis and Mr Petros Petridis who contributed in parts of the research work described in the chapter.

## References

- Ambroseys, N. and Menu, J. (1988). "Earthquake induced ground displacements, *Earthquake engineering and structural dynamics*, **16**, 7, 985-1006.
- Ambroseys N., Srbulov M. (1995). "Earthquake induced displacements of slopes," *Soil Dynamics and Earthquake Engineering*; **14**, pp. 59-71.
- Aubry, D., A., Modaressi, H., Modaressi, A. (1990). Constitutive model for cyclic behaviour of interfaces with variable dilatancy, *Computers and Geotechnics*, **9**, pp. 47-58.
- Aubry, D., Benzenati, I., and Modaressi, A. (1993). Numerical predictions for model No. 1, Verification of numerical procedures for the analysis of liquefaction problems. Arulanandan K. and Scott R. F. (editors), Balkema, Rotterdam, pp. 45-54.
- BRGM (French Geological Survey) Software (1998) "Cyberquake, Version 1.1", User's Guide", France.
- Dahlquist, G. and Bjorck, A., translated by Andeson, N. (1974) "Numerical methods", Prentice-Hall Inc., New Jersey.
- Dawson, E. M., Roth W.H., Drescher A. (1999) "Slope Stability Analysis by Strength Reduction", *Geotechnique*, **49**(6), pp 835-840.
- Foester E. and Modaressi H. (2001). Large motion assessment in soils under dynamic loading. *Fourth International Conference on Recent Advances in Geotechnical Earthquake Engineering and Soil Dynamics*, San Diego, California. (on CD, 6 pages)
- Gerolymos N. and Gazetas G. (2007). A model for grain-crushing-induced landslides - Application to Nikawa, Kobe 1995, *Soil Dynamics and Earthquake Engineering*; **27**, Iai, S. (2001). "Recent studies on seismic analysis and design of retaining structures", Fourth International Conference on Recent Advances in Geotechnical Earthquake Engineering and Soil Dynamics, San Diego, California, March 26-31.
- ITASCA Consultants (2005). FLAC (Fast Lagrangian Analysis of Continua), S. A. ,Version 5.0 .
- Kallou P.B., and Gazetas G., (2001). "Dynamic Analysis of Nikawa Landslide, Kobe 1995". *Proceedings of the 4 th Hellenic Conference on Geotechnical and Geoenvironmental Engineering*, Athens , Vol. 2, pp.171-178.
- Kramer S. (1996). *Geotechnical Earthquake Engineering*. Prentice-Hall, pp 438-447
- Kotta N., Tsamis V., Gazetas G. (1988). "Seismic Failure of Kalamata Harbour Quaywall", *Proceedings: First Hellenic Conference on Geotechnical Engineering*, Vol II, pp 117-122.
- Lopez-Caballero, F. and Modaressi, A. (2002). "Importance of site effects in seismic induced displacements of gravity walls", *12th European Conference on Earthquake Engineering*, Elsevier Science Ltd.

- Modaressi, A. and Lopez-Caballero, F. (2001). Final Report for the project "Seismic Ground Displacements as a tool for town planning, design and mitigation", Work performed by Ecole Centrale Paris, European Commission, DG12.
- Mononobe, N. and Matsuo, H (1924). "On the determination of earth pressures during earthquakes," *Proc., World Engineering Congress*, Vol. 9.
- Modaressi, H., Aubry, D, Faccioli, E., Noret, C. (1995). Numerical modelling approaches for the analysis of earthquake triggered landslides. Proceedings: *Third International Conference on Recent Advances in Geotechnical Earthquake Engineering and Soil Dynamics*, April 2-7, Volume II, St. Louis, Missouri.
- Modaressi, A., and Lopez-Caballero, F. (2001). Global methodology for soil behavior identification and its application to the study of site effects. *Proceedings: Fourth International Conference of Recent Advances in Geotechnical earthquake engineering*, San Diego, California, March (CD-ROM).
- Modaressi, A. (1998). Second Progress Report, performed under the grant of the European Commission Project ENV4-CT97-0392, November.
- Newmark, N. M. (1965). "Effect of earthquakes on dams and embankments", *Geotechnique*, Vol. 15, No. 2, London, England, June, pp. 139-160.
- Nishimura Y., Fukui S., Sato M., Kurose H. (1995). "Shaking table tests and numerical simulation of seismic response of the seawall", *Proceedings, Third Int. Conf. On Recent Advances in Geotechnical Earthquake Engineering and Soil Dynamics*.
- Okabe, S. (1926). "General Theory of earth pressures," *J. of Japan Society of Civil Engineering*, Vol.12, No.1.
- Papadimitriou A., Bouckovalas G., Dafalias Y. (2001). Plasticity model for sand under small and large cyclic strains. *Journal of Geotechnical and Geoenvironmental Engineering, ASCE*; Vol.127, No. 11, pp. 973-983.
- Richards, R. and Elms, D. (1979). "Seismic behaviour of gravity retaining walls," *Journal of the Geotechnical Engineering Division, ASCE*, Vol. 105, No GT4, pp. 449-464.
- Stark, T.-D., Contreras, I.-A. (1998) Fourth Avenue Landslide during 1964 Alaskan Earthquake. *Journal of Geotechnical and Geoenvironmental Engineering*, Vol. 124, No. 2, pp. 99-109.
- Sarma S.K. and Chlimitzas G. (2001a) Co-seismic & post-seismic displacements of slopes, 15th ICSMGE TC4 Satellite Conference on "Lessons Learned from Recent Strong Earthquakes", 2001, 25 August, Istanbul, Turkey
- Sarma, S. K. and Chlimitzas, G. (2001b) Analysis of seismic displacement of slopes using multi-block model. Final report performed under the grant of the European Commission Project ENV4-CT97-0392, 2001, January.
- Sarma S.K. (1979). Stability analysis of embankments and slopes. *Journal of Geotechnical Engineering ASCE*; Vol.105, No. 12, pp. 1511-1524.
- Sarma, S.K. (1975). Seismic Stability of Earth Dams and Embankments", *Geotechnique*, Vol. 25, No. 4, pp.743-761
- Sarma S. K. , Tan D. (2006). Determination of critical slip surface in slope analysis *Géotechnique*, Vol 56, No 8, pp 539 - 550.
- Sarma, S. K. (1999). "Seismic slope stability - The critical acceleration", *Proceedings of the Second International Conference on Earthquake Geotechnical Engineering*, Balkema, Lisbon, 1999, pp. 1077-1082.

- 
- Sassa, K., Fukuoka, H., Scarascia-Mugnozza, G., Evans, S. (1996) "Earthquake-induced landslides: Distribution, motion and mechanisms" Special Issue of Soils and Foundations, *Japan Geotechnical Society*, pp. 53-64.
- Sassa, K., Fukuoka, H., Sakamoto, T. (1995). The rapid and disastrous Nikawa landslide," *Landslide News*, No. 9, pp 6-9.
- Stamatopoulos, C. A. (1996). Sliding System Predicting Large Permanent Co-Seismic Movements of Slopes. *Earthquake Engineering and Structural Dynamics*, Vol. 25, No, 10, pp 1075-1093.
- Stamatopoulos C. (1992). Analysis of a slide parallel to the slope. *Proc. 2nd Greek National Conference of Geotechnical Engineering*. Vol. 1, pp. 481-488. (in Greek)
- Stamatopoulos C., Velgaki E., and Sarma S. (2000) "Sliding-block back analysis of earthquake induced slides". *Soils and foundations, The Japanese Geotechnical Society*, Vol. 40, No. 6, pp 61-75.
- Stamatopoulos, C. A., Stamatopoulos A. C., Aneroussis S. and Velgaki, E. G., (2001). Final Report for the project "Seismic Ground Displacements as a tool for town planning, design and mitigation", Work performed by Kotzias-Stamatopoulos Co., European Commission, DG12.
- Tika, T.-E., and Hutchinson, J.-N (1999). Ring shear tests on soil from the Vaiont landslide slip surface, *Geotechnique*, pp. 59-74.
- Vucetic, M. and Dobry, R. (1991). "Effect of soil plasticity on cyclic response, *Journal of the Geotechnical Division, ASCE*, 117 (1).



*Chapter 3*

## GEOTECHNICAL SEISMIC ISOLATION

*Hing-Ho Tsang*\*

Department of Civil Engineering, University of Hong Kong,  
Pokfulam Road, Hong Kong, China

### Abstract

Traditionally, seismic isolation is a flexible or sliding interface positioned between a structure and its foundation for the purpose of decoupling the motions of the ground from that of the structure. In recent years, novel seismic isolation methods have been proposed, in which the flexible or sliding interface is in direct contact with geological sediments and the isolation mechanism primarily involves geotechnics.

Smooth synthetic liners have been proposed beneath foundations or between soil layers for dissipating seismic energy through sliding. Rubber-soil mixtures have also been proposed around foundations for absorbing seismic energy with a function similar to that of a cushion. The low cost of these proposed seismic isolation methods can greatly benefit developing countries where resources and technology are not adequate for earthquake mitigation using well-developed, yet expensive, techniques.

In this chapter, the background and principles of these new methods will be introduced, followed by the latest research findings. Potential problems and further research directions will be identified and discussed.

### Introduction

A large proportion of the world's population is living under the threat of earthquakes. In the past century, earthquakes have killed an average of over 20,000 people a year throughout the world, with 90% of fatalities occurring in developing countries. It is impossible to prevent earthquakes from occurring, but it is possible to mitigate the disastrous effects of strong earthquake shaking in order to save lives and properties.

---

\* E-mail address: [tsanghh@hku.hk](mailto:tsanghh@hku.hk). Fax: +852 2559 5337

In conventional earthquake resistant design, ductile capacity is provided by proper design and construction of structural members, some of which are expected to experience inelastic deformation. Hence, extensive damage can result in enormous repair costs. In contrast, seismic isolation aims at reducing seismic loads induced by earthquake excitations, which can greatly minimize the damage induced in a structure, and hence save on costs of repair.

### Overview of Seismic Isolation System

A seismic isolation system is defined as a flexible or sliding interface positioned between a structure and its foundation, for the purpose of decoupling the horizontal motions of the ground from the horizontal motions of the structure, thereby reducing earthquake damage to the structure and its contents (Taylor and Igusa, 2004), as shown in Figure 1. Various mechanisms of this type have been invented over the past century, including those using rollers and layers of sand. For example, a building in China with a sand layer between the foundation and the building has been built (Lee, 1987).

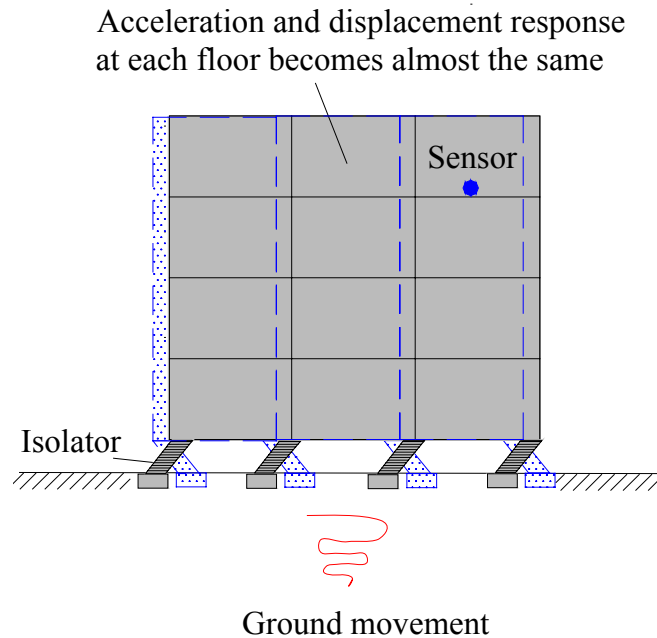


Figure 1. Schematic description of a seismic isolation system.

The early development of seismic isolation involving the use of bearings can be dated back to the late 1960's in New Zealand. The concept was considered to be very impractical by most structural engineers in those days. Nowadays, it has become a major technique in earthquake resistant design protecting human lives in the world (Kelly, 1998a; Martelli and Forni, 1998; Fujita, 1998; Robinson, 2000; Zhou, 2001). Comprehensive reviews of research and development of seismic isolation methods can be found in Buckle and Mayes (1990), Skinner *et al.* (1993), Jangid and Datta (1995), Robinson (1996), Kelly (1998b), and Naeim and Kelly (1999).

Rubber has been used as a base bearing over the past three decades. Laminated rubber bearings (refer Figure 2) are currently the most commonly adopted system due to the strength requirement in the vertical direction to support the full weight of the building. Another type of seismic isolation technique is typified by a sliding system (refer Figure 3), such as the friction-pendulum system, which limits the transfer of shear across the isolation interface. Nowadays, due to the high cost of implementation, these base isolation techniques are only applied in structures with critical or expensive contents.

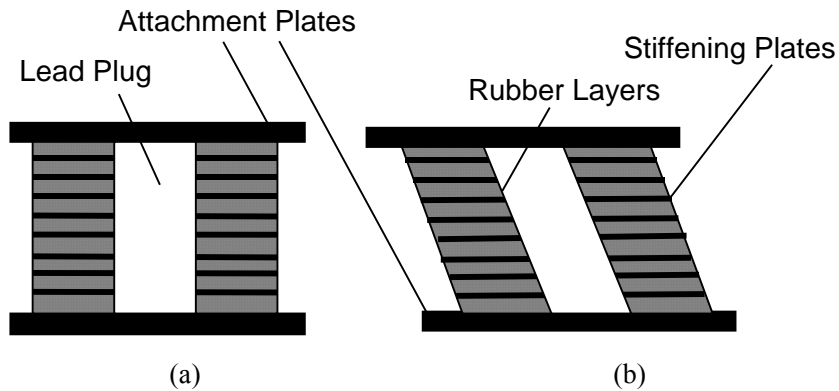


Figure 2. A typical laminated rubber bearing.

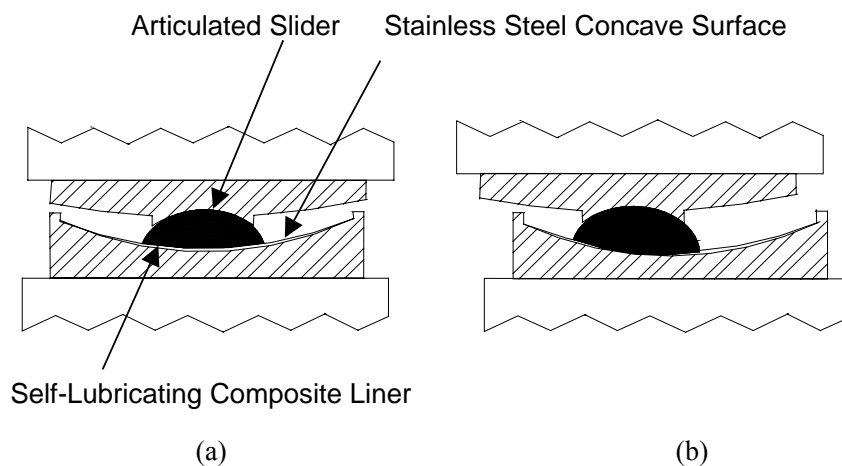


Figure 3. A typical spherical sliding bearing.

### Seismic Isolation for Developing Countries

Earthquakes have been causing unacceptably large numbers of deaths and injuries in developing countries. Bozorgnia and Bertero (2004) stated, “*The international earthquake engineering community is facing a major challenge of improving the knowledge and practice in developing countries with the goal of reducing the seismic risks to socioeconomically acceptable levels. Ensuring life safety is the thrust of this goal. This is a grand challenge for*

*industrialised countries in particular to find a way to help developing countries to achieve the modern goal of earthquake engineering, especially reduction in loss of lives.”*

There is an increasing interest in applying seismic isolation technology to public housing, schools and hospitals in developing countries where the replacement costs due to earthquake damage could be significant. United Nations Industrial Development Organization (UNIDO) has been instrumental in developing low-cost seismic isolation systems using natural rubber-based bearings for the protection of housing and other structures in earthquake-prone developing countries, including Egypt (UNIDO, 1993), India (UNIDO, 1994) and Indonesia (UNIDO, 1995). For any innovative system to be widely adopted in those countries, it must be cost-effective and technically efficient.

Efforts have been put in to develop low-cost base isolation systems for developing countries (Kelly, 2002), and several demonstration projects are in place in countries such as Indonesia (Taniwangsa and Kelly, 1996) and the People’s Republic of China (Kelly, 1994). A new kind of base isolator made from high-damping natural rubber has been developed. For example in Chile, apartment buildings with this kind of low-cost seismic isolator have been constructed (De la Llera *et al.*, 2004).

On the other hand, there is a patented method for using rubber for seismic isolation, in which the whole used tire, filled with a particular rock aggregate, is utilized as the bearing (Lang and Sargent, 2005). Aimed at providing low-cost seismic protection for residential buildings in developing countries and economically distressed areas within the United States, this invention is a very convenient method as it requires minimal treatment of scrap tires. Experimental results showed that the acceleration response of a structure with short natural period could be reduced by more than 70%. However, one potential problem is that the structure has to be detached from the ground, which is impractical for small residential houses. The feasibility of this method for large structures is also doubtful.

## **New Seismic Isolation Methods**

In recent years, novel seismic isolation methods have been proposed, of which the flexible or sliding interface is in direct contact with geological sediments and the isolation mechanism primarily involves geotechnics. For example, Kim and Konagai (2001) has proposed a method of covering a tunnel lining with a soft and thin coating for reducing deformation under earthquake shaking.

Additionally, there are two recently proposed distinctive and promising methods. Smooth synthetic liners have been proposed underneath the foundation of structures or between soil layers for dissipating seismic energy through sliding (Yegian and Kadakal, 2004; Yegian and Catan, 2004); and rubber-soil mixtures (RSM) have been proposed around the foundation of structures for absorbing seismic energy and exerting a function similar to that of a cushion (Tsang, 2008). The low cost of these proposed seismic isolation methods can greatly benefit developing countries where resources and technology are not adequate for earthquake mitigation using well-developed, yet expensive, techniques.

The aforementioned seismic isolation methods involving geotechnics could be collectively named “*Geotechnical Seismic Isolation*”, in contrast to the commonly used “*Structural Seismic Isolation*”. In the following sections, the background and principles of the two new geotechnical methods will be introduced, followed by the latest research findings.

For newly proposed technologies, it is reasonable that some hidden problems may exist and it is essential to carefully evaluate, investigate and criticize the proposed methods. Potential problems related to the concept and feasibility of the proposed seismic isolation methods, as well as further research directions, will be identified and discussed.

## Seismic Isolation by Geosynthetics

Sliding systems are one of the most common types of seismic isolation systems adopted in practice. Based on friction, these systems are designed such that transmission of shear forces is limited to a particular level, beyond which sliding occurs and further transmission is prohibited. Despite their effectiveness in limiting the damage caused by earthquake excitations, conventional base isolators are too expensive such that their use in seismic protection is not widespread.

Analogous to sliding systems, the new concept of utilizing geosynthetics as base isolation evolved in the early 1990's with the advancement in research on dynamic interface properties between geosynthetics. Yegian and Lahlaf (1992) demonstrated the idea by conducting shaking table tests on two sheets of smooth geomembrane and the test results showed that the shear force transmitted from one geomembrane to another was limited. The research program was then expanded and two possible schemes were proposed (Yegian and Kadakal, 2004; Yegian and Catan, 2004). The first one, which can be referred to as *foundation isolation*, involves the placement of the synthetic liner immediately underneath the foundations of a structure. The other approach is *soil isolation*, in which the liner is placed within the soil at some depth below the foundations so as to prevent seismic energy from reaching the building or the ground surface. These two concepts are shown schematically in Figures 4 and 5 respectively. Relying on the low friction coefficient of the interface between two synthetic liners, the two similar yet distinct concepts aim to dissipate earthquake energy through slip deformations along the liner interface and thus reduce the magnitude of accelerations transmitted to the structure.

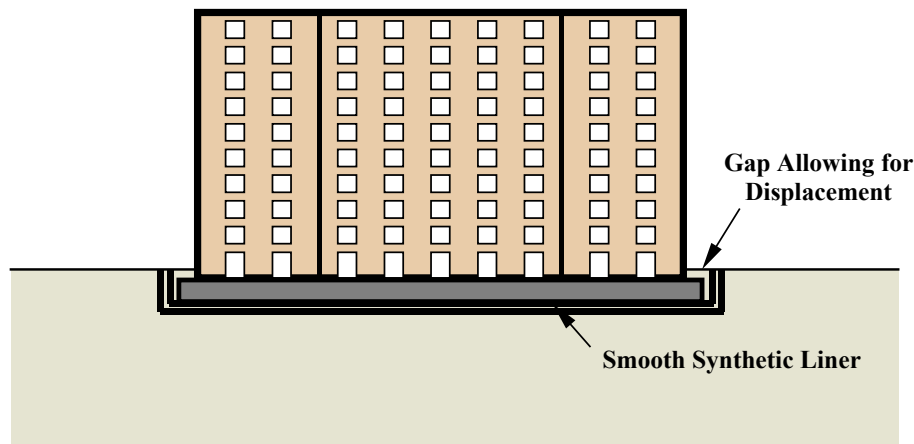


Figure 4. Schematic drawing of foundation isolation using smooth synthetic liner (Yegian and Kadakal, 2004).

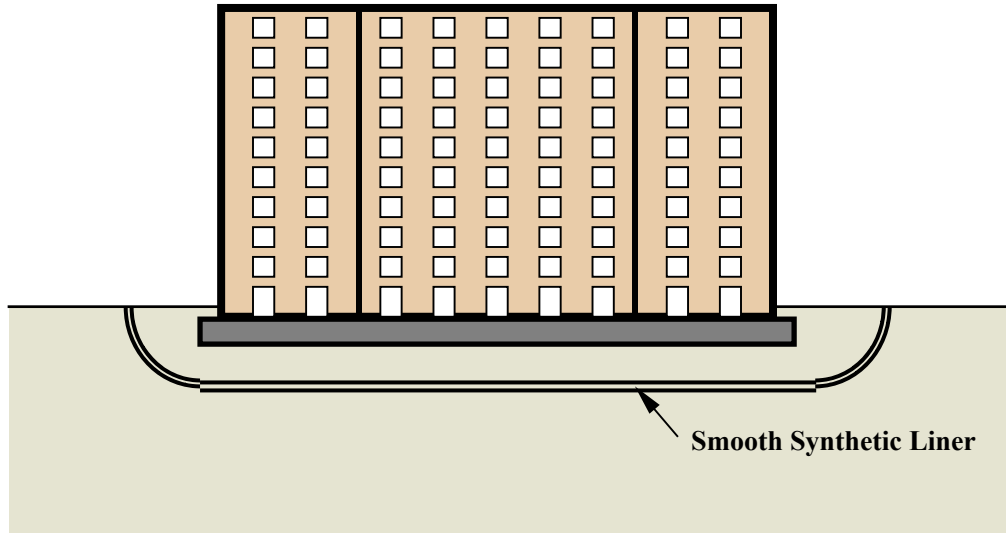


Figure 5. Schematic drawing of soil isolation using smooth tub-shaped synthetic liner (Yegian and Catan, 2004).

### **Selection of Suitable Geosynthetic Liners**

The selection of suitable types of geosynthetics is critical to the implementation of the proposed isolation schemes. Yegian and Kadakal (2004) suggested using materials with low friction coefficients to minimize the acceleration transmitted through the interface. Slip displacements induced by seismic loads should also be minimal to prevent any damage to the structure and utilities.

To investigate their suitability as base isolators, four different interfaces including geotextile/HDPE (high density polyethylene), PTFE/PTFE (polypropylene), UHMWPE/UHMWPE (ultrahigh molecular weight polypropylene) and geotextile/UHMWPE were selected and tested using cyclic load tests (Yegian and Kadakal, 2004). In the cyclic load tests, the influence of normal stress, number of cycles and sliding velocity on the friction coefficients of the chosen interfaces was explored. The results indicated that the geotextile/UHMWPE interface was the most promising given that its friction coefficient was the smallest and the magnitude varied very slightly with different loading conditions.

### **Investigations of Foundation Isolation**

Cyclic load experiments could only provide information about the variation of friction coefficients of geosynthetic interfaces but not the dynamic response of the liners. Therefore, shaking table tests were conducted on the geotextile/UHMWPE interface in order to determine permanent deformations and transmitted accelerations under dynamic loads.

The feasibility of foundation isolation was first investigated. By placing a rigid block on the synthetic liner and allowing sliding along the fixed UHMWPE sheet, variations of transmitted accelerations and slip displacements with excitation frequency were examined. From Figure 6, it was discovered that under harmonic excitations, sliding was initiated when the table

acceleration was beyond around  $0.11g$ , implying a static friction coefficient of  $0.11$ . After the table acceleration exceeded  $0.11g$ , the transmitted acceleration was maintained at around  $0.08g$  regardless of frequency, indicating a dynamic friction coefficient of  $0.08$ . Moreover, larger slip displacements were resulted from lower excitation frequencies (Figure 7).

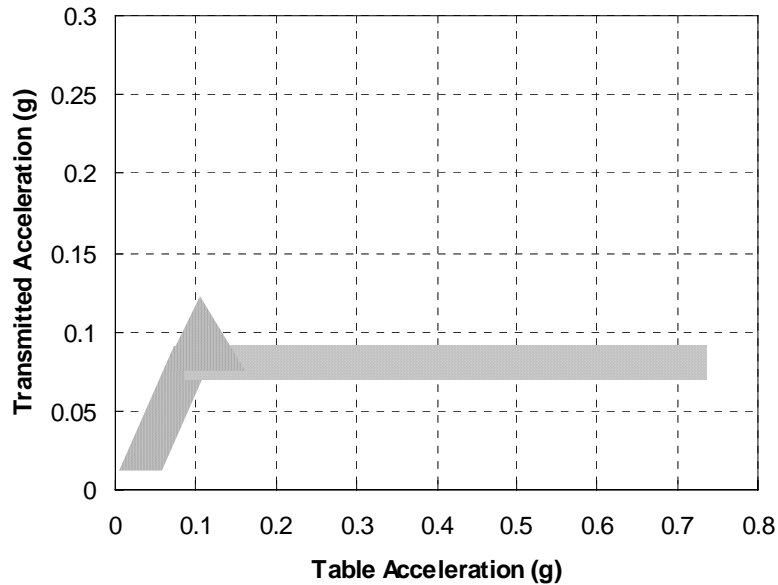


Figure 6. Variation of transmitted acceleration with table acceleration from rigid block tests on geotextile/UHMWPE interface under harmonic excitations (Yegian and Kadakal, 2004).

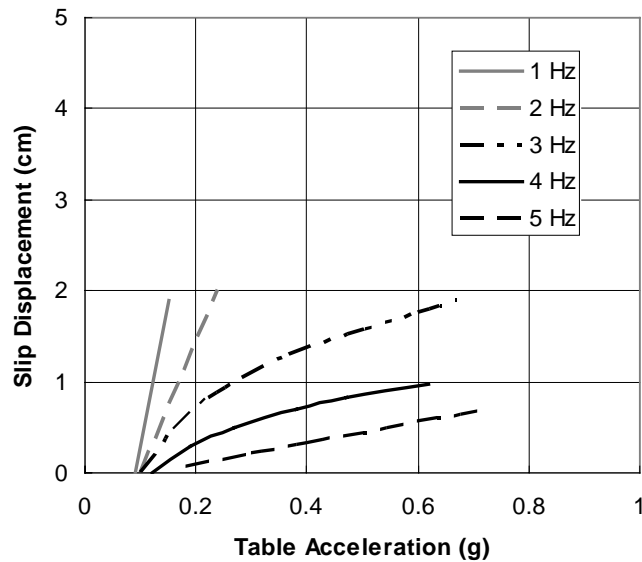


Figure 7. Variation of slip displacement with table acceleration from rigid block tests on geotextile/UHMWPE interface under harmonic excitations (Yegian and Kadakal, 2004).

To simulate the response under more realistic transient motions, the rigid block tests were repeated using earthquake excitations. Three earthquake records with different frequency bands were chosen for the table motions, namely the Corralitos, Capitola, and Santa Cruz records of the 1989 Loma Prieta Earthquake. In general, the results obtained had the same trend as those of harmonic excitations. It is likely that the geotextile/UHMWPE interface is a suitable liner for foundation isolation.

In reality, due to the inertial forces induced by upper storey masses, the dynamic response of a structure is much more complicated than those obtained from cyclic load tests and rigid block tests. For this reason, a simple single-storey building model was constructed and tested using shaking table tests. Figure 8 shows the comparison of the peak drift (distortion of columns) of the fixed-base and foundation-isolated models as a function of the peak acceleration of the three earthquake records. It was noted that the peak drift of the model with foundation isolation was almost constant and much smaller than that without isolation, resulting in a large reduction in column shear forces induced by an earthquake. Similar to rigid block tests, lower excitation frequencies produced greater peak-to-peak (maximum slip during shaking) and permanent slip displacements (slip at the end of shaking) in the foundation-isolated model.

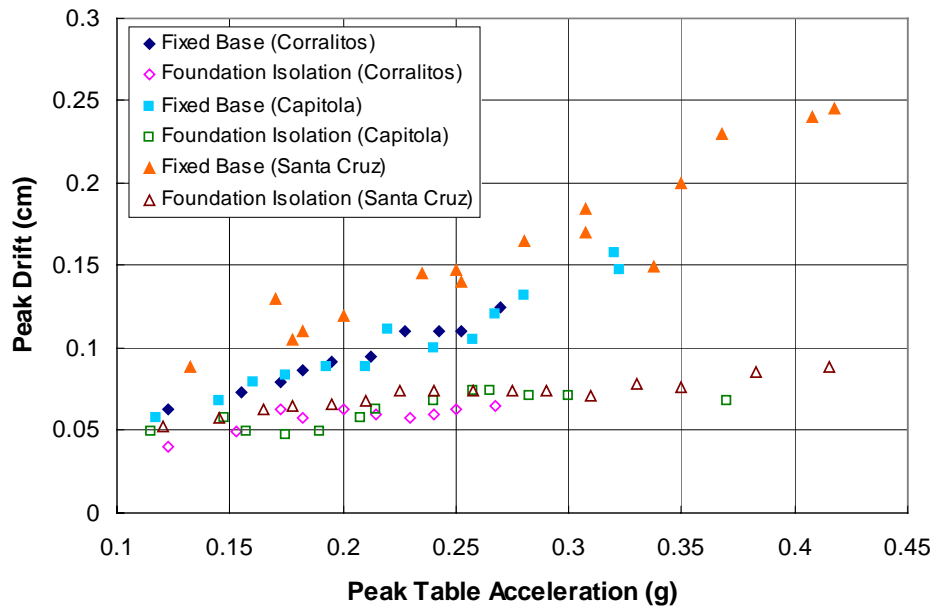


Figure 8. Comparisons of peak drifts from fixed-base and foundation-isolated structure under earthquake excitations based on Corralitos, Capitola, and Santa Cruz records (Yegian and Kadakal, 2004).

Since permanent slip displacements can cause damage to the isolated building and its surroundings, it is essential to reduce permanent slips by introducing a restoring system. To investigate the effect of a restoring force, steel springs were attached to the base of the single-storey model and shaking table tests were carried out using earthquake excitations stated

above. The results demonstrated that the use of the restoring spring significantly reduced the amount of permanent slip while the effect of foundation isolation was not affected. However, more research is required to determine a suitable restoring system for foundation isolation.

### Investigations of Soil Isolation

Soil isolation is another seismic isolation method utilizing geosynthetics, in which the soil layer above the liner is isolated from the underlying soil deposits. The scope of application of soil isolation is potentially wider than foundation isolation and it can be extended to the construction of reclaimed land, slopes and embankments.

To minimize permanent slips along the synthetic liner after an earthquake, it was proposed to place the liner in a curved manner instead of placing it horizontally so that a restoring gravitational force could bring the isolated soil back to its original position after sliding. Two different shapes of the geotextile/UHMWPE liner were investigated by Yegian and Catan (2004), namely the cylindrical-shaped (Figure 9) and the tub-shaped liners (Figure 5). Shaking table experiments were performed on the liners to explore their effectiveness as soil isolation.

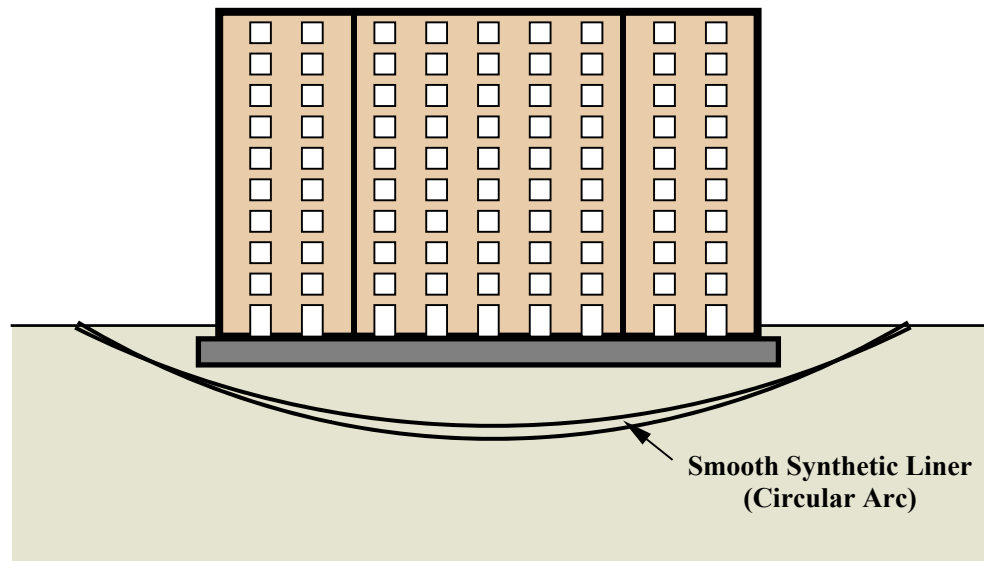


Figure 9. Schematic drawing of soil isolation using cylindrical-shaped synthetic liner (Yegian and Catan, 2004).

For the cylindrical-shaped liner, the shaking table test results showed that the isolated sand layer experienced pure rotation as a rigid block. From Figure 10, the friction coefficient obtained in the harmonic tests ( $0.18g$ ) was larger than that of a horizontal liner due to the curved shape of the liner and the side friction in the system. Similar to foundation isolation, the transmitted acceleration was independent of frequency. However, a slight increase in the transmitted acceleration was noted with an increase in table acceleration. To find out the amount of permanent slips, the shaking table was excited using records of the 1989 Loma

Prieta Earthquake (East-West component) and the 1994 Northridge Earthquake (East-West component). It was observed that permanent slips were almost zero, proving that the curved liner shape was effective to provide a restoring force.

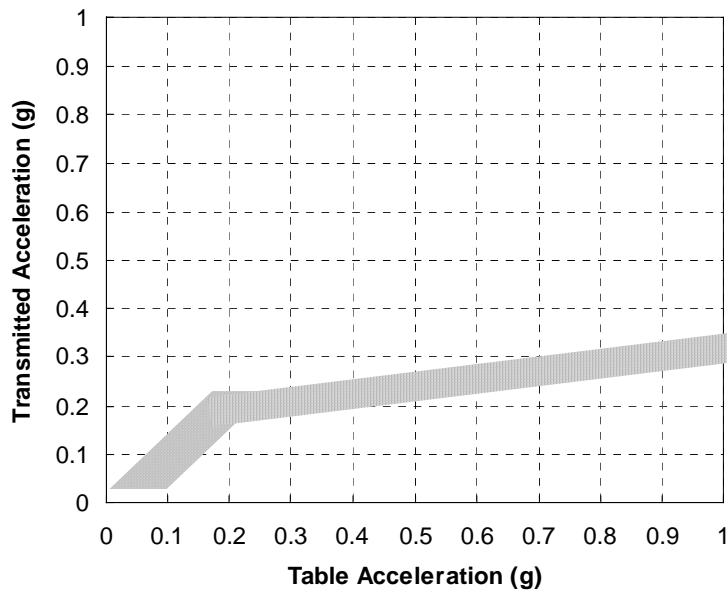


Figure 10. Variation of transmitted acceleration with table acceleration from shaking table tests using cylindrical-shaped liner under harmonic excitations (Yegian and Catan, 2004).

Nevertheless, the installation of a cylindrical-shaped liner might not be practical in field applications. A tub-shaped liner with the central part placed horizontally was thus proposed, and the shaking table tests were repeated using this alternative shape of the liner. As observed in the tests using harmonic and earthquake-based excitations, the transmitted accelerations in the central part of the isolated soil were much smaller than the table acceleration, but the transmitted accelerations measured near the edges were considerably larger than those in the middle due to edge effects. Such differences in strains led to the formation of failure lines on the sand surface. On the other hand, permanent slips induced by earthquake excitations were almost zero, indicating that a restoring effect could still be provided.

Georgarakos *et al.* (2005) further examined the optimal geometry of the synthetic liner using an analytical approach. Among the proposed liner geometries, apart from the cylindrical liner, the compound trapezoidal shape was found to be the most effective. As shown in Figure 11, the basic geometry of this liner was trapezoidal with a side angle of  $60^\circ$ . In view of the formation of cracks in the soil above the tub-shaped liner, the middle core of the isolated soil (in the form of a truncated pyramid) was compacted or reinforced, whereas the space between the core and the non-isolated free-field soil was filled with soil of lower stiffness. The same synthetic liner was also inserted between the core and the lower stiffness soil. From the dynamic analyses, it was discovered that the decrease in transmitted acceleration was substantial and a restoring force was supplied to the system through the movement of loose soil at both sides to reduce permanent slip. Furthermore, no local failure zones were found.

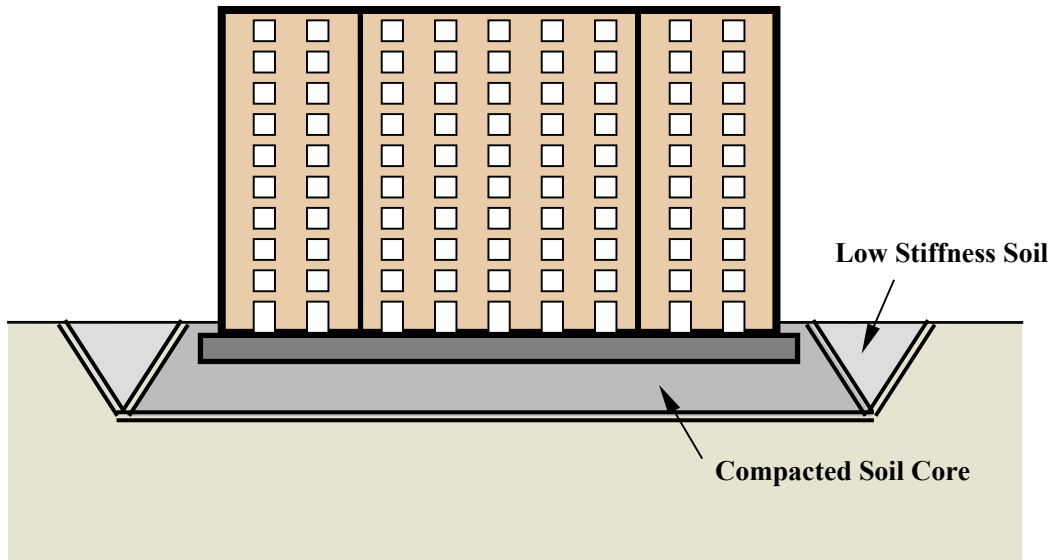


Figure 11. Schematic drawing of soil isolation using trapezoidal synthetic liner with reinforced core (Georgarakos *et al.*, 2005).

## Discussion on Seismic Isolation by Geosynthetics

### Soil-Geosynthetic Interaction

In the case of soil isolation, it is essential to ensure that the bond between the soil and the synthetic liner is sufficient so that the relative displacement between the liner and the soil in direct contact with the liner can be minimized. In other words, the soil mass should be prevented from sliding over the geosynthetic and the pulling out of the liners from the soil should be avoided. Traditionally, the interface friction in these two situations is checked by the direct shear test and the pullout test respectively.

The frictional resistance of soil-geosynthetic interfaces varies with different types of soil and geosynthetic as well as the texture and condition of geosynthetic. Ling *et al.* (2002) measured the friction angle between a PVC geomembrane and three different kinds of sand using tilting table tests, and the value obtained ranged from about  $32^\circ$  to  $40^\circ$ . Pullout tests conducted by Perkins and Cuelho (1999) between gravel and a geotextile indicated that the peak friction angle varied from  $37^\circ$  to  $53^\circ$ . On the other hand, the static friction angle between a typical geotextile and a smooth HDPE geomembrane was measured to be  $10.7^\circ$  (Yegian and Lahlaf, 1992). Regardless of the type of tests and the differences in the kind of soil and geosynthetics, the frictional resistance between a soil and a geosynthetic is generally greater than that between two geosynthetic sheets, implying that sliding between the soil and the liner is not likely to happen.

## Creep and Stress Relaxation

Creep refers to the time-dependent elongation of a material when subjected to a sustained load, whereas stress relaxation implies a reduction in stress under constant strain. Since synthetic liners manufactured from polymers are viscoelastic materials, they are susceptible to both creep and stress relaxation, which can affect the performance of geosynthetics under service conditions.

Creep is an important factor to consider when geosynthetics are designed for a long service life, of say 50 years. The creep rate of geosynthetics is dependent on temperature: Higher temperatures result in greater creep rates, producing larger strains to rupture the synthetic liner. The level of load exerted on the polymer can also affect the creep rate (Greenwood and Myles, 1986; Mikki *et al.*, 1990). Under the same confining pressure, the larger the creep load, the greater the amount of creep (Chang *et al.*, 1996). On the other hand, for constant creep load, creep decreases with an increase in confining pressure. McGown *et al.* (1982) reported that creep of non-woven geotextiles is reduced under confinement in soil. A possible reason for this phenomenon is the significant increase of frictional resistance between the geotextile and the soil. Therefore, for the case of soil isolation, it can be deduced that creep of synthetic liners would not be excessive in static conditions provided that non-woven geotextiles are used.

It is also essential to examine the cyclic creep behaviour of geosynthetics used for seismic isolation. For both woven and non-woven geosynthetics, creep strain generally increases with an increase in the number of load applications (Kabir and Ahmed, 1994). However to date, very few discussions on the cyclic creep response can be found. It is necessary to conduct more research on this subject.

A synthetic liner placed below buildings may also be subjected to stress relaxation, especially when there is a soft soil layer underneath (Paulson, 1987). Once most of the settlement occurs, strain experienced by the basal geosynthetics would tend to be constant. As a result, there may be loss of tensile stress within the liner. However, the soil layer under the liner gains strength through consolidation and is therefore able to offer greater resistance to failure.

## Installation

Previous experience indicates that many failures associated with the use of geosynthetics are related to construction and installation (Shukla, 2002). One major problem is the loss of strength due to damage and ultraviolet exposure.

Being relatively delicate construction materials, geosynthetics are prone to damage during installation, such as cuts, tears and punctures, which can adversely affect the functionality of geosynthetics during their service life. The frequency of defects can be minimized through appropriate construction measures. For example, before placing any synthetic liner, large angular soil particles and tree branches should be removed on site to prevent any damage. For the method of soil isolation, care must also be taken when spreading and compacting soil layers above the polymer liner to avoid any unnecessary damage. It may not be practical to adopt such isolation schemes on rocky grounds.

Synthetic liners are also vulnerable to ultraviolet attack. To prevent premature degradation, all the rolls of geosynthetics should be shielded from sunlight before use and they should be wrapped with opaque materials if possible.

### **Water Infiltration**

For the method of soil isolation, a synthetic liner composed of a geotextile and a geomembrane is placed within the soil at some depth below the foundation. If the soil above the liner is not compacted properly, it would be permeable enough to allow water to infiltrate into the soil. However, due to the impermeable geomembrane underneath, water can be trapped within the soil mass which is bounded by the liner, causing the so-called “bathtub” effect. Rapid premature failure may thus be resulted in the overlying soil. It is recommended that soil above the liners be compacted to its maximum possible density and drainage be installed around the isolated soil to minimize water infiltration.

### **Effects on the Surrounding**

In order to allow relative displacements between the superstructure and the ground during an earthquake, both foundation isolation and soil isolation require a clearance (called “seismic gap”) around protected structures throughout the service life of the isolation system. It may not be feasible, or even impossible, to adopt such seismic isolation schemes in heavily constructed areas with high density of superstructures and underground utilities due to lack of space for such a clearance to be provided. Wherever foundation isolation or soil isolation is applicable, it should be ensured that the system does not damage and collide with the surrounding structures and utilities. Special design may also be necessary in some situations to enable the use of these seismic isolation methods. For example, the synthetic liners buried within the slope should be protected from horizontal soil pressure which can adversely affect the performance of the isolation system.

### **Endurance**

Due to the polymeric nature of geosynthetics, the synthetic liner used as foundation isolation or soil isolation is prone to attacks of various sources including ultraviolet, radioactivity, oxidation, as well as organisms and chemicals in soil. Most of these degradation mechanisms adversely affect the long-term performance of geosynthetics through polymeric chain scission or bond breaking within the polymer structure. Certain properties of geosynthetics may also be altered by changes in the surrounding temperature.

#### **1. Ultraviolet**

Natural sunlight containing ultraviolet can cause degradation of geosynthetics by penetrating the polymer structure and breaking the bonds within the structure. This phenomenon is more severe in geotextiles than geomembranes due to the difference in the nature of their constituents. However, the liner used for seismic isolation is either placed under buildings or

buried within the soil strata, without being exposed to sunlight. Moreover, during manufacture of geosynthetics, carbon black or pigments are often introduced to screen the polymer structure from ultraviolet rays. As long as the synthetic liners are carefully handled and shielded from sunlight before placement, ultraviolet degradation is not a concern.

## **2. Radioactivity**

Although there is very little discussion on radioactive degradation in the literature, it is likely that radioactivity greater than  $10^6$  to  $10^7$  rads can cause polymer chain scission (Koerner, 1998). This is certainly not a problem for greenfield land, but care must be taken when dealing with brownfield sites especially when little is known about how they are used in the past. Before construction and installation of synthetic liners on brownfields, ground investigation specific to the site should be conducted to ensure that the level of radioactive waste is minimal.

## **3. Oxidation**

Unlike other mechanisms, oxidation of geosynthetics is unavoidable. As the synthetic liner is usually placed at shallow depths and thus likely to be in contact with unsaturated soil, oxygen in the air voids can react with a free radical created on a carbon atom in the polymer chain to form a hydroperoxy radical, which will further react with another polymer chain to give a new free radical. This kind of chain reaction will continuously cause chain scission of the polymer structure and eventually degrade the liner. Peggs *et al.* (1989) recorded that a non-woven polypropylene geotextile exhumed after 12-13 years of service showed a small amount of oxidation in the polypropylene fibres under scanning electron microscopy (SEM). Nevertheless, the oxidation process normally takes hundreds of years to complete, far longer than the service life of the polymer products. Antioxidants can also be added to the liners to help retard degradation.

## **4. Living Organisms**

Since there are numerous living organisms in the soil, it is important to consider the biological resistance of the synthetic liner. Geosynthetics are relatively vulnerable to attacks of burrowing animals, fungi and bacteria. In contrast with the above factors, living organisms do not cause polymeric degradation of synthetic liners but the loss of functionality. There are not any established test methods to evaluate the degree of damage caused by burrowing animals, but it is intuitively believed that geosynthetics harder than the animals' teeth or claws have a better resistance to animal attack. As for fungi and bacteria, the concern lies on the possible clogging of geotextiles due to their huge population, restricting seepage flow and resulting in soil failure.

## **5. Chemicals**

Unavoidably there are various chemicals including acids, salts and heavy metals in the soil. However, as the synthetic liner in the application of seismic isolation will not be constantly attacked by a large concentration of chemicals, chemical resistance is not as important as that

in landfill sites. Polypropylene (PP), the most common raw material of geotextile, has good chemical and pH range resistance. Common polymers for geomembranes such as polyvinyl chloride (PVC), chlorosulfonated polyethylene (CSPE) and polyethylene (PE) are also resistant to most organic solvents and chemicals (Vandervoort, 1992), with PE having the best chemical resistance. In addition, polymers of higher density have better chemical resistance. If chemical resistance is a concern in a particular site, geomembranes manufactured from HDPE (high-density polyethylene) can be adopted.

## 6. Thermal Effects

Both high and low temperatures may affect the performance of geosynthetics. Heat can cause changes in physical, mechanical and chemical properties of synthetics liners. The extent of such changes should be assessed before installation to ensure the liners will not deform excessively during the service life. On the contrary, there is no adverse effect on geomembranes to cyclic cold temperatures. Although ice may cause puncturing and tearing problems, a thick needle-punched non-woven geotextile placed above the geomembrane can act as a cushion and provide sufficient puncture resistance.

If the polymeric liner is placed where temperature difference is large, thermal expansion and contraction should be allowed for. For example, slack as significant as 50mm should be added for every 10m during the installation of a HDPE liner to accommodate a temperature change of 40°C (Koerner, 1998).

## Seismic Isolation by Rubber-Soil Mixtures

This section introduces an alternative geotechnical seismic isolation scheme using rubber-soil mixtures (RSM). Firstly, the background and principles of this new method will be introduced. It will then be followed by a review of the mechanical and dynamic properties of RSM. Results of a series of numerical simulations will also be presented to demonstrate the effectiveness and robustness of the proposed system. Finally, a number of important issues regarding the concept and feasibility of the proposed method will be identified and discussed.

### Principle

The proposed method is shown schematically in Figure 12. The building structure has a typical dimension [10-storey and 40 m width ( $w$ )] of a residential or office building. Surrounding the footing of a low-rise building, a layer of soil was replaced by soil mixed with a designated proportion of rubber (i.e. RSM) of thickness ( $t$ ) in the order of 10 m. For high-rise building, RSM layer could be placed around the pile cap.

The rationale of this method can be explained by fundamental wave theory [refer Tsang (2008) for details], in which transfer function  $\mathbf{T}(f)$  can be defined to describe the ratio of displacement amplitudes at any two points in the RSM layer. In this case, the transfer function is given by choosing the two points to be the top (surface) and bottom (top of halfspace) of the RSM layer. The ratio between transfer functions of placing RSM and pure sand, respectively, as the overlying material, has been plotted in Figure 13, which was

obtained from the two-dimensional finite element modeling for the **Reference** scenario to be presented in later sub-section. This ratio would be exactly the same as that between the *Fourier* amplitude spectrum (*FAS*) which describes the frequency content of the respective ground motion. The potential of the proposed method can be demonstrated in Figure 13 that only a narrow bandwidth of seismic waves (at around 1–2 Hz) would be amplified, while significant reduction can be seen for other frequency ranges.

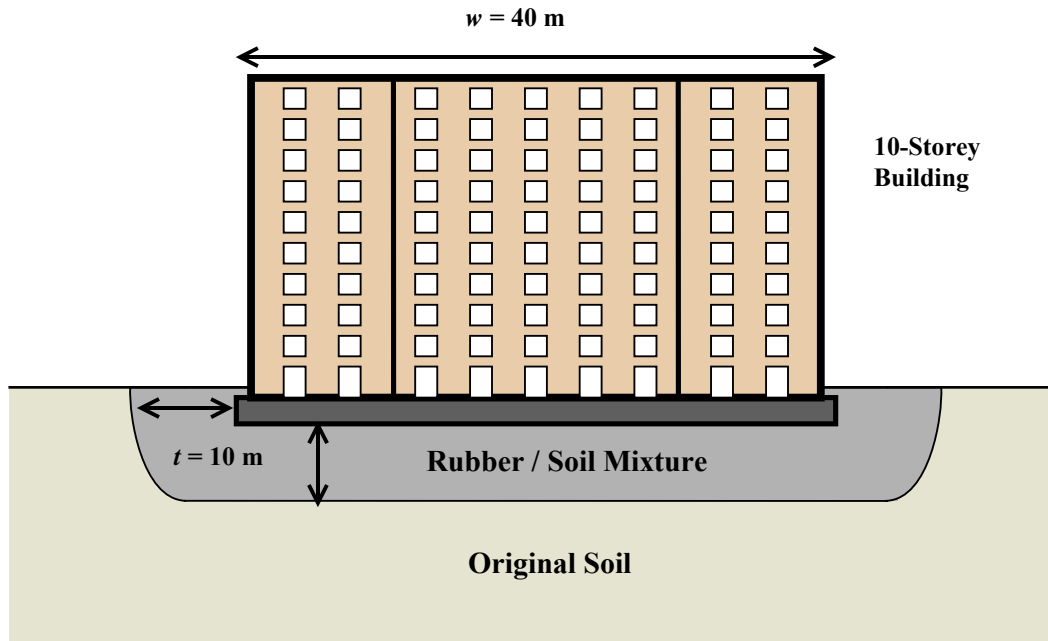


Figure 12. Seismic isolation by a layer of rubber-soil mixture (RSM) (Tsang, 2008).

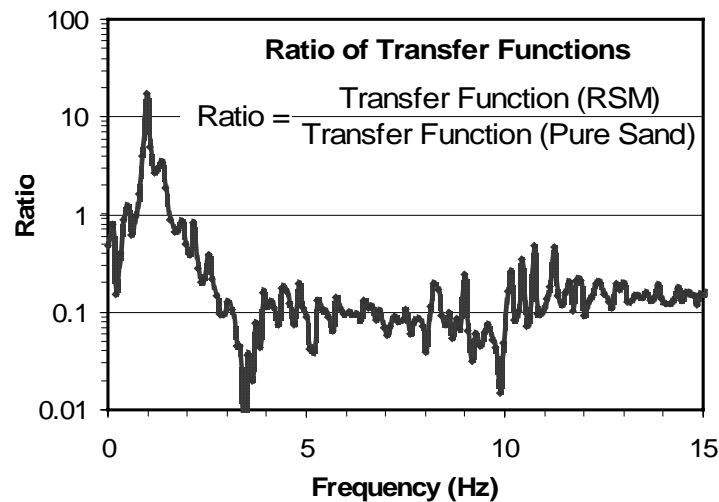


Figure 13. The ratio between the transfer functions of placing RSM and pure sand, respectively, as the overlying material (Tsang, 2008).

It is noted that the amplification function is expected to be dependent on the geometry and the material dynamic properties of the RSM layer. The importance of the material damping property leads to the proposed use of rubber, which will be further discussed next.

### **Use of Rubber**

Energy dissipation is the primary mechanism attributing to the reduction of seismic ground shaking. Rubber is known for its excellent energy absorption capability, and hence its uses for vibration control and dampening such as in automotive components have been extensive. Rubber was first used for earthquake protection of building structure in the 1960's. In Macedonia, a 3-storey concrete structure was built on large blocks of unreinforced natural rubber. The major drawback of this method was that the building would bounce and rock backwards and forwards in an earthquake. However, this phenomenon could be avoided with the use of RSM since the rubber solids could be reinforced by normal soil materials. This concept of reinforcing rubber is actually similar to that of the commonly adopted laminated rubber bearing. It should be noted that the use of pure rubber is not recommended for RSM.

In fact, rubber solids and soil particles are complementary in their functions. Comparing with normal soils, soil reinforced with rubber demonstrates a significant increase in shear strength (Edil and Bosscher, 1994; Masad *et al.*, 1996; Foose *et al.*, 1996), and more importantly a tremendous increase in energy dissipating capability. More details of the engineering properties of rubber-reinforced soils will be discussed later.

### **Use of Scrap Tires**

It is generally believed that recycled rubber will become an important component in base isolation in the near future, and scrap tire potentially provides a huge source of rubber material required for the proposed method. The durability of tires is ensured, for instance, they are termite proof, fireproof and do not outgas once they are buried. Possible environmental effects will be discussed in a later section.

In recent years, the disposal of scrap tires has become a significant environmental problem. Hundreds of millions of scrap tires are disposed of every year worldwide as a consequence of the huge increase in the number of vehicles. Just in the United States, about 300 million scrap tires were generated in 2005 (Rubber Manufacturers Association, 2006) and the number is expected to rise by approximately 2% every year, let alone the whole world.

Since the ban of used tires from landfills in the European Union and several states in the United States (European Commission, 1999; Masad *et al.*, 1996; USEPA), proper uses of scrap tires have become a hot topic among the engineering community to utilize the huge stockpile. Owing to the high energy content of tires, uses of scrap tires as fuel for energy recovery have been the main outlet of the stockpile in the United States and several European countries such as Sweden (Van Beukering and Janssen, 2001). Despite the reduction in emissions of nitrogen oxides, uncontrolled burning of tires can generate black smoke and sulphur dioxide which will worsen air pollution.

From the perspective of sustainability, reusing and recycling of waste tires is preferred to energy recovery. Tire shreds can be applied in highway embankments, landslide stabilization

and backfill for retaining walls and bridge abutments (Humphrey, 2005), and the rubber component of scrap tires can also be blended with asphalt in pavement constructions (Ahmed and Lovell, 1992). However, the amount of tires used in these civil engineering applications is limited.

The use of RSM in earthquake protection provides a promising way to reduce the huge stockpile as a large volume of tires can be utilized in each project. Taking the **Reference** scenario in Figure 12 as an example, the bulk volume occupied by RSM is around 42,000 m<sup>3</sup>. Assuming a bulk density of 0.8 for the RSM, for RSM with 75% rubber by volume, 25,200 m<sup>3</sup> of solid volume of rubber is required. Since a typical passenger tire weighs 9.1 kg and contains around 70% of rubber (Dhir *et al.*, 2001), over four million passenger tire equivalents (equivalent to 40,000 tons) can be consumed, given the density of rubber of 1,100 kg/m<sup>3</sup>. This amount is well beyond the consumption of scrap tires in typical civil engineering projects (Ahmed and Lovell, 1993).

### Material Properties of RSM

Extensive research has been conducted to investigate fundamental engineering properties of RSM, such as compaction characteristics, compressibility, permeability, shear strength, modulus of elasticity and Poisson's ratio (Edil and Bosscher, 1994; Masad *et al.*, 1996; Humphrey and Manion, 1992; Lee *et al.*, 1999). Based on Masad *et al.* (1996), the values of density of sand and RSM with 75% rubber by volume (abbreviated as RSM75) selected for finite element modeling in Tsang (2008) are 17.4 and 9.5 kN/m<sup>3</sup> respectively. Given the fact that Poisson's ratio has little effects on the results, different values for different materials were deemed not essential and a single value of 0.3 was chosen.

Dynamic properties of soils are well known for their significant dependence on soil shear strains. The computer program used in the finite element analysis, *QUAD4M*, employs the commonly adopted equivalent linear method, in which the nonlinear characteristics of soils can be captured by two strain-compatible material parameters, namely, secant shear modulus  $G$  and damping ratio  $\xi$ . These important properties of RSM have been investigated by Feng and Sutter (2000).

The shear modulus of soil ( $G_{\max}$ ) is maximum when shear strains are very small ( $10^{-5}$  –  $10^{-3}$  %). The maximum values adopted for sand and RSM75 in Tsang (2008) are 222 and 7.5 MPa respectively. The  $G/G_{\max}$  ratio defining the strain dependent degradation of the shear modulus has been plotted in Figure 14(a).

Soil damping is composed of two parts (Vucetic and Dobry, 1991): (i) the viscous component which is independent of the shear straining of the soil layers and is represented by a constant term, namely initial damping ratio ( $\xi_i$ ), and (ii) the hysteretic component which is associated with the degradation in the shear modulus and is dependent on shear strain. Details of the dynamic properties of RSM can be found in Tsang (2008).

Large uncertainty in estimating the dynamic properties of soil materials is unavoidable, and thus tolerance of around plus and minus 10% has been allowed in modeling the shear modulus degradation and damping. The notional upper bound and lower bound curves have been plotted with dashed lines in Figure 14.

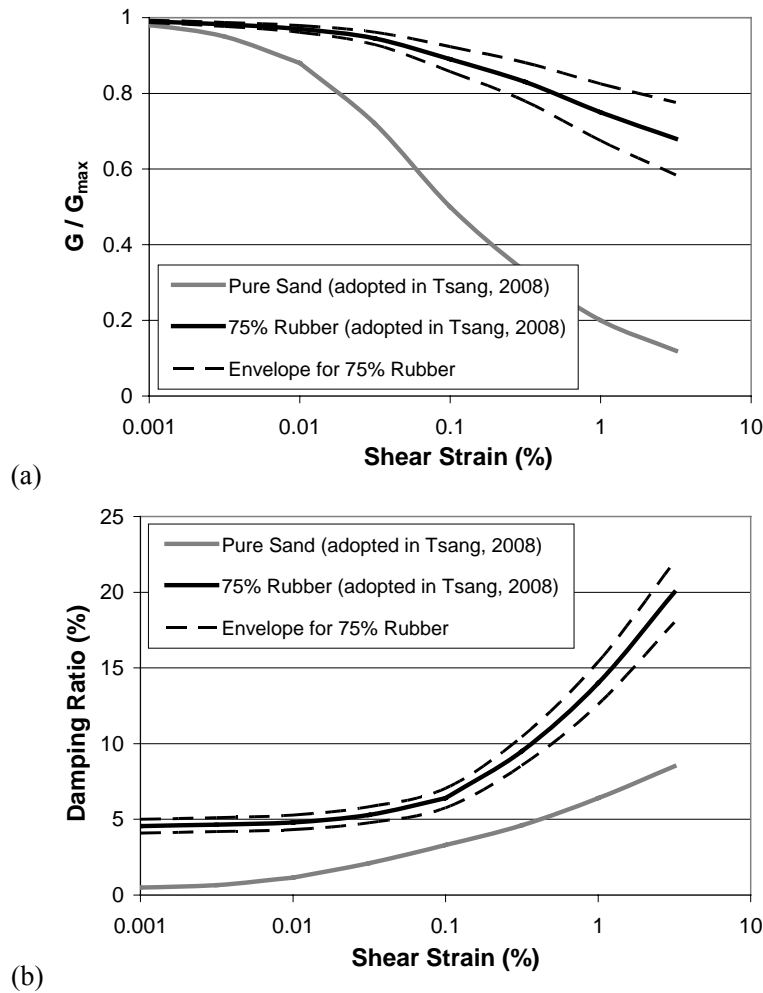


Figure 14. (a) Shear modulus degradation curves and (b) damping curves (Tsang, 2008).

### Investigations on Seismic Isolation by Rubber-Soil Mixtures

The computer program *QUAD4M* (Hudson, 1994) was employed to model the dynamic response of the isolation system involving RSM. *QUAD4M* is a dynamic, time-domain, equivalent linear two-dimensional finite element program. It is a robust analysis tool that has been extensively used in the past few decades.

To demonstrate the feasibility of the isolation system, a series of numerical simulations were performed. The configuration described in Figure 12 was adopted as the **Reference** model. Moreover, robustness analysis was conducted to examine a number of important variables, which included number of storeys and width of the building, depth of underground structure (annotated as  $F$  in Figure 15), thickness of RSM, discrepancies in dynamic properties of RSM, earthquake ground motions with different shaking levels and frequency contents. Details can be found in Table I. It is noted that only one input parameter was varied in each case, whereas all other input parameters were held constant at the default values

specified for the **Reference** scenario (bolded in Tables I and II). The purpose of this comparative analysis was to test the robustness of the results to each input parameter.

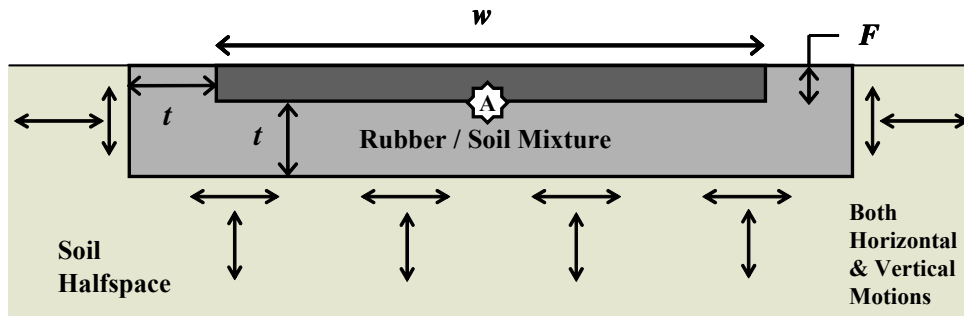


Figure 15. Simplified model for finite element analysis using *QUAD4M*.

**Table I. Input parameters used in the parametric study (Tsang, 2008).**

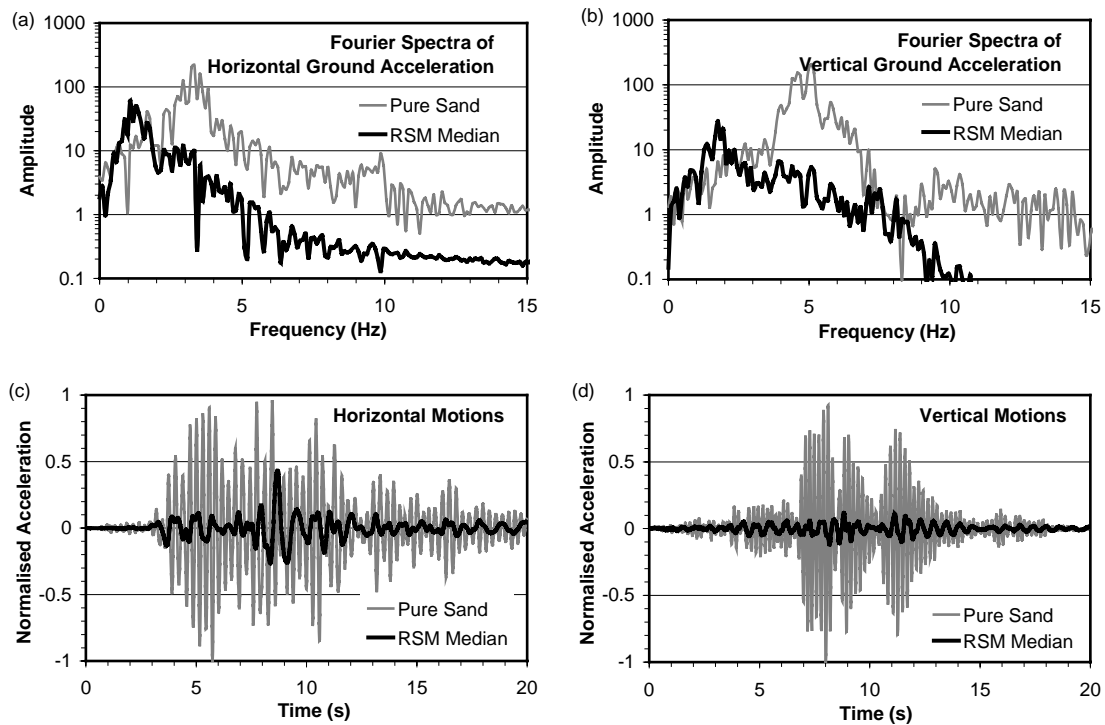
Input Parameter		Reference		
Thickness of RSM (m)	5	<b>10</b>	20	
Dynamic Properties of RSM	Lower Tolerance	<b>Median</b>	Upper Tolerance	
Building Width (m)	20	<b>40</b>	80	
Number of Storeys (Equivalent Density of Elements; kN/m <sup>2</sup> )	5 (40)	<b>10</b> <b>(60)</b>	15 (80)	
Depth of Underground Structure $F$ (m) (Equivalent Density of Elements; kN/m <sup>2</sup> )		<b>3</b> <b>(60)</b>	7 (30)	10 (23)
Peak Horizontal Acceleration (g)	0.45 – 3.56 (refer Table II)			
Peak Vertical Acceleration (g)	0.33 – 2.10 (refer Table II)			

**Table II. Details of earthquake strong-motion data (Tsang, 2008).**

	Northridge, California	Valparaiso, Chile	Duzce, Turkey
Date of Earthquake	<b>1994-01-17</b>	1985-03-03	1999-11-12
Earthquake Magnitude	<b>6.7 (Mw)</b>	7.8 (Ms)	7.1 (Mw)
Peak Horizontal Acceleration (g)	<b>1.78</b>	0.45	1.03
Peak Vertical Acceleration (g)	<b>1.05</b>	0.87	0.33

In most cases, the most severe damages were caused by near-field earthquakes with strong ground shaking, so ground motions which are rich in high frequency seismic wave components were the focus of the analysis (Tsang, 2008). Peak and root-mean-square ground accelerations, both horizontal and vertical, were chosen for the comparison of the effectiveness in different scenarios. Normally, the location where earthquake motion is applied for structural analysis is at the base of the footing or pile cap. Hence, in the following analysis, the acceleration time histories were collected at the point annotated by the letter “A” in Figure 15. For simplicity, the weight of the whole building structure was condensed to the footing, leading to different “equivalent” densities of elements for different scenarios listed in Table I. This simplification is reasonable provided that ground accelerations, but not structural responses, were chosen for comparison.

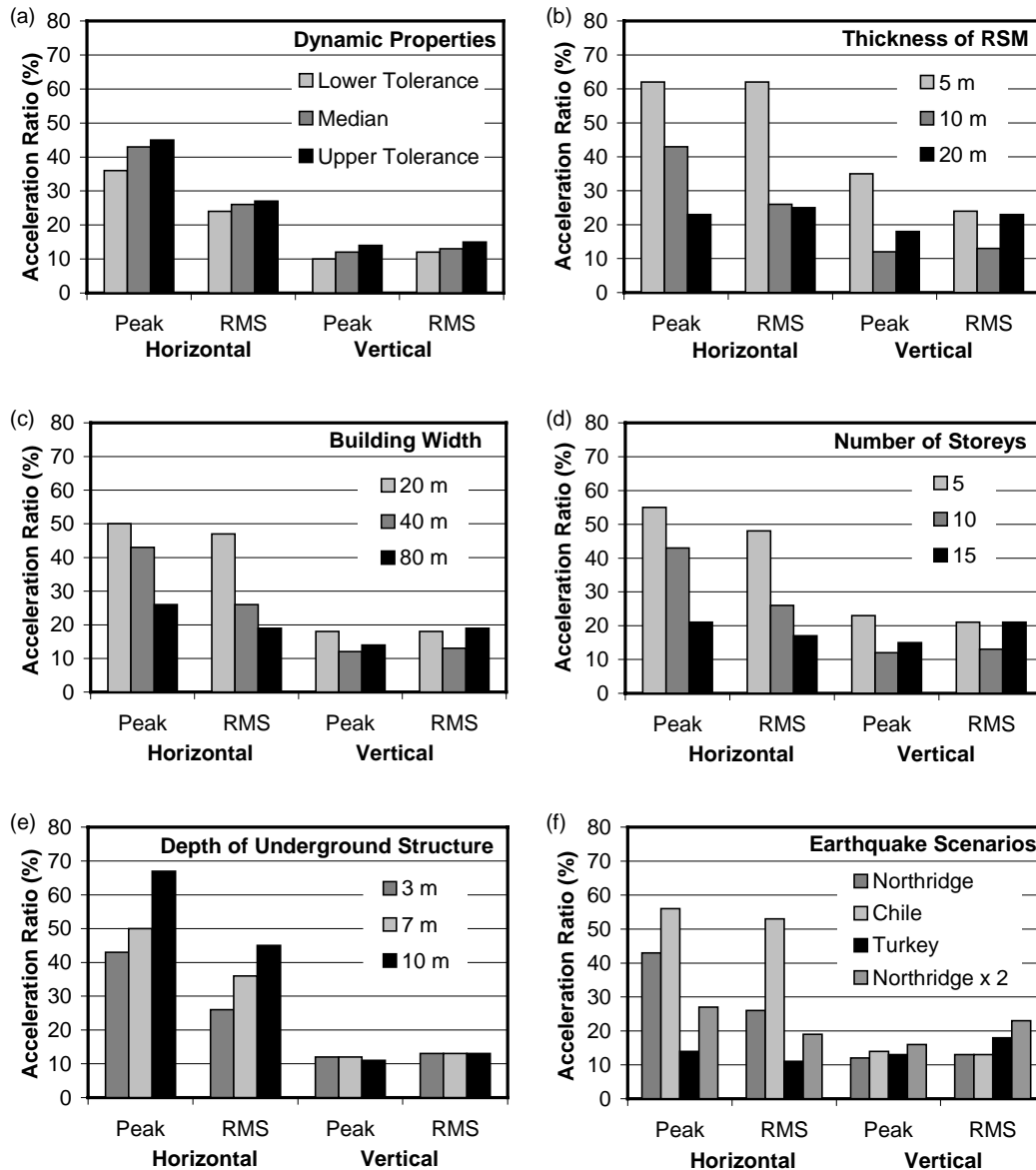
The model was subjected to three earthquake ground excitations, which cover different frequency contents and a wide range of ground shaking levels, both horizontal and vertical, as shown in Table I. They are, respectively, 1994 Northridge, California earthquake, 1985 Valparaiso, Chile earthquake and 1999 Duzce, Turkey earthquake. An additional set of strong-motion data was obtained by multiplying the 1994 Northridge, California earthquake (bolded in Table II) by a factor of two (equivalent to around one unit increase in earthquake magnitude), in order to give a stronger shaking level.



**Note:** In each figure, the scenarios of placing RSM and pure sand were plotted. Each time history was normalized by the respective maximum absolute ground acceleration of the scenario with pure sand.

Figure 16. The *Fourier* amplitude spectra (FAS) of the (a) horizontal and (b) vertical ground accelerations; and the corresponding normalized (c) horizontal and (d) vertical ground acceleration time histories for the Reference scenario (Tsang, 2008).

Figures 16(a)–(b) show the *FAS* of the horizontal and vertical ground accelerations respectively, in which the *FAS* of the scenarios of placing RSM and pure sand were plotted. Figures 16(c)–(d) present the corresponding normalized horizontal and vertical ground acceleration time histories of the two scenarios. Each time history was normalized by the respective maximum absolute ground acceleration of the scenario with pure sand for convenient observation of the reduction ratio and for direct comparison.



**Note:** Only one input parameter was varied in each case, while all other input parameters were held constant at the default values specified for the **Reference** scenario (bolded in Tables I and II).

Figure 17. Comparison of the acceleration ratio, with respect to different (a) dynamic properties of RSM; (b) thicknesses of RSM; (c) building widths; (d) number of storeys; (e) depths of underground structure; and (f) earthquake scenarios (Tsang, 2008).

In Figures 17(a)–(f), the effectiveness of acceleration reduction is shown. The “Acceleration Ratio” (in %) refers to the ratio of the ground acceleration obtained from the model with RSM to that obtained from the model with sand. It is obvious that the isolation system can effectively reduce both horizontal and vertical ground accelerations in all cases, even for the worst-case scenarios presented. On average, the acceleration ratio is in the order of 30–40% for horizontal motion and 10–20% for vertical motion. This has demonstrated the unique advantage of the seismic isolation method using RSM as all conventional seismic isolation schemes normally cannot reduce the vertical acceleration. The importance of vertical ground motion will be further discussed in the following sub-section.

It is noted in Figure 17(b) that the result is most sensitive to the thickness of RSM. In particular, the horizontal acceleration ratio changes from around 20% to 60% with respect to the thickness of RSM of 5 to 20 m. In Figures 17(c)–(d), significantly higher effectiveness can be observed in reducing horizontal acceleration for heavier structures which are represented by a greater height or width of building, but the vertical acceleration ratio only varies slightly. On the other hand, increasing the depth of underground structure is relatively ineffective in the reduction of acceleration (Figure 17(e)). A clear trend is yet to be seen in different earthquake scenarios which include a wide range of shaking levels and frequency contents (Figure 17(f)).

## Vertical Ground Motion

In the past few decades, characteristics of horizontal earthquake ground motion, as well as their effects on structures, have been extensively examined. It was not until recently that investigations on vertical ground motion were initiated. Strong vertical ground motion was studied by Papazoglous and Elnashai (1996) and field evidence from recent earthquakes on their destructive effects on structures was collated. It was discovered that vertical motion might increase axial column forces, moment and shear demands and also reduce the ductility level in columns and moment/shear capacity in beams (Papazoglous and Elnashai, 1996; Abdelkareem and Machida, 2000; Diotallevi and Landi, 2000; Quek *et al.*, 2002). Other studies on the effects of vertical ground motion on structures were also conducted, details of which can be found in Xie (2001), Collier and Elnashai (2001), and Podestà *et al.* (2006).

It was also learnt that the ratio of vertical to horizontal (V/H) response spectra increases with decreasing source-site distance at high frequencies (Bozorgnia and Niazi, 1993; Bozorgnia *et al.*, 1995). This means that the effects of vertical ground motion are more critical to structures with short natural periods under near-field earthquakes. In view of this characteristic, both short-period structures and near-field earthquakes with strong shaking levels were chosen for demonstration in this study. More studies on the characteristics of vertical ground motion can be found in Beresnev *et al.*, 2002; Ambraseys and Douglas (2003), and Elgamal and He (2004).

In commonly used seismic isolation systems, the reduction of energy transfer to the structure is achieved by allowing horizontal movement at the bearing but not vertical movement. As illustrated in the numerical simulations in the previous sub-section, it can thus be concluded that using RSM could be a promising strategy for reducing both horizontal and vertical shaking.

## Discussion on Seismic Isolation by Rubber-Soil Mixtures

### Nonlinear Site Response

It is well recognized that a nonlinear response can result from soils yielding at moderate to high levels of strains (Idriss, 1990; Beresnev and Wen, 1996; Field *et al.*, 1997; Field *et al.*, 1998). As stated in Hauksson and Gross (1991), most damage was caused by soft, near-surface ground conditions. Hence, it might be reasonable to deduce that RSM may not be beneficial in reducing the shaking level. However, Trifunac and Todorovska (1998) and Trifunac (2003) illustrated that buildings on softer soils were damaged to a lesser degree under strong shaking (e.g. peak ground velocity > 200 mm/s) due to energy absorption of incident seismic waves by nonlinear soil response. In fact, soft soils can potentially act as a natural mechanism for passive isolation, especially for near-field earthquakes that are rich in high-frequency wave components. This is supported by evidence in the simulations presented in the form of *FAS* in Figures 13 and 16(a)–(b), from which significant reduction in amplitudes could be observed in high-frequency range. Considering the excellent energy absorption capability of rubber, it is therefore believed that seismic isolation using RSM should be feasible.

### Soil Resonance Effects

Earthquakes produce seismic waves with a wide spectrum of frequencies. If a certain seismic wave component with high energy matches the natural frequency of the surface geological deposits, the interaction could potentially amplify the level of shaking, commonly referred to as soil resonance. Considering the replacement of certain thickness of surface geological deposits with RSM, the stiffness (and in turn the natural frequency) of the materials beneath the structure would be significantly modified and the potential harmful effects should not be ignored. Although this problem could not be seen in the numerical simulations mentioned in the previous section, further investigation on soil resonance effects is required.

If the natural frequency of the site can be modified, with specific design of the configuration and properties of the RSM layer, to a frequency which is not close to the dominant frequency of the incident seismic waves, the level of shaking can then be further reduced in addition to energy dissipation by RSM. This is actually the underlying philosophy of the commonly adopted seismic isolation system.

### Liquefaction

Liquefaction is the state when saturated sandy soil loses shear strength and effective stresses are reduced as a result of increased pore water pressure. The two most important factors accounting for the occurrence of liquefaction include (1) the cohesiveness and density of the soil deposit and (2) the level of shaking (Japanese Geotechnical Society, 1998). As this isolation method requires partial replacement of the soil materials with RSM, it is essential to consider whether it would increase the liquefaction potential during earthquakes.

As mentioned in the previous section, the density of RSM is reduced from  $17.4 \text{ kN/m}^3$  (of pure sand) to  $9.5 \text{ kN/m}^3$ . This may lead to a decrease in the shear strength and potentially enhance the possibility of liquefaction occurrence. Preliminary studies by Promputthangkoon and Hyde (2007) have shown that the addition of small quantity of tire chips reduces the cyclic shear strength of RSM. However, there is evidence to show that the shear strength of loose sand becomes greater than that of dense sand with an addition of more than 10% tire chips (Edil and Bosscher, 1994). Various studies of the engineering properties of RSM have also demonstrated a significant increase in the cohesion intercept (commonly referred to as the  $c$ -value) (Masad *et al.*, 1996). Moreover, rubbers normally have higher frictional angles (commonly referred to as the  $\phi$ -value) than normal soils (Edil and Bosscher, 1994) and the  $\phi$ -value increases with the percentage of shred content (Foose *et al.*, 1996).

In addition, randomly mixing tire chips can reinforce sand, resulting in greater shear strength than that of pure sand at its densest state. Densification can be carried out to reduce the void ratio and thus increase the density in order to minimize liquefaction. Details of various densification methods can be found in Japanese Geotechnical Society (1998).

Concerning the ground shaking intensity, it is noted from the previous section that both the peak and root-mean-square ground accelerations are lowered due to the damping effects of RSM, thus reducing the probability of liquefaction occurrence. Nevertheless, remedial measures against liquefaction could still be carried out during the construction process.

## Ground Settlement

Since tire shreds and RSM are highly compressible (Promputthangkoon and Hyde, 2007), they are prone to ground settlement. However, it has been demonstrated that the compressibility of tire shreds decreases substantially upon one load application (Edil and Bosscher, 1994; Humphrey and Manion, 1992). Preloading can thus be adopted after the construction of fill to eliminate plastic compression. Although an embankment constructed with pure tire shreds settles slightly more than that constructed with soils, embankment sections composed of tire shreds that are overlain with a soil cap (of the order of 1 m thickness) can significantly reduce the compressibility and deflections, performing equally well as those constructed with soils (Bosscher *et al.*, 1993).

In addition, settlement can be decreased by compaction, through which soil particles are packed more closely and air voids are reduced with the addition of either static or dynamic forces (Bergado *et al.*, 1996). It has been reported that tire shreds and soil-tire shred mixtures can be compacted using common compaction procedures (Ahmed and Lovell, 1993; Humphrey and Manion, 1992; Bosscher *et al.*, 1993), such as dynamic compaction and vibratory tamper methods (Japanese Geotechnical Society, 1998; Bergado *et al.*, 1996). Among currently available compaction methods, surface compaction (e.g. rolling and ramming) is the cheapest and simplest, rendering it particularly suitable for developing countries. Apart from the increase in density, compaction leads to a higher internal frictional angle and greater cohesion for cohesionless soils and cohesive soils respectively.

## Environmental Effects

Long term environmental issues associated with the use of recycled rubber, such as groundwater contamination and impacts on local ecology, have been the subjects of intense debate. From previous laboratory tests and field studies (Liu, 2000), both the concentrations of metallic components and the organics were well below the standards specified in two protocols in the United States, namely, Toxicity Characteristics Leaching Procedure Regulatory Limits and Extraction Procedure Toxicity, proving that recycled scrap tire is not a hazardous recycled material.

The increase in iron and manganese levels arising from the use of scrap tires is also a common concern. However, iron level is only specified in the aesthetic drinking water standard (taste), rather than of health concern. Furthermore, manganese is naturally present in ground water in many areas. It can thus be concluded that there is little or no likelihood of significant leaching of substances that are of specific public health concern from tire chips.

## New Classification of Seismic Isolation Systems

An interesting feature of the two new types of geotechnical seismic isolation systems is that they are analogous to the conventional structural seismic isolation systems using laminated rubber bearings and spherical sliding bearings (refer Figure 18 for comparison). Both laminated rubber bearings and RSM decouple the building or structure from ground motions by interposing elements or materials of low stiffness in between. While the rubber bearings shift the fundamental frequency of the isolated structure and concentrate the deformation and energy dissipation demands in the isolation system, RSM modifies the dominant frequency of the incident seismic waves and dissipates the seismic energy of high frequency components in particular. On the other hand, both spherical sliding bearings and geosynthetic liners limit the transfer of shear across the isolation interface which has a low level of frictional resistance, and hence, the levels of shaking transmitted to the structure could be reduced.

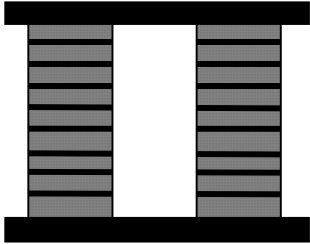
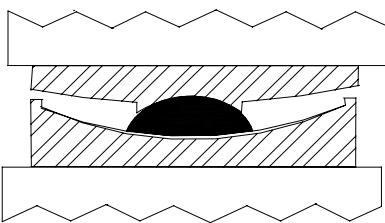
	Stiffness / Damping	Sliding / Friction
Conventional "Structural"	<p>Laminated Rubber Bearing</p> 	<p>Spherical Sliding Bearing</p> 

Figure 18. Continued on next page.

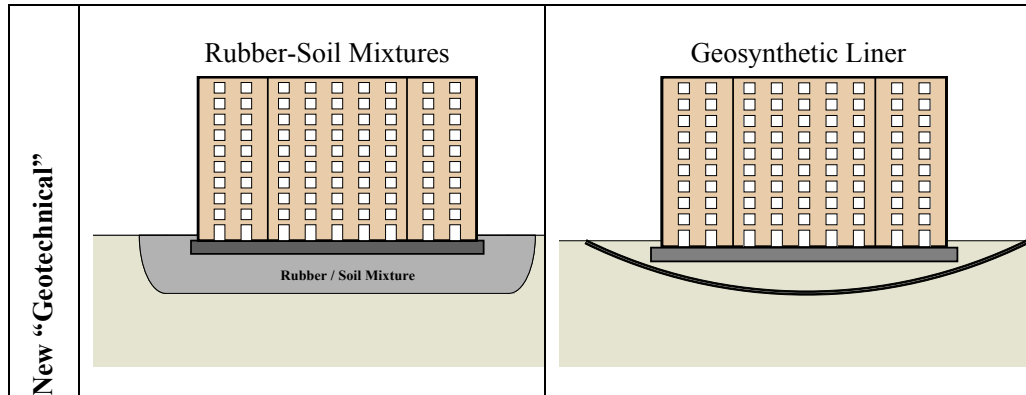


Figure 18. Proposed classification of seismic isolation systems.

On the other hand, the two methods presented in the chapter can be generalized as a *distributed seismic isolation system*, which involves isolating the entire contact surface of the foundation structure. This feature is clearly distinctive from the conventional systems which are based on isolation of certain discrete supporting points. Further research can be directed to the development of the *distributed seismic isolation system*.

## Conclusion and Closing Remarks

Conventional seismic isolation systems make use of a flexible or sliding interface positioned between a structure and its foundation for the purpose of decoupling the motions of the ground from that of the structure. This chapter presents new geotechnical seismic isolation methods, which comprise of a flexible or sliding interface in direct contact with geological sediments and of which the isolation mechanism primarily involves geotechnics. The principles and details of the two geotechnical methods have been described. Some of the latest research findings associated with these methods have also been presented.

New inventions are always viewed conservatively, especially in the field of civil engineering where risks to human life, in the case of malfunction, cannot be neglected. The concept of seismic isolation was considered to be very impractical by most structural engineers in the days of early development. Nowadays, it has become a major strategy of earthquake-resistant design protecting human lives all over the world. Hence, it is of particular importance to identify and evaluate if there are any drawbacks or hidden problems with these new methods, on which further discussion and research are required.

## The Most Important Challenge Ahead

Undoubtedly, there is a huge difference in loss of lives and properties from earthquakes between developing and developed countries. The vulnerability of megacities in the developing world is much greater where the average number of victims can be 150 times larger than that in the developed world, and the economic loss (as a percent of Gross National Product) 20 times greater (Wenzel *et al.*, 2007).

In the past few decades, rapid urbanization can be seen all over the world, while most of this has occurred in developing countries, owing to the breakdown of the rural economy and the consequential migration of rural population to urban areas, leading to the emergence of megacities, such as Mumbai, Dhaka and Jakarta. It is foreseen that the vulnerability in developing countries will continue to increase. Severe devastation and high death tolls could result if a major earthquake occurs in one of these megacities, where fragile buildings and infrastructures prevail.

It is believed to be the most important, yet underrated, challenge that the global earthquake engineering community is facing. More efforts are indeed required to address this problem by, for example, forming international networks to promote collaboration and information sharing, putting greater emphasis on small-scale local advocacy, and so forth. Another way is to encourage more research into inadequately engineered construction and low-cost earthquake protection techniques.

The editors of the World Housing Encyclopedia have published an inspiring article entitled “A Challenge to Earthquake Engineering Professionals” (Comartin *et al.*, 2004). Some sentences are quoted below as closing remarks.

“..... all of us, as earthquake professionals, have a responsibility to make the built environment safer worldwide.”

“In 2003, at least 26,000 people died in the Bam earthquake in Iran, ....., we find these high death tolls emotionally wrenching and simply unacceptable. .... It is time for us to meet the challenge head on.”

“..... United Nations Commission on Human Rights (UNCHR) Principle #10 states, ‘All persons have the right to adequate housing, land tenure and living conditions in a secure, healthy and ecologically sound environment.’”

“Not only are urban populations in developing countries becoming increasingly more vulnerable, but also the number of disasters is increasing.”

“We admit that the challenge can seem daunting. .... If we do not face this challenge with the knowledge and resources that we have collectively, who will? Is there anything that we could be doing that is more important?”

## References

- Abdelkareem, K. H.; Machida, A. Effects of vertical motion of earthquake on failure mode and ductility of RC bridge piers. In *Proceedings of the 12<sup>th</sup> World Conference on Earthquake Engineering*, New Zealand Society for Earthquake Engineering, Upper Hutt, New Zealand, 2000, Paper No. 0463.
- Ahmed, I.; Lovell, C. W. Use of waste materials in highway construction: state of the practice an evaluation of the selected waste products. In *Transportation Research Record* No. 1345; Transportation Research Board; National Academy Press: Washington, DC, 1992; pp. 1-9.
- Ahmed, I.; Lovell, C. W. Use of rubber tires in highway construction. In *Utilization of Waste Materials in Civil Engineering Construction*; Inyang, H. I.; Bergeson, K. L.; Ed.; ASCE: New York, 1993; pp. 166-181.
- Ambraseys, N. N.; Douglas, J. Near-field horizontal and vertical earthquake ground motions. *Soil Dyn. Earthquake Eng.* 2003, 23(1), 1-18.

- Beresnev, I. A.; Wen, K. L. Nonlinear soil response – A reality? *Bulletin of the Seismological Society of America* 1996, 86(6), 1964-1978.
- Beresnev, I. A.; Nightengale, A. M.; Silva, W. J. Properties of vertical ground motions. *Bull. Seism. Soc. Am.* 2002, 92(8), 3152-3164.
- Bergado, D. T.; Anderson, L. R.; Miura, N.; Balasubramaniam, A. S. *Soft Ground Improvement in Lowland and Other Environments*; ASCE: New York, 1996.
- Bosscher, P. J.; Edil, T. B.; Eldin, N. Construction and performance of shredded waste tire test embankment. In *Transportation Research Record No. 1345*; Transportation Research Board; National Academy Press: Washington, DC, 1993; pp. 44-52.
- Bozorgnia, Y.; Niazi, M. Distance scaling of vertical and horizontal response spectra of the Loma Prieta earthquake. *Earthquake Eng. Struct. Dyn.* 1993, 22(8), 695-707.
- Bozorgnia, Y.; Niazi, M.; Campbell, K.W. Characteristics of free-field vertical ground motion during the Northridge earthquake. *Earthquake Spectra* 1995, 11(4), 515-525.
- Bozorgnia, Y.; Bertero, V. V. (Ed.) *Earthquake Engineering: from Engineering Seismology to Performance-based Engineering*; CRC Press LLC: Boca Raton, FL, 2004.
- Buckle, I. G.; Mayes, R. L. Seismic isolation: history, application, and performance – a world view. *Earthquake Spectra* 1990, 6(2), 161-201.
- Chang, D. T. T.; Chen, C. A.; Fu, Y. C. The creep behaviour of geotextiles under confined and unconfined conditions. In *Proceedings of the International Symposium on Earth Reinforcement, Fukuoka, Japan, 1996*, pp. 19-24.
- Collier, C. J.; Elnashai, A. S. A procedure for combining vertical and horizontal seismic action effects. *J. Earthquake Eng.* 2001, 5(4), 521-539.
- Comartin, C.; Brzev, S.; Naeim, F.; Greene, M.; Blondet, M.; Cherry, S.; D'Ayala, D.; Farsi, M.; Jain, S. K.; Pantelic, J.; Samant, L.; Sassu, M. A challenge to earthquake engineering professionals. *Earthquake Spectra* 2004, 20(4), 1049-1056.
- De la Llera, J. C.; Lüders, C.; Leigh, P.; Sady, H. Analysis, testing, and implementation of seismic isolation of buildings in Chile. *Earthquake Eng. Struct. Dyn.* 2004, 33(5), 543-574.
- Dhir, R. K.; Limbachiya, M. C.; Paine, K. A. (Ed.) *Recycling and Reuse of Used Tyres*; Proceedings of the international symposium organized by the Concrete Technology Unit and University of Dundee, University of Dundee, Scotland, 19-20 March 2001; Thomas Telford: London, 2001.
- Diotallevi, P. P.; Landi, L. Effect of the axial force and of the vertical ground motion component on the seismic response of R/C frames. In *Proceedings of the 12<sup>th</sup> World Conference on Earthquake Engineering*, New Zealand Society for Earthquake Engineering, Upper Hutt, New Zealand, 2000, Paper No. 1026.
- Edil, T. B.; Bosscher, P. J. Engineering properties of tire chips and soil mixtures. *Geotech. Test. J.* 1994, 17(4), 453-464.
- Elgamal, A.; He, L. Vertical earthquake ground motion records: an overview. *J. Earthquake Eng.* 2004, 8(5), 663-697.
- European Commission. Council Directive 1999/31/EC of 26 April 1999 on the Landfill of Waste. *Official Journal of the European Communities L182* (16.07.1999) 1999, 1-19.
- Feng, Z. Y.; Sutter, K. G. Dynamic properties of granulated rubber/sand mixtures. *Geotechnical Testing Journal* 2000, 23(3), 338-344.
- Field, E. H.; Johnson, P. A.; Beresnev, I. A.; Zeng, Y. Nonlinear ground-motion amplification by sediments during the 1994 Northridge earthquake. *Nature* 1997, 390(6660), 599-602.

- Field, E. H.; Kramer, S.; Elgamal, A.-W.; Bray, J. D.; Matasovic, N.; Johnson, P. A.; Cramer, C.; Roblee, C.; Wald, D. J.; Bonilla, L. F.; Dimitriu, P. P.; Anderson, J. G. Nonlinear site response: where we're at (a report from a SCEC/PEER seminar and workshop). *Seismological Research Letters* 1998, 69, 230-234.
- Foose, G. J.; Benson, C. H.; Bosscher, P. J. Sand reinforced with shredded waste tires. *J. Geotech. Eng. (ASCE)* 1996, 122(9), 760-767.
- Fujita, T. Seismic isolation of civil buildings in Japan. *Progress in Structural Engineering and Materials* 1998, 1(3), 295-300.
- Georgarakos, P.; Yegian, M. K.; Gazetas, G. In-ground isolation using geosynthetic liners. In *9th World Seminar on Seismic Isolation, Energy Dissipation and Active Vibration Control of Structures, Kobe, Japan, 2005*.
- Greenwood, J. H.; Myles, B. Creep and stress relaxation of geotextiles. In *Proceedings of the 3rd International Conference on Geotextiles, Vienna, Austria, 1986*, pp. 821-826.
- Hauksson, E.; Gross, S. Source parameters of the 1933 Long Beach earthquake. *Bull. Seism. Soc. Am.* 1991, 81(1), 81-98.
- Hudson, M.; Idriss, I. M.; Beikae, M. *User's Manual for QUAD4M: a computer program to evaluate the seismic response of soil structures using finite element procedures and incorporating a compliant base*; University of California, Davis, U.S.A., 1994.
- Humphrey, D.; Manion W. Properties of tire chips for light-weight fill. *Grouting, Soil Improvement, and Geosynthetics*; ASCE: New York, 1992; Vol. 2, pp. 1344-1355.
- Humphrey, D. N. Effectiveness of Design Guidelines for Use of Tire Derived Aggregate as Lightweight Embankment Fill. In *Recycled Materials in Geotechnics*; Aydilek, A. H.; Wartman, J.; Ed.; ASCE: Reston, VA, 2005; pp. 61-74.
- Idriss, I.M. Response of soft soil sites during earthquakes. In *H.B. Seed Memorial Symposium Proceedings*; Duncan J. M.; Ed.; Bitech Publisher: Vancouver, BC, 1990; Vol. 2.
- Jangid, R. S.; Datta, T. K. Seismic behaviour of base-isolated buildings: a state-of-the-art review. *Proceedings of the Institution of Civil Engineers – Structures and Buildings* 1995, 110(2), 186-203.
- Japanese Geotechnical Society (JGS). *Remedial Measures against Soil Liquefaction: From Investigation and Design to Implementation*; JGS: Rotterdam, Netherlands, 1998.
- Kabir, M. H.; Ahmed, K. Dynamic creep behaviour of geosynthetics. In *Proceedings of the 5th International Conference on Geotextiles, Geomembranes and Related Products, Singapore, 1994*, pp. 1139-1144.
- Kelly, J. M. The tests of natural rubber isolators for the UNIDO demonstration building in Shantou City, Guangdong Province, P.R. China. In *Proceedings of International Workshop on the Use of Rubber-Based Bearings for the Earthquake Protection of Small Buildings, Shantou City, P.R. China, 1994*.
- Kelly, J. M. Seismic isolation of civil buildings in the USA. *Progress in Structural Engineering and Materials* 1998a, 1(3), 279-285.
- Kelly, J. M. (1998b) Base Isolation: Origins and Development. National Information Service for Earthquake Engineering (NISEE), University of California, Berkeley. Available from: <http://nisee.berkeley.edu/lessons/kelly.html> (last accessed March 2008).
- Kelly, J. M. Seismic isolation systems for developing countries. EERI Distinguished Lecture 2001. *Earthquake Spectra* 2002, 18(3), 385-406.
- Kim, D. S.; Konagai, K. Key parameters governing the performance of soft tunnel coating for seismic isolation. *Earthquake Eng. Struct. Dyn.* 2001, 30(9), 1333-1343.

- Koerner, R. M. (1998) *Designing with Geosynthetics*; Prentice Hall: Upper Saddle River, NJ, 1998.
- Lang, A. F.; Sargent, J. D. Method and apparatus for reducing earthquake damage in developing nations using recycled tires. United States Patent Number: 6,862,848 B1. Date of Patent: 8 March 2005.
- Lee, L. Advances in base isolation in China. In *Soil-Structure Interaction*; Cakmak, A. S.; Ed.; Elsevier Science Publishers: Amsterdam, Netherlands, 1987.
- Lee, J. H.; Salgado, R.; Bernal, A.; Lovell, C. W. Shredded tires and rubber-sand as lightweight backfill. *Journal of Geotechnical and Geoenvironmental Engineering* (ASCE) 1999, 125(2), 132-141.
- Ling, H. I.; Burke, C.; Mohri, Y.; Matsushima, K. Shear strength parameters of soil-geosynthetic interfaces under low confining pressure using a tilting table. *Geosynthetics International* 2002, 9(4), 373-380.
- Liu, H. S.; Mead, J. L.; Stacer, R. G. Environmental effects of recycled rubber in light-fill applications. *Rubber Chem. Tech.* 2000, 73(3), 551-564.
- Martelli, A.; Forni, M. Seismic isolation of civil buildings in Europe. *Progress in Structural Engineering and Materials* 1998, 1(3), 286-294.
- Masad, E.; Taha, R.; Ho, C.; Papagiannakis, T. Engineering properties of tire/soil mixtures as a lightweight fill material. *Geotech. Test. J.* 1996, 19(3), 297-304.
- McGown, A.; Andrawes, K. Z.; Kabir, M. H. Load-extension testing of geotextiles confined in soil. In *Proceedings of the 2nd International Conference on Geotextiles, Las Vegas*, 1982, pp. 793-796.
- Mikki, H.; Hayashi, Y.; Yamada, K.; Takasago; Shido, H. Plane strain tensile strength and creep of spun-bonded nonwovens. In *Proceedings of the 4th International Conference on Geotextiles, Geomembranes and Related Products, The Hague*, 1990, pp. 667-672.
- Naeim, F.; Kelly, J. M. *Design of Seismic Isolated Structures: From Theory to Practice*; John Wiley & Sons: New York, 1999.
- Papazoglous, A. J.; Elnashai, A. S. Analytical and field evidence of the damaging effect of vertical earthquake ground motion. *Earthquake Eng. Struct. Dyn.* 1996, 25(10), 1109-1137.
- Paulson, J. N. Geosynthetic material and physical properties relevant to soil reinforcement applications. *Geotextiles and Geomembranes* 1987, 6, 211-223.
- Peggs, I. D.; Tisinger, L. G.; Bonaparte, R. Durability of a polypropylene geotextile in an unpaved road structure. In *Transportation Research Record No. 1248*; Transportation Research Board; National Academy Press: Washington, DC, 1993; pp. 1-12.
- Perkins, S. W.; Cuelho, E. V. Soil-geosynthetic interface strength and stiffness relationships from pullout tests. *Geosynthetics International* 1999, 6(5), 321-346.
- Podestà, S.; Resemini, S.; Bindi, D.; Spallarossa, D. Influence of ground motion characteristics on monumental building damage: the 2002 Molise earthquake (Southern Italy). *J. Earthquake Eng.* 2006, 10(3), 381-409.
- Promptthangkoon, P.; Hyde, A. F. L. Compressibility and liquefaction potential of rubber composite soils. In *International Workshop on Tire Derived GeoMaterials, PARI, Kurihama, Japan*, 2007.
- Quek, S. T.; Bian, C. M.; Lu, X. L.; Lu, W. S.; Xiong, H. B. Tests on low-ductility RC frames under high- and low-frequency excitations. *Earthquake Eng. Struct. Dyn.* 2002, 31(2), 459-474.

- Robinson, W. H. Latest advances in seismic isolation. In *Proceedings of the 11th World Conference on Earthquake Engineering, Acapulco, Mexico*, July 1996, Paper No. 270.
- Robinson, W. H. Seismic isolation of civil buildings in New Zealand. *Progress in Structural Engineering and Materials* 2000, 2(3), 328-334.
- Rubber Manufacturers Association (2006). Scrap Tire Markets in the United States. Available from: <http://www.rma.org/getfile.cfm?ID=894&type=publication> (last accessed March 2008).
- Shukla, S. K. (Ed.) *Geosynthetics and their Applications*; Thomas Telford: London, 2002.
- Skinner, R. I.; Robinson, W. H.; McVerry, G. H. *Seismic Isolation*; John Wiley and Sons: Chichester, England, 1993.
- Taniwangsa, W.; Kelly, J. M. Studies on seismic isolation for housing in developing regions. In *Proceedings of the 11th World Conference on Earthquake Engineering, Acapulco, Mexico*, July 1996, Paper No. 261.
- Taylor, A. W.; Igusa, T. (Ed.) *Primer on Seismic Isolation*; American Society of Civil Engineers (ASCE): Reston, VA, 2004.
- Trifunac, M. D.; Todorovska, M. I. Nonlinear soil response as a natural passive isolation mechanism – the 1994 Northridge, California earthquake. *Soil Dyn. Earthquake Eng.* 1998, 17(1), 41-51.
- Trifunac, M. D. Nonlinear soil response as a natural passive isolation mechanism. Paper II. The 1933, Long Beach, California earthquake. *Soil Dyn. Earthquake Eng.* 2003, 23(7), 549-562.
- Tsang, H. H. Seismic isolation by rubber-soil mixtures for developing countries. *Earthquake Eng. Struct. Dyn.* 2008, 37(2), 283-303.
- UNIDO (1993). Use of Natural Rubber-based Bearings for Earthquake Protection of Buildings, Project SI/EGY/93/801. Available from: <http://www.unido.org/data/Project/Project.cfm?c=6337> (last accessed March 2008).
- UNIDO (1994). Use of Natural Rubber-based Bearings for Earthquake Protection of Buildings, Project SI/IND/94/801. Available from: <http://www.unido.org/Data/Project/Project.cfm?c=6895> (last accessed March 2008).
- UNIDO (1995). Advisory Services for Seismic Isolation of Hospital Buildings using Natural Rubber-based Bearings, Project US/INS/95/101. Available from: <http://www.unido.org/Data/Project/Project.cfm?c=7770> (last accessed March 2008).
- United States Environmental Protection Agency (USEPA). Management of Scrap Tires. Available from: <http://www.epa.gov/garbage/tires/basic.htm> (last accessed March 2008).
- Van Beukering, P. J. H.; Janssen, M. A. Trade and recycling of used tyres in Western and Eastern Europe. *Resources, Conservation and Recycling* 2001, 33(4), 235-265.
- Vandervoort, J. The Use of Extruded Polymers in the Containment of Hazardous Wastes; Schlegel Lining Technology, Inc.: The Woodlands, TX, 1992.
- Vucetic, M.; Dobry, R. Effect of soil plasticity on cyclic response. *J. Geotech. Eng.* (ASCE) 1991, 117(1), 89-107.
- Wenzel, F.; Bendimerad, F.; Sinha, R. Megacities – megarisks. *Natural Hazards* 2007, 42(3), 481-491.
- Xie, G.M. Effects of strong ground motions of near source earthquakes on response of thin-walled L-shaped steel bridge piers. *Structural Engineering and Mechanics* 2001, 12(3), 341-346.

- 
- Yegian, M. K.; Lahlaf, A. Geomembranes as base isolation. *Geotechnical Fabrics Report* 1992, 10(6), 17-21.
- Yegian, M. K.; Catan, M. Soil isolation for seismic protection using a smooth synthetic liner. *Journal of Geotechnical and Geoenvironmental Engineering* 2004, 130(11), 1131-1139.
- Yegian, M. K.; Kadakal, U. Foundation isolation for seismic protection using a smooth synthetic liner. *Journal of Geotechnical and Geoenvironmental Engineering* 2004, 130(11), 1121-1130.
- Zhou, F. L. Seismic isolation of civil buildings in the People's Republic of China. *Progress in Structural Engineering and Materials* 2001, 3(3), 268-276.

*Reviewed by:*

Adrian F. L. Hyde, BSc, PhD, MICE, CEng  
Professor of Geotechnical Engineering  
Department of Civil and Structural Engineering  
University of Sheffield



*Chapter 4*

**DYNAMIC RESPONSES OF HIGH-SPEED RAILWAY  
BRIDGES UNDER EARTHQUAKES  
AND THEIR INFLUENCES ON RUNNING SAFETY  
OF TRAIN VEHICLES**

*Weiwei Guo, He Xia\* and Chaoyi Xia*

School of Civil Engineering, Beijing Jiaotong University, Beijing 100044, China

**Abstract**

In this paper, the current situation, problems to be studied and further research trend in the field of dynamic interaction of vehicles and bridges under seismic excitations are summarized. A seismic analysis model of a simply-supported beam subjected to movable wheel with sprung mass is presented and the solution is deduced. A dynamic model of coupled train-bridge system subjected to earthquakes is then established, in which the bridge is modeled with the modal comprehension analysis technique, and each vehicle is modeled with 31 degrees of freedom. The seismic loads are imposed on the bridge by using the influence matrix and exerted on the vehicles through the dynamic wheel-rail interaction relationships. The normal wheel-rail interaction is tackled by using the Hertzian contact theory, and the tangent wheel-rail interaction by the Kalker linear theory and the Shen-Hedrick-Elkins theory. Case studies are performed to several actual bridges in China, including the simply-supported bridges with different span-lengths on the Qinghuangdao-Shenyang Special Passenger railway, and the continuous PC girder bridges on the planned Beijing-Shanghai high-speed railway. Through input of typical seismic waves with different propagation velocities to the train-bridge system, the histories of the train running through the bridge are simulated and the dynamic responses of the bridge and the vehicles are calculated. The influences of different train speeds and earthquake wave propagation velocities in non-uniform seismic excitations on the dynamic responses of the train-bridge system are studied. The critical train speeds are proposed for running safety on high-speed railway bridges under earthquakes of various intensities.

---

\* E-mail address: hxia88@163.com; Tel: (86) 10-82161656; Fax: (86) 10-51683340 (Corresponding author).

## 1. Introduction

The high-speed railway, owing to its fast speed, safely running, comfortable riding, high transportation capacity, low environmental pollution and less land use, is concerned by more and more countries, and thus the construction of high-speed railways is becoming a new trend of railway development in the world.

The design of the high-speed railway requires of more strict design conditions than the conventional railway, for it needs large curve radius and fully closed train running operation, resulting in much more bridges than the conventional railway.

In high-speed railways, the percentage of the total length of bridges to the overall road-length is considerable. In Germany, this percentage from Honnover to Würzburg is 12.5%. In France, the percentage of bridge length is 6.0% in TGV Southeast Line from Paris to Lyon, 21.5% in TGV Northern Line from Paris to Lille, and 32.2% in TGV South-East Extension Line from Lyon to Valence, respectively. In Japan, the average percentage of high-speed railway bridges is 48%, and this value is continuously increasing. In the earliest Tokaido Shinkansen, the bridges and elevated roads occupied 33.6% of the overall road-length, while in the Joetsu Shinkansen, the percentage increased to 61.5%, and in the Tohoku Shinkansen 58.1%, respectively. In the Korea high-speed railway from Seoul to Pusan, the percentage of bridge length is 27.1%. In Taiwan, the North-to-South high-speed railway from Taipei to Kaohsiung, this percentage is as high as 73%. In China mainland, there are 13 high-speed railways being constructed, with the total bridge length of 3607 km, which is 54.0% of the total length of the railways 6801 km. In the 1318 km's Beijing-Shanghai High-speed Railway, there are 230 bridges, with the total length being 1060.9 km, occupying 80.5% of the overall road-length. In the recently opened high-speed railway from Beijing to Tianjin, there are 35 bridges with the total length of 100.2 km, the percentage is as high as 87.7%.

Since 1964, the opening of the first high-speed railway in the world, the operation train speed has developed from 210 km/h in the Japanese Tokaido Shinkansen to 320 km/h in French TGV, while the highest experimental train speed reached as high as 574.8 km/h. In the current high-speed railways under construction, the infrastructures are normally designed for train speed of 300-350 km/h. In China, the operation train speed for the Qinghuangdao-Shenyang high-speed railway is 200 km/h, with that for its experimental section being 300 km/h. The operation train speed for the Beijing-Shanghai high-speed railway is 300 km/h, with that for the infrastructures being 350 km/h. Owing to the high speed, the high-speed trains produce much higher dynamic impact on the bridge structures than the common speed trains.

Earthquake is a suddenly arising and highly destructive natural disaster that harms the people's lives and properties while bridges are an important facility for the traffic and transportation system. When an earthquake occurs, the induced ground movements may cause intense bridge vibrations, which would affect the safety of bridge structures and the running trains. With the upgrade of railway design standards, bridges play more and more important roles in railway engineering. Especially with the development of high-speed railways, elevated bridges stretching tens of kilometers are commonly built to ensure the smoothness of track and the safety and stability of running trains, which greatly increases the probability of trains on bridges when an earthquake occurs. During the Niigata Earthquake on October 23, 2004, a Shinkansen high-speed train derailed when running on the elevated bridge at

200km/h, breaking the 40 years' safety record of the Shinkansen railways. Cases like this, as closely noticed by railway engineers, sufficiently testify the importance of studying the effect of earthquakes on the safety of trains running on bridges.



Figure 1. Derailment of a Shinkansen high-speed train during the Niigata Earthquake [4]

The dynamic interaction between railway bridges and trains has been an important subject of research since the early 20<sup>th</sup> century. During the past two decades, a number of sophisticated models have been developed to investigate the dynamic interaction between bridges and trains, and many useful results published. Diana and Cheli (1989) presented a finite element based numerical model in conjunction with a direct integration method to investigate dynamic interaction between a long suspension bridge and trains. Yang and Yau (1997) developed a special vehicle-bridge interaction element for dynamic analysis of coupled train and bridge systems. Xia et al (2000) investigated the dynamic interaction between a long suspension bridge and trains. They used four-axle vehicle models of 27 degrees of freedom and a mode superposition technique, and the measured track vertical, lateral, and torsional irregularities from one of the main railways in China in their work. Au et al (2001) carried out the impact study of a cable-stayed bridge under railway traffic using various vehicle models from 2 degrees-of-freedom systems to 4-axle systems of 10 degrees of freedom. Frýba (1996) took into account the track irregularities to simulate the vehicle-bridge dynamic interaction. Zhang et al (2001), however, simulated track irregularities based on the power spectral density functions.

With the successful operation of high-speed railways worldwide, the dynamic responses of railway bridges are receiving much more attentions from researchers than ever. When a high-speed railway bridge is located in prone-earthquake area, the dynamic interaction between seismic excitation, running trains and the bridge should be considered. However, most research has been focused on either the bridge aseismic design problem or the dynamic behavior of train-bridge coupling system excluding seismic excitation. In contrast, comparatively few works have been conducted on the dynamic responses of train-bridge system during earthquakes. Diana and Cheli (1989) analyzed the dynamic behavior of a row of train vehicles running over a long span suspension bridge at the speed of 60 km/h under a 4-hundred-year-once earthquake. They concluded that the bridge vibrations would induce the rolling movements of train vehicles during earthquakes. When the vibration amplitude of the

bridge exceeded some degree, the train vehicles would take the risk of derailment. Miura (1996) put emphasis on the deformation characteristics of railway tracks in earthquakes. From his point of view, earthquakes mainly induced the track movements and damaged the vehicles. Miyamoto (1997) adopted a 3-D simplified vehicle model to investigate the running safety of the railway trains subjected to earthquakes by representing the seismic excitations with sine waves. Yang and Wu (2002) developed a vehicle–rails–bridge interaction model to study the dynamic behaviors of the trains traveling over a bridge shaken by an earthquake excitation, and evaluated the risk of derailment for moving trains on the bridge. Luo (2001) presented a simple and convenient assessment method for running safety of the railway vehicles during earthquakes based on the energy balance theory.

Most of the research works cited above considered only the uniform seismic excitations. However, bridges are linear-shaped spatial structures composed of bridge spans, piers and their foundations. In fact, the foundations of a bridge may be built on soils of different properties, thus the earthquake waves onto different foundations may not be identical. For long bridges with large spans, or multiple simple spans or continuous spans, phase differences may exist between the foundations, due to the arrival time intervals of the earthquake waves propagating through the subsoil. The longitudinal phase differences of the seismic waves may lead to out-of-phase vibrations of the bridge piers and thus increase the danger of span collapse. The lateral phase differences of the seismic waves may lead to out-of-phase displacements of two adjacent piers and thus directly influence the running safety of the train on the bridge. Xia et al. researched the dynamic behavior of train-bridge coupling system under earthquakes over a long period of time (Xia, 1992; Xia, 1994; Zhang and Xia, 2001; Han and Xia, 2004; Han and Xia, 2005; Xia et al, 2006). They established a 3-D dynamic model of coupled train-bridge system subjected to earthquakes, in which the non-uniform characteristics of the seismic waves from different foundations are firstly considered. The vibrations of the railway bridges due to earthquakes and the runnability of the moving trains on the bridge were thus analyzed.

## 2. Seismic Analysis of a Simple Beam Subjected to Movable Wheel with Sprung Mass

In this section, discussion is concentrated on the seismic responses of a simple beam subjected to a movable wheel (movable mass) with a sprung mass (and a dashpot). For the case herein only the vertical vibration of the system is concerned. Suppose  $\ddot{y}_g(t)$  the seismic acceleration of the ground, and that the seismic excitations at two bearings of the bridge are identical.

The analysis is made of a simply-supported beam with span  $L$  subjected to a moving load system, consisted of the moving mass  $M_1$ , the moving sprung mass  $M_2$ , the spring  $k_1$ , and the dashpot  $c_1$ , moving at speed  $V$  from the left to the right-hand side, to simulate the loading actions of a movable wheel with sprung mass on the bridge. The analysis model is seen in Figure 2, where  $y(x, t)$  is the deflection of the beam at the point  $x$  and time  $t$ , and  $Z(t)$  the vertical displacement response of the moving sprung mass  $M_2$ , respectively. Suppose the moving mass  $M_1$  moves along the axis of the beam at a constant speed  $V$  and always keep contact with the beam, the displacement of  $M_1$  can thus be written as  $y(Vt, t)$ .

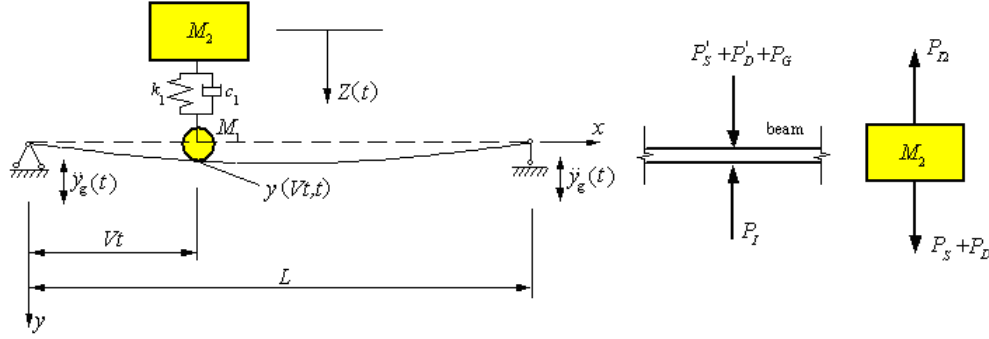


Figure 2. Seismic analysis model of a simple beam subjected to movable wheel with sprung mass.

The inertia force  $P_{I2}$ , elastic force  $P_S$ , and damping force  $P_D$  acting on the moving sprung mass  $M_2$  can be written as:

$$P_{I2} = M_2[\ddot{Z}(t) + \ddot{y}_g(t)] \quad (1a)$$

$$P_S = k_1[y(x,t) - Z(t)]\Big|_{x=Vt} \quad (1b)$$

$$P_D = c_1\left[\frac{dy(x,t)}{dt} - \dot{Z}(t)\right]\Big|_{x=Vt} \quad (1c)$$

The equation of motion for the moving sprung mass  $M_2$  can be expressed as:

$$M_2\ddot{Z}(t) + k_1[Z(t) - y(x,t)]\Big|_{x=Vt} + c_1\left[\dot{Z}(t) - \frac{dy(x,t)}{dt}\Big|_{x=Vt}\right] = -M_2\ddot{y}_g(t) \quad (2)$$

Noticed that  $\frac{dy}{dt} = \frac{\partial y(x,t)}{\partial t} + \frac{\partial y(x,t)}{\partial x}V$ , in which the first term of the right-hand side represents the vibration velocity of the beam, while the second term indicates the additional velocity due to the moving load, and for the general bridge span length and the current train speed, the influence of the second term can be neglected. Consequently, Equation (2) can be written as

$$M_2\ddot{Z}(t) + k_1[Z(t) - y(x,t)]\Big|_{x=Vt} + c_1\left[\dot{Z}(t) - \frac{\partial y(x,t)}{\partial t}\Big|_{x=Vt}\right] = -M_2\ddot{y}_g(t) \quad (3)$$

As the sprung mass model moved through the beam at a constant speed, the load on beam is composed of the inertia force  $P_{I1}$ , elastic force  $P'_S$ , damping force  $P'_D$ , and the gravity of the moving mass system  $P_G$ . It can be expressed in terms of

$$P(x,t) = \delta(x-Vt)[P_G - P_1 + P'_s + P'_D] \quad (4)$$

The expressions for the forces  $P_{11}$ ,  $P'_s$ ,  $P'_D$ , and  $P_G$  can be found in equation (5).

$$P_{11} = M_1 \left[ \frac{\partial^2 y(x,t)}{\partial t^2} \Big|_{x=Vt} + \ddot{y}_g(t) \right] \quad (5a)$$

$$P'_s = P_s \quad (5b)$$

$$P'_D = P_D \quad (5c)$$

$$P_G = (M_1 + M_2)g \quad (5d)$$

Equation (4) can thus be written as:

$$P(x,t) = \delta(x-Vt) \left\{ (M_1 + M_2)g - M_1 \left[ \frac{\partial^2 y(x,t)}{\partial t^2} + \ddot{y}_g(t) \right] + k_1 [Z(t) - y(x,t)] + c_1 \left[ \dot{Z}(t) - \frac{\partial y(x,t)}{\partial t} \right] \right\} \quad (6)$$

Therefore, the equation of motion for the simple beam subjected to a moving mass supported by a spring-dashpot unit under seismic excitation can be expressed as:

$$\begin{aligned} EI \frac{\partial^4 y(x,t)}{\partial x^4} + \bar{m} \left[ \frac{\partial^2 y(x,t)}{\partial t^2} + \ddot{y}_g(t) \right] + c \frac{\partial y(x,t)}{\partial t} \\ = \delta(x-Vt) \left\{ (M_1 + M_2)g - M_1 \left[ \frac{\partial^2 y(x,t)}{\partial t^2} + \ddot{y}_g(t) \right] + k_1 [Z(t) - y(x,t)] + c_1 \left[ \dot{Z}(t) - \frac{\partial y(x,t)}{\partial t} \right] \right\} \end{aligned} \quad (7)$$

Herein the modal superposition method was applied for analysis of the simple beam. Let  $q_i$  denote the generalized co-ordinate of the  $i$ th mode, the vertical displacement response of the beam  $y(x, t)$  can be expressed as:

$$y(x,t) = \sum_{i=1}^{\infty} \sin \frac{i\pi x}{L} q_i(t) \quad (8)$$

The equation of motion of the bridge deck related to the  $n$ th mode can be derived based on Equation (7) as:

$$\frac{L}{2} \bar{m} \ddot{q}_n(t) + \frac{L}{2} c \dot{q}_n(t) + \frac{L}{2} \frac{n^4 \pi^4}{L^4} q_n(t) = P_{gbn} n(t) + P_{gwn}(t) + P_{n1}(t) + P_{n2}(t) \quad (9)$$

in which  $P_{n1}(t)$  and  $P_{n2}(t)$  are the  $n$ th generalized force on the bridge without earthquake excitation, and can be found in equation (10):

$$P_{n1}(t) = \int_0^L \delta(x-Vt) \left[ (M_1 + M_2)g - M_1 \sum_{i=1}^{\infty} \ddot{q}_i(t) \phi_i(x) \right] \phi_n(x) dx \quad (10a)$$

$$P_{n2}(t) = \int_0^L \delta(x-Vt) \left\{ k_1 Z(t) + c_1 \dot{Z}(t) - \sum_{i=1}^{\infty} [k_i q_i(t) + c_i \dot{q}_i(t)] \phi_i(x) \right\} \phi_n(x) dx \quad (10b)$$

$P_{gbn}(t)$  is the  $n$ th generalized seismic force on the bridge and can be expressed as:

$$P_{gbn}(t) = \frac{2\bar{m}L}{n\pi} \ddot{y}_g(t) \quad (n=1,3,5,\dots) \quad (11)$$

$P_{gwn}(t)$  is the  $n$ th generalized seismic force from the moving mass  $M_1$  to the bridge and can be expressed as:

$$P_{gwn}(t) = -M_1 \ddot{y}_g(t) \sin \frac{n\pi Vt}{L} \quad (12)$$

The equation of motion for the moving sprung mass  $M_2$  can be in terms of:

$$M_2 \ddot{Z}(t) + c_1 \dot{Z}(t) + k_1 Z(t) - c_1 \sum_{i=1}^{\infty} \dot{q}_i(t) \sin \frac{i\pi Vt}{L} - k_1 \sum_{i=1}^{\infty} q_i(t) \sin \frac{i\pi Vt}{L} = -M_2 \ddot{y}_g(t) \quad (13)$$

Equations (9) and (13) thus constitute the basic equations of the simple beam subjected to movable wheel with a sprung mass under earthquakes. Thus the coupled equations of motion for the system can be expressed as:

$$\mathbf{M}\{\ddot{X}\} + \mathbf{C}\{\dot{X}\} + \mathbf{K}\{X\} = \{F\} \quad (14)$$

where  $\{X\}$  is the generalized displacement vector of the bridge and in term of

$$\{X\} = [q_1, q_2, \dots, q_N, Z]^T$$

$\mathbf{M}$  is the generalized mass matrix and in term of

$$\mathbf{M} = \begin{bmatrix} 1 + \rho_M \Phi_{11} & \rho_M \Phi_{12} & \cdots & \rho_M \Phi_{1N} & 0 \\ \rho_M \Phi_{21} & 1 + \rho_M \Phi_{22} & \cdots & \rho_M \Phi_{2N} & 0 \\ \cdots & \cdots & \ddots & \cdots & 0 \\ \rho_M \Phi_{N1} & \rho_M \Phi_{N2} & \cdots & 1 + \rho_M \Phi_{NN} & 0 \\ 0 & 0 & 0 & 0 & M_2 \end{bmatrix}$$

$\mathbf{C}$  is the generalized damping matrix and in term of

$$\mathbf{C} = \begin{bmatrix} 2\xi_1\omega_1 + \rho_c\Phi_{11} & \rho_c\Phi_{12} & \cdots & \rho_c\Phi_{1N} & -\rho_c\phi_1 \\ \rho_c\Phi_{21} & 2\xi_2\omega_2 + \rho_c\Phi_{22} & \cdots & \rho_c\Phi_{2N} & -\rho_c\phi_2 \\ \cdots & \cdots & \ddots & \cdots & \cdots \\ \rho_c\Phi_{N1} & \rho_c\Phi_{N2} & \cdots & 2\xi_N\omega_N + \rho_c\Phi_{NN} & -\rho_c\phi_N \\ -c_1\phi_1 & -c_1\phi_2 & \cdots & -c_1\phi_N & c_1 \end{bmatrix}$$

$\mathbf{K}$  is the generalized stiffness matrix and in term of

$$\mathbf{K} = \begin{bmatrix} \omega_1^2 + \rho_k\Phi_{11} & \rho_k\Phi_{12} & \cdots & \rho_k\Phi_{1N} & -\rho_k\phi_1 \\ \rho_k\Phi_{21} & \omega_2^2 + \rho_k\Phi_{22} & \cdots & \rho_k\Phi_{2N} & -\rho_k\phi_2 \\ \cdots & \cdots & \ddots & \cdots & \cdots \\ \rho_k\Phi_{N1} & \rho_k\Phi_{N2} & \cdots & \omega_N^2 + \rho_k\Phi_{NN} & -\rho_k\phi_N \\ -k_1\phi_1 & -k_1\phi_2 & \cdots & -k_1\phi_N & k_1 \end{bmatrix}$$

in which  $\rho_M = \frac{2M_1}{\bar{m}L}$ ,  $\rho_c = \frac{2c_1}{\bar{m}L}$ ,  $\rho_k = \frac{2k_1}{\bar{m}L}$ ,  $\Phi_{NM} = \phi_N\phi_M$ , and  $\phi_N = \sin \frac{n\pi Vt}{L}$  is the value of the  $n$ th bridge mode at the position of  $x = Vt$ .

$\{F\}$  is the generalized force vector, consisting of two parts:

$$\{F\} = \{F_0\} + \{F_g\} \quad (15)$$

where  $\{F_0\}$  is the vector of generalized forces from the wheels on the bridge deck and can be expressed as:

$$\{F_0\} = [\rho_F\phi_1, \rho_F\phi_2, \cdots, \rho_F\phi_N, 0]^T \quad (16)$$

where  $\rho_F = \frac{2(M_1 + M_2)}{\bar{m}L}g$ .

$\{F_g\}$  is the vector of generalized forces excited by earthquakes and can be expressed as:

$$\{F_g\} = [\rho_{g1} \quad \rho_{g2} \quad \cdots \quad \rho_{gN} \quad M_2]^T \ddot{y}_g(t) \quad (17)$$

in which

$$\rho_{gn} = \begin{cases} \frac{2}{\bar{m}L}M_1 \sin \frac{n\pi Vt}{L} + \frac{4}{n\pi} & (n = 1,3,5,7,\dots) \\ \frac{2}{\bar{m}L}M_1 \sin \frac{n\pi Vt}{L} & (n = 2,4,6,8,\dots) \end{cases} \quad (18)$$

From the equations deduced above, one can find that:

1. In the analysis of a simple beam and a movable wheel (movable mass) with a sprung mass (and a dashpot) system subjected to earthquakes, the dynamic model can be established by simply introducing the seismic forces into the motion equations of the system without considering earthquakes.
2. For a beam discretized with concentrated masses, the seismic forces equal to the seismic inertial forces of the masses multiplied by the earthquake ground acceleration.
3. For a simple beam discretized with generalized coordinates, the seismic forces are the generalized seismic inertial forces of the modes concerned.
4. For the wheel on the beam moving as a movable mass without any independent degree of freedom, the generalized seismic forces acting on the beam equal to the products of the seismic inertial forces of wheel masses multiplied by the modal function values at the wheel position.

These conclusions provide very convenient conditions for the establishment of the dynamic model of train-bridge system subjected to earthquakes.

### **3. Dynamic Model of Train-Bridge System Subjected to Earthquakes**

The behavior of train-bridge system under earthquakes is a coupled, complex time-varying dynamic problem. Such a problem is generally solved by computer simulating method based on establishing a dynamic interaction model for the train-bridge subjected to earthquakes. Theoretically, the analysis model can be regarded as a united big spatial dynamic system composed of two subsystems, the bridge model and the moving vehicle model, which are simulated as two elastic structures, with each characterized by some frequencies of vibration. The two subsystems interact with each other through the contact forces, i.e., the forces induced at the contact points between the wheels and rails surface of the railway bridge. The seismic actions on the train-bridge system are considered as the external excitations from different foundations of the bridge.

#### **3.1. Dynamic Model of Train Vehicles**

The train model is composed of several locomotives and cars. Each vehicle is a complicated MDOF vibration system consisting of car body, bogies, wheel-sets, suspension springs and dashpots.

There are two types of bogies used in railway trains: (1) The independent bogies which are used in the vehicles for most of conventional and high-speed railway trains, where the vehicles are independent with each other. (2) The articulated bogies which are used in the vehicles for high-speed trains such as in French TGV and the Korea High-speed railway, where the trains are composed of the articulated vehicles coupled with each other by the bogies.

The vehicle model with independent bogies is shown in Figure 3.

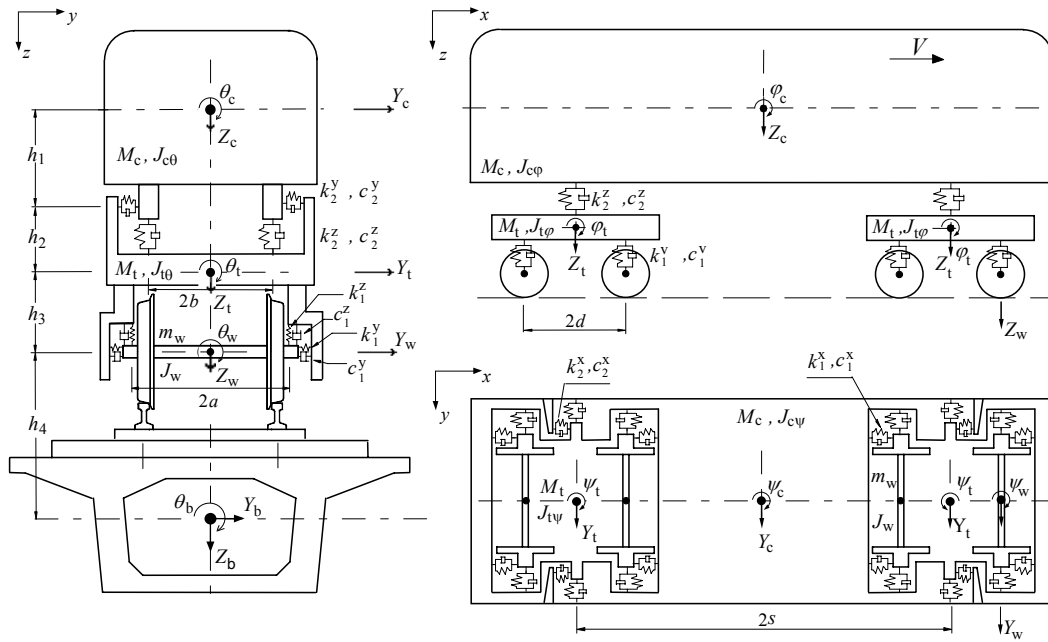


Figure 3. Dynamic analysis model of vehicle-girder system.

### 3.1.1. Basic Assumptions for Vehicle Model

To simplify the analysis but with enough accuracy, the following assumptions are used in modeling the train vehicles in this study (Ref. Figures 2 and 3):

1. The car body, bogies and wheel-sets in each vehicle are regarded as rigid components, neglecting their elastic deformation during vibration.
2. The connections between the car body and a bogie are represented by two linear springs and two viscous dashpots of the same properties in either the horizontal direction or the vertical direction.
3. The connections between a bogie and a wheel-set are characterized as two linear springs and two viscous dashpots of the same properties in either the horizontal direction or the vertical direction.
4. The train runs over the bridge at a constant speed so that the position of the train in the longitudinal direction (in the  $x$ -direction in Figure 3) can be determined accurately at any given time as long as the initial position of the trains is known. In this connection, the degrees of freedom of the train in the longitudinal direction are not included.
5. The vibration amplitude of each component in a coach is small.
6. A total of 5 DOFs is assigned to the car body, to account for the lateral movement  $Y_c$ , rolling  $\theta_c$ , yawing  $\Psi_c$ , floating  $Z_c$  and pitching  $\phi_c$ . Each bogie also has 5 DOFs of lateral movement  $Y_t$ , rolling  $\theta_t$ , yawing  $\Psi_t$ , floating  $Z_t$  and

pitching  $\varphi$ . In contrast, only 4 DOFs are assigned to each wheel-set, which relate to the lateral movement  $Y_w$ , rolling  $\theta_w$ , floating  $Z_w$  and yawing  $\Psi_w$ . The idealized configuration for each 4-axle 2-bogie vehicle in a train can therefore be modeled by a 31-DOFs dynamic system, as shown in Figure 3.

### 3.1.2. Motion Equations of Vehicle Model

By assuming that the vibration amplitude of each component in a vehicle is small and using the equilibrium conditions, the equations of motion for the car body and two bogies in the  $i$ th vehicle can be derived as follows:

$$\begin{aligned} & \begin{bmatrix} \mathbf{M}_{cci} & \mathbf{0} & \mathbf{0} \\ \mathbf{0} & \mathbf{M}_{t_1t_1i} & \mathbf{0} \\ \mathbf{0} & \mathbf{0} & \mathbf{M}_{t_2t_2i} \end{bmatrix} \begin{Bmatrix} \ddot{\mathbf{v}}_{ci} \\ \ddot{\mathbf{v}}_{t_1i} \\ \ddot{\mathbf{v}}_{t_2i} \end{Bmatrix} + \begin{bmatrix} \mathbf{C}_{cci} & \mathbf{C}_{t_1ci} & \mathbf{C}_{t_2ci} \\ \mathbf{C}_{ct_1i} & \mathbf{C}_{t_1t_1i} & \mathbf{0} \\ \mathbf{C}_{ct_2i} & \mathbf{0} & \mathbf{C}_{t_2t_2i} \end{bmatrix} \begin{Bmatrix} \dot{\mathbf{v}}_{ci} \\ \dot{\mathbf{v}}_{t_1i} \\ \dot{\mathbf{v}}_{t_2i} \end{Bmatrix} \\ & + \begin{bmatrix} \mathbf{K}_{cci} & \mathbf{K}_{t_1ci} & \mathbf{K}_{t_2ci} \\ \mathbf{K}_{ct_1i} & \mathbf{K}_{t_1t_1i} & \mathbf{0} \\ \mathbf{K}_{ct_2i} & \mathbf{0} & \mathbf{K}_{t_2t_2i} \end{bmatrix} \begin{Bmatrix} \mathbf{v}_{ci} \\ \mathbf{v}_{t_1i} \\ \mathbf{v}_{t_2i} \end{Bmatrix} = \begin{Bmatrix} \mathbf{F}_{ci} \\ \mathbf{F}_{t_1i} \\ \mathbf{F}_{t_2i} \end{Bmatrix} \end{aligned} \quad (19)$$

where the subscripts c, t<sub>1</sub>, t<sub>2</sub> represent the car body, the front and rear bogies of the vehicle, respectively,  $i=1,2,\dots,N_v$ , and  $N_v$  is the number of vehicles on the bridge.  $\mathbf{v}_i$ ,  $\dot{\mathbf{v}}_i$ , and  $\ddot{\mathbf{v}}_i$  are the displacement, velocity and acceleration vectors of the  $i$ th vehicle respectively. The sub-displacement vectors for the car body and two bogies in the  $i$ th vehicle can be expressed as

$$\mathbf{v}_{ci} = [Y_{ci} \quad \theta_{ci} \quad \psi_{ci} \quad Z_{ci} \quad \varphi_{ci}]^T \quad (20a)$$

$$\mathbf{v}_{t_1i} = [Y_{t_1i} \quad \theta_{t_1i} \quad \psi_{t_1i} \quad Z_{t_1i} \quad \varphi_{t_1i}]^T \quad (20b)$$

$$\mathbf{v}_{t_2i} = [Y_{t_2i} \quad \theta_{t_2i} \quad \psi_{t_2i} \quad Z_{t_2i} \quad \varphi_{t_2i}]^T \quad (20c)$$

Each sub-mass matrix is a diagonal matrix, expressed as

$$\mathbf{M}_{cci} = \text{diag}[M_{ci} \quad J_{c\theta i} \quad J_{c\psi i} \quad M_{ci} \quad J_{c\varphi i}] \quad (21a)$$

$$\mathbf{M}_{t_jt_ji} = \text{diag}[M_{t_ji} \quad J_{t_j\theta ij} \quad J_{t_j\psi ij} \quad M_{t_ji} \quad J_{t_j\varphi ij}] \quad (21b)$$

where  $M_{ci}$ ,  $J_{c\theta i}$ ,  $J_{c\psi i}$ , and  $J_{c\varphi i}$  are the mass, mass moment about the  $x$ -axis, mass moment about the  $z$ -axis, and mass moment about the  $y$ -axis of the car body of the  $i$ th vehicle respectively.  $M_{t_ji}$ ,  $J_{t_j\theta ij}$ ,  $J_{t_j\psi ij}$  and  $J_{t_j\varphi ij}$  are the mass, mass moment about the  $x$ -axis, mass moment about the  $z$ -axis, and mass moment about the  $y$ -axis of the  $j$ th bogie in the  $i$ th vehicle respectively. In this study,  $j=1, 2$ .

The sub-stiffness matrices are expressed as

$$\mathbf{K}_{cei} = \begin{bmatrix} k_{2i1}^h + k_{2i2}^h & -h_i(k_{2i1}^h + k_{2i2}^h) & 0 & 0 & 0 \\ -h_i(k_{2i1}^h + k_{2i2}^h) & h_i^2(k_{2i1}^h + k_{2i2}^h) + b_i^2(k_{2i1}^v + k_{2i2}^v) & 0 & 0 & 0 \\ 0 & 0 & s_i^2(k_{2i1}^h + k_{2i2}^h) & 0 & 0 \\ 0 & 0 & 0 & k_{2i1}^v + k_{2i2}^v & 0 \\ 0 & 0 & 0 & 0 & s_i^2(k_{2i1}^v + k_{2i2}^v) \end{bmatrix} \quad (22a)$$

$$\mathbf{K}_{t_j, j, i} = \begin{bmatrix} k_{2ij}^h + 2k_{1ij}^h & h_{2i}k_{2ij}^h - 2h_{3i}k_{1ij}^h & 0 & 0 & 0 \\ h_{2i}k_{2ij}^h - 2h_{3i}k_{1ij}^h & h_{2i}^2k_{2ij}^h + b_i^2k_{2ij}^v + 2h_{3i}^2k_{1ij}^h + 2a_i^2k_{1ij}^v & 0 & 0 & 0 \\ 0 & 0 & 2d_i^2k_{1ij}^h & 0 & 0 \\ 0 & 0 & 0 & 2k_{1ij}^v + k_{2ij}^v & 0 \\ 0 & 0 & 0 & 0 & 2d_i^2k_{1ij}^v \end{bmatrix} \quad (22b)$$

$$\mathbf{K}_{ct_1} = \mathbf{K}_{t_1, c}^T = \begin{bmatrix} -k_{2i1}^h & h_{1i}k_{2i1}^h & -s_i k_{2i1}^h & 0 & 0 \\ -h_{2i}k_{2i1}^h & h_{1i}h_{2i}k_{2i1}^h - b_i^2k_{2i1}^v & -h_{2i}s_i k_{2i1}^h & 0 & 0 \\ 0 & 0 & 0 & 0 & 0 \\ 0 & 0 & 0 & -k_{2i1}^v & -s_i k_{2i1}^v \\ 0 & 0 & 0 & 0 & 0 \end{bmatrix} \quad (22c)$$

$$\mathbf{K}_{ct_2} = \mathbf{K}_{t_2, c}^T = \begin{bmatrix} -k_{2i2}^h & h_{1i}k_{2i2}^h & s_i k_{2i2}^h & 0 & 0 \\ -h_{2i}k_{2i2}^h & h_{1i}h_{2i}k_{2i2}^h - b_i^2k_{2i2}^v & h_{2i}s_i k_{2i2}^h & 0 & 0 \\ 0 & 0 & 0 & 0 & 0 \\ 0 & 0 & 0 & -k_{2i2}^v & s_i k_{2i2}^v \\ 0 & 0 & 0 & 0 & 0 \end{bmatrix} \quad (22d)$$

where  $h_{1i}$ ,  $h_{2i}$ , and  $h_{3i}$  are the vertical distances between the three components in the  $i$ th vehicle;  $a_i$ ,  $b_i$ ,  $d_i$ , and  $s_i$  are the longitudinal and lateral distances between various axes of the  $i$ th vehicle, as defined in Figure 3.

The sub-damping matrix can be obtained by simply replacing “ $k$ ” in the corresponding sub-stiffness matrix by “ $c$ ”.

The force vector consists of two parts:

$$\begin{Bmatrix} \mathbf{F}_{ci} \\ \mathbf{F}_{t_1, i} \\ \mathbf{F}_{t_2, i} \end{Bmatrix} = \begin{Bmatrix} \mathbf{F}_{cei} \\ \mathbf{F}_{t_1, ei} \\ \mathbf{F}_{t_2, ei} \end{Bmatrix} + \begin{Bmatrix} \mathbf{0} \\ \mathbf{F}_{t_1, wi} \\ \mathbf{F}_{t_2, wi} \end{Bmatrix} \quad (23)$$

The components in the first part,  $\mathbf{F}_{cei}$ ,  $\mathbf{F}_{t_1, ei}$ , and  $\mathbf{F}_{t_2, ei}$  are the vectors of external forces (such as wind forces) acting on the car body, the front and rear bogies of the vehicle respectively.  $\mathbf{F}_{t_1, wi}$  and  $\mathbf{F}_{t_2, wi}$  are the vectors of forces transmitted from the wheels through the primary springs and dashpots to the front and rear bogies respectively. The forces transmitted from the wheels to the bogies can be expressed in terms of the displacements and velocities of the wheels.

$$\mathbf{F}_{i,w_i} = \sum_{l=1}^{N_{wij}} \left\{ \begin{array}{l} (k_{1ij}^h Y_{w_{ijl}} + c_{1ij}^h \dot{Y}_{w_{ijl}}) \\ 2a_i^2 (k_{1ij}^v \theta_{w_{ijl}} + c_{1ij}^v \dot{\theta}_{w_{ijl}}) - h_{4i} (k_{1ij}^h Y_{w_{ijl}} + c_{1ij}^h \dot{Y}_{w_{ijl}}) \\ 2\eta_{jl} d_i (k_{1ij}^h Y_{w_{ijl}} + c_{1ij}^h \dot{Y}_{w_{ijl}}) \\ (k_{1ij}^v Z_{w_{ijl}} + c_{1ij}^v \dot{Z}_{w_{ijl}}) \\ 2\eta_{jl} d_i (k_{1ij}^v Z_{w_{ijl}} + c_{1ij}^v \dot{Z}_{w_{ijl}}) \end{array} \right\} \quad (j=1,2) \quad (24)$$

where  $N_{wij}$  is the number of wheel-sets in the  $j$ th bogie of the  $i$ th vehicle.  $\eta_l$  is the sign function with  $\eta_l = 1$  when the wheel is in the front bogie and  $\eta_l = -1$  when it is in the rear bogie, respectively.

### 3.2. Dynamic Model of Bridge Structure

A railway bridge consists mainly of piers, beams, decks, and tracks. The forces from the wheels of a train will be transmitted to the bridge deck through the track. Nowadays, bridges are usually analyzed and designed with the help of finite element method. In this analysis, the modal comprehension analysis is performed for modelling the track-bridge system. First, the free vibration frequencies and modes of the system are solved. Upon the orthogonality of the modes, the FEM equations coupled with each other can then be decoupled, which makes the bridge model become the superposition of independent modal equations. Owing to the fact that the dynamic response of a structure is dominantly influenced by its several lowest modes, this method has a very great advantage that an adequate estimation on the dynamic response can be obtained by considering only a few modes of vibration, even for a spatial structure having hundreds of DOFs. Therefore, the computational effort can be significantly reduced.

The number of mode shapes of the bridge deck taken into account in the computation should be large enough to include the effects of both the global deformation of the bridge and the local deformation of the structural elements supporting the track. This decision may be made through a convergent study of the effects of the number of mode shapes or through a comparison with the measurement data.

#### 3.2.1. Basic Assumptions for Railway Bridge

The following assumptions have been used in the modeling of the railway bridge in this study:

1. There is no relative displacement between the track and bridge deck. The elastic effects of the track system are also neglected.
2. The mode shape between the deck nodes obtained from the eigenvalue analysis is determined using the Lagrange interpolation.
3. The deformation in cross-section of the beam is neglected in vibration analysis for the solid-web girder bridge.

### 3.2.2. Motion Equations for Railway Bridge Subjected to Multiple Seismic Excitations

In the model, the seismic movement of the bridge foundations excites the superstructure of the bridge through the influence matrix, and acts on the vehicles through the dynamic interactions between the wheels and the rails, and in turn, the vehicle vibration also affects the vibrations of the bridge structures.

In the previous studies of train-bridge systems subjected to earthquakes, the seismic waves were considered as identical for all foundations of the bridge, which is reasonable for short bridges. While for bridges stretching long distances, the seismic waves input to different foundations may differ from one another, and thus should be treated as multiple different excitations (Figure 4).

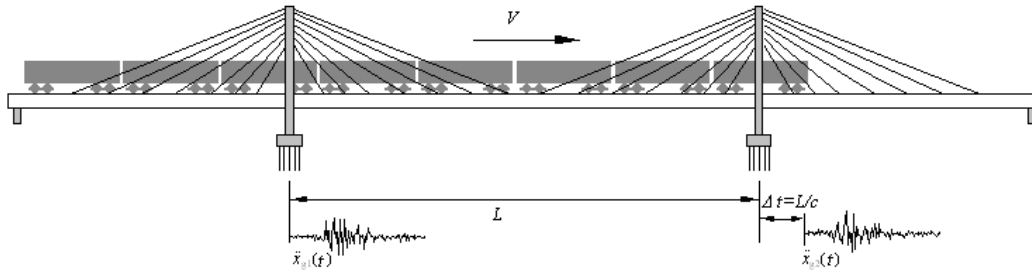


Figure 4. Non-uniform seismic excitations for long span bridge.

In this study, the non-uniformity of the ground accelerations is realized by using the same seismic waves but with time delays, and can be expressed as

$$\ddot{x}_{g_i}(t) = \ddot{x}_{g_j}\left(t - \frac{\Delta x}{c_s}\right) \quad (25)$$

where,  $\ddot{x}_{g_i}(t)$  and  $\ddot{x}_{g_j}(t)$  are the input accelerations to the  $i$ th and the  $j$ th foundations of the bridge, respectively;  $c_s$  is the propagating velocity of the seismic wave in the soil; and  $\Delta x$  the distance between the two foundations.

In the analysis, by separating the bridge subsystem into a supporting part and a non-supporting part, the dynamic equations of the bridge subjected to earthquakes can be expressed as:

$$\begin{bmatrix} \mathbf{M}_{bb} & \mathbf{0} \\ \mathbf{0} & \mathbf{M}_{ss} \end{bmatrix} \begin{Bmatrix} \ddot{\mathbf{X}}_b \\ \ddot{\mathbf{X}}_s \end{Bmatrix} + \begin{bmatrix} \mathbf{C}_{bb} & \mathbf{C}_{bs} \\ \mathbf{C}_{sb} & \mathbf{C}_{ss} \end{bmatrix} \begin{Bmatrix} \dot{\mathbf{X}}_b \\ \dot{\mathbf{X}}_s \end{Bmatrix} + \begin{bmatrix} \mathbf{K}_{bb} & \mathbf{K}_{bs} \\ \mathbf{K}_{sb} & \mathbf{K}_{ss} \end{bmatrix} \begin{Bmatrix} \mathbf{X}_b \\ \mathbf{X}_s \end{Bmatrix} = \begin{Bmatrix} \mathbf{0} \\ \mathbf{F}_s \end{Bmatrix} \quad (26)$$

where  $\mathbf{M}$ ,  $\mathbf{C}$  and  $\mathbf{K}$  denote the mass, damping and stiffness matrices of the bridge, respectively;  $\ddot{\mathbf{X}}$ ,  $\dot{\mathbf{X}}$  and  $\mathbf{X}$  the absolute acceleration, velocity and displacement vectors of the bridge, with the subscripts bb, ss and bs (sb) representing the non-supporting part, the

supporting part and the interaction part, respectively;  $\mathbf{F}_s$  is the reaction force vector of the supporting part.

Based on the concept of pseudo-static displacement, the total displacement of the bridge under multi-excitations can be divided into two parts, the pseudo-static displacement and the dynamic response displacement. Thus the total displacement vector can be expressed as:

$$\mathbf{X} = \begin{Bmatrix} \mathbf{X}_b \\ \mathbf{X}_s \end{Bmatrix} = \begin{Bmatrix} \mathbf{X}_b^p \\ \mathbf{X}_{sg} \end{Bmatrix} + \begin{Bmatrix} \mathbf{X}_b^d \\ \mathbf{0} \end{Bmatrix} \quad (27)$$

where the superscripts p and d represent the pseudo-static response component and the dynamic response component, respectively;  $\mathbf{X}_{sg}$  is the movement vector of the bridge supporting foundations, a known quantity for a given earthquake input.

By substituting Equation (27) into Equation (26), the upper part of Equation (26) can be written as:

$$\mathbf{M}_{bb}(\ddot{\mathbf{X}}_b^p + \ddot{\mathbf{X}}_b^d) + \mathbf{C}_{bb}(\dot{\mathbf{X}}_b^p + \dot{\mathbf{X}}_b^d) + \mathbf{C}_{bs}\dot{\mathbf{X}}_{sg} + \mathbf{K}_{bb}(\mathbf{X}_b^p + \mathbf{X}_b^d) + \mathbf{K}_{bs}\mathbf{X}_{sg} = \mathbf{0} \quad (28)$$

For a structure with only the static displacement at the supporting points and without any other loads, the static equilibrium equations can be written as:

$$\mathbf{K}_{bb}\mathbf{X}_b^p + \mathbf{K}_{bs}\mathbf{X}_{sg} = \mathbf{0} \quad (29)$$

Let  $\mathbf{R}_{bs} = -\mathbf{K}_{bb}^{-1}\mathbf{K}_{bs}$  denote the pseudo-static displacement influence matrix, one has:

$$\mathbf{X}_b^p = \mathbf{R}_{bs}\mathbf{X}_{sg} \quad (30)$$

Equation (28) can thus be expressed as:

$$\mathbf{M}_{bb}\ddot{\mathbf{X}}_b^d + \mathbf{C}_{bb}\dot{\mathbf{X}}_b^d + \mathbf{K}_{bb}\mathbf{X}_b^d = -(\mathbf{M}_{bb}\mathbf{R}_{bs} + \mathbf{M}_{bs})\ddot{\mathbf{X}}_{sg} - (\mathbf{C}_{bb}\mathbf{R}_{bs} + \mathbf{C}_{bs})\dot{\mathbf{X}}_{sg} \quad (31)$$

For common civil engineering structures, the contribution of the damping forces caused by the velocity of the supporting part is very small and can be neglected from the right hand side of Equation (31). Thus the dynamic equations can be written as:

$$\mathbf{M}_{bb}\ddot{\mathbf{X}}_b^d + \mathbf{C}_{bb}\dot{\mathbf{X}}_b^d + \mathbf{K}_{bb}\mathbf{X}_b^d = -(\mathbf{M}_{bb}\mathbf{R}_{bs} + \mathbf{M}_{bs})\ddot{\mathbf{X}}_{sg} \quad (32)$$

When lumped masses are adopted,  $\mathbf{M}_{bs}$  is a zero matrix and Equation (32) can be simplified as:

$$\mathbf{M}_{bb}\ddot{\mathbf{X}}_b^d + \mathbf{C}_{bb}\dot{\mathbf{X}}_b^d + \mathbf{K}_{bb}\mathbf{X}_b^d = -\mathbf{M}_{bb}\mathbf{R}_{bs}\ddot{\mathbf{X}}_{sg} \quad (33)$$

where  $\ddot{\mathbf{X}}_{sg}$  is the excitation vector composed of ground accelerations to different bridge foundations. These accelerations are in fact non-uniform for different foundations.

As there are no measured ground accelerations available for foundations at different locations, in this analysis, the non-uniformity of the ground accelerations is expressed as Equation (25).

### 3.3. Wheel/Rail Inter-forces

In studying the dynamic response of a train-bridge system, two sets of equations of motion can be written, one for the bridge and the other for the vehicles. It is the interaction or contact forces existing at the contact points of the two subsystems that make the two sets of equations coupled.

The passage of a train on a bridge is a complicated dynamic course. The dynamic action of the train makes the bridge deform, while the deformation of the bridge in turn affected the responses of the train vehicles, which are dynamically coupled with each other through the contact of the wheels and the rails. Therefore, the analysis model of wheel/rail contact relationship and the corresponding inter-forces are one of the key problems to be solved in the train-bridge system analysis.

In determining the interactions between the wheel and rail of the train-bridge system, there are two types of contact forces between the wheel and the rail: the normal interaction force and the tangent creep force.

When a vehicle moves on the track, there occurs a normal force between the two closely inter-pressed elastic bodies of the wheel and the rail.

In this study, the normal interaction is treated according to the nonlinear elastic Hertzian contact theory, in which the normal interaction force between the wheel and rail can be expressed as:

$$N_z(t) = \left[ \frac{1}{G} \delta Z(t) \right]^{3/2} \quad (34)$$

where  $\delta Z(t)$  is the compression between wheel and rail, and  $G$  the Hertzian wheel-rail contact constant.

During a vehicle moves on the track, there also occurs a contact spot between the two closely inter-pressed elastic bodies of the wheel and the rail. When there is a relative movement or a trend of relative movement between the two elastic bodies, and owing to the friction action, a tangent force appears at the contact spot surface, which is called as creep force. The relationship between the creep forces and the relative wheel/rail sliding is studied by the wheel/rail rolling contact mechanics, which plays an important role in the dynamic analysis of train-bridge system.

In the past decades, many researchers performed a lot of theoretical and experimental studies on the behaviors of creep forces from the rolling contact of elastic bodies, and proposed various algorithms. Kalker, a Netherlands scholar, made excellent contribution to the development of wheel/rail rolling contact theory. Since 1960's, Kalker has proposed a

series of linear, nonlinear, accurate and simplified wheel-rail creep theories, systemically solved the rolling contact problem of two elastic bodies under dry friction, and thus promote the application of the creep theory to the engineering practice. His researches are regarded as useful references in this field.

The tangent interaction is treated firstly by the Kalker linear theory under small creep and then corrected by the Shen-Hedrick-Elkins nonlinear theory, to make it applicable to the conditions with large creep (Kalker, 1989; Zhai, 1996). According to the Kalker theory and the Shen-Hedrick-Elkins theory, the tangent interaction force between wheel and rail can be expressed as:

$$\begin{cases} F_x = -\varepsilon \cdot f_{11} \xi_x \\ F_y = -\varepsilon \cdot f_{22} \xi_y - \varepsilon \cdot f_{23} \xi_{sp} \\ M_z = \varepsilon \cdot f_{23} \xi_y - \varepsilon \cdot f_{33} \xi_{sp} \end{cases} \quad (35)$$

where,  $F_x$  and  $F_y$  are the creep forces in longitudinal and lateral directions, respectively;  $M_z$  stands for the rolling creep moment;  $f_{11}$  and  $f_{22}$  are the longitudinal and lateral creep factors, respectively;  $f_{23}$  the rotation/lateral-displacement creep factor, and  $f_{33}$  the rolling creep factor;  $\xi$  stands for the relative velocity difference between the contact surfaces of the wheel and the rail, with the subscripts x, y and sp representing the longitudinal, lateral and rolling directions, respectively; and  $\varepsilon$  is a correcting factor.

When Equations (34) and (35) are employed to calculate the wheel-rail interaction forces, the wheel-rail contact point and the corresponding contact geometry parameters must be determined first. The contact points in left and right wheels can be only in the trace (Ref. Figure 5):

$$\begin{cases} x_C = d_{L,R} \cdot l_x + l_x R_w \tan \delta_{L,R} \\ y_C = d_{L,R} \cdot l_y - R_w (l_x^2 l_y \tan \delta_{L,R} + l_z m) / (1 - l_x^2) + Y_w \\ z_C = d_{L,R} \cdot l_z - R_w (l_x^2 l_z \tan \delta_{L,R} - l_y m) / (1 - l_x^2) \end{cases} \quad (36)$$

where,  $m = \sqrt{1 - l_x^2 (1 + \tan^2 \delta_{L,R})}$ ;  $l_x$ ,  $l_y$  and  $l_z$  are the direction cosines of wheel axis, respectively;  $Y_w$  the lateral displacement,  $R_w$  the rotation angle of wheel-set,  $\delta$  the contact angle between wheel and rail, with the subscripts L and R representing the left and the right wheels, respectively.

In the analysis, the actual contact point can be obtained by changing the position of the rolling center and searching for the point nearest to the rail surface, with the irregularity of the rail taken into account.

By introducing the measured wheel-rail section profile data and graphing with the third-order spline approximation in the fixed coordinate system, the coordinates of the wheel-rail contact point can be identified by calculating the minimum perpendicular distance of the left or right wheel-rail at a given time.

Following the above analysis and using Equations (35) and (36), the wheel-rail contact forces can be determined. Details of the calculation process can be found in Xia (2005) and Zhai (1996).



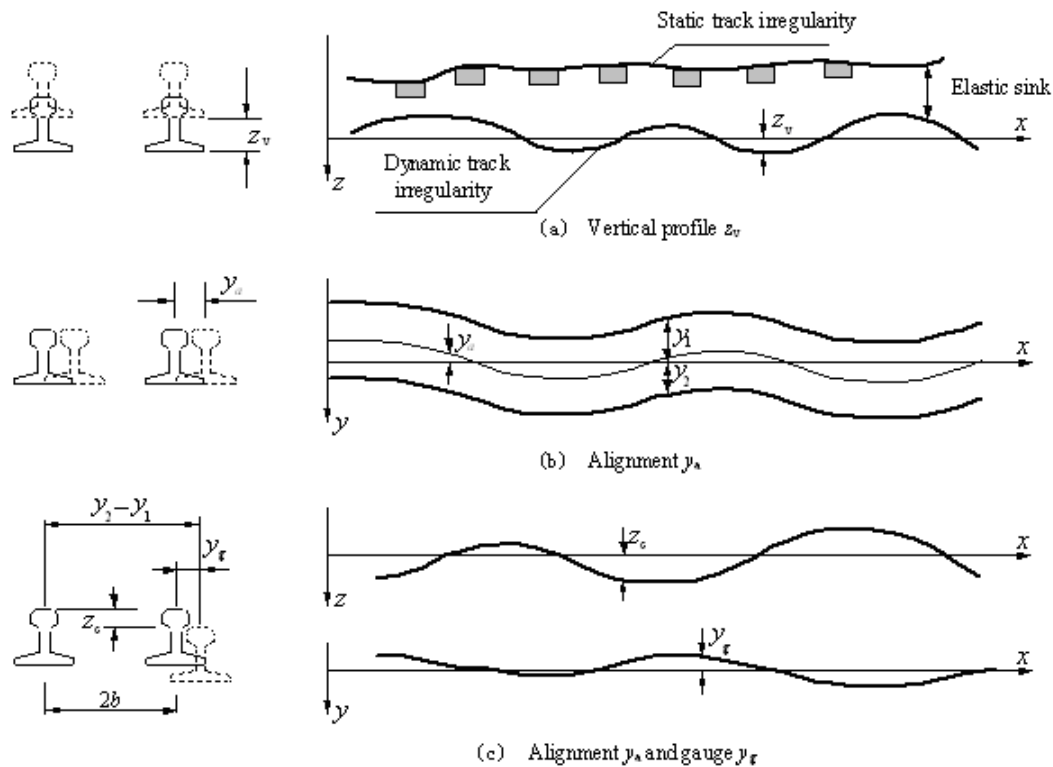


Figure 6. Illustration of track irregularities.

In the analysis, the track irregularities are used as the input to the dynamic model. The track irregularity input could be the measured irregularities from the actual tracks, or the simulated ones based on the power spectral density functions of the track irregularity.

### 3.4.2. Wheel Hunting Movement

The occurrence of wheel hunting movement of railway vehicles is a consequence of the wheel with reversed conic wheel tread running on the straight track, and the gap between the wheel rim and the side surface of rail. When the vehicle runs, if the wheel-set drifts off the central line of the track, the wheel that finds itself closer to the rail will have a larger rolling diameter than the other one, which rolls on a smaller diameter. The wheel rolling on a larger diameter will advance quicker than the other one, which will always stay behind. Therefore, the two wheels, the left wheel and the right wheel, on the same wheel-set will move at different rolling diameters, which makes the two wheels move different distances. The unequal moving distances of the two wheels in turn make the wheel-set drift to the other side of the track. In this way, when a wheel-set runs on the track, it emerges, at the same time, a lateral movement and a yawing movement in horizontal plane, and thus forming a sinusoid curve, as shown in Figure 7. This phenomenon is the so-called hunting movement of wheel-set.

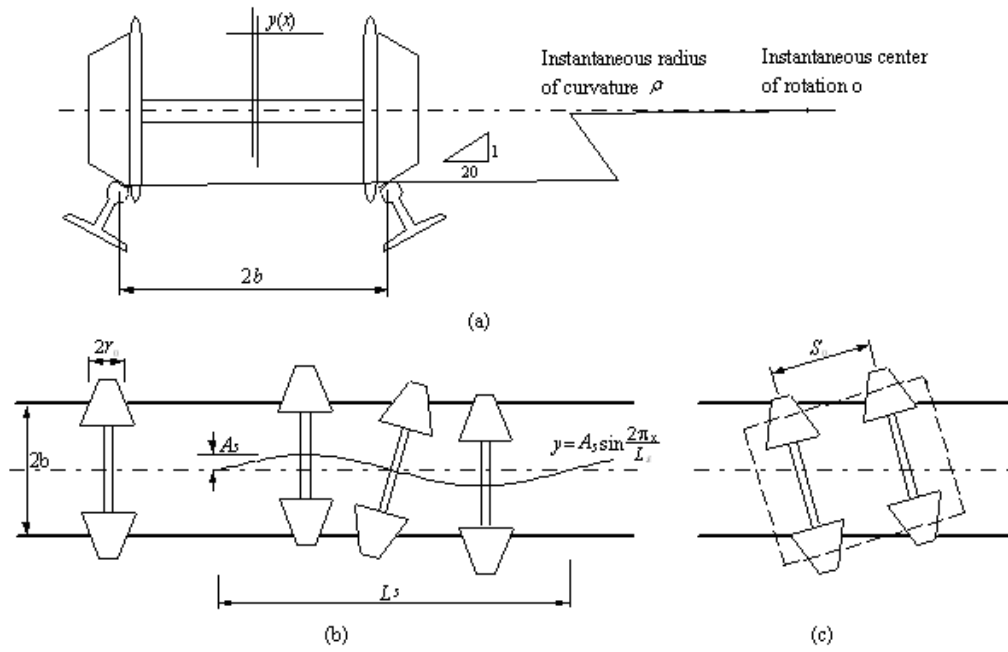


Figure 7. Illustration of wheel hunting movement.

Generally speaking, the hunting movement of a railway vehicle wheel-set in a straight and uniform motion is one of the main factors that induce the lateral vibration of the train-bridge system. The loss of control of this phenomenon by an unstable evolution is harmful for the running safety and riding comfort of vehicles.

In this study, the wheel hunting displacement  $Y_h$  (in the lateral direction) is assumed as a sinusoid function with a certain amplitude and a random phase:

$$Y_h(t) = A_h \sin\left(\frac{2\pi Vt}{L_h} + \phi_{hij}\right) \quad (37)$$

where  $A_h$  is the hunting amplitude;  $L_h$  is the hunting wavelength;  $\phi_{hij}$  is the random phase of the  $j$ th wheel-set in the  $i$ th bogie of the coach ranging between 0 and  $2\pi$ ; and  $V$  is the traveling speed of the vehicle.

### 3.4.3 Consideration in equation of motion

In consideration of both the wheel hunting and track irregularities, the relations between the  $l$ th wheel displacements and the bridge deck displacements can be deduced as (Ref Figure 8):

$$\begin{cases} Y_{wijl} \\ \theta_{wijl} \\ Z_{wijl} \end{cases} = \begin{cases} Y_b(x_{ijl}) + h_{4i}\theta_b(x_{ijl}) + Y_s(x_{ijl}) + Y_h(x_{ijl}) \\ \theta_b(x_{ijl}) + \theta_s(x_{ijl}) \\ Z_b(x_{ijl}) + e_i\theta_b(x_{ijl}) + Z_s(x_{ijl}) \end{cases} \quad (38)$$

where the track irregularities consist of the lateral irregularity  $Y_s(x)$ , vertical irregularity  $Z_s(x)$ , and rotational irregularity  $\theta_s(x)$ ;  $x_{ijl}$  is the co-ordinate of the  $l$ th wheel of the  $j$ th bogie in the  $i$ th vehicle along the bridge deck;  $Y_b, Z_b$ , and  $\theta_b$  are the lateral, vertical, and rotational displacement of the bridge deck, respectively.

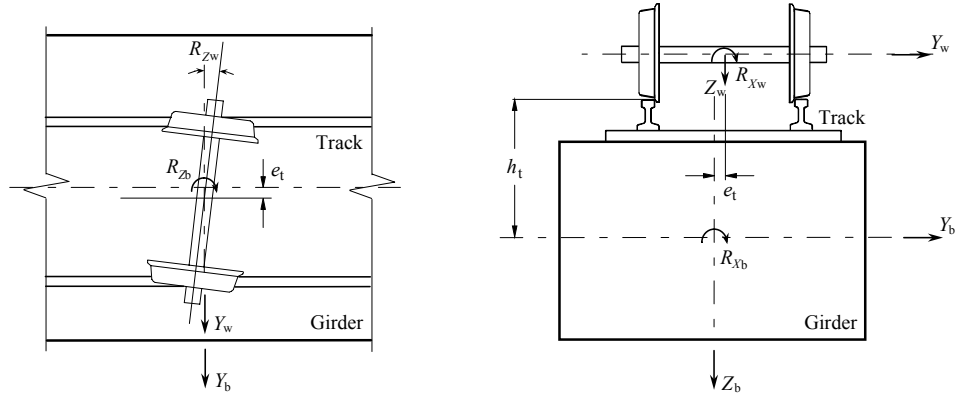


Figure 8. Relationship between wheel-set and bridge girder.

### 3.5. Dynamic Analysis Model for Train-Bridge System Subjected to Earthquakes

By combining the vehicle subsystem Equation (19) and the bridge subsystem Equation (26), together with the wheel-rail contact forces [Equations (34) and (35)], and track irregularities and wheel hunting movement [Equations (38)], the dynamic equations of the coupled train-bridge system subjected to earthquakes can be obtained.

In analyzing the running safety of train vehicles on high-speed railway bridges during earthquakes, the deformation of the bridge can be approximately considered within the elastic range. Therefore, the modal comprehension analysis method can be adopted for modeling the bridge subsystem. The vehicle equations are combined with the modal equations, instead of the direct finite element equations of the bridge.

The dynamic equations of the coupled train-bridge system subjected to earthquakes can thus be expressed as:

$$\begin{bmatrix} \mathbf{M}_{vv} & \mathbf{0} \\ \mathbf{0} & \mathbf{M}_{bb} \end{bmatrix} \begin{Bmatrix} \ddot{\mathbf{X}}_v \\ \ddot{\mathbf{X}}_b \end{Bmatrix} + \begin{bmatrix} \mathbf{C}_{vv} & \mathbf{C}_{vb} \\ \mathbf{C}_{bv} & \mathbf{C}_{bb} \end{bmatrix} \begin{Bmatrix} \dot{\mathbf{X}}_v \\ \dot{\mathbf{X}}_b \end{Bmatrix} + \begin{bmatrix} \mathbf{K}_{vv} & \mathbf{K}_{vb} \\ \mathbf{K}_{vb} & \mathbf{K}_{bb} \end{bmatrix} \begin{Bmatrix} \mathbf{X}_v \\ \mathbf{X}_b \end{Bmatrix} = \begin{Bmatrix} \mathbf{F}_v \\ \mathbf{F}_b \end{Bmatrix} \quad (39)$$

where,  $\mathbf{M}$ ,  $\mathbf{C}$  and  $\mathbf{K}$  are the mass, damping and stiffness matrices, with the subscripts  $v$  representing vehicles, and  $b$  the non-supporting part of the bridge, respectively.

Assume that the number of vehicles on the bridge is  $N_v$  and the number of concerned vibration modes of the bridges is  $N_b$ , the sub-displacement vectors can be expressed as

$$\mathbf{X}_v = [\mathbf{X}_{v1} \quad \mathbf{X}_{v2} \quad \cdots \quad \mathbf{X}_{vN_v}]^T \quad (40a)$$

$$\mathbf{X}_b = [q_1 \quad q_2 \quad \cdots \quad q_{N_b}]^T \quad (40b)$$

where  $\mathbf{X}_{v_i} = [v_{c_i} \quad v_{t_1 i} \quad v_{t_2 i}]^T, i = 1, 2, \dots, N_v$ . The sub-mass and stiffness matrices of the vehicles are listed as follows:

$$\mathbf{M}_{vv} = \begin{bmatrix} \mathbf{M}_{v_1} & \mathbf{0} & \mathbf{0} & \mathbf{0} \\ \mathbf{0} & \mathbf{M}_{v_2} & \mathbf{0} & \mathbf{0} \\ \mathbf{0} & \mathbf{0} & \ddots & \mathbf{0} \\ \mathbf{0} & \mathbf{0} & \mathbf{0} & \mathbf{M}_{v_{N_v}} \end{bmatrix} \quad \mathbf{K}_{vv} = \begin{bmatrix} \mathbf{K}_{v_1} & \mathbf{0} & \mathbf{0} & \mathbf{0} \\ \mathbf{0} & \mathbf{K}_{v_2} & \mathbf{0} & \mathbf{0} \\ \mathbf{0} & \mathbf{0} & \ddots & \mathbf{0} \\ \mathbf{0} & \mathbf{0} & \mathbf{0} & \mathbf{K}_{v_{N_v}} \end{bmatrix} \quad (41)$$

where

$$\mathbf{M}_{v_i} = \begin{bmatrix} \mathbf{M}_{cc_i} & \mathbf{0} & \mathbf{0} \\ \mathbf{0} & \mathbf{M}_{t_1 t_1 i} & \mathbf{0} \\ \mathbf{0} & \mathbf{0} & \mathbf{M}_{t_2 t_2 i} \end{bmatrix} \quad \mathbf{K}_{v_i} = \begin{bmatrix} \mathbf{K}_{cc_i} & \mathbf{K}_{t_1 c_i} & \mathbf{K}_{t_2 c_i} \\ \mathbf{K}_{c t_1 i} & \mathbf{K}_{t_1 t_1 i} & \mathbf{0} \\ \mathbf{K}_{c t_2 i} & \mathbf{0} & \mathbf{K}_{t_2 t_2 i} \end{bmatrix} \quad (42)$$

The sub-damping matrix of the vehicle can be achieved by simply replacing ‘K’ in the stiffness matrix by ‘C’. The sub-mass, sub-stiffness, and sub-damping matrices of the bridge are deduced as follows:

$$\mathbf{M}_{bb} = \begin{bmatrix} 1 + M_b^{11} & M_b^{12} & \cdots & M_b^{1N_b} \\ M_b^{21} & 1 + M_b^{22} & \cdots & M_b^{2N_b} \\ \cdots & \cdots & \ddots & \cdots \\ M_b^{N_b 1} & M_b^{N_b 2} & \cdots & 1 + M_b^{N_b N_b} \end{bmatrix} \quad (43)$$

$$M_b^{nm} = \sum_{i=1}^{N_v} \sum_{j=1}^2 \sum_{l=1}^{N_{w_i}} (\Phi_{hijl}^{nm} m_{w_{ijl}} + \phi_{bijl}^{nm} J_{w_{ijl}} + \Phi_{vijl}^{nm} m_{w_{ijl}}) \quad (44)$$

$$\mathbf{K}_{bb} = \begin{bmatrix} \omega_1^2 + K_b^{11} & K_b^{12} & \cdots & K_b^{1N_b} \\ K_b^{21} & \omega_2^2 + K_b^{22} & \cdots & K_b^{2N_b} \\ \cdots & \cdots & \ddots & \cdots \\ K_b^{N_b 1} & K_b^{N_b 2} & \cdots & \omega_{N_b}^2 + K_b^{N_b N_b} \end{bmatrix} \quad (45)$$

$$K_b^{nm} = \sum_{i=1}^{N_v} \sum_{j=1}^2 \sum_{l=1}^{N_{w_i}} (\Phi_{hijl}^{nm} k_{ij}^h + 2\phi_{bijl}^{nm} k_{ij}^v a_i^2 + \Phi_{vijl}^{nm} k_{ij}^v) \quad (46)$$

$$\mathbf{C}_{bb} = \begin{bmatrix} 2\xi\omega_1 + C_b^{11} & C_b^{12} & \cdots & C_b^{1N_b} \\ C_b^{21} & 2\xi\omega_2 + C_b^{22} & \cdots & C_b^{2N_b} \\ \cdots & \cdots & \ddots & \cdots \\ C_b^{N_b 1} & C_b^{N_b 2} & \cdots & 2\xi\omega_{N_b} + C_b^{N_b N_b} \end{bmatrix} \quad (47)$$

$$C_b^{nm} = \sum_{i=1}^{N_v} \sum_{j=1}^2 \sum_{l=1}^{N_{wi}} (\Phi_{hijl}^{nm} c_{lij}^h + 2\phi_{\theta ij}^{nm} c_{lij}^v \alpha_i^2 + \Phi_{vijl}^{nm} c_{lij}^v) \quad (48)$$

The sub-stiffness matrices attributed to the interaction between the bridge and the vehicles can be derived as follows:

$$\mathbf{K}_{vb} = \{\mathbf{K}_{bv}\}^T = \begin{bmatrix} \mathbf{K}_{vb1} \\ \mathbf{K}_{vb2} \\ \dots \\ \mathbf{K}_{vbN_v} \end{bmatrix} \quad (49)$$

$$\mathbf{K}_{vbi} = \begin{bmatrix} \mathbf{0} & \mathbf{0} & \dots & \mathbf{0} \\ \mathbf{K}_{t_1 q_1}^i & \mathbf{K}_{t_1 q_2}^i & \dots & \mathbf{K}_{t_1 q_{N_b}}^i \\ \mathbf{K}_{t_2 q_1}^i & \mathbf{K}_{t_2 q_2}^i & \dots & \mathbf{K}_{t_2 q_{N_b}}^i \end{bmatrix} \quad (50)$$

$$\mathbf{K}_{t_j q_n}^i = \{\mathbf{K}_{q_n t_j}^i\}^T = - \sum_{l=1}^{N_{wi}} \begin{bmatrix} (\phi_{hijl}^n + h_{4i} \phi_{\theta ij}^n) k_{lij}^h \\ 2\phi_{\theta ij}^n \alpha_i^2 k_{lij}^v - h_{4i} \phi_{hijl}^n k_{lij}^h \\ 2\eta_{jl} d_i \phi_{hijl}^n k_{lij}^h \\ (\phi_{vijl}^n + e_i \phi_{\theta ij}^n) k_{lij}^v \\ 2\eta_{jl} d_i \phi_{vijl}^n k_{lij}^v \end{bmatrix} \quad (51)$$

where  $i = 1, 2, \dots, N_v$ ,  $n = 1, 2, \dots, N_b$ , and  $j = 1, 2$ . The sub-damping matrices attributed to the interaction between the bridge and vehicles can be obtained by simply replacing “ $k$ ” in upper Equation (49) to (51) by “ $c$ ”.

$\mathbf{F}_v$  is the wheel-rail contact forces acting on the wheel set, which is determined by the relative displacement between the wheel and the rail.  $\mathbf{F}_b$  is the generalized seismic force vector acting on the non-supporting parts of bridge, consisting of the generalized wheel-rail contact forces vector  $\mathbf{F}_{bv}$  and the generalized seismic forces vector  $\mathbf{F}_{bs}$ , transmitted by the influence matrix from the supporting parts of the bridge.

Suppose there are  $N_v$  vehicles traveling on the bridge when an earthquake occurs, the wheel-rail contact force vector  $\mathbf{F}_v$  acting on the vehicle can be expressed as:

$$\mathbf{F}_v = [\mathbf{F}_{v1} \quad \mathbf{F}_{v2} \quad \dots \quad \mathbf{F}_{vN_v}]^T \quad (52)$$

where  $\mathbf{F}_{vi}$  is the wheel-rail contact force vector of the  $i$ th vehicle, and can be expressed as:

$$\mathbf{F}_{vi} = [\mathbf{F}_c \quad \mathbf{F}_{t1} \quad \mathbf{F}_{t2} \quad \mathbf{F}_{wi1} \quad \mathbf{F}_{wi2} \quad \mathbf{F}_{wi3} \quad \mathbf{F}_{wi4}]^T \quad (53)$$

where,  $F_c$ ,  $F_{t1}$  and  $F_{t2}$  are zero vectors, since there are no external forces directly transmitted to the car body and the two bogies;  $F_{wij}$  is the wheel-rail force vector of the  $j$ th wheel-set of the  $i$ th vehicle on the bridge, and can be expressed as:

$$\mathbf{F}_{wij} = \left\{ \begin{array}{l} -F_{Lij}^y - F_{Rij}^y - N_{Lij}^y - N_{Rij}^y \\ a_{Li}(F_{Lij}^z + N_{Lij}^z) - a_{Ri}(F_{Rij}^z + N_{Rij}^z) - r_{Lij}(F_{Lij}^y + N_{Lij}^y) - r_{Rij}(F_{Rij}^y + N_{Rij}^y) \\ a_{Li}(F_{Lij}^x + N_{Lij}^x) - a_{Ri}(F_{Rij}^x + N_{Rij}^x) + M_{Lij}^z + M_{Rij}^z + \psi_{wij}[a_{Li}(F_{Lij}^y + N_{Lij}^y) - a_{Ri}(F_{Rij}^y + N_{Rij}^y)] \\ -F_{Lij}^z - F_{Rij}^z - N_{Lij}^z - N_{Rij}^z \end{array} \right\} \quad (54)$$

where,  $N$  and  $F$  are, respectively, the normal and tangent interaction forces between the  $j$ th wheel-set of the  $i$ th vehicle and the rail, with the subscripts L and R standing for the left and right wheels of the wheel-set, and the superscripts  $x$ ,  $y$ ,  $z$  denoting the coordinate axes in the fixed coordinate system, respectively. The relationship between the wheel and the rail in the local coordinate system is shown in Figure 5, where  $A$  and  $B$  are contact points of the left and right wheels with the corresponding rails;  $a_{Li}$  and  $a_{Ri}$  are the horizontal projections of the distance from the  $i$ th left and right wheel-rail contact points to the centroid of the wheel-set, respectively.

Let  $N_q$  denote the mode number concerned in the analysis of the finite element model of the bridge, the modal force vector of the bridge can be expressed as:

$$\mathbf{F}_b = [F_{b1} \quad F_{b2} \quad \cdots \quad F_{bN_q}]^T \quad (55)$$

where,  $F_{bn}$  ( $n=1,2,\dots, N_q$ ) is the generalized force of the  $n$ th mode, consisting of the generalized wheel-rail contact forces  $F_{bvn}$  and the generalized seismic forces  $F_{bsn}$ , transmitted by the influence matrix from the supporting parts of the bridge. They can be expressed as:

$$F_{bn} = F_{bsn} + F_{bvn} \quad (56)$$

where:

$$F_{bsn} = -\Phi_n^T \mathbf{M}_{bb} \mathbf{R}_{bs} \ddot{\mathbf{X}}_{sg} \quad (57)$$

in which,  $\Phi_n^T$  is the transposition of the  $n$ th mode vector for all non-supporting nodes of the bridge;  $\mathbf{M}_{bb}$  the mass matrix of the corresponding nodes; and  $\mathbf{R}_{bs}$  the pseudo-static displacement influence matrix of the bridge supporting nodes on the non-supporting nodes. The minus sign in the right hand side of this equation indicates that the force is in opposite direction to the ground acceleration. In practice this has little significance inasmuch as the engineer is interested in the maximum absolute value of  $\ddot{\mathbf{X}}_{sg}$ , therefore, the minus sign is omitted in the following descriptions.

The horizontal and vertical seismic excitations are considered in the analysis. When multi-point excitations are considered, the following expression can be found:

$$F_{bsn} = \sum_{i=1}^{N_h} \sum_{j=1}^{N_s} m_{bbi} r_{bsij} (\phi_{ni}^h \ddot{X}_{sgj}^h + \phi_{ni}^v \ddot{X}_{sgj}^v) \quad (n=1,2,\dots,N_q) \quad (58)$$

where,  $N_b$  and  $N_s$  are the node numbers of the non-supporting part and supporting part in the finite element model of the bridge, respectively;  $m_{bbi}$  the mass of the  $i$ th node of the non-supporting parts of the bridge;  $\phi_{ni}^h$  and  $\phi_{ni}^v$  the values of the horizontal and vertical components of the  $n$ th bridge mode vector at the  $i$ th node of the non-supporting part of the bridge, respectively;  $\ddot{X}_{sgj}^h$  and  $\ddot{X}_{sgj}^v$  the horizontal and vertical acceleration components of the earthquake input from the  $j$ th supporting node of the bridge, respectively; and  $r_{bsij}$  the influence matrix element of the  $j$ th supporting node on the  $i$ th non-supporting node.

The generalized wheel-rail force acting on the bridge can be written as:

$$F_{bvn} = \sum_{i=1}^{N_b} \sum_{j=1}^4 F_{nij} \quad (59)$$

where  $F_{nij}$  is the  $n$ th generalized wheel-rail force of the  $j$ th wheel-set of the  $i$ th vehicle on the bridge deck. When the wheel deviates from the rail,  $F_{nij}$  equals to zero; and when the wheel keeps contact with the rail,  $F_{nij}$  can be calculated as:

$$\begin{aligned} F_{nij} = & \phi_n^h(x_{ij})(N_{L,yij} + F_{L,yij} + N_{R,yij} + F_{R,yij}) \\ & + [\phi_n^v(x_{ij}) + e_t \phi_n^\theta(x_{ij})](N_{L,zij} + F_{L,zij} + N_{R,zij} + F_{R,zij}) \\ & + \phi_n^\theta(x_{ij})[-a_{Li}(N_{L,zij} + F_{L,zij}) + a_{Ri}(N_{R,zij} + F_{R,zij}) + (N_{L,yij} + F_{L,yij} + N_{R,yij} + F_{R,yij})h_t] \end{aligned} \quad (60)$$

where,  $\phi_n^h(x_{ik})$ ,  $\phi_n^v(x_{ik})$  and  $\phi_n^\theta(x_{ik})$  are, respectively, the values of the horizontal, vertical and rotational components of the  $n$ th bridge mode shape at the  $j$ th wheel of the  $i$ th vehicle on the bridge deck;  $e_t$  the eccentric distance from the track center line to the centroid of the girder cross section; and  $h_t$  the vertical distance from the wheel-rail contact point to the centroid of girder cross section. The relative position between the wheel-set and bridge deck can be seen in Figure 8.

Equation (39) can be solved by the step-by-step integration method. In each time step, the responses of the vehicle and the bridge are calculated separately, and then the iterative processes are adopted to meet the convergence allowances of the two subsystems in the following way: first a displacement vector of the bridge and the vehicle at the wheel-rail contact point is assumed and the wheel-rail contact forces are calculated, from which the new displacement vector can be obtained by solving the equations; when the maximum errors between the solved displacements and the assumed ones are within the prescribed allowance, the solved displacements at this time step are taken as the actual ones and the calculation continues to the next step.

Details of the calculation process for the above equations can be found in Han (2005) and Xia (2005).

A computer code of the train-bridge system subjected to earthquakes is developed based on the formulations described above and is employed to perform a case study.

## 4. Case Study

### 4.1. Case Study I: Dynamic Responses of Simply-Supported Bridges Subjected to Uniform Seismic Excitations

#### 4.1.1. Bridge Description and Calculation Method

With the construction of quasi-high speed railways and high-speed railways in China, various types of bridges suitable for high-speed trains emerge as the times require. More and more multi-span simply-supported beam bridges with various structural styles, span-lengths and lateral deck widths have been designed and built.

In Northeast China, the 404 km Qin-Shen Special Passenger Railway (Qin-Shen Railway) from Qinhuangdao to Shenyang, with the design train speed of 200 km/h and an 83 km high speed experimental section of 300 km/h, has been completed and put into operation. There were ten types of simply-supported beam bridges adopted in the Qin-Shen Railway, including two types of T-shaped beams and eight types of box beams (see Table 1).

**Table 1. Maximum responses of bridges**

Bridge type		Span length (m)	Beam height (m)	Track type
Double-track railway bridge	T-shaped beam	12.0	1.3	Ballast track
		16.0	1.6	
	Box beam	20.0	1.8	
		24.0	2.0	Integrated slab track
		24.0	2.2	
		24.0	2.2	Long-sleeper buried ballastless track
Single-track railway bridge	Box beam	32.0	2.6	Ballast track
		20.0	1.8	Ballast track
		24.0	2.0	
		32.0	2.7	

During the design of the Qin-Shen Railway, the dynamic characteristics of the high-speed railway bridges were systematically studied through theoretical analysis, numerical simulations and field experiments, to ensure the safety of bridge structure and the running safety and stability of high-speed trains. The dynamic analysis models of the train-bridge system were established, by which the dynamic characteristics and time history responses of the train-bridge coupling system were calculated and analyzed. Furthermore, the running safety and riding comfort of the moving trains on the bridge with different types and speeds were investigated.

In September and November 2002, two field experiments were carried out in the experimental section of the Qin-Shen Railway. In the experiments, the China-made high-speed trains, called “China-star” and “Pioneer” were used, with the highest train speeds

reaching 290 km/h and 321.5 km/h, respectively. Many useful results have been achieved from the experimental data, which verified the train-bridge system analysis model and the calculated results (Xia and Zhang, 2005).

Since this railway line is located in the Bohai Rim earthquake sensitive region in China, the consideration of seismic excitations is necessary.

The case study analyzes the runnability of the moving trains on the ten types of simply-supported beam bridges subjected to earthquakes, with each bridge having five spans and four 12m-height-piers.

By normalizing the maximum acceleration as 0.1g in lateral direction and 0.05g in vertical, the seismic waves are input along the lateral and vertical directions from the bridge foundations identically (see Figure 9).

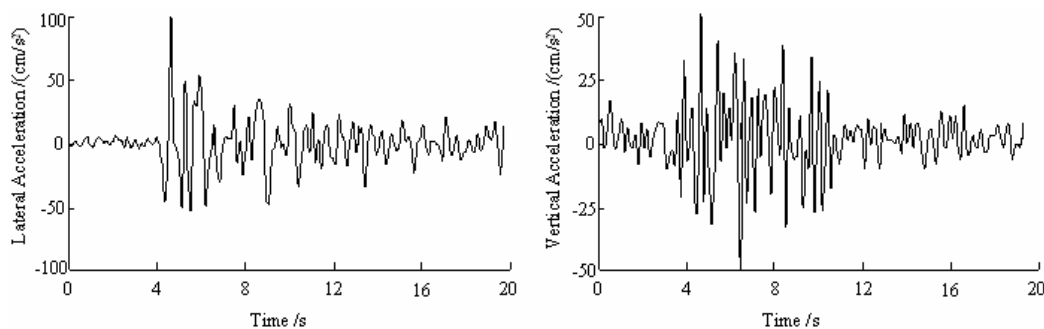


Figure 9. Input seismic accelerations: (left) lateral acceleration; (right) vertical acceleration.

The vertical, lateral and torsional irregularities of the track on the bridge are taken into consideration as the self-excitation by using the measured data from the Qinghuangdao-Shenyang Special Passenger Railway in China. The wheel hunting displacement  $Y_h$  (in the lateral direction) is assumed as a sinusoid function with a certain amplitude and a random phase, expressed as Equation (37), in which the hunting wavelength and amplitude are 15 m and 3 mm, respectively. Then the whole time histories of the running trains through the multi-span simple beam bridges are simulated on computers by using the real parameters of the bridge structures and the train vehicles. The dynamic responses of the bridge and the train vehicles, including the displacement and accelerations of the bridge and the derailment factors, the offload factors, and the wheel/rail lateral forces are obtained.

#### 4.1.2. Calculation Results

##### Dynamic Responses of Train-Bridge System under Earthquake Loads

The dynamic responses of the train-bridge coupling system when the power-concentrated train composed of 2 locomotive + 10 passenger cars, running on the bridge at a constant speed of 200 km/h with or without seismic excitations are both calculated, for the purpose of investigating the behaviors of various types of bridge structures subjected to earthquakes.

Shown in Figure 10 and Figure 11 are the lateral and vertical dynamic responses of the bridge at the middle mid-span as the train runs through with and without seismic excitations (designated by the dashed line and the continuous line, respectively). Displayed in Figure 12

are the comparisons of the lateral and vertical acceleration responses of the first locomotive. It is seen from the response time histories that under the earthquake action, there are remarkable rises in the dynamic responses of the bridge and the vehicle.

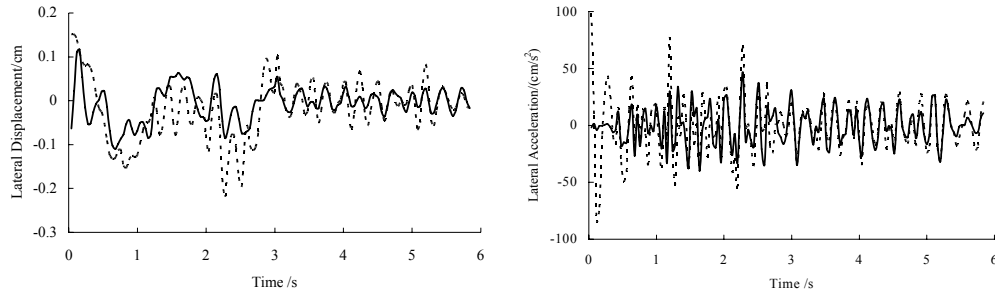


Figure 10. Comparisons of lateral responses of bridge at mid-span with and without earthquakes.

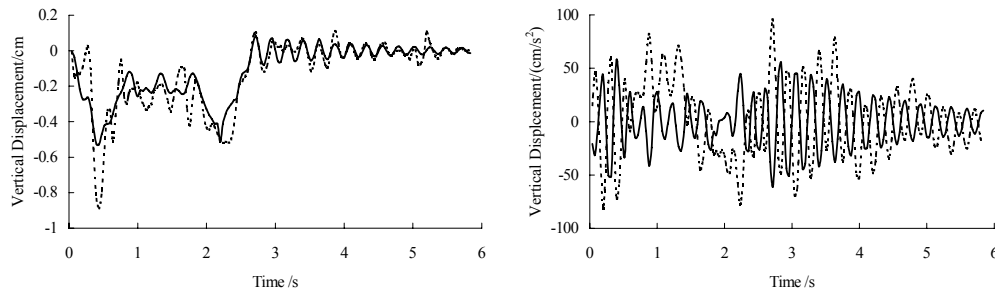


Figure 11. Comparisons of vertical responses of bridge at mid-span with and without earthquakes.

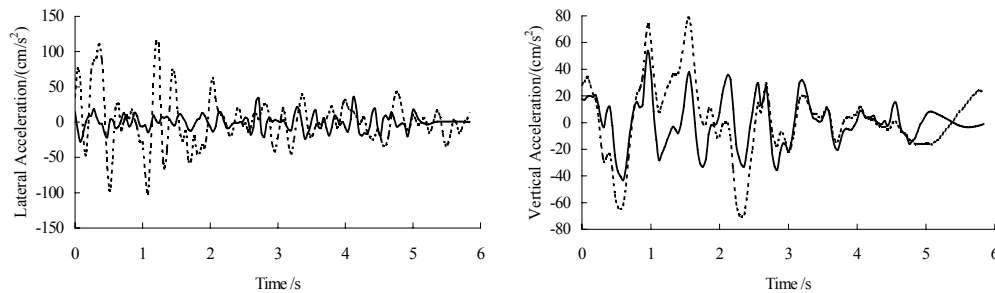


Figure 12. Comparisons of vehicle accelerations with and without earthquakes.

The maximum responses of the ten types of bridges with and without seismic excitations are listed in Table 2. It is found that the seismic actions have great influences on the dynamic responses of the bridge, especially for the single-track railway bridges. This may be because the lateral stiffness of the single-track bridge structures is weaker than that of the double-track ones. As a result, the vibration displacements and accelerations subjected to earthquakes are more prominent. In addition, the higher-frequency components occupy the majority of the input seismic waves, and the natural frequencies of the simple beam bridge are comparatively higher than long span bridges, these kinds of bridges are therefore more sensitive to the seismic excitation.

**Table 2. Maximum responses of Bridges**

Bridge type		Displacement (cm)				Acceleration (cm/s <sup>2</sup> )			
		Lateral		Vertical		Lateral		Vertical	
		1*	2*	1*	2*	1*	2*	1*	2*
Double-track railway bridge	T-shaped beam, span 12m, height 1.3m	0.102	0.068	0.196	0.112	59.8	36.6	154.1	118.0
	T-shaped beam, span 16m, height 1.6m	0.133	0.070	0.369	0.277	61.2	39.9	221.8	170.2
	Box beam, span 20m, height 1.8m	0.154	0.076	0.440	0.265	55.4	33.1	134.2	98.5
	Box beam, span 24m, height 2.0m	0.151	0.073	0.500	0.303	53.2	29.0	141.8	105.4
	Box beam, span 24m, height 2.2m, integrated slab track	0.138	0.065	0.390	0.268	51.5	27.9	133.0	101.4
	Box beam, span 24m, height 2.2m, long-sleeper buried ballastless track	0.134	0.065	0.395	0.274	50.9	28.6	135.5	102.3
	Box beam, span 32m, height 2.6m	0.198	0.097	0.865	0.554	52.6	28.9	90.2	63.4
Single-track railway bridge	Box beam, span 20m, height 1.8m	0.315	0.179	0.380	0.262	106.0	56.4	141.1	109.8
	Box beam, span 24m, height 2.0m	0.288	0.141	0.553	0.392	111.8	53.3	128.5	99.7
	Box beam, span 32m, height 2.7m	0.219	0.117	0.887	0.528	98.8	46.5	95.7	61.1

The maximum responses of the vehicles with and without seismic excitations are listed in Table 3. It is also found that earthquake actions have significant influences on the dynamic responses of the vehicle.

The evaluation indices for the running safety of train vehicles currently adopted for the high-speed railways in China include the derailment factor  $Q/P$  (defined as the ratio of the lateral wheel-rail force to the vertical wheel-rail force), the offload factor  $\Delta P/P$  (defined as the ratio of the offload vertical wheel-rail force to the static vertical wheel-rail force), and the lateral wheel-rail force  $Q$ . The expressions and allowances of these indices are as follows:

$$\begin{aligned}
 \text{Derail factor :} & \quad Q/P \leq 0.8 \\
 \text{Offload factor :} & \quad \Delta P/P \leq 0.6 \\
 \text{Wheel/rail force :} & \quad Q \leq 0.85(10 + P_{st}/3)
 \end{aligned} \tag{61}$$

where,  $P_{st}$  denotes the static wheel-set load in kN.

**Table 3. Maximum responses of vehicles**

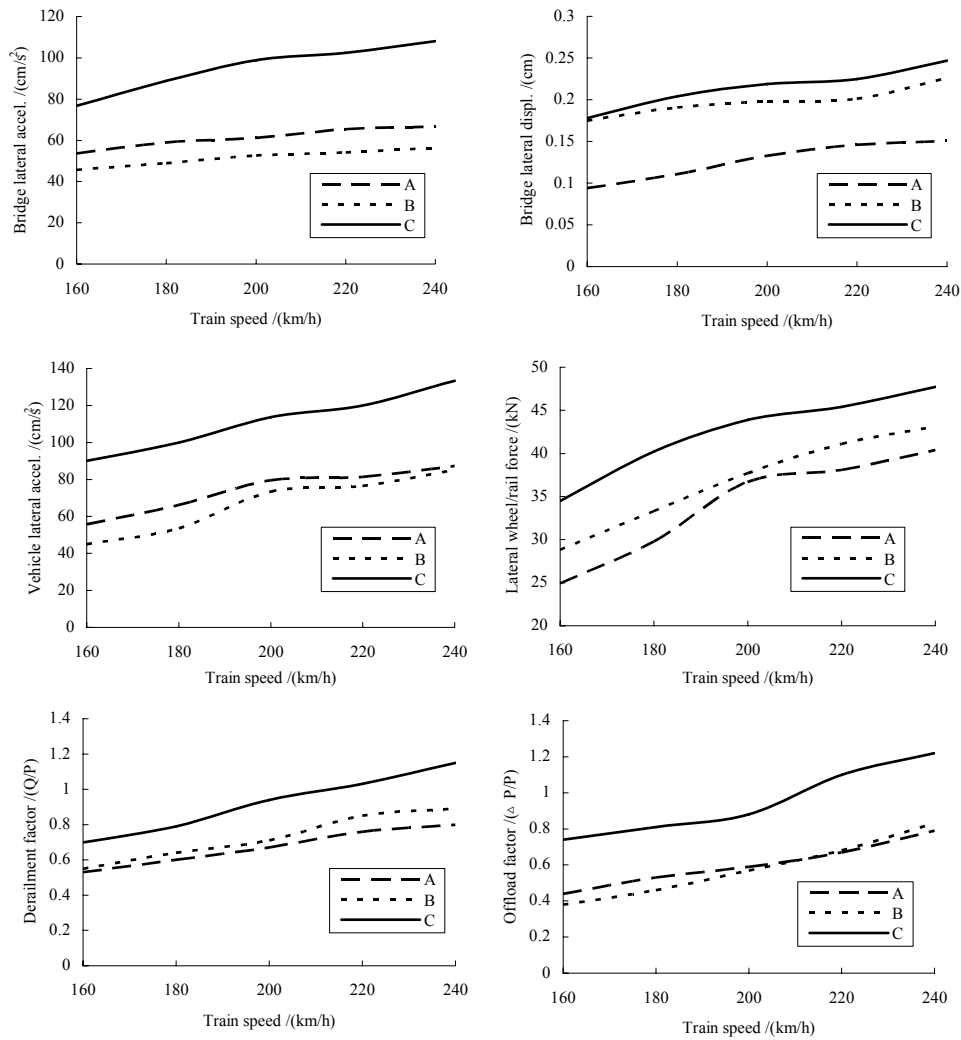
Bridge type		Derailment Factor (Q/P)		Offload Factor ( $\Delta P/P$ )		Lateral Wheel/rail Force (Q)		Lateral Acceleration ( $\text{cm/s}^2$ )		Vertical Acceleration ( $\text{cm/s}^2$ )	
		1*	2*	1*	2*	1*	2*	1*	2*	1*	2*
Double-track railway bridge	T-shaped beam, span 12m, height 1.3m	0.64	0.25	0.56	0.30	35.3	16.4	76.3	28.8	99.4	61.5
	T-shaped beam, span 16m, height 1.6m	0.67	0.26	0.59	0.34	36.7	18.2	79.5	33.1	81.5	42.0
	Box beam, span 20m, height 1.8m	0.63	0.32	0.53	0.35	40.4	24.1	80.8	34.0	88.4	49.3
	Box beam, span 24m, height 2.0m	0.66	0.31	0.52	0.36	41.5	23.6	80.2	36.7	74.0	46.3
	Box beam, span 24m, height 2.2m, integrated slab track	0.65	0.28	0.52	0.40	38.9	22.2	74.5	33.5	67.5	37.8
	Box beam, span 24m, height 2.2m, long sleeper buried ballastless track	0.65	0.28	0.52	0.35	37.6	21.0	73.1	30.2	66.6	38.7
	Box beam, span 32m, height 2.6m	0.71	0.38	0.57	0.35	37.7	21.0	73.4	29.9	80.2	55.3
Single-track railway bridge	Box beam, span 20m, height 1.8m	0.97	0.39	0.92	0.46	50.5	28.7	126.0	55.5	70.0	48.1
	Box beam, span 24m, height 2.0m	0.96	0.45	0.89	0.49	39.7	25.1	129.4	51.0	84.4	53.2
	Box beam, span 32m, height 2.7m	0.94	0.45	0.88	0.52	43.9	22.9	113.7	42.8	78.7	54.0

Note: 1\* indicates the case with seismic excitation, while 2\* without.

### Influences of Train Speed

Taking three kinds of simply-supported beam bridges as examples, i.e., the T-shaped beam bridge with double-tracks (span: 16m, height: 1.6m), the box beam bridge with double-tracks (span: 32m, height: 2.6m), and the box beam bridge with single-track (span: 32m, height: 2.7m), to study the dynamic behaviors of the train-bridge coupling system subjected to earthquakes with different train speeds.

Displayed in Figure 13 are the distributions of the maximum responses of the bridge and the vehicle with respect to the train speed. The results show that the dynamic indices all increase with the train speed.



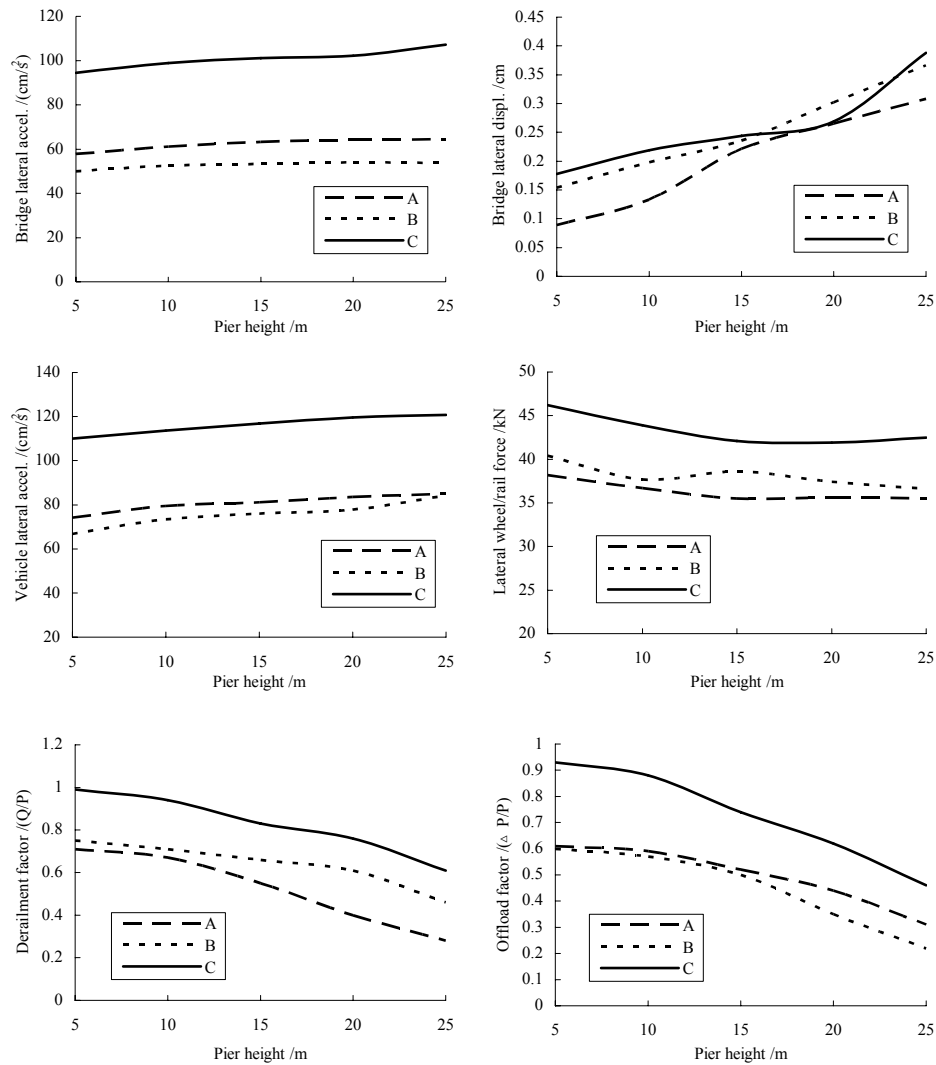
**Note:** A represents the T-shaped beam bridge with double-tracks (span: 16m, height: 1.6m);  
 B represents the box beam bridge with double-tracks (span: 32m, height: 2.6m);  
 C represents the box beam bridge with single-tracks (span: 32m, height: 2.7m).

Figure 13. Dynamic responses of train-bridge system vs train speed.

### Influences of Pier Height

The relationship between the pier height and the seismic responses of the superstructure is more complex. In this section, taking three kinds of simple beam bridges described above as examples, to study the dynamic behaviors of the train-bridge coupling system subjected to earthquakes with different pier heights.

Displayed in Figure 14 are the distributions of the maximum responses of the bridge and the vehicle with respect to the pier height.



**Note:** A represents the T-shaped beam bridge with double-tracks (span: 16m, height: 1.6m);  
 B represents the box beam bridge with double-tracks (span: 32m, height: 2.6m);  
 C represents the box beam bridge with single-tracks (span: 32m, height: 2.7m).

Figure 14. Dynamic responses of train-bridge system vs pier height.

#### 4.1.3. Summary of Analytical Results for Case Study I

The main conclusions are summarized for the case study of dynamic responses of simply-supported bridges subjected to uniform seismic excitations as follows:

1. For the ten kinds of simple beam bridges with the span-length ranging from 12 m to 32 m adopted in the Qinghuangdao-Shenyang Special Passenger Railway in China, earthquake actions have significant influences on the train-bridge coupling system,

which results in the increase of the system responses, while the decrease of the structure safety.

2. The train speed and the pier heights have significant effects on the dynamic responses of the train-bridge coupling system subjected to earthquakes.
3. Due to that the seismic accelerations used in the case study are normalized as  $100 \text{ cm/s}^2$  in horizontal and  $50 \text{ cm/s}^2$  in vertical, respectively, the results are only adapted to the analysis of the response mechanism and rules of train-bridge system under earthquakes. For the safety assessment of the system, further analysis should be performed using actual earthquake records.

## 4.2. Case Study II: Dynamic Responses of a Continuous Bridge Subjected to Non-uniform seismic Excitations

The case study on the train-bridge system subjected to non-uniform seismic excitations concerns a continuous bridge across the Huaihe River on the Beijing-Shanghai High-speed Railway in China, which is now under construction.

### 4.2.1. Bridge Description and Calculation Parameters

The bridge consists of seven spans of continuous PC box girders,  $48+5\times 80+48 \text{ m}$ , as is shown in Figure 15, which is also one of the most commonly used structural types of bridges in the high-speed railways in China.

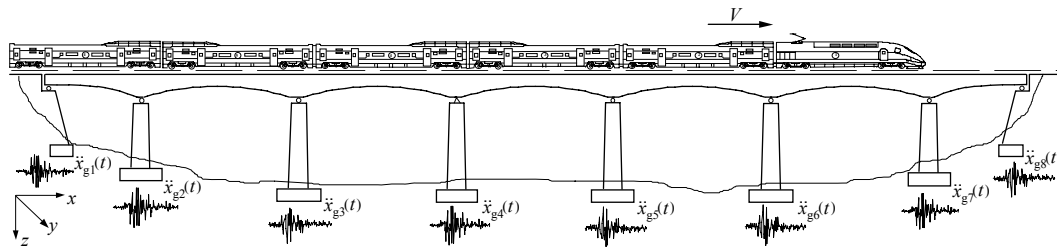


Figure 15. Model of train-bridge system subjected to earthquake.

The bridge is located on the site with Class-II subsoil. The piers are 16~22 m high, with round-end sections and pile foundations.

The continuous box girders have variable sections that are 6.1 m high at the support position and 3.8 m at the mid-span (see Figure 16). Mounted on the third pier are fixed pot neoprene bearings, while the rest are moveable ones.

The ANSYS software is employed in establishing the finite element model of the bridge, with the girders and piers being all dispersed by using the Beam 4 elements, and the secondary loads of the bridge distributed on the girders as supplementary mass.

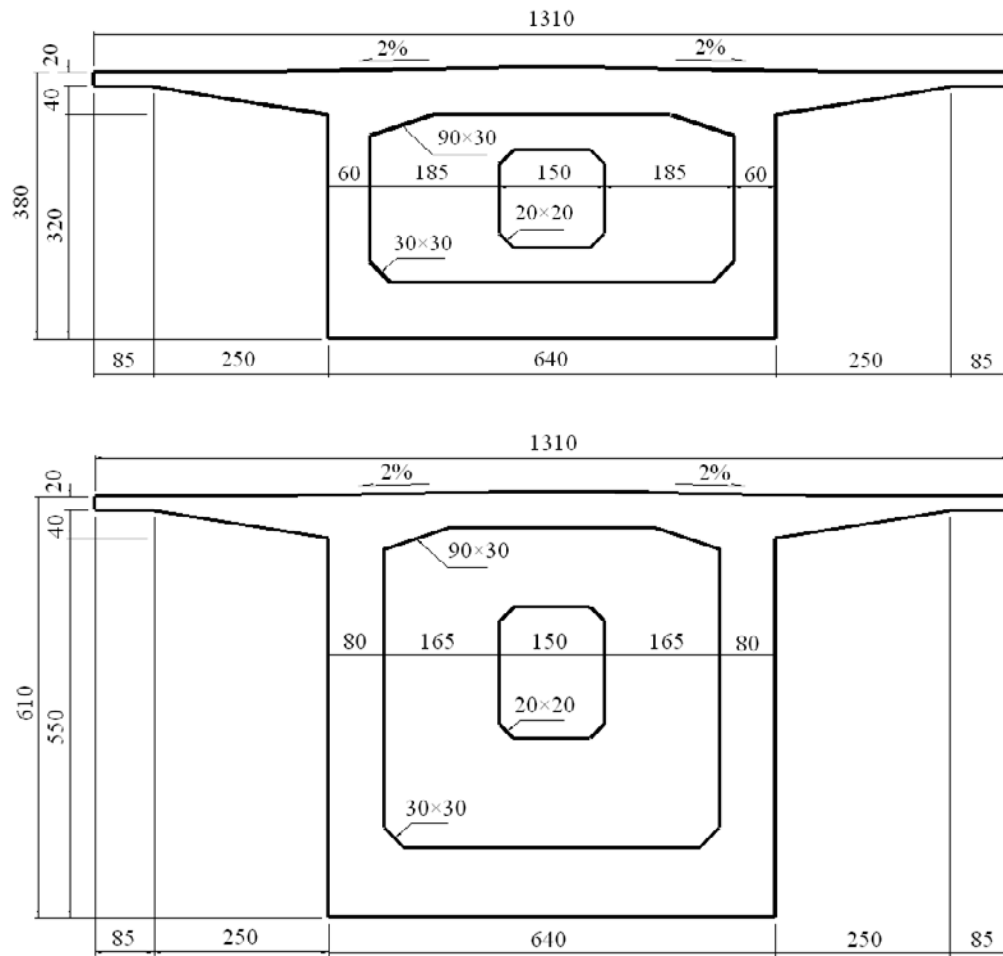


Figure 16. Typical cross-section of bridge deck: (upper) mid-span; (lower) support.

For the movable bearings, the translational displacements along the longitudinal axis  $x$  are free, and so are the rotations with respect to the vertical axis  $z$  and the transverse axis  $y$  of the girder ends; while the translational displacements along the other two axes are taken as the master-and-slave freedoms with the pier-tops, and so is the rotation with respect to the longitudinal axis  $x$ .

For the fixed bearings, the rotations with respect to the vertical axis  $z$  and the transverse axis  $y$  of the girder ends are free; while the other three translational displacements and one rotation are taken as the master-and-slave freedoms with the pier-top.

The interactions between the foundations and the soils are modeled by the Matrix 27 elements. The parameters of the elements are determined according to the dimensions and the properties of the surrounding soils. The natural vibration properties of the bridge are analyzed and there are altogether 60 frequencies and mode shapes obtained for such a long seven-span bridge, and are included in the calculation. The first vertical and lateral frequencies of the girders are 1.24 Hz and 2.33 Hz, respectively (see Table 4).

**Table 4. Modal analysis summary of the bridge**

Mode number	Natural Frequency (Hz)	Description of mode shape
1	0.90	Longitudinal vibration of bridge deck and piers
2	1.24	Vertical vibration of bridge deck
3	1.57	Vertical vibration of bridge deck
4	2.01	Vertical vibration of bridge deck
5	2.33	Lateral vibration of bridge deck
6	2.52	Vertical vibration of bridge deck
7	2.57	Lateral vibration of bridge deck
8	2.90	Lateral vibration of bridge deck
9	3.05	Vertical vibration of bridge deck
10	3.06	Longitudinal vibration of piers
11	3.09	Lateral vibration of bridge deck and piers
12	3.21	Lateral vibration of bridge deck and piers
13	4.16	Vertical vibration of bridge deck
14	4.26	Vertical vibration of bridge deck
15	5.25	Lateral vibration of bridge deck and piers
16	5.35	Vertical vibration of bridge deck
17	5.58	Lateral vibration of bridge deck and piers
18	5.83	Lateral vibration of bridge deck and piers
19	5.91	Lateral vibration of bridge deck and piers
20	6.07	Vertical vibration of bridge deck

A seismic acceleration record from the Kern County earthquake, which took place on July 21, 1952, is selected for the study. The time record and the power spectrum of this earthquake are shown in Figure 17, from which one can see that the main frequency of the earthquake is 2.78Hz. The maximum accelerations in the analysis are normalized as 0.1g in the horizontal direction (perpendicular to the longitudinal axis of the bridge) and 0.05g in the vertical direction.

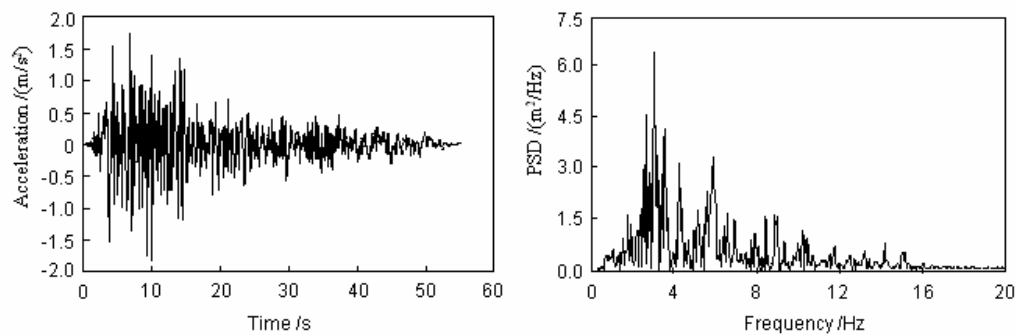


Figure 17. Seismic acceleration (left) and its PSD (right) curves.

Three classes of subsoil, Class-I, Class-II and Class-III, are considered in the analysis. Assuming that the earthquake wave propagates in the subsoil from one end of the bridge to the other, for each class of subsoil, three propagating velocities of the seismic wave are used in the simulations, which are 800m/s, 1000m/s and 1500m/s for Class-I subsoil; 400m/s, 500m/s and 600m/s for Class-II subsoil; and 180m/s, 250m/s and 360m/s for Class-III subsoil, respectively. The wavelengths corresponding to the main frequency of 2.78Hz can thus be estimated as 288m, 360m and 432m for Class-I subsoil; 144m, 180m and 216m for Class-II subsoil; and 65m, 90m and 130m for Class-III subsoil, which are longer than the distances between the adjacent bridge piers, but shorter than the total length of the bridge. The seismic waves with phase differences are input along the horizontal and vertical directions to the bridge foundations. For the concerned continuous bridge, the maximum time delays between the seismic waves arriving at the foundations are 0.62s, 0.49s and 0.33s for Class-I subsoil; 1.24s, 0.99s and 0.83s for Class-II subsoil; and 2.76s, 1.98s and 1.38s for Class-III subsoil, respectively.

The high-speed train China-Star, used in the calculation, consists of one front locomotive, nine passenger cars and one rear locomotive, with the average axle loads being 195kN for the locomotive and 142.5kN for the passenger car, respectively. The lateral and vertical natural frequencies are 1.23 Hz and 0.952 Hz for the locomotive, and 1.05 Hz and 0.734 Hz for the passenger car, respectively. Figure 18 illustrates the dimensions of the first locomotive and the two passenger cars. The calculation train speeds are 120, 160, 200, 240, 280 and 320 km/h, respectively.

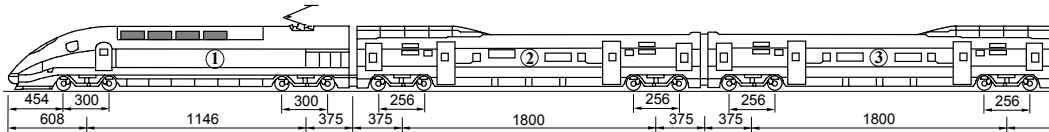


Figure 18. Composition of the China-Star high-speed train (unit: cm).

The track irregularities measured from the Qinghuangdao-Shenyang Special Passenger Railway in China are used in the calculation (Xia and Zhang, 2005). There are four groups of irregularities, including left vertical, right vertical, left lateral and right lateral, used for the left and right rails, respectively. Displaced in Figure 19 are the lateral irregularity curve and its power spectrum.

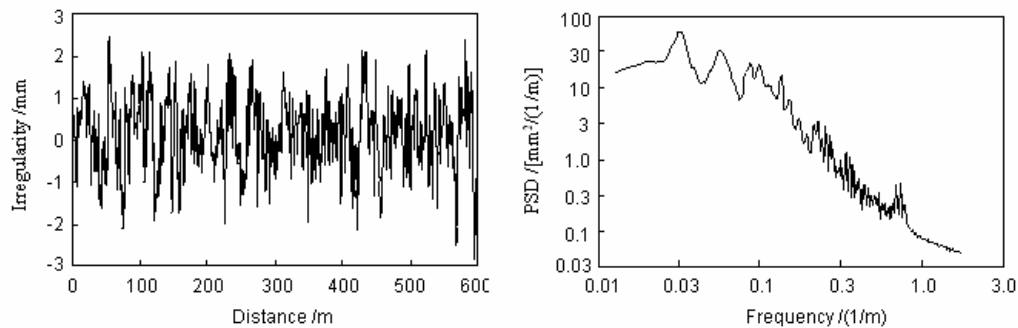


Figure 19. Rail irregularity (left) and its PSD (right) curves.

Assume that the earthquake takes place as the train moves onto the bridge. The starting times of the input seismic waves are adjusted in the calculation to assure that the maximum seismic acceleration occurs while the train is traveling on the bridge. The damping ratio of the bridge structure is taken as 3% in reference of the measured value in Xia and Zhang (2005), and is introduced into Equation (33) by using the Rayleigh damping. The damping parameters of the vehicles can be found in Han (2005). The integration time step is taken as 0.00005s.

#### 4.2.2. Dynamic Responses of the Train-Bridge System under Seismic Loads

The displacement and acceleration histories of the bridge at the mid section of the mid-span (mid-span for short) are presented in Figures 20 and 21, when the train runs on the bridge at a constant speed of 200km/h.

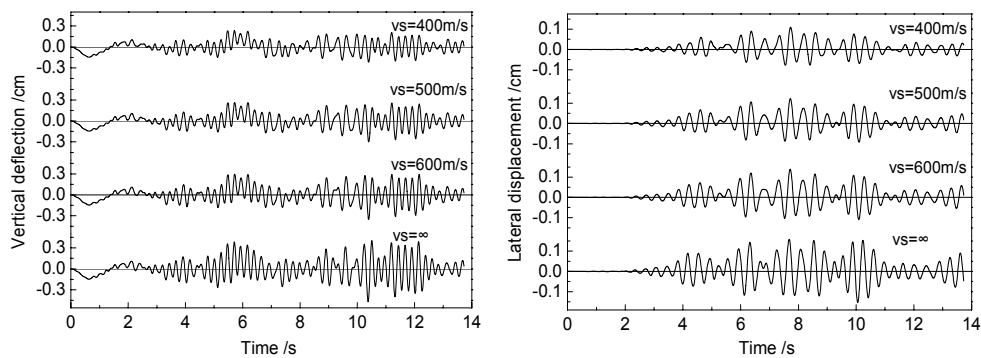


Figure 20. Vertical deflection (left) and lateral displacement (right) of bridge at mid-span.

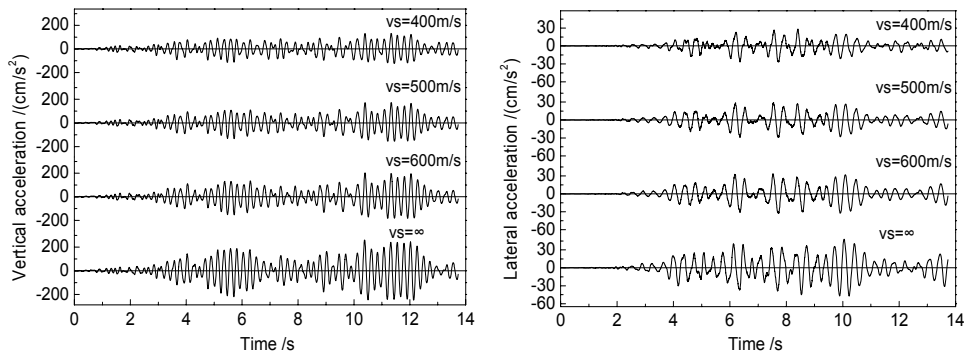


Figure 21. Vertical (left) and lateral (right) accelerations of bridge at mid-span.

In the above and the following figures,  $v_s$  represents the propagating velocity of the seismic waves, and  $v_s = \infty$  denotes the uniform excitation. The results indicate that the time histories of vertical deflections and accelerations at the mid-span of the bridge assume almost the same form for different seismic traveling wave excitations. For vertical deflections and accelerations, the bridge vibrates more intensively with the increase of the seismic propagating velocity, reaching maximum values under the uniform excitations. The time

history curves of the lateral accelerations of the bridge at mid-span show similar properties under seismic excitations of different propagating velocities.

The vertical and lateral acceleration histories of the first vehicle are presented in Figure 22, when the train runs on the bridge at a speed of 200 km/h. Under the same seismic excitation, the time history curves of the vertical and the lateral car-body accelerations vary with the seismic wave propagating velocities.

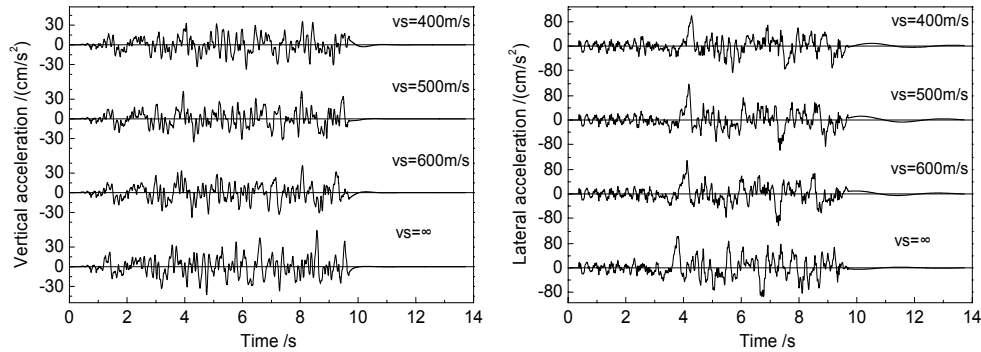


Figure 22. Vertical (left) and lateral (right) accelerations of vehicle.

Three evaluation indices for the running safety of train vehicles, including the derailment factor  $Q/P$ , the offload factor  $\Delta P/P$ , and the lateral wheel-rail force  $Q$  are calculated in the case study. The expressions and allowances of these indices are in terms of Equation (61). The allowable lateral wheel-rail forces for the China-Star locomotives and passenger cars are 63.75 kN and 45.33 kN, corresponding to their static loads 195.0 kN and 130.0 kN, respectively.

The wheel-rail contact model can deal with the instantaneous digression of the wheel from the rail. But for the calculated derailment factors, only those corresponding to the digressing time shorter than 0.015s are taken into account in the following analysis, considering that very short digression of a wheel from the rail has no significant influence on the running safety of the vehicle.

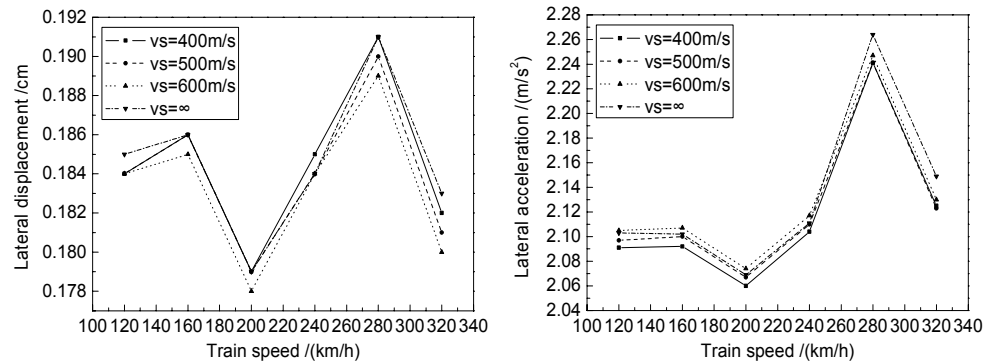


Figure 23. Maximum bridge displacement (left) and acceleration (right) vs train speed.

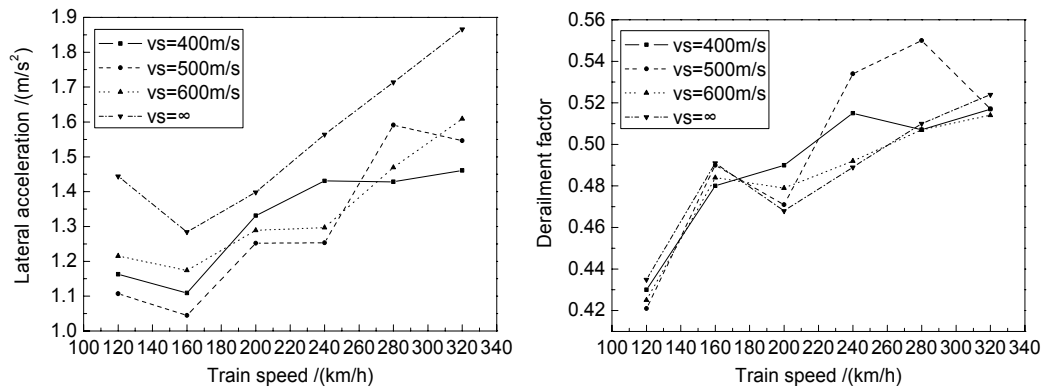


Figure 24. Maximum vehicle acceleration (left) and derailment factor vs train speed.

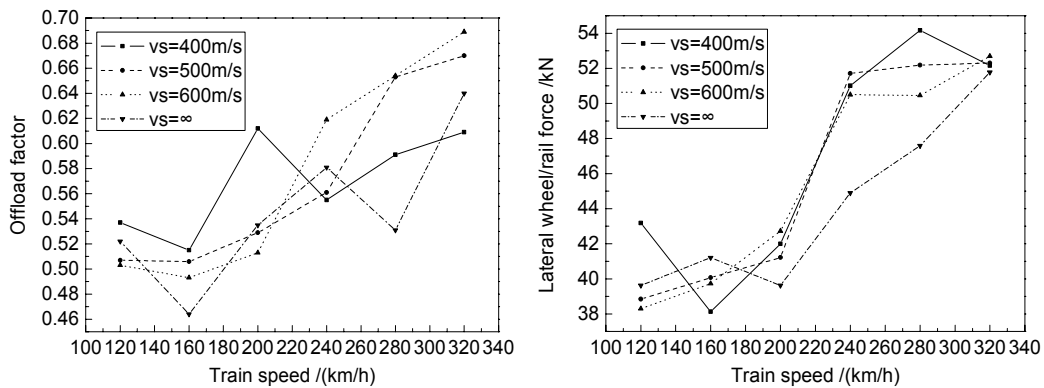


Figure 25. Maximum offload factor (left) and wheel/rail force (right) vs train speed.

Shown in Figures 23 to 25 are the distributions of the maximum lateral responses of the bridge and the evaluation indices of the vehicles with respect to the train speed and the seismic wave propagating velocity.

Referring to the above figures, it is clear that the influences of seismic wave propagating velocity on the dynamic responses of the bridge and the vehicles can be summarized as follows.

1. For the bridge, the lateral displacements and accelerations change only slightly with the seismic wave propagating velocity, with lower velocity tending to induce greater displacements but smaller accelerations. The maximum lateral displacements and accelerations change with the train speed and assume peak values at a train speed of 280 km/h under different seismic wave propagating velocities. For a bridge with such long spans, the peak responses can neither be explained by the loading speed nor by the regularly arranged train vehicle wheel axles as in the bridge-train resonance cases. Instead, they are induced by the rail irregularity (Guo, 2005). From Figure 18 one can see that the peak wavelength of the rail irregularity is about 34 m. Assuming a lateral frequency of 2.33 Hz for

the bridge, the resonance train speed can thus be estimated to be  $3.6 \times 2.33 \times 34 \approx 280$  km/h.

2. For the vehicles, the accelerations of the car body are influenced by the seismic wave propagating velocity, but with no obvious fixed pattern. For example, when the train speed equals 200 km/h, the lateral acceleration of the car body is  $1.289 \text{ m/s}^2$  under  $v_s = 600 \text{ m/s}$ , which is greater than  $1.252 \text{ m/s}^2$  under  $v_s = 500 \text{ m/s}$  and less than  $1.331 \text{ m/s}^2$  under  $v_s = 400 \text{ m/s}$ ; however, when the train speed equals 280 km/h, the lateral acceleration of the car body is  $1.469 \text{ m/s}^2$  under  $v_s = 600 \text{ m/s}$ , which is less than  $1.591 \text{ m/s}^2$  under  $v_s = 500 \text{ m/s}$  and greater than  $1.428 \text{ m/s}^2$  under  $v_s = 400 \text{ m/s}$ , respectively. Under all the seismic wave propagating velocities employed in the calculations, the lateral accelerations of the car body tend to increase with the train speed.
3. The running safety indices of the train vehicles under earthquakes, including derailment factors, offload factors and lateral wheel-rail forces, all generally increase with the train speed. Under given train speeds, no obvious patterns can be identified for the effects of the seismic wave propagating velocity on the running safety indices of vehicles. The estimated indices by calculation may be apparently smaller if the effect of seismic traveling wave is not considered. For instance, at a train speed of 240 km/h, the offload factors are calculated as 0.581 under  $v_s = \infty$  and 0.619 under  $v_s = 600 \text{ m/s}$ . Obviously, when the Chinese Code GB5599-85, which stipulates that the offload factor should be smaller than 0.6, is employed to assess train safety, an erroneous conclusion may be reached if without considering the effect of seismic traveling wave.

Therefore, the effect of seismic traveling wave should be considered in evaluating the running safety of trains on the bridge during earthquakes.

#### 4.2.3. Safety Control of Train Vehicles Traveling on Bridge during Earthquakes

The running safety of train vehicles on high-speed railway bridges during earthquakes is a concerned issue in railway engineering.

By taking the earthquakes intensity (acceleration) and the train speed as the main parameters that control the running safety of train vehicles, the threshold speed of train vehicles traveling on bridge during earthquakes can be determined according to the safety evaluation indices given in Equation (61) in the following way:

1. Firstly, keeping the earthquake intensity as a constant at each stage, the dynamic responses of the train vehicles are calculated by changing the train speed from 40 km/h to 360 km/h with an increment of 20 km/h. If any of the three indices is exceeded, the previous train speed is considered as the critical train speed for the corresponding earthquake intensity.
2. The earthquakes peak intensity is then changed from 0.0g (without seismic excitation) with an increment of 0.02g in the horizontal and 0.01g in the vertical directions, respectively. The dynamic responses of the train vehicles are calculated at different train speeds under each earthquake intensity and each seismic wave propagating velocity.

- The relationship between the earthquake intensity and the critical train speed can thus be obtained, by plotting the above calculated results under all seismic wave propagating velocities in an identical coordinate system, with the abscissa representing the earthquake intensity and the ordinate the train speed.

The results are shown in Figures 26-28, corresponding to the first-class, second-class and third subsoils, respectively.

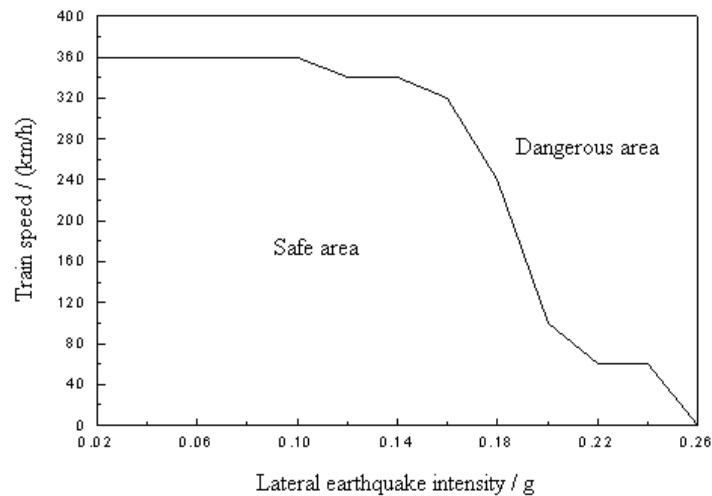


Figure 26. Critical train speed for vehicle safety vs earthquake intensity on site soil of Class I.

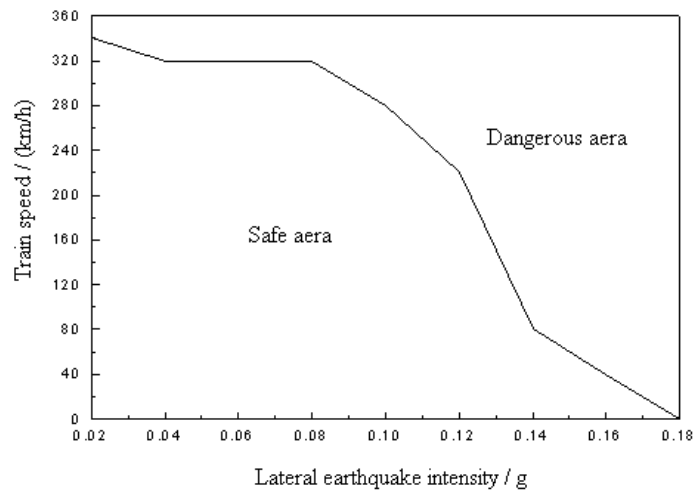


Figure 27. Critical train speed for vehicle safety vs earthquake intensity on site soil of Class II.

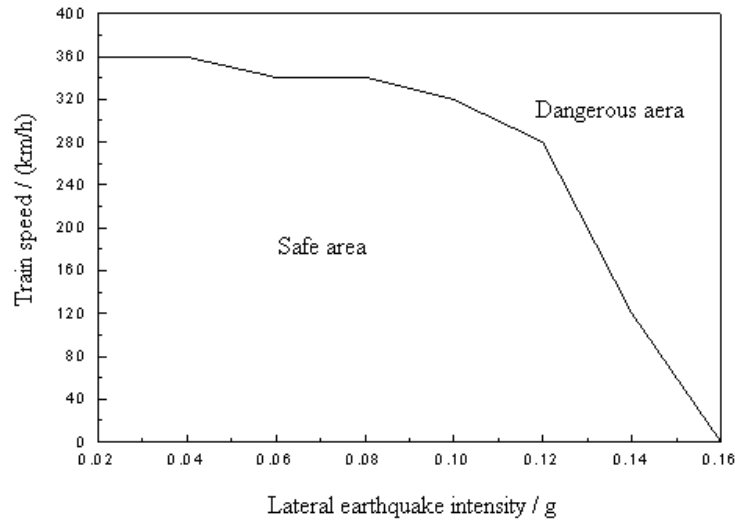


Figure 28. Critical train speed for vehicle safety vs earthquake intensity on site soil of Class III.

From Figures 26-28 one can see that for different earthquake intensities, the critical speeds of the train on the bridge are also different. The results show that the critical train speed is controlled by the offload factor with respect to the earthquake intensities of 0.0-0.12g, and by the lateral wheel-rail force with respect to the earthquake intensities of 0.14-0.18g, respectively. For the China-Star train, within the train speed range of 40~360 km/h, the critical train speed decreases with the increase of the earthquake intensity, and the decrease rate becomes larger when the earthquake intensity is greater than 0.08g. In this example, the maximum earthquake intensity can be estimated as 0.12g for the train speed of 160 km/h, and 0.08g for the train speed of 260 km/h.

By referencing this example, this method can be applied to other bridges to determine their critical train speed curves by taking into account of the soil conditions and the dynamic properties of the bridges.

#### 4.2.4. Summary of Analytical Results for Case Study II

The main conclusions are summarized for the case study of dynamic responses of a continuous bridge subjected to non-uniform seismic excitations as follows:

1. Seismic traveling waves affect the dynamic responses of the coupled train-bridge system. Lack of considering the traveling wave effect may lead to unsafe conclusions. It is not always true that the faster the seismic wave propagating velocity, the closer the dynamic response of the train-bridge system is to the corresponding ones under the uniform seismic excitations. Therefore, the seismic wave propagating velocity should be considered according to the property of the subsoil in calculation of the dynamic response of train-bridge system subjected to earthquakes.
2. For the dynamic response of train vehicles, the lateral car body accelerations, derailment factors, offload factors and lateral wheel-rail forces all increase with the

train speed. Therefore, the influences of train speed should be taken into account in evaluating the runnability of vehicles on the bridge during earthquakes.

3. Dynamic analysis of coupled train-bridge systems subjected to earthquakes is quite complicated. The proposed analysis model and the calculation results may provide a reference for the dynamic design of railway bridges.

## 5. Conclusion

In this chapter, the previous and current development of the research on the dynamic responses of railway bridges under running trains and earthquakes and their influences on running safety of train vehicles are investigated and summarized. Based on the studies of predecessors, a dynamic model of coupled train-bridge system subjected to earthquakes is established by connecting the motion equations of the bridge under earthquakes and the vehicles through the nonlinear contact relationships between the wheels and rails, in which the non-uniform characteristics of the seismic wave input from different foundations are considered. The seismic loads are imposed on the bridge by using the influence matrix and exerted on the vehicles through the dynamic wheel-rail interaction relationships. A computer code is developed. Two case studies are then performed to several actual bridges in China, including the simply-supported girder bridges with different span-lengths in the Qinghuangdao-Shenyang Special Passenger railway, and the continuous PC girder bridges on the planned Beijing-Shanghai high-speed railway. Through input of typical seismic waves with different propagation velocities to the train-bridge system, the histories of the train running through the bridge are simulated and the dynamic responses of the bridge and the vehicles are calculated. The influences of different train speeds and earthquake wave propagation velocities in non-uniform seismic excitations on the dynamic responses of the bridge-vehicle system are studied. The critical train speeds are proposed for running safety on high-speed railway bridges under earthquakes of various intensities.

## Acknowledgements

This study is sponsored by the National Natural Science Foundation of China (Grant No. 90715008) and the Flander (Belgium)-China Bilateral Project (Grant No. BIL07/07).

## References

- [1] Biggs M. (1964). Introduction to Structural Dynamics. New York: McGraw-Hill Inc.
- [2] Cakmak A.S. (1985). Modeling earthquake ground motions in California using parametric time series methods. *Journal of Soil Dynamics & Earthquake Engineering*, **4**, 124-131.
- [3] Cheung Y.K., Au F.T.K., Zheng D.Y., Cheng Y.S. (1999). Vibration of multi-span bridges under moving vehicles and trains by using modified beam vibration functions. *Journal of Sound & Vibration*, **228**, 611-628.

- 
- [4] China News. (2004). A high-speed train derailed at the Shinkansen in Japan. <http://China news.com/news.21cn.com/world/ guojisaomiao/2004/10/24/1821310.shtml>.
- [5] Clough R.W., Penzien J. (1993). Dynamics of Structures. New York: McGraw-Hill Inc.
- [6] Diana G., Cheli F. (1989). Dynamic interaction of railway systems with large bridges. *Journal of Vehicle System Dynamics*, **18**, 71-106.
- [7] Findell K.L., Cakmak A.S. (1993). Modeling and simulating earthquake accelerograms using strong-motion data from the Istanbul, Turkey, Region. *Journal of Soil Dynamics & Earthquake Engineering*, **12**, 51-59.
- [8] Frýba L. Nonstationary response of a beam to moving random force. *Journal of Sound & Vibration*, 1976, 46: 323-338.
- [9] Frýba L. (1996). Dynamics of Railway Bridges. London: Thomas Telford.
- [10] Frýba L. (1996). Vibration of Solids and Structures under Moving Loads. London: Thomas Telford.
- [11] Guo W.W., Xia H., Zhang N. (2005). Resonance analysis of train-bridge dynamic interaction system. *Proc. of Environmental Vibrations*, Okayama, 181-187.
- [12] Han Y., Xia H. (2004). Running safety of trains on half-through arch bridge during earthquakes. *Proc. of Progress in Safety Science & Technology*, Shanghai, 1945-1951.
- [13] Han Y. (2005). Dynamic Response of High-speed Railway Bridges and Running Safety of Vehicles during Earthquakes. *Ph.D Thesis*, Beijing Jiaotong University.
- [14] Han Y., Xia H., Guo W.W. (2003). Dynamic analysis of cable-stayed bridge subjected to running trains and earthquakes. *Proc. of Environmental Vibrations*, Beijing, 242-251.
- [15] Ju S.H., Lin H.T. (2007). Resonance characteristics of high-speed trains passing simply supported bridges. *Journal of Sound & Vibration*, **267**, 1127-1141. DOI: 10.1016/S0022-460X(02)01463-3.
- [16] Kalker J.J. (1989). Some new results in rolling contact. *Journal of Vehicle System Dynamics*, **18**(4), 223-242.
- [17] Luo X. (2001). An application of assessment methodology for running safety of railway vehicles during earthquakes. *Journal of JSCE*, **197-206**.
- [18] Mark K. (1982). ARMA models for earthquake ground motions. *Journal of Earthquake Engineering & Structural Dynamics*, **10**, 651-662.
- [19] Miyamoto T., Ishida H., Matsuo M. (1997). Running safety of railway vehicles as earthquake occurs. *Report of RTRI: Tokyo*, **38**(3), 117-122.
- [20] MIURA S. (1996). Deformation of Track and the Safety of Train in Earthquake. *Report of RTRI: Tokyo*, **37**(3), 139-146.
- [21] Matsumoto N., Okano M., Okuda H., Wakui H. (2000). New Railway viaduct providing superior running safety at earthquake, *Proc. of 16<sup>th</sup> Congress of IABSE*, Lucerne, CD-ROM.
- [22] Newmark N.M., Rosenblueth E. (1971). Fundamentals of Earthquake Engineering. New York: Prentice-Hall Inc, Englewood Cliffs.
- [23] Polhemus N.W., Cakmak A.S. (1981). Simulation of earthquake ground motions using ARMA models. *Journal of Earthquake Engineering & Structural Dynamics*, **9**, 343-354.
- [24] Saiidi M., Maragakis E., Connor D.O. (1995). Seismic performance of the Madrone bridge during the 1989 Loma Prieta Earthquake. *Journal of Structural Engineering Review*, **7**(3), 219-230.

- 
- [25] Tanabe M., Matsumoto N. (2005). Dynamic interaction analysis of a Shinkansen train and the railway structure under seismic loads. *Structural Dynamics, Proc. EURODYN' 2005*, 1001-1007.
- [26] Wiriyachai A., Chu K.H., Garg V.K. (1982). Bridge impact due to wheel and track irregularities. *Journal of Engineering Mechanics Division, ASCE*, **108**(4), 648-665.
- [27] Xia H., Han Y., Zhang N., Guo W.W. (2006). Dynamic analysis of train-bridge system subjected to non-uniform seismic excitation. *Journal of Earthquake Engineering & Structural Dynamics*, **35**, 1563-1579.
- [28] Xia H., De Roeck G. (1997). System identification of mechanical structures by a multivariate autoregressive model. *Computers & Structures*, **1-4**, 341-351.
- [29] Xia H., De Roeck G. (1993). Multivariate AR Model and its application to modal parameter identification of structures. *Structural Dynamics, Proc. EURODYN'93*. Rotterdam: Balkema Publisher, 811-817.
- [30] Xia H., Yan G.P. (1994). Numerical aseismic analysis of grade-separation structures. *Proc. of Computer Methods in Structural & Geotechnical Engineering*, Hong Kong, 1331-1336.
- [31] Xia H., Zhang N. (2005). Dynamic analysis of railway bridge under high-speed trains. *Computers & Structures*, **83**: 1891-1901. DOI: 10.1016/j.compstruc.2005.02.014.
- [32] Xia H., Zhang N. (2005). *Dynamic Interaction of Vehicles and Structures*. 2<sup>nd</sup> ed. Beijing: Science Press, 252-288.
- [33] Xia H., Xu Y.L. (2000). Dynamic interaction of long suspension bridges with running trains. *Journal of Sound & Vibration*, **237**(2), 263-280.
- [34] Xia H., Chen Y.J., Yan G.P. (1992). Dynamic interaction of train and a flexible arch stiffened steel truss bridge during earthquakes. *Proc. of JSSC-4*, Tokyo, Japan, 763-770.
- [35] Xu Z.X., Hu Z.L. (1993). *Analysis of Structures under Earthquakes*. Beijing: Superior Education Press, 80-84.
- [36] Yang Y.B., Wu Y.S. (2002). Dynamic stability of trains moving over bridges shaken by earthquakes. *Journal of Sound & Vibration*, **258**(1), 65-94. DOI: 10.1006/jsvi.5089.
- [37] Yau J.D., Yang Y.B. (2002). *Theory of Vehicle-Bridge Interaction for High Speed Railway*. Taipei: DNE Publisher.
- [38] Yu D.M., Xia H. (1998). Generation of artificial earthquake waves by time series method. *Proc. of Theories and Practice of Structural Engineering*, Beijing: Seismic Press, 195-203.
- [39] Zhai W.M., Cai C.B., Guo S.Z. (1996). Coupling model of vertical and lateral vehicle/track interactions. *Vehicle System Dynamics*, **26**(1), 61-79.
- [40] Zhang N., Xia H. (2001). Dynamic responses of train-bridge system under earthquakes. *Proc. of Traffic Induced Vibrations & Controls*, Beijing, 99-106.
- [41] Zhang N. Xia H. (2008). Vehicle-bridge interaction analysis under high-speed trains. *Journal of Sound and Vibration*, **309**, 407-425.
- [42] Zhang Q.L., Vrouwenvelder A., Wardenier J. (2001). Numerical simulation of train-bridge interactive dynamics. *Computers and Structures*, **79**, 1059-1075.



*Chapter 5*

**ON THE SEISMIC ATTENUATION  
WITH CONSIDERATION OF THE PREDICTION  
MODEL COMPLEXITY**

***Ka-Veng Yuen\* and He-Qing Mu***

Faculty of Science and Technology, University of Macau, Macao, China

**Abstract**

Estimation of peak ground acceleration is one of the main issues in civil and earthquake engineering practice. The Boore-Joyner-Fumal empirical formula is well known for this purpose by estimating the peak ground acceleration using information such as the magnitude of earthquake, the site-to-fault distance and the site foundation properties. The complexity of this prediction formula is investigated in this study. For example, should we use a first-order or a second-order polynomial for the earthquake magnitude? It is obvious that a more complicated prediction model class (i.e., a formula with more free parameters) possesses smaller fitting error for a set of data. However, this does not imply that the complicated predictive formula is more realistic since over-fitting may occur if there are too many free parameters. In this chapter we propose to use the Bayesian probabilistic model class selection approach to obtain the most suitable prediction model class for the seismic attenuation formula. In this approach, each prediction model class is evaluated by the plausibility given the dataset. A complicated model class is penalized by the “Ockham factor”, which is a natural consequence of the aforementioned plausibility, instead of any ad-hoc penalty terms. The optimal model class is robust in the sense that there is balance between the data fitting capability and the sensitivity to noise. A database of strong-motion records, obtained from the China Earthquake Data Center, is utilized for the analysis. The optimal prediction model class and its most plausible model parameters are determined. Quantification of the uncertainty of the parameters is allowed by the Bayesian probabilistic methodology and this can be used for uncertainty analysis of the predicted peak ground acceleration. It turns out that the optimal model class is simpler than the full order attenuation model suggested by Boore, Joyner and Fumal (1993).

**Keywords:** Bayesian inference, Boore-Joyner-Fumal formula; model class selection; peak ground acceleration; seismic attenuation

---

\* E-mail address: kvuyen@umac.mo. Tel: (853) 83974468 Phone: (853) 28838314. (Corresponding author)

## 1. Introduction

Prediction of peak ground acceleration (PGA) has received great attention in the society of civil engineering, earthquake engineering and seismology in the previous decades. Significant amount of work can be found in predicting the PGA by using the magnitude of earthquake, station-to-hypocenter distance, and the properties of the site foundation [1-8]. In particular, the Boore-Joyner-Fumal seismic attenuation formula is a well-known regression model for estimation of the PGA and it is given by [6, 7]

$$\log_{10} PGA = b_1 + b_2(M - M_0) + b_3(M - M_0)^2 + b_4r + b_5 \log_{10} r + b_6G_B + b_7G_C + \varepsilon \quad (1)$$

where  $M$  is the moment magnitude of the earthquake [9];  $M_0$  is a shifting constant and  $M_0 = 6$  is used in [6, 7];  $r$  is the observation station-to-hypocenter distance (in km);  $G_B$  and  $G_C$  are site foundation classification variables:  $G_B = 1$  for class B and 0 otherwise, and  $G_C = 1$  for class C and 0 otherwise [6, 7] (the classification of foundation will be discussed further in Section 4); and  $\varepsilon$  is a zero-mean Normal random variable to model the prediction error. In this model, the parameters to be identified are  $b_k, k = 1, 2, \dots, 7$  and the standard deviation  $\sigma_\varepsilon$  for the prediction error  $\varepsilon$ . The parameters of this model can be estimated by maximum likelihood method with the strong-motion records.

In [10-13], the Crouse and McGuire model [14] was used for the attenuation model with the strong-motion records from different areas of China and this model has essentially a different functional form from Eq. (1):

$$\ln PGA = c_1 + c_2M + c_3 \ln[r + c_4 \exp(c_5M)] + \varepsilon \quad (2)$$

where the variables  $M$  and  $r$  are defined in the same way as in Eq. (1). Note the prediction models in Eq. (1) and Eq. (2) are both empirical models. One may wonder if better results can be obtained by adding/erasing terms to these models or by considering a different functional form. A good prediction model class should be capable to fit the strong-motion records and at the same time be insensitive to observation and modeling error. If the number of free parameters in a model class is very large, this model class possesses powerful data fitting capability but may become very sensitive to the noise in the dataset, referred to as “over-fitting”. This is because the identified parameters of this model class depend highly on the detail of the data (including the measurement noise and modeling errors) and it may cause large errors in future predictions.

In this work, the regression formula given in [6, 7] is examined. Thirty two model classes are constructed by including subsets of terms in the regression equation (Eq. (1)). Bayesian statistical methods have been widely used in many areas in science and engineering [15]. In this chapter, we propose to use the Bayesian model class selection approach [16, 17] to select among these thirty two model classes. This approach has been shown promising in several research areas, such as artificial neural networks [16, 18], structural dynamics and model updating [17], damage detection [19], fracture mechanics [20], and air quality prediction [21],

etc. As will be shown in Section 3, it considers the plausibility of each model class conditional on the database. The plausibility of a model class can be factorized as a product of the likelihood and a measure of the robustness of the model class (namely the ‘‘Ockham factor’’). The Ockham factor penalizes those model classes that are over-parameterized and therefore prone to error due to the noise in the dataset. As a result, the optimal model class has the best tradeoff between the data fitting capability and the robustness to measurement noise and modeling error. A database of 266 strong-motion records from the China Earthquake Data Center [22] is utilized for this study. The observation stations are located in three regions of China (Tangshan, Xinjiang and Guangdong) with different geological condition. Investigations are performed with records of individual regions as well as the full database.

## 2. Prediction Model Class Candidates

In order to examine the suitability of the prediction model class in Eq. (1) and to propose the most suitable one, model class candidates are constructed. A prediction model class is referred to a prediction formula with free parameters governed by a probability density function (PDF). On the other hand, a prediction model is a prediction formula with fixed parameters so the former is a set of (infinitely many) prediction models/formulae. Here, we consider prediction model classes in similar functional forms of Eq. (1) but to include different combinations of terms in different model classes. First of all, the constant  $b_1$  is necessary to serve as the scaling factor of the PGA for any model class so all model classes include  $b_1$ . As will be discussed later in Section 4 that only strong-motion records with moment magnitude  $M > 3.5$  are utilized,  $M_0 = 3.5$  is taken in this study. There are four possibilities for the contribution of  $M$ , namely without any terms for  $M$ ,  $b_2(M - M_0)$ ,  $b_3(M - M_0)^2$  and  $b_2(M - M_0) + b_3(M - M_0)^2$ . For the contribution of  $r$ , there will be also four possibilities, namely without any terms for  $r$ ,  $b_4r$ ,  $b_5 \log_{10} r$  and  $b_4r + b_5 \log_{10} r$ . For the site properties, we either consider or not consider both terms ( $b_6G_B$  and  $b_7G_C$ ) at the same time. Therefore, there are totally  $4 \times 4 \times 2 = 32$  candidates of model class, namely  $C_1, C_2, \dots, C_{32}$ .

## 3. Selection of the Prediction Model Class

Let  $D$  denote the data that includes the measured PGA and the corresponding earthquake magnitude, observation station-to-hypocenter distance and site foundation properties. We attempt to use  $D$  to select the most suitable prediction model class among the aforementioned model class candidates  $C_1, C_2, \dots, C_{32}$ . Since probability may be interpreted as a measure of plausibility [21], the plausibility of a prediction model class  $C_k$  given the data  $D$  is given by [16]

$$P(C_k|D) = \frac{p(D|C_k)P(C_k)}{p(D)} \quad (3)$$

where  $P(C_k)$  is a prior plausibility of a model class and it is treated as a uniform prior in this study, i.e.,  $P(C_k) = \frac{1}{32}$ ,  $k=1,2,\dots,32$ . The factor  $p(D)$  is a normalizing constant regardless of the model class so that  $\sum_{k=1}^{32} P(C_k|D) = 1$ . The factor  $p(D|C_k)$  is called the evidence for model class  $C_k$  given the data  $D$ . Since uniform prior is used in this case, the plausibility of a model class is proportional to the evidence. By the theorem of total probability [24], the evidence of model class  $C_k$ ,  $p(D|C_k)$ , is given by

$$p(D|C_k) = \int_{\Theta} p(D|\theta, C_k)p(\theta|C_k)d\theta, \quad k=1,2,\dots,32 \quad (4)$$

where  $\theta$  is the parameter vector in the parameter space  $\Theta$  that defines each model in  $C_k$ . Note that the parameter vector  $\theta$  and the parameter space  $\Theta$  depend on the model class  $C_k$  even though this is not explicitly reflected in the symbol. This is done for the purpose of simplifying the notation only. The prior PDF  $p(\theta|C_k)$  is specified by the user and  $p(D|\theta, C_k)$  is the likelihood that will be introduced in Section 3.1. In the current situation that the predicted PGA is a linear function of the uncertain parameters, unique global maximum exists for the integrand in Eq. (4) (i.e.,  $p(D|\theta, C_k)p(\theta|C_k)$ ). This is referred to the globally identifiable case and  $p(D|\theta, C_k)p(\theta|C_k)$  can be well approximated by a Normal PDF when the number of data points is large [25, 26]. As a result, the integral in Eq. (4) can be well approximated by using Laplace's method [27]:

$$p(D|C_k) = p(D|\hat{\theta}, C_k)p(\hat{\theta}|C_k)(2\pi)^{\frac{N_k}{2}} |H_k(\hat{\theta})|^{-\frac{1}{2}}, \quad k=1,2,\dots,32 \quad (5)$$

where  $N_k$  is the number of parameters to be determined in the model class  $C_k$ ;  $\hat{\theta}$  is the optimal parameter vector found by maximizing  $p(D|\theta, C_k)p(\theta|C_k)$  (equivalent to minimizing the negative of its natural logarithm  $-\ln[p(\hat{\theta}|C_k)p(D|\hat{\theta}, C_k)]$  for better numerical condition);  $H_k(\hat{\theta})$  is the Hessian matrix of the objective function  $-\ln[p(\hat{\theta}|C_k)p(D|\hat{\theta}, C_k)]$  with  $\theta$  evaluated at  $\hat{\theta}$  and  $\sigma_\varepsilon$  evaluated at  $\hat{\sigma}_\varepsilon$ . Specifically, the  $(i, j)$  component of the Hessian matrix  $H_k(\hat{\theta})$  is given by

$$H_k^{(i,j)}(\hat{\theta}) = - \frac{\partial^2}{\partial \theta_i \partial \theta_j} \ln [p(\theta | C_k) p(D | \theta, C_k)] \Big|_{\theta = \hat{\theta}} \quad (6)$$

where  $\theta_i$  is the  $i^{\text{th}}$  component of the parameter vector  $\theta$ . In Eq. (5), the factor  $p(\hat{\theta} | C_k) (2\pi)^{\frac{N_k}{2}} |H_k(\hat{\theta})|^{-\frac{1}{2}}$  is called the Ockham factor:

$$Oc_k = p(\hat{\theta} | C_k) (2\pi)^{\frac{N_k}{2}} |H_k(\hat{\theta})|^{-\frac{1}{2}} \quad (7)$$

The Ockham factor serves as a measure of the robustness of a model class. It penalizes the model classes that depend too sensitively on their parameters because the robustness of this model class is low (sensitive to noise and modeling error) and over-fitting/over-parameterization may occur. In such case, small changes of the dataset may substantially affect the parameter identification results. This is not preferable since future prediction will be sensitive to the modeling error and measurement noise of the dataset.

### 3.1. Identification of Prediction Model Parameters

Given a model class  $C_k$ , the optimal parameter vector  $\hat{\theta}$  for a given model class is the one that maximizes the posterior PDF  $p(\theta | D, C_k)$ . The posterior PDF provides a measure of the relative plausibility of the values of the parameters in  $\theta$ . Note that the posterior PDF is proportional to the integrand of Eq. (4). By Bayes' theorem, this PDF is given by [25]

$$p(\theta | D, C_k) = c_0 p(\theta | C_k) (2\pi)^{\frac{N}{2}} \sigma_\varepsilon^{-N} \exp \left[ - \frac{N}{2\sigma_\varepsilon^2} J(\theta | D, C_k) \right] \quad (8)$$

where  $c_0$  is a normalizing constant,  $N$  is the number of strong-motion records in  $D$  and  $p(\theta | C_k)$  is the prior PDF of the model parameters expressing the user's judgment about the relative plausibility of the values of the prediction model parameters without using the data. In this study, a flat prior PDF is used for not biasing the results prior to the data. The error function  $J(\theta | D, C_k)$  is given by

$$J(\theta | D, C_k) = \frac{1}{N} \sum_{l=1}^N [\log_{10} PGA(l; \theta, C_k) - \log_{10} PGA_o(l)]^2 \quad (9)$$

where  $PGA_o(l)$  is the  $l^{\text{th}}$  observed record while  $PGA(l; \theta, C_k)$  is the corresponding model predicted PGA with the parameter vector  $\theta$ . The most plausible model parameters  $\hat{\theta}$  are obtained by maximizing the posterior PDF  $p(\theta|D, C_k)$  in Eq. (8). This is equivalent to minimizing the error function  $J(\theta|D, C_k)$  in Eq. (9) over all the parameters in  $\theta$ , because a flat prior PDF is used. The most plausible value of the prediction error variance can be found by solving  $\frac{\partial p(\theta|D, C_k)}{\partial \sigma_\varepsilon} = 0$  and it is readily obtained by  $\hat{\sigma}_\varepsilon^2 = \min_{\theta} J(\theta|D, C_k) = J(\hat{\theta}|D, C_k)$ . For large  $N$ , the posterior PDF  $p(\theta|D, C_k)$  can be well approximated by a Normal PDF centered at its optimal point [25, 26]. Therefore, the uncertainty of the parameter estimation can be represented by its covariance matrix given by  $\Sigma_\theta = H_k(\hat{\theta})^{-1}$ , where  $H_k(\hat{\theta})$  is given in Eq. (6). Note that the diagonal elements of  $\Sigma_\theta$  are the marginal variance of the corresponding element of  $\theta$  and the quantification of the uncertainty of the model parameters can be used for the uncertainty analysis of the predicted PGA.

## 4. Results

### 4.1. Description of the Database

A database of strong-motion records is obtained from the China Earthquake Data Center [22]. In this study, we consider the horizontal components of the PGA records and only the records with  $M > 3.5$  are utilized so  $M_0 = 3.5$  is taken in Eq. (1). Table 1 summarizes the information of the records in this database. Note that some records correspond to the same earthquake observed in the same station but with different machines and the numbers in the bracket denote the independent records (i.e., excluding the records with the same earthquake observed at the same station). There are totally 266 records, observed from 34 stations in the Tangshan, Xinjiang, and Guangdong region. Figure 1 shows the magnitude of the earthquake versus the site-to-hypocenter distance for each record. The symbols “□”, “o”, and “□” denote the records in the Tangshan, Xinjiang and Guangdong region, respectively.

**Table 1. Information of the database**

Region	Records	Earthquakes	Stations	Class A	Class B	Class C
Tangshan	94 (91)	18	19	8	6	5
Xinjiang	155 (155)	125	13	4	6	3
Guangdong	17 (4)	4	2	2	0	0

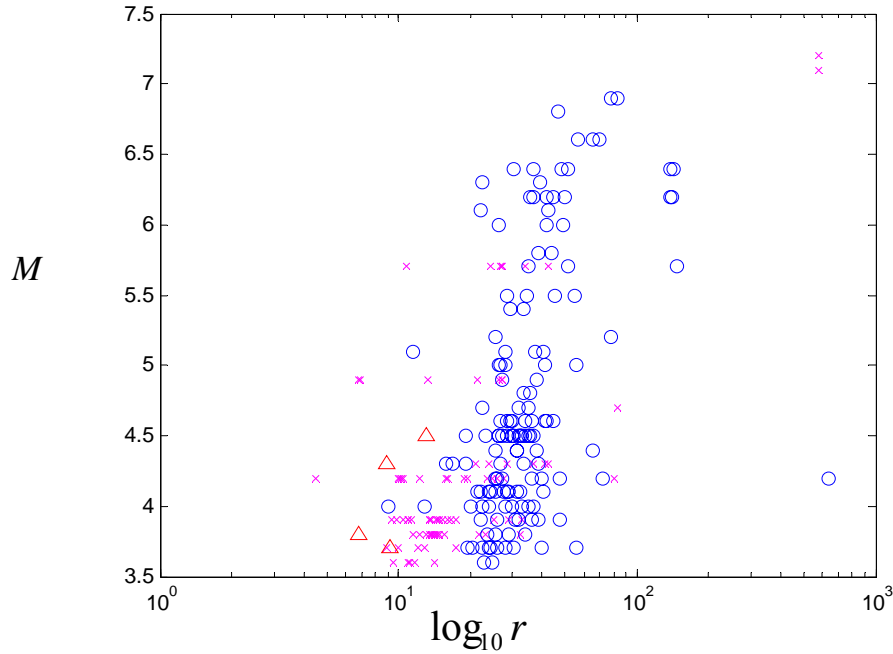


Figure 1. Distribution of  $M$  and  $r$  in the database.

The classification of the site foundation depends on its stiffness and the averaged shear velocity over the upper 30 m is used as its measure [6]. Since only the soil/rock types are given in the data center, the site class is defined in a slightly different way from the original definition by [6]. Specifically, granite, sandstone, bedrock, siltstone, and conglomerate are classified as class A. Alluvium, diluvium, and weathering conglomerate are included in class B. Soft soil, clay and sub-clay are classified as class C. In this study, we will perform independent study of the prediction model class selection using the data from the Tangshan region and the Xinjiang region but not the Guangdong region since all the records in the Guangdong region are obtained from stations on granite (site class A) only. Therefore, it is not possible to obtain the parameters  $b_6$  and  $b_7$  by using the records from the Guangdong region alone because  $G_B = 0$  and  $G_C = 0$  in this case. However, we will perform the prediction model selection with the full set of data including records from all these three regions.

Note that the range of  $\log_{10} PGA$  in the dataset lies in the interval of  $[-1, 3]$ . The prior PDF for  $b_1$  in Eq. (1) is taken to be a uniform distribution in the range from -1 to 3. For the other parameters (if they are included in a prediction model class), they are also taken as uniform distribution in order to let the dataset to infer the parameter values. By considering the previous work in [1-8], the range of the uniform distribution is taken as  $[-1, 1]$  for  $b_2$ ,  $b_3$ ,  $b_5$ ,  $b_6$  and  $b_7$ . For  $b_4$ , it was observed that it is much smaller from previous study. This is also expected to happen in this case because  $r$  is much larger than  $\log_{10} r$  in the range of

our dataset (Figure 1). Specifically, the range for its uniform distribution is taken to be  $[-0.01, 0.01]$ . Note that as long as the range is large enough, the values of the bounds do not affect the identification results for the parameter vector  $\theta$ .

## 4.2. Tangshan Region

Tangshan city is located in the North China Plain. Table 2 shows the results of the prediction model class selection using the horizontal records of the Tangshan region. The first column shows the ranking of each prediction model class. A smaller number of the ranking corresponds to a higher plausibility of the model class. The second column shows the parameters being included in that model class, e.g., “1 2 3 5” denotes a model class with free parameters  $b_1$ ,  $b_2$ ,  $b_3$ , and  $b_5$  in Eq. (1), i.e.,  $\log_{10} PGA = b_1 + b_2(M - M_0) + b_3(M - M_0)^2 + b_5 \log_{10} r$ . The third and fourth columns show the likelihood factor and the corresponding standard deviation of the fitting error. The fifth column shows the value of the Ockham factor  $Oc_k$  in Eq. (6), that indicates the robustness of the model class, and the last column shows the plausibility of each model class. The full model class with all the seven parameters has the largest likelihood value because it has the highest capability to fit the data. This is intuitive because the full model class has the largest solution space so it is capable to fit the dataset at least as well as any other model classes with less free parameters. However, its robustness is not as good as the other model classes and its Ockham factor (measure of robustness) is  $5.79 \times 10^{-10}$ , which is the smallest among all the model class candidates. Table 3 shows the optimal parameters of each model class. The numbers in parenthesis denote the standard deviation of that parameter calculated using the Bayesian probabilistic approach described at the end of Section 3.1. In order to balance the data fitting capability and robustness, a relatively simple model class is selected and its optimal model is given by

$$\log_{10} PGA = 1.9 + 0.76(M - 3.5) - 0.19(M - 3.5)^2 - 0.86 \log_{10} r \quad (10)$$

where PGA is in  $\text{cm/s}^2$ . The term  $-0.86 \log_{10} r$  indicates that the PGA decreases with an increasing site-hypocenter distance. The PGA decreases by 45% ( $\approx (1 - 2^{-0.86}) \times 100\%$ ) when  $r$  increases by 2 times if all the other factors remain. This prediction model class has plausibility over 0.7 by the Bayesian model selection approach.

Note that the terms  $b_6 G_B$  and  $b_7 G_C$  are not included in this model. By observing the model classes that include the parameters  $b_6$  and  $b_7$ , one can see that the optimal values of these parameters are of similar order of its standard deviation of the estimates. This implies that the data does not provide significant evidence for such terms to be included. Furthermore, some of the values of  $b_7$  (in some of the model classes with low plausibility) are negative. This seems to contradict with physics at the first glance. However, this is only due to the large posterior uncertainty of this parameter, i.e., the dataset does not have much saying on the value of this parameter.

**Table 2. Model class selection results (Tangshan)**

	Parameters	$p(D \hat{\theta}, C_k)$	$\hat{\sigma}_\varepsilon$	$O_{C_k}$	$P(C_k D)$
1	1 2 3 5	5.54E-09	0.30	4.74E-07	7.04E-01
2	1 2 4 5	7.65E-10	0.30	7.88E-07	1.61E-01
3	1 2 3 4 5	5.72E-09	0.30	7.35E-08	1.13E-01
4	1 2 3 5 6 7	1.15E-08	0.29	3.72E-09	1.14E-02
5	1 2 5	1.27E-12	0.32	1.25E-05	4.24E-03
6	1 2 4 5 6 7	1.09E-09	0.30	6.61E-09	1.94E-03
7	1 2 3 4 5 6 7	1.15E-08	0.29	5.79E-10	1.78E-03
8	1 3 4 5	1.23E-11	0.32	4.06E-07	1.34E-03
9	1 2 4	7.42E-13	0.33	4.95E-06	9.84E-04
10	1 3 4	2.49E-13	0.33	2.21E-06	1.48E-04
11	1 2 3 4	7.43E-13	0.33	5.06E-07	1.01E-04
12	1 2 5 6 7	2.00E-12	0.32	1.19E-07	6.38E-05
13	1 3 4 5 6 7	1.65E-11	0.32	3.76E-09	1.67E-05
14	1 2 4 6 7	1.16E-12	0.32	4.79E-08	1.49E-05
15	1 5	1.14E-16	0.36	2.20E-04	6.72E-06
16	1 4 5	6.81E-16	0.35	1.92E-05	3.51E-06
17	1 3 4 6 7	3.40E-13	0.33	2.23E-08	2.03E-06
18	1 4	8.58E-17	0.36	8.62E-05	1.98E-06
19	1 3 5	1.19E-15	0.35	5.73E-06	1.83E-06
20	1 2 3 4 6 7	1.19E-12	0.32	4.93E-09	1.57E-06
21	1 2 3	2.74E-16	0.35	5.73E-06	4.20E-07
22	1 5 6 7	3.16E-16	0.35	2.47E-06	2.09E-07
23	1 4 5 6 7	2.02E-15	0.35	2.06E-07	1.12E-07
24	1 4 6 7	2.41E-16	0.35	9.74E-07	6.29E-08
25	1 3 5 6 7	2.34E-15	0.35	6.28E-08	3.95E-08
26	1 2 3 6 7	8.50E-16	0.35	6.27E-08	1.43E-08
27	1	4.91E-23	0.42	2.06E-03	2.72E-11
28	1 3	5.88E-22	0.41	4.58E-05	7.23E-12
29	1 2	5.55E-23	0.42	1.56E-04	2.32E-12
30	1 6 7	8.42E-23	0.42	3.26E-05	7.36E-13
31	1 3 6 7	1.54E-21	0.40	6.75E-07	2.78E-13
32	1 2 6 7	1.04E-22	0.41	2.45E-06	6.81E-14

Another noteworthy point is on the model class with parameters  $b_1$  and  $b_2$  only, i.e., the twenty eighth model class. The optimal value for  $b_2$  is negative and it seems to imply that the larger the moment magnitude of an earthquake the smaller the PGA. However, this is only due to the non-uniform distribution of  $M$  and  $r$  in the dataset. Specifically, the correlation coefficient between the  $M$  and  $r$  is 0.64 in this dataset. This implies that large value of  $M$  in a record often associates with large value of  $r$ , that reduces the PGA. Furthermore, the correlation coefficient between the  $\log_{10} PGA$  and  $M$  is -0.0511 and hence the optimal

coefficient  $b_2$  is negative. Therefore, a model class with too few free parameters may cause under-fitting to the data. Figure 2 shows the logarithm of the predicted PGA values ( $\log_{10} PGA_p$ ) versus their observation values ( $\log_{10} PGA_o$ ) for the most plausible model class along with the 45° line.

**Table 3. Optimal parameters of each prediction model class (Tangshan)**

	$b_1$	$b_2$	$b_3$	$b_4$	$b_5$	$b_6$	$b_7$
1	1.9 (0.17)	0.76 (0.13)	-0.19 (0.043)	---	-0.86 (0.14)	---	---
2	1.8 (0.19)	0.34 (0.06)	---	-0.0025 (0.00066)	-0.66 (0.17)	---	---
3	1.9 (0.19)	0.73 (0.20)	-0.17 (0.083)	-0.00031 (0.0012)	-0.83 (0.19)	---	---
4	1.8 (0.18)	0.76 (0.13)	-0.19 (0.043)	---	-0.85 (0.13)	0.081 (0.07)	0.0033 (0.08)
5	2.3 (0.15)	0.28 (0.06)	---	---	-1.1 (0.14)	---	---
6	1.8 (0.20)	0.33 (0.06)	---	-0.0024 (0.00066)	-0.66 (0.17)	0.06 (0.07)	0.0082 (0.08)
7	1.8 (0.19)	0.75 (0.20)	-0.18 (0.083)	-0.00011 (0.0012)	-0.83 (0.19)	0.08 (0.07)	0.0031 (0.08)
8	1.8 (0.20)	---	0.12 (0.026)	-0.0038 (0.00084)	-0.49 (0.17)	---	---
9	1.1 (0.05)	0.27 (0.06)	---	-0.0041 (0.00053)	---	---	---
10	1.2 (0.04)	---	0.11 (0.026)	-0.0051 (0.00073)	---	---	---
11	1.1 (0.09)	0.28 (0.19)	-0.005 (0.082)	-0.0041 (0.00099)	---	---	---
12	2.3 (0.16)	0.27 (0.06)	---	---	-1.1 (0.14)	0.074 (0.08)	0.037 (0.09)
13	1.8 (0.20)	---	0.12 (0.026)	-0.0037 (0.00084)	-0.49 (0.17)	0.058 (0.08)	0.012 (0.08)
14	1.1 (0.06)	0.27 (0.06)	---	-0.0041 (0.00053)	---	0.062 (0.08)	-0.016 (0.09)
15	2.0 (0.15)	---	---	---	-0.68 (0.12)	---	---
16	1.7 (0.22)	---	---	-0.0014 (0.00074)	-0.39 (0.19)	---	---
17	1.2 (0.05)	---	0.11 (0.027)	-0.005 (0.00073)	---	0.056 (0.08)	-0.008 (0.09)
18	1.3 (0.04)	---	---	-0.0026 (0.00045)	---	---	---
19	2.3 (0.19)	---	0.049 (0.022)	---	-0.93 (0.16)	---	---
20	1.1 (0.10)	0.30 (0.19)	-0.018 (0.082)	-0.0039 (0.0010)	---	0.064 (0.08)	-0.017 (0.09)
21	0.86 (0.08)	0.83 (0.15)	-0.29 (0.048)	---	---	---	---
22	2.0 (0.15)	---	---	---	-0.69 (0.12)	0.12 (0.08)	0.027 (0.09)
23	1.7 (0.22)	---	---	-0.0014 (0.00073)	-0.39 (0.19)	0.12 (0.08)	0.0094 (0.09)
24	1.2 (0.06)	---	---	-0.0027 (0.00045)	---	0.11 (0.08)	-0.0064 (0.10)
25	2.2 (0.19)	---	0.046 (0.023)	---	-0.91 (0.16)	0.10 (0.08)	0.040 (0.09)
26	0.84 (0.08)	0.83 (0.15)	-0.29 (0.048)	---	---	0.11 (0.08)	-0.024 (0.09)
27	1.2 (0.04)	---	---	---	---	---	---
28	1.2 (0.05)	---	-0.042 (0.019)	---	---	---	---
29	1.2 (0.06)	-0.03 (0.06)	---	---	---	---	---
30	1.1 (0.06)	---	---	---	---	0.10 (0.10)	0.026 (0.11)
31	1.2 (0.06)	---	-0.046 (0.019)	---	---	0.13 (0.10)	0.014 (0.11)
32	1.2 (0.08)	-0.039 (0.06)	---	---	---	0.11 (0.10)	0.024 (0.11)

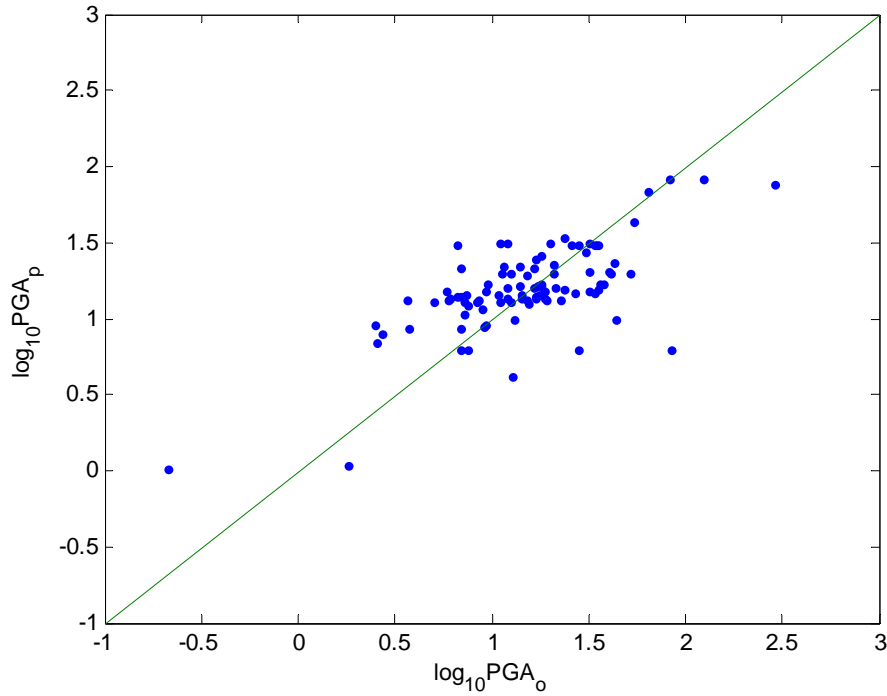


Figure 2. Model prediction results with their observed values (Tangshan).

### 4.3. Xinjiang Region

Xinjiang is in the North West of China. In the same fashion as in Table 2 and 3, Table 4 and 5 show the prediction model class selection results and the optimal parameters of each model class, respectively. From Table 5, the optimal prediction model for the PGA is given by

$$\log_{10} PGA = 1.9 + 0.22(M - 3.5) - 0.4 \log_{10} r + 0.24G_B + 0.06G_C \quad (11)$$

Note that the first four model classes possess similar plausibility, implying that the Bayesian model selection method does not have strong preference on the optimal model class. This is in contrast to the previous case in the Tangshan region, in which the plausibility of the optimal model class is over 0.7. In this case with the data of Xinjiang, a multi-model prediction formula can be used as follows:

$$\log_{10} PGA = \sum_{k=1}^4 (\log_{10} PGA)_k K_0 P(C_k | D) \quad (12)$$

where  $(\log_{10} PGA)_k$  is the prediction of PGA using the  $k^{\text{th}}$  most plausible model class and  $K_0 = 1 / \sum_{k=1}^4 P(C_k | D)$  is a normalizing constant so that the sum of the weightings is equal to

unity. In other words, the PGA is estimated using four model classes with the weightings being the relative plausibility given the data. Specifically, this model is given by

$$\log_{10} PGA = 2.21 + 0.122(M - 3.5) + 0.0327(M - 3.5)^2 + 0.00071r - 0.56\log_{10} r + 0.26G_B + 0.076G_C \quad (13)$$

and the associated uncertainty of the parameters  $b_1, \dots, b_7$  are: 0.21, 0.02, 0.006, 0.00047, 0.15, 0.08 and 0.097, respectively.

**Table 4. Model class selection results (Xinjiang)**

	Parameters	$p(D \hat{\theta}, C_k)$	$\hat{\sigma}_\varepsilon$	$Oc_k$	$P(C_k D)$
1	1 2 5 6 7	4.47E-05	0.26	1.66E-08	2.23E-01
2	1 2 4 5 6 7	5.30E-04	0.25	1.28E-09	2.04E-01
3	1 3 5 6 7	1.39E-04	0.26	4.76E-09	2.00E-01
4	1 3 4 5 6 7	1.61E-03	0.25	3.63E-10	1.76E-01
5	1 2 5	6.64E-08	0.27	2.26E-06	4.52E-02
6	1 3 5	1.67E-07	0.27	6.62E-07	3.32E-02
7	1 2 3 5 6 7	1.75E-04	0.26	5.75E-10	3.04E-02
8	1 2 3 4 5 6 7	2.31E-03	0.25	4.30E-11	3.00E-02
9	1 2 4 5	3.95E-07	0.27	1.86E-07	2.22E-02
10	1 3 4 5	1.07E-06	0.26	5.41E-08	1.75E-02
11	1 2 6 7	1.21E-07	0.27	1.41E-07	5.15E-03
12	1 2 3 5	1.75E-07	0.27	8.39E-08	4.43E-03
13	1 3 6 7	2.73E-07	0.27	4.13E-08	3.40E-03
14	1 2 3 4 5	1.18E-06	0.26	6.77E-09	2.41E-03
15	1 2	1.72E-10	0.28	1.78E-05	9.23E-04
16	1 2 4 6 7	3.74E-07	0.27	7.07E-09	7.98E-04
17	1 3 4 6 7	9.44E-07	0.26	2.05E-09	5.83E-04
18	1 2 3 6 7	3.12E-07	0.27	5.22E-09	4.92E-04
19	1 3	2.83E-10	0.28	5.28E-06	4.51E-04
20	1 2 4	6.60E-10	0.28	9.36E-07	1.86E-04
21	1 3 4	1.21E-09	0.28	2.76E-07	1.01E-04
22	1 2 3 4 6 7	1.07E-06	0.26	2.57E-10	8.31E-05
23	1 2 3	2.88E-10	0.28	6.98E-07	6.07E-05
24	1 2 3 4	1.23E-09	0.28	3.61E-08	1.34E-05
25	1	2.46E-15	0.30	6.48E-04	4.81E-07
26	1 5	3.23E-15	0.30	9.11E-05	8.87E-08
27	1 4	3.17E-15	0.30	3.70E-05	3.53E-08
28	1 4 5	3.31E-15	0.30	8.37E-06	8.35E-09
29	1 6 7	4.73E-15	0.30	5.81E-06	8.27E-09
30	1 5 6 7	9.16E-15	0.30	8.87E-07	2.45E-09
31	1 4 6 7	6.58E-15	0.30	3.34E-07	6.62E-10
32	1 4 5 6 7	9.29E-15	0.30	8.50E-08	2.38E-10

Of course, one may consider to include five or even more model classes in Eq. (12) but the results will be virtually the same since the plausibilities of the fifth and below model classes are small. One important point is that this multi-mode prediction formula includes all seven parameters but it is not the “optimal model” in the full model class (eighth model class in Table 5) as their parameter values are not the same. This multi-model prediction formula (along with the posterior uncertainty of the parameters) does not have the most powerful data fitting capability but it possesses higher level of robustness than the “optimal model” in the full model class. Figure 3 shows the predicted PGA values versus their observed values with the 45° line.

**Table 5. Optimal parameters of each prediction model class (Xinjiang)**

	$b_1$	$b_2$	$b_3$	$b_4$	$b_5$	$b_6$	$b_7$
1	1.9 (0.17)	0.22 (0.03)	---	---	-0.4 (0.11)	0.24 (0.08)	0.06 (0.10)
2	2.4 (0.25)	0.24 (0.03)	---	0.0015 (0.00068)	-0.74 (0.19)	0.28 (0.08)	0.11 (0.10)
3	2.1 (0.17)	---	0.067 (0.009)	---	-0.4 (0.11)	0.24 (0.08)	0.043 (0.10)
4	2.5 (0.25)	---	0.073 (0.009)	0.0015 (0.00067)	-0.75 (0.19)	0.27 (0.08)	0.092 (0.10)
5	2.2 (0.16)	0.17 (0.03)	---	---	-0.4 (0.11)	---	---
6	2.3 (0.17)	---	0.052 (0.008)	---	-0.41 (0.11)	---	---
7	2.0 (0.18)	0.066 (0.10)	0.049 (0.029)	---	-0.41 (0.11)	0.24 (0.08)	0.046 (0.10)
8	2.5 (0.25)	0.082 (0.10)	0.05 (0.029)	0.0015 (0.00067)	-0.76 (0.19)	0.27 (0.08)	0.097 (0.10)
9	2.6 (0.25)	0.19 (0.03)	---	0.0013 (0.00069)	-0.68 (0.19)	---	---
10	2.7 (0.25)	---	0.057 (0.0085)	0.0013 (0.00068)	-0.70 (0.19)	---	---
11	1.4 (0.09)	0.19 (0.03)	---	---	---	0.20 (0.08)	-0.03 (0.10)
12	2.3 (0.17)	0.032 (0.10)	0.042 (0.03)	---	-0.41 (0.11)	---	---
13	1.5 (0.08)	---	0.057 (0.009)	---	---	0.20 (0.08)	-0.046 (0.10)
14	2.7 (0.26)	0.044 (0.10)	0.045 (0.03)	0.0013 (0.00068)	-0.71 (0.19)	---	---
15	1.6 (0.04)	0.12 (0.03)	---	---	---	---	---
16	1.4 (0.09)	0.19 (0.03)	---	-0.00062 (0.00041)	---	0.20 (0.08)	-0.018 (0.10)
17	1.6 (0.08)	---	0.059 (0.009)	-0.00065 (0.00041)	---	0.20 (0.08)	-0.035 (0.10)
18	1.5 (0.10)	0.053 (0.10)	0.042 (0.03)	---	---	0.20 (0.08)	-0.045 (0.10)
19	1.7 (0.03)	---	0.038 (0.008)	---	---	---	---
20	1.7 (0.04)	0.13 (0.03)	---	-0.00071 (0.00043)	---	---	---
21	1.7 (0.03)	---	0.04 (0.008)	-0.00073 (0.00043)	---	---	---
22	1.5 (0.10)	0.051 (0.10)	0.044 (0.03)	-0.00065 (0.00041)	---	0.20 (0.08)	-0.033 (0.10)
23	1.7 (0.07)	0.02 (0.11)	0.032 (0.032)	---	---	---	---
24	1.7 (0.07)	0.018 (0.10)	0.035 (0.031)	-0.00073 (0.00043)	---	---	---
25	1.8 (0.02)	---	---	---	---	---	---
26	1.9 (0.17)	---	---	---	-0.083 (0.11)	---	---
27	1.8 (0.03)	---	---	-0.00032 (0.00046)	---	---	---
28	1.9 (0.25)	---	---	-0.00016 (0.00073)	-0.053 (0.18)	---	---
29	1.7 (0.09)	---	---	---	---	0.093 (0.09)	0.12 (0.10)
30	1.9 (0.20)	---	---	---	-0.14 (0.12)	0.10 (0.09)	0.16 (0.11)
31	1.7 (0.09)	---	---	-0.00038 (0.00046)	---	0.093 (0.09)	0.13 (0.10)
32	2.0 (0.29)	---	---	0.00013 (0.00076)	-0.17 (0.21)	0.10 (0.09)	0.16 (0.11)

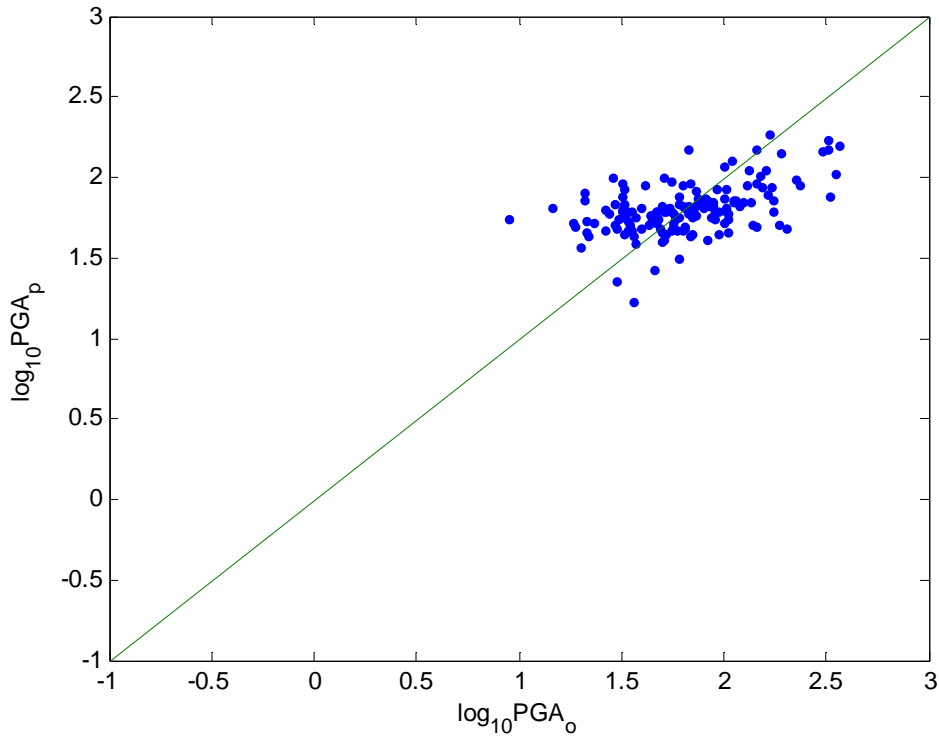


Figure 3. Model prediction results with their observed values (Xinjiang).

#### 4.4. Full Set of Data

Table 6 and 7 show the prediction model class selection results and the optimal parameters of each model class, respectively. From Table 7, the most plausible prediction model for the PGA is given by

$$\log_{10} PGA = 1.2 + 0.26(M - 3.5) - 0.0027r + 0.31G_B + 0.011G_c \quad (14)$$

where the terms  $b_3(M - M_0)^2$  and  $b_5 \log_{10} r$  are not included. From Table 6, the plausibility of this model class is over 0.7, and it is much higher than the full model class. Note that the standard deviation of the prediction error  $\hat{\sigma}_\varepsilon$  is 0.38 for the optimal model, which is significantly larger than the previous cases because a single model is used to predict the PGA in three different regions that are significantly different in terms of the geological and terrestrial condition. Figure 4 shows the predicted PGA compared with their measured values for the most probable model class along with the 45° line.

**Table 6. Model class selection results (Full dataset)**

	Parameters	$p(D \hat{\theta}_s, C_k)$	$\hat{\sigma}_\varepsilon$	$O_{C_k}$	$P(C_k D)$
1	1 2 4 6 7	2.70E-53	0.38	5.80E-09	7.03E-01
2	1 2 4 5 6 7	3.22E-53	0.38	1.02E-09	1.48E-01
3	1 2 3 4 6 7	1.10E-52	0.38	2.35E-10	1.16E-01
4	1 2 3 4 5 6 7	1.68E-52	0.38	4.16E-11	3.14E-02
5	1 2 3 5 6 7	3.28E-55	0.39	6.62E-10	9.78E-04
6	1 3 4 6 7	2.85E-56	0.39	2.18E-09	2.80E-04
7	1 2 5 6 7	2.08E-57	0.4	1.83E-08	1.71E-04
8	1 3 4 5 6 7	3.14E-56	0.39	3.82E-10	5.39E-05
9	1 2 3 4	2.61E-60	0.41	5.79E-08	6.79E-07
10	1 2 4	5.50E-62	0.41	1.40E-06	3.47E-07
11	1 2 4 5	2.07E-61	0.41	2.35E-07	2.18E-07
12	1 2 3 4 5	4.52E-60	0.4	9.90E-09	2.01E-07
13	1 2 3 6 7	5.48E-60	0.4	6.56E-09	1.62E-07
14	1 2 6 7	1.09E-62	0.41	1.75E-07	8.58E-09
15	1 3 5 6 7	5.29E-62	0.41	7.24E-09	1.72E-09
16	1 2 3 5	4.71E-64	0.42	1.55E-07	3.29E-10
17	1 3 4 5	8.54E-64	0.42	8.01E-08	3.07E-10
18	1 2 3	1.85E-65	0.42	1.25E-06	1.04E-10
19	1 3 4	2.59E-65	0.42	5.07E-07	5.89E-11
20	1 4 5 6 7	1.14E-64	0.42	4.18E-08	2.15E-11
21	1 3 6 7	2.18E-65	0.42	6.14E-08	6.03E-12
22	1 4 6 7	1.30E-66	0.43	2.62E-07	1.53E-12
23	1 2 5	6.91E-68	0.43	4.13E-06	1.28E-12
24	1 4 5	2.16E-68	0.43	6.56E-06	6.36E-13
25	1 2	2.12E-69	0.44	3.18E-05	3.03E-13
26	1 6 7	1.99E-69	0.44	5.57E-06	4.98E-14
27	1 5 6 7	2.58E-69	0.44	6.68E-07	7.76E-15
28	1 3	4.12E-72	0.45	1.07E-05	1.97E-16
29	1 3 5	1.35E-71	0.45	1.45E-06	8.81E-17
30	1 4	3.12E-73	0.45	4.70E-05	6.58E-17
31	1	2.25E-75	0.46	8.90E-04	9.01E-18
32	1 5	3.48E-75	0.46	1.04E-04	1.62E-18

**Table 7. Optimal parameters of each prediction model class (Full dataset)**

	$b_1$	$b_2$	$b_3$	$b_4$	$b_5$	$b_6$	$b_7$
1	1.2 (0.05)	0.26 (0.03)	---	-0.0027 (0.0004)	---	0.31 (0.06)	0.011 (0.08)
2	1.3 (0.16)	0.27 (0.04)	---	-0.0025 (0.00056)	-0.084 (0.14)	0.33 (0.06)	0.026 (0.08)
3	1.2 (0.07)	0.43 (0.10)	-0.056 (0.033)	-0.0025 (0.00042)	---	0.30 (0.06)	0.014 (0.08)
4	1.3 (0.16)	0.46 (0.11)	-0.062 (0.034)	-0.0021 (0.00059)	-0.13 (0.14)	0.32 (0.06)	0.036 (0.08)
5	1.6 (0.13)	0.60 (0.10)	-0.10 (0.032)	---	-0.49 (0.10)	0.38 (0.06)	0.11 (0.08)
6	1.3 (0.05)	---	0.075 (0.01)	-0.0028 (0.00042)	---	0.34 (0.06)	0.037 (0.08)
7	1.8 (0.12)	0.29 (0.04)	---	---	-0.53 (0.10)	0.41 (0.06)	0.11 (0.08)
8	1.3 (0.16)	---	0.073 (0.011)	-0.003 (0.00057)	0.061 (0.14)	0.33 (0.06)	0.026 (0.08)
9	1.3 (0.06)	0.53 (0.11)	-0.098 (0.035)	-0.0022 (0.00044)	---	---	---
10	1.4 (0.04)	0.24 (0.03)	---	-0.0026 (0.00043)	---	---	---
11	1.2 (0.16)	0.21 (0.04)	---	-0.0032 (0.00057)	0.22 (0.14)	---	---
12	1.1 (0.16)	0.49 (0.12)	-0.089 (0.036)	-0.0026 (0.0006)	0.14 (0.14)	---	---
13	1.1 (0.07)	0.55 (0.11)	-0.12 (0.034)	---	---	0.27 (0.06)	0.036 (0.08)
14	1.2 (0.06)	0.18 (0.03)	---	---	---	0.31 (0.06)	0.035 (0.08)
15	1.8 (0.13)	---	0.071 (0.012)	---	-0.44 (0.11)	0.42 (0.06)	0.14 (0.08)
16	1.5 (0.14)	0.68 (0.11)	-0.15 (0.034)	---	-0.27 (0.10)	---	---
17	1.1 (0.17)	---	0.054 (0.011)	-0.0036 (0.00058)	0.35 (0.13)	---	---
18	1.2 (0.06)	0.63 (0.11)	-0.15 (0.035)	---	---	---	---
19	1.5 (0.03)	---	0.066 (0.011)	-0.0026 (0.00045)	---	---	---
20	0.93 (0.16)	---	---	-0.0029 (0.00061)	0.42 (0.14)	0.26 (0.07)	0.10 (0.09)
21	1.3 (0.05)	---	0.044 (0.010)	---	---	0.33 (0.06)	0.072 (0.08)
22	1.4 (0.05)	---	---	-0.0015 (0.00041)	---	0.35 (0.06)	0.21 (0.08)
23	1.7 (0.13)	0.23 (0.04)	---	---	-0.29 (0.11)	---	---
24	0.84 (0.16)	---	---	-0.0035 (0.0006)	0.61 (0.13)	---	---
25	1.4 (0.04)	0.17 (0.03)	---	---	---	---	---
26	1.4 (0.05)	---	---	---	---	0.34 (0.06)	0.18 (0.08)
27	1.4 (0.13)	---	---	---	-0.07 (0.10)	0.35 (0.07)	0.21 (0.09)
28	1.5 (0.03)	---	0.04 (0.010)	---	---	---	---
29	1.7 (0.14)	---	0.05 (0.012)	---	-0.17 (0.11)	---	---
30	1.6 (0.03)	---	---	-0.0014 (0.00044)	---	---	---
31	1.6 (0.03)	---	---	---	---	---	---
32	1.5 (0.13)	---	---	---	0.087 (0.093)	---	---

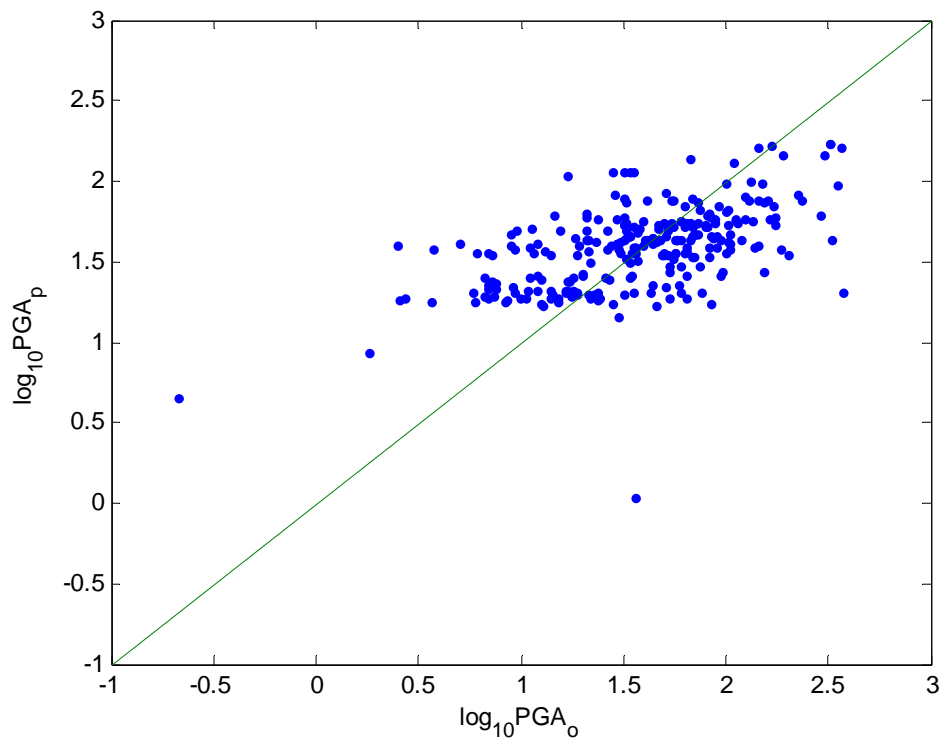


Figure 4. Model prediction results with their observed values (Full dataset)

## 5. Conclusion

A Bayesian probabilistic approach for model class selection is applied to select the seismic attenuation model. In order to balance between the capability of data fitting and the robustness to noise and modeling error, the prediction model class is selected by maximizing the plausibility of the model class given the strong-motion records. A database with 266 strong-motion records in three regions of China is utilized for analysis. It turns out that the optimal model is not the full model even though the full model gives the smallest fitting error. The optimal model is less prone to noise so more reliable future prediction can be anticipated. If several prediction model classes possess similar plausibility given the dataset, one can consider a multi-model prediction formula as in the case of the Xinjiang region. The Bayesian approach allows to obtain not only the optimal parameters within a model class but also the associated uncertainty of the parameter values. The quantified uncertainty can be further used for uncertainty analysis of the prediction.

## Acknowledgement

The work described in this chapter was fully supported by the Research Committee of University of Macau under grant RG077/07-08S/YKV/FST UMAC. The generous financial support is gratefully acknowledged.

## References

- [1] Joyner, W.B., & Boore, D.M. (1981). Peak horizontal acceleration and velocity from strong-motion records including records from the 1979 Imperial Valley, California, earthquake. *Bulletin of the Seismological Society of America*, **71**, 469-487.
- [2] Brillinger, D.R., & Preisler, H.K. (1984). An exploratory analysis of the Joyner-Boore attenuation data. *Bulletin of the Seismological Society of America*, **74**(4), 1441-1450.
- [3] Brillinger, D.R., & Preisler, H.K. (1985). Further analysis of the Joyner-Boore attenuation data. *Bulletin of the Seismological Society of America*, **75**(2), 611-614.
- [4] McLaughlin, K.L. (1991). Maximum likelihood estimation of strong motion attenuation relationships. *Earthquake Spectra*, **7**, 267-279.
- [5] Joyner, W.B., & Boore, D.M. (1993). Methods for regression analysis of strong motion data. *Bulletin of the Seismological Society of America*, **83**(2), 469-487.
- [6] Boore, D.M., Joyner, W.B., & Fumal, T.E. (1993). Estimation of response spectra and peak accelerations from Western North American earthquakes: an interim report. U.S. Geological Survey Open-File Report 93-509.
- [7] Boore, D.M., Joyner, W.B., & Fumal, T.E. (1994). Estimation of response spectra and peak accelerations from Western North American earthquakes: an interim report, part 2. U.S. Geological Survey Open-File Report 94-127.
- [8] Boore, D. M., Joyner, W. B., & Fumal, T. E. (1997). Equations for estimating horizontal response spectra and peak acceleration from western North American earthquakes: a summary of recent work (with 2005 erratum), *Seismology Research Letters*, **68**, 128-153.
- [9] Hanks, T.C. and Kanomori, H. (1979). A moment magnitude scale. *Journal of Geophysical Research*, **84**, 2348-2350.
- [10] Wang, S., Yu Y., Gao A., & Yan, X. (2000). Development of attenuation relations for ground motion in China. *Earthquake Research in China*, **16**(2), 99-106 (in Chinese).
- [11] Wong, Y.L., Zhao, J.X., & Luo, Q. (2002). Attenuation characteristics of ground motions in northern China. *Earthquake Engineering and Engineering Vibration*, **1**(2), 161-166.
- [12] Zheng, S., & Wong, Y.L. (2004). Seismic ground motion relationships in southern China based on stochastic finite-fault model. *Earthquake Engineering and Engineering Vibration*, **3**(1), 11-22.
- [13] Shi, S. & Shen, J. (2004). Study on ground motion attenuation relation in Shanghai and its adjacent region. *Earthquake Research in China*, **18**(2), 105-113.
- [14] Crouse, C.B., & McGuire, J.W. (1996). Site response studies for purpose of revising NEHRP seismic provisions. *Earthquake Spectra*, **12**(3), 407-439.
- [15] Field, R.V. Jr. (2004). Methods for model selection in applied science and engineering. Technical report SAND 2004-5082, Sandia National Laboratories.
- [16] Mackay, D.J.C. (1992). Bayesian interpolation. *Neural Computation*, **4**(3), 415-447.
- [17] Beck, J.L., & Yuen, K.V. (2004). Model selection using response measurements: Bayesian probabilistic approach. *ASCE Journal of Engineering Mechanics*, **130**(2), 192-203.
- [18] Yuen, K.V., & Lam, H.F. (2006). On the complexity of artificial neural networks for smart structures monitoring. *Engineering Structures*, **28**(7), 977-984.

- [19] Lam, H.F., Yuen, K.V., & Beck, J.L. (2006). Structural health monitoring via measured Ritz vectors utilizing artificial neural networks. *Computer-Aided Civil and Infrastructure Engineering*, **21**(4), 232-241.
- [20] Lecampion, B., & Gunning, J. (2007). Model selection in fracture mapping from elastostatic data. *International Journal of Solids and Structures*, **44**, 1391-1408.
- [21] Hoi, K.I., Yuen, K.V., & Mok, K.M. (2007). Applying Kalman filter to forecast short-term air quality in Macau. Proc. 10th International Conference on Environmental Science and Technology, Cos island, Greece, Volume A, pp. 504-511.
- [22] China Earthquake Data Center. <http://smsd-iem.net/eqkview.asp>
- [23] Cox, R.T. (1961). *The Algebra of Probable Inference*. Baltimore: Johns Hopkins University Press.
- [24] Ross, S.M. (2003). *Introduction to Probability Models (8th edition)*. San Diego: Academic Press.
- [25] Beck, J.L., & Katafygiotis, L.S. (1998). Updating models and their uncertainties. I: Bayesian statistical framework. *ASCE Journal of Engineering Mechanics*, **124**(4), 455-461.
- [26] Katafygiotis, L.S., & Beck, J.L. (1998). Updating models and their uncertainties. II: Model identifiability. *ASCE Journal of Engineering Mechanics*, **124**(4), 463-467.
- [27] Papadimitriou, C., Beck, J.L., & Katafygiotis, L.S. (1997). Asymptotic expansions for reliability and moments of uncertain systems. *ASCE Journal of Engineering Mechanics*, **123**(12), 1219-1229.



*Chapter 6*

**USING AMBIENT NOISE MEASUREMENTS  
IN THE PROCESS OF ASSESSING EARTHQUAKE  
HAZARDS IN URBAN AREAS: EXAMPLES  
FROM ISRAEL**

***Y. Zaslavsky, A. Shapira, G. Ataev, M. Gorstein, T. Aksinenko,  
M. Kalmanovich, N. Perelman and R. Hofstetter***

Seismology Division, Geophysical Institute of Israel, P.O. Box 182, Lod 71100, Israel

**Abstract**

Ground motion amplifications due to soft soils, common in urban areas, are a major contributor to increasing damage and number of casualties. The great variability in the subsurface conditions across a town/city and the relatively high costs associated with obtaining the appropriate information about the subsurface, strongly limit proper hazard assessments. Direct information from strong motion recordings in urban areas is usually unavailable. Such is the situation in Israel which is small and its population centers are in close proximity to the seismically active Dead Sea Fault system, capable of generating earthquakes with magnitude as high as 7.5.

Heavily limited with relevant local recordings of strong ground motions, we adhere to the use of simplified modelling of the earthquake processes. More precisely, we generate synthetic spectra of the expected ground motions by implementing the so called Stochastic Approach (e.g. Boore, 2000), in which we integrate analytical models to determine the nonlinear response of the site under investigation that requires modelling of subsurface. Then, Monte-Carlo simulations are used to obtain the uniform hazard, site-specific acceleration spectrum.

Over the years, we have conducted site investigations in several thousands of sites across Israel. These investigations demonstrate the usefulness of using horizontal-to-vertical (H/V) spectra of ambient noise measurements to identify sites with high potential for being vulnerable to amplification effects and characterize the sites with respect to their expected resonance frequencies and the corresponding H/V levels. This information, together with any available geological, geotechnical and geophysical information, helps building a reliable model of the subsurface, which is then integrated in the processes of the seismic hazard assessment.

Modeling the subsurface and assessing the earthquake hazards in urban areas involves systematic ambient noise measurements on a grid with spacing of 500 m. At instances where high variations are observed, the spatial density of measurements is significantly increased. In doing so, we are able to develop a regional subsurface model, which is systematic with all additional information we compile, i.e., geological maps, borehole information, seismic refraction surveys etc.

In order to reduce the scatter in H/V observations, the processing scheme involves continuous recording of ambient noise for about 1-2 hours and careful selection of time windows from which H/V functions are calculated. To assure stability in H/V observations, measurements are repeated in different times and dates. At several occasions, while measuring the ambient noise or when we deliberately aimed at recording seismic events, it is possible to support ambient noise spectral ratios with spectral H/V observations from earthquakes (often considered transfer functions) and explosions recorded by accelerometers and seismometers. In all cases, we obtained similar H/V spectral ratios from the different data sets.

At the final stage of the hazard assessment process, we divide the study region into zones of similar hazard characteristics, which are used for earthquake scenarios and better represent the design acceleration spectra for safer buildings.

## Introduction

Israel is small and its population centers are in proximity to the seismically active Dead Sea Fault system. Deformation of young sediments, paleoseismic and historical records indicate that the Dead Sea Fault has been continuously active and was the source of several destructive earthquakes that shook the entire region throughout geological times (Begin, 2005). Over the past three centuries, large earthquakes with intensities reaching X on the MM scale occurred in the area. The earthquake on October 30, 1759 (Amiran et al., 1994), located probably in southern Lebanon, affected most of today Lebanon, Israel and Syria with damage extended as south as Jaffa. Some sources report a death toll of 10,000-40,000 people. According to Ambraseys and Barazangi (1989) losses were certainly considerable. The earthquake that occurred on January 1, 1837, was the strongest earthquake to occur in the region since the 19th century (Amiran et al., 1994), where most of the damage is reported to occur in Safed and Tiberias. The Jericho earthquake on July 11, 1927, with magnitude  $M=6.2$ , was the most destructive regional seismic event in the 20th century. The effects of the earthquake were devastating, particularly in Jerusalem, Nablus, Lod and Ramle. In Lod and Ramle, which at that time were small towns, many buildings were destroyed and 50 people were killed (Avni et al., 2002). We note that these towns are relatively distant from the epicentre, i.e., about 60 km away. In the earthquake on January 18, 749, which had possibly a similar magnitude, the flourishing Roman-Byzantine town of Bet Shean was destroyed. Figure 1 presents mapped active faults (after Bartov et al., 2002) along with suggested epicentres of historical earthquakes (after Ben-Menahem, 1979) and the earthquake epicentre on July 11, 1927 (Shapira et al., 1993). Consequently, today more than 15 million people surrounding the Dead Sea Transform fault system are vulnerable to earthquakes.

In order to mitigate earthquake risk and assess the site specific seismic hazard in urban areas, we must estimate the possible consequences of strong earthquakes, i.e., implement our accumulated experience of past earthquakes to present a scenario of an eventual earthquake. Despite the fact that the Holy Land has a long documented history of destructive earthquakes its usefulness with respect to seismic hazard assessment is limited. The demographic

conditions, engineering characteristics of the buildings and structures and even the geographical sites are different from those that existed in the past.

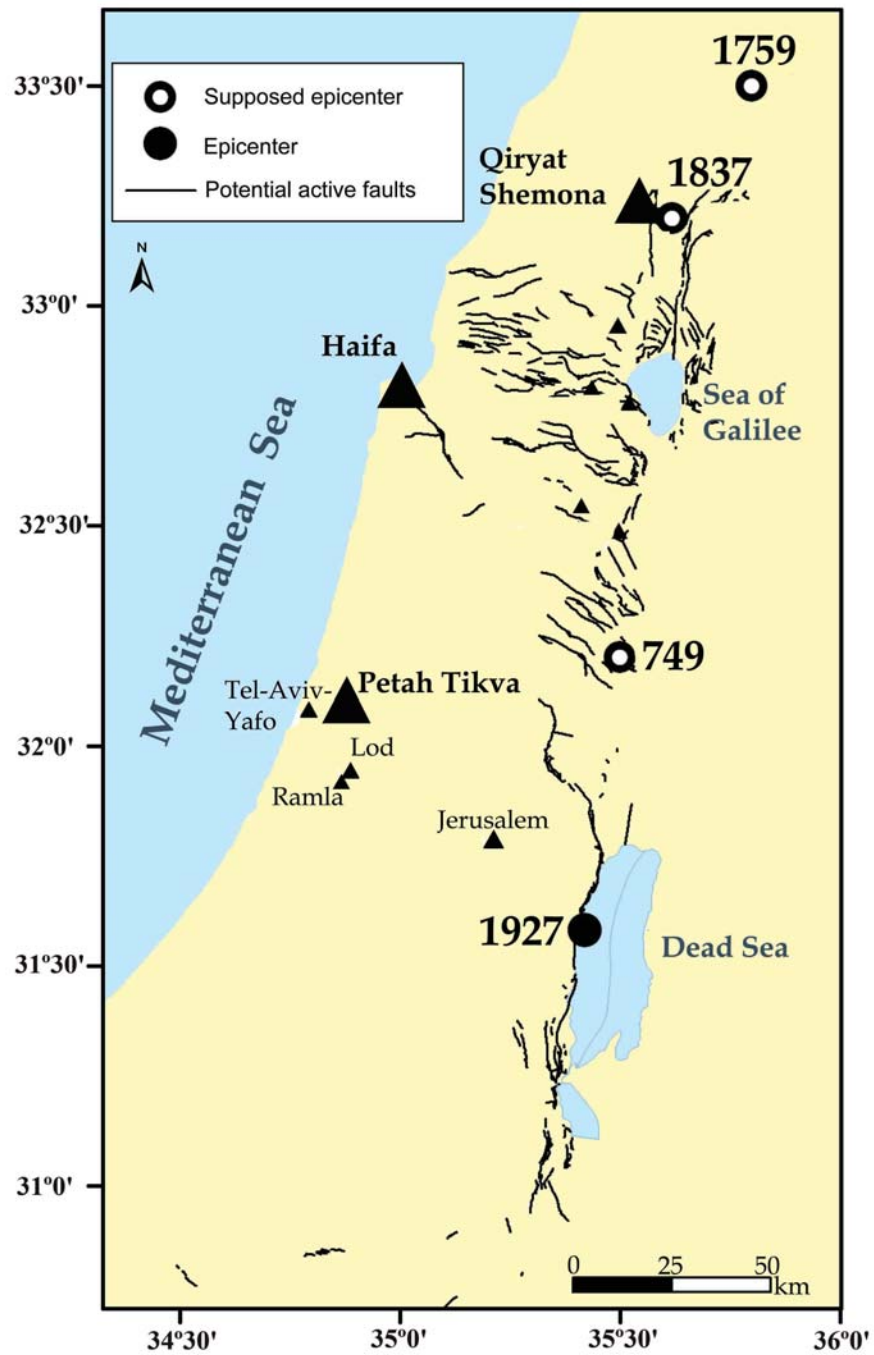


Figure 1. Location of assumed active faults and epicenters. Solid triangle indicates investigated urban area.

The detailed investigation of the Jericho earthquake (Avni, 1999) is probably the most accurate and complete macroseismic study of the region. And yet, it is of limited use because of the great changes the region has undergone in the last 80 years.

Several well known examples of destructive earthquakes during the last two decades like the Mexico City, 1985 (Singh et al., 1988; Reinoso and Ordaz, 1999), Spitak, Armenia, 1988 (Borcherdt et al., 1989), California, Loma Prieta, 1989 (Hough et al., 1990) and Northridge, 1994 (Hartzell et al., 1996), Kobe, Japan, 1995 (Iwata et al., 1996), Kocaeli (Izmit), Turkey, 1999 (Ozel et al., 2002), Algeria, 2003 (Hamadche et al., 2004) and many others have clearly shown that local site conditions are an important factor in determining the seismic hazard. The Seismology Division, of the Geophysical Institute of Israel, took the lead in the site specific seismic hazard assessment in Israel and in the last decade has launched a number of projects to identify and map areas, which are expected to amplify seismic ground motion across Israel (i.e., Zaslavsky et al., 1995, 2004, 2005; Shapira et al., 2001).

In this study we present a few examples of our methodology in using ambient noise records as an aid to determine seismic hazard in intensely populated areas. This methodology is based on integrating data from the extensive ambient noise measurements, information about the regional geology and S-wave velocity profiles derived from refraction profiles, borehole data and any additional relevant information that enabled the construction of systematic and coherent multi-layer soil-column models that consequently yield analytical site response functions. It should be emphasized that those analytical response functions are consistent with the observed horizontal-to-vertical spectral ratios and often almost identical in the range of fundamental and second frequencies. We divide the study areas into zones and characterize each of them by a generalized soil column model. The obtained seismic hazard zonation maps are thus closely tied to actually measured site effects, and therefore may lead to realistic site specific seismic hazard assessments, in spite of the paucity of borehole, refraction data and other subsurface information.

## **Empirical Approaches Implemented in the Analysis of Site Effects**

Various empirical techniques for site response estimations were summarized and discussed by Field and Jacob (1995), Kudo (1995), Lachet et al. (1996), Satoh et al. (2001) and others. There is no doubt that the best evaluation of site effect is based on dense strong motion observations using spectral ratio of seismic records from sedimentary sites and bedrock reference sites, because the nonlinear effect is included (Jarpe et al., 1988, 1989; Darragh and Shakal, 1991; Satoh et al., 1995; Hartzell, 1998; Reinoso and Ordaz, 1999; and others). In most cases, mainly in regions where the seismic activity is relatively low as in Israel, this type of analysis is usually impractical. The best known empirical techniques used for the assessments of site effects are:

### **S-Wave Spectral Ratio with Respect to Reference Site**

The most common technique for estimating site response is the standard (classic) spectral ratio procedure first introduced by Borcherdt (1970). This approach considers the ratio  $R_b$ ,

between the Fourier spectra of a seismogram recorded in the site of interest  $S_s$  and the spectrum of a seismogram recorded at a reference site, which is usually the rock outcrop  $S_r$ :

$$R_b(\omega) = \frac{|S_s(\omega)|}{|S_r(\omega)|} \quad (1)$$

This ratio can be considered as the transfer function between the bedrock and the surface assuming that the two recordings correspond to the same source, the same path effect and that the reference site has a negligible site effect. It is very difficult to implement all these assumptions in real conditions. First, in many cases we do not have a nearby bedrock site and therefore the condition that the path of the propagating seismic waves is the same is not fulfilled; second, it is known (e.g., Steidl et al., 1996, Zaslavsky et al., 2002) that weathered and cracked bedrock site exhibits a significant site effect, associated with frequency-selective ground motion amplification; third, there are many cases in Israel, when nearby bedrock outcrop is not the same rock at the base of the soil layer which is responsible for amplifying seismic waves amplitudes. It should also be noted that performing simultaneous measurements at two sites is often relatively costly. Nevertheless, when all the conditions are observed, this method maybe considered the most reliable estimate of the empirical transfer function of site. Many investigators used this method and evaluated site response functions from moderate to weak motion recording of earthquakes (Tucker and King, 1984; McGarr et al., 1991; Field et al., 1992; Liu et al., 1992; Carver and Hartzell, 1996; Hartzell et al., 1996; Steidl et al., 1996; Zaslavsky et al., 2000 and others).

### Horizontal-to-Vertical S-Wave Spectral Ratio (Receiver Function)

This technique is applied by Lermo and Chávez-García (1993):

$$R_s(\omega) = \frac{|S_{sh}(\omega)|}{|S_{sv}(\omega)|} \quad (2)$$

where  $S_{sh}$  and  $S_{sv}$  denote horizontal and vertical amplitude spectra computed at the same investigated site from S-waves, respectively.

Receiver function was introduced by Langston (1979) to determine the velocity structure of the crust and upper mantle from P-waves of teleseisms. Langston made the assumption that the vertical component of motion is not influenced by the local structure, whereas the horizontal components, owing to the geological layering, contain the P to S conversion. In the spectral domain this corresponds to a simple division of the horizontal spectrum by the vertical (equation 2). Many studies report that the frequency dependence of site response can thus be obtained from measurements made at only one station at the analysed site (Lermo and Chavez-Garcia 1994; Malagnini et al., 1996; Seekins, et al., 1996; Theodulidis et al., 1996; Castro et al. 1997; Yamazaki and Ansary, 1997; and others). Their results confirm the validity of the method to estimate S-wave site response. We obtained similar conclusion in our

investigations (Zaslavsky et al., 2000). Nevertheless, the implementation of this approach still requires a rather frequent occurrence of earthquakes. This requirement becomes an obstacle in regions of low seismicity.

### Spectral Analysis of Ambient Noise

Spectral analysis of ambient noise is an alternative tool to quantify site effects because it is much cheaper, less time-consuming than the classical technique and effective for seismic risk mitigation. Kanai and Tanaka (1961) pointed out that predominant frequencies of horizontal spectra of ambient vibrations measured on thick sediment deposits (up to several kilometers thick) are well correlated with the dominant frequencies of spectra of measured strong motions obtained at the same site. Since then, it has been reported that this technique has proved to be effective in estimating the fundamental frequency of site effects (Tanaka et al., 1968; Katz, 1976; Katz and Bellon, 1978; Ohta et al., 1978; Kagami et al., 1982; Zaslavsky, 1987; Morales et al., 1991; Yamanaka et al., 1994; Kobayashi, 1995). It should be noted, however, that dominant frequencies of ambient noise in urban areas may result from a variety of possible artificial sources and interference of the waves they generate and therefore, predominant frequencies in the spectrum are not necessarily due to local site effects.

### Noise Spectral Ratio with Respect to Reference Site

Kagami et al. (1982) proposed that the ratio of the spectra of the horizontal ground motions of the noise at the investigated site to those of a reference site can be used as a measure of the site response function:

$$R_k(\omega) = \frac{|H_S(\omega)|}{|H_r(\omega)|} \quad (3)$$

where  $H_S$  and  $H_r$  denote spectral amplitudes of the horizontal components of motion at the investigated site and those of the reference site, respectively. This method can be successfully applied for long period microtremors with period ranging from 1.0 to 10 sec. When higher frequencies are of interest, the distance between the measured sites should not exceed few hundred meters.

The reliability of this method depends on whether or not the simultaneously measured motions at each site are from the same source and propagation path. This technique is widely used for site response estimates (Lermo et al., 1988; Field et al., 1990, 1995; Rovelli et al., 1991; Dravinski et al., 1995, 2003; Gaull et al., 1995;). However, experimental study of site effect by sediment-to-bedrock spectral ratio in urban and suburban regions can be successful only under particular circumstances, because ambient noise would be influenced by local artificial sources generated by human activities which essentially change from place to place.

## Horizontal-to-Vertical Ambient Noise Spectral Ratio

Nakamura (1989) proposed the hypothesis that site response function under low strain can be determined as the spectral ratio of the horizontal versus the vertical component (H/V) of motion observed at the same site. He hypothesized that the vertical component of ambient noise is relatively unaffected by the unconsolidated near-surface layers. Hence, the site response is the spectral ratio between the horizontal component of microseisms  $H_h$  and vertical component of microseisms  $H_v$  recorded at the same location:

$$R_n(\omega) = \frac{|H_h(\omega)|}{|H_v(\omega)|} \quad (4)$$

In analogy to the other approaches, the vertical component of the surface motions retains the characteristics of horizontal components of ambient noise at depth on the bedrock (reference site). Many authors, among them Lermo and Chávez-García (1994), Seekins et al. (1996), Toshinawa et al. (1997), Chávez-García and Cuenca (1998), Enomoto et al. (2000), Shapira et al. (2001), Mucciarelli and Gallipoli (2004), Murphy and Eaton (2005), Maresca, (2006), show that the H/V spectral ratio technique can be a useful tool for the assessment of ground motion characteristics on soft sediments. However, other authors (for example, Bonilla et al. 1997; Horike et al. 2001, Satoh et al. 2001) conclude that whereas the predominant peak of H/V ratio is well correlated with the fundamental resonance frequency, the amplitude of this peak is not necessarily the amplification level as obtained from sediment-to-bedrock spectral ratio of earthquake records. In a recent comprehensive study by SESAME European project (Atakan et al., 2004; Bard et al., 2004) it has been shown that H/V spectral ratio from ambient noise can be used to obtain reliable information about the amplification of sedimentary layers, provided that no non-linear processes occur. The Nakamura approach has gained great interest, primarily due to the simplicity in its implementation. However, it is a controversial issue which is heavily debated among the specialists.

## The Semi-empirical Approach

Application of empirical approaches which involves measuring strong motions of engineering interest is not practical in regions with low or even moderate seismicity as in Israel. Following site investigations in thousands sites across Israel, we adopt the concept that the site response be determined by analytical tools. In our studies we use either the well known program SHAKE or the non-linear site response computations by Joyner (1973). It has to be emphasized that both computer codes yield exactly the same results for the same give model of a stratified subsurface. Implementation of such programs enables the assessment of the site response also in cases when the soils change their response in accordance with the intensity of the propagating seismic waves, i.e., susceptible to non-linear effects. At low stresses, however, as in the case of macroseismic noise and low magnitude earthquakes, the empirically obtained site response by any of the specified above methods should be similar to

the site response function which is obtained analytically. Furthermore, we require that the observed fundamental resonance frequency of the site will be identical to the one obtained by modeling and computations. In practice, we use ambient noise measurements and H/V computations to specify and/or control a stratified subsurface model which best characterizes the site. That model is used for calculating the site response. The applicability of this semi-analytical concept is demonstrated in the following.

In the process of implementing information from ambient noise measurements, we observe, like many other investigators, that the H/V spectral ratio of ambient noise is sensitive to variations in the subsurface over very short distances. Consequently, it is possible to integrate H/V observations with other site specific data from e.g. surface geology, seismic refraction surveys, borehole data etc, to derive realistic models of the subsurface, especially at sites where other direct information is missing. Furthermore, as demonstrated in the following, ambient noise measurements over a dense grid reveals a reliable 3D model of the investigated area and is useful for detecting discontinuities such as faults which are currently not mapped.

## Observation and Processing

Ambient noise measurements are conducted using portable instruments (Shapira and Avirav, 1995) consisting of a multi channel amplifier, Global Positioning System (GPS) for timing and a laptop computer with 16-bit analogue-to-digital conversion card to digitize and store the data. In our experimental set-up, each seismograph station consists of three (one vertical and two horizontal) L4C velocity transducers (Mark Products) with a natural frequency of 1.0 Hz and damping ratio 70% of critical. The recorded signals are sampled at 100 samples per second and band-pass filtered between 0.2 Hz and 25 Hz. All the equipment: sensors, power supply, amplifiers, personal computer and connectors are carried in a vehicle, which also serves as a recording centre. The seismometers are fixed on levelled metal plate placed directly on the ground. Prior to performing measurements, the individual seismometer constants (natural frequency, damping and motor constant) are determined using sine and step calibration signals, and then the frequency response functions of all channels are computed. This procedure allows evaluating change of natural frequency and motor constant (voltage sensitivity) during long time of measurements in harsh conditions in the free field. As a final test, all seismometers are placed at the same location and in the same orientation to record the same waves. It so happens that the differences between the seismic channels are marginal even without “correcting” for the instrumentation response. In fact, at frequencies below the natural frequency of the seismometers, correcting for the instrument response may increase variability and scattering. It is necessary to remind that all channels (horizontal and vertical) have practically the same frequency response function and amplifiers are set to the same gain level. Hence, spectral ratio may be calculated on the recorded signals. Moreover, it is possible to assess the predominant frequencies in the H/V spectra also at frequencies much lower than the natural frequency of the seismometer.

During the first projects for site investigations and in order to validate interpretations based on ambient noise measurements, we used to install seismometers at 3-6 points in an around the investigated site. Soon it became apparent that this practice significantly manifested the reliability of the results. At a later stage, when performing seismic

microzonation studies, we could appreciate the value of a dense grid of points where we conducted ambient noise measurements. In today practice, to provide a good coverage of the study area, the measurement sites are designed with a grid spacing of 500 m. Different surface sedimentary deposits, thickness of sediments and shear wave velocity contrast between sediments and bedrock are also considered in the design stage. High variation in the observations can lead us to increase the spatial density to a grid spacing of 250 m and in some locations 150-100 m. This dense network of monitored sites reflects (a) the high variability of the subsurface properties in the urban areas we study and (b) the relatively high sensitivity of H/V spectra to variations at depth.

To study the characteristics of spectra of the ambient noise signals, we compute Fourier spectra and spectral ratios. The record length (time window) used for spectral calculations depends on the fundamental frequency. The basic criterion is to choose the minimal time window which yields spectra that practically do not change when increasing the record length. We have concluded that at sites with fundamental frequencies of 1 Hz (or more) we should use a record of at least 30 sec. At sites with lower frequencies, the time window should be increased to 60 sec. The selected time windows are Fourier transformed, using cosine-tapering (1 sec at each end) before transformation and then smoothed with a triangular moving Hanning window. More precisely, we apply “window closing” procedure (see Jenkins and Watts, 1968) for smart smoothing of spectral estimates so that any significant spectral peaks are not distorted.

The H/V spectral ratios are obtained by dividing the individual spectrum of each of the horizontal components [ $S_{NS}(f)$  and  $S_{EW}(f)$ ] by the spectrum of the vertical component [ $S_V(f)$ ]:

$$A_{NS}(f) = \frac{S_{NS}(f)}{S_V(f)} \quad A_{EW}(f) = \frac{S_{EW}(f)}{S_V(f)} \quad (5)$$

The average spectral ratio for each of two horizontal components is computed, if the curves of average spectral ratios of the two components are similar then the average of the two horizontal-to-vertical ratios is defined as:

$$A(f) = \frac{1}{2n} \left[ \sum_{i=1}^n \frac{S_{NS}(f)_i}{S_V(f)_i} + \sum_{i=1}^n \frac{S_{EW}(f)_i}{S_V(f)_i} \right] \quad (6)$$

The length of recorded ground motions (ambient noise) may affect the results and influence the reliability and applicability of the technique. According to Teves Costa et al. (1996), Teves Costa and Senos (2000) and Dravinski et al. (2003), a total ambient noise recording of five minutes is sufficient. Lebrun et al. (2004) and Garcia-Jerez et al. (2006) advocated recording time of 10 minutes, while many authors (e.g., Parolai et al., 2001; Ferretti et al., 2007, and others) suggest that signals should be recorded for at least 30 minutes. Figure 2 illustrates the influence of the recording time on the variability of the average H/V spectrum. In this example, the ambient noise is recorded continuously for 60-70 minutes, stored in a series of data files of 3 minutes each. We can compile a set of up to 50 selected time windows and then average the spectral ratio. From comparison between the

average H/V curves obtained from ambient noise recordings of different durations we conclude that recording for about 1-2 hours provides enough time segments for reliable calculation of the average H/V function.

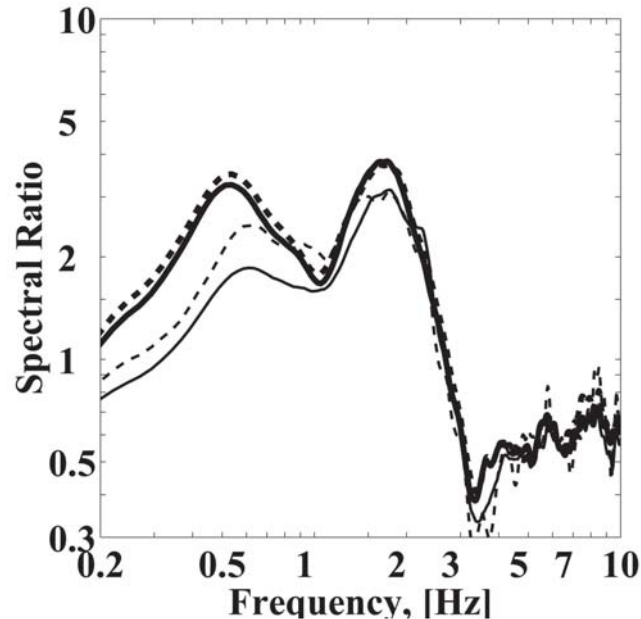


Figure 2. Comparison between the average H/V curves obtained from ambient noise recordings of different durations: 5, 20, 60, 360 minutes presented by dotted thin line, continuous thin line, continuous thick line, and dotted thick line, respectively.

A set of 25 - 50 selected time windows, for each site provide the average H/V spectral function. Computations are made using program SEISPECT (Perelman and Zaslavsky, 2001), which was specially developed for routine analysis and site investigations. SEISPECT is a MATLAB based application for spectral analysis and processing of ground motions recorded by a variety of seismic instruments. The main modules realized in the program are visualizing and editing the input data, selecting time window and computing Fourier spectra and H/V spectral ratios, saving and displaying results.

The reliability and applicability of the method to determine the fundamental frequency and the corresponding amplitude of the H/V spectral function may be influenced by various factors such as anthropoid noise, underground pipe lines and constructions, soil structure interaction, effects of rain, wind, coupling between seismometer and soil. Some of these interferences may be detected already in the field and then the measurements could be relocated. Figure 3 shows an example of ambient noise records and average spectral ratios obtained at a station located over a buried pipe-line and at a station located in "free field" conditions 50 m away from the pipeline. One can see that H/V ratios from the "free field" station exhibits the predominant peak at frequency 2.8 Hz with amplitude up to 3.

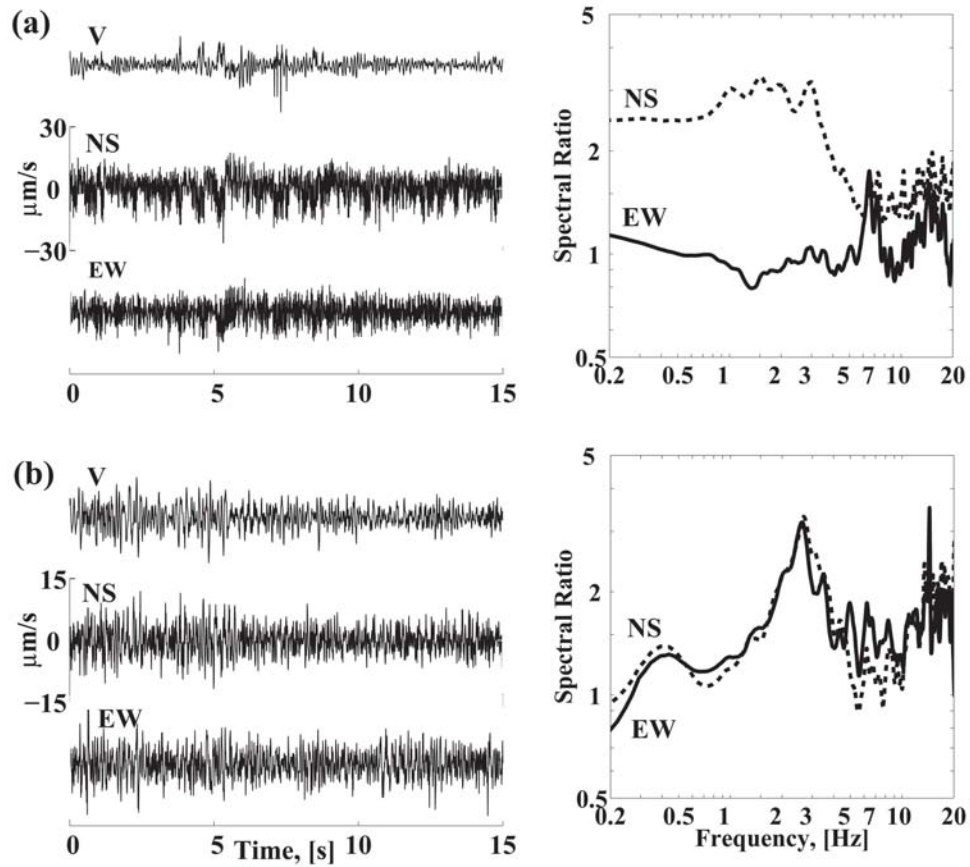


Figure 3. Comparison between ambient noise records and average spectral ratios obtained at station located (a) over underground pipeline and (b) 50 m away from pipe line at "free field".

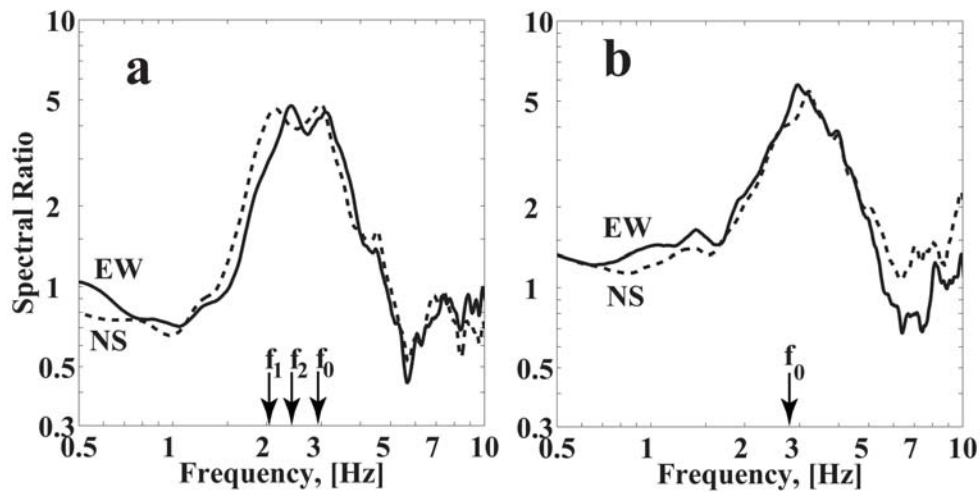


Figure 4. Comparison of the average H/V spectral ratio from ambient vibration recorded at station located at a distance of (a) 10 m from eight stories prefabricated residential building and (b) about 70 m from the building.

Estimation of site effect may be strongly influenced by soil-structure interaction when measurements are made close to buildings. Needless to say that real free field conditions in urban areas are hard to find. Examples of the average H/V spectral ratios for two horizontal components calculated for station deployed at a site about 10 m from a rectangular eight stories, prefabricated residential building located in the town of Qiryat Shemona are shown in Figure 4a. These spectral ratios are characterized by three peaks appearing at frequencies  $f_1=2.1$  Hz in NS component,  $f_2=2.4$  Hz in EW components and  $f_0=3.0$  Hz in both components. The frequencies  $f_1$  and  $f_2$  are actually the natural frequencies of the building. This is revealed by simply installing horizontal seismometers on the roof of the building and measuring its response to ambient noise. The frequency  $f_0$  which is clearly seen in the H/V spectral ratios should be attributed to the site. In order to avoid the effects of the building, the measured point should be located away from the building as demonstrated in Figure 4b, where the free field station is located about 70 m away. As a rule of thumb the free field station should be located at a distance greater than twice the height of the structure.

As already observed by many researchers, there is high scatter in the H/V spectra. The source of the scatter is debated between the researchers. Mucciarelli (1998), for example, claims that traffic is not a major reason for the scatter and Horice et al. (2001) used noise originated by passing traffic in their analysis. In a recent study, Parolai and Galiana-Merino (2006) showed that the influence of transients on the H/V spectral ratio is insignificant.

Our observations indicate that the effect of transients is almost unnoticeable. In order to reduce the scatter and increase stability, our processing scheme involves a careful manual selection of the time windows from which we obtain the H/V functions. In selecting the time windows, the analysts follow the concept that sites with no site effect should exhibit spectra of the H and V components that are of the same level throughout the spectrum. At sites with significant site effect, the spectra of the two components should differ only within a certain limited frequency band, probably at the neighbourhood of the resonance frequency. Time windows with spectra that exhibit such or similar conditions are selected. Evidently, this practice has yielded an appreciated reduction in the H/V scatter. An example of the spectral ratio functions, obtained at sites in the town of Kefar Sava, from automatic and careful manual selection is shown in Figure 5.

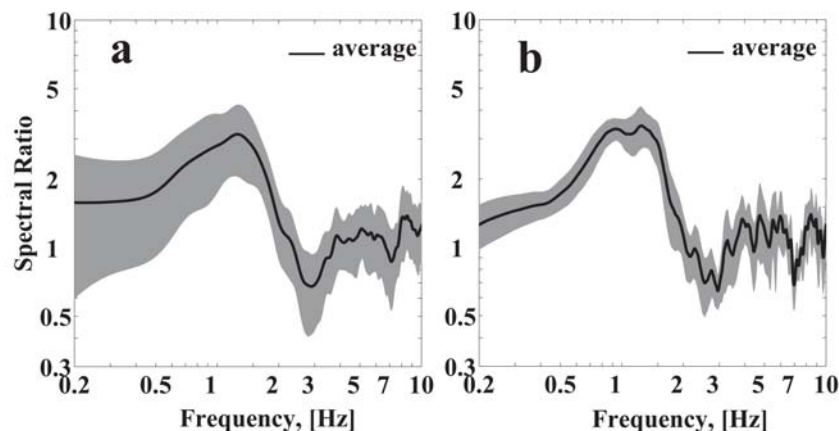


Figure 5. H/V spectral ratios  $\pm$  one standard deviation (shaded area) of automatic (a) and manual (b) selected time window.

## Stability of H/V Spectral Ratio Functions

The stability and reproducibility of H/V ratio from ambient noise must be confirmed before analyzing and interpreting ambient noise measurements. The next examples show measurements made in the town Petah Tikva at sites of different geology (sites locations and their I.D. numbers are shown in Figure 29). In those sites, H/V spectral ratios are obtained from ambient noise recorded in different months but in similar weather conditions. Examples of the spectral ratios obtained at point 420 from measurements made in March and in August 2006 are shown in Figure 6a. Variations of individual functions are small and all curves are similar in shape. Here, the dominant feature of the spectral ratios is a peak near 0.6 Hz with H/V ratio of 4.0-4.5. Comparison between average spectral ratios for two sets of measurements demonstrates the resemblance (Figure 6b).

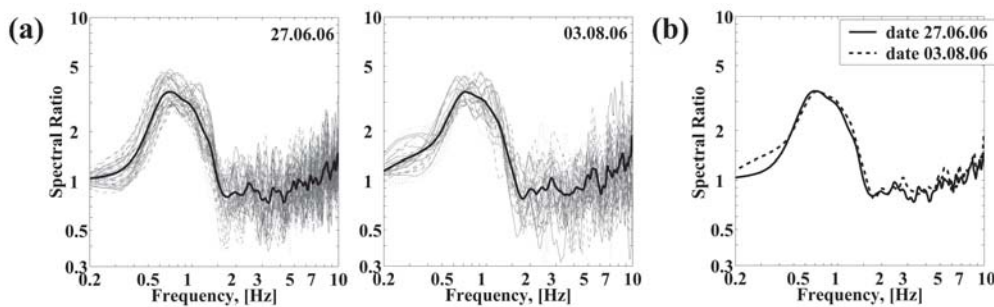


Figure 6. Comparison of (a) individual and (b) average H/V spectral ratio from ambient noise observed at point 420 in different months.

Figure 7a shows the average spectra of horizontal and vertical components calculated from records of ambient noise at point 253 in different months. Comparing the spectra, we can see that for both sets of records the frequency range, where horizontal and vertical spectra deviate, is 0.4-2.0 Hz, whereas the maximum levels of the spectra are similar. The amplitudes of horizontal spectra increase at frequencies near 0.8 and 1.2 Hz, and consequently the average spectral ratios (Figure 7b) have peaks at those frequencies. One can see that the shapes of the average spectral ratios are in a good agreement not only in the range of predominant frequencies but throughout the frequency range from 0.1 to 10 Hz.

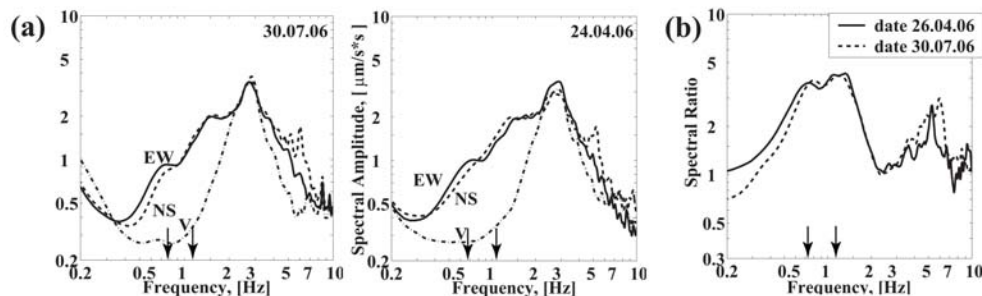


Figure 7. Comparison of (a) average Fourier spectra of three components of motions and (b) average H/V spectral ratios from ambient noise observed at point 253 in different months.

Individual and average spectral ratios of the ambient noise obtained at point 262 in April and August 2006 are displayed in Figure. 8. Once again, we can see that variations of the individual spectral ratios are small and average curves are very similar in shape.

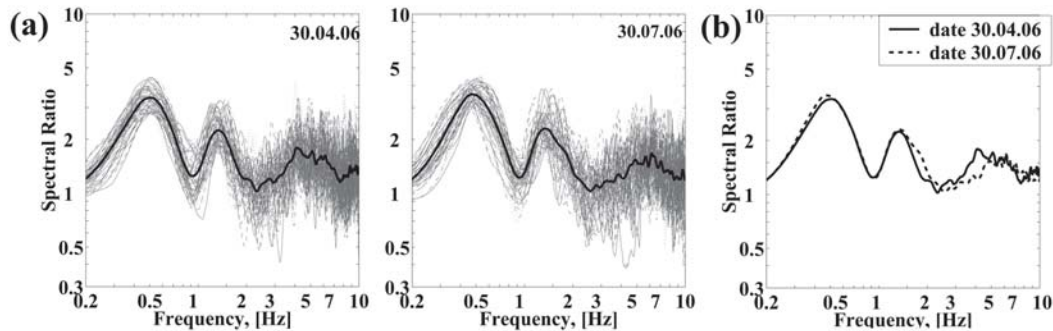


Figure 8. Comparison of (a) individual and (b) average H/V spectral ratios from ambient noise observed at point 262 in different months.

Figure 9a shows the average noise spectra at point 329 obtained in different months. The NS and EW components at this site for both sets of records have a sharp peak near 7.0 Hz. In addition, the spectra of the vertical component have narrow-bandwidth trough near 7.0 Hz., yielding a sharp peak in the H/V spectrum at about 7.0 Hz (Figure 9b). Note that the average curves are identical.

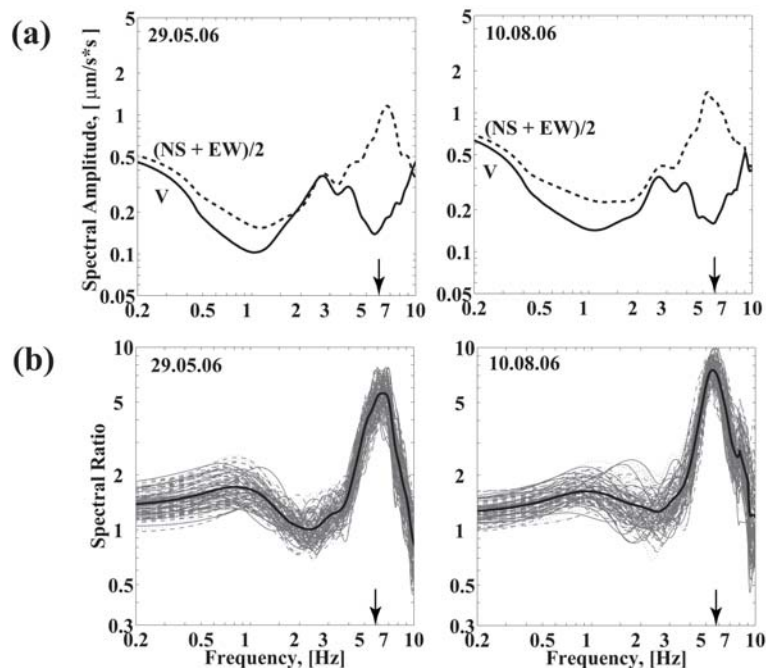


Figure 9. Comparison of (a) average Fourier spectra of three (NS and EW - horizontal and V - vertical) components of motions and (b) individual and average H/V spectral ratios observed at point 329 in different months.

Another example of the average spectra is obtained at point 81 and is displayed in Figure 10a. In this case the spectral shapes of all the components show a sharp peak near 3.0 Hz. This peak is related to noise generated somewhere in the town. At the same time, the vertical spectra are flat in frequency range 0.2-1.3 Hz. As demonstrated in Fig. 10, the evaluated amplitude spectra and the spectral ratios for a given site are the same although the ambient noise measurements were made on different dates.

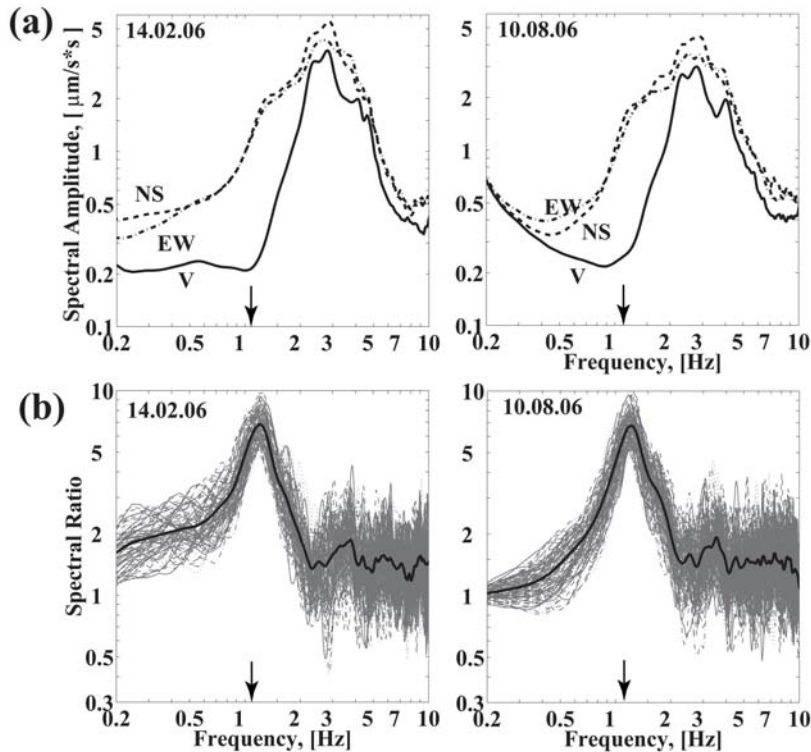


Figure 10. Comparison of (a) average Fourier spectra of three components of motion and (b) H/V spectral ratio from ambient noise observed at point 81 in different months.

## Variations of H/V Ratio Shapes with Different Geology

The spectral analysis of ambient noise provides important information that helps to characterize the site response especially in places where the local geological conditions may be responsible for intense ground motions. Qualitative analysis of the distribution of parameters that characterize amplitude spectra and spectral ratios over the study areas shows a high correlation with geological conditions and may be used to roughly delimit areas with different subsurface structure prior to the modeling.

Figure 11 displays the average amplitude spectra of two horizontal (NS and EW), the vertical components of motion and spectral ratios obtained at some sites in the towns Petah Tikva and Qiryat Shemona. A common feature to the presented examples is the appearance of a single peak in the H/V spectral function which also coincides with a peak in the amplitude spectrum of the horizontal motion. Such spectra correspond to a simple model of the

subsurface where a soft layer overlay hard rock. In such a simple model, the frequency will correspond to the fundamental resonance frequency of the soil, be proportional to the S wave velocity in that layer and inversely proportional to its thickness. The height of the H/V peak is proportional to the seismic impedance between the soil and the rock. Hence, the variations in the spectra and spectral ratios at the sites are directly associated with variations in the geological structure of the subsurface. In the presented cases, alluvium with  $V_s=200$  m/sec overlays basalt with  $V_s=2,000$  m/sec (points Q47 and Q241 in Qiryat Shemona) and alluvium overlays the limestone and dolomite of the Judea Gr. with  $V_s=1,900$ /sec (points P501 and P331 in Petah Tikva).

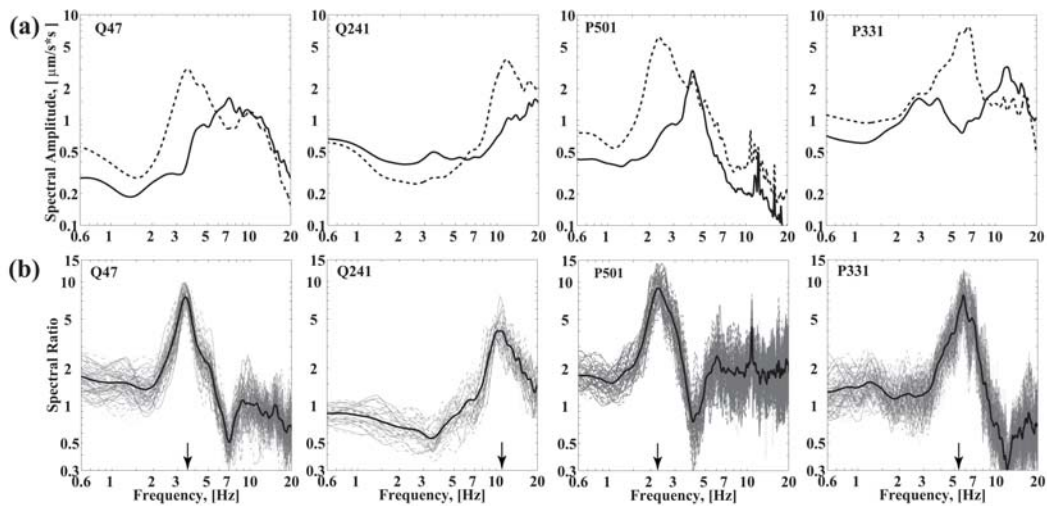


Figure 11. Examples of (a) average Fourier spectra and (b) H/V spectral ratios at sites whose subsurface structure may be approximated by one-layer models. The solid line indicates a vertical spectral component; the dashed line indicates the average of NS and EW horizontal components of motion. Indices Q and P in the point number refer to Qiryat Shemona and Petah Tikva, respectively.

Careful selection of ambient noise time windows and their analysis may reveal resonance effect of the soil layer(s) even when the seismic impedance is relatively low. Such is the case at site P382. Comparing the horizontal and vertical Fourier spectra of point P382 (Figure 12) one can see at the frequency range 0.6-2.5 Hz that the horizontal components are considerably higher than the vertical. This feature, emphasized in the H/V spectral ratio, relates to amplification of ground motion at frequency 1.5 Hz. For points P373 and P382, the vertical component practically coincides with the horizontal, in the whole frequency band 0.1-10 Hz, excluding the area where there is a trough in the vertical component near 1.5 Hz, which is responsible for the peak in the H/V spectrum. In these points the subsurface structure consists of sandy loam ( $V_s=200-300$  m/sec) overlying calcareous sandstone ( $V_s=700$  m/sec). Despite a low velocity contrast between soils and a hard rock, H/V spectral ratio shows clear peaks. For point H682 in the Haifa Bay, located on the outcrop of Eocene chalk ( $V_s=1,000$  m/sec) and underlain by limestone and dolomite of the Judea Gr. ( $V_s=1,900$  m/sec), H/V spectral ratio shows apparent peak with amplitude 2 at 0.8 Hz.

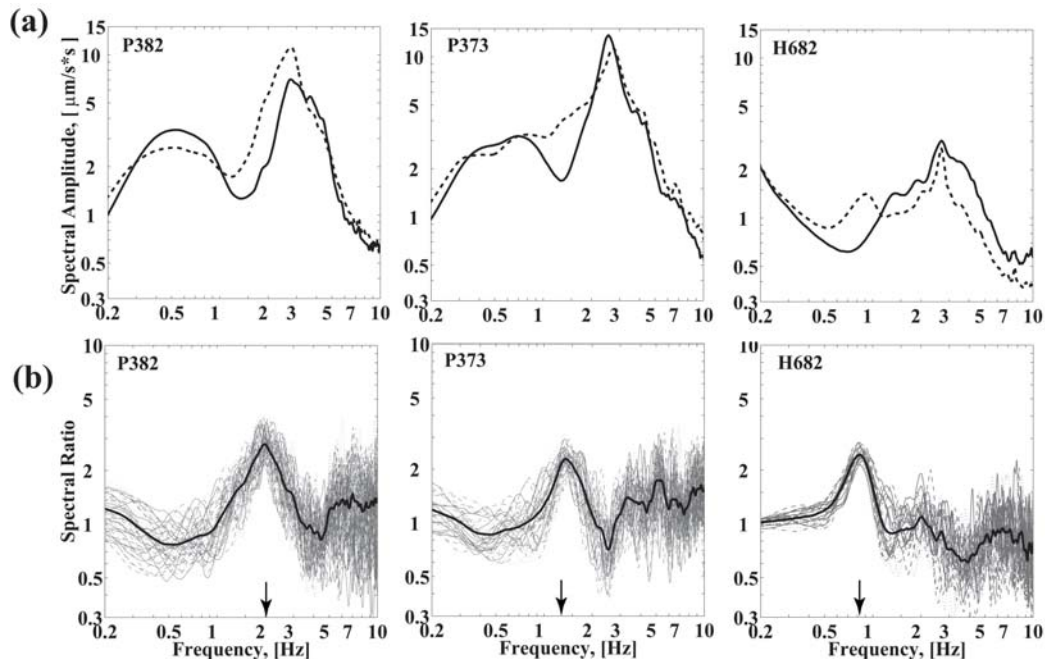


Figure 12. Examples of (a) average Fourier spectra and (b) individual and average H/V spectral ratios for sites whose subsurface structure yields low impedance contrast between soil and rock. The solid line indicates a vertical spectral component; the dashed line indicates the average of NS and EW horizontal components of motion. Indices P and H refer to Petah Tikva and Haifa Bay, respectively.

There are many cases where the Fourier spectra show two frequency bands of site effect, manifested on the H/V curves by two resonance peaks. The second peak is most likely caused by an intermediate hard layer in the subsurface. While the first resonance frequency is related to the hard rock at depth, the position of the second resonance peak depends mainly on the thickness of the intermediate hard layer. Amplitude level of both peaks is determined mainly by the S wave velocity in the soft sediments.

Figure 13 displays some examples from Petah Tikva, where the Quaternary sediments ( $V_s=300-450$  m/sec) together with the Pliocene clay-marl ( $V_s=600-700$  m/sec), prevailing in the lithological section of the western part of the area, determine the shape of H/V ratio curve. The chalky limestone ( $V_s=1,200$  m/sec) and marl-chalk ( $V_s=900$  m/sec) overlying the limestone and dolomite of the Judea Gr. ( $V_s=1,900$  m/sec) is an intermediate layer. Here we observe two separate peaks with amplitude 3-5.

Thickness increase of the intermediate hard layer leads to a merge of the peaks. In such cases we observe a broad peak in the Fourier spectra and two inseparable peaks in the H/V ratio curves (see example in Figure 14). The width of the frequency band where the peaks are observed varies depending on the proportion between the thickness and  $V_s$  of the soft sediments and the intermediate hard layer. In the Haifa Bay the intermediate hard layer is represented by sandy limestone and marl-chalk with  $V_s=1,100-1,300$  m/sec and  $800-900$  m/sec, respectively. There, the limestone and dolomite of the Judea Gr. is the fundamental reflector. In Qiryat Shemona the soft sediments ( $V_s=450$  m/sec) overlays the weathered basalt ( $V_s=900-1,000$  m/sec), which in turn covers the Pleistocene basalt ( $V_s=2,000$  m/sec).

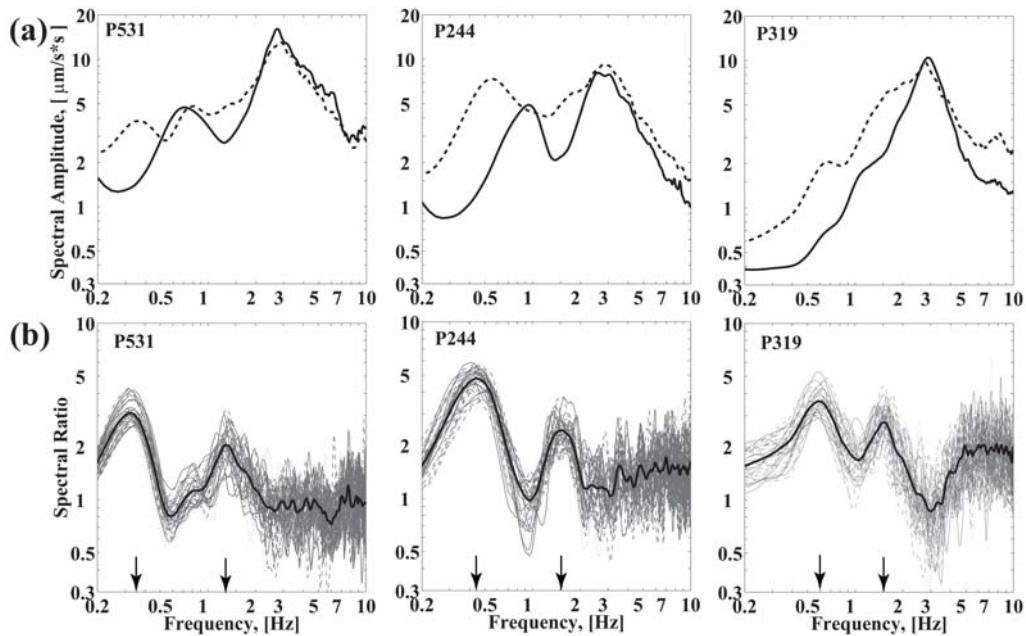


Figure 13. Examples of (a) average Fourier spectra and (b) individual and average H/V spectral ratios for sites whose soil column comprises the soft sediment layer significantly thicker than the intermediate hard layer. The solid line indicates a vertical spectral component; the dashed line indicates the average of NS and EW horizontal components of motion. Index P in point number indicates Petah Tikva.

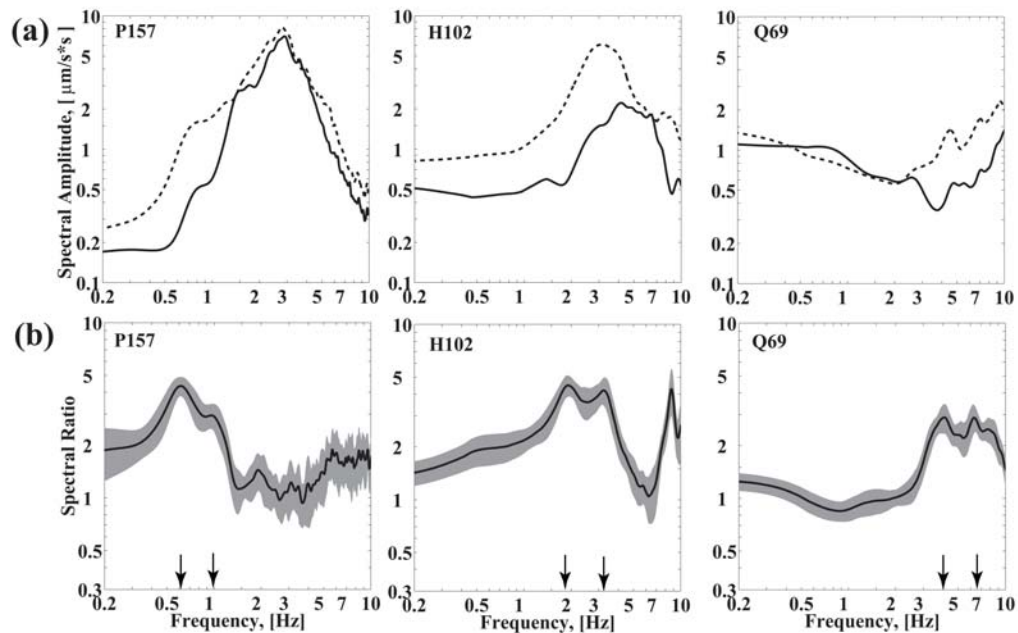


Figure 14. Examples of (a) average Fourier spectra and (b) H/V spectral ratios  $\pm$  one standard deviation (shaded area) at sites for which the intermediate hard layer is comparable in thickness to the soft sediment layer. Indices Q, H and P in the point number refer to Qyriat Shemona, Haifa Bay and Petah Tikva, respectively.

We present examples where the intermediate hard layer dominates, and again we observe two separate peaks (Figure 15). Position and amplitude of the second peak is determined by the  $V_s$  velocity and thickness of the upper soft layer. We note that in order to simplify the presentation, instead of a collection of individual ratios we present a shaded area with bounds that correspond to the standard deviation. In this case, the amplitude of the fundamental peak is normally smaller than the second one. At site Q673, alluvium of 7 m thick with  $V_s=280$  m/sec overlays 260 m of marl-chalk layer. At site P461 the thickness of alluvium is 20 m, while the marl-chalk layer is 120 m thick. Certainly, both are underlain by limestone and dolomite of the Judea Gr.

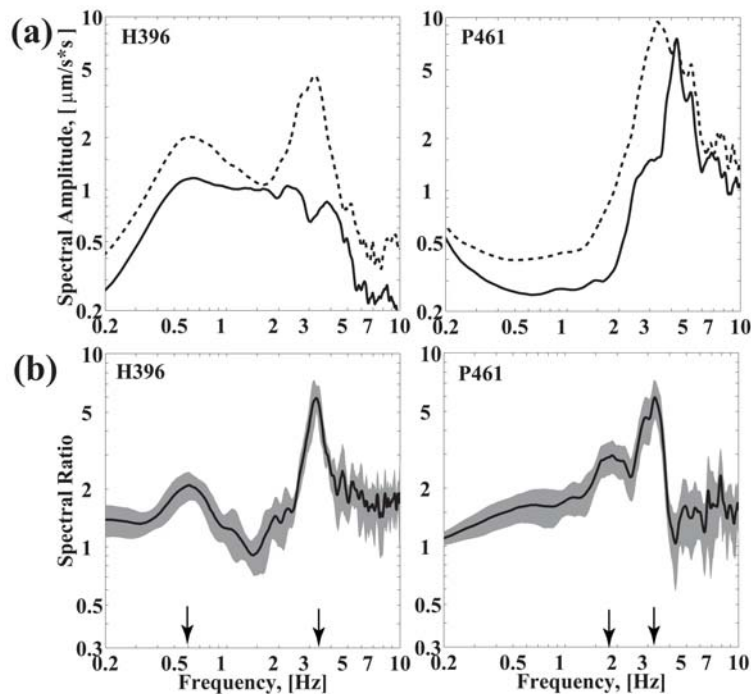


Figure 15. Examples of (a) average Fourier spectra and (b) individual and average H/V spectral ratios  $\pm$  one standard deviation (shaded area) at sites for which thickness of the intermediate hard layer significantly exceeds thickness of the soft sediments. The solid line indicates a vertical spectral component; the dashed line indicates the average of NS and EW horizontal components of motion. Indices H and P in the point number refer to Haifa Bay and Petah Tikva, respectively.

## Comparison of H/V Spectral Ratios from Ambient Noise and Seismic Events

The theoretical background for use of ambient noise measurements in site response investigations is debated. Not likewise, the association of H/V spectral ratio from earthquake signals. The latter clearly explains why H/V spectral ratios of S waves, often known as receiver functions, are also representing the site amplification. It is thus interesting to compare H/V spectral functions as obtained from ambient noise and earthquake recordings.

In our studies we analyze the H/V spectral ratios from ambient noise measurements and from ground motion measurements generated by different sources of excitation: Local and regional earthquakes and quarry explosions recorded by different sensors i.e.; accelerometers and seismometers. The strong motion stations that recorded felt earthquakes and used in this study are listed in Table 1. The recorded earthquakes and explosions are presented in Table 2.

As an example, Figure 16 presents the calculated receiver function of a site in Qiryat Shemona, as evaluated from the spectral ratio of strong motion recordings:

- a. The H/V spectral ratio from two horizontal components of accelerograms of the Beirut earthquake (record 1 in Table 1). This H/V function shows prominent peak near 4 Hz ( $f_1$ ) with an amplification factor of about 4.5 and with a second peak near 8.0 Hz.
- b. The average spectral ratio obtained from eight earthquakes (events 1 to 8 in Table 2). The average function also yields two peaks at frequency 4.5 Hz (with amplitude 4.5) and 8.0 Hz.
- c. The horizontal-to-vertical spectral ratio from ambient noise shows two prominent peaks near 4.5 Hz and 8.0 Hz in agreement with the resonance frequencies identified by the receiver function.

As mentioned above, site effect may be strongly influenced by soil structure interaction. In our case the strong motion station is located in a cellar of a two-stories building. The Fourier amplitude spectra from wind excitation recorded on the roof allowed establishing that  $f_2 \sim 8$  Hz is the fundamental frequency of the building. Seismograms of the earthquakes and explosions (events No. 9-15 in Table 2) and ambient noise, all recorded in the town of Kefar Saba, show an agreement between the different evaluation techniques. These are presented in Figure 17.

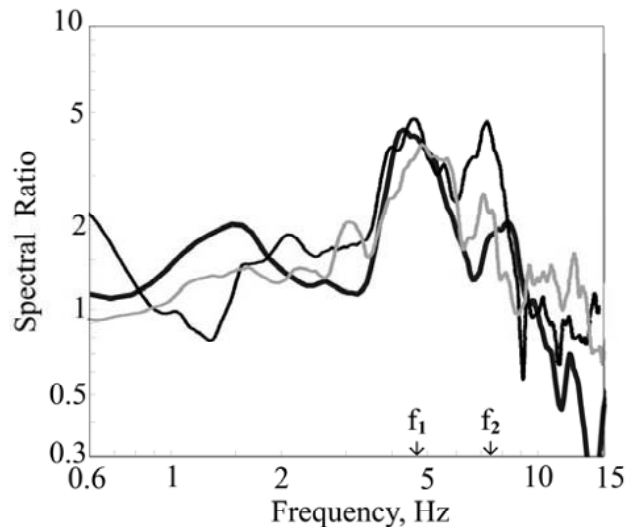


Figure 16. Average H/V spectral ratios for Qiryat Shemona strong motion stations obtained from: two horizontal accelerograms of Beirut earthquake (thick line), seismogram of eight local and regional earthquakes (shaded line) and ambient noise (thin line).

**Table 1. Parameters of earthquakes recorded by accelerometer stations and used in this study. Distance is to the surface projection of the rupture.**

No.	Recording site	Date yr/mo/dy	Origin time hr:mn:sec	$M_w$	Geographic coordinates		Distance (km)	Epicentre region
					Lat.(N)	Long.(E)		
1	Qiryat Shemona	97/08/04	11:29:46	4.0	33.26	35.73	14	Beirut
2	Lod	04/02/11	08:15:03	5.1	31.70	35.56	70	Dead Sea
3	Lod	04/07/07	09:23 55	4.7	31.97	35.55	55	Dead Sea
4	Petach-Tikva				32.01	34.98	65	
5	Lod	07/11/23	23:19:54	4.2	31.86	34.94	11	Samaria
6	Petach-Tikva						26	

**Table 2. List of earthquakes and explosions used in this study. Eq. - earthquake; Ex. – explosion;  $M_d$  – duration magnitude;  $M_w$  – moment magnitude.**

No.	Recording site	Date yr/mo/dy	Origin time hr:mn:sec	$M_d$	Geographic coordinates		Distance km	Epicentre region	Type
					Lat.(N)	Long.(E)			
1	Qiryat Shemona.	99/03/25	16:37:11	3.6	36.46	31.04	560	East Mediterr.	Eq.
2		99/03/27	13:42:29	3.6	34.61	33.25	270	Cyprus	Eq.
3		99/03/28	19:54:11	2.5	33.71	32.73	300	East Mediterr.	Eq.
4		99/04/06	00:08:25	w5.2	39.50	37.90	700	Turkey	Eq.
5		99/04/07	08:55:48	3.0	34.01	21.89	350	East Mediterr	Eq.
6		99/04/08	00:13:17	3.9	35.92	27.02	830-	Crete	Eq.
7		99/04/10	22:46:09	3.4	35.68	28.16	740	East Crete	Eq.
8		99/04/11	19:45:05	3.6	33.16	35.64	10	Golan	Eq.
9	KS12	00/06/13	14:03:20	5.4	34.86	27.44	750	Mediterr. Sea	Eq.
10		00/06/15	09:24:17	2.0	32.01	34.98	20	Samaria	Ex.
11		00/06/15	21:30:45	5.2	34.44	20.18	1400	Greece	Eq.
12	KS70	00/08/31	09:23 55	2.0	32.01	34.98	20	Samaria	Ex.
13		00/09/02	04:02:47	2.1	32.22	35.41	50	Samaria	Eq.
14	KS234	00/10/06	12:13:24	2.0	31.02	36.14	150	Jordan	Ex.
15		00/10/15	11:49:02	2.4	32.01	34.98	20	Samaria	Ex.
16	Ramle	06/01/08	11:34:59	w6.4	35.50	24.40	1000	Mediterr. Sea	Eq.
17		06/02/02	09:49:42	w4.6	27.34	35.13	500	Red Sea	Eq.

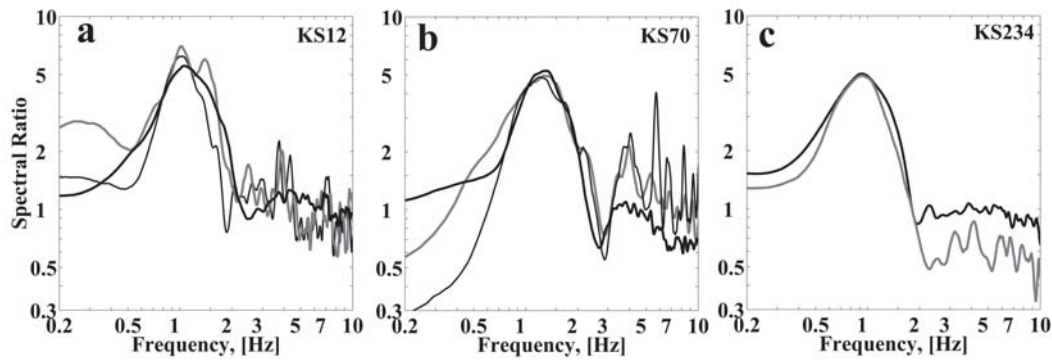


Figure 17. Comparison between the average H/V ratios obtained at three sites in the town of Kefar Sava from ambient noise and seismic events (see Table 1). Solid, thin and shaded lines correspond to ambient noise, earthquake and explosion sources, respectively.

During a seismic microzoning study in the towns of Lod and Ramle (Zaslavsky et al., 2005) that was carried out in 2001, there were no strong motion records available in these towns from regional or local seismic events. A seismic station was installed in the town of Ramle and continuously recorded for 2 months. Eventually we recorded two regional earthquakes (Records 16-17 in Table 2). In Figure 18 we compare the H/V spectral ratios for the two from seismograms of the earthquakes and of ambient noise. The main feature of the spectral ratios is the two resonance peaks at frequencies near 0.9 Hz and 1.4 Hz. These are associated with two (deep and shallow) impedance contrasts. We can see that the dominant frequencies and their level evaluated from ambient noise are similar to those derived from S-waves. We note that there is an additional peak in the frequency range 2.5-3.0 Hz in the H/V ratios of S-waves. It is possibly a higher mode of vibration.

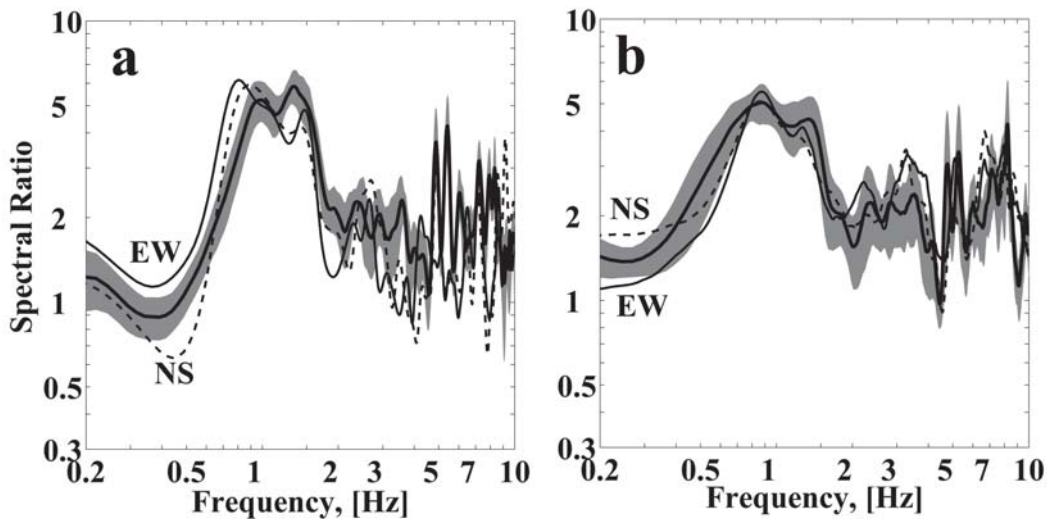


Figure 18. H/V ratios observed in the town of Ramle from seismogram of two regional earthquakes occurred in the Mediterranean Sea (a) and the Red Sea (b) and the average spectral ratio from ambient noise measurements (thick line). The shaded area represents  $\pm$  one standard deviation.

At present, the Seismology Division of the Geophysical Institute of Israel operates 62 strong motion stations. Two earthquakes that occurred on February 11, 2004 ( $M_d=5.2$ ) and on July 7, 2004 ( $M_d=4.7$ ), in the Dead Sea Transform Fault triggered 24 and 14 accelerometers, respectively, including one located in Lod. This station was installed in the basement of a seven-storey building of the Geophysical Institute of Israel. According to borehole data the site is characterized by Quaternary soft sediments of 40 m thick and Eocene-Senonian chalk-marl of 60 m thick overlying the hard carbonates of the Judea Gr. (Turonian-Cenomanian age). The accelerograms and the corresponding H/V spectral ratios for NS and EW components are shown in Figure 19. In the time domain, there are noticeable differences in the duration, frequency content and amplitude of shear waves on vertical and horizontal components. Relative to the vertical component, the motion on the horizontal components exhibits many cycles with large amplitudes with low frequencies. The H/V ratios of EW component of the two earthquakes show two prominent peaks:  $f_1=1.7$  Hz with amplitude ratio 3.0 and 4.5 for the first and second earthquakes, respectively. The H/V ratios of NS component from the two earthquakes clearly exhibit the resonance peak near 1.8-2.0 Hz with amplitude up to 5.0. The increase of spectral ratio amplitudes in the frequency range 5.0-9.0 Hz can be explained as being higher modes of soil vibration.

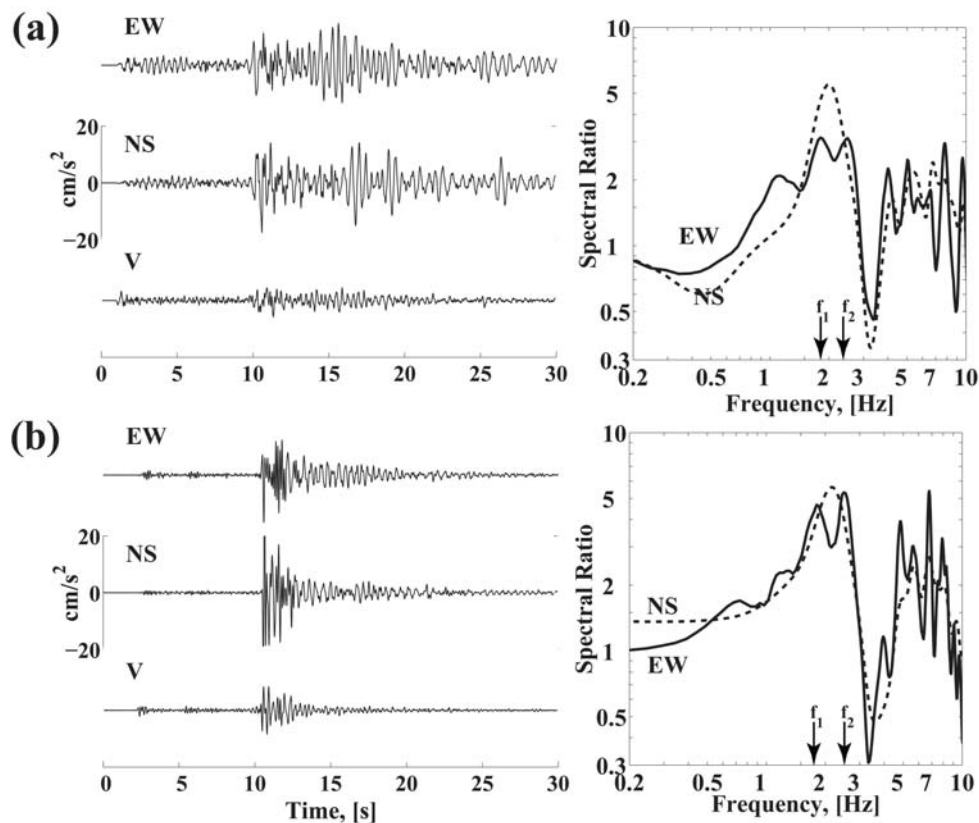


Figure 19. Accelerograms and their spectral ratios recorded at the location of the Lod strong motion station: (a) recordings of the earthquake on Feb. 11, 2004;  $M_w=5.2$ , at epicentral distance of 70 km. (b) recordings of the earthquake on July 7, 2004;  $M_w=4.7$ , at an epicentral distance of 55 km.

One feature that is consistently observed in the results obtained from the two earthquakes is a systematic peak at  $f_2=2.5$  Hz on the EW component of H/V ratios. As indicated above, the peak at 2.5 Hz is most likely a result of soil-structure interaction. To confirm it, an ambient vibration test was conducted by placing on the roof three stations. Each station is equipped with a pair of horizontal seismometers, placed perpendicular to each other and parallel to the outer walls of the structure. The average Fourier spectra show maximum amplitudes of vibrations at  $f_2=2.5$  Hz for both horizontal components. The peak is interpreted as the fundamental frequency of the building. An earthquake that occurred on November 23, 2007 ( $M_d=4.2$ ) at epicentral distance of 12 km southeast of Lod, triggered again the strong motion station. At that time two horizontal accelerometers were installed on the roof of the building parallel to the outer walls of the structure. We define the longitudinal axis as the EW component and the transverse axis as the NS component of motion. Figure 20a shows the two horizontal component accelerograms of this earthquake recorded on the roof and the three components recorded at the basement. The figure also shows the Fourier spectra of the building vibrations and H/V spectral ratios of the basement obtained from this event. The prominent feature of the roof spectra (Figure 20a) is high amplitude in the frequency 2.5 Hz for NS and EW axes.

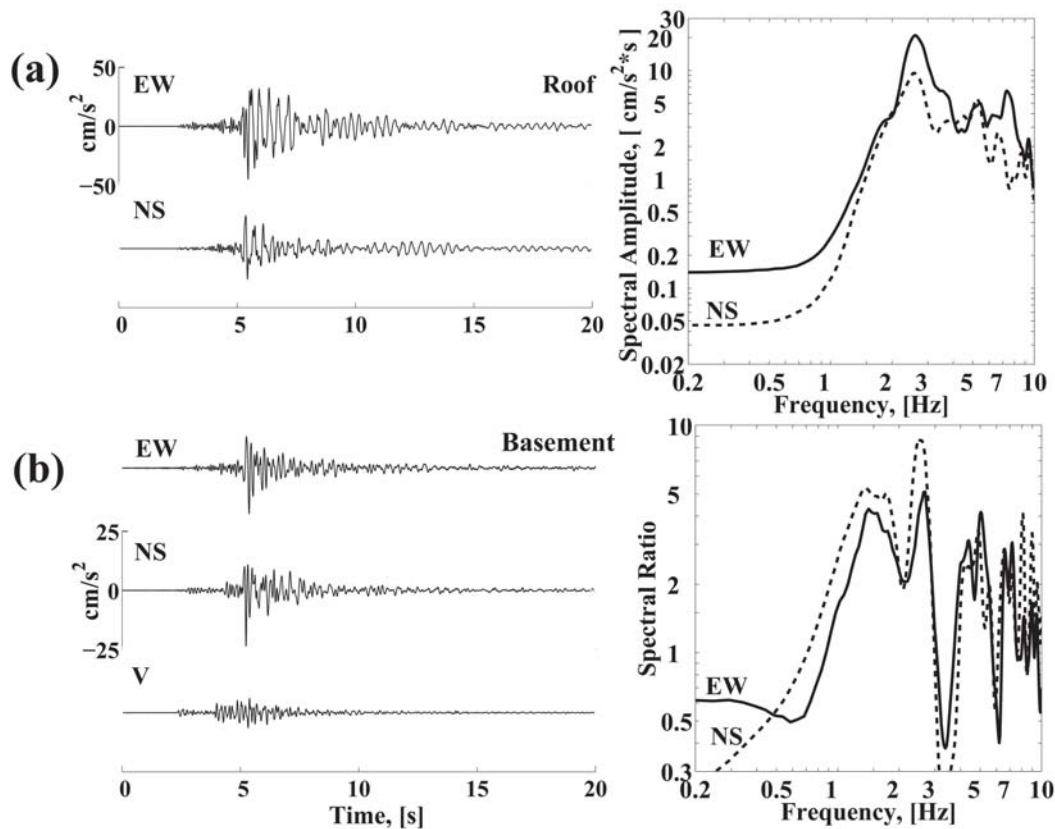


Figure 20. Accelerations from the earthquake on November 23, 2007,  $M_w=4.2$ , distance 12 km, recorded at the Lod strong motion station (a) at the roof and (b) at the basement; and corresponding H/V spectral ratios.

The transient signals produced by the earthquake yield the same assessment of the resonance frequency as from the ambient noise. This H/V spectral ratio (Figure 20b) as well as previous earthquakes reveals significant response of the sediments in the frequency range 1.5-1.8 Hz. It is worth noting that the site response is controlled by two additional prominent peaks at frequencies near 5.0 and 8.0 Hz where the second and third resonant modes of the sedimentary layers are presented.

Figure 21 presents a comparison between the average H/V spectral ratio of the EW component from accelerograms of the three earthquakes and ambient noise recorded at a station installed on natural soil about 100 m away from the building. Both curves show prominent peak in the frequency range 1.5-2.0 Hz, with amplitudes reaching 4.5.

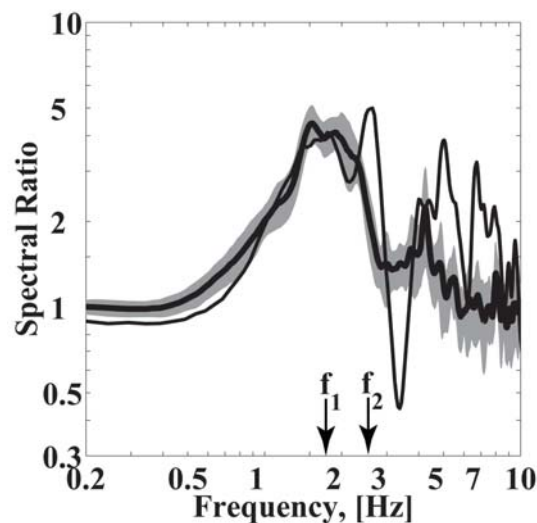


Figure 21. Comparison between average H/V ratio obtained from accelerograms of three earthquakes recorded by the Lod strong motion station (thin line) and ambient noise H/V ratio  $\pm$  standard deviation recorded at "free field" seismic stations located about 70 m away.

Another example is the case of the strong motion station in Petah Tikva (Figure 22). The station recorded two earthquakes that occurred in the Dead Sea Fault on July 7, 2004,  $M_d=4.7$ , at a distance of 65 km, and in the Shfela region on November 23, 2007,  $M_d=4.2$ , at a distance of 25 km. Here we compare the average H/V spectral ratios obtained from accelerograms of horizontal components and from ambient noise, which were recorded at the same site. This comparison shows a good agreement in both predominant frequency and H/V ratio shape obtained from the first earthquake and ambient noise. The H/V ratio for the second earthquake produces a similar shape; however the spectral ratios amplitude is about a factor 2 less than that from ambient noise. As pointed out by Field et al. (1992) the ensemble of spectral ratios obtained with respect to reference site from weak earthquakes reveal great variability between the individual spectra. Therefore, in cases where we have only one or two records of earthquakes, one has to be very careful in reaching conclusions. Additional ambient noise measurements may help clarifying the observations. We note that the examples above are only few out of many similar cases we observed.

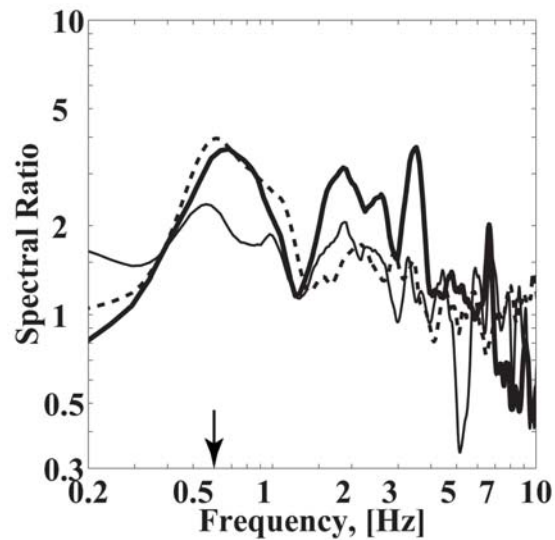


Figure 22. Spectral ratios from the earthquake on July 7, 2004,  $M_d=4.7$ , distance 65 km (thick line), earthquake on November 23, 2007,  $M_d=4.2$ , distance 25 km (thin line) and ambient noise (dashed line) observed in the Petah Tikva town.

## Examples of Distribution of H/V Resonance Frequencies and their Associated Amplitude Levels in Different Urban Areas

### Town of Qiryat Shemona

Qiryat Shemona is a relatively small town (about 25,000 inhabitants), which occupies a territory of 25 km<sup>2</sup> and is situated in the northern part of Israel alongside the Hula Valley between two major segments of the Dead Sea fault system. Two most recent destructive earthquakes in this region occurred in 1759 and in 1837 (Amiran et al., 1994). These earthquakes had a maximum intensity X on the MM scale and caused severe damage and loss of life in the northern Levant, presently Israel, Syria, Jordan and Lebanon. The Qiryat Shemona fault (Figure 23) crossing the town in the west is a manifestation of the main transform fault, which separates the African plate from the Arabian plate (Sneh and Weinberger, 2003). The local young faults of Tel-Hay and Shehumit trending in the north-south direction are also part of the Dead Sea fault system and separate the Qiryat Shemona graben from the Hula valley. The geology of the investigated area is characterized by outcrops of basalt flow of Pleistocene age. Hard conglomerate of Miocene age and carbonate of Paleogene age crop out in the north-western part of the town. There are talus cones composed of loam and talus breccias of 0-20 m thick, which cover the basalt and conglomerate. Thickness of the alluvium deposits accumulated in the Qiryat Shemona graben merging with the Hula Valley in the southern part of the study area, reaches 150 meters. These deposits overlay Plio-Pleistocene basalt flows.

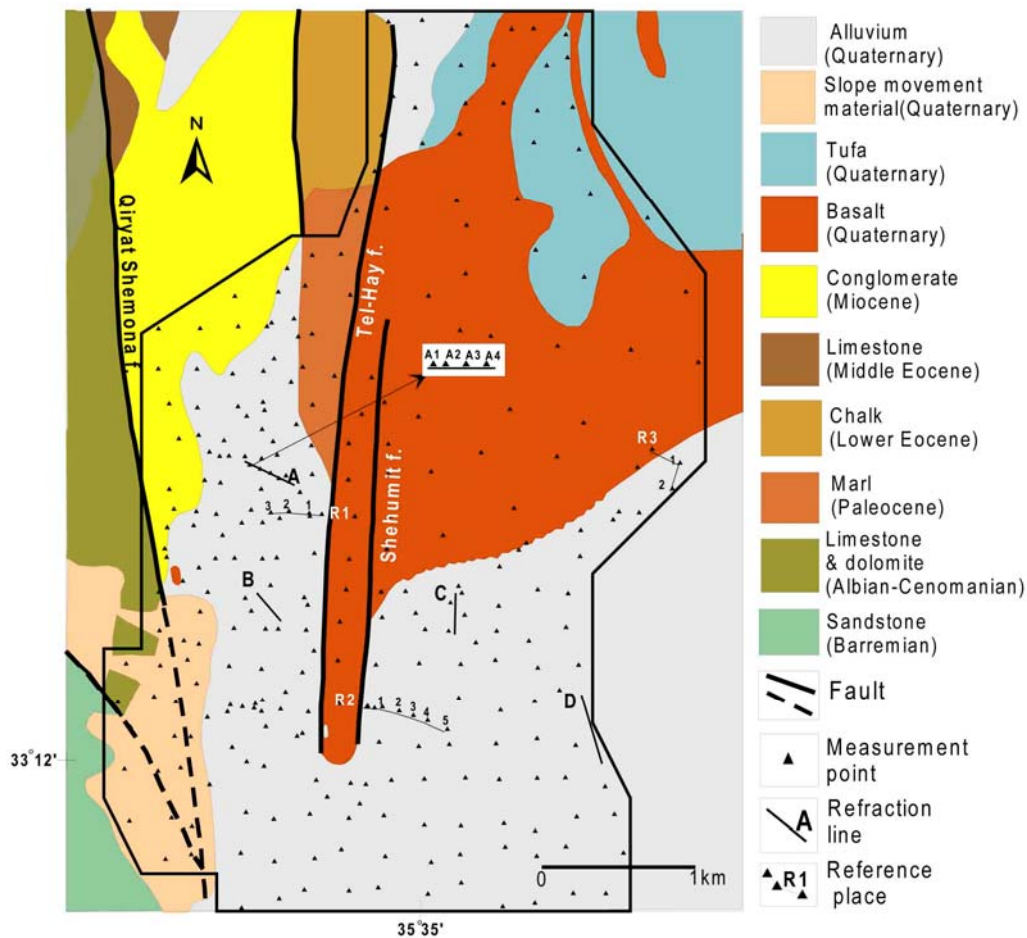


Figure 23. Geological map of the town of Qiryat Shemona. The black line is borders of the study area.

A microzonation study to investigate possible site effect was carried out through ambient noise survey at 300 sites across the town. Two methods are used to estimate the site effects:  $H/V$  spectral ratio and  $H_{\text{site}}/H_{\text{bedrock}}$ . In applying the second technique, one station that serves as a reference station is located on a basalt outcrop throughout the duration of the experiment, while the other station is moved from point to point. Due to practical limitations, we are able to carry out only three such sets of measurements where the reference station is within 400 meters from the investigated sites. Figure 24 shows the comparison between the average  $H_{\text{site}}/H_{\text{bedrock}}$  and  $H/V$  spectral ratios for different points on those three places, marked as R1, R2 and R3 (see Fig. 24). The two functions showed similar peak values at the same fundamental frequency clearly indicating that the two methods reflect the same characteristics of the local site response. It is important to note that there are no significant differences in shapes of spectral ratios. The marked rise in the  $H/V$  spectral ratios observed at a frequency near 0.3 Hz (R2 place) is normally associated with ocean waves. Therefore, this peak is negligible in the  $H_{\text{site}}/H_{\text{bedrock}}$  spectral ratios.

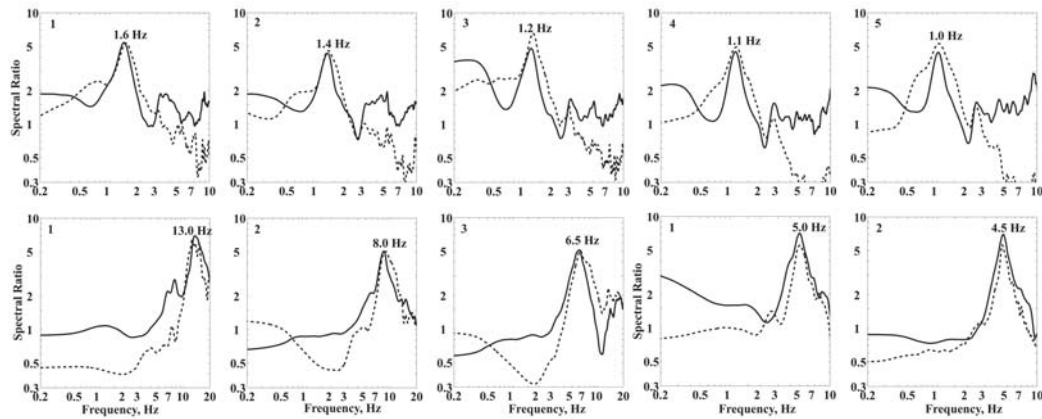


Figure 24. Comparison between average H/V (solid line) and H<sub>site</sub>/H<sub>bedrock</sub> spectral ratios (dashed line) obtained at 3 places R1, R2 and R3 indicated in Figure 23.

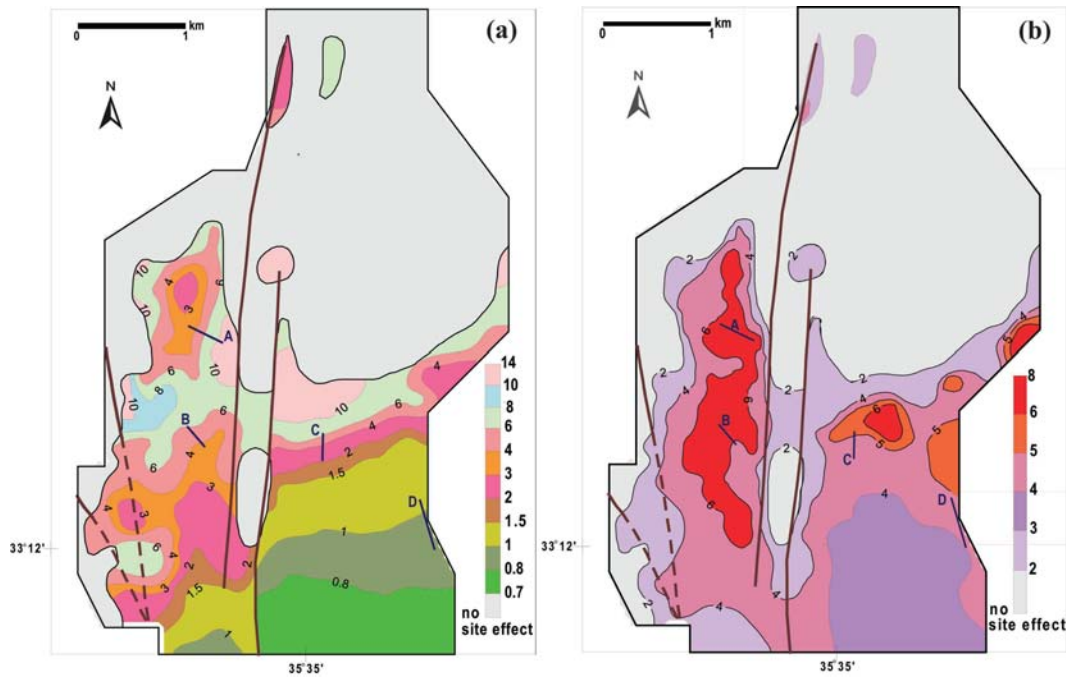


Figure 25. Maps showing the distributions of (a) predominant frequency and (b) associated maximum amplitude level.

The observed fundamental frequencies and the associated amplitude levels are depicted on the regional maps and contoured (see Figures 25a and 25b). The data exhibit peaks changing from 2 to 8, occurring at frequencies 0.8 -15 Hz. We obtained almost flat H/V ratios at sites where basalt, conglomerates, limestone and travertine are outcropped. These results suggest that, with respect to the expected site effects, the area can be divided into two zones separated by the Shehumit and Tel Hay faults. The first zone constitutes the built area of the town and is located in the graben. This zone is characterized by frequency anomalies with general trend to decrease from 14 Hz in the north to 1 Hz in the south. These variations seem

to coincide with the variations in the depth to the basement. The significant increase of H/V ratios, reaching 8 in the central part of Qiryat Shemona is probably associated with the heterogeneities of loose alluvium sediments deposited (i.e., low S-velocity) in the graben. The second zone is located to the east of the Shehumit and Tel Hay faults and south to the basalt outcropping. Gradual decrease of resonance frequency from 14 Hz to 0.7 Hz from the north to the south is correlated with dipping of the basalts. The great part of this zone is generally characterized by lesser variability and lower H/V spectral ratios (a level of 3-4).

## Haifa Bay

The Haifa Bay area is one of the more densely populated urban areas in Israel, and which also include the Haifa port, airport, large scale chemical industry and underground pipelines containing flammable gas or potentially pollutant liquids. The coastal strip of Haifa bay has about 170,000 inhabitants. The proximity to the possibly active Carmel fault and a few tens of kilometers from the active Dead Sea Transform fault, imply that this region is considered to be a high seismic risk zone.

The Carmel Fault, a branch of the Dead Sea Fault, accommodates the movements along the Dead Sea Transform faults. The movements were accompanied by the formation of elongated sub-parallel horsts and grabens dissected by faults (see Figure 26). In August 1984 a magnitude 5.2 earthquake occurred south-east to the bay. There is no historical evidence of  $M \geq 5$  earthquakes prior to this event, but it has been suggested that this fault is capable of producing earthquakes with magnitude up to 6.5 (Hofstetter et al., 1996). Considering the local site conditions as an important factor in determining the seismic hazard specific to a given site, it is particularly important for the Haifa bay area because there we have a sedimentary basin with strong impedance contrast between the soft sediments and the underlying bedrock. In addition, over the area of study the soil conditions change considerably from place to place. In the sedimentary column characterizing the study area five lithostratigraphic units, of Cretaceous to Quaternary age represented by limestone and calcareous sandstone may be presumed to be potential reflectors of seismic waves capable of producing site effects. The deep reflector is limestone and dolomite of the Cretaceous age (Judea Group). Its depth increases westward from several meters up to 1,500 meters, according the structural map (Fleischer and Gafsu, 2003).

Maps showing distribution of frequency and its associated amplitude for two resonance peaks (Figures 27-28) are constructed on the base of 450 measurements. Results show that the study area may be divided into two zones: western and eastern characterized by different subsurface structures. While there is no big difference in the distribution of the first resonance frequency, the second one behaves differently, showing significantly larger variability in the eastern part. Distribution of the first resonance frequency associated with a deep reflector of seismic waves exhibits maximum of both frequency and amplitude in the southwestern edge of the area, where the thin layer of the alluvial deposits directly overly the hard carbonates. Towards the west the limestone of the Judea Gr. is dipping and at a depth of 800-1000 m, a sharp change in the first frequency associated with fault is observed. This fault directed north-south is the boundary between two regional geological structures. In the western part, the Miocene limestone is the fundamental reflector.

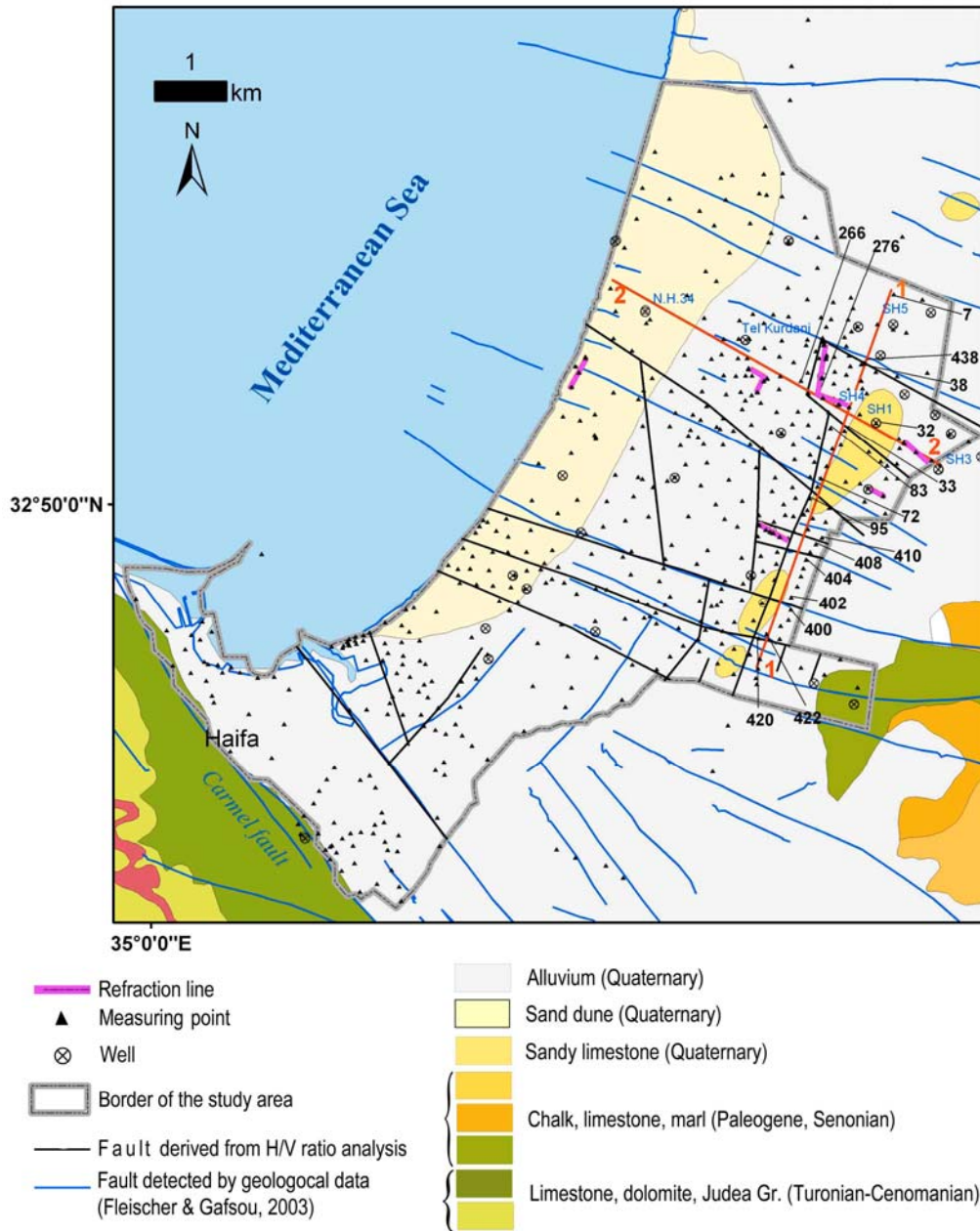


Figure 26. Geological map of the Haifa Bay area. The straight lines 1-1 and 2-2 show position of the geological cross sections in Figures 46 and 48. Numbered sites refer to Figure 46.

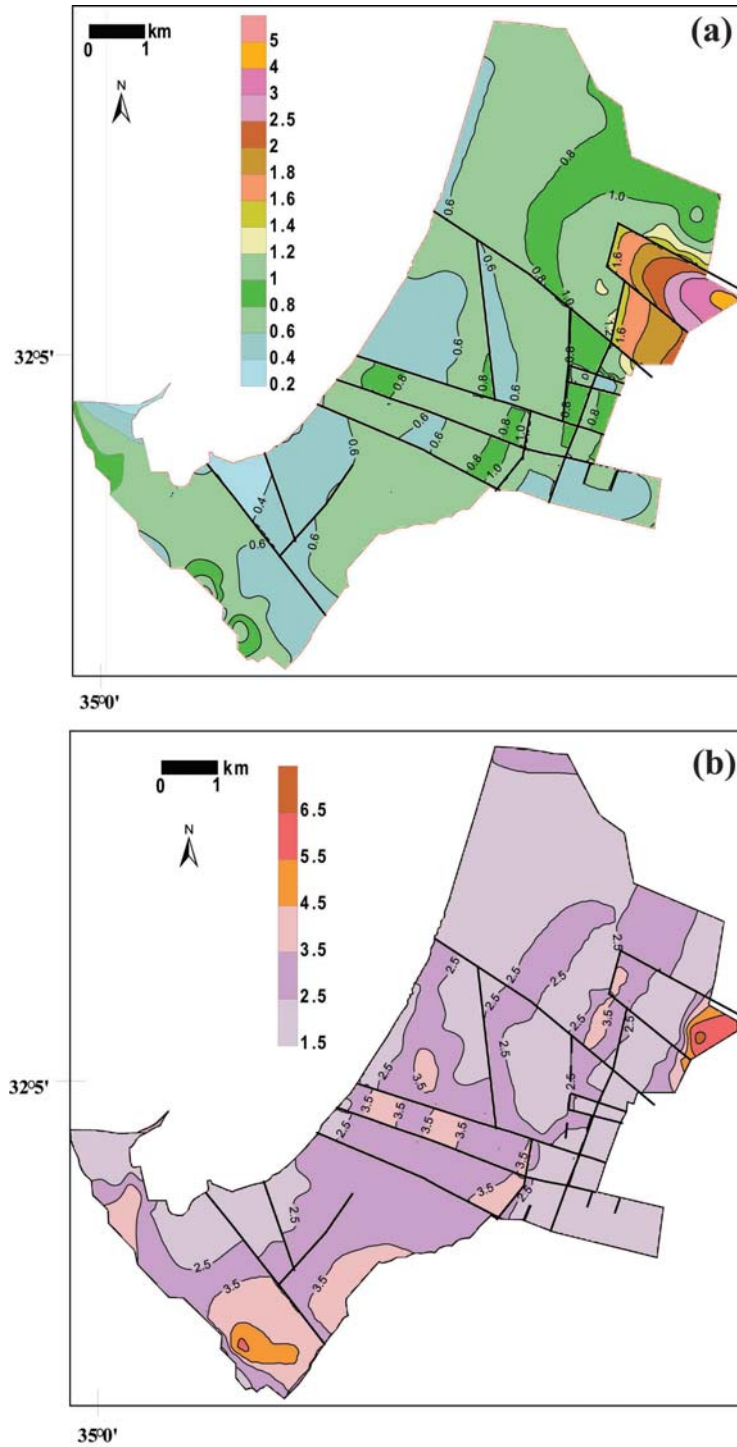


Figure 27. Haifa bay area: distribution of the first H/V resonance frequency (a) and its associated amplitude (b)

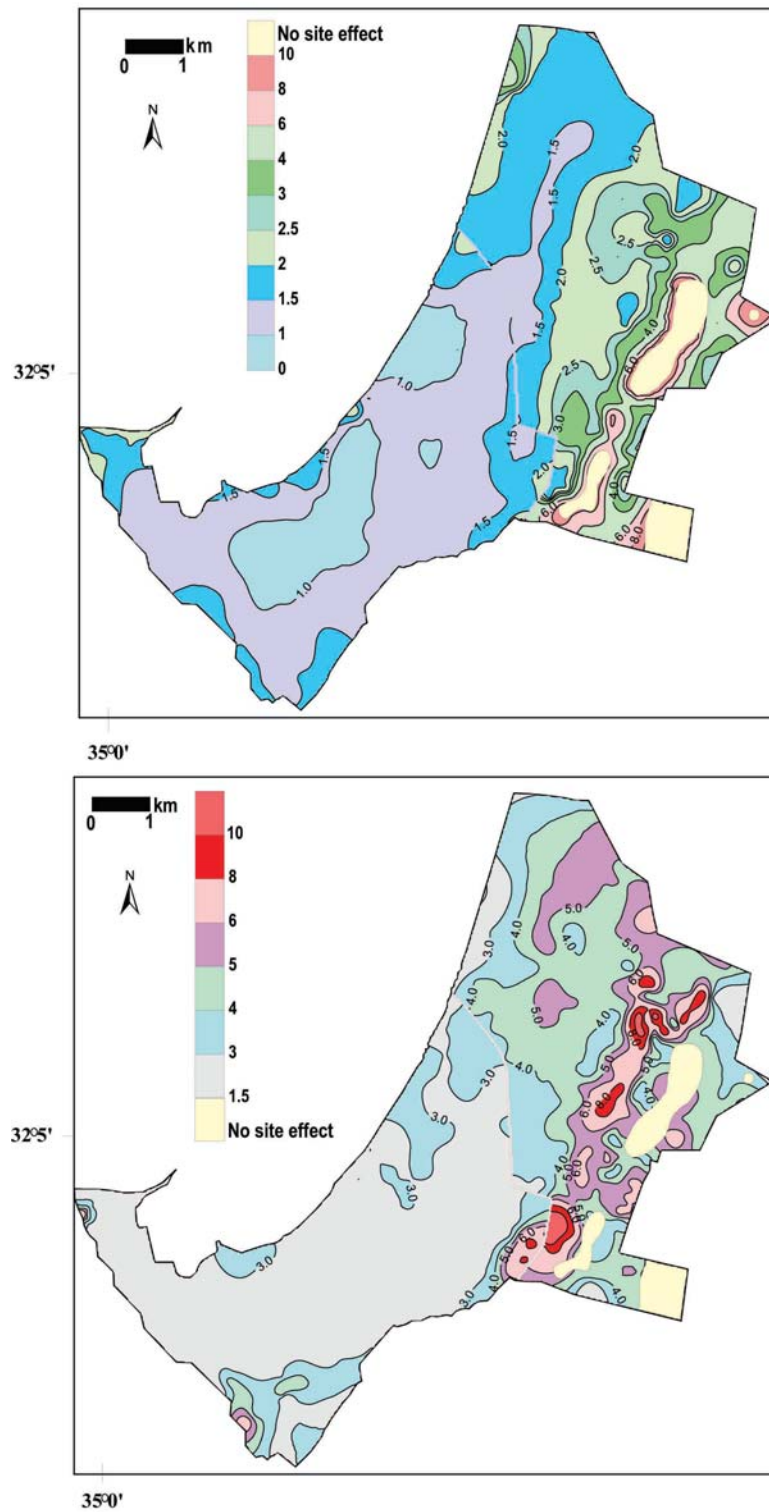


Figure 28. Haifa bay area: distribution of the second resonance frequency (a) and its associated amplitude (b).

The second resonance frequency varying from 2 Hz up to 10 Hz in the eastern part of the study area is correlated with the shallower limestone layer (see Figure 28a). In the western part, the second frequency is related to the Pleistocene calcareous sandstone and shows values from 0.8 Hz to 1.5 Hz.

The map of H/V amplitudes reflects variations of impedance between bedrock and overlying soft sediments. The amplitude values are in the range 2.0-2.5 in the western part and up to 7 in the eastern one. It strongly depends on the geotechnical characteristics of the upper layer (Figure 27b). The amplitude of the second peak shows a general decrease to the west due to increasing  $V_s$  of the upper layer (Figure 28b). We note that in a multilayer medium with intermediate hard layer the first and second resonance peaks are linked and variations in velocity of the upper layer are immediately reflected in amplitudes of both peaks. Only joint interpretation of these parameters gives a clear concept of the spatial distribution of site response characteristics.

### **Petah Tikva, Neighboring Towns and Settlements**

For microzoning purposes about 550 ambient noise measurements were carried out across an area of 128 km<sup>2</sup> including the Petah Tikva town, adjoining four towns and more than 10 villages (Figure 29). The significance of the project lies in the fact that heavily populated urban areas of the country are subject to earthquake risk. Petah Tikva is relatively a new town. It is located in proximity of the towns of Ramla and Lod, at roughly the same distance from the sources of future earthquakes and in the similar geological conditions. We remind that the towns of Ramla and Lod throughout their long history have been severely affected by strong earthquakes (Amiran, 1994). The last destructive earthquake occurred on July 11, 1927, and caused major damage in large parts of these towns, reaching a seismic intensity of VIII-IX on the MSK scale (Avni, 1999). Such a high intensity from a relative distant earthquake (about 70 km) of magnitude 6.2 is the result of local site effects of the sedimentary layers that may have significantly enhanced earthquake ground motions.

Geological analysis shows that the investigated area may be divided into five areas based on the structural configuration of the bedrock, which is limestone and dolomite of the Judea Gr. (Cretaceous age) and lithostratigraphic composition of the sediment cover rocks. The areas are indicated on the simplified schematic cross section over the study area (Figure 30) and may be defined as follow:

- Zone 1 is an outcrop of the bedrock (Judea Gr.);
- Zone 2 is characterized by the Quaternary soft sediments directly overlying the Judea Gr.;
- In Zone 3, the sedimentary substrate is formed by the Quaternary deposits, Pliocene clay and Paleogene chalk-marl overlying the Judea Gr.;
- Zones 4 and 5 have the similar lithostratigraphic composition of the soft sediments represented by the Quaternary soils and clay, but differ significantly by depth of the Judea Gr.

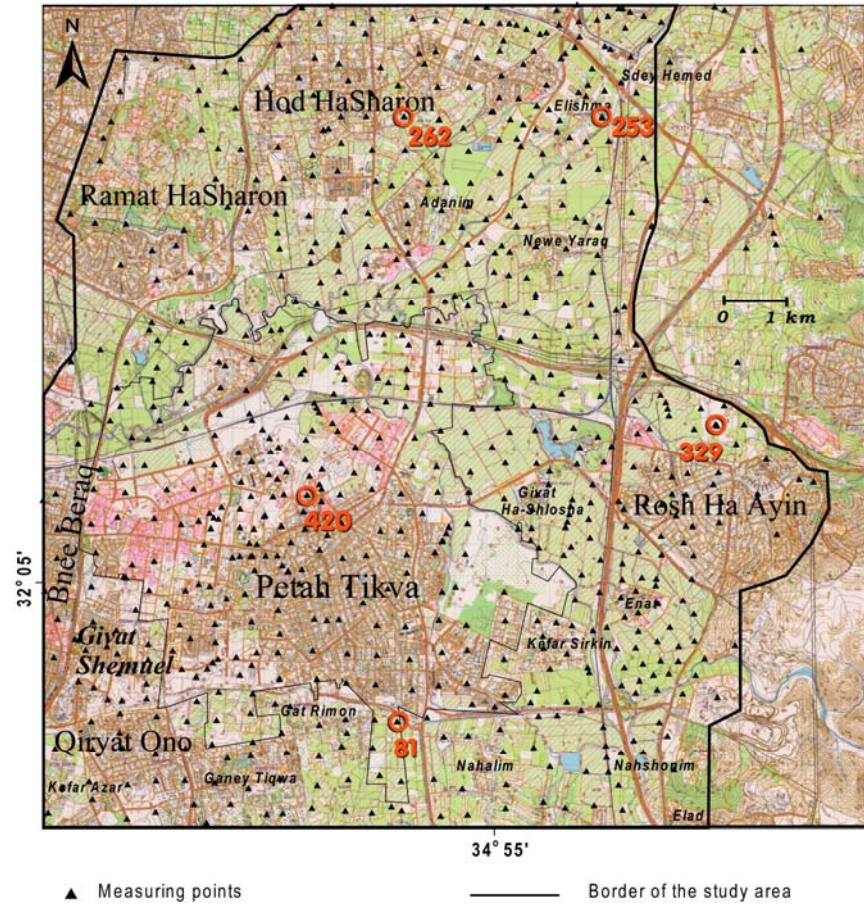


Figure 29. Topographical map of the Petah Tikva study area with measuring sites and towns.

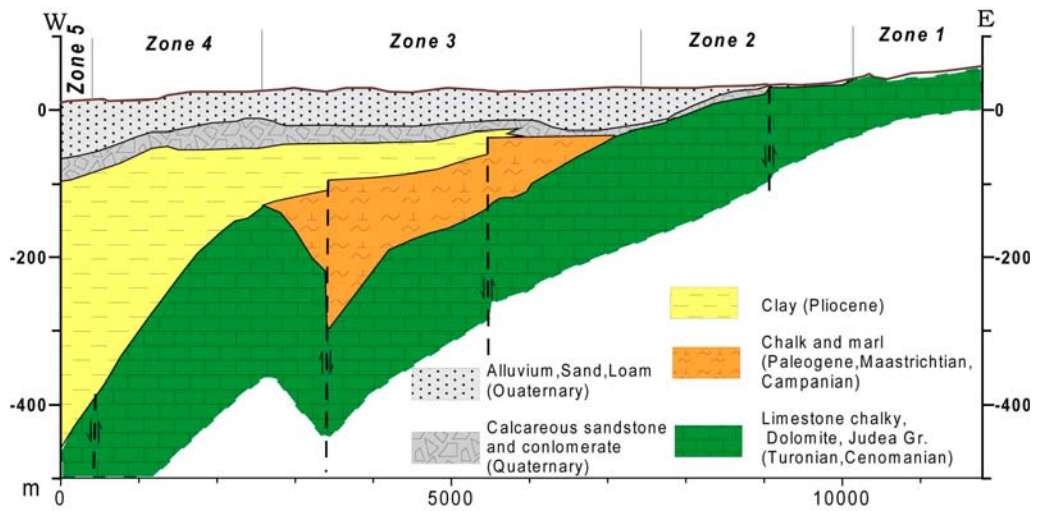


Figure 30. Geological division of the Petah Tikva study area shown on the cross section in the east-west direction.

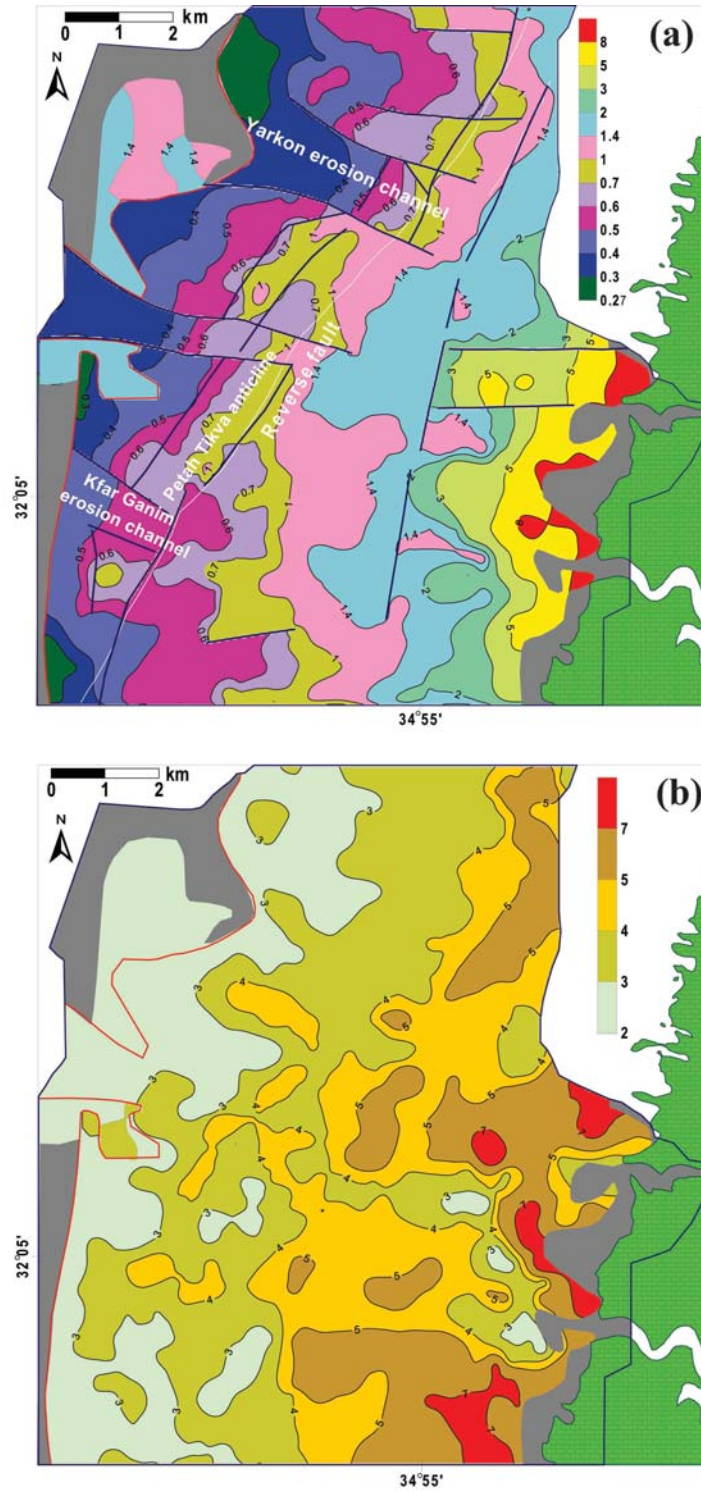


Figure 31. Distributions of the (a) fundamental frequency and (b) its associated amplitude level in the Petah Tikva study area.

The map of spatial distribution of H/V frequency over the study area (Figure 31) shows in the first approximation a correlation between frequency contours directed SW-NE and depth of the bedrock. However, complicated indented shape of the frequency iso-lines reflects the block structure of the Judea Gr. and suggests the presence of faults.

The main reverse fault of SW-NE strike which is traced in the structural map of Fleischer and Gafsou (2003) divides the study area into the western and eastern parts with characteristic resonance frequency of 0.3-1 Hz and 1.0-13 Hz respectively. We also note that this fault is a boundary between two types of the H/V spectral ratio introduced in Figs. 13 and 14. A series of sublatitudinal faults divides the main reverse fault into separate parts, which delineate the structural blocks of different depth. A local areas characterized by the lower resonance frequencies trending NW-SE are associated with erosion channels. Sites located in erosion channels show typical H/V shape with two separate peaks like in Figure 13.

Sharp increase in the fundamental frequency from 0.3-0.4 Hz to 1.2-1.7 Hz is observed in the western edge of the study area. This trend of change may be explained by appearance of the Quaternary calcareous sandstone layer. While the Judea Gr. keeps dipping to depths of 800-1500 meters, this shallower, relatively high velocity layer becomes a main reflector and provides the indicated increase in the fundamental frequency.

Sites where the site effect has not been detected are on the sandstone outcrop in the west or limestone and dolomite of the Judea Gr. in the east.

Distribution of maximum amplitude associated with fundamental H/V peak retains the general trend characterizing the frequency map, i.e. SW-NE strike of contours (see Figure 31b). The amplitude values decrease from 7 to 2 in the direction of dipping bedrock. The variations of amplitude values in the west, where the Judea Gr. occurs at a big depth, are probably connected with local variations of Vs in the upper part of the geological section. Erosion channels are indicated by amplitude of about factor 2.5.

## On the Applicability of Relationship between H/V Fundamental Frequency and Sediment Thickness

In recent years different studies (Ibs-von Seht and Wohlenberg, 1999; Delgado et al., 2000; Fäh, et al., 2000; Kobayashi et al., 2000; Parolai et al., 2002; D'Amico et al., 2004; Hinzen et al., 2004; García-Jerez et al., 2006) showed that the resonance frequency of the site obtained from horizontal-to-vertical spectral ratios of ambient vibration can be used to map the thickness of soft sediments. The resonance frequency  $f$  is related to thickness of soil layer  $h$  through the relationship

$$h = af^{-b} \quad (7)$$

To determine to what extent such a relationship is appropriate for the Petah Tikva area we correlate in Figure 32a resonance frequency and depth to the bedrock (Judea Gr.) according to the structural map (Fleischer and Gafsou, 2003). Range of the sediment thickness over the Judea Gr. is from a few meters up to 800 m. The best fit is expressed as

$$h = 155f^{-1.04} \quad (8)$$

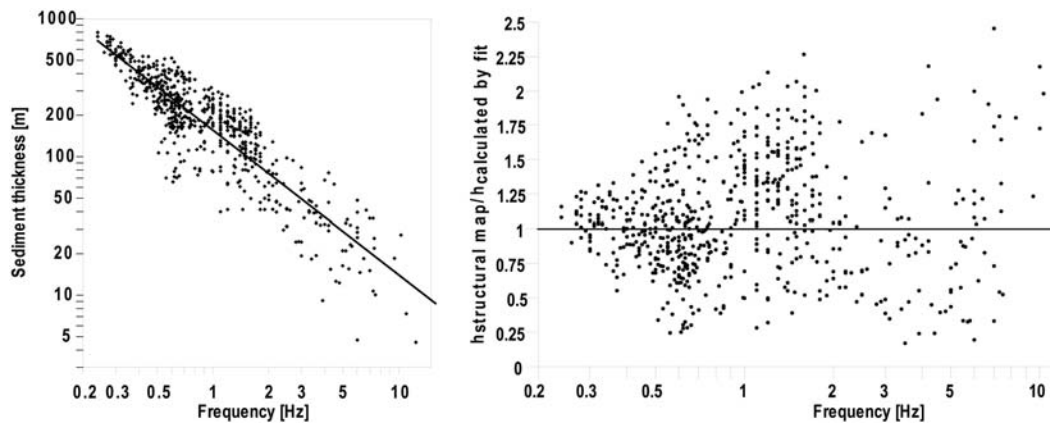


Figure 32. (a) - Fundamental frequency vs. thickness of sediments from the structural map of the Judea Gr. (Fleischer and Gafso, 2003); (b) distribution deviation of the reflector depth from the structural map normalized by that calculated from the empirical expression (8) with respect to fundamental frequency.

Figure 32 shows a clear correlation between the fundamental frequency and sediment thickness with correlation coefficient of almost 0.8. Nevertheless, scatter in both parameters is large and use of this relationship for predicting subsurface model is very questionable. Figure 32b shows the factor of deviation of the depth to the seismic waves reflector according to the structural map and the depth calculated from the empirical expression (8). Error of depth estimations is different for different frequency ranges and reaches values up to factor 4. The deviation is higher at the higher frequencies.

It is of importance to analyze depth variability in the context of the study area. We should note that initial data on sediment thickness taken from the regional structural map contribute to the great scatter. The others factors influencing deviation are associated with the use of a one-layer model and/or the assumption of smooth vertical variations of velocity and the lateral homogeneous  $V_s$  velocities. We use some examples of borehole locations to examine these conditions in our study area.

Example in Figure 33 presents two boreholes of different lithological composition. The reflector depths in the well PT44 and well Lod20 are 110 m and 40 m, respectively. However H/V ratios obtained at borehole locations show very close fundamental frequencies near 2 Hz. Analytical functions, calculated using borehole and refraction survey data are superimposed on the H/V spectral ratios in Figures 33a and 33b. Another example is a comparison between well 234 and well 238 shown in Figure 34. The soft sediment thickness in well 234 is 12 meters vs. 6 m in well 238. However, H/V spectra of these points show 7 Hz and 5.5 Hz respectively. Since  $V_s$  of upper alluvium layer do not differ significantly, this is a result of the presence of 8-meter gravel layer with  $V_s=480$  m/sec, which changes the velocity structure.

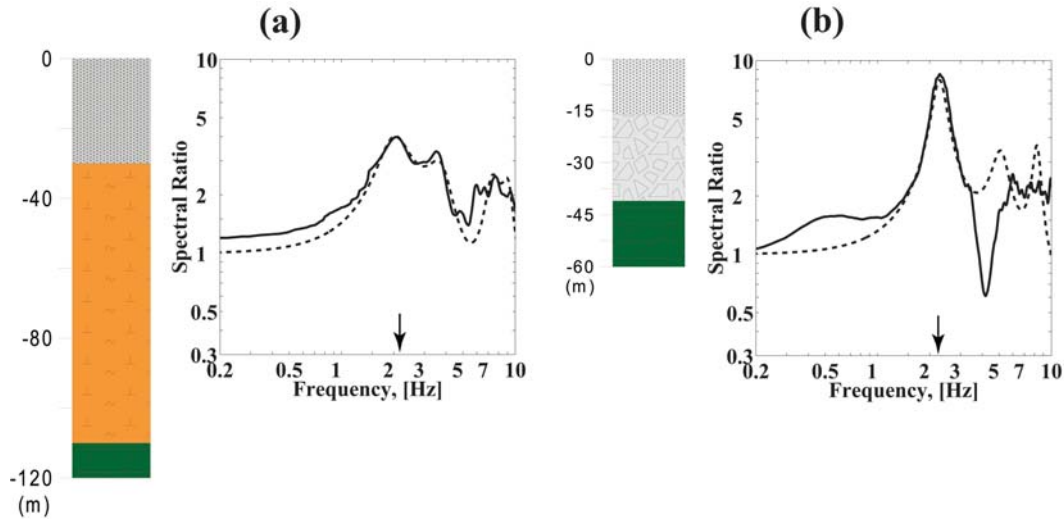


Figure 33. Columnar section and H/V spectral ratio (solid line) superimposed on analytical transfer function (dashed line) calculated on the base of borehole and refraction survey data for well PT44 – (a) and well Lod20– (b).

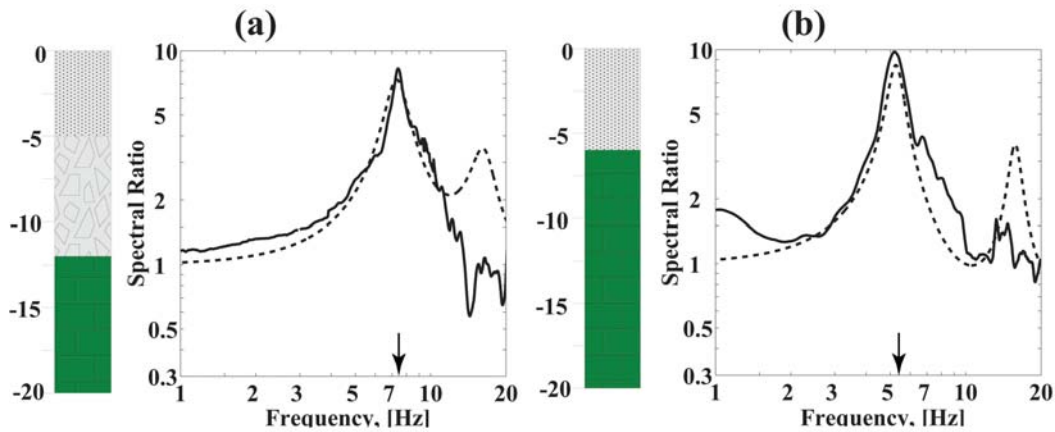


Figure 34. Columnar section and H/V spectral ratio (solid line) superimposed on analytical transfer function (dashed line) calculated on the base of borehole and refraction survey data for well 234 – (a) and well 238– (b).

Next example concerns divergence in the identification of the fundamental reflector by available geological data (Fleischer and Gafsou, 2003) and by the H/V analysis. H/V spectral ratio in Figure 35 obtained at well PT-2 exhibits wide spectral shape, which is result of two resonance frequencies: 0.65 Hz and 1 Hz. One can see that the site response function calculated by modeling the depth to the main reflector to be at 220 m which is the depth to limestone of the Judea Gr., according to the borehole data, does not approximate the spectral ratios neither by frequency nor by amplitude. We supposed the main reflector is top dolomite of the Judea Gr. found at a depth of 415 m, while the top limestone is an intermediate interface. The new model yields two resonance peaks and provides a good fit to the H/V

observations. We figure that the well stratigraphy was possibly misinterpreting a sharp break in the resistivity log.

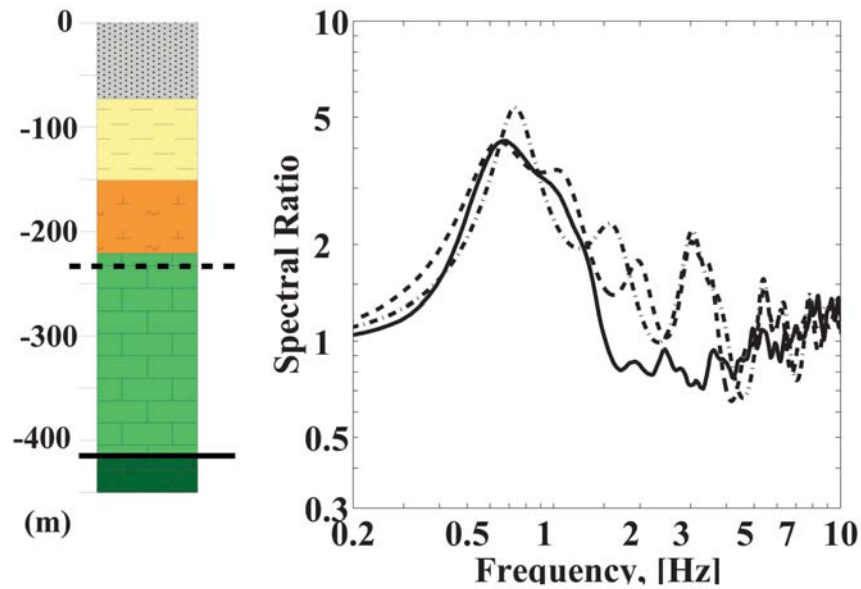


Figure 35. Columnar section of well Pt-2 and comparison between the H/V spectral ratio (thick line), trial analytical function (thin line) and optimal analytical function (dashed line) calculated assuming limestone at a depth of 220 m and dolomite at a depth of 420m as fundamental reflector, respectively.

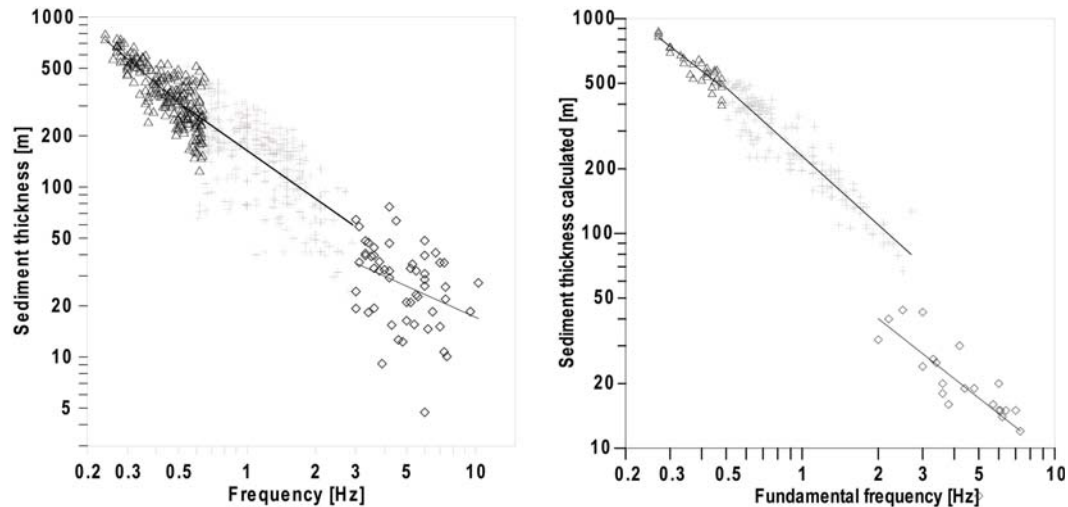


Figure 36. (a)- Fundamental frequency vs. sediment thickness from the structural map fitted separately for three groups with similar subsurface structure; (b) - fundamental frequency vs. sediment thickness calculated by modeling.

We have a lot of similar examples in the study area. Thus, we divide all the measured sites into three groups, based on correlation between the fundamental frequency, the shape of the H/V functions and the subsurface structure established throughout analysis of the

measurement results in Petah Tikva. Fundamental frequencies vs. soft sediment thickness of each group are shown in Figure 36a. We assume that each group may be roughly characterized by quasi-homogeneous subsurface structure. We specify some reasons for the large scatter. Among others the presence of the limestone layer up to 300 m thick, which being a part of the Judea Gr. is, nevertheless, not fundamental reflector for groups characterized by frequencies 0.3-0.6 Hz and 0.7-3 Hz (see Fig. 35); several local geological structures, not identified previously by geological mapping. For the high frequency group (3-8 Hz) we suppose to be crucial presence of Quaternary gravel layer, which is distributed irregularly (see Fig. 34) and leads to the significant discordance between frequency and reflector depth correlation.

The differences in estimating depth to the main reflector we observe within the groups of similar subsurface structure as well. In Figure 36b, we plot the fundamental frequency vs. sediment thickness derived from 1-D modeling, carried out at majority of the measured sites. After best-fitting of each group the scatter is reduced to a factor 2 that, however, is still large for predicting site amplification.

In example given in Figure 37, two sites are characterized by the same fundamental frequency  $f_1=1.4$  Hz and similar lithological cross section consisting of alluvium layer and chalk-marl layer over the bedrock. Variations in S-velocity from 850 m/sec up to 1000 m/sec for chalk-marl lithological unit and 200-300 m/sec for the upper layer at p34 and p123, respectively, are common in the Petah Tikva area. Modeling shows that a fair agreement between the analytical functions and H/V curve is reached with the reflector depth is 150 m for P34 and 208 m for P123.

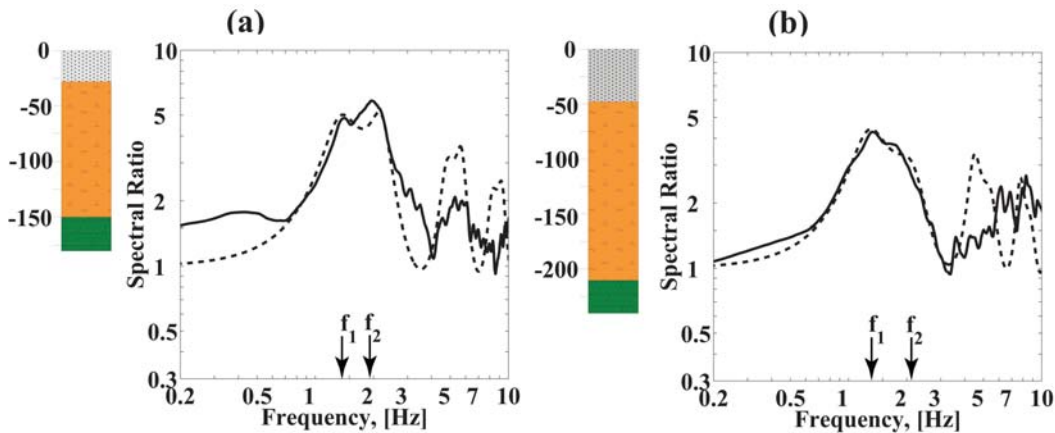


Figure 37. H/V spectral ratio (solid line), analytical transfer function (dashed line) and soil column derived from modeling of p34 (a) and p123 (b) sites with similar lithological composition yielding the same fundamental frequency  $f_1$ .

Hence, the demonstrated above shows that it is not recommended estimating depths by applying empirical relationships such that given in Eq. 8. Here again, ambient noise measurements can be of great use.

## Estimation of Shear-Wave Velocity Models and Reconstruction of Subsurface Structure

The key parameters to analytically evaluate site effects by using computer codes such as SHAKE (Schnabel et al., 1972) are the S-wave velocities of the unconsolidated sediments, thickness of each layers, density and specific attenuation in different lithological units as well as S-wave and density of the hard rock acting as a seismic reflector. Densities and specific attenuation in different lithological units were selected from literature sources (Borcherdt et al., 1989; McGarr et al., 1991; Theodulidis et al., 1996; Reinozo and Ordas, 1999; Pergalani et al., 2000 and many others). Recently, Pratt and Brocher (2006) used spectral decay in the shear-wave spectral ratio with respect to reference site amplification curves and estimated Q-values for shallow sedimentary deposits. They concluded that the range of Q values is 10-40. These values agree well with those used in our studies.

Data collected from a few seismic refraction profiles provide information on the S-wave velocities and thickness of shallow sediments within the accuracy and resolution of the geophysical technique. Refraction profiles are normally designed to obtain maximum information on Vs of the lithological units represented in the study area and in the vicinity of boreholes.

Measurements of ambient vibrations are also carried out either very close to or directly at drilling sites where detailed information on the subsurface is available. Available logging data are incorporated to obtain more detailed and reliable information about the subsurface. At that point, we combine the borehole and geophysical information with the observed spectral ratios to estimate the S-wave velocity profile at-depth. Then propagate by means of extrapolation to neighbouring sites, using H/V spectral observations and information about the regional geology to constraint S-wave velocities of the lithological units present in the area.

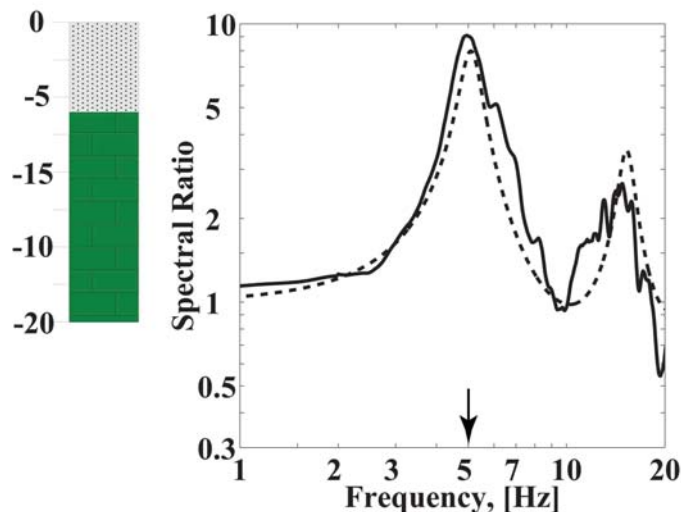


Figure 38. (a) - Lithological section of well 238 and (b) - analytical transfer function (dashed line) compared with H/V spectral ratio (solid line) obtained at this well.

The first example is one-layer subsurface model with the main reflector being dolomite of the Judea Gr. overlain by silt (well 238 in Petah Tikva).  $V_s=160$  m/sec for the silt layer is taken from a refraction survey carried out not far from well 238. Lacking direct  $V_s$  measurements of the dolomite in the well, we adhere to  $V_s$  assigned to dolomite in near-by Lod (Zaslavsky et al., 2005). In the Lod-Ramle area the geological conditions are similar to those in Petah Tikva, where  $V_s=1900\pm 80$  m/sec was derived at eight boreholes. We note that  $V_s=1970$  m/sec for dolomite is also suggested by a refraction survey in the Parsa area located in the Dead Sea area (Zaslavsky et al., 2000) and in the town of Dimona (Zaslavsky et al., 2008).  $V_s=160$  m/sec for silt and  $V_s=1900$  m/sec for limestone-dolomite of the Judea Gr. provide a quite well agreement between the analytical transfer function and H/V spectral ratio obtained at well 238 (see Figure 38, Table 3).

**Table 3. Geotechnical data and soil column model for well 238 (Petah Tikva).**

Well 238		Derived soil column model			
Lithology	Depth m	Thickness m	$V_s$ m/sec	Density gr/cm <sup>3</sup>	Damping %
Silt	0-6	6	160	1.6	4
Limestone and dolomite (Judea Gr.)	6 and below	-	1900	2.3	

S-velocities for gravel and chalky limestone of the Judea Gr. overlying the dolomites at a great part of the Petah Tikva area, but not everywhere, are obtained at well 70 using refraction profile RL-3. We note that borehole description does not separate the Judea Gr. into chalky limestone and dolomite. Thus, the thickness of the chalky limestone as the only unknown parameter is fitted - (Figure 39, Table 4).

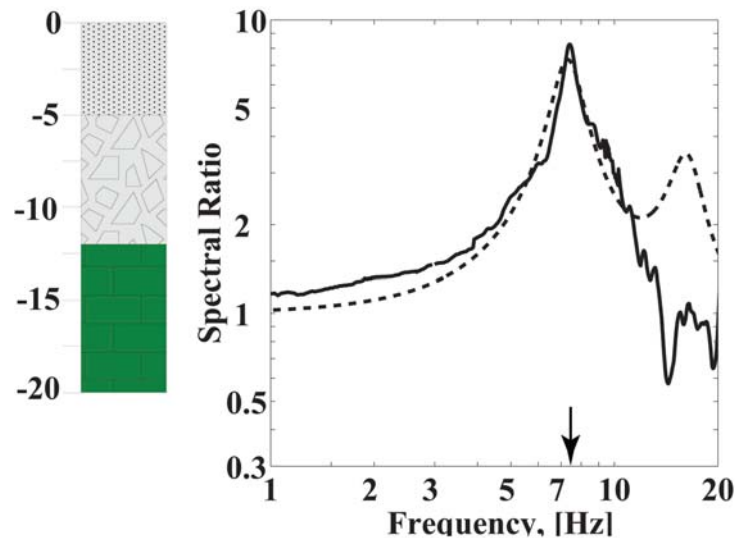


Figure 39. (a) Lithological cross section of well 70; (b) - comparison between H/V spectral ratio obtained at well 70 (solid line) and analytical transfer functions calculated using well data and velocities from refraction data (dashed line).

**Table 4. Geotechnical data and soil column model for well 70 (Petah Tikva).**

Well 70		Refraction survey	Derived soil column model			
Lithology	Depth m	Vs m/sec	Thickness m	Vs m/sec	Density gr/cm <sup>3</sup>	Damping %
Clay and silt	0-5	160	5	160	1.6	4
Gravel and conglomerate	5-12	480	7	500	1.8	3
Chalky limestone and dolomite (Judea Gr.)	12 and below	1200	20	1200	2.1	1
			-	1900	2.3	

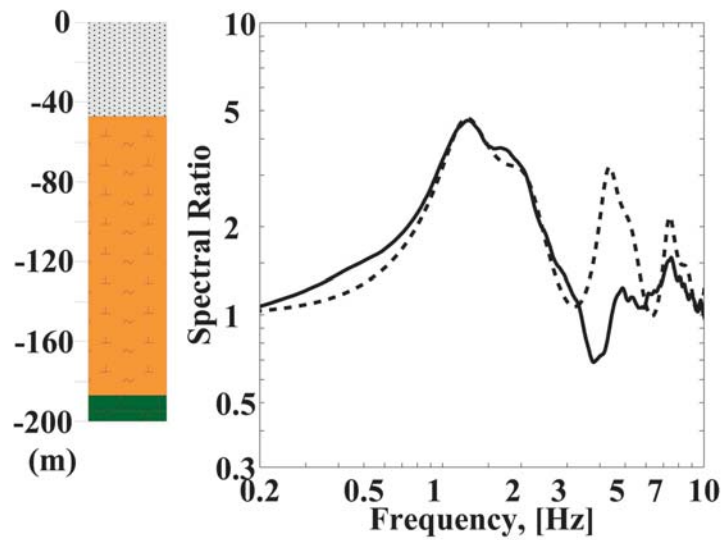


Figure 40. (a) -Lithological cross section of well PT-12; (b) - comparison between H/V spectral ratio (solid line) and analytical transfer functions calculated using well and refraction survey data (dashed line).

**Table 5. Geotechnical data and soil column model for well PT-12 (Petah Tikva).**

Well PT-12		Refraction survey	Derived soil column model			
Lithology	Depth interval m	Vs m/sec	Thickness m	Vs m/sec	Density gr/cm <sup>3</sup>	Damping %
Sand, loam	0-47	280	47	280	1.7	4
Marl-chalk	47-187	880	140	880	2.0	2
Limestone and dolomite (Judea Gr.)	187 and below	1900	-	1900	2.3	

Lithological column of well 111 shown in Figure 40a contains 140-meters marl-chalk layer. Using of  $V_s=880$  m/sec from the refraction profile provides a good match between the calculated transfer function and H/V ratio. This refraction profile provides us information on  $V_s$  of sand and loam layer as well. For geotechnical data and model parameters see Table 5. The analytical and experimental functions are plotted in Figure 40. We note that refraction survey carried out in the Haifa Bay area provides  $V_s$  values up to 1050 m/sec for the chalk layer, while south of Petah Tikva we have  $V_s=800$  m/sec for the marl layer. Therefore, to facilitate site effect analytical estimation the sediments represented by marl-chalk facies are merged into one layer characterized by  $V_s$  range of 800-1050 m/sec.

Since there is no refraction survey determining S-velocity for the clay (Pliocene age) neither in Petah Tikva nor Haifa Bay area, we adjust  $V_s$  at wells, for which all the velocities with the exception of the clay layer are fixed. Examples of the wells marked Lod-25 and Saqiye-2 containing the clay layer of different thickness are presented in Figures 41ab. The borehole data and model parameters are given in Table 6. We note that  $V_s=700$  m/sec for calcareous sandstone is known from down-hole measurements.

**Table 6. Geotechnical data and soil-column models for wells Lod 25 and Saqiye 2 (Petah Tikva).**

Well Lod 25		Derived soil column model			
Lithology	Depth interval m	Thickness m	$V_s$ m/sec	Density gr/cm <sup>3</sup>	Damping %
Loam	0-23	25	415	1.8	3
Conglomerate	23-28	7	500	1.8	2
Clay	28-80	55	600	1.8	2
Chalk	80-125	40	800	1.9	2
Chalky limestone (Judea Gr.)	125-164	40	1250	2.1	1
Limestone and dolomite (Judea Gr.)	172 and below	-	1900	2.3	
Well Saqiye 2		Derived soil column model			
Loam, clay	0-45	45	440	1.8	3
Sandstone	45-90	45	700	1.9	2
Clay	90-365	250	650	1.9	2
Chalky limestone (Judea Gr.)	Below 365	200	1200	2.1	1
Limestone and dolomite (Judea Gr.)	?	-	1900	2.3	

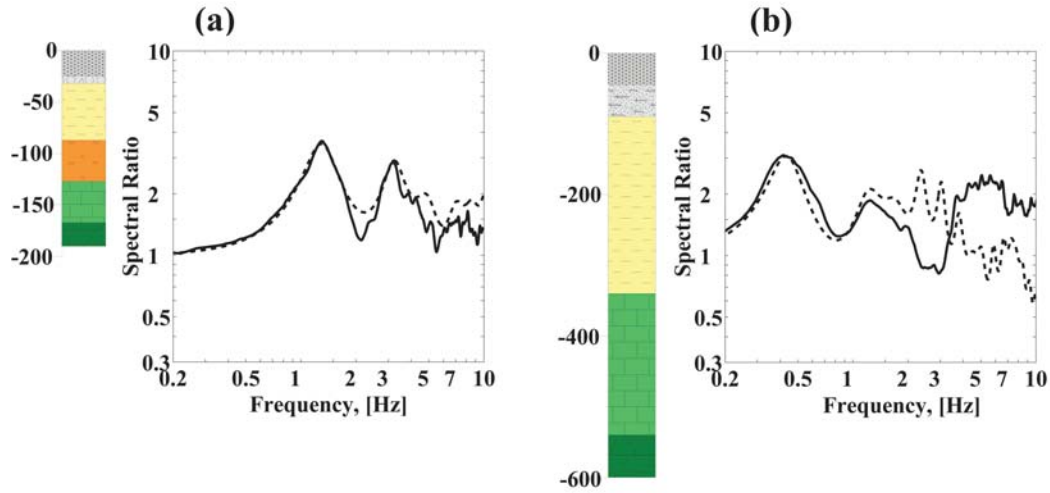


Figure 41. Soil columns and the analytical functions (dashed line) superimposed on H/V spectral ratios (solid line) of wells Lod 25 (a) and Saqiye 2 (b).

**Table 7. Geotechnical data and soil-column model for well SH-4 (Haifa Bay).**

Well SH-4		Refraction survey		Derived soil column model	
Lithology	Depth interval m	Thickness m	Vs m/sec	Thickness m	Vs m/sec
Alluvium	0-10	4	160	4	160
		14	290	8	290
Sandy limestone	10-37	Below 18 meters	1290	25	1290
Marl-chalk	37-95			60	850
Limestone and dolomite (Judea Gr.)	-				1900

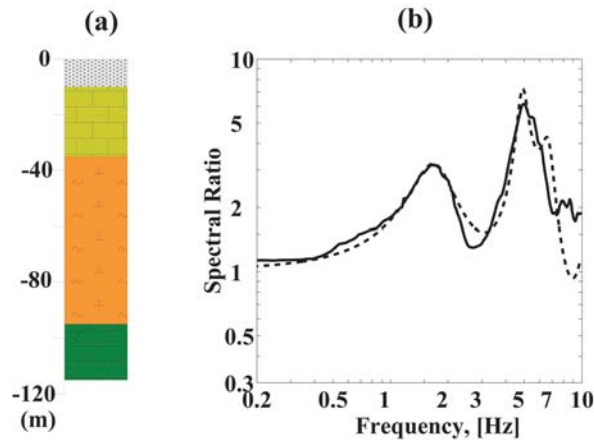


Figure 42. (a) - Lithological cross section of well SH-4; (b) - comparison between H/V spectral ratio (solid line) and analytical transfer functions calculated using well SH-4 and refraction survey data (dashed line).

The next example of well SH-4 shown in Figure 42 is taken from the eastern part of Haifa Bay area. We note that H/V spectral ratio yields two resonance peaks. The first, fundamental one is related to the limestone of the Judea Gr. The second peak is produced by the shallower velocity contrast between the alluvial deposits and Quaternary sandy limestone. Its  $V_s$  is also determined from refraction profiles close to the well. Table 7 contains results of the refraction survey, borehole data and derived soil-column model. The analytical function calculated on the base of data from Table 5 matches pretty well the spectral ratio and is also shown in Figure 42.

For another structural element of Haifa Bay area, the Qishon graben, the Miocene limestone is the main reflector. Its S-velocity is adopted from the refraction survey carried out in the similar geological conditions. This refraction survey yields  $V_s=650$  m/sec for the clay layer that agrees quite well with  $V_s$  obtained in Petah Tikva. Velocities are verified at well SY-3 (Figure 43, Table 8).  $V_s$  for the upper layer is taken based on lithological description of the well.

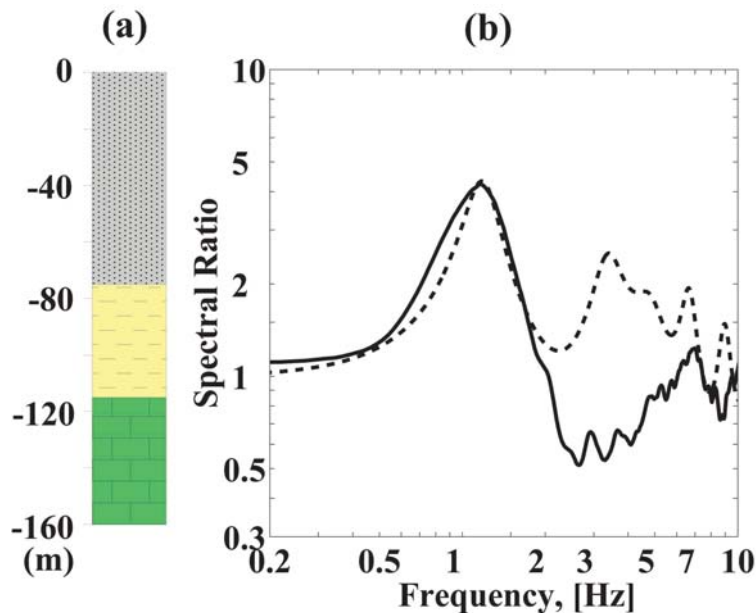


Figure 43. (a) - Lithological section of well SY-3 and (b) - comparison between average H/V spectral ratio (solid line) and analytical transfer function (dashed line).

**Table 8. Geotechnical data and soil column model for well SY-3 (Haifa Bay).**

Well SY-3		Derived soil column model	
Lithology	Thickness m	Thickness m	$V_s$ m/sec
Silt & clay, gravel	80	75	370
Clay	40	40	650
Miocene limestone	60	-	1500

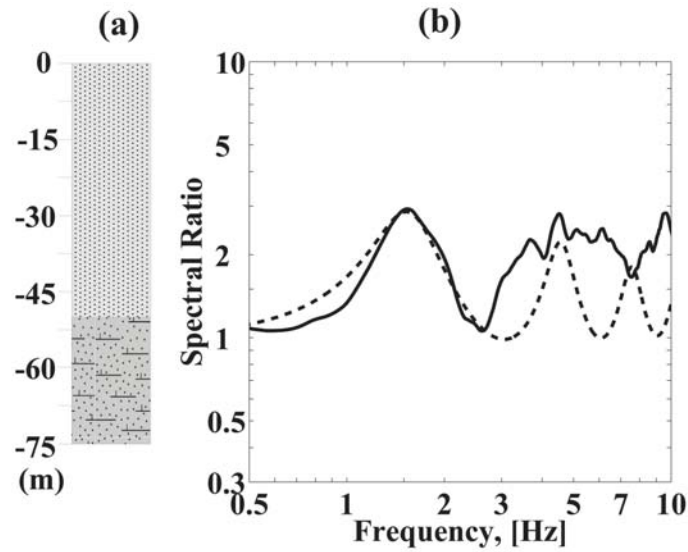


Figure 44. (a) Lithological section of well Saqiye 53 and (b) analytical function (dashed line) compared with H/V spectral ratio (solid line).

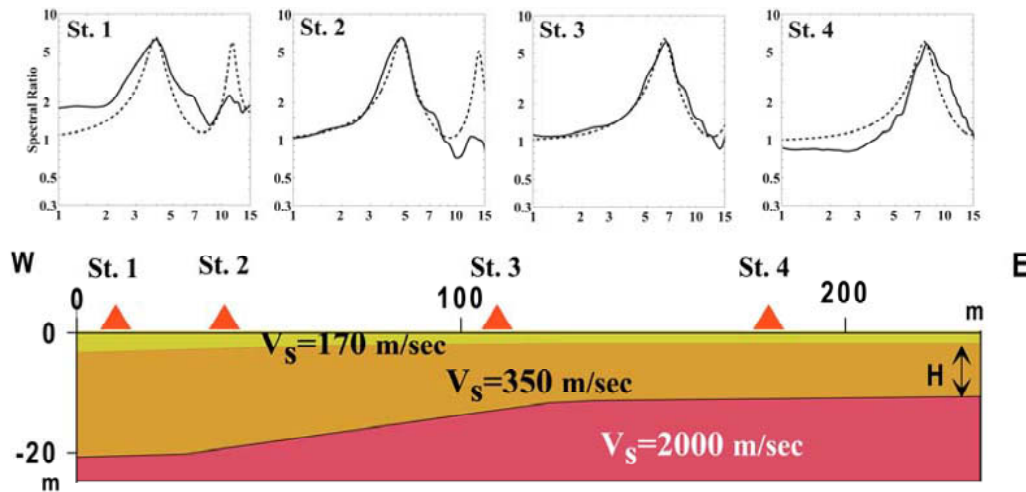


Figure 45.  $V_s$ -depth section along refraction profile A (Qiryat Shemona) and comparison between analytical transfer functions (dashed lines) and H/V spectral ratios (solid lines).

**Table 9. Well Saqiye 53 data and soil-column model (Petah Tikva).**

Well Saqiye 53		Derived soil column model	
Lithology	Depth interval m	Thickness m	$V_s$ m/sec
Loam, sand	0-50	50	280
Calcareous sandstone	50-57		700

**Table 10. Geotechnical data from refraction profile A and soil-column model (Qiryat Shemona).**

Refraction survey		Derived soil column model	
Lithology	Depth interval m	Thickness m	Vs m/sec
Silt	0-5	2-5	170
Loam	5-20	5-15	350
Basalt	Below 20m		2000

The well Saqiye-53 is located in the western part of Petah Tikva, where velocity contrast producing site effect is between the sandy loam and Quaternary calcareous sandstone. As mentioned above Vs of 700 m/sec for the calcareous sandstone is obtained by down-hole measurements. Borehole data and model are given in Table 9. Comparison of the H/V ratio with the analytical function is shown in Figure 44.

According to the refraction survey carried out in Qiryat Shemona, the Quaternary sediments represented by alluvium, loam and slope movement material accumulated in the west of the town are characterized by Vs of 170-180 m/sec; 300-400 m/sec and 650-700 m/sec, respectively. S-velocity of the Pleistocene basalt is 2000 m/sec.

**Table 11. S-velocities of lithological units represented in the study area.**

Age	Lithology	Vs range		
		Petach Tikva	Haifa Bay	Qiryat Shemona
Quaternary	Alluvium, silt, sand, sandy loam, gravel	160-200		
		250-450		
	Slope movement material			650-700
	Gravel, clay, conglomerate	400-550		450-600
	Calcareous sandstone	650-700		
	Weathered basalt			1000
	Basalt			2000
Neogene	Pliocene	Clay, marl		600-850
	Miocene	Gypsum, limestone		1500
Paleogene	Oligocene	Chalk-marl		800-1050
	Eocene			
	Paleocene			
Cretaceous	Senonian			
	Turonian	Judea	Chalky limestone, limestone	1100-1300
	Cenomanian		Limestone and dolomite	1900

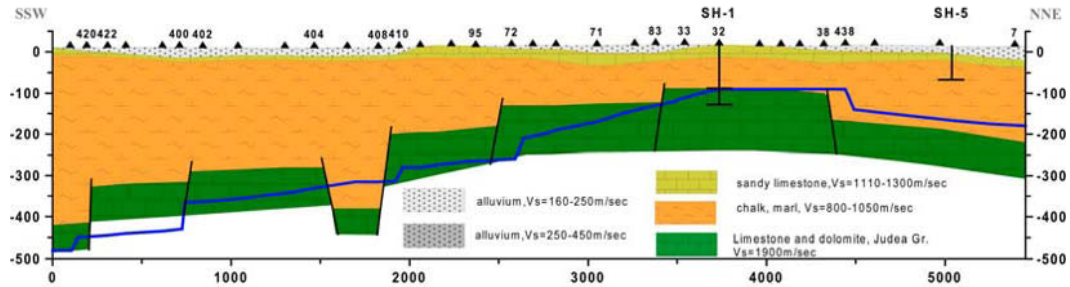


Figure 46. Schematic geological cross section beneath profile 1 (Haifa Bay area). The blue line represents the top of the basement according to the structural map of the Judea Gr. (Fleischer and Gafsou, 2003).

Figure 46 shows cross section along profile 1 reconstructed on the base of H/V ratio analysis. For comparison we superimpose a line showing top of the main reflector (limestone and dolomite of the Judea Gr.) outlined by the available geological data. Figure 47 displays examples of the H/V ratios at points located on different sides of suggested faults, which are associated with sharp changes of H/V ratio characteristics over a short distance. We note that the majority of H/V spectral ratios show two resonance peaks. The fundamental one is associated with the limestone and dolomite of the Judea Gr. (Cenomanian-Turonian age). Its amplitude is formed mainly by the velocity contrast between the Judea Gr. characterized by  $V_s=1900$  m/sec (see Table 4) and chalk-marl ( $V_s=850-1050$  m/sec). Quaternary sandy limestone with  $V_s=1100-1300$  m/sec represents the shallower reflector and decrease the amplitude of the fundamental frequency if its thickness is more than 40 m. Frequency of the second resonance peak is strongly correlated with thickness of the alluvial sediments overlying the limestone. Therefore, for sites located on the limestone outcrop, the second resonance peak does not exist and we observe the fundamental peak only (see points 95 and 32 in Figure 47). Point 420 is located in the southern part of profile 1 and is characterised by the fundamental frequency of 0.5 Hz (see Figure 47). At point 422, the fundamental frequency sharply increases up to 0.7 Hz that corresponds to rising of the top Judea Gr from 425 m to 340 m. Such a sharp changes in the fundamental frequency suggests the existence of a fault. We note that this fault is slightly shifted relatively to its position on the geological map (see Figure 26). The second frequencies at both points are 7 Hz, that corresponds to thickness of the soft sediments of 8m. We note that approximating the H/V ratios by the analytical functions at points Q420 and Q422 we seek the best fit considering only the fundamental and second resonance peaks corresponding to the deep and shallow reflector and marked by arrows. At point Q400, while the fundamental frequency does not change, the second one decreases to 3.2 Hz. Our calculations yield increase of the alluvium thickness up to 25 m.

Sharp shift in the fundamental frequency between neighboring points is identified several times at profile 1. Increase in the fundamental frequency from 0.7 Hz up to 0.9 Hz is observed between points 400 and 402. It corresponds to decrease in the reflector depth from 330 m to 290 m respectively and is accompanied by a fault, which is identified also by seismic and well data. A decrease and further increase in the fundamental frequency (0.9 Hz - 0.55 Hz - 1.0 Hz) between points 404-408-410, respectively, form the local graben with corresponding vertical displacements of 100m and 180m. The faults are a continuation of those shown in the geological map west of profile 1. The further gradual increase in the fundamental frequency

and consequent decrease in the reflector depth up to point 32 (SH-4 well) is complicated by steps. Some of the faults are detected by the geological data. Comparison of H/V ratios at points 38, 438 and 7 is of special interest. Here the influence of the upper alluvium layer on the H/V function is apparent. In particular, significant increase in amplitude (from 5 up to 9.5) and simultaneous decrease in frequency (from 8 Hz to 3 Hz) of the second resonance peak which can be explained by both low-velocity ( $V_s=160$  m/sec) and thickening of sediments above the shallow reflector, cause increase in amplitude of the fundamental peak.

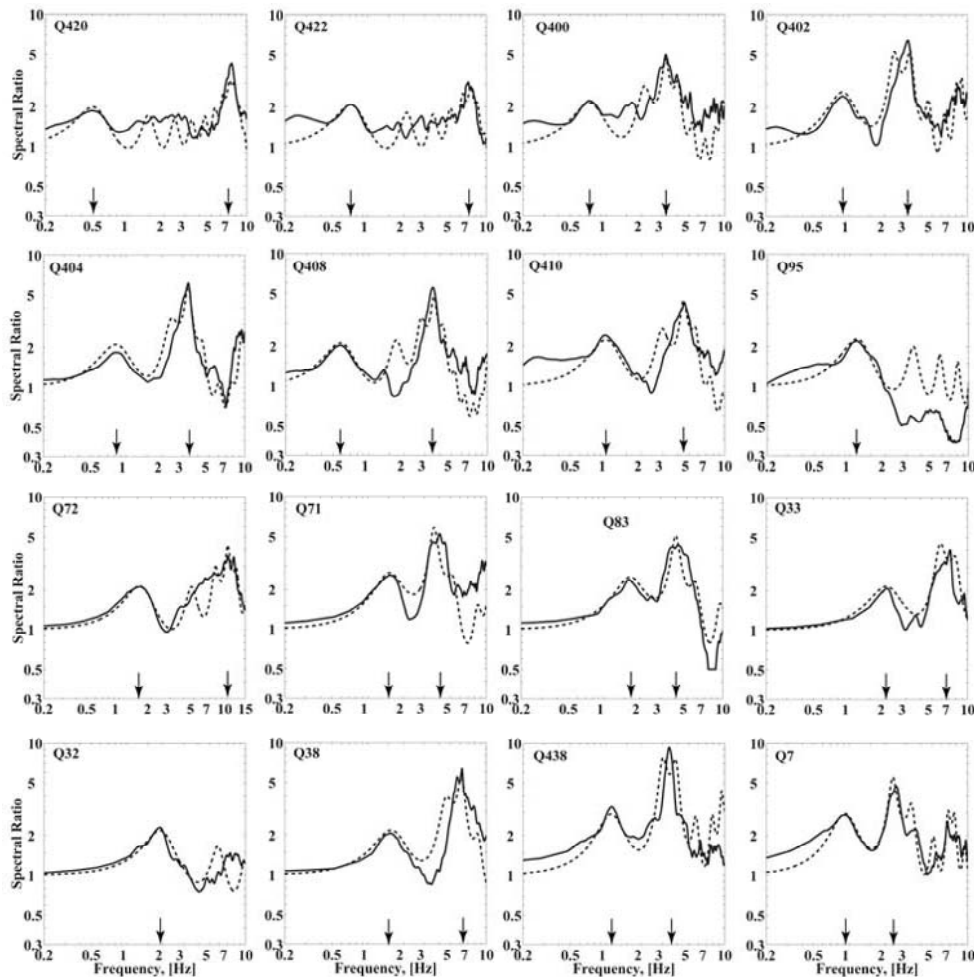


Figure 47. H/V spectral ratio (solid line) and analytical transfer function (dashed line) for representative points of profile 1 (Haifa Bay).

The cross section along profile 2 oriented NW-SE is shown in Figure 48. One can see two geological versions of the top Judea Gr., which practically coincide in the southeastern segment of profile and significantly diverge in the central and northwestern segments. According to the structural map of Mero (1983), Judea Gr. keeps gradually dipping to the northwest, while Fleischer and Gafsou (2003) suggest a sharp fall. We present another interpretation of this cross section based on the H/V analysis. According to this interpretation, increase of the fundamental frequency from 1 Hz (point 266) to 1.5 Hz (point 276) implies a

vertical displacement of 60 meters (Figure 49). This fault is, in a sense, a prototype of several faults of N-S direction, which are detected by ambient noise data, while neither geological nor seismic surveys provide information about the presence of these longitudinal faults.

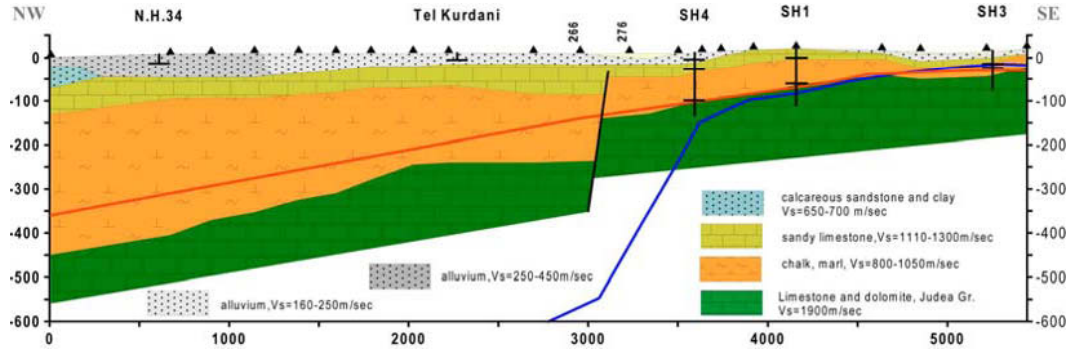


Figure 48. Schematic geological cross section along profile 2 (Haifa Bay area). The red and blue lines indicate two different geological versions of the basement surface.

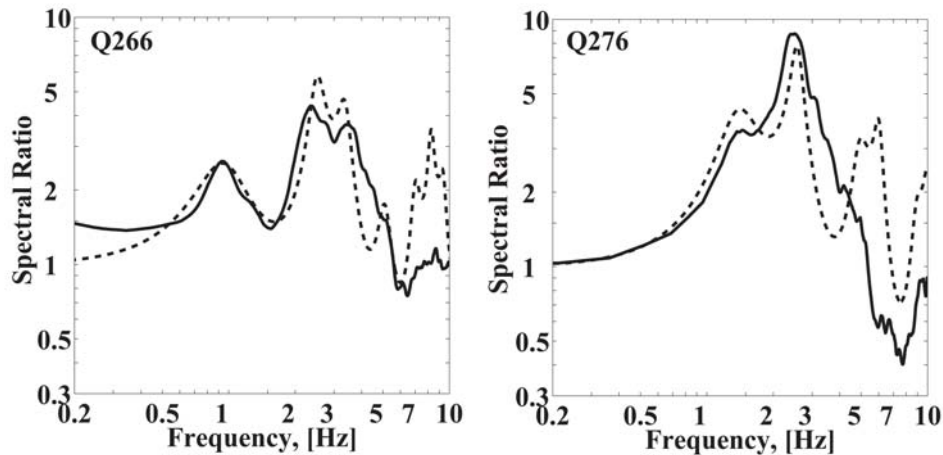


Figure 49. Analytical transfer function (dashed line) superimposed on H/V spectral ratio (solid line) for points Q266 and Q276 located on different sides of fault.

## Seismic Hazard Microzonation

The amplification of the ground motion during earthquakes due to geological site conditions makes it necessary for urban areas to perform detailed seismic hazard assessment. Under seismic hazard microzonation we understand subdividing of an area into zones with respect to geological characteristics of the sites and thus characterize the site specific seismic hazard at different locations. We used H/V measurements of ambient noise together with available geological and geophysical information to construct subsurface models for the investigated regions. These models may be used for seismic hazard microzonation across the study areas.

The grouping of H/V observations is done manually taking into consideration the fundamental frequency, amplitude and the shape of H/V spectral functions. As examples, the assemble of H/V spectral ratios and averaged analytical response function for Zone 4 in Qiryat Shemona, Zone 11 in Haifa bay and Zone 5 in Petah Tikva are depicted in Figure 50a. Soil column models corresponding to these analytical response functions are shown in Figure 50b. Seismic microzonation maps, presenting zones each of which is characterizes by soil column model were prepared for all investigated urban areas. Such maps for Qiryat Shemona, Haifa bay and Petah Tikva are presented in Figures 51-53.

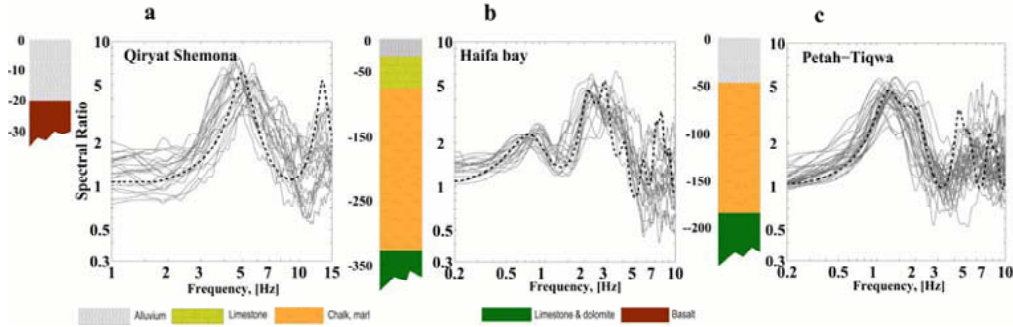


Figure 50. H/V spectral ratios from different sites (thin line), generalized analytical transfer functions (the dotted line) and 1D soil column models for Zone 4 (Qiryat Shemona) – (a); Zone 11 (Haifa bay) – (b); and Zone 5 (Petah Tikva) – (c).

The site specific acceleration spectra of a given site may be obtained by convolution of the analytical response function with observed and/or synthesized strong motions. Boore et al. (1997) presented equations to predict horizontal response spectra:

$$\ln Y = b_1 + b_2(M - 6) + b_3(M - 6)^2 + b_5 \ln r + b_v \ln V_s / V_A \quad (9)$$

Where  $Y$  is the response spectra (g) for the random horizontal component at 5% damping,  $r = (r_{jb}^2 + h^2)^{1/2}$ ;  $r_{jb}$  – is the distance to the rupture in km;  $b_1 = b_{ISS}$  for strike-slip earthquakes;  $b_2 = b_{2RS}$  for reverse-slip earthquake;  $b_1 = b_{1ALL}$  if mechanism is not specified;  $V_s$  is average shear wave velocity to a depth of 30 m;  $V_A$  shear wave velocity of rock.

The coefficients  $b_2$ ,  $b_3$ ,  $h$  and  $V_A$  were estimated using weighted, two stage regression procedure (Joyner and Boore, 1993; 1994) and based on the data set contains 213 accelerograms from 23 earthquakes of moment magnitude from 5.2 to 7.3 which occurred in western North America. In order to verify the applicability of equation (9) in our region, it has been used to predict the horizontal acceleration response spectrum at the strong motion station in Lod where  $V_s(30)=350\text{m/sec}$  from the earthquake of  $M_w=5.1$  (February 11, 2004). This function is compared with response spectra obtained from real accelerograms of this earthquake recorded at the station in Lod. In Figure 54a we show comparison between two response spectra. The prediction failed delineating both the frequency of maximum and its amplitude.

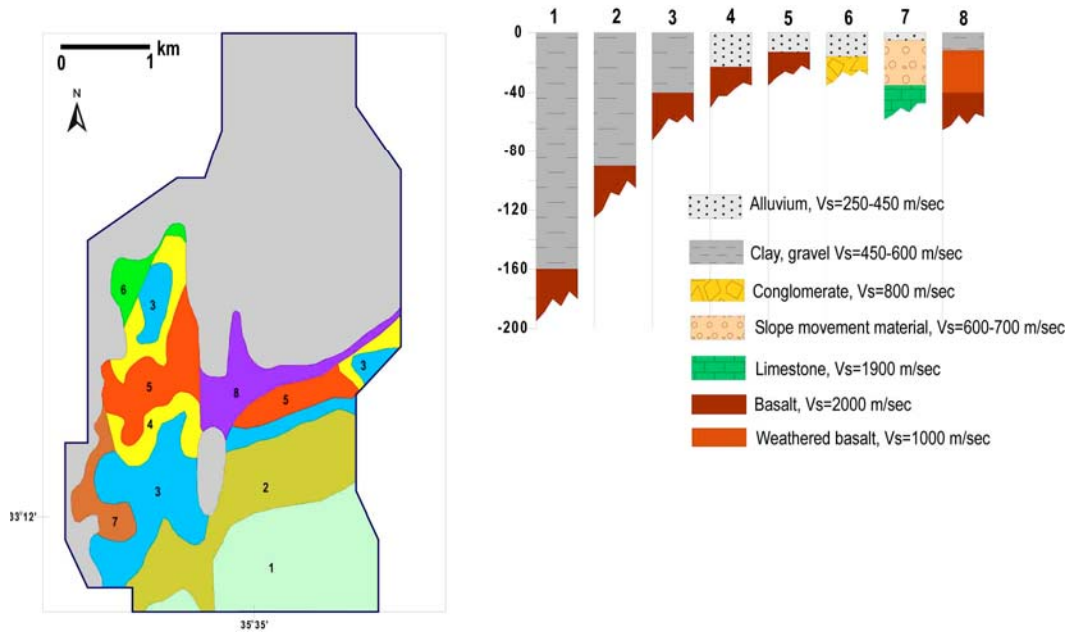


Figure 51. Seismic microzoning map of Qiryat Shemona, presenting zones of common site effect characteristics (a) and the characteristic 1D soil column model for each zone (b).

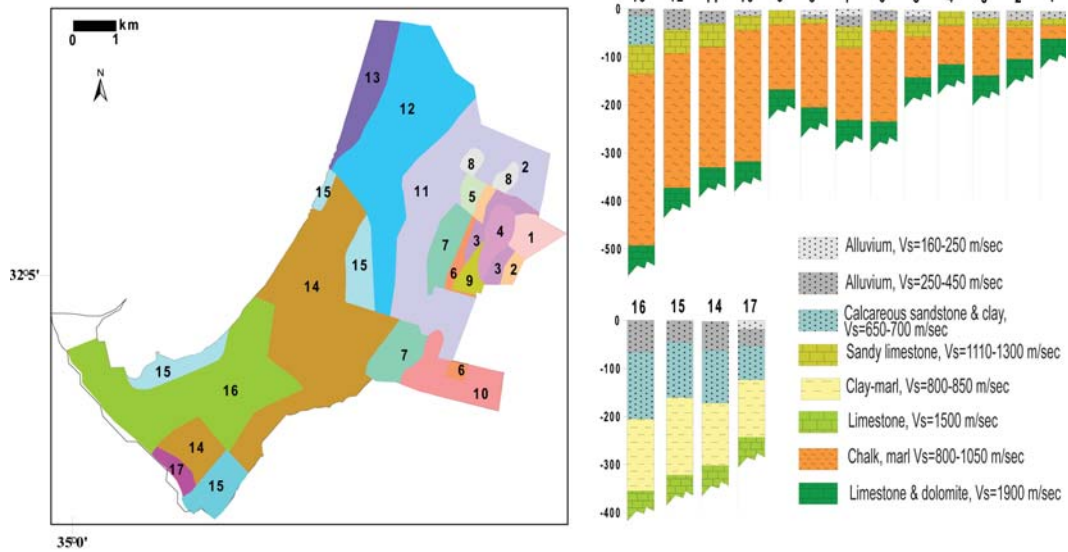


Figure 52. Seismic microzoning map of the Haifa Bay area, presenting zones of common site effect characteristics (a) and the characteristic 1D soil column models for each zone (b).

From data set which consists of 595 strong motion records caused by shallow crustal earthquakes with magnitudes  $\geq 5$  recorded in Europe and Middle East, Ambraseys et al., (2005) obtained the equation:

$$\log y = a_1 + a_2 M_w + (a_3 + a_4 M_w) * \log(d^2 + a_5^2)^{1/2} + a_6 S_S + a_7 S_A + a_8 F_N + a_9 F_T + a_{10} F_0 \quad (10)$$

Where  $y$  is the acceleration response spectra for 5% damping,  $S_S = 1$  for soft soil site and 0 otherwise,  $S_A = 1$  for stiff soil sites and 0 otherwise,  $F_N = 1$  for normal faulting earthquakes and 0 otherwise and  $F_0 = 1$  for odd faulting earthquakes and 0 otherwise.

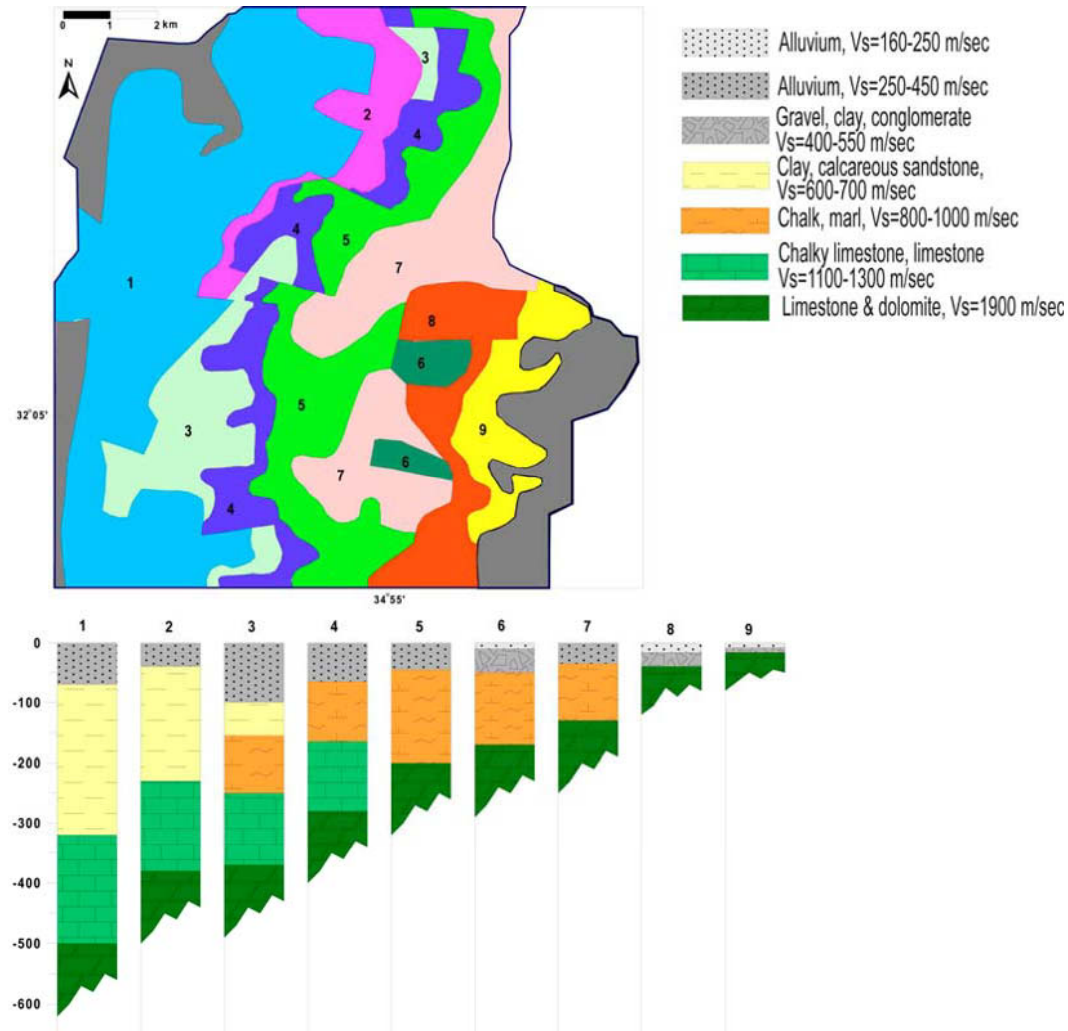


Figure 53. Seismic microzoning map of Petah Tikva, presenting zones of common site effect characteristics (a) and the characteristic 1D soil column models for each zone (b).

As shown in Figure 54a, estimations using formulae (10) and the response spectra from accelerograms of the earthquake are not similar. The strong motion station located in the town of Eilat recorded the main shock of the Gulf of Aqaba earthquake (95-11-22 04:15,  $M_W = 7.2$ , epicentral distance of 70 km). According to borehole and geophysical information (Zaslavsky et al., 2003) this site consist of three layers: alluvium (thickness of 5 m and  $V_S$  of 250 m/sec), sand (thickness of 30 m and  $V_S$  of 420 m/sec), and conglomerates (thickness of 25 m and  $V_S$  of 1,100 m/sec), overlying granite with  $V_S$  equal to 2,400 m/sec. Here,  $V_S(30)=400$  m/sec. The acceleration response spectra are shown in Figure 54b. Again, we can see significant discrepancy between the spectrum obtained from accelerograms of the earthquake and the

spectra predicted by equations (6) and (7). This is not surprising because these equations cannot take into account actual site amplification.

A series of studies (Boore, 1983; Boore and Atkinson, 1987; Boore and Joyner, 1991 and others) described and demonstrated the stochastic method for synthesizing accelerograms of the S-wavetrain. The stochastic approach has been applied to predict the acceleration response spectrum of the signals from the the Feb. 11, 2004 and Nov. 22, 1995 earthquakes and compared the predicted functions with the observations. Figure 54 shows the average response spectrum obtained by the stochastic method, which also demonstrate the high resemblance between the predicted and the actual functions. The examples shown in Figure 54 also suggest that the site related coefficients used in the prediction equations discussed are possibly not applicable to the investigated sites. In general, one should be extremely careful when estimating ground motions on the surface of site that may exhibit site effects and amplification of seismic motions. This finding, if confirmed by additional measurements, may cast a great shadow on the world wide practice to copy site correction values associated with  $V_s(30)$  from the USA building codes. The values of these parameters may not valid to other parts of the world.

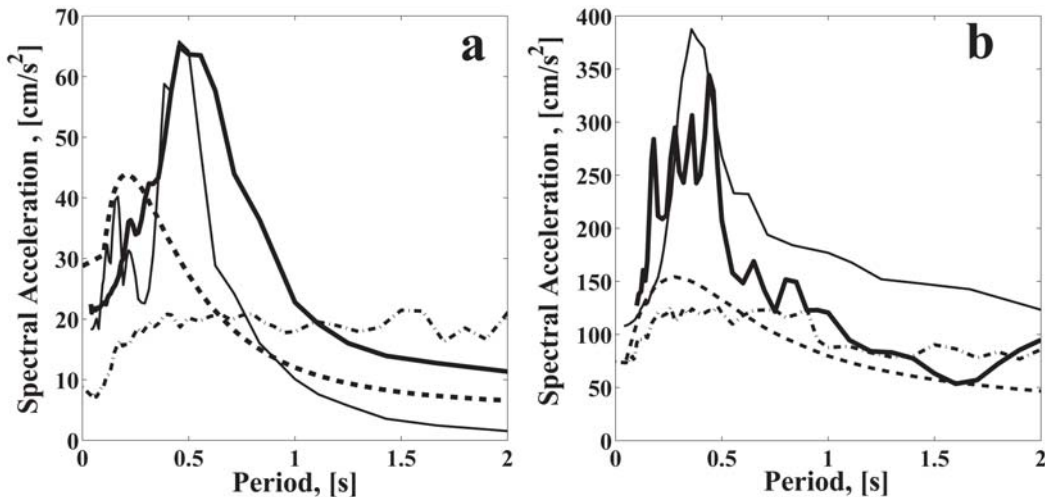


Figure 54. Comparison between response spectra obtained from earthquakes and predicted by different methods: earthquake on Feb. 11, 2004, recorded in Lod and (a) and earthquake on Nov. 22, 1995, recorded in Eilat (b). Thin line denotes response spectra calculated from accelerograms; dashed line indicated response spectra calculated by equation (9); dashed-dotted line refers to equation (10) and thick line is the average response spectra computed using SEEH method.

Based on this Stochastic method, Shapira and van Eck (1993) developed the SEEH process (SEEH- Stochastic Estimation of the Earthquake Hazard) to predict the site specific acceleration response spectra computed for 10% probability of exceedence during an exposure time of 50 years and for a damping ratio of 5%.

The SEEH computations require information on several seismological parameters such as spatial distribution of seismogenic zones and their seismicity characteristics, stress drop,  $Q$ -values, seismic moment – local magnitude relationships, etc. Estimation of these parameters are based on seismological data (local and regional earthquake) provided by the local seismic

networks. The SEEH applies Monte Carlo simulation to simulate the seismicity in the different seismogenic zones surrounding the investigated area over several thousands of years and applies the stochastic method to synthesize ground motions for each of the simulated events. At the final stage of the simulations, the synthetic horizontal accelerations propagate to the surface of the site through the soil layers constituting the site's sub-surface. The SEEH also incorporates the uncertainties associated with almost every parameter needed in the computations.

## Conclusions

Ground motion amplifications of soft soils layers, common in urban areas, are a major contributor to increasing damages and number of casualties during earthquakes. The great variability in the subsurface conditions across a town/city and the relatively high costs associated with obtaining the appropriate information about the subsurface, strongly limit proper hazard assessments. Direct information from strong motions recordings in urban areas are usually not available. Such is the situation in Israel which is small and its population centers are in close proximity to the seismically active Dead Sea Fault system, capable of generating earthquakes with magnitude as high as 7.5.

Over the years, we have conducted site investigations in several thousands of sites across Israel. These investigations demonstrated the usefulness of using horizontal-to-vertical (H/V) spectra of ambient noise measurements to identify sites with high potential for being vulnerable to amplification effects and characterize the sites with respect to their expected resonance frequencies and the corresponding H/V levels. This information, together with any available geological, geotechnical and geophysical information helps building a reliable model of the subsurface which is then integrated in the processes of the seismic hazard assessment.

Our conclusions may be summarized as follows:

- Reliability and applicability of the ambient noise H/V spectral ratio may be influenced by different factors such as anthropoid noise, underground pipe lines and constructions, soil structure interaction etc. and heavily depended on the amount of data. Assessing the condition of ambient noise waveform by computing spectra and H/V spectral ratio for many time windows allows identifying these factors already in the field. It is essential to monitor the ambient noise at least during one hour and thus increase the chances of selecting the time windows to be used in the analysis. Here, quantity is a necessity to achieve quality.
- One of the problems associated with ambient noise measurements and analysis is the stability and reproducibility of measurements. Data from continuous measurements during several months as well as repeated measurements in different days, months and years show that the shapes of average spectral ratios obtained at the same site under the same conditions of measurements yield almost identical results.
- Another problem in analysing ambient noise measurements is the large scatter of the maximum H/V spectral amplitudes. Apparently, this instability is related to

non-stationary character of the sources which are randomly distributed in time and space. In order to reduce the scatter and increase stability, our processing scheme involved a careful manual selection of the time window from which we obtain reliable H/V functions.

- H/V and  $H_{\text{site}}/H_{\text{bedrock}}$  curves from ambient noise showed consistent results. However, since the source of ambient noise varies significantly from place to place, the  $H_{\text{site}}/H_{\text{bedrock}}$  ratio technique can only be applied within a limited area and within 200-300 m from a reference site.
- Qualitative analysis of the distribution of the Fourier spectra and H/V spectral ratios of ambient noise over the study areas shows high correlation between shape of spectra and geological site conditions. This can be used to contour areas of similar subsurface structure.
- Maps of the spatial distribution of the fundamental frequency and their associated H/V amplitude delineate potentially vulnerable sites. This information is useful for land use considerations in urban planning and for identifying sites which require in depth site investigations to better evaluate the seismic hazard.
- The structure and properties of the underlying soils inferred only from geological and geophysical information may still lead to wrong assessments of the site response, especially when based on 1D model. Reliable modeling to be used in site response analysis is those obtained by combining different empirical approaches, supplemented with geophysical and geological data.
- Limited data on S-wave velocities and sediment thickness obtained from seismic refraction surveys carried out at boreholes enable the calibration of the H/V spectral ratio with an analytical site response derived from a 1D subsurface model. It is also used to justify further H/V ratios utilization, by velocities extrapolation, to study other sites, away from refraction profiles and boreholes. A stochastic optimization algorithm is applied to calculate the layer thickness, yielding transfer functions to match in the best way the observed H/V curves, considering all resonance peaks.
- It is interesting to note that the modeling results, obtained in studies which used ambient noise measurements, lead to suggest a revision of existing concepts as regards to the subsurface structure in the region.
- Analysis of an empirical relationship between fundamental frequency and thickness of the soft sediments performed on the extensive database of ambient vibration measurements have demonstrated that the assessment of layers thickness based on regression functions correlating fundamental frequency with depth does not allow a reliable construction of a realistic model to be used to determine the site response function.
- The ambient noise measurements enable identifying discontinuity in the subsurface and locate faults. These are associated with significant change in all three characteristics of the H/V spectra, i.e. fundamental frequency, amplitude and shape corresponding to both vertical displacement and change in the velocity profile.
- When relevant, the average H/V spectral ratio obtained from ambient vibrations, reliably identified the fundamental resonance frequency of the investigated site

and provide a fair estimate of the expected amplification level, similar to those assessed by other techniques and similar to the analytically obtained response functions, provided that all processes remain linear.

- H/V spectral ratio from ambient noise adds very useful information that when integrated with other different data sources, often limited in quantity and quality, enable obtaining a systematic picture of the characteristics of site effects in the investigated region. The application of this methodology is very important in regions where strong earthquake occur over a long return period, but might exhibit a very high risk.

## Acknowledgements

Our thanks to Dr. V. Pinsky for help and fruitful discussions. We are thankful to our colleagues at the Geophysical Institute of Israel, especially L. Feldman, V. Avirav, C. Ben-Sasson, B. Reich, U. Peled, D. Kadosh, D. Levy, Y. Schwartz. The dedication and enthusiasm of V. Giller, I. Livshits and A Shvartsburg who made the ambient noise measurements were the main force behind the success of the study. We are grateful to D. Giller and I. Dan for the data processing. Many of our studies were financed by the Israel Ministry for Absorption and the Earth Sciences Research Administration of the Israel Ministry for National Infrastructure.

## References

- Ambraseys, N.N.; Barazangi B. The 1979 earthquake in the Bekaa Valley: implications for earthquake hazard assessment in the eastern Mediterranean region. *J. Geophys.* 1989, Res.94, 4007-4013.
- Ambraseys, N.N.; Douglas, J.; Sarma, S. K.; Smit, P.M. Equation for the estimation of strong ground motions from shallow crustal earthquakes using data fro Europe and the Middle East: horizontal peak ground acceleration and spectral acceleration. *Bull. of Earth. Engin.* 2005, 3, 55-73.
- Amiran, D.H.K.; Arieh, E.; Turcotte, T. Earthquakes in Israel and Adjacent Areas: Macroseismic Observations since 100 B.C.E. *Israel Exploration Journal.* 1994, 44, 261-305.
- Atakan, K.; Duval, A-M.; Theodulidis, N.; Guillier, B.; Chatelan, J-L.; Bard, P-Y.; the SESAME-Team. The H/V spectral ratio technique: experimental conditions, data processing and empirical reliability assessment. *Proc. of 13<sup>th</sup> World Conference of Earthquake Engineering.* Vancouver, B.C., Canada. 2004, Paper 2268.
- Avni, R. The 1927 Jericho Earthquake. Comprehensive macroseismic analysis based on contemporary sources. Ph.D. Thesis, Ben-Gurion University, Beer-Sheva, 1999.
- Avni, R.; Bowman, D.; Shapira, A.; Nur, A. Erroneous interpretation of historical documents related to the epicenter of the 1927 Jericho earthquake in the Holy Land. *Journal of Seismology.* 2002, 6, 469-476.
- Bard, P.-Y.; 76 SESAME participants. The SESAME project: An overview and main results. *Proc. of 13<sup>th</sup> World Conference of Earthquake Engineering.* 2004, Vancouver, B.C., Canada, Ppr. 2207.

- Bartov, Y.; Sneh, L.; Fleisher, L.; Arad, V.; Rosensaft, M. *Map of fault in Israel, geological Survey of Israel*. Rep. GSI/29/2002
- Begin, Z. B. *Destructive earthquakes in the Jordan Valley and the Dead Sea – their recurrence intervals and the probability of their occurrence*. Rprt. GSI 12/2005.
- Ben-Menahem, A. Earthquake catalog for the Middle-East (92 B.C. – 1980 A.D.). *Boll. Geof. Theor. Appl.* 1979, 21, 245-310.
- Bonilla, L. F.; Steidl, J. H.; Lindley, G.T.; Tumarkin, A. G.; Archuleta, R. J. Site amplification in the San Fernando Valley, California: Variability of site effect estimation using S-wave, Coda, and H/V method. *Seism. Soc. Am.* 1997, 87, 710-730.
- Boore, D. M. Stochastic simulation of high-frequency ground motions. *Bull. Seism. Soc. Am.* 1983, 73, 1865-1894.
- Boore, D. M.; Atkinson G.M. Stochastic prediction of ground motion and spectral response parameters at hard-rock sites in eastern North America. *Bull. Seism. Soc. Am.* 1987, 86, 440-467.
- Boore, D. M.; Joyner, W.B. Estimation of ground motion at deep-soil sites in the eastern North America. *Bull. Seism. Soc.* 1991, 81, 2167-2185.
- Boore, D. M., Joyner, W.B., and Fumal, T.E. Equations for estimating horizontal response spectra and peak acceleration from Western North American earthquakes: a summary of recent work. *Seism. Res. Lett.* 1997, 68(1), 128-153.
- Borcherdt, R. D. Effects of local geology on ground motion near San Francisco bay. *Seism. Soc. Am.* 1970, 60, 29-61.
- Borcherdt, R.; Glassmoyer, G.; Andrews, M.; Cranswick, E. Effect of site conditions on ground motion and damage. Earthquake spectra, Special supplement, *Armenia earthquake reconnaissance report*. 1989, 23-42.
- Carver, D.; Hartzell, S. H. Earthquake site response in Santa Cruz, California. *Bull. Seism. Soc. Am.* 1996, 86, 55-65.
- Castro, R.R.; Mucciarelli, M.; Pacor, F.; Petrongaro, C. S-wave site-response estimates using horizontal-to vertical spectral ratios *Bull. Seism. Soc. Am.* 1997, 87(1), 256-260.
- Chávez-García, F. J.; Cuenca, J. Site effects and microzonation in Acapulco. *Earthquake Spectra*. 1998, 14(1), 75-93.
- Chávez-García, F.J.; Domínguez, T.; Rodríguez, M.; Pérez, F. Site effects in a volcanic environment: A comparison between HVSR and array techniques at Colima, Mexico. *Bull. Seism. Soc. Am.* 2007, 97(2), 591-604.
- D'amico, V.; Picozzi, M.; Albarello, D. Quick estimates of soft sediments thickness from ambient noise horizontal to vertical spectral ratios; a case study in southern Italy. *Journal of Earthquake Engineering*. 2004, 8(6), 895-908.
- Darragh, R. B.; Shakal, A. F. The site response of two rock and soil station pairs to strong and weak motion. *Bull. Seism. Soc. Am.* 1991, 81, 1885-1889.
- Delgado, J.; López Casado, C.; Giner, J.; Estévez, A.; Cuenca, A.; Molina, S. Microtremors as a exploration tool: application and limitations. *Pure and Applied Geophysics*. 2000, 157, 1445-1462.
- Dravinski, M.; Ding, G.; Wen, K.-L. Ground motion amplification in the San Fernando Valley from dense array measurements of microtremors. *5th International Conference on Seismic Zonation*, Nice, France. 1995, 723-730.
- Dravinski, M.; Ding, G.; Biswas, N. N. Site amplification factor in Anchorage, Alaska based on long period microtremors. *Journ. of Earth. Eng.* 2003, 7 (4), 555-571.

- Enomoto T.; Kuriyama, T.; Abeki, N.; Iwatate, T.; Navarro, M.; Nagumo, M. Study on microtremor characteristics based on simultaneous measurements between basement and surface using borehole. *Proc. of 12th World Conference on Earthquake Engineering*, Auckland, New Zealand. 2000, 1522, 8.
- Field, E. H.; Hough, S. E.; Jacob, K. H. Using microtremors to assess potential earthquake site response: a case study in flushing meadows, New York City. *Bull. Seism. Soc. Am.* 1990, 80, 1456-1480.
- Field, E. H.; Jacob, K. H.; Hough, S. E. Earthquake site response estimation: a weak-motion case study. *Bull. Seism. Soc. Am.* 1992, 82, 2283-2306.
- Field, E. H.; Jacob, K. H. A comparison and test of various site-response estimation techniques, including three that are not reference-site dependent. *Bull. Seism. Soc. Am.* 1995, 85, 1127-1143.
- Fleischer, L.; Gafsou, R. *Top Judea Group – digital structural map of Israel*. The Geophysical Institute of Israel; Rprt 753/312/2003.
- García-Jerez, A.; Luzón, F.; Navarro, M.; Pérez-Ruiz, A. Characterization of the sedimentary cover of the Zafarraya basin, Southern Spain by means of ambient noise. *Bull. Seism. Soc. Am.* 2006, 96(3), 957-967.
- Gaull, B. A.; Kagami, H.; Taniguchi, H. The microzonation of Perth, Western Australia, using microtremor spectral ratio. *Earthquake Spectra*. 1995, 11, 173-191.
- Gill, D. The subsurface geology of the Petah Tikva area. M.Sc.Thesis. Heb. Univ. Jerusalem. 1965.
- Hamdache, M.; Palaez, J.A.; Yelles-Chauche, A.K. The Algiers, Algeria Earthquake (Mw 6.8) of 21 May 2003. Preliminary Report. *Seism. Research Letters*. 2004, 75(3), 360-367.
- Hartzell, S. H.; Leeds, A.; Frankel, A.; Michael, J. Site response for urban Los Angeles using aftershocks of the Northridge earthquake. *Bull. Seism. Soc. Am.* 1996, 86, 168-192.
- Hartzell, S. Variability in nonlinear sediment response during the 1994 Northridge, California. Earthquake. *Bull. Seism. Soc. Am.* 1998, 88, 1426-1437.
- Hinzen, K-G.; Weber, B.; Scherbaum, B. On the resolution of H/V measurements to determine sediment thickness, a case study across a normal fault in the lower Rhine embayment, Germany. *Journal of Earthquake Engineering*. 2004, 8 (6), 909-926.
- Hofstetter, A.; van Eck, T.; Shapira, A. Seismic activity along fault branches of the Dead Sea-Jordan transform system: The Carmel-Tirtza fault system. *Tectonophysics*. 1996, 267, 317-330.
- Horike, M.; Zhao, B.; Kawase, H. Comparison of site response characteristics inferred from microtremors and earthquake shear wave. *Bull. Seism. Soc. Am.* 2001, 91, 1526-1536.
- Hough, S. E.; Friberg, P.A.; Busby, R.; Field, E. F.; Jacob K.H.; Borchardt R.D. Sediment-induced amplification and the collapse of the Nimitz Freeway. *Nature*. 1990, 344, 853-855.
- Ibs-von Seht, M.; Wohlenberg J. Microtremor measurements used to map thickness of soft sediments. *Bull. Seism. Soc. Am.* 1999, 89, 250-259.
- Iwata, T.; Hatayama, K.; Kawase H.; Irikura K. Site amplification of ground motions during aftershocks of the 1995 Hyogo-ken Nanbu Earthquake in several damaged zone – array observation of ground motions at Higashinada ward, Kobe city, Japan. *Journal of Physics of the Earth*. 1996, 44(5), 553-61.

- Jarpe, S. P.; Cramer, C. H.; Tucker, B. E.; Shakal, A. F. A comparison of observations of ground response to weak and strong motion at Coalinga, California. *Bull. Seism. Soc. Am.* 1988, 78, 421-435.
- Jarpe, S. P.; Hutchings, L. J.; Hauk, T. F.; Shakal, A. F. Selected strong- and weak-motion data from the Loma Prieta earthquake sequence. *Seism. Research Letters.* 1989, 60(4), 167-176.
- Jenkins, M. G.; Watts, D. G. Spectral analysis and its applications; Holden-Day: San Francisco, CA, 1968.
- Kagami, H.; Duke C.M.; Liang, G.C.; Ohta, Y. Observation of 1- to 5-second microtremors and their application to earthquake engineering. Part II. Evaluation of site effect upon seismic wave amplification deep soil deposits. *Bull. Seism. Soc. Am.* 1982, 72, 987-998.
- Kanai, K.; Tanaka, T. On microtremors VIII. *Bull. Earthquake Res. Inst.* 1961, 39, 97-114.
- Katz, L. J. Microtremor analysis of local geological conditions. *Bull. Seism. Soc. Am.* 1976, 66, 45-60.
- Katz, L. J.; Bellon, R.S. Microtremor site analysis study at Beatty, Nevada. *Bull. Seism. Soc. Am.* 1978, 68, 757-565.
- Kobayashi, H. Application of microtremors measurements for urban planning. *Proceedings of 5th International Conference on Seismic Zonation*, Nice, France. 1995, October 17-19, 778-785.
- Kobayashi, K.; Uetake, T.; Mashimo, M.; Kobayashi, H. 2000. Estimation of deep underground velocity structures by inversion of spectral ratio of horizontal to vertical component in p-wave part of earthquake ground motion. *Proc. of 12th World Conference on Earthquake Engineering*, Auckland, New Zealand. 2000, 2658, 9.
- Kudo, K. Practical estimates of site response. State-of-art Report. *Proceedings of 5th International Conference on Seismic Zonation*, Nice, France, October 17-19. 1995, 1878-1907.
- Lachet, C.; Hatzfeld, D.; Bard, P-Y.; Theodulidis, N.; Papaioannou, C.; Savvaidis, A. Site effects and microzonation in the City of Thessaloniki (Greece). Comparison of different approaches. *Bull. Seismol. Soc. Am.* 1996, 86 (6), 1692-1703.
- Langston, C. A. Structure under Mount Rainier, Washington, inferred from teleseismic body waves. *J. Geophys. Res.* 1979, 84, 4749-4762.
- Lebrun, B.; Duval, A-M.; Bard, P-Y.; Monge, O.; Bour, M.; Vidal, S.; Fabriol, H. Seismic microzonation: A comparison between geotechnical and seismological approaches in Pointe-à-Pitre (French West Indies). *Bull. of Eart. Engin.* 2004, 2, 27-50.
- Lermo, J.; Chávez-García, F. J. Site effect evaluation using spectral ratios with only one station. *Bull. Seism. Soc. Am.* 1993, 83, 1574-1594.
- Lermo, J.; Chávez-García, F. J. Are microtremors useful in site response evaluation? *Bull. Seism. Soc. Am.* 1994, 84, 1350-1364.
- Lermo, J.; Rodriguez, M.; Singh, S.K. 1988. The Mexico earthquake of September 19, 1985: natural period of sites in the valley of Mexico from microtremor measurements and from strong motion data. *Earthquake Spectra.* 4, 805-814.
- Liu, H. -P.; Warrick, R. E.; Westerlund, R. E.; Sembera, E. D.; Wennerberg, L. Observation of local site effects at a downhole-and-surface station in the marina district of San Francisco, *Bull. Seism. Soc. Am.* 1992, 82, 1563-1591.
- Malagnini, L.; Tricarico, P.; Rovelli, A. ; Herrmann, R. B.; Opice, S.; Biella G.; de Franco, R. Explosion, earthquake, and ambient noise recording in a pliocene sediment-filled valley:

- inferences on seismic response properties by reference- and non-reference-site techniques. *Bull. Seism. Soc. Am.* 1996, 86, 670-682.
- Maresca, R.; Galluzzo, D.; Del Pezzo, E. H/V spectral ratio and array techniques applied to ambient noise recorded in the Colfiorito basin, Central Italy. *Bull. Seism. Soc. Am.* 2006, 96(2), 490-505.
- McGarr, A.; Celebi, M.; Sembera, E.; Noce, T.; Mueller, C. Ground motion at the San Francisco international airport from the Loma Prieta earthquake, sequence. *Bull. Seism. Soc. Am.* 1991, 81, 1923-1944.
- Morales, J.; Vidal, V.; Peña, J. A.; Alguacil, G.; Iwañez, J.M. Microtremor study in the sediment-filled basin of Zavarraza, Genada (southern Spain). *Bull. Seism. Soc. Am.* 1991, 81, 2, 687-693.
- Mucciarelli, M. Reliability and applicability of Nakamura's technique using microtremors: an experimental approach. *Journal of Earthquake Engineering.* 1998, 4, 625-638.
- Mucciarelli, M.; Gallipoli, M. R. The HVSR technique from microtremor to strong motion: empirical and statistical considerations. *Proc. of 13th World Conference of Earthquake Engineering*, Vancouver, B.C., Canada. 2004, Paper 45.
- Murphy, C.; Eaton, D. Empirical site response for POLARIS stations in Southern Ontario, Canada. *Seismological Research Letters.* 2005, 76, 1, 99-109.
- Nakamura, Y. A method for dynamic characteristics estimation of subsurface using microtremor on the ground surface. *Quarterly Report of Railway Technical Research.* 1989, 30(1), 25-33.
- Ohta, Y.; Kagami, H.; Goto, N.; Kudo, K. Observation of 1 to 5 second microtremors and their application to earthquake engineering. Part I: Comparison with long period accelerations at the Tokachi-Oki earthquake of 1968. *Bull. Seism. Soc. Am.* 1978, 68, 767-779.
- Ozel, O.; Cranswick, E.; Meremonte, M.; Erdik, M.; Safak, E. Site effects in Avcilar, west of Istanbul, Turkey, from strong-and weak-motion, *Bull. Seism. Soc. Am. (Special Issue).* 2002, 92(1), 499-508.
- Parolai, S.; Bormann, P.; Milkereit, C. Assessment of the natural frequency of the sedimentary cover in the Cologne area (Germany) using noise measurements. *Journal of Earth. Engin.* 2001, 5(4), 541-564.
- Parolai, S.; Bormann, P.; Milkereit, C. New relationship between VS, thickness of sediments, and resonance frequency calculated by the H/V ratio of seismic noise for the Cologne area (Germany), *Bull. Seism. Soc. Am.* 2002, 92 (6), 2521-2527.
- Parolai, S.; Galiano-Merino, J.J. Effect of transient seismic noise on estimates on H/V spectral ratios. *Bull. Bull. Seism. Soc. Am.* 2006, 96, 228-236.
- Perelman, N.; Zaslavsky, Y. Analysis of seismic signals in frequency domain, (SEISPECT). GII Report 569/345/01. 2001.
- Pergalani, F.; Pomeo, R. ; Luzi, L. ; Petrini, V. ; Pugliese, A. ; Sano, T. Criteria for seismic microzoning of a large area in central Italy. *Proc. of 12th World Conf. of Eart. Eng.,* Auckland. January, 2000. CD-Rom
- Pratt, T. L.; Brocher, T. M. Site response and attenuation in the Puget Lowland, Washington state. *Bull. Seism. Soc. Am.* 2006, 96, 536-552.
- Reinoso, E.; Ordaz, M. Spectral amplification for Mexico City from free-field recordings, *Earthquake Spectra.* 1999, 15 (2), 273-295.

- Rovelli, A.; Singh S. K.; Malagnini, L.; Amato, A.; Cocco, M. Feasibility of the use microtremors in estimating site response during earthquakes: some test in Italy. *Earthquake Spectra*. 1991, 7, 551-561.
- Satoh, T.; Sato, T.; Kawase, H. Nonlinear behavior of soil sediments identified by using borehole records observed at the Ashigara valley, Japan. *Bull. Seism. Soc. Am.* 1995, 85, 1821-1834.
- Satoh, T.; Kawase, H.; Matsushima, S. Difference between site characteristics obtained from microtremors, S-wave, P-waves, and codas. *Bull. Seism. Soc. Am.* 2001, 91, 313-334.
- Schnabel, P.B.; Lysmer, J.; Seed, H.B. SHAKE – a computer program for earthquake response analysis of horizontal layered sites. 1972; Rpt. EERC 71-12, Earthquake Engineering Research Center, Berkeley, CA.
- Seekins, L. C.; Wennerberg, L.; Margheriti, L.; Liu, Hsi-Ping. Site amplification at five locations in San Francisco, California: a comparison of S waves, codas and microtremors, *Bull. Seism. Soc. Am.* 1996, 86, 627-635.
- Shapira, A.; Avirav, V. PS-SDA *Operation Manual*. 1995, IPRG Rpt. Z1/567/79.
- Shapira, A.; Avni, R.; Nur, A. A new estimate for the epicenter of the Jericho earthquake of 11 July 1927. *Isr. Journ. Earth Sci.*, 1993, 93-96.
- Shapira, A. and van Eck, T. Synthetic uniform hazard site specific response spectrum. *Natural Hazard*. 1993, 8, 201-205.
- Shapira, A.; Feldman L.; Zaslavsky, Y.; Malitzky, A. Application of a stochastic method for the development of earthquake damage scenarios: Eilat, Israel test case. The Problems of Lithosphere Dynamics and Seismicity, *Computational Seismology*. 2001, 32, 58-73.
- Singh, S. K.; Lermo, J.; Dominguez, T.; Ordaz, M.; Espinosa, J. M.; Mena, E.; Quaas, R. A study of amplification of seismic waves in the Valley of Mexico with respect to a hill zone site. *Earthquake spectra*. 1988, 4, 653-673.
- Singh, S. K.; Mena E.; Castro, R. Some aspects of source characteristics of the 19 September 1985 Michoacán earthquakes and ground motion amplification in and near Mexico City from strong motion data. *Bull. Seism. Soc. Am.* 1988, 78, 451-477.
- Sneh, A.; Rosensaft M. Geological map of Kefar Sava 1:50 000. 1993, Sheet 8-1.
- Steidl J. H.; Tumarkin, A.G.; Archuleta R. J. What is reference site? *Bull. Seism. Soc. Am.* 1996, 86, 1733-1748.
- Tanaka, T.; Kanai, K.; Osada, K.; Leeds D. J. Observation of microtremors. XII. (Case of the U.S.A.) *Bull. of the Earth. Research Inst.* 1968, 46, 1127-1147.
- Teves-Costa, P.; Matias, L.; Bard, P.-Y. Seismic behavior estimation of thin alluvium layers using microtremor recordings, *Soil Dynamics and Earthquake Engineering*. 1996, 15, 201-209.
- Teves-Costa, P.; Senos M.L. Estimating site effects using microtremor measurements and analytical modeling – application to the Lower Tagus valley, Portugal. *Proc. of 12th World Conference on Earthquake Engineering*, Auckland, New Zealand. 2000, 1250, 8.
- Theodulidis, N.; Bard, P.Y.; Archuleta, R.; Bouchon, M. Horizontal-to-vertical spectral ratio and geological conditions: the case of Garner valley downhole in Southern California. *Bull. Seism. Soc. Am.* 1996, 68, 767-779.
- Toshinawa, T.; Taber J. J.; Berrill, J. B. 1997. Distribution of ground motion intensity inferred from questionnaire survey, earthquake recordings, and microtremor measurements- a case study in Christchurch, New Zealand, during 1994 Arthurs pass earthquake. *Bull. Seism. Soc. Am.*, **87**, 356-369.

- Tucker, B. E.; King, J. L. Dependence of sediment-filled valley response on input amplitude and valley properties. *Bull. Seism. Soc. Am.* 1984, 74, 153-165.
- Yamanaka, H.; Takemura, M.; Ishida, H.; Niva, M. Characteristics of long-period microtremors and their applicability in exploration of deep sedimentary layers. *Bull. Seism. Soc. Am.* 1994, 84, 1831-1841.
- Yamazaki, F.; Ansary, A.A. Horizontal-to-vertical spectral ratio of earthquake ground motion for site characterization. *Earthquake Engineering and Structural Dynamics*. 1997, 26, 671-689.
- Zaslavsky, Y. Analysis of microseisms at the Dushanbe seismological observatory, *Instruments and methods of earthquake registration (Moscow)*. 1987, 19, 152-157.
- Zaslavsky, Y.; Gitterman, Y.; Shapira, A. Site response estimations using weak motion measurements. Proceedings of 5th International Conference on Seismic Zonation, Nice, France, October 17-19. 1995, 1713-1722.
- Zaslavsky, Y.; Shapira, A.; Arzi, A. Amplification effects from earthquakes and ambient noise in Dead Sea Fault (Israel). *Soil Dynamics and Earthquake Engineering*, 2000, 20, 187-207.
- Zaslavsky, Y.; Shapira, A.; Arzi, A.. Earthquake site response on hard rock – empirical study. *Proceeding of 5 the International Conference on analysis of Discontinuous Deformation*, ICADD, 6-10 October, Beer-Sheba, Israel. 2002, 133-144.
- Zaslavsky, Y.; Shapira, A.; Gorstein, M.; Kalmanovich, M. Estimation of site effects in the Israel seacoast area by ambient noise records for microzonation. *Proceeding of 5th International Conference on Case Histories in Geotechnical Engineering*, New York, April 13-17. 2004, 12A-4.
- Zaslavsky, Y.; Shapira, A.; Gorstein, M.; Kalmanovich, M.; Giller, V.; Perelman, N.; Livshits, I.; Giller D.; Dan, I. Site response from ambient vibrations in the towns Lod and Ramle (Israel) and earthquake hazard assessment. *Bulletin of Earthquake Engineering*. 2005, 3(3), 355-381.
- Zaslavsky, Y.; Ataev, G.; Gorstein, M.; Kalmanovich, M.; Hofstetter, A.; Perelman, N.; Aksinenko, T.; Giller, V.; Dan H.; Giller, D.; Livshits I.; Shvartsburg, A.; Shapira A. Microzoning of site response parameters in the towns of Dimona and Bet Shean (Israel). *Bollettino di Geofisica, Teorica e Applicata* 2008, 109-130.

*Chapter 7*

**SEISMIC RESISTANT BRACED FRAME  
STRUCTURES WITH SHAPE  
MEMORY ALLOY-BASED  
SELF-CENTERING DAMPING DEVICE**

*Yunfeng Zhang<sup>1,\*</sup> and Songye Zhu<sup>2</sup>*

<sup>1</sup>Department of Civil & Environmental Engineering, University of Maryland,  
College Park, MD, USA

<sup>2</sup>Department of Civil & Structural Engineering, The Hong Kong Polytechnic University,  
Hung Hom, Kowloon, Hong Kong

**Abstract**

This article deals with seismic resistant braced frame structures with a special type of bracing element termed self-centering friction damping brace (SFDB). The SFDB provides a passive form of energy dissipation with its core re-centering component made of stranded superelastic shape memory alloy (SMA) wires while enhanced energy dissipation mechanism is provided through friction. Superelastic Nitinol is selected as the SMA material for SFDB because of its superb superelastic property and excellent fatigue life. The mechanical property of superelastic Nitinol wires was experimentally investigated through a series of uniaxial cyclic tests. The fatigue life and the effect of loading rate and ambient temperature are studied as a part of the experimental program. Three types of constitutive models for superelastic SMAs with increasing complexity and modeling details are discussed. Based on the calibrated constitutive model for superelastic Nitinol wires, analytical model for SFDB has been developed to simulate the unique flag-shaped hysteresis of SFDB. The seismic performance of SFDB frames is evaluated through nonlinear pushover and time history analysis of two prototype buildings—a 3-story and a 6-story concentrically braced frames, at different seismic intensity levels. A displacement-based design procedure for SFDB frame is also presented, in which SFDBs are proportioned based on the target performance level under design basis earthquakes. The simulation results demonstrate that SFDB frame has a few desirable performance characteristics such as minimal residual drift after frequent and design basis earthquakes due to its self-centering capability. SFDB frame has the potential to withstand

---

\* E-mail address: zyf@umd.edu; Tel: (301) 405-1955; Fax: (301) 405-2585 (Corresponding author)

several design basis earthquakes without the need for repair or replacement of SFDB if properly designed.

## 1. Introduction

In the past decade, passive dampers that utilize shape memory alloys (SMA) for energy dissipation have been attracting growing interest in civil engineering, particularly for seismic hazard mitigation application (e.g., Graesser and Cozzarelli 1991; Aiken et al. 1992, 1993; Witting and Cozzarelli 1992; Clark et al. 1995; Whittaker et al. 1995; Higashino 1996; Wilde et al. 2000; Dolce et al. 2000, 2005; Castellano et al. 2001; Ocel et al. 2004; DesRoches et al. 2004; Zhang and Zhu 2007; Zhu and Zhang 2008). For example, Krumme et al. (1995) have developed a SMA damping device termed center-tapped device for passive control of the dynamic response of civil structures. The center-tapped device comprises a simple slider mechanism in which resistance to linear sliding is provided by two pairs of opposed SMA tension elements. Whittaker et al (1995) developed two conceptual designs for SMA dampers, the effectiveness of which to mitigate the seismic hazard was demonstrated by the nonlinear time history analysis of an existing reinforced concrete frame retrofitted using these SMA dampers under moderate earthquake ground motions. Dolce et al. (2000) tested Nitinol-based devices with full re-centering and good energy dissipation capabilities. Their experimental results have shown that SMA braces can provide a performance level at least comparable to those of steel braces, while having an additional self-centering feature. In Italy, superelastic SMA damping devices have also been implemented in several masonry cultural heritage structures to enhance their seismic resistance capacities during recent restoration (Castellano et al. 2001; Indirli et al. 2001). DesRoches and Delemont (2002) have tested the efficacy of superelastic NiTi bars as bridge restrainers to reduce the risk of collapse from unseating of bridge superstructures at the hinges. Additionally, two full-scale partially restrained steel beam-column connections using SMA bars for providing additional energy dissipation were tested by Ocel et al. (2004). The connection consists of four large diameter Nitinol SMA bars connecting the beam flange to the column flange and serve as the primary moment transfer mechanism. The connections exhibited a high level of energy dissipation, large ductility capacity, and no strength degradation after being subjected to cycles up to 4% drift.

New trends in seismic design have resulted in proposals of several innovative seismic protection strategies, among which buckling-restrained braces (BRB) and the concept of self-centering system have recently received a great deal of attention. BRB, which are capable of yielding in both tension and compression, have been developed to overcome the buckling problems of conventional braces in concentrically braced frame (CBF) systems (Clark et al. 1999; Sabelli et al. 2003; Fahnestock et al. 2003; Uang et al. 2004). In comparison with conventional CBFs, BRB frames have much more ductile performance and a larger energy dissipating capacity, and thus are desirable for seismic design and rehabilitation. BRBF has been used extensively for seismic applications in Japan after the 1995 Kobe earthquake (Reina and Normile 1997) and is quickly gaining popularity in the US after the 1994 Northridge earthquake. However, some researchers have identified several potential problems for BRBF (Sabelli et al. 2003; Kiggins and Uang 2004) including large residual story drifts that could be as high as 40% to 60% of the peak drifts (Sabelli et al. 2003) and tendency of

BRBs to yield at frequent earthquakes under which continued occupancy might be expected. Additionally, about 10% difference exists between the tensile and compressive capacities of BRB. This raises issues of the beam design in chevron-braced configurations which is often governed by the unbalanced forces in the braces (Sabelli et al. 2003).

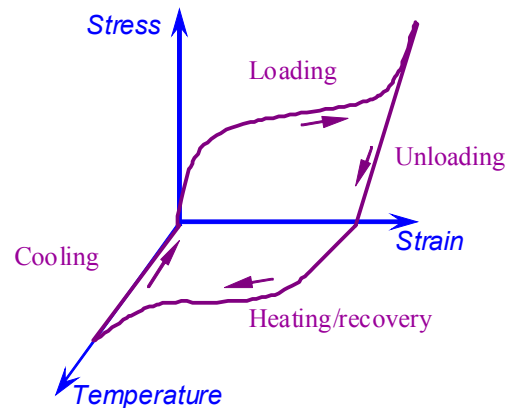
Recently, an alternative seismic resisting system with self-centering behavior has attracted considerable interests (e.g., Stanton et al 1997; Cheok et al 1998; Kurama et al. 1999; Ricles et al. 2001; Christopoulos et al. 2002a; Lee and Billington 2006; Sakai et al 2006). A flag-shaped hysteresis loop is typical of such self-centering systems with energy dissipation capability. Self-centering systems can be achieved by utilizing post-tensioning, special energy dissipating dampers or special material such as SMAs. Researchers in US (Stanton et al 1997; Ricles et al 2001; Christopoulos et al. 2002b; Garlock et al. 2005; Restrepo 2006; Sakai et al 2006) have studied a family of post-tensioned systems with self-centering capabilities, such as steel frame system with post-tensioned moment connections. In general, these systems use gap-opening behavior at selected critical joints between main structural members, along with complementary energy dissipation elements, to provide nonlinear softening behavior, ductility, and energy dissipation without significant inelastic deformation and related damage to the main structural members. Elastic restoring forces are provided by post-tensioning at these joints return the structure to its original position. Self-centering systems have the ability to control damage and to reduce (or even eliminate) residual structural deformation after strong earthquake events. It is worth noting that residual structural deformation is emphasized as a fundamental complementary parameter in the evaluation of structural (and non-structural) damage in performance-based seismic design and assessment approaches (Pampanin et al. 2003). Special metals such as superelastic SMAs inherently possess the self-centering hysteresis behavior.

This article presents the seismic behavior and design of steel CBF buildings with a special type of bracing element termed self-centering friction damping brace (SFDB). SFDB is capable of re-centering itself because of the use of superelastic SMA wire strands and features enhanced energy dissipation capacity through friction. SFDB would be typically installed in a CBF building as part of the bracing system which resists lateral seismic loads. A brief introduction of the material properties of superelastic SMA are described first in this paper, followed by a discussion of three types of constitutive models for superelastic SMAs with increasing complexity and modeling details. Next, seismic analysis and design of buildings with SFDB is presented, including the configurations of SFDB and a displacement-based design procedure for buildings with such SMA-based damping devices. The results of the nonlinear pushover analysis and time history analysis in this study suggest that SFDB frame can achieve a seismic response level comparable to that of other CBF systems (e.g., buckling-restrained-braced frame) while having significantly reduced residual drifts under design basis earthquakes.

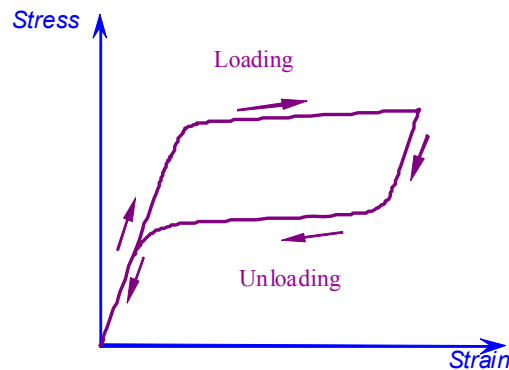
## 2. Mechanical Properties of SMA

Shape memory alloys (SMA) refer to a unique group of alloys with the ability to return to some pre-defined shape when subjected to an appropriate thermal-mechanical procedure. This shape recovery is due to a micromechanical phase transformation in the material that can be either temperature- or stress-induced. SMAs generally demonstrate two types of

unique behavior at different temperatures. For example, at ambient temperatures  $T < M_f$ , where  $M_f$  refers to martensite finish temperature, the microstructure of SMA materials is fully martensitic and SMA exhibits a large hysteresis loop similar to other conventional metal alloys such as mild steel, but the residual deformation after unloading can be fully recovered by an increase in temperature (as shown in Figure 1-(a)). This shape recovery effect is called shape memory effect, which is due to a micromechanical phase transformation from the martensite phase to the parent austenite phase. Another important characteristic of SMA materials is called superelasticity or pseudoelasticity, which involves rate-dependent hysteresis damping with zero residual strain upon unloading. SMA exhibits the superelastic behavior at ambient temperatures  $T > A_f$ , where  $A_f$  is termed austenite finish temperature, above which the microstructure of SMA is fully austenitic. The superelastic behavior of SMA is due to a stress-induced solid phase transformation from austenite to martensite. Since martensite is stable only at the presence of the externally applied load, a reverse transformation takes place upon unloading, and after fully unloading, the material will return to its original undeformed shape (as shown in Figure 1-(b)).



(a) Shape memory effect



(b) Superelastic effect

Figure 1. Typical hysteresis shape of shape memory alloy.

Among several available SMAs, the most common one that has received considerable interests in industrial applications is the alloy of nickel and titanium called Nitinol, which exhibits good hysteresis damping effect, outstanding fatigue properties and excellent corrosion resistance. The transformation temperatures of Nitinol such as the aforementioned  $M_f$  and  $A_f$  can be adjusted in the range from less than  $-100^\circ\text{C}$  to over  $100^\circ\text{C}$ . Nitinol alloys tend to have much higher corrosion resistance and ductility and excellent fatigue performance (both low-cycle and high-cycle fatigue), compared to other SMA materials. The prominent properties of Nitinol materials have made them a promising candidate for use in energy dissipation device. Zhu (2007) studied the stress-strain relationship of superelastic Nitinol wires through a series of cyclic tests conducted under different loading rates and ambient temperatures. This section summarizes the test program and findings on the fatigue life, maximum recoverable strain, training, loading rate effect, temperature effect of superelastic Nitinol wires. These properties are of importance to the proposed civil engineering applications.

## 2.1. Test Program

Nitinol wires with a diameter of 0.58 mm (0.23 in) were cyclically tested using an MTS universal testing machine. In this experimental study, two types of Nitinol wires were acquired from two different manufacturers, designated as Type A and Type B wires respectively. Both types of Nitinol wires have a similar chemical composition (about 56% nickel and 44% titanium) that leads to exhibiting superelastic behavior at room temperature.

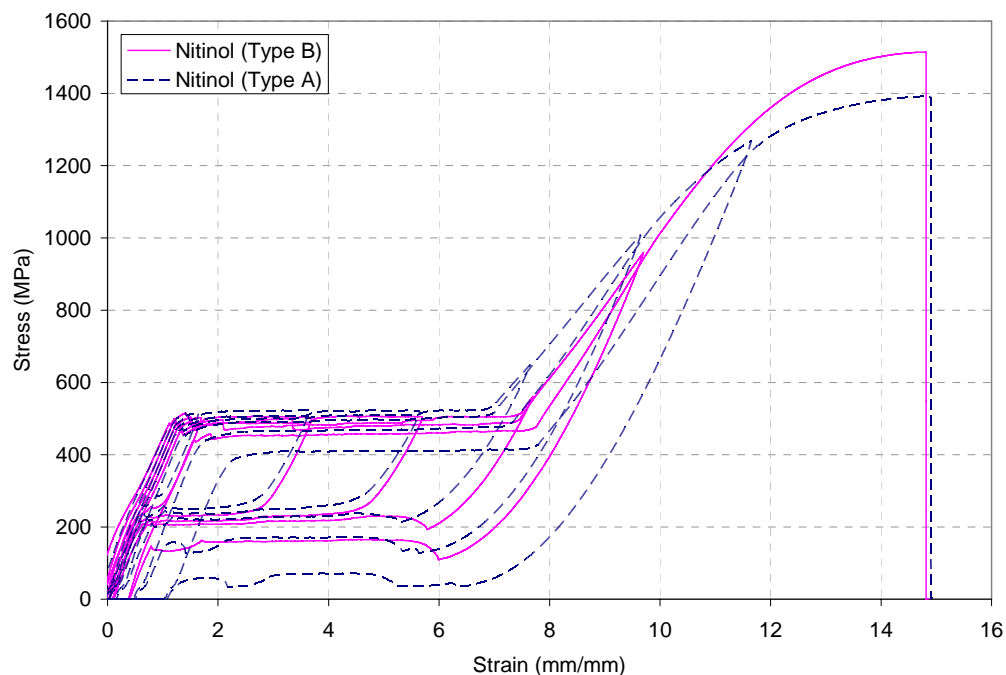


Figure 2. Cyclic quasi-static test of Nitinol wires at room temperature.

Figure 2 shows the stress-strain curves of both types of superelastic Nitinol wires from cyclic tests conducted at quasi-static loading rates. Figure 2 indicates that the superelastic Nitinol wires under test can regain its initial shape without permanent deformation when unloaded from strain amplitudes as high as 8%. This is because the yield-like plateau in Figure 2 is due to solid phase transformation in superelastic Nitinol rather than yielding. Therefore below 8% strain, no apparent damage is observed in superelastic Nitinol wires. Beyond 8% strain, strain hardening occurs in superelastic Nitinol wires and noticeable residual strains after unloading can be observed due to plastic deformation of Nitinol wires. The ultimate strain of both types of superelastic Nitinol wires can reach up to 15%, which provides a reasonably large safety margin to seismic application of Nitinol wires. The ultimate stress of both wires is about 1400-1500 MPa, which is almost three times the ‘yield’ stress (i.e., the forward transformation stress). Such a significant strain hardening behavior of superelastic Nitinol wires needs special attention when designing SMA-based energy dissipation device and may cause potential overloading to the adjoined members if not well accounted for.

The tests by Funakubo (1987) indicated that the high-cycle fatigue life of Nitinol under cyclic strain  $\epsilon_{\max} = 0.02$  can reach as high as  $1 \times 10^5$  cycles. Zhu and Zhang (2007a) tested the low-cycle fatigue life of Nitinol wires which is of more interest for seismic application. In their experiments, the superelastic Nitinol wire samples were tested under 8% strain cycles at a loading frequency of 1 Hz. All superelastic Nitinol wires tested can withstand over 2000 cycles under such 8% strain cycles.

In comparison with other SMAs, superelastic Nitinol wires have much higher fatigue life and larger recoverable strain level. These unique properties enable superelastic Nitinol wires to sustain several strong earthquakes without the need of repair or replacement of SMA-based energy dissipation device if carefully designed. This reusability can considerably reduce the repair cost after earthquakes and is very appealing from a life-cycle cost perspective.

## 2.2. Training of Nitinol Alloy

Figure 3 shows the change in mechanical properties of superelastic Nitinol wires with increasing number of load cycles. The wires were tested under 8% strain cycles with a loading frequency of 1 Hz. Observable changes for both types of wires include strain shift at zero stress (i.e., after unloading), decrease of ‘yield’ stress (i.e., forward transformation stress) and hysteresis area, and increase of ‘post-yield’ stiffness as seen from the first eighty loading cycles, although generally the degradation of Type A is more substantial than the Type B. However, after the first 50 to 80 load cycles the hysteresis behavior of superelastic Nitinol wires stabilizes to its steady-state hysteresis loop. These observations are consistent with the findings made by other researchers (e.g., Miyazaki 1990; McCormick et al. 2006). To overcome the potential problems in implementation that may arise from these observed degradation behaviors of superelastic SMA, training (i.e., cyclic preloading) of superelastic Nitinol wires should be performed before their use for energy dissipation device.

Figure 4 shows the hysteresis behavior of the superelastic Nitinol wires after 80 cycles of training with peak strain equal to 8%. The loading frequency was 2 Hz for this test. The displacement-controlled test process comprises four separate load sequences with different strain amplitudes, and within each load sequence the wire was cyclically loaded at constant

amplitude for over ten cycles. It is seen that stable hysteresis loops were obtained after training and no noticeable degradation effect such as residual deformation or change in transformation stress, were observed in the test results.

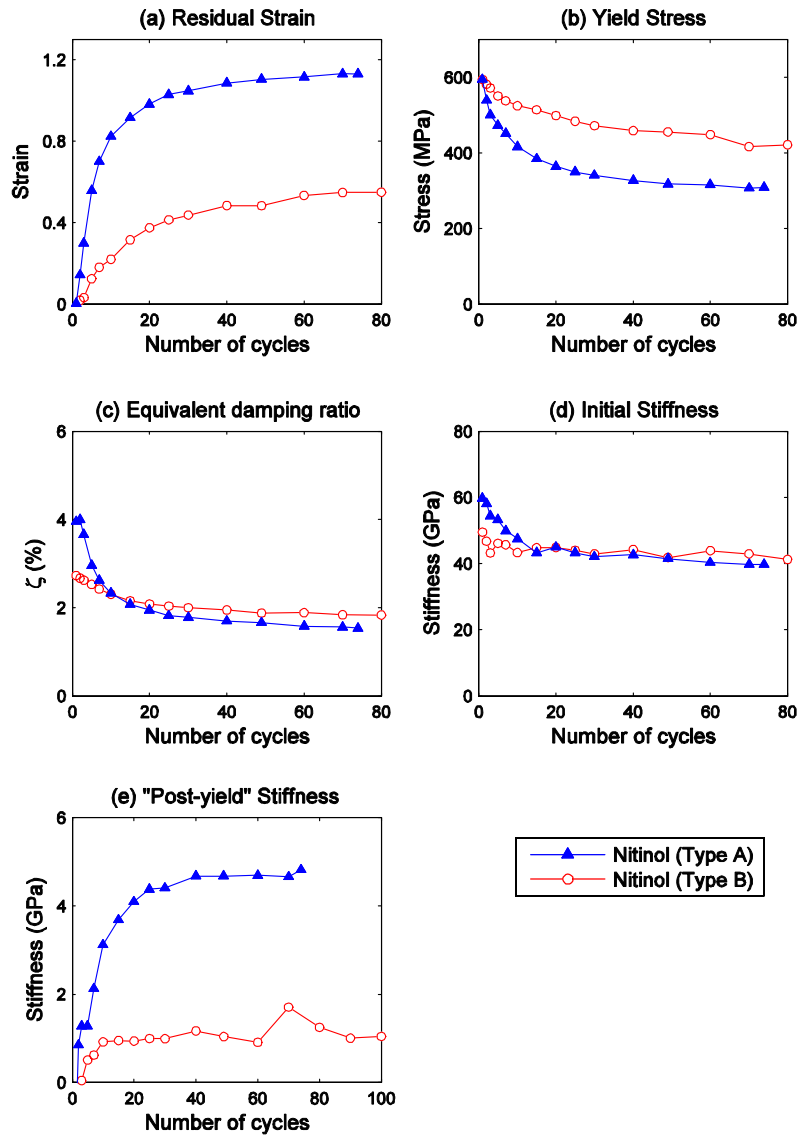


Figure 3. Change of mechanical behaviors of Nitinol wires with increasing number of load cycles.

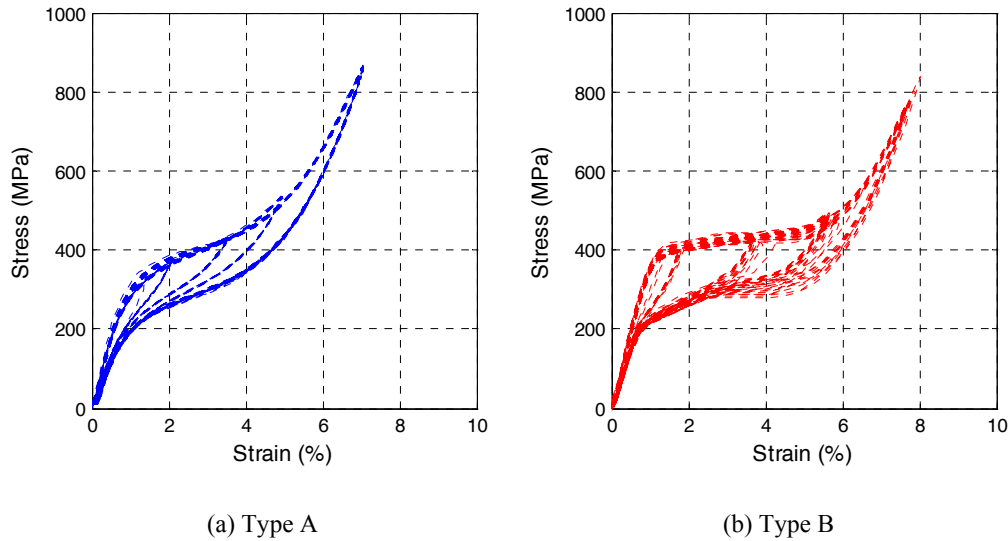


Figure 4. Stress-strain curve of trained superelastic Nitinol wires at 2-Hz loading frequency.

### 2.3. Loading Rate Effect

Most SMAs have a strong loading rate-dependence of mechanical properties, such as hysteresis shape, transformation stress, energy dissipation capacity and temperature rise. This section deals with the loading rate-induced thermal effect on superelastic Nitinol wires.

Zhu and Zhang (2007b) tested the superelastic Nitinol wires (Type A) under a variety of predetermined loading rates. Before the formal test, the Nitinol wires were trained with 80 cycles of preloading in order to minimize the accumulation of residual strain and stabilize its hysteresis behavior. The uniaxial tension test was carried out at six loading frequencies - 0.001 Hz, 0.01 Hz, 0.1 Hz, 1 Hz, 2 Hz and 5 Hz for constant 7% strain cycles. Figure 5 shows the stress-strain curve of superelastic Nitinol wires under these loading frequencies. During the cyclic test a K-type thermocouple with a diameter of 0.0254-mm (0.001 in) was mounted onto the test wire surface to measure its temperature. Figure 6 presents the experimental results of temperature variation in superelastic Nitinol wire specimens at three loading frequencies of 0.001 Hz, 0.01 Hz and 0.1 Hz respectively. Figure 6-(a), (b) and (c) show the temperature-strain profile for these three loading frequencies respectively, while Figure 6-(d) shows the corresponding time history of the wire specimen temperature. The temperature variation under higher loading frequencies was not measured due to the limitation of thermocouple measurement under dynamic loading. Torra et al (2007) performed a test of Nitinol wires with a diameter 2.46 mm under a loading frequency of 0.25 Hz. The strain cycle amplitude of their test was 0.032 and their measurement indicates that the temperature oscillation in the Nitinol wire specimen was about 15°C, which is consistent with the experimental data shown in Figure 6-(c).

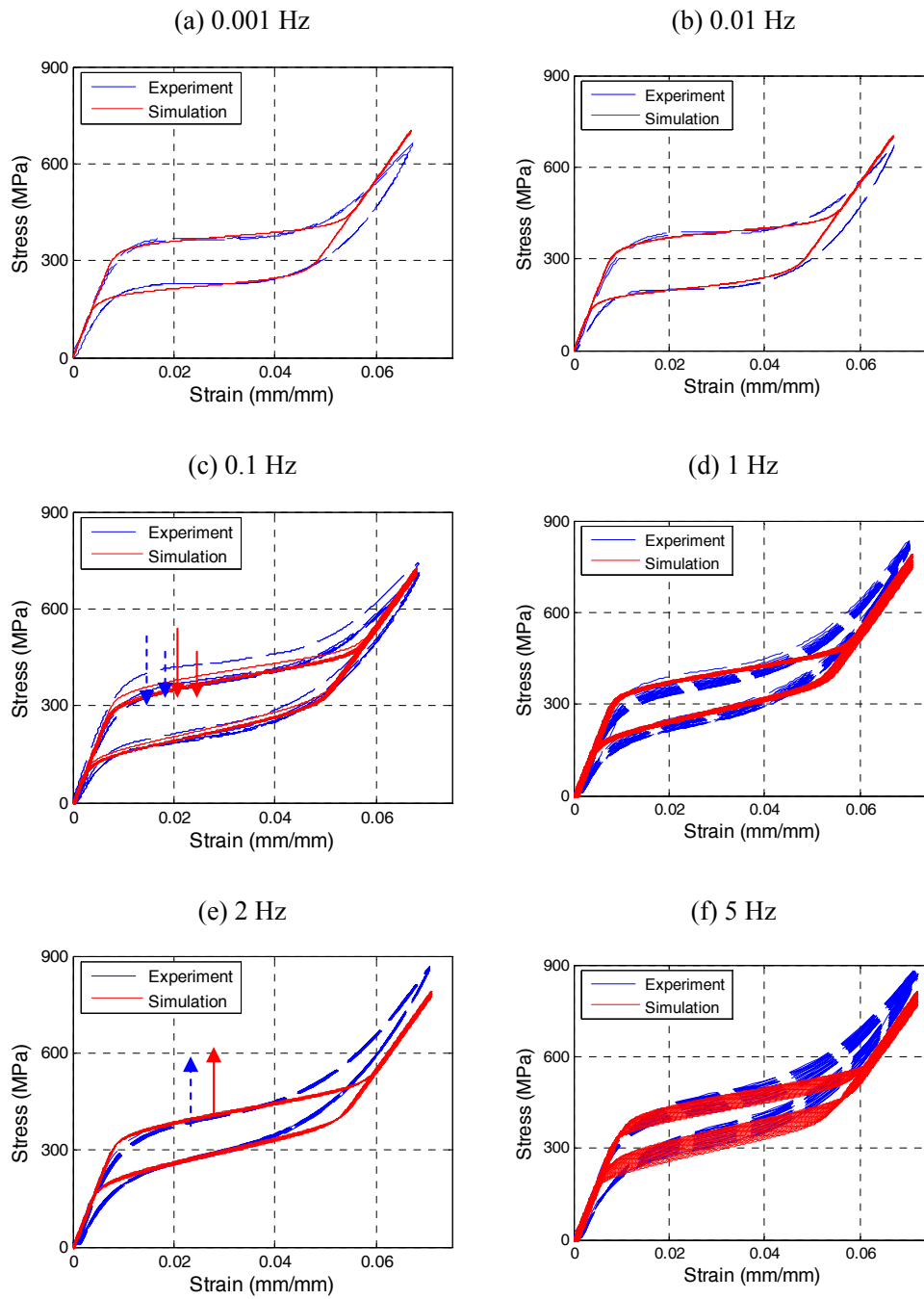


Figure 5. Stress-strain curves of Nitinol wires (Type A) at various loading frequencies.

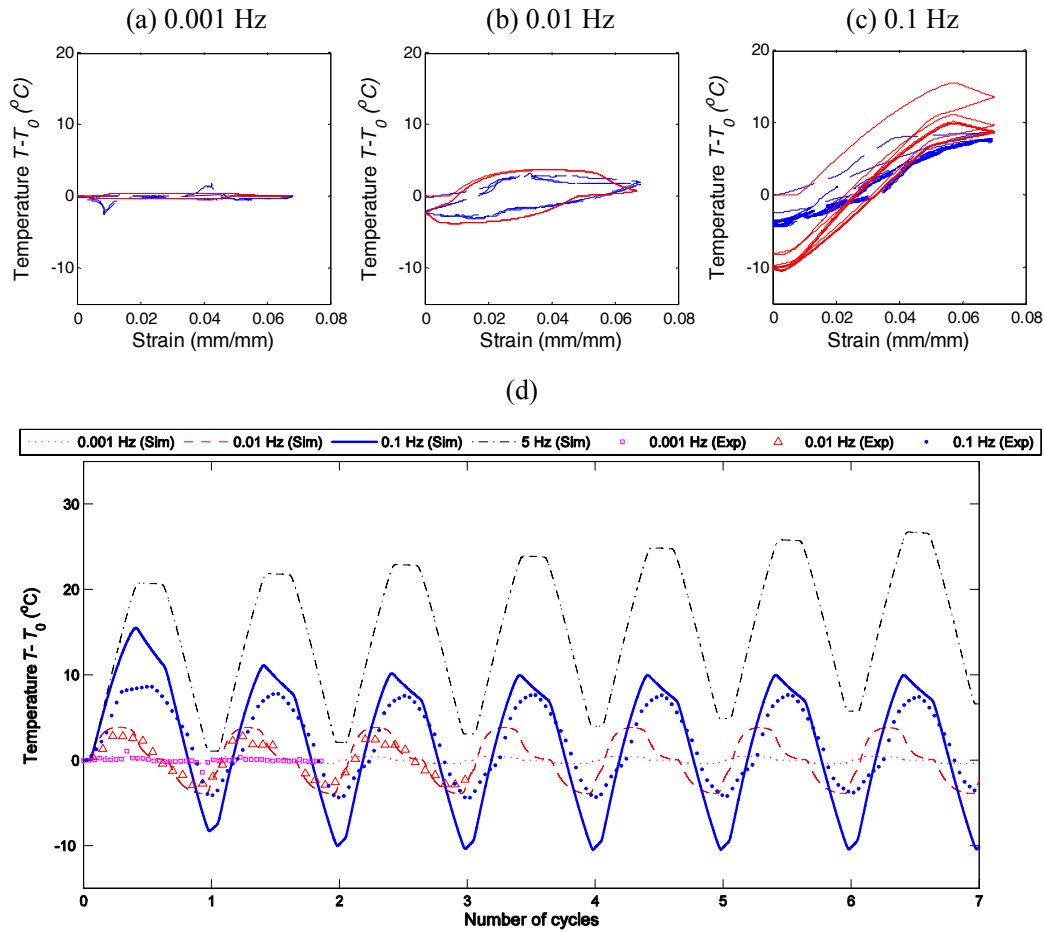


Figure 6. Experimental and simulated temperature variation of superelastic Nitinol wires (Type A) during the loading process.

The test with a loading frequency of 0.001 Hz was a quasi-static test. During the quasi-static test, the temperature change was negligible, and the slopes of both the upper and lower transformation plateau in the stress-strain curve are essentially horizontal. Compared with the quasi-static test results, the slope of the loading and unloading plateaus becomes increased and the amount of energy dissipation (i.e. the enclosed hysteresis area by each cycle) gets reduced for the tests with higher loading rates. The increased slope of loading/unloading plateau (or post-‘yield’ stiffness) which is often considered a favorable effect for seismic application is caused by the self-heating phenomena due to latent heat. The austenite to martensite phase transformation in the forward loading path is exothermic, while the martensite to austenite phase transformation in the unloading path is endothermic. Therefore, the loading path is accompanied with a rise in wire temperature while the unloading path is associated with a temperature drop (as shown in Figure 6). Such a temperature variation in each cycle results in the observed increase in the post-‘yield’ stiffness. For quasi-static tests, nonetheless, temperature fluctuation is negligible which leads to relatively flat transformation plateau.

It is also seen in Figure 5 that under certain loading rates the hysteresis loops of superelastic Nitinol wires are not stable in the first several load cycles. Compared with the first cycle, the hysteresis loops of the tenth cycle shift downwards for the loading frequencies of 0.1 Hz and 1 Hz, while the hysteresis loop shifts upwards for the loading frequency of 5 Hz; for the loading frequency of 2 Hz and quasi-static loading, the hysteresis loops of the first and following cycles are almost identical. The energy dissipation capacity is slightly reduced with the increasing number of loading cycles for all loading frequencies considered. It is noted that the tenth cycle of hysteresis loop is quite stable and repeatable in the subsequent cycles except for the loading frequency of 5 Hz. At the loading frequency of 5 Hz the successive loading after the tenth loading cycle makes the hysteresis loop continue to shift upwards.

The variation in the hysteresis shapes was attributed to the temperature change associated with the increasing number of loading cycles. According to energy equilibrium, the absorbed specific heat has to be equal to the latent heat generation and mechanical energy dissipation, subtracted by the heat loss to the surrounding environment. After superelastic Nitinol wire is fully unloaded, the latent heat generation should be equal to zero. If the heat generated by mechanical energy dissipation has different values than the heat loss in one cycle, the temperature at zero strain will be different at the start and end of this particular cycle. Such a variation of zero-strain temperature results in the shift of hysteresis loops with the increasing number of loading cycles until the mechanical energy dissipation is equal to the heat loss in one cycle, i.e., the temperature cycles get stabilized. For example, for the wire test results shown in Figure 5, the zero-strain temperature drops in the first several cycles for the loading frequencies of 0.1 Hz and 1 Hz, and rises for the loading frequency of 5 Hz. The zero-strain temperature does not differ much for the loading frequency of 2 Hz, which leads to quite repeatable hysteresis loops under this loading rate. Under the slow loading frequencies (0.001 Hz and 0.01 Hz), temperature variation is very small and the hysteresis loop is quite repeatable. As a result, such temperature cycles cause the shift of hysteresis loops correspondingly in the first several load cycles since the transformation stress is also dependent on the wire temperature.

#### 2.4. Temperature Effect

Zhu (2007) tested superelastic Nitinol wires at various temperatures in order to evaluate the temperature effect on their mechanical behavior. Figure 7 shows the hysteresis loops of the superelastic Nitinol wires at different test temperatures: 24°C (room temperature), 16°C, 8°C and 0°C. The wires were tested under a loading frequency of 1 Hz. Before formal tests, all Nitinol wire specimens were trained by 80 cycles of preloading at room temperature. It is seen that the hysteresis loop of superelastic Nitinol wires shift downwards with decreasing test temperatures. The stresses at 2% strain on both the forward transformation plateau and reverse transformation plateau were recorded, denoted as  $\sigma_U$  and  $\sigma_L$  respectively, and their variation pattern with the change of ambient temperature is shown in Figure 7-(b). A linear relationship can be observed between the stress and ambient test temperature.

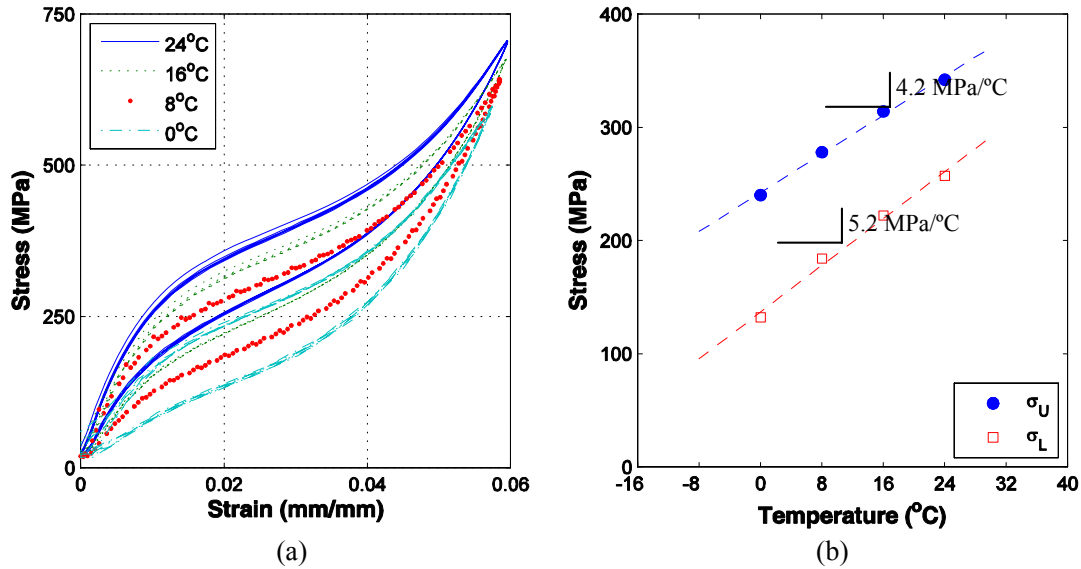


Figure 7. Temperature effect on the hysteresis behavior of superelastic Nitinol wires (Type A): (a) stress-strain curves at various ambient temperatures; (b) stress-strain relationship (where  $\sigma_U$  = stress on upper plateau corresponding 2% strain,  $\sigma_L$  = stress on lower plateau corresponding 2% strain).

The transformation stress of superelastic Nitinol alloy is observed to strongly depend on ambient temperature. The Nitinol wires tested in this study exhibits the superelastic behavior as long as the ambient temperature is above 0°C. However below 0°C they would be partially or completely martensite and lose their re-centering properties, namely, residual deformation would take place after unloading. Therefore, this type of Nitinol wires is not suitable for outdoor applications if its superelastic behavior is desired. Other superelastic SMA materials such as copper-based alloy (Zhang et al. 2008) are available for use in cold regions.

### 3. Constitutive Model for Superelastic SMA

The implementation of SMA materials and need for design and analysis tool have motivated the development of constitutive models that can describe the mechanical behavior of SMAs with acceptable accuracy. The mechanical property of SMAs is usually modeled following either a phenomenological or a micromechanical approach (Brocca et al. 2002). Micromechanics-based constitutive models are much more sophisticated than the phenomenological models and usually are computationally demanding. Phenomenological models are often ad hoc descriptions aimed at fitting experimental data and are usually quite accurate in predicting the uniaxial response of SMAs.

Research and application of SMAs have generally been focused on one-dimensional case in order to obtain maximum recoverable deformation. This section describes several one-dimensional phenomenological constitutive models for superelastic SMA wires, which are relatively simple and suitable for civil engineering applications. Based on the ability to capture the loading rate-induced effect, they are generally divided into two categories: rate-independent models and rate-dependent models.

### 3.1. Flag-shaped Model

The piecewise-linear flag-shaped hysteresis model is perhaps the simplest rate-independent constitutive model for superelastic SMA materials. It has been widely used in the study of various self-centering systems, such as rocking walls, post-tensioned concrete or steel frames, SMA devices, and etc, for the sake of simplicity (e.g. Christopoulos et al 2002; Seo and Sause 2005; Mao and Li 2005; Andrawes and DesRoches 2005). A typical flag-shaped hysteresis model for describing the stress-strain relationship of superelastic Nitinol wires can be fully defined with five parameters: elastic modulus of austenite  $E_a$ , elastic modulus of martensite  $E_m$ , 'yield' stress  $\sigma_y$ , post-'yield' stiffness coefficient  $\alpha$  and energy dissipation coefficient  $\beta$  (as shown in Figure 8). Figure 9-(a) shows the stress-strain curves of superelastic Nitinol wires obtained from a simulation of the flag-shaped model and test data under a loading frequency of 2 Hz. Although the flag-shaped model can predict reasonably well the key features of superelastic Nitinol wires such as initial stiffness, post-'yield' stiffness, forward and reverse transformation stress, apparent discrepancy can be observed between the test data and prediction from the flag-shaped model along the unloading path, which may lead to the overestimation of dissipated energy. As a rate-independent constitutive model, the flag-shaped model is unable to capture the hysteresis behavior under varying loading rates.

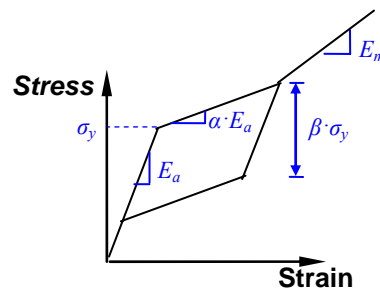


Figure 8. Typical flag-shaped hysteresis loop for superelastic Nitinol wires.

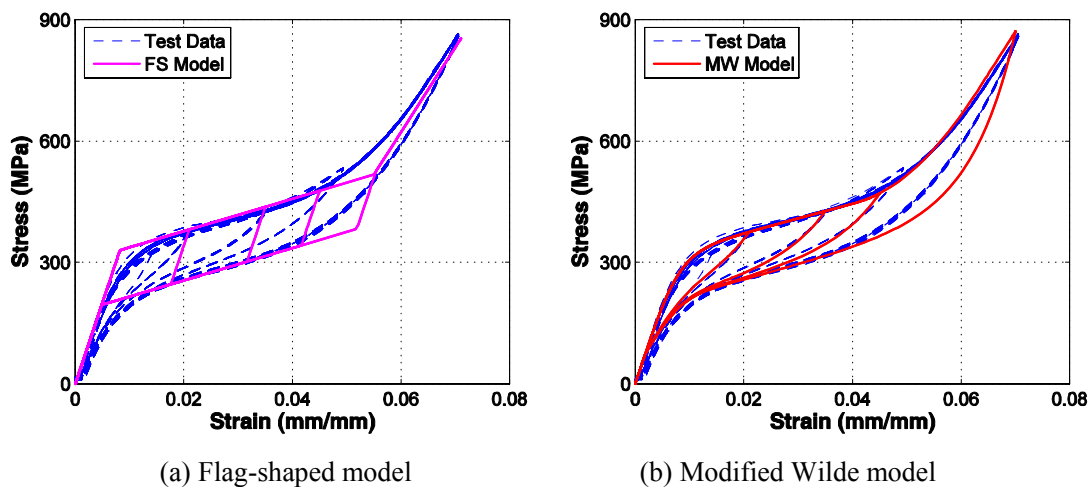


Figure 9. Stress-strain curve simulated by the flag-shaped model and modified Wilde model.

### 3.2. Modified Wilde Model

This is a modified version of the constitutive model for SMA initially developed by Graesser and Cozzarelli (1991). The Graesser-Cozzarelli model for SMA is an extension of a rate-independent model for hysteresis proposed by Ozdemir (1976). The Graesser-Cozzarelli model was extended by Wilde et al. (2000) to include the hardening behavior of SMA material after the transition from austenite to martensite is completed. The Wilde model for SMA is furthermore modified by Zhang and Zhu (2007) to enhance the stability of numerical simulation and speed up the computation time. The modified Wilde model which simulates the one-dimensional stress-strain relationship of superelastic SMA wires is expressed as follows:

$$\dot{\sigma} = E \cdot \left[ \dot{\varepsilon} - K \cdot |\dot{\varepsilon}| \cdot \text{sgn}(\sigma - \beta) \cdot \left( \frac{|\sigma - \beta|}{Y} \right)^n \right] \cdot u_I(\varepsilon) + E_m \cdot \dot{\varepsilon} \cdot u_{II}(\varepsilon) \quad (1a)$$

$$+ \left( E_y \frac{\varepsilon_m - \varepsilon}{\varepsilon_m - \varepsilon_1} + E_m \frac{\varepsilon - \varepsilon_1}{\varepsilon_m - \varepsilon_1} \right) \cdot \dot{\varepsilon} \cdot u_{III}(\varepsilon) \quad (1b)$$

$$\beta = \alpha \cdot E \cdot [\varepsilon_{in} + f_T \cdot H(-\varepsilon \dot{\varepsilon}) \cdot \text{sgn}(\varepsilon) \cdot g(a \cdot \varepsilon_{in} + \text{sgn}(\varepsilon) \cdot b)]$$

where  $\sigma$  and  $\varepsilon$  are the one-dimensional stress and strain, respectively;  $\beta$  is the one-dimensional backstress;  $E$  is the initial modulus of elasticity of SMA;  $Y$  is the upper (loading) plateau stress (i.e., the ‘yielding’-like plateau in the loading stage);  $\alpha = E_y/(E-E_y)$  is a constant that controls the slope of the stress-strain curve, where  $E_y$  is the slope after yielding;  $f_T$ ,  $a$  and  $b$  are material constants controlling the recovery of the inelastic strain upon unloading;  $n$  is a constant controlling the sharpness of transition between different phases; dot implies ordinary time derivative;  $E_m$  is the elastic modulus of martensite; strain  $\varepsilon_m$  defines the point where the transition of SMA from austenite to martensite is completed.

$\text{sgn}(\cdot)$  and  $H(\cdot)$  is the Signum function and unit step function (i.e., Heaviside function);  $\varepsilon_{in}$  is the inelastic strain, which is expressed as follows,

$$\varepsilon_{in} = \varepsilon - \frac{\sigma}{E} \quad (2)$$

function  $g(\cdot)$  is defined as

$$g(t) = 1 - e^{-t^2} \quad (3)$$

and coefficient  $K$  is defined by

$$K = \begin{cases} 1 & \text{if } \varepsilon \dot{\varepsilon} > 0, \text{ loading} \\ H(\varepsilon_{in} \varepsilon) & \text{if } \varepsilon \dot{\varepsilon} \leq 0, \text{ unloading} \end{cases} \quad (4)$$

and the functions  $u_I(\varepsilon)$ ,  $u_{II}(\varepsilon)$  and  $u_{III}(\varepsilon)$  are expressed respectively as,

$$u_I(\varepsilon) = 1 - u_{II}(\varepsilon) - u_{III}(\varepsilon) \quad (5)$$

$$u_{II}(\varepsilon) = \begin{cases} 1 & \text{if } \varepsilon \dot{\varepsilon} > 0 \text{ and } |\varepsilon| \geq \varepsilon_m \\ 0 & \text{otherwise} \end{cases} \quad (6)$$

$$u_{III}(\varepsilon) = \begin{cases} 1 & \text{if } \varepsilon \cdot \dot{\varepsilon} > 0 \text{ and } \varepsilon_1 < |\varepsilon| < \varepsilon_m \\ 0 & \text{otherwise} \end{cases} \quad (7)$$

If we assume that SMA wires can only undertake tension force, i.e.,  $\sigma = 0$  if  $\varepsilon < 0$ . Equation (1) can be rewritten as follows when  $\varepsilon > 0$ ,

if  $\dot{\varepsilon} > 0$ , loading

$$\begin{cases} \dot{\sigma} = E \cdot \left[ \dot{\varepsilon} - \dot{\varepsilon} \cdot \left( \frac{\sigma - \beta}{Y} \right)^n \right] \cdot u_I(\varepsilon) + E_m \cdot \dot{\varepsilon} \cdot u_{II}(\varepsilon) + \left( E_y \frac{\varepsilon_m - \varepsilon}{\varepsilon_m - \varepsilon_1} + E_m \frac{\varepsilon - \varepsilon_1}{\varepsilon_m - \varepsilon_1} \right) \cdot \dot{\varepsilon} \cdot u_{III}(\varepsilon) \\ \beta = \alpha \cdot E \cdot \varepsilon_{in} \end{cases} \quad (8a)$$

if  $\dot{\varepsilon} < 0$ , unloading

$$\begin{cases} \dot{\sigma} = E \cdot \left[ \dot{\varepsilon} + \dot{\varepsilon} \cdot H(\varepsilon_{in}) \cdot \text{sgn}(\sigma - \beta) \left( \frac{|\sigma - \beta|}{Y} \right)^n \right] \\ \beta = \alpha \cdot E \cdot [\varepsilon_{in} + f_T \cdot g(a\varepsilon_{in} + b)] \end{cases} \quad (8b)$$

if different stiffness or sharpness of transition are demanded for the loading and unloading stages,  $\alpha$ ,  $E$  and  $n$  can take different values during the loading and unloading stages.

Figure 9-(b) shows the stress-strain curves of superelastic Nitinol wires obtained from a simulation of the modified Wilde model and test data under a loading frequency of 2 Hz. It is seen that the modified Wilde model agrees well with the experimentally measured hysteresis loops. However, it is also noted that the modified Wilde model does not account for the loading rate and temperature effect, and thus it is unable to capture hysteresis behavior under varying loading rates.

### 3.3. Thermomechanical Model

In order to accurately capture the loading rate-induced thermo-mechanical effect of SMAs, a number of rate-dependent thermomechanical models for SMAs have been proposed by researchers (e.g. Brocca et al. 2002; Auricchio et al. 1999, 2006; Prahlad and Chopra 2003;

Sadjadpour and Bhattacharya 2006; Zhu and Zhang 2007b). These uniaxial thermo-mechanical models usually make use of measurable quantities as parameters.

The typical frequency range of interest to seismic application is from 0.1 Hz to 5 Hz. Zhu and Zhang (2007b) proposed a thermo-mechanical constitutive model which can fairly accurately predict the strain-rate dependent behavior of superelastic SMA wires in this frequency range. This rate-dependent constitutive model for superelastic SMA was derived within a thermo-mechanical framework from Helmholtz free energy. It comprises three key components – a mechanical law, an energy balance equation and a transformation kinetics rule.

Following Tanaka (1986), it is assumed that the thermo-mechanical process of SMAs can be fully described by a set of state variables  $(\varepsilon, T, \xi)$ , where  $\varepsilon$  is the Green strain,  $T$  is the temperature of SMA specimens, and  $\xi$  is an internal variable which is often defined as the fraction of martensite. Then the mathematical expression of this thermo-mechanical model is described as follows. Interested readers are referred to the article by Zhu and Zhang (2007b) for details.

### 3.3.1. Mechanical Law

The mechanical law which governs the stress-strain relationship of SMAs can be expressed as

$$\sigma = E(\xi)\varepsilon_{el} \quad (9a)$$

$$E(\xi) = E_a + \xi(E_m - E_a) \quad (9b)$$

$$\varepsilon_{el} = \varepsilon - \varepsilon_l \xi \quad (9c)$$

where  $\sigma$  is the second Piola-Kirchhoff stress which is energy conjugate to the Green strain;  $E(\xi)$  is the Young's modulus of SMAs which is experimentally found to be strongly dependent on the martensite fraction,  $\xi$ . Following Liang (1990), its expression is as Equation (9b). Constants  $E_a$  and  $E_m$  are Young's modulus for austenite and martensite respectively. In the case of small deformation the strain of SMA material can be decomposed into two parts:  $\varepsilon_{el}$ , the thermo-elastic strain, and  $\varepsilon_{in}$ , the inelastic strain due to phase transformation. The expression of inelastic strain is  $\varepsilon_{in} = \varepsilon_l \xi$ , where  $\varepsilon_l$  is the maximum residual strain which is generally considered as a time-independent material constant of SMAs. Thus the elastic strain  $\varepsilon_{el}$  can be expressed as Equation (9c).

The rate form of mechanical law is obtained by differentiating the two sides of Equation (9a) simultaneously,

$$\dot{\sigma} = E(\xi)\dot{\varepsilon} + \Omega(\varepsilon, \xi)\dot{\xi} \quad (10)$$

where material property function  $\Omega(\varepsilon, \xi)$  is defined by

$$\Omega(\varepsilon, \xi) = -\varepsilon_l \cdot E(\xi) + (E_m - E_a)(\varepsilon - \varepsilon_l \xi)$$

### 3.3.2. Energy Balance Equation

The energy balance equation describes the rate-dependent thermal effect, and its rate form is as follows

$$\varepsilon_l E(\xi) \cdot (\varepsilon - \varepsilon_l \xi) \dot{\xi} + \frac{E_a - E_m}{2} (\varepsilon - \varepsilon_l \xi)^2 \dot{\xi} = \rho_0 C_p \dot{T} - \rho_0 L \dot{\xi} + \frac{k}{V} (T - T_0) \quad (11)$$

or

$$\sigma \dot{\varepsilon}_{in} + \frac{E_a - E_m}{2} \varepsilon_{el}^2 \dot{\xi} = \rho_0 C_p \dot{T} - \rho_0 L \dot{\xi} + \frac{k}{V} (T - T_0) \quad (12)$$

where  $\rho_0$ ,  $L$  and  $C_p$  represent material density, latent heat of phase transformation and specific heat of the material respectively, which are all assumed to be equal for both the austenite and the martensite here;  $T_0$  is the ambient temperature;  $V$  is the volume of the SMA specimen;  $k$  is the heat transfer coefficient which should include not only the effect of heat convection but also the heat contact conduction between the SMA specimen and the gripping fixtures at the end of wire specimen.

The terms on the left-hand side of the Equation (12) represent the mechanical energy dissipation due to the phase transformation. The term  $\rho_0 L \dot{\xi}$  represents the rate of latent heat and the negative sign means the austenite to martensite transformation is exothermic, while the martensite to austenite transformation is endothermic. Such energy dissipation and latent heat usually contributes to the temperature variation of SMA wire specimens during loading procedure, and thus affects the material behaviors of SMA. Thus Equation (12) means at any instant the heat generation due to the mechanical dissipation and latent heat is equal to the specific heat absorbed by the specimen plus the heat loss to the environment.

### 3.3.3. Transformation Kinetics

Transformation kinetics of SMAs describes the evolution rule of martensite fraction  $\xi$  for both the transformation from austenite to martensite and the reverse transformation from martensite to austenite. To achieve a smooth transition at critical stress, Zhu and Zhang (2007b) proposed a new form of transformation kinetics, whose rate form is defined by

Austenite  $\rightarrow$  Martensite:

$$\dot{\xi} = (1 - \xi_0) \cdot \left( a_M \dot{T} - \frac{a_M}{c_M} \dot{\sigma} \right) \cdot \mathfrak{g} \left[ a_M \left( T - T_M - \frac{\sigma}{c_M} \right) \right] \quad (13a)$$

Martensite  $\rightarrow$  Austenite:

$$\dot{\xi} = \xi_0 \cdot \left( a_A \dot{T} - \frac{a_A}{c_A} \dot{\sigma} \right) \cdot \mathfrak{g} \left[ a_A \left( T - T_A - \frac{\sigma}{c_A} \right) \right] \quad (13b)$$

where the function  $g(\cdot)$  is defined as

$$g(x) \equiv \frac{-e^x}{(1+e^x)^2}$$

The critical temperatures  $T_M$  and  $T_A$  are defined as

$$T_M = \frac{M_s + M_f}{2}, \quad T_A = \frac{A_s + A_f}{2}$$

where transformation temperatures  $M_s$ ,  $M_f$ ,  $A_s$  and  $A_f$  are referred to the martensite start temperature, martensite finish temperature, austenite start temperature and austenite finish temperature, respectively;  $\zeta_0$  is the initial martensite fraction at the beginning of the current transformation; the material constants  $c_A$  and  $c_M$  are the slopes of the critical stress-temperature curve; the material constants  $a_M$  and  $a_A$  are defined here as

$$a_M = \frac{\ln(10000)}{M_f - M_s}, \quad a_A = \frac{\ln(10000)}{A_f - A_s}$$

This results in a starting point and finishing point of transformation that corresponds to the martensite fraction of 0.01 and 0.99 respectively.

### 3.3.4. Numerical Example

Figure 5 shows the simulation results using the thermo-mechanical model in comparison with the test data of superelastic Nitinol wires under a variety of loading frequencies. It is seen that this thermo-mechanical constitutive model can predict the superelastic behavior of Nitinol wires quite well for a variety of loading rates. It is capable of capturing two major thermo-mechanical behaviors of superelastic Nitinol wires under varying loading rates – reduction of hysteresis area and thus energy dissipation capacity as well as increased slope of transformation plateau with increasing loading rates. It can also replicate the phenomenon of change in hysteresis loops with increasing number of load cycles, which is due to the temperature change in superelastic Nitinol wires. Notable discrepancy between the experimental results and simulation results can be observed in the hysteresis shape at large strains (>5%). This is due to the difference between the evolution of martensite fraction in the experiment data and that described by Equation (13) at large strains. Improved transformation kinetics equations (often with increased sophistication) would have to be used to minimize the discrepancy.

Figure 6 presents the experimental and simulation results of temperature oscillation in superelastic Nitinol wire specimens. It is seen that the proposed constitutive model can properly predict the trend of temperature change in superelastic Nitinol wires: negligible temperature fluctuation under quasi-static loading (0.001 Hz); slight cooling down at medium loading frequency (0.01 Hz, 0.1 Hz) in terms of zero-strain temperature and slight heating up at further increased loading frequency (5 Hz). This cooling or heating trend caused the hysteresis loops to shift downwards or upwards with increasing number of load cycles until the temperature cycles are stabilized (as shown in Figure 5). Although the simulated

temperature agrees fairly well with the test results for the loading frequencies of 0.001 Hz and 0.01 Hz, the simulation seems to over-predict the temperature variation at the loading frequency of 0.1 Hz. Such a discrepancy may arise from either inaccuracy of the identified model parameters or error in temperature measurement.

### 3.4. Comparative Study of Constitutive Models

Although the rate-dependent thermo-mechanical constitutive model described earlier can fairly well reproduce the hysteresis behavior of superelastic SMA materials under various loading rates, it is derived in a thermo-dynamics framework and the associated complexity often deters the use of this kind of model by engineers for seismic application. Furthermore, the rate-dependent constitutive models for SMA cannot be directly used in nonlinear static analysis procedures such as push-over analyses, even if these models can yield accurate and reliable results in nonlinear dynamic analyses. On the other hand, rate-independent phenomenological models for SMA cannot explicitly consider the temperature and loading rate effects, but they are very appealing to seismic applications because of their simpler mathematical expression and computationally less demanding than thermo-mechanical constitutive models.

In order to investigate a feasibility of using rate-independent constitutive models for superelastic SMA in seismic response analyses of structures, Zhu (2007) conducted a comparative study of three nonlinear constitutive models described previously in this section: (i) the rate-dependent thermo-mechanical model (TM model); (ii) the modified Wilde model (MW model); (iii) a piecewise linear flag-shaped model (FS model). For the rate-independent constitutive models (i.e. MW model and FS model), the parameters of the models are tuned with the dynamic test results at a loading frequency of 2 Hz (as shown in Figure 9).

Parametric study of single-degree-of-freedom (SDOF) systems was carried out with varying initial elastic periods and strength reduction factors. The restoring force of the SDOF system is assumed to be solely from a superelastic Nitinol element. Two key parameters—the initial elastic period  $T_0$  and strength reduction factor  $R$  were considered in the parametric study. The range of  $T_0$  considered is  $0.2 \text{ sec} \leq T_0 \leq 2.5 \text{ sec}$ . The values of  $R$  considered are 2, 4 and 6 respectively. The nonlinear time history analyses employed the suite of ground motions developed by Somerville et al. (1997). This earthquake suite contains 20 records, corresponding to design basis earthquakes (DBE) at downtown, Los Angeles.

Three response indices of SDOF system were evaluated in the comparative study: peak displacement ductility  $\mu$ , peak acceleration  $a_{\max}$  and normalized dissipated energy  $e_{dis}$ . Figure 10 shows the statistical results (including mean, mean  $\pm$  standard deviation) of three response indices for SDOF system with three constitutive models respectively. Here the ensemble average and standard deviation are calculated based on the system response under the twenty earthquake ground motions. The maximum difference between the ensemble average curves of the peak displacement ductility and peak acceleration corresponding to the three constitutive models is observed to be less than 8%. Similarly, only very little difference is observed in the curves corresponding to a standard deviation away from the ensemble average curve. In terms of energy dissipation, however, notable difference exists between the response index curves corresponding to the three constitutive models, especially for the case of  $R = 6$ .

The simulations predicted by the TM model indicate that no significant shift of the hysteresis loops would occur during earthquakes. This is because the shift of the hysteresis

loops or the change in zero-strain temperature is a gradual progress, and larger amplitude vibration always leads to larger temperature variation including change of zero-strain temperature; however, structural response of larger amplitude under strong earthquakes usually lasts for a very limited time period which is insufficient to induce the considerable change of zero-strain temperature as well as shift of hysteresis loops.

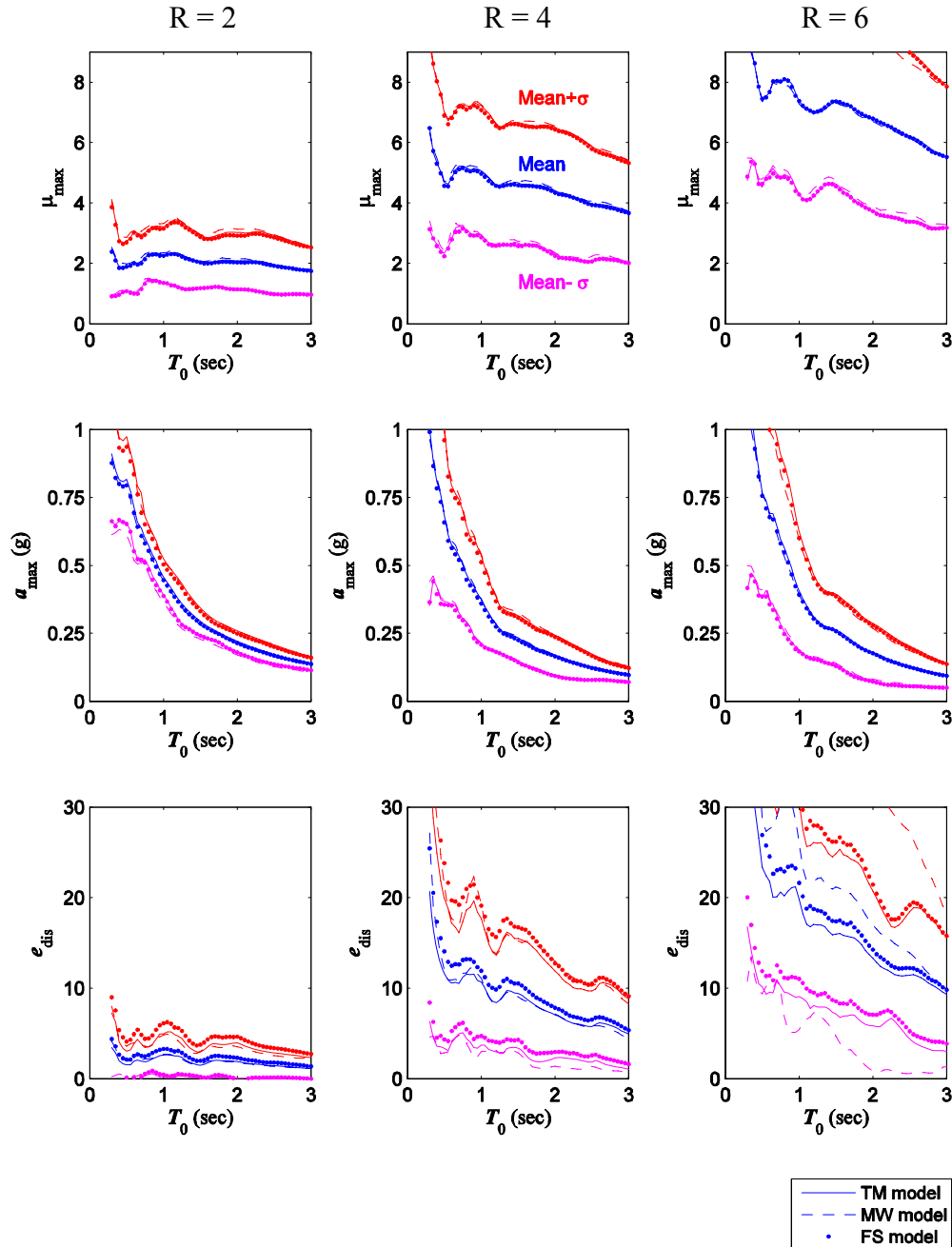


Figure 10. Statistical results of the response indices for SDOF system with different models.

In summary, replacing rate-dependent constitutive model with rate-independent models such as the MW model or FS model appears to be acceptable for seismic analyses of structures with SMA-based energy dissipation element. However, the use of more sophisticated thermo-mechanical constitutive models for SMA is still required in certain situations such as where significant change in environmental temperature is expected.

## 4. Seismic Performance and Design of SFDB Frame

Zhu and Zhang (2008) proposed a special type of bracing element termed self-centering friction damping brace (SFDB). The SFDB, with its core component made of superelastic Nitinol wires, exhibits a flag-shaped hysteresis loop, and thus it has a potential to establish a new type of CBF systems with self-centering behavior. The superior properties of superelastic Nitinol wires, such as inherent self-centering capability, high ductility and corrosion resistance, and very long fatigue life, form the physical basis on which properly designed SFDB can re-center itself and withstand several design basis earthquakes without performance deterioration. The reusability of SFDB for several frequent and design level earthquakes is very appealing in the sense that it can enhance the robustness of structural system performance during strong aftershocks following a significant earthquake event, thus leading to minimized service interruption after strong earthquakes. Additionally, self-centering behavior is able to reduce (or even eliminate) residual structural deformation which is emphasized as a fundamental complementary parameter in the evaluation of structural (and non-structural) damage in the performance-based seismic design and assessment approach.

### 4.1. Mechanics of SFDB

The mechanical configuration of SFDB is schematically illustrated in Figure 11. The SFDB comprises three major steel parts, designated as block “A”, block “B” and block “C” respectively. The slot on the block “B” enables these three parts to slide past each other at the contact surface. Stranded superelastic Nitinol wires are attached to block “A” and “B” using anchoring fixtures. In order to enhance its energy dissipation capacity, a pre-determined amount of normal force is applied at the sliding surface 1 by tightening the bolts (as shown in Figure 11) and thus produces a specified level of friction force at the sliding surface 1 of the SFDB. Such a specified level of friction force is generally less than the ‘yield’ force of Nitinol wire strands in order to maintain the nearly self-centering effect of the brace. Meanwhile, much larger friction coefficient and normal force is applied at the sliding surface 2 to result in a friction force level that is much larger than the ‘yield’ force of Nitinol wire strand by a pre-specified amount. Under low external force two parts—blocks “B” and “C”—will move as one piece. Therefore without sliding of surface 2, the hysteresis behavior of the SFDB is the superposition of the superelastic behavior of Nitinol wire strands and the friction effect at sliding surface 1, as illustrated in Figure 12. By properly adjusting the ratio between the ‘yield’ strength of Nitinol wire strands and the friction forces, the final combined hysteresis loop exhibits a nearly self-centering behavior with enhanced energy dissipation, as illustrated in Figure 12-(c).

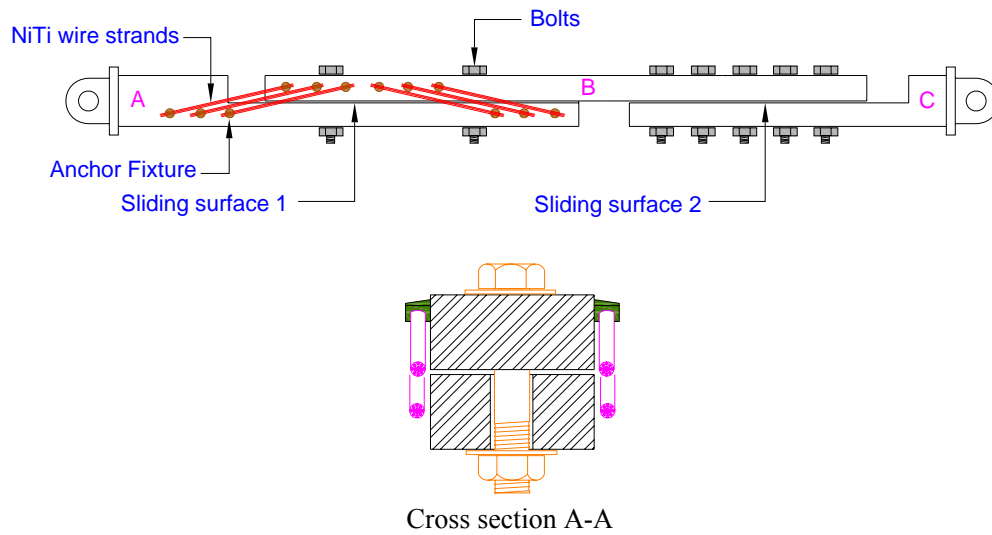


Figure 11. Schematic of the mechanical configuration of SFDB.

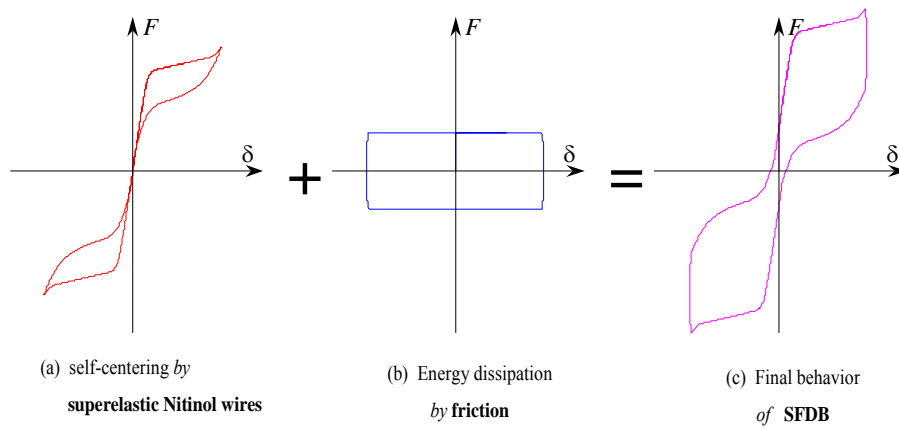


Figure 12. Illustration of the self-centering mechanism of SFDB.

Figure 13 shows the experimental validation of scaled SFDB specimens which was cyclically tested using a servo-controlled MTS test machine. Figure 13-(a), (b) and (c) show the measured hysteresis loops of the SFDB specimens with different levels of friction force. The friction force was measured with the same loading protocol after removing the Nitinol wires. Figure 13-(d), (e) and (f) show the hysteresis of friction forces corresponding to Figure 13-(a), (b) and (c) respectively. The friction force in Figure 13-(a) and (d) is negligible and this SFDB specimen has very limited energy dissipation capacity. With increasing level of friction force, the SFDB specimens exhibit a hysteresis loop with enhanced energy dissipation capacity, as shown in Figure 13-(b) and (c).

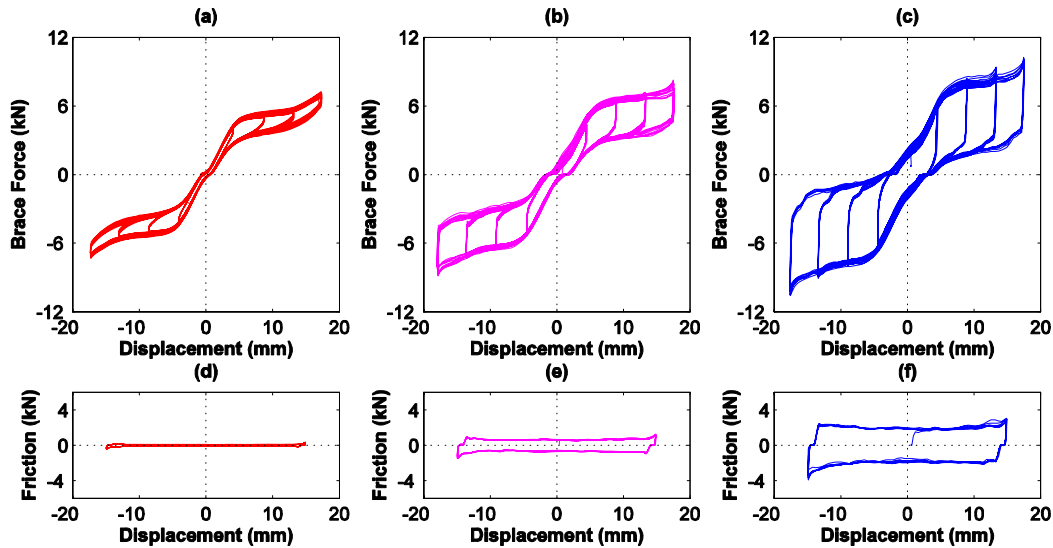


Figure 13. Test results of SFDB specimens.

It is observed that the load-displacement behaviors of both the friction force and the SFDB device were quite repeatable during the cyclic loading. No obvious residual strain and strength degradation in Nitinol wires were observed after 50-cycle training. As shown in Figure 13-(a), (b) and (c), the behavior of SFDB is almost symmetrical under tension and compression, which is another advantage of SFDB derived from its unique mechanical configuration in contrast to directly using SMA bars as bracing members in a CBF structure. The unique configuration of SFDB enables the direct transfer of applied load to the Nitinol wire strands in tension. Although SMA bars can undertake both tension and compression forces, a significant difference in the behavior of SMA bars under compression and tension stresses has been observed by Cardone et al. (1999), which may cause problems in beam design due to the unbalanced forces in chevron-braced configurations of framed structures.

#### 4.2. Displacement-based Design Procedure for SFDB Frame

Engineering structures with SMA-based damping devices usually show quite different seismic behavior compared with conventional structural systems. In order to implement these SMA-based devices in a real structural system, it is necessary to formulate some specific design guideline and procedures. In this regard, Zhu (2007) developed a displacement-based design (DBD) procedure for SFDB frame buildings. The DBD approach is based on the use of inelastic design spectra. The inter-story drift ratios and brace ductility demands are selected as the performance objective in this DBD approach. The flow chart of the DBD approach is shown in Figure 14. The details of this DBD procedure for SFDB frame is given as follows:

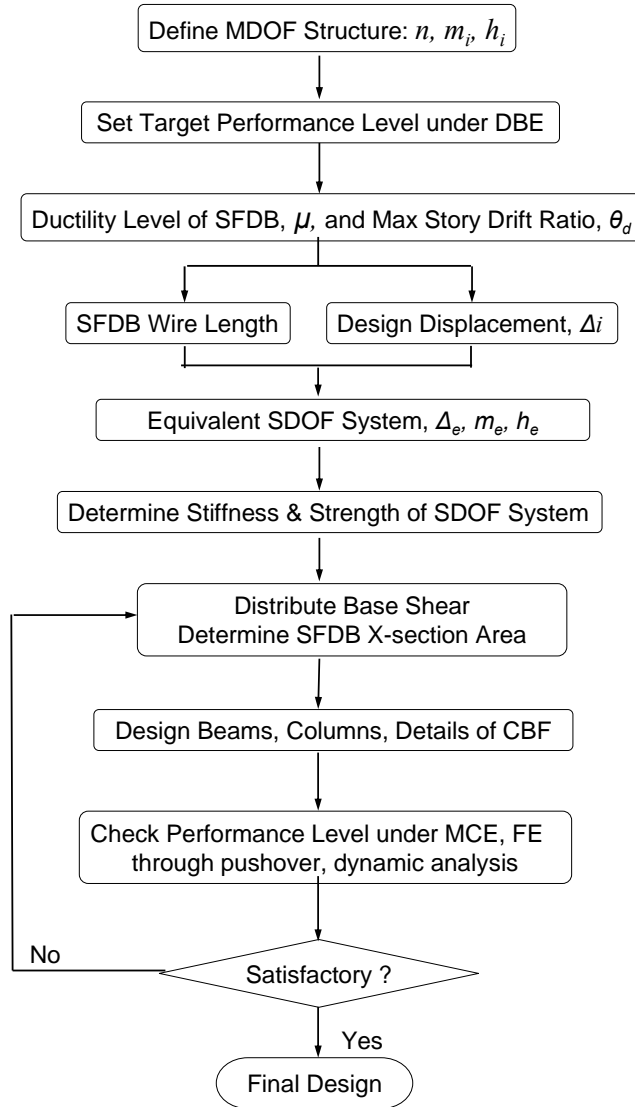


Figure 14. Flow chart for the displacement-based design procedure.

#### STEP 1: Design Data

The design parameters of the SFDB frame building under consideration such as the total number of stories  $n$ , number of braced bays, seismic mass at each floor level (i.e.,  $m_i$ ), story height (i.e.,  $h_i$ ), need to be specified first. Consequently, a planar MDOF model can be defined for the SFDB frame, as illustrated in Figure 15-(b). The design response spectrum should be determined based on the site conditions using the seismic hazard maps (NEHRP 2003).

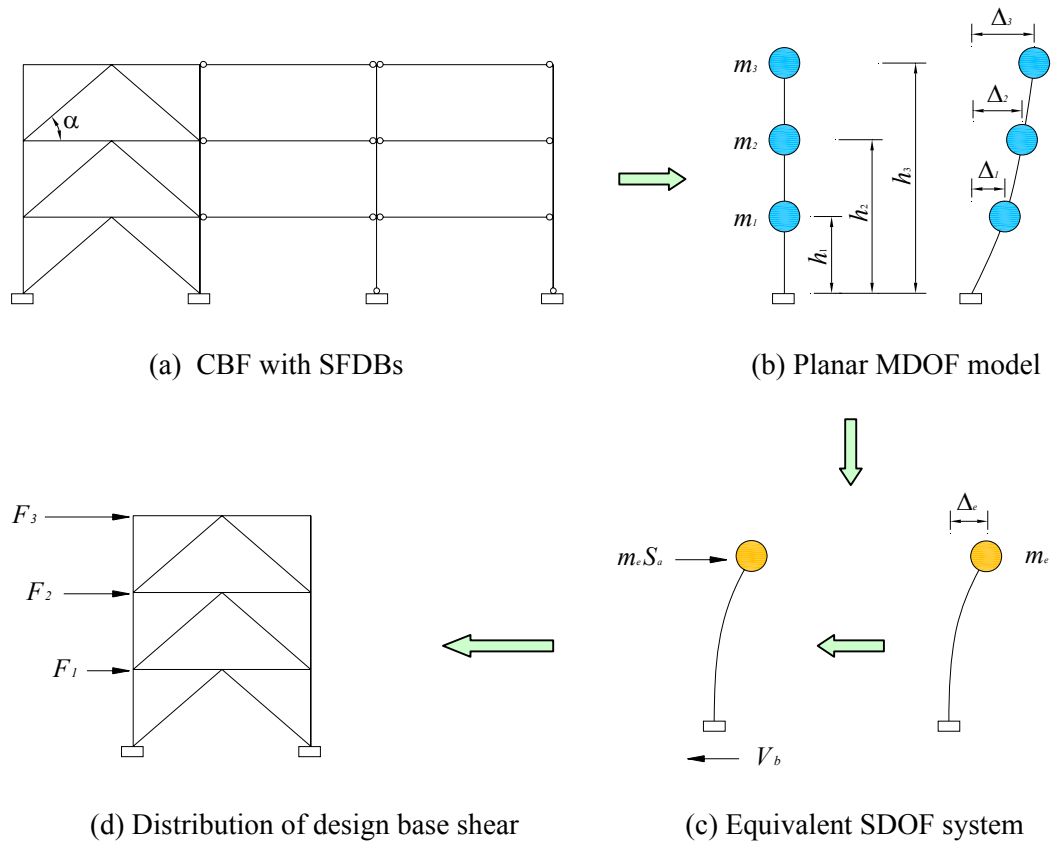


Figure 15. Schematic diagram of displacement-based seismic design procedure.

### STEP 2: Set Target Performance Level

The target performance indices include the design ductility demand of SFDB (i.e.,  $\mu$ ) and design maximum inter-story drift ratio (i.e.,  $\theta_d$ ) under the design basis earthquake (DBE). In order to minimize the residual deformation and provide a safety margin, the maximum brace ductility of SFDB has to be limited within a certain range. Since the maximum inter-story drift ratio offers an important measure of both the structural and non-structural damage, the limiting values for these two performance indices should be selected to meet the desired performance level. Once the design inter-story drift is determined, the displacement profile of the multistory frame structure needs to be approximately estimated. A linear displacement profile is usually assumed for low-rise buildings; however, a nonlinear displacement profile suitable to CBFs should be assumed in the design of medium-rise or high-rise SFDB frames.

Given the design displacement profile and the ductility of SFDB, the length of SMA wires in SFDB can be determined by:

$$l_i = \frac{(\Delta_i - \Delta_{i-1}) \cdot \cos(\alpha)}{\mu \cdot \varepsilon_y} \quad (9)$$

where  $\varepsilon_y$  is the ‘yield’ strain (i.e., transformation stress) of SMA wires and  $\alpha$  is the angle formed by the brace and beams of the braced frame (see Figure 15-(a)).

### STEP 3: Transform to Equivalent SDOF System

Assuming the seismic response of the frame building is dominated by the fundamental mode, the effective displacement and mass of the equivalent SDOF system is given by

$$\Delta_e = \sum (m_i \Delta_i^2) / \sum (m_i \Delta_i) \quad (10)$$

$$m_e = \sum (m_i \Delta_i) / \Delta_e \quad (11)$$

### STEP 4: Calculate Design Base Shear

Nonlinear response spectra of SDOF system with flag-shaped hysteresis (representing SFDBs’ self-centering hysteresis behavior) need to be calculated for specified value of the ductility level  $\mu$  (as shown in Figure 16). The derivation and regression functions of equivalent SDOF system can be found in Zhu (2007) in more details. With the target displacement  $\Delta_e$ , the required initial period  $T_i$  and the corresponding acceleration  $S_a$  are to be determined from the nonlinear response spectrum (as illustrated in Figure 16). Here  $S_a = S_{de}/R_\mu$  is the acceleration corresponding to the ‘yield’ strength of the equivalent SDOF system. The design base shear of the equivalent SDOF system is given as,

$$V_b = m_e S_a \quad (12)$$

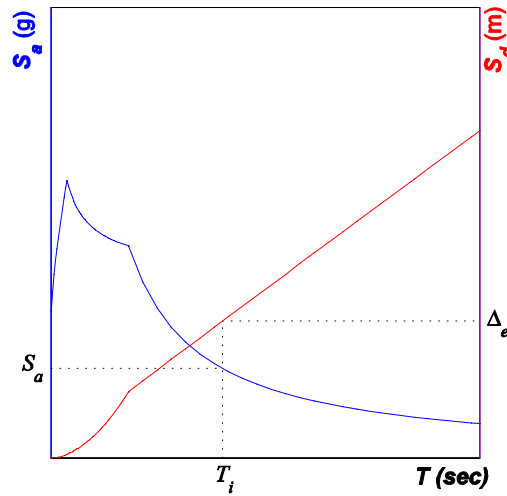


Figure 16. Nonlinear response spectrum for SDOF system.

#### STEP 5: Design Strength of SFDB

The base shear calculated in the last step can be distributed over the braced frame height in proportion to the seismic mass and displacement profile in accordance with the following relationship,

$$F_i = V_b \frac{m_i \Delta_i}{\sum (m_i \Delta_i)} \quad (13)$$

Such a force distribution is based on the fundamental mode shape and does not account for the contribution of higher modes. In the design of SFDB frame, it is assumed that all design story shear is to be resisted by the concentric braces – SFDBs. Thus the required ‘yield’ strength of the SFDB, and the cross sectional area of SMA wires in the SFDB can be determined based on the nominal ‘yield’ stress of SMA wires.

#### STEP 6: Design for Other Members in SFDB frame

Since the SFDBs are the primary lateral load resisting and energy dissipating elements of the braced frame building, bracing connections and adjoining beams and columns shall be designed to resist the maximum possible brace strength instead of yield forces of SFDBs.

#### STEP 7: Check Performance Level under MCE and FE

The seismic performance levels of the SFDB frame under maximum considered earthquakes (MCE) and frequent earthquakes (FE) need to be checked through inelastic analysis procedures such as pushover analysis or nonlinear time-history analysis. If the performance levels under the MCE and FE are not acceptable, the revision of brace strength, i.e., the cross-sectional area of the SMA wires in SFDBs, would have to be made in order to achieve satisfactory performance levels under the MCE and FE. Accordingly, the design of adjoining members and bracing connections also need to be modified.

### **4.3. Design Examples**

A 3-story and a 6-story office building were designed using the above DBD procedure (Zhu 2007). These two steel braced frame buildings are designed for a location in downtown Los Angeles with site class D (firm soil). The nonlinear static analyses (i.e., pushover analyses) and nonlinear time history analyses of these two design examples were carried out to evaluate the effectiveness of the proposed design procedure. In both analyses, the modified Wilde model was used to describe the stress-strain relationship of superelastic Nitinol wires in SFDB.

### 4.3.1. Pushover Analyses

Nonlinear pushover analyses of the prototype buildings with SFDBs were conducted to evaluate the lateral load response and failure mechanisms of the SFDB frames. Figure 17 shows the pushover curves (base shear versus roof drift ratio) for one of the prototype buildings—3-story SFDB frame. Various characteristic points such as the slip at friction surface of SFDB, ‘yielding’ of SFDBs, yielding at beams and columns, are indicated in Figure 17.

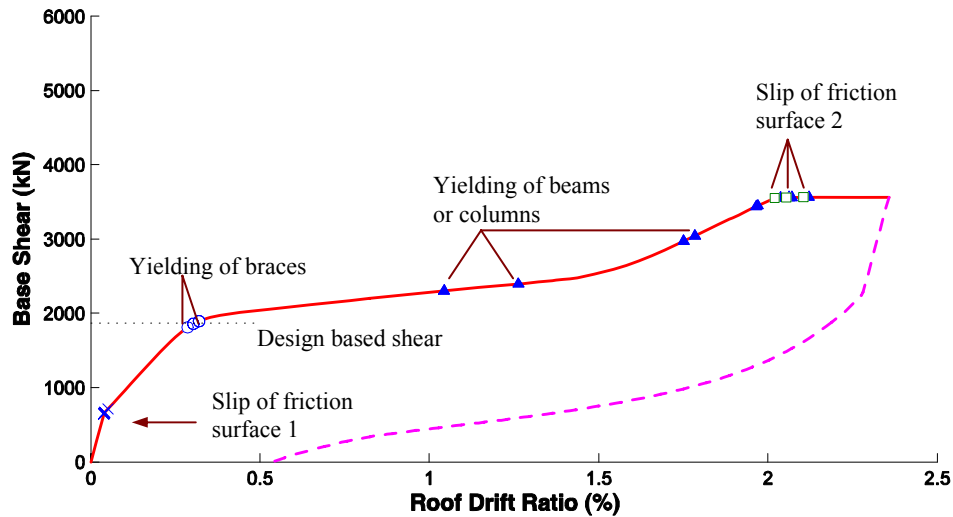


Figure 17. Pushover analyses of the 3-story SFDB frames.

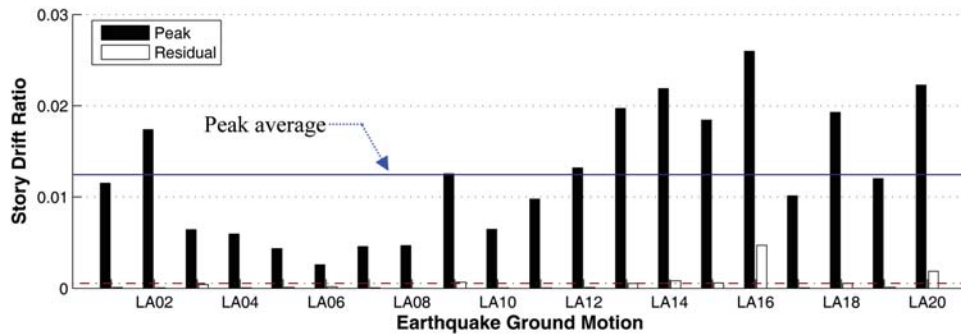
Initial stiffness change in the SFDB frame can be observed from its pushover curve due to the slip of friction surface 1 in SFDBs at very small roof displacement. The SFDB frame yield at relatively small roof drift ratios (about 0.25%). The ‘yield’-like plateau of SFDB frames is caused by the solid phase transformation in superelastic SMA wires instead of plastic deformation. Before the occurrence of plastic deformation in beams and columns, there is essentially no damage in the SFDB frame. Therefore the SFDB frame has the potential to achieve a damage-free structural system for FE and DBE earthquakes, which would lead to considerably reduced repair cost and service interruption after design-level earthquakes, particularly in earthquake-prone regions.

The slip of friction surface 2 in SFDBs occurs at a roof drift ratio around 2%. The strain hardening and plastic deformation associated with the superelastic Nitinol wire at large strain would cause certain undesirable effects in the SFDB frame if the sliding surface 2 is not activated at this point, e.g., the potential overloading to brace connections and adjacent members. Below this roof drift ratio value, the SFDBs in the frames do not have appreciable residual deformation after earthquakes and thus need not be repaired. However, above this roof drift ratio value the SFDBs lose their self-centering capacity and residual deformation will occur. The corresponding pushover curves with unloading path (in dashed line) are also shown in Figure 17, and apparent residual roof drift ratio after unloading can be observed.

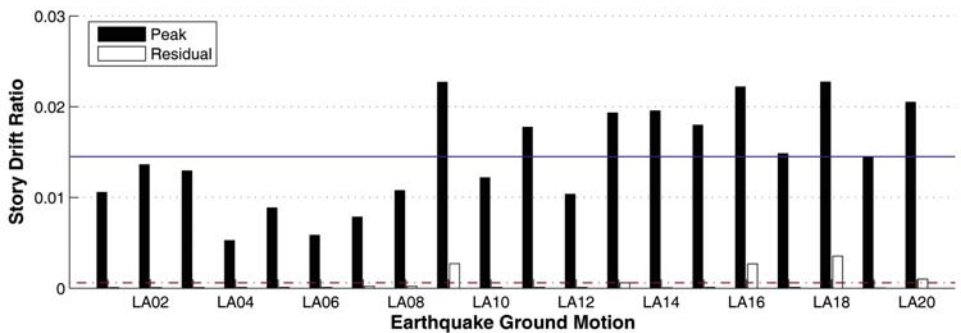
### 4.3.2. Nonlinear Time History Analyses

The time history analyses employ the suites of earthquake ground motions developed previously for use in the SAC project on steel moment-resisting frames. Two earthquake suites corresponding to downtown Los Angeles, California, were selected in this study and they are designated as LA01 - LA20 (for DBE), and LA21 - LA40 (for MCE), respectively (Somerville et al. 1997).

Figure 18 shows the maximum story drift ratios and residual story drift ratios for 3-story and 6-story SFDB frames subjected to the DBE suite of earthquake ground motions. Only the maximum value in three stories of the SFDB frame is presented. For the DBE suite, the mean value of the maximum inter-story drift ratios is 1.25% and 1.45% for the 3-story and 6-story frames respectively. The residual story drifts are almost negligible under around 17 ground motions for both frames. This significant reduction of residual drifts in the SFDB frame manifests the benefit of SFDB which is derived from its self-centering capability. In this study the slip of friction surface 1 in SFDB correspond to a transient inter-story drift ratio value of 2% for the prototype building structures. For 16 ground motions in the DBE suite, the peak story drift ratios of both SFDB frame are less than 2.0% and the SFDBs need not be repaired. Therefore the reusability of SFDB is validated in a statistical sense.



(a) 3-story SFDB frame



(b) 6-story SFDB frame

Figure 18. Maximum and residual drift ratios of SFDB frames under DBE earthquakes.

Figure 19 and Figure 20 show the smooth-median response (Seo 2005) of the 3- and 6-story buildings respectively under the DBE earthquake suite. It can be seen that the SFDB frame buildings designed using the proposed DBD approach can achieve the target displacement pattern specified in the design procedure. In terms of the peak inter-story drift ratios and ductility levels of the SFDB braces, the 3-story frame buildings can meet the design target performance reasonably well. For the 6-story buildings, the proposed DBD method tends to underestimate the peak inter-story drift ratios and brace ductility demands for both the SFDB and SFDB-NF frames. Here SFDB-NF denotes the SFDB device with zero friction level at friction surface 1 (Zhu 2007). This discrepancy can be attributed to the exclusion of concentration of story drift due to inelastic behavior and higher mode contribution in this simplified design method. These effects have a larger impact on the maximum inter-story drift ratios than the displacement profile. In general, their effects increase with the displacement ductility ratio and the number of stories. Therefore special caution should be exercised when designing medium-rise SFDB frame buildings using the proposed DBD approach.

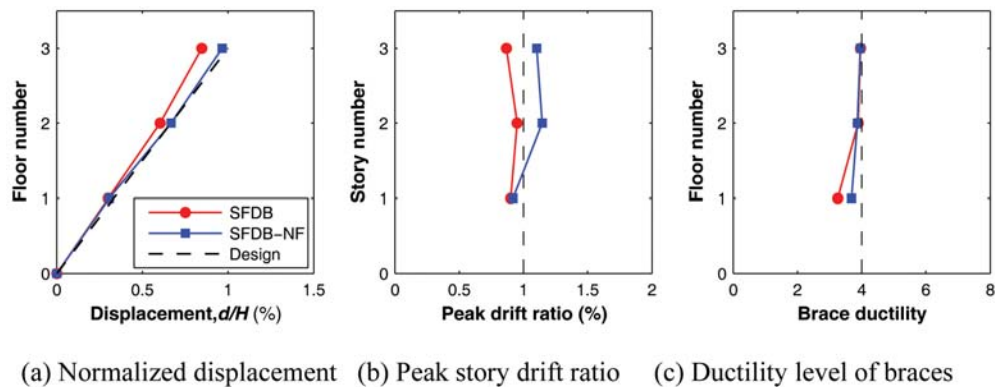


Figure 19. Smooth-median response of 3-story frames under DBE earthquakes.

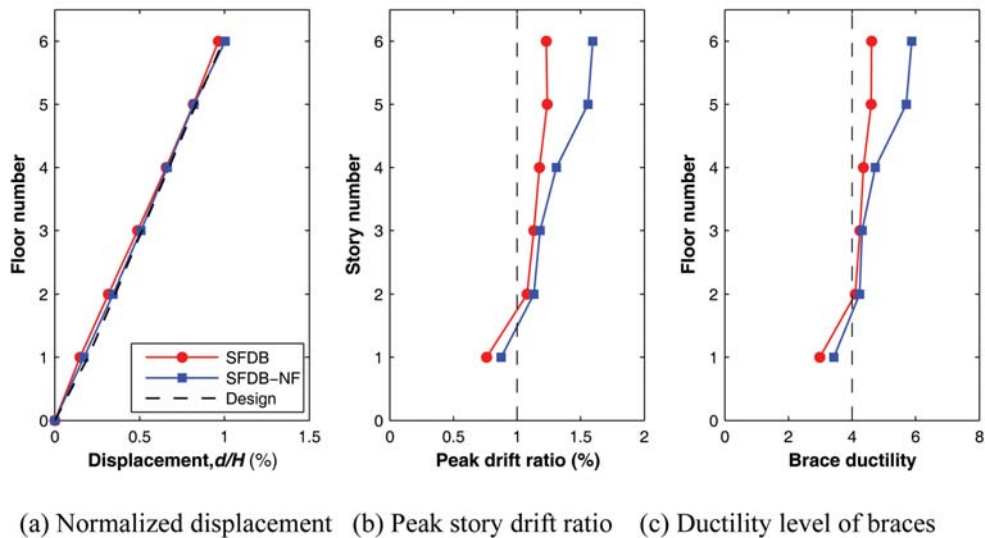


Figure 20. Smooth-median response of 6-story frames under DBE earthquakes.

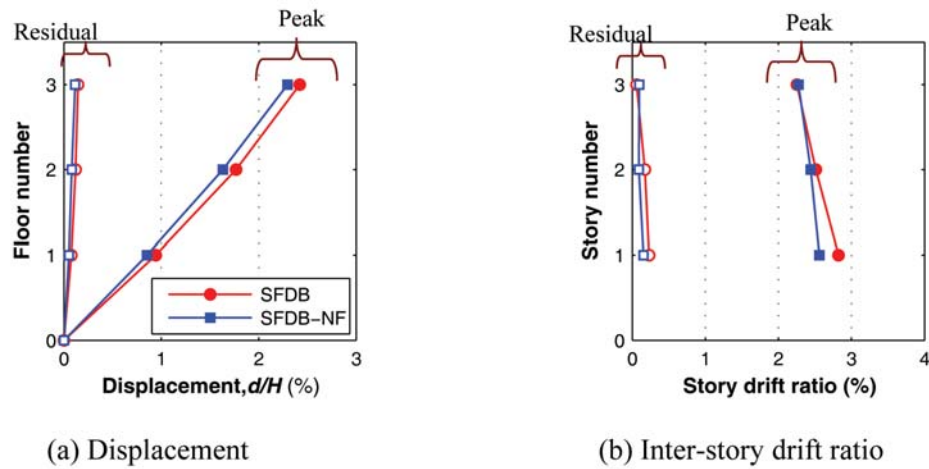


Figure 21. Smooth-median response of 3-story building under MCE earthquakes.

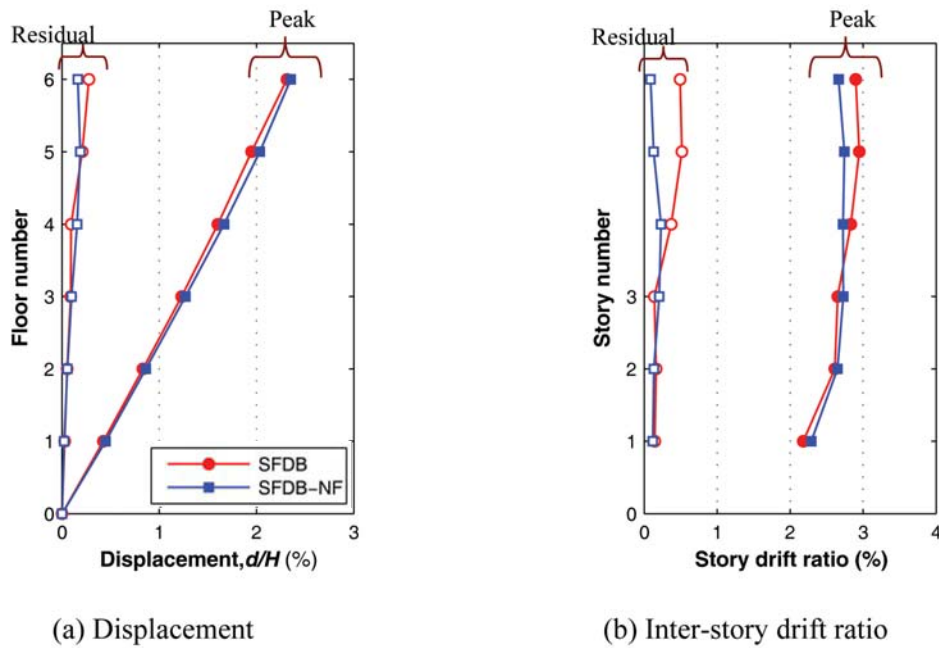


Figure 22. Smooth-median response of 6-story building under MCE earthquakes.

Figure 21 and Figure 22 show the statistical results of the nonlinear seismic response of 3-story and 6-story SFDB frames under the MCE suite. Figure 21-(a) and (b) show the distribution of the smooth-median of the peak displacements and residual story drift ratios along the height of the 3-story SFDB frame building. The smooth median was calculated based on the twenty earthquake ground motions in the corresponding earthquake suite. Although the SFDB frames have minimal residual inter-story drift ratios under the FE and DBE suites, the peak roof drift ratio exceeds 2% and the friction surface 2 is activated during MCE earthquakes. Consequently residual inter-story drift ratios can be observed in all three

stories after the MCE earthquakes. Similar observation can also be made to the results of 6-story SFDB frame (as shown in Figure 22).

The results of the nonlinear time history analysis also show that the SFDB frame can achieve a seismic response level comparable to that of the buckling restrained braced frame while having significantly reduced residual drifts. The SFDB has a potential to establish a new type of self-centering CBF systems with higher seismic performance.

## 5. Conclusion

The concept of self-centering seismic resisting system has recently attracted growing interest. A flag-shaped hysteresis loop is typical of such self-centering structural systems. Special metals like shape memory alloys (SMA) also exhibit flag-shaped stress-strain curve. This paper presents the seismic analysis and design of steel concentrically braced frame (CBF) buildings with a special SMA based damping device termed self-centering friction damping brace (SFDB). SFDB has its core re-centering component made of stranded superelastic SMA wires. SFDB would be typically installed as part of the bracing system to resist seismic-induced lateral load. Through proper design, flag-shaped hysteresis loops exhibiting nearly self-centering behavior can be obtained for SFDB.

It is found in this study that the temperature variation in superelastic Nitinol wires under dynamic tests affects to some extent the hysteresis behaviors at different loading frequencies. The thermo-mechanical constitutive model concerned shows a good agreement with experimental stress-strain relationship of superelastic SMA wires at a variety of specified loading rates. The loading rate-induced thermo-mechanical effect, such as the temperature variation, the reduction in hysteresis area, rise of the transformation plateau and the increased slope of the loading transformation plateau with increasing loading rates can be predicted reasonably well by this thermo-mechanical constitutive model. The modified Wilde model is capable of simulating the experimental hysteresis behavior of superelastic SMA wires at a specified loading rate through data fitting. This study also shows that using rate-independent constitutive models for superelastic SMA wires for seismic response analyses of structures gives fairly accurate results. Considering the mathematical complexity for numerical implementation, intensive computational demand and infeasibility for nonlinear dynamic analyses associated with the rate-dependent constitutive models, the rate-independent constitutive models (e.g., the modified Wilde model) for superelastic SMA materials are very appealing to structural engineers for seismic simulation study of SMA-based energy dissipation devices.

The proposed displacement-based design procedure involves the proportioning of SFDB frame based on the target performance level specified for design basis earthquakes, such as target building inter-story drift ratio and target ductility level of SFDBs. The results of nonlinear pushover and dynamic analyses of a 3-story and 6-story CBF building validate the effectiveness of the proposed design method. However, the current simplified design approach only considers the participation of the fundamental mode and assumes a constant displacement profile for the entire earthquake duration, and thus it tends to give underestimated values for the maximum story drift ratios and brace ductility demands for medium-rise braced frame buildings. The time history analyses involve two suites of earthquake ground motions each containing 20 earthquake records which represent the design

basis and maximum considered earthquakes in Los Angeles, California respectively. The results of the nonlinear time history analysis show that SFDB frames have minimal residual story drifts while still capable of achieving a seismic response control level comparable to that of conventional CBF frames in terms of peak story drifts. The pushover analysis results disclose the nonlinear lateral load response behavior and failure mechanism of the SFDB frame. Characteristic performance points of the SFDB frame such as slip at friction surfaces, 'yielding' of braces, yielding at beams and columns, are indicated in the pushover curve. In summary, the SFDB frames, if properly designed, have minimal residual drifts under frequent and design basis earthquakes, and SFDBs are able to withstand several design level earthquakes without the need for repair or replacement.

## Reference

- Aiken, I. D., Nims, D. K., & Kelly, J. M. (1992) Comparative study of four passive energy dissipation systems. *Bulletin of the New Zealand National Society for Earthquake Engineering*, **25**(3), 175-192.
- Aiken, I. D., Nims, D. K., Whittaker A.S., & Kelly, J. M. (1993) Testing of passive energy dissipation systems. *Earthquake Spectra*, **9**(3), 335-370.
- Andrawes, B., & DesRoches, R. (2005) Unseating prevention for multiple frame bridges using superelastic devices. *Smart Mater. Struct.*, **14**, S60-S67.
- Auricchio, F., & Sacco, E. (1999) Modelling of the rate-dependent superelastic behavior of Shape-Memory Alloys. *ECCM '99, European Conference on Computational Mechanics*, August 31-September 3, Munchen, Germany.
- Auricchio, F., Fugazza, D., & DesRoches, R. (2006) Numerical and experimental evaluation of the damping properties of shape-memory alloys. *Journal of Engineering Materials and Technology*, **128**, 312-319.
- Brinson, L. C., & Huang, M. S. (1996) Simplifications and comparisons of shape memory alloy constitutive models. *J. Intell. Mater. Syst. Struct.*, **7**(1), 108-114.
- Brocca, M., Brinson, L. C., & Bazant, Z. P. (2002) Three-dimensional constitutive model for shape memory alloys based on microplane model. *Journal of the Mechanics and Physics of Solids*, **50**, 1051-1077.
- Cardone, D., Coelho, E., Dolce, M., & Ponzo, F. (2004) Experimental behaviour of RC frames retrofitted with dissipating and re-centring braces. *Journal of Earthquake Engineering*, **8**(3), 361-396.
- Castellano, M. G., Indirli, M., & Martelli, A. (2001) Progress of application, research and development and design guideline for shape memory alloy devices for cultural heritage structures in Italy. *Proc. SPIE* **4330**, 250-261.
- Cheok, G. S., Stone, W. C., & Kunnath, S. K. (1998) Seismic response of precast concrete frames with hybrid connections. *ACI Structural Journal*, **95**(5), 527-539.
- Christopoulos, C., Filiatrault, A., & Folz, B. (2002a) Seismic response of self-centering hysteretic SDOF systems. *Earthquake Engineering and Structural Dynamics*, **31**, 1131-1150.
- Christopoulos, C., Filiatrault, A., Folz, B., & Uang, C. M. (2002b) Post-Tensioned Energy Dissipating Connections for Moment-Resisting Steel Frames. *ASCE Journal of Structural Engineering*, **128**(9), 1111-1120.

- Clark, P. W., Aiken, I. D., Kelly, J. M., Higashimo, M., & Krumme, R. C. (1995) Experimental and analytical studies of shape memory alloy dampers for structural control. *Proc., the 1995 Conference on Smart Structures and Materials, SPIE*, **2445**, 241-251.
- Clark, P. W., Aiken, I. D., Kasai, K., Ko, E., & Kimura, I. (1999) Design procedures for buildings incorporating hysteretic damping devices. *Proc., the 69<sup>th</sup> SEAOC Annual Convention*, Sacramento, CA.
- DesRoches, R., McCormick, J., & Delemont, M. (2004) Cyclic properties of superelastic shape memory alloy wires and bars. *ASCE Journal of Structural Engineering*, **130**(1), 38-46.
- DesRoches, R., & Delemont, M. (2002) Seismic retrofit of simply supported bridges using shape memory alloys. *Eng. Struct.*, **24**, 325-332.
- Dolce, M., Cardone, D., & Marnetto, R. (2000) Implementation and testing of passive control devices based on shape memory alloys. *Earthquake Engrg. Struct. Dyn.*, **29**(7), 945-968.
- Dolce, M., Cardone, D., Ponzio, F. C., & Valente, C. (2005) Shaking table tests on reinforced concrete frames without and with passive control systems. *Earthquake Engineering and Structural Dynamics*, **34**(14), 1687-1717.
- Fahnestock, L. A., Sause, R., & Ricles, J. M. (2003) Analytical and Experimental Studies on Buckling Restrained Braced Composite Frames. *Proceedings, International Workshop on Steel and Concrete Composite Construction*, Taipei, Taiwan, October 8-9, 2003.
- FEMA (2003) *NEHRP recommended provisions for seismic regulations for new buildings and other structures*. FEMA-450, Federal Emergency Management Agency, Washington D.C.
- Funakubo, H. (1987) *Shape memory alloys*. Gordon and Breach Science Publishers. New York, NY.
- Garlock, M. M., Ricles, J. M., & Sause, R. (2005) Experimental Studies of Full-Scale Post-tensioned Steel Connections. *J. Struct. Engrg.*, **131**(3), 438-448.
- Graesser, E. J., & Cozzarelli, F.A. (1991) Shape-memory alloys as new materials for aseismic isolation. *ASCE J. Eng. Mech.*, **117**(11), 2590-2608.
- Higashino, M., Aizawa, S., Clark, P. W., Whittaker, A. S., Aiken, I. D., & Kelly, J. M. (1996) Experimental and analytical studies of structural control system using shape memory alloy. *Proc. 2nd International Workshop on Structural Control*, Hong Kong, December, 221-232.
- Indirli, M., Castellano, M. G., Clemente, P., & Martelli, A. (2001) Application of shape memory alloy devices: the rehabilitation of the S. Giorgio church bell-tower. *Proc. SPIE* **4330**, 262-272.
- Kiggins, S., & Uang, C. M. (2004) Reducing residual drifts in BRBF systems. *Proc., 73<sup>rd</sup> SEAOC Annual Convention*, Sacramento, CA. 481-492.
- Krumme, R., Hayes, J., & Sweeney, S. (1995) Structural damping with shape-memory alloys: one class of devices. *Proc. SPIE* **2445**, 225-240
- Kurama, Y., Sause, R., Pessiki, S., & Lu, L. W. (1999) Lateral load behavior and seismic design of unbonded post-tensioned precast concrete walls. *ACI Structural Journal*, **96**(4), 622-632.
- Lee, W. K., & Billington, S. L. (2006) Performance-based assessment of a self-centering bridge pier system for seismic regions. *Proc. 8NCEE*, San Francisco, CA, April 18-21, 2006.

- Liang, C. (1990) The constitutive modeling of shape memory alloys. *Ph.D. thesis*, Virginia Tech.
- Mao, C., & Li, H. (2005) SMA-based smart damper/displacement transducer. *Smart Structures and Materials 2005: Sensors and Smart structures Technologies for Civil, Mechanical and Aerospace Systems*, Proc. of SPIE Vol. 5765, Bellingham, WA. pp: 442-452
- McCormick, J., DesRoches, R., Fugazza, D., & Auricchio, F. (2006) Seismic vibration control using superelastic shape memory alloys. *ASME J. Engineering Materials and Technology*, **128**, 294-301.
- Miyazaki, S. (1990) *Thermal and stress cycling effects and fatigue properties of Ni-Ti alloys, engineering aspects of shape memory alloys*. T. W. Duerig, K. N. Melton, D. Stockel, & C. M. Wayman, eds., Butterworth-Heinemann, London, 394-413.
- Ocel, J., DesRoches, R., Leon, R. T., Hess, W. G., Krumme, R., Hayes, J. R., & Sweeney, S. (2004) Steel beam-column connections using shape memory alloys. *ASCE J. Struct. Eng.*, **130**, 732-740
- Ozdemir, H. (1976) Nonlinear transient dynamic analysis of yielding structures. *PhD Thesis*, University of California, Berkeley, CA.
- Pampanin S., Christopoulos, C., & Priestley, M. J. N. (2003) Performance-based seismic response of frame structures including residual deformations. Part II: multi-degree of freedom systems. *Journal of Earthquake Engineering*, **7**(1), 119-147.
- Prahlad, H., & Chopra, I. (2003) Development of a strain-rate dependent model for uniaxial loading of SMA wires. *J. Intell. Mater. Syst. Struct.*, **14**, 429-442.
- Reina, P., & Normile, D. (1997) Fully braced for seismic survival. *Engineering News Record*, July 21, pp. 34-36.
- Restrepo, J. I. (2006) New generation of structural concrete systems for seismic resistance. *Proc. First European Conference on Earthquake Engineering and Seismology*, Geneva, Switzerland, 3-8 September 2006.
- Ricles, J. M., Sause, R., Garlock, M. M., & Zhao, C. (2001) Posttensioned seismic-resistant connections for steel frames. *Journal of Structural Engineering*, **127**(2), 113-121.
- Sabelli, R., Mahin, S.A., & Chang, C. (2003) Seismic demands on steel-braced buildings with buckling-restrained braces. *Engineering Structures*. **25**, 655-666.
- Sadjadpour, A., & Bhattacharya, K. (2006) A micromechanics inspired constitutive model for shapememory alloys: the one-dimensional case. *Smart Mat. Struct.*, **16**, S51-S62
- Sakai, J., Jeong, H., & Mahin, S. A. (2006) Reinforced concrete bridge columns that re-center following earthquakes. *Proc. 8NCEE*, San Francisco, CA, April 18-21, 2006.
- Seo, C. Y. (2005) Influence of ground motion characteristics and structural parameters on seismic responses of SDOF systems. *Ph.D. thesis*, Lehigh University, Bethlehem, PA.
- Seo, C. Y., & Sause, R. (2005) Ductility demands on self-centering systems under earthquake loading. *ACI Structural Journal*, **102**(2), 275-285
- Sommerville, P., Smith, N., Punyamurthula, S., & Sun, J. (1997) Development of ground motion time histories for Phase 2 of the FEAM/SAC steel project. *SAC Background document SAC/BD-91/04*, SAC joint venture, Sacramento, California.
- Stanton, J., Stone, W. C., & Cheok, G. S. (1997) A hybrid reinforced precast frame for seismic region. *PCI Journal*, **42**(2), 20-32.
- Tanaka, K. (1986) A thermomechanical sketch of shape memory effect: one-dimensional tensile behavior. *Res. Mechanica*, **18**, 251-263.

- Torra, V., Isalgue, A., Lovey, F. C., & Martorell, F. (2007) Phase metastability in shape memory alloys. Dampers in engineering via SMAs. *Proc. Estonian Acad. Sci. Phys. Math.*, **56**(2), 177–196.
- Uang, C. M., Nakashima, M., & Tsai, K. C. (2004) Research and application of buckling-restrained braced frames. *International Journal of Steel Structures*, **4**, 301-313.
- Whittaker, A. S., Krumme, R., Sweeney, S. C., & Hayes, J. R. (1995) Structural control of building response using shape-memory alloys. Phase 1. *USACERL Technical Report 95/22*, Construction Engineer Research Laboratories, US Army Corps of Engineers, Champaign, IL.
- Wilde, K., Gardoni, P., & Fujino, Y. (2000) Base isolation system with shape memory alloy device for elevated highway bridges. *Eng. Struct.*, **22**(3), 222-229.
- Witting, P. R., & Cozzarelli, F. A. (1992) Shape memory structural dampers: material properties, design and seismic testing. *NCEER Report No. 92/13*, State University of New York, Buffalo, USA.
- Zhang, Y., & Zhu, S. (2007) A shape memory alloy-based reusable hysteretic damper for seismic hazard mitigation. *Smart Mater. Struct.*, **16**, 1603-1613.
- Zhang, Y., Camilleri, J. A., & Zhu, S. (2008) Mechanical properties of superelastic Cu-Al-Be wires at cold temperatures for seismic protection of bridges. *Smart Materials and Structures*, **17**, 025008.
- Zhu, S. (2007) Seismic behavior of framed structural systems with self-centering friction damping braces. *Ph.D. thesis*, Lehigh University, Bethlehem, PA
- Zhu, S., & Zhang, Y. (2007a) Seismic behavior of self-centering braced frame buildings with reusable hysteretic damping brace. *Earthquake Engineering and Structural Dynamics*, **36**, 1329-1346
- Zhu, S., & Zhang, Y. (2007b) A thermomechanical constitutive model for superelastic SMA wire with strain-rate dependency. *Smart Materials and Structures*, **16**, 1696- 1707
- Zhu, S., & Zhang, Y. (2008) Seismic analysis of concentrically braced frame system with self-centering friction damping braces. *ASCE Journal of Structural Engineering*, **134**(1), 121-131

*Chapter 8*

# APPLICATION OF NUMERICAL TOOLS FOR THE MODELLING OF GRANULAR SOIL BEHAVIOUR UNDER EARTHQUAKES: THE STATE-OF-THE-ART

*S. López-Querol\**

Dept. of Civil Engineering, Univ. de Castilla - La Mancha,  
Avda. Camilo José Cela, s/n, 13071, Ciudad Real, Spain

## Abstract

Granular soils suffer changes in their mechanical properties when they are subjected to seismic loadings. There are two extreme situations related to the soil saturation conditions, i.e. dry and saturated soil, for which densification and liquefaction phenomena, respectively, may happen. Densification is due to the solid skeleton rearrangement as the shaking goes on, which produces a reduction of the initial soil volume to occur and, typically, the soil stiffness to increase. Conversely, liquefaction may be found in saturated sandy soils not enough drained or totally undrained; the same trend of the solid particles to rearrange during vibrations causes the accumulation of excess pore water pressure to develop, and consequently, a reduction of both initial effective stress and soil stiffness, until the soil does not behave like a solid any more but like a fluid. Both phenomena may result in important negative effects on natural and man made geo-structures (like dams, road and railway embankments or foundations). Therefore, numerical codes capable to model them may constitute useful tools for diminishing possible casualties and excessive material resources to be spent at seismic sites. Constitutive laws for soils specifically developed for dynamic loadings are needed for accurately reproduce the physics of these processes. In this chapter, several examples of densification and liquefaction cases in the history are provided, after which a state-of-the-art on the most important and used constitutive laws, coupled formulations, and examples of applications are given.

## 1. Introduction

It is well known that dry sands subjected to dynamic loadings tend to suffer the rearrangement of its solid skeleton, acquiring denser configurations than at the beginning of the

---

\*E-mail address: MariaSusana.Lopez@uclm.es. Tel.: 34 926 29 53 00 ext. 6263, Fax:34 926 29 53 91

solicitation, but also suffering high volumetric strains and soil surface settlements which may cause the failure of foundations, structures and geo-structures. An increase of the sand relative density due to the decreasing trend of the void ratio, produce the soil bearing capacity to increase at the end of the shaking. This phenomenon is known as “densification” or dynamic compaction.

On the other hand, the process of liquefaction occurs in saturated and not enough drained sand, and can be summarized as follows: when it is subjected to vibrations, tends to suffer densification, and therefore, the void ratio diminishes and the volume occupied by the fluid phase decreases. If drainage is not enough, an increase of the pore fluid pressure takes place, which produces the solid skeleton stresses to decrease (effective stress) as well as the soil stiffness; finally, when the effective stress totally disappear, it can be said that liquefaction has occurred.

This chapter shows several field evidences of densification and liquefaction. The experimental research of these phenomena is summarized next, as well as the most important and used constitutive models. Biot’s equations and their main formulations are explained, highlighting their main advantages and countermeasures. Finally, several examples of computations of densification and liquefaction are given.

## 2. Dry Sandy Soils: Densification

### 2.1. Field Evidences of Dry Soil Settlements after Earthquakes

There are a lot of field evidences of huge strains suffered by dry sandy soil layers after earthquakes. These strains may produce the infrastructures to collapse, as well as settlements of crest concrete and earthfill dams, and differential vertical movements of building foundations to occur. After San Fernando earthquake, in 1971, settlements of the range of 10 to 15 centimeters were observed in a dry 12 meters deep sandy layer, whereas in Skopje earthquake (1963), most of the observed structural damages were suffered on those founded over dry sandy layers (46; 53). Table 1 (53) summarizes some field data reported after several earthquakes, also providing the magnitude of the corresponding earthquake and the maximum recorded acceleration.

Roads and highways are exceptional witnesses in what strains suffered during an earthquake concerns, because comparing their geometry before and after the event is very easy. An example of the failure of a highway, taken place during the San Fernando earthquake,

**Table 1. Recorded settlements on dry sandy layers after several earthquakes (53)**

Earthquake	Tokachioki	Tokachioki	Niigata	Niigata	Miyagiken Oki
Year	1968	1968	1964	1964	1968
Magnitude	7.9	7.9	7.5	7.5	7.4
Site	Hachinohe	Hachinohe	Niigata	Niigata	Arahama
Max. acc. (g)	0.20	0.23	0.16	0.18	0.20
Thickness (m)	5	2	9	9	9
Settlement (m)	0.40-0.50	0.01-0.02	0.20	0.00	0.20



Figure 1. Settlement in a highway after the San Fernando earthquake, in 1971. (Courtesy of the National Information Service for Earthquake Engineering, EERC, University of California, Berkeley).

in 1971, is shown in Fig.1.

In Fig.2, a similar circumstance in a road after the Niigata earthquake, in 2004, is given. In this case it is very easy to calculate the final settlement, by comparing the final road surface elevation and the culvert.

## 2.2. Experimental Research

During the last 60's and first 70's, the densification begun to be deeply analysed by means of a huge number of field and laboratory tests. These researches aimed to point out the dependence of this phenomenon on the factors it is controlled by.

One of the first experimental investigations was performed by Viering (55), who tried to identify the cohesionless soil behaviour when subjected to high and medium frequencies of loading (10-80 Hz). To achieved that, this researcher took several field measurements at several distances from a source of vibration. Following this path, several soil stiffness parameters, based on the main soil resonant frequency, were determined. Correlations between relative density and settlements were also obtained, as well as the soil behaviour due to vibrations. As a main conclusion of this research, it was obtained that a minimum relative density of 0.7 is desirable, not only for reducing the settlements, but also for improving the soil bearing capacity.

Ko and Scott (29) carried out cyclic hydrostatic compression tests on cubic sand samples. They demonstrated that, during the first cycles, a small non recoverable volumetric strain takes place, after what it performs non linearly, but elastically. Thus, this investigation points out that cycles of hydrostatic loading do not have too much influence on the final volumetric strain of the sand.

One of the first researchers who carried out laboratory tests on sand under shear stresses



Figure 2. Settlement of a road surface after the Niigata 2004 earthquake (Courtesy of James Arendt, Japan).

was Drnevich (20). This author investigated the sand behaviour by means of resonant column tests, using high cyclic strain amplitudes. The conclusion was that the sand displays elastic behaviour for very small shear strains (of about 0.0001 for the analysed materials). For higher shear strains, plastic volumetric strain (densification) appears.

Soon after, Greenfield and Misaszek (25) developed a study on Ottawa sand with four different grading curves, in order to identify the relationship between grading and sand performance under vibrations. Thus, several sandy, dry samples were subjected to fifty cycles of harmonic, horizontal loadings with different frequencies ranging from 10 to 50 Hz. As the main results of this analysis, it was concluded that: 1) different gradings produce different densification values to appear; 2) for a constant amplitude of applied shear strain, there is a resonant frequency (of about 30 Hz for the analysed sand) for which densification reaches a maximum value; and 3) if the critical acceleration for the obtained resonant frequency with constant amplitude tests remains constant, the final value of densification seems to be independent of the frequency of loading.

During the next four years, several analysis on dry sand densification were made, all of them by means of cyclic shear strain apparatus. These researches gave some light on the basis of this phenomena and the factors which mainly control it. The first investigation of this type was done by Anderson (2), who carried out a set of tests on dune sand, applying cyclic shear strain amplitudes ranging from 0.01 and 0.07, and frequencies of loading from 3 to 7 Hz. Silver and Seed (51) and Seed and Silver (46) tested dry Crystal Silica N20 sand, applying until 300 cycles to samples with different initial relative density, shear strain amplitudes and vertical stresses (Fig.3 and 4). The main conclusion was that densification is mainly related to the initial relative density, shear strain and number of cycles, and they found almost no influence of the vertical stress on the final amount of densification. In both

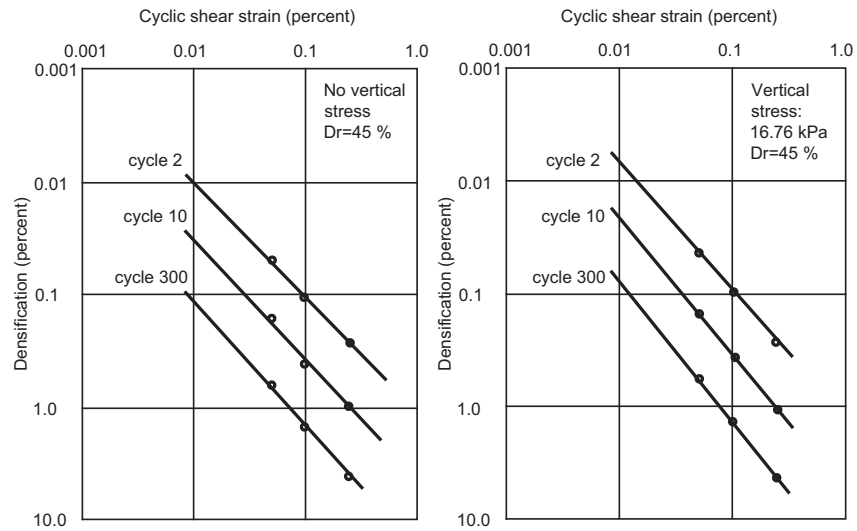


Figure 3. Densification of Crystal Silica N 20 sand with  $Dr = 45\%$ , subjected to cyclic shear strain tests (after (46))

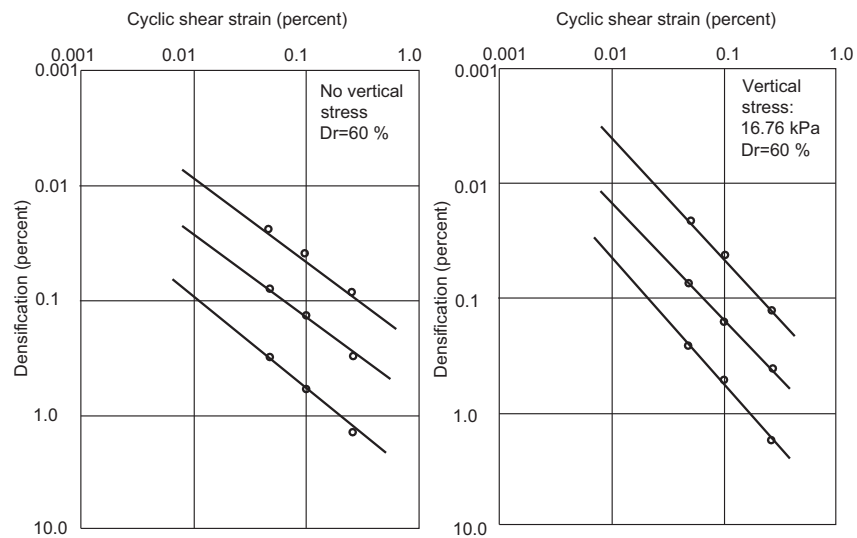


Figure 4. Densification of Crystal Silica N 20 sand with  $Dr = 60\%$ , subjected to cyclic shear strain tests (after (46))

Figs.3 and 4, left graph displays the results of tests without vertical loading, while the right one shows the results with a  $16.76 \text{ kPa}$  vertical loading.

Following this path, Youd (60) studied dry and saturated, totally drained Ottawa sand. This researcher also used cyclic shear strain tests, but in this case, applying until 15000 cycles, and a higher range of cyclic shear strain amplitudes (between 0.001 and 0.09). Again, some of the derived conclusions were the same: he found a strong dependence of the den-

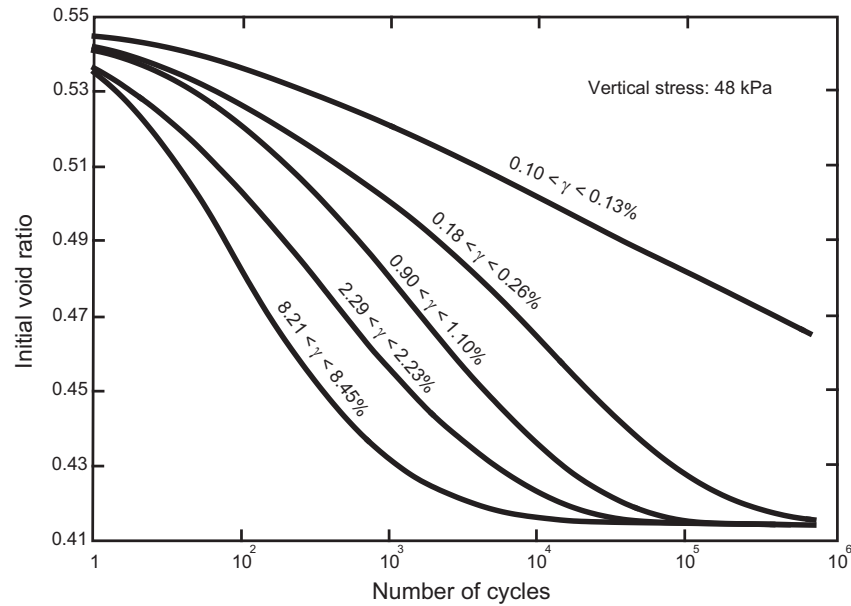


Figure 5. Densification of Ottawa sand subjected to cyclic shear strain tests (after (60))

sification on the amplitude of shear strains, as well as the number of applied cycles (Fig.5). However, this researcher also found a negligible dependence of the final result on dry sand and the frequency of loading, for frequencies ranging from 0.2 to 2.0 Hz (Fig.6).

Pyke *et al.* (43) used a shaking table to investigate the densification of dry Monterrey N. 0 sand. These authors analysed cylindrical samples vertically overloaded by a steel plate. The conducted tests were performed under stress controlled conditions, and the obtained shear strains at the end of the tests were not reported. The influence of multidirectional loading (two horizontal and one vertical components) was intended to be found with these tests. They concluded that the densification obtained by the two horizontal components of loading, applied together, is equivalent to the addition of the results obtained after separately subjecting the sample to both components. Therefore, densification can be decoupled into the horizontal components of loading (Fig.7a). In addition, a vertical dynamic acceleration applied together with a horizontal acceleration, can produce increments of around 50% in the final amount of densification (Fig.7b).

Joining all the described experimental results together, it is possible to identify the key factors controlling this phenomenon, in order to develop an accurate constitutive law. The next summary was firstly presented by Youd (60) and completed by Cuéllar (18), and it is the beginning of a rational approach to the problem of the numerical modelling of the densification:

1. Dynamic volumetric strains applied to a sample do not produce a significant densification to occur.
2. Dynamic shear strains applied to a sample are one of the most important factors controlling densification. All the conducted experimental researches in the literature

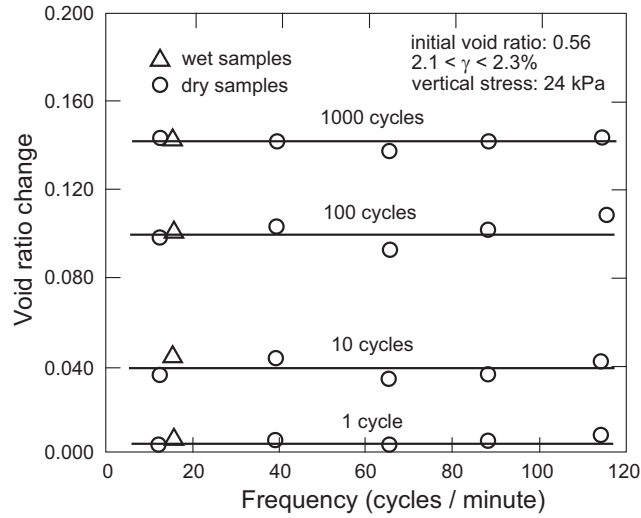


Figure 6. Change of void ratio against frequency of loading for Ottawa sand subjected to cyclic shear strain tests (after (60))

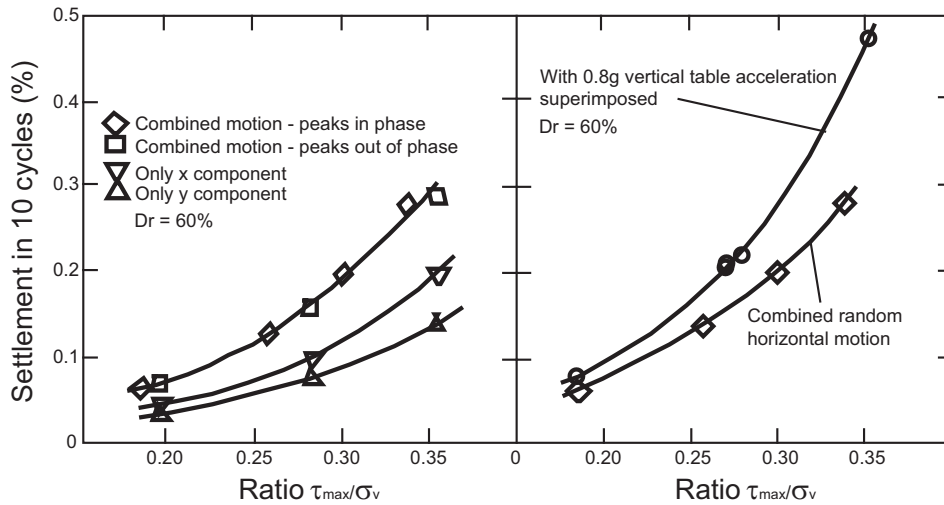


Figure 7. Comparison of settlements of sand subjected to shaking table stress controlled tests. a) 1-D and 2-D loading. b) 3-D loading (after (43))

have correlated the amplitude of dynamic shear strains (in cyclic shear strain tests, resonant column and drained dynamic triaxial test) and the densification. The bigger the amplitude of dynamic shear strain, the bigger the densification.

3. The initial relative density of a sample is other of the main factors. The bigger the initial relative density, the smaller the densification.
4. The confining stress does not seem to be a key factor, attending to most of the exper-

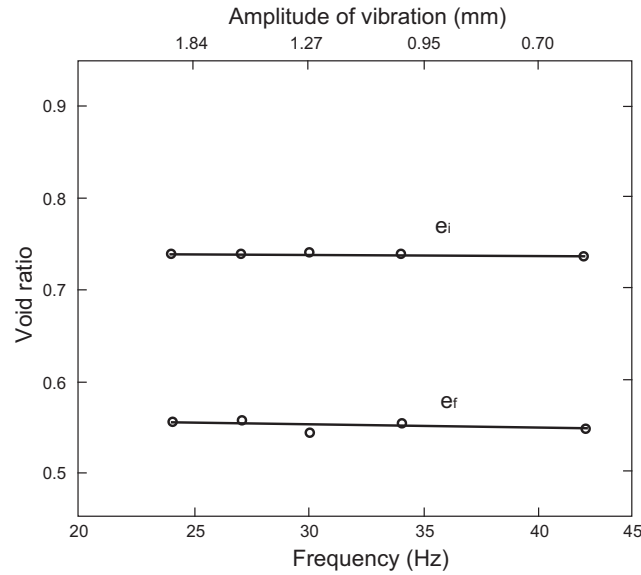


Figure 8. Initial and final void ratio of Ottawa sand subjected to constant acceleration, variable frequency vibrations (after (25))

imental research given in the literature.

5. Attending to the experimental results presented by Youd (60), the frequency of loading does not have a significant influence on the final amount of densification. It is worth to point out, however, that this author presented results for low values of frequency (until 2 Hz). Greenfield and Misiaszek (25) found an important influence of the frequency for higher values (until 80 Hz). On the other hand, these authors showed that the peak acceleration is more relevant than the frequency of loading, and, for a given acceleration, keeping constant the frequency, the densification does not almost suffer changes of consideration (Fig.8).
6. The number of cycles has been identified by all the authors as one of the key factors controlling densification.

### 2.3. Constitutive Models

The first constitutive laws developed for specifically modelling the sandy soil densification were semi-empirical approaches. These models were derived on the base of the above mentioned experimental researches, and by the same authors.

Seed and Silver (46) proposed a method based on extrapolating the cyclic shear strain tests results to the sandy soil layers. In order to achieve that, it is necessary to depart from the densification for certain values of initial relative density, amplitude of shear strain and number of cycles. After that, a sandy soil layer is vertically divided into several parts (the more divided, the more accurate the method); equivalent shear strain and number of

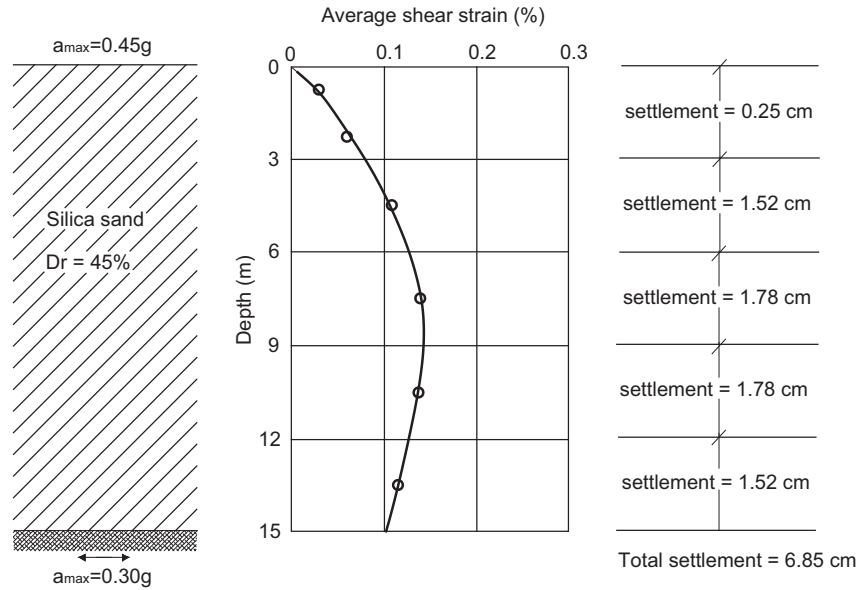


Figure 9. Computation of the settlement suffered by a Crystal Silica N20 sandy layer in the Sand Fernando (1971) earthquake, by using the Seed and Silver method (after (46))

cycles must be estimated in each one of these parts, and the corresponding experimental densification is then associated to each sub-layer. The total layer settlement is then obtained by adding all the settlements of the sub-layers (Fig.9).

Youd (60) proposes a very similar approach, applying it to the analysis of a sandy layer compaction by static and dynamic loadings, as well as vibrations produced by the Niigata (1964) earthquake. In all the cases, volumetric strains at several layer elevations are computed by correlating field and experimental results, and again, the total settlement is computed by adding all the sub-layer results.

Other authors presented purely empirical and quasi-empirical models, correlating shear strains and densification. Martin *et al.* (33) also took into account the strain history suffered by the soil layer. Finn and Byrne (22) used a “equivalent elastic method”, by means of which the increment of densification was estimated using the Martin *et al.* (33) formula.

Tokimatsu and Seed (53) developed a simplified method, based on SPT data. Again, a layer is subdivided into several parts, and shear strain due to an earthquake is estimated in each one of them, by means of the elastic shear modulus and the peak acceleration. Pradel (41) made several analytical adjustments to Tokimatsu and Seed’s method, simplifying the computation process.

All of the above mentioned models are very difficulty applicable in a numerical model using the general dynamic equations, because of the high number of tables and graphics with empirical data involved. Trying to shorten this disadvantage, rational numerical models were developed.

One of the first rational densification numerical model was presented by Cuéllar (18). This author approaches the problem from the endochronic theory framework. This for-

mulation in based on two endochronic functions, namely: rearrangement function,  $\xi$ , and densification function,  $\zeta$ . Both values are incrementally determined in time, and are positive and monotonically increasing:

$$d\xi = |d\gamma| \quad (1)$$

$$d\zeta = \frac{n}{4} \cdot |100 \cdot \gamma|^{n-1} \cdot |d\gamma| \quad (2)$$

In the above equations,  $\gamma$  stands for current shear strain, and  $n$  is one of the densification law parameters. The densification,  $\varepsilon_v$ , is incrementally computed as follows:

$$d\varepsilon_v = -\frac{n}{4} \cdot \frac{|100 \cdot \gamma|^{n-1}}{1 + \alpha \cdot \zeta} \cdot |d\gamma| \quad (3)$$

where  $\alpha$  is the second law parameter. Both  $n$  and  $\alpha$  parameters were considered by Cuéllar to be constant for each sand, and dependent on its initial relative density. However, this author only analysed data for a few number of cycles. It has been recently demonstrated that, for quartzitic sands, these parameters are not independent of the number of cycles of loading, and also, this law can be generalized, yielding only one single parameter which needs to be calibrated for each type of sand (8). Thus,  $n$  and  $\alpha$  can be expressed as follows:

$$n = A \cdot \ln(N) + B \quad (4)$$

$$\alpha = C \cdot N^{-D} \quad (5)$$

where:

$$A = \frac{1}{2} \left( \frac{e_{max}^2 - e_{min}^2}{1 + e_{max} - Dr_0 \cdot (e_{max} - e_{min})} \right) \quad (6)$$

$$D = \frac{1}{2} (e_{max}^2 - e_{min}^2) \quad (7)$$

$$B = D + 1 \quad (8)$$

$C$  is a parameter lineally dependent on the initial relative density,  $Dr_0$ :

$$C = -C_0 + 50 \cdot Dr_0 \quad (9)$$

In the above equations,  $N$  is denotes the current equivalent number of cycles, which must be determined every time step,  $Dr_0$  is the initial relative density, and  $C_0$  is the only type of sand dependent densification law parameter.

Working along this path, Zienkiewicz *et al.* (62) proposed a very similar densification model, but in this case, dependent on three parameters instead of two. These authors also implemented their model in a coupled numerical code in order to compute liquefaction problems.

It is self evident that, solving a densification model together with the general dynamic equations represents a very non linear problem, which requires advanced numerical tools,

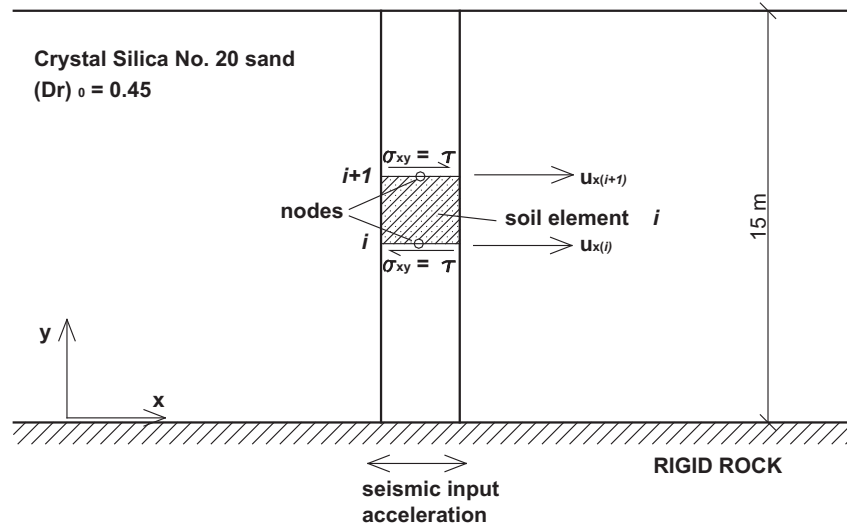


Figure 10. Sandy layer geometry and finite element scheme, used in the numerical model of the densification (8) in the San Fernando (1971) earthquake.

and only in very few cases an analytical solution exists. Przewlocki and Knabe (42) proposed an analytical solution, departing from the peak acceleration at the rigid base of the layer and the number of equivalent cycles. This analytical solution needs very strong mathematical simplifications, and therefore, the solution is very far from being trustable.

Finally, Vincens *et al.* (56) proposed a model based on obtained the first vibration mode and the maximum amplitude of the soil answer, as well as the equivalent number of cycles. The main contribution of this method is that it also considers the second mode of vibration in addition to the first one.

## 2.4. Example of Computation

The soil layer sketched in Figs.9 and 10 has been analysed by several of the above mentioned authors. It consists of a 15 meters deep layer of Crystal Silica N20 sand, with  $Dr_0 = 45\%$ . This layer rests over rigid rock, which is horizontally subjected to the San Fernando earthquake (1971). Figure 10 also shows the 1-D finite element configuration used by Blázquez and López-Querol method (8). The applied horizontal accelerogram, recorded at the Castaic Station (N69W component) during this earthquake, is given in Fig.11. All the authors obtained similar values of final settlement at the layer surface, which are also in good agreement with field observations. These computed values are given in Table 2.

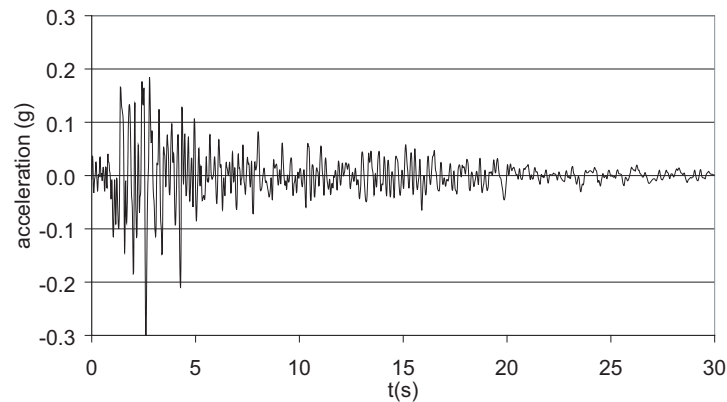


Figure 11. Accelerogram recorded on rock at the Castaic Station in the San Fernando earthquake (1971). Horizontal N69W component.

**Table 2. Computed settlements in the San Fernando earthquake (1971) by several authors.**

Authors	Computed settlement (cm)
Seed and Silver (46)	6.8
Tokimatsu and Seed (53)	8.6
Vincens <i>et al.</i> (56)	6.9
Blázquez and López-Querol (8)	8.0

### 3. Saturate Sandy Soils: Liquefaction

#### 3.1. Field Evidences of Liquefaction during Earthquakes

When liquefaction takes place in sandy soil, there exists a rearrangement in its solid skeleton, and as a result, the modification of its initial internal structure. Sometimes, sand boils at a sandy soil layer surface which suffer liquefaction can be observed after an earthquake. They are the most trustable field evidence that this phenomenon has taken place. The Paleoseismology allows us to identify and date these typical geological structures, and then it is possible to know if a soil has undergone liquefaction or not, and when it approximately took place. An example of the application of these techniques are the fossil sand boils found in Santa Cruz de Tenerife (Spain), which seem to be 10000 years old (24).

Earthquakes are as old as the Earth. Unfortunately, graphical evidences are not that antique. The first documents related to liquefaction phenomenon which we can find are drawings depicting sand boils after earthquakes, sometimes forming little lakes. Figure 12 is an example, corresponding to Calabria earthquake, in 1783. Figure 13 shows sand boils appeared after Corinto earthquake, in 1861.

The first pictures on liquefaction which can be found in the literature are dated on the end of the XIX century. Figures 14 and 15 respectively show field evidences found after Assam (1987) and San Francisco (1906) earthquakes.



Figure 12. Drawing of a little lake appeared after the Calabria earthquake (1783). Authors: Pompeo Schiantarelli and Ignazio Stile. (Courtesy of the National Information Service for Earthquake Engineering, EERC, University of California, Berkeley).

One of the most famous case of liquefaction occurred during Niigata earthquake, in 1964. Figure 16 represents the most typical and known case of liquefaction related to building and foundations. This picture shows structurally undamaged buildings which have tilted and floated within their liquified sandy base. Figure 17 also shows sand boils appeared after the same earthquake.

In addition to sand boils and buildings floating, another field evidence of liquefaction are the lateral spreading, with longitudinal fissures appearing at the soil surface. Figure 18



Figure 13. Drawing of sand boils after the Corintio earthquake (1861). (Courtesy of the National Information Service for Earthquake Engineering, EERC, University of California, Berkeley).



Figure 14. Sand boil after the Assam earthquake (1897). (Courtesy of the National Information Service for Earthquake Engineering, EERC, University of California, Berkeley).



Figure 15. Sand boil after the San Francisco earthquake (1906). (Courtesy of the National Information Service for Earthquake Engineering, EERC, University of California, Berkeley).



Figure 16. Liquefaction at buildings foundation, Niigata earthquake (1964). (Courtesy of the National Information Service for Earthquake Engineering, EERC, University of California, Berkeley).



Figure 17. Sand boils due to liquefaction, after the Niigata earthquake (1964). (Courtesy of the National Information Service for Earthquake Engineering, EERC, University of California, Berkeley).

shows an example of this kind of phenomenon, in Caracas earthquake (1967).

Another one of the most famous cases of liquefaction was the failure of the upstream sand fill of the Lower San Fernando dam (Los Angeles area), which happened several minutes after San Fernando earthquake in 1971. It was an around 50 meters height, heterogeneous earth fill dam. Around 8000 people who lived downstream were evacuated during the next days after the earthquake, because the reservoir was almost full of water, and the collapse of the whole dam seemed to be very likely to occur. However, the dam finally did not fail, and was successfully repaired. This case study has been deeply analysed by a lot of researches, because the characteristics of the soil, the geometries before and after the failure, and an approximate acceleration record are available (47; 48; 49; 15; 63; 16; 26; 28; 9). Figure 19 shows a picture of the dam after the earthquake.

Although the Lower Sand Fernando dam is the most famous case of liquefaction in earth dams, it is not the only one (35; 36). Another possible failure of dams due to liquefaction happened at the Niteko Complex (Japan), during the Kobe earthquake, in 1995. Although there was not any evidence of liquefaction within the dams, there appeared sand boils in the proximities, showing liquefaction in the surrounding soils. A picture of these dams after their failure is provided in Fig. 20.

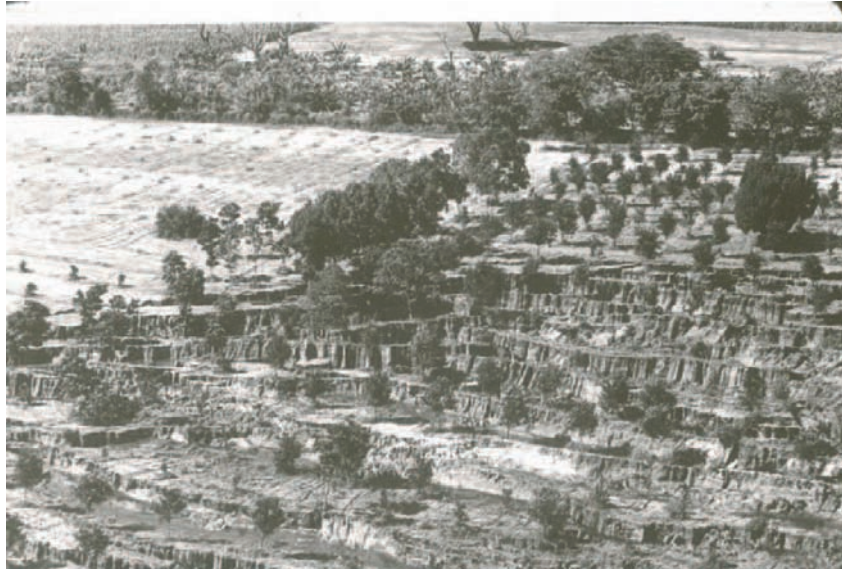


Figure 18. Lateral spreading in a sandy layer after the Caracas earthquake (1967). (Courtesy of the National Information Service for Earthquake Engineering, EERC, University of California, Berkeley).



Figure 19. Lower San Fernando dam after the San Fernando earthquake (1971). (Courtesy of the National Information Service for Earthquake Engineering, EERC, University of California, Berkeley).



Figure 20. Niteko earth dams complex, after the Kobe earthquake (1995). (Courtesy of the National Information Service for Earthquake Engineering, EERC, University of California, Berkeley).

Roads are geo-structures very sensitive to earthquakes. In gradings of the granular layers it is unusual to find a high fine content. It means that, if these layers are dry, they are likely to densify, and if they are saturated and not enough drained, to liquefy. If the road pavement is an asphaltic or concrete layer, the smallest deformability of the pavement may cause its failure when the lower layers undergo high volumetric strains. Then, roads usually suffer a very characteristic type of failure, which consists of longitudinal fissures not exactly located at the road axis, but a bite displaced (31). Figure 21 shows a detail of a road pavement failure due to the liquefaction of the granular layer.

### 3.2. Experimental Research: Historical Review

The first researcher who reported liquefaction in soils was Terzaghi (52), who introduced the “meta-stability” concept to justify the instability of submerged slopes. According to this author, meta-stable soil structure takes place during the sedimentation of fine, cohesionless sand over high void ratio preexisting soil. If a small grain slowly falls and finds a first point of contact, the reactions at the support may be enough for preventing the grain to roll or slide, and therefore, to find a more stable location (Fig.22). High void ratio, small grain



Figure 21. Detail of a failed road due to liquefaction after the Loma Prieta earthquake (1989); Moss Landing State Beach. (Photo: Dan Orange; Courtesy of Justin Revenaugh, Earth Sciences, University of California).

size and very collapsible behaviour are the main features of this kind of soils. Excess pore fluid pressure suddenly increases after collapse, causing liquefaction to occur. This theory explains the so called “static” liquefaction, but does not give answers to the causes of the liquefaction due to vibrations, which may take place in soils stable under static loadings.

Casagrande pointed out that, on one hand, shear stresses more likely cause liquefaction to occur than compression stresses, and, on the other, fine sands liquefy more frequently than coarse sands. This researcher was the first one on developing the concept of “critical state”: loose sands, when sheared, tend to acquire a denser configuration, while dense sands tend to dilate. For a given sand, there is a void ratio, confining stress dependent, for which neither contraction nor dilation takes place under shear loadings. This void ratio is known as critical state. Following this line of thought, if a sand initially displays a void ratio higher than the critical state, may suffer liquefaction under monotonic shear stress. This theory is not capable to explain liquefaction due to cycles of loading, since a dense sand subjected to enough number of cycles, may liquefy if the amplitude of loading is strong enough, as it was demonstrated by Seed and Lee (45) amongst others.

Of relevant importance was the research developed by Ishihara *et al.* (27). These authors conducted undrained monotonic and cyclic triaxial tests on several samples of sand under the same initial conditions of density and stress. Figure 23 summarizes this investigation; it provides the results of three tests, in terms of stress paths:  $p'$  (effective confining stress) against  $q$  (deviatoric stress). The initial state of isotropic stress is common in all the samples, and it is depicted with point 1 in the figure. For the sample sketched with triangles, compression was applied until reaching point 2, after what unloading took place. From 1 to 2,  $p'$  diminishes, and therefore, the pore fluid pressure increases. Another sample (this one sketched with solid circles) was tested under exactly the same isotropic stress initial conditions, but in this case the amplitude of cyclic loading was higher. Thus, after reaching

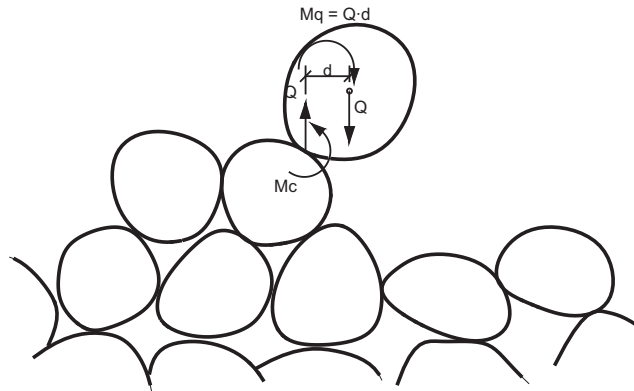


Figure 22. Sketch of the metastable structure origine.

point 2, instead of unloading, loading went on. In point 3, the stress path suffers an elbow: the effective mean principal stress,  $p'$ , begins to increase at this point (pore fluid pressure begins to decrease). This change of behaviour was defined by Ishihara *et al.* as “phase transformation”. In this second sample, unloading takes place at point 4. It is noticeable how, for these two samples, which have exactly the same initial conditions, the slope of the stress path in unloading is quite different: after suffering phase transformation, a sample is weaker, and the slope 2-3' is steeper than 4-6; it means that liquefaction takes place faster after than before reaching phase transformation. It is also worth to point out that the third sample (sketched with empty circles), which is loading in extension instead of compression, reaches point 6 in the first cycle of loading, which means that it is weaker than the samples firstly loaded in compression.

During the 1980s, a lot of experimental research was conducted, looking for the relationship between monotonic and cyclic sand behaviour, a problem unsolved since Casagrande's times. In this sense, it is remarkable the investigation conducted by Castro (12; 13; 14), followed by Alarcon-Guzman *et al.* (1). These authors tried to investigate the liquefaction from the critical state framework (called by them “steady state” and critical void ratio). These researchers used the state diagram  $p' - e$  (mean effective stress against void ratio). Depending on the initial state of a given sample of sand, and its relative location respect steady-state line (determined by monotonic undrained triaxial tests) and critical void ratio line (by monotonic drained triaxial tests), the sample initially tends to contract or dilate when subjected to cyclic shear stress. In addition, they pointed out that, for two initially identical samples, one of them subjected to monotonic loading, and the other, to cyclic loading, both under undrained conditions, if the stress path of the second one touches the stress path of the first one, the cyclic loading path follows the monotonic one until failure, which may be interpreted as a “collapse”. This circumstance is depicted in Fig.24, where both pore fluid pressure evolution and monotonic and cyclic stress paths are sketched.

Joining the researches of Ishihara *et al.* (27) and Alarcon-Guzman *et al.* (1), the types of failure of saturated sand under cyclic loading can be summarized as follows:

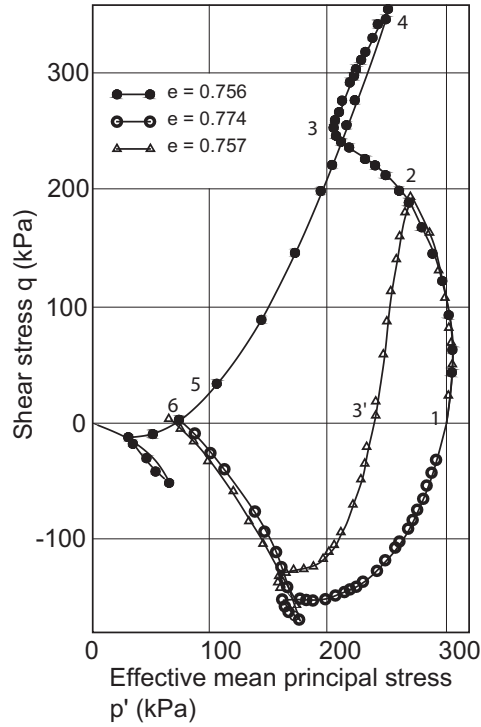


Figure 23. Experimental evidence of phase transformation in sands (after (27)).

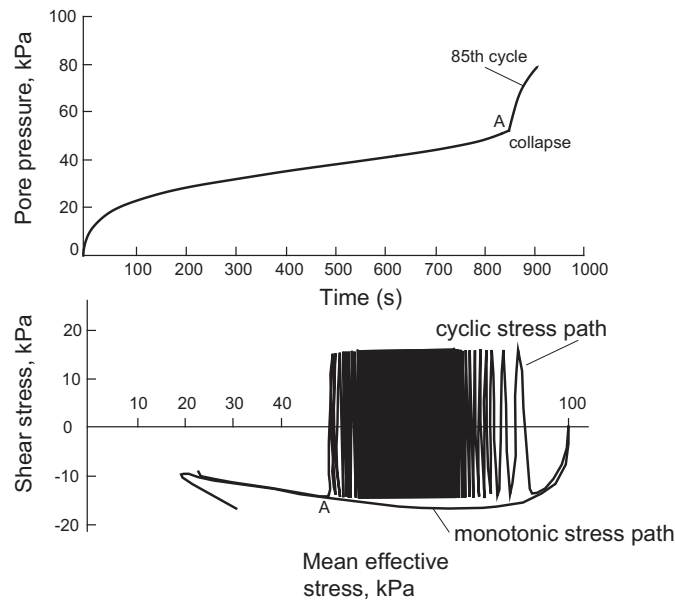


Figure 24. Result of an undrained cyclic torsional test: collapse of the sample (after (1)). a) Evolution of the pore fluid pressure in time. b) Shear stress against effective stress.

- Continuous loss of effective stress, cycle by cycle, until the stress path crosses the phase transformation line. Depending on the nearness of this line to the failure line, liquefaction after very few more cycles (loose sand; Fig.25) or cyclic mobility (dense sand); Fig.26), will occur. It is worth to point out that the difference between liquefaction and cyclic mobility is that, in the former one, shear strains tends to infinity when failure takes place, while in cyclic mobility they are limited.
- Loss of effective stress, cycle by cycle, until the stress path crosses the monotonic line. In this case, the sand collapses and no more cycles of loading are necessary for reaching the failure due to liquefaction (Fig.27).

Nowadays some attempts have been made trying to establish a critical state framework for the undrained cyclic sand behaviour. In this sense, it is remarkable the research performed by Qadimi and Coop (44) on Dogs Bay Sand (a carbonate sand), which has been deeply analysed under monotonic loadings. However, the drained cyclic sand behaviour relation with the critical state is still far from being clarified.

All the above mentioned experimental research aimed to better understand the saturated sand behaviour under vibrations, in order to develop accurate constitutive laws which take into account all possible mechanisms of failure. However, only models subjected to validation are trustable enough for numerical modelling engineering designs or to prevent possible liquefaction risks. Unfortunately it is very difficult to validate a liquefaction numerical model with field measurements, because of the great dimensions of the prototypes, and because earthquakes are most of the times very unexpected circumstances. On the other hand, soil behaviour is very stress dependent, and therefore scaled models lack of accuracy and are only able to qualitatively reproduce the investigated phenomenon. Thus, apparatus like the shaking table have been very employed in earthquake research, but more successfully from the structural than geotechnical point of view. In order to overcome this countermeasure, the centrifuge equipment was developed to create scale models in which its initial stress state is reproduced by scaling the gravity acceleration (until  $100g$ ), by rotating at high velocities. Thus, since the 1990s until nowadays, this apparatus is of generalized use in soil dynamics (64). The following centrifuge projects are of special importance in what verification of numerical models concerns:

- VELACS (*VERification of Liquefaction Analysis by Centrifuge Studies*): Nevada sand samples with different initial relative densities were tested under undrained monotonic and cyclic shear stress and triaxial tests (3). First, investigation teams from all over the world developed numerical modelling, after what the experimental research on centrifuge was carry out, and compared to the numerical results. After the end of this project, a lot of verifications of numerical codes using these experimental data have been made (37; 38; 58; 59; 21; 11).
- Earthquake Induced Damage Mitigation from Soil Liquefaction (10). The analysed material in this case was Fraser River sand. It is remarkable the high number of conducted cyclic shear stress tests with different initial relative density and confining stress conditions for constitutive model calibration purposes. Again, the conducted centrifuge tests have been used for verification (39; 32).

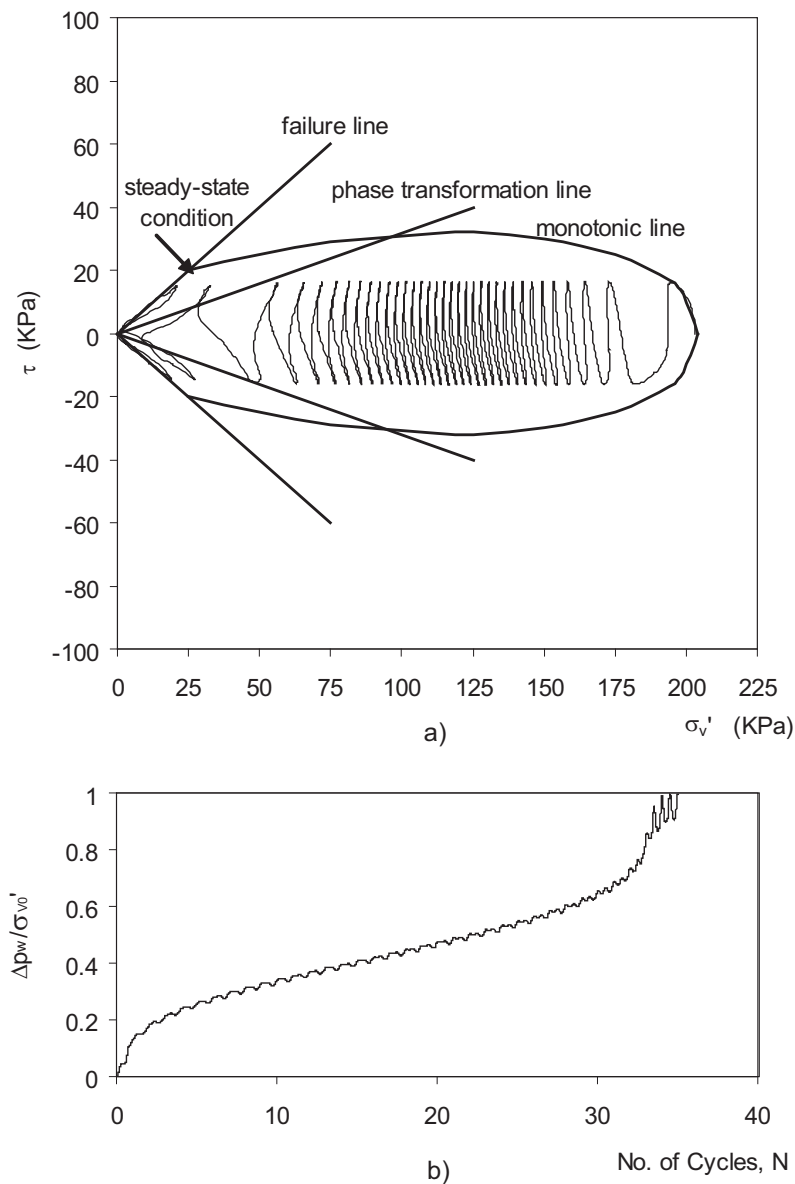


Figure 25. Undrained cyclic shear stress test for Fraser River Sand (after (57))  $Dr_0 = 0.44$ ;  $\sigma'_{v0} = 200 \text{ kPa}$ ;  $CSR = 0.08$  a) Stress path. Failure, monotonic and phase transformation lines sketched. b) Excess pore water pressure

On the other hand, there is another research line in the identification of the soil performance against liquefaction by means of numerical models based on field data. This investigation is based in the non-alteration of the material at its field location, trying to decrease the degree of uncertainties due to the laboratory tests and sample reconstitution. The most used field test is the SPT, which can establish correlations with soil bearing capacity

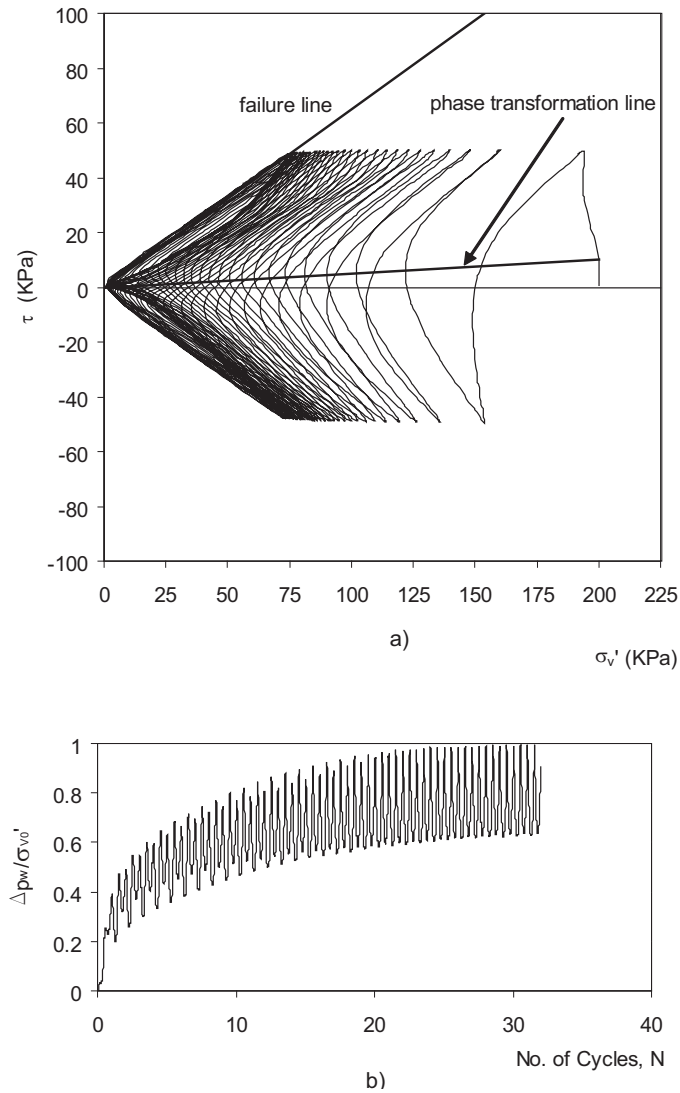


Figure 26. Undrained cyclic shear stress test for Fraser River Sand (after (57))  $Dr_0 = 0.81$ ;  $\sigma'_{v0} = 200 \text{ kPa}$ ;  $CSR = 0.25$  a) Stress path. Failure and phase transformation lines sketched. b) Excess pore water pressure

and mechanical features (61).

### 3.3. Constitutive Laws

It is well established that sand behaviour undergoes plastic strains even for very small loadings. Thus, a plastic numerical model is always needed for modelling purposes.

Models based on classic plasticity theories, which are of general use in static or monotonic problems, are unable to reproduce sand performance under dynamic loadings, since

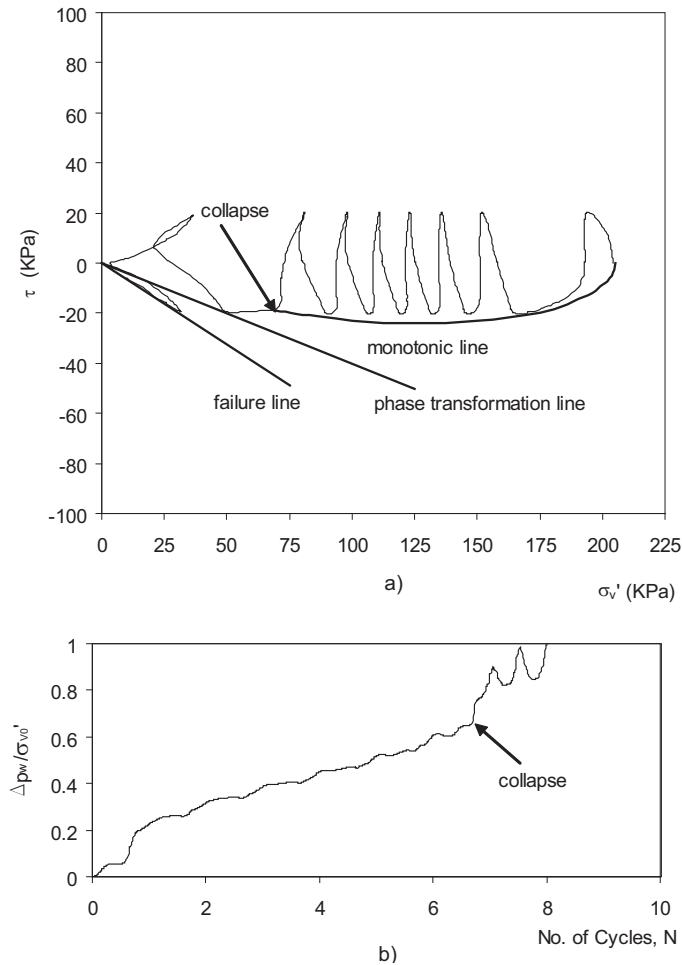


Figure 27. Undrained cyclic shear stress test for Fraser River Sand (after (57))  $Dr_0 = 0.44$ ;  $\sigma'_{v0} = 200kPa$ ;  $CSR = 0.1$  a) Stress path. Failure, monotonic and phase transformation lines sketched. b) Excess pore water pressure

in unloading, for example, these models give no plastic strains which occur in reality. Advanced models specifically developed for dynamic loading are required. The most relevant ones are enumerated next.

### 3.3.1. Bounding Surface Models

Bounding surface models are of very generalized use. They need the analytical definition of yield and potential surfaces, but allow plastic deformations inside the potential surface. They usually include hardening and softening rules (19). However, these laws usually lack of efficiency in the time required for numerical computations.

### 3.3.2. Generalized Plasticity Based Models

Generalized plasticity based models have been successfully developed for dynamic problems of soils. These laws do not need to analytically define yield and potential surfaces, and just require to establish their normal vectors. This circumstance usually makes these laws very efficient from the computational point of view. They may also include hardening and softening rules, which complete all the possible patterns of soil behaviour, including contraction and dilation performances. Pastor-Zienkiewicz model for sands (PZ) is a very good example of this type of model, and it has been very used and validated, reason why it is of generalized use. This constitutive law is explained in detail in (40).

### 3.3.3. Densification Based Models

The first constitutive laws for liquefaction were based on theories specifically developed for representing the plastic behaviour of metals (54). These laws were later extended to sands by means of the endochronic theory (4; 5; 62; 7). A correlation between densification and evolution of excess pore fluid pressure is made with these models by means of the constrained modulus of drained sand, in unloading, obtained with oedometer test devices. This kind of models try to reproduce the physical process of the liquefaction and/or cyclic mobility (33; 50). Usually they correctly represent the contractive sand behaviour (loose sand), but lack of accuracy when mainly dilative sands are to be modelled. Some attempts have been recently made trying to overcome this countermeasure. An example is the law developed by López-Querol and Blázquez (30), which is summarized next. This model is based on the densification model developed by Cuéllar (18), and generalized to quartzitic sands by Blázquez and López-Querol (8), which has been previously explained in this chapter. Equations 1-2 and 4-9 are applicable. In addition, the relationship between the increment of excess pore pressure,  $p_w$ , and the densification,  $\epsilon_v$ , is given by:

$$dp_w = -M_d \cdot d\epsilon_v \quad (10)$$

$$M_d = \frac{K_d \cdot \sigma_v^{0.5}}{\sigma_{v0}^{m^*}} \quad (11)$$

where  $M_d$  is the constrained modulus of the drained sand in unloading, and  $K_d$  and  $m^*$  are constitutive model parameters. The plastic shear strains,  $\gamma^p$ , are obtained as:

$$d\gamma^p = d\tau/H \quad (12)$$

where  $\tau$  is the current shear stress, and  $H$  is the plastic modulus, defined as:

$$H = G \cdot \left( \frac{1 - K_q}{K_q} \right) \quad (13)$$

$$K_q = \frac{\tau \cdot \text{sign}(d\gamma)}{G \cdot \tau_D \left( 1 + \frac{\alpha'}{\beta} \cdot \xi \right)^\beta} \quad (14)$$

In the above equations,  $\tau_D$ ,  $\alpha'$  and  $\beta$  are constants, and  $G$  denotes the tangent shear elastic module variation law:

$$G = \frac{G_{max}}{T} \quad (15)$$

$$G_{max} = \frac{B_g \cdot p_a}{0.3 + 0.7 \cdot e^2} \cdot \left( \frac{p'}{p_a} \right)^2 \quad (16)$$

$B_g$  is another model parameter,  $e$  is the current void ratio, and  $p_a$  is the atmospheric pressure, expressed in the same units than  $p'$ .  $T$  is given by:

- First loading:

$$T = 1 + 2 \cdot C_t \cdot |\eta - \eta_0| \quad (17)$$

- Unloading and reloading:

$$T = 1 + C_t \cdot |\eta - \eta_{sr}| \quad (18)$$

where  $C_t$  is a model parameter, and  $\eta$ ,  $\eta_0$  and  $\eta_{sr}$  denote, respectively, the current, initial and at last reversal values of  $\tau/\sigma'_v$ . For modelling the contractive sand behaviour, a slight modification of eq.3 is required:

$$d\varepsilon_v = -I_s \cdot \frac{d\zeta}{1 + \alpha \cdot \zeta} \cdot |d\gamma| = -I_s \cdot \frac{n}{4} \cdot \frac{|100 \cdot \gamma|^{(n-1)}}{1 + \alpha \cdot \zeta} \cdot |d\gamma| \quad (19)$$

where  $I_s$  another model parameter, which needs calibration after phase transformation and/or collapse, and:

- before phase transformation and/or collapse:  $I_s = 1$
- after phase transformation and/or collapse:  $I_s > 1$

To represent dilation and/or collapse, the next equations of application:

$$\psi = \frac{G_0}{G_0 - G} \quad (20)$$

$$\phi = \left| \frac{d\tau}{dp'} \right| \quad (21)$$

$$\phi = \psi \cdot M_p \quad (22)$$

$$d = (1 + \alpha_p) \cdot \psi \quad (23)$$

$$d = \left| \frac{d\varepsilon_v}{d\gamma_p} \right| \quad (24)$$

$G_0$  is the initial tangent shear elastic modulus;  $M_p$  is the slope of the failure line in the stress plane;  $d$  is the soil dilation; and  $\alpha_p$  is the last model parameter.

### 3.4. Coupled Numerical Models. Different Formulations of Biot's Equations

For taking into consideration the interaction between fluid and solid phases when a saturated sand is subjected to dynamic loading, the different constitutive law must implemented in a coupled code, based on Biot's equations for saturated soils (6). The governing equations are summarized below, formulated according to (64; 30). In a two-dimensional approach, under the assumption of plane strain, the unknowns are  $u$  (vector of absolute displacements of solid phase, in  $x$  and  $y$  components),  $w$  (vector of displacements of fluid phase relative to the solid phase, also in  $x$  and  $y$ ) and  $p_w$  (excess pore water pressure).

The following equation stands for the equilibrium of the solid+fluid mixture, neglecting convective terms, and expressed incrementally:

$$S^T d\sigma - \rho d\ddot{u} - \rho_f d\ddot{w} + \rho db = \{0\} \quad (25)$$

On the other hand, the equilibrium of the fluid phase is expressed as:

$$-\nabla dp_w - k^{-1} d\dot{w} - \rho_f d\ddot{u} - \frac{\rho_f}{n} d\ddot{w} + \rho_f db = \{0\} \quad (26)$$

Finally, the continuity equation is:

$$\nabla^T d\dot{w} + m^T d\dot{\varepsilon} + \frac{dp_w}{Q} = 0 \quad (27)$$

In the above equations,  $\rho$  and  $\rho_f$  denote mixture and fluid phase densities, respectively,  $b$  is the vector of external accelerations,  $S$  is the matrix operator of stress equilibrium within an infinitesimal volume of soil,  $k$  is the permeability matrix (the components of which are expressed in  $[length]^3[time]/[mass]$  units),  $Q$  is the compressibility of the mixture, and  $m$  is a vector which, in two-dimensional plane strain conditions, is given by:

$$m^T = (1, 1, 0) \quad (28)$$

In the above approach, extension is considered positive for both stresses,  $\sigma$ , and strains,  $\varepsilon$ , and conversely excess pore water pressure is taken positive in compression. Thus, applying the effective stress concept given by Terzaghi, for saturated soils:

$$\sigma = \sigma'_0 - p_w \quad (29)$$

(where  $\sigma'_0$  denotes the initial effective stress), relating increments of effective stresses and strains by means of the constitutive law (given by tensor  $D^{ep}$ )

$$d\sigma' = D^{ep} d\varepsilon \quad (30)$$

and expressing strains as a function of the solid phase displacements

$$d\varepsilon = S du \quad (31)$$

eq. 25 is finally arranged as follows:

$$S^T D^{ep} S du - \nabla^T dp_w - \rho d\ddot{u} - \rho_f d\ddot{w} + \rho db = \{0\} \quad (32)$$

The set of eqs. 32, 26 and 27 is called  $u - w - p_w$  or complete formulation. It can also be expressed in terms of the absolute displacement of the fluid phase, usually denoted as  $U$ . The number of degrees of freedom, in a 2-D case, is five:  $u_x, u_y, w_x, w_y$  and  $p_w$ . In a 3-D model, it is seven (three components in each vector). It is possible to rearrange these equations in order to reduce this number. The most extended approach is the  $u - p_w$  formulation, which consist of rearranging eqs. 32, 26 and 27 after neglecting the increment of flow acceleration,  $d\ddot{w}$ . Following this path, the number of degrees of freedom becomes three in 2-D, and four in 3-D. The new set of equations is:

$$S^T D^{ep} S du - \nabla^T dp_w - \rho d\ddot{u} + \rho db = \{0\} \quad (33)$$

$$\nabla^T [k \cdot (-\nabla dp_w - \rho_f d\ddot{u} + \rho_f db)] + m^T S d\dot{u} + \frac{dp_w}{Q} = 0 \quad (34)$$

Another possible approach is the  $u - w$  formulation: integrating in time eq.27, from an initial zero value of the excess pore water pressure, and substituting  $dp_w$  into eqs.32 and 26, the problem is expressed as a  $u - w$  formulation according to the following equations:

$$(S^T D^{ep} S) \cdot du + Q \cdot \nabla(\nabla^T du) + Q \cdot \nabla(\nabla^T dw) - \rho \cdot d\ddot{u} - \rho_f \cdot d\ddot{w} + \rho \cdot db = 0 \quad (35)$$

$$Q \cdot \nabla(\nabla^T du) + Q \cdot \nabla(\nabla^T dw) - k^{-1} \cdot d\dot{w} - \rho_f \cdot d\ddot{u} - \frac{\rho_f}{n} \cdot d\ddot{w} + \rho_f \cdot db = 0 \quad (36)$$

After solving these equations at every time step,  $dp_w$  can be computed by using eq.(27) integrated in time, and the effective water pore pressure is then updated.

It is worth pointing out that in the  $u - w$  formulation it is not necessary to assume negligible relative acceleration of the fluid, which represents a more accurate approach compared to  $u - p_w$  formulation for high permeability values or high external acceleration imposed to the mixture. In addition, it does not require stabilization algorithms (34) when soil permeability is too low and/or the fluid is almost incompressible if the same order of approximation is to be considered in the whole unknowns field (30). This formulation has been demonstrated to provide almost identical results than the complete one when both pore fluid and solid grains are not incompressible, for a wide range of soil permeabilities (23). However, one of the main weaknesses of  $u - w$  formulation is that it involves a higher number of degrees of freedom than  $u - p_w$ , (four in 2-D and six in 3-D), making the model numerically less efficient.

In order to solve these sets of equations in time domain, usually Newmark's integration schemes are implemented. It can be formulated according (64). To solve the equations in space domain, finite element methods are the most employed tools.

### 3.5. Numerical Examples

#### 3.5.1. Verification of a Numerical Model Using Centrifuge Tests Data

The set of centrifuge tests conducted at the University of British Columbia (10) have been used to validate the numerical model developed by López-Querol and Blázquez (30), implemented in a coupled code formulated in terms of  $u - w$ . The geometry of the modelled

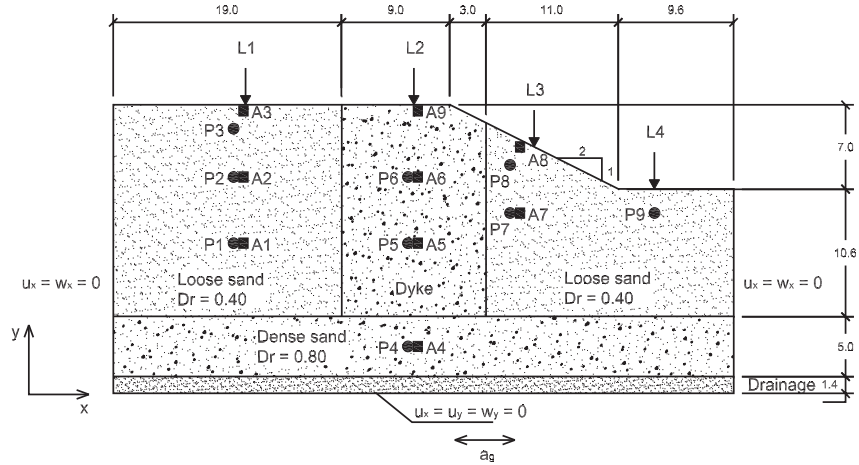


Figure 28. Geometry of the analysed centrifuge tests (dimensions in meters), boundary conditions and locations of the transducers (after (17))

prototype, the involved materials, the location of the transducers (P: pressure; A: acceleration; L: displacement) and the boundary conditions of the numerical model, are sketched in Fig.28. Two types of soil are involved in the models: Fraser River sand, and a drainage material. The set of parameters for modelling purposes, after calibrating the model by means of standard identification and constant volume cyclic shear stress tests, are given in Table 3. Three sets of tests were performed, changing the material of the central dyke: loose sand, dense sand and drainage material. The accelerogram, used for both physical and numerical models, is given in Fig.29.

**Table 3. Soil model parameters of the soils involved in the centrifuge tests (30)**

Parameter	Fraser River sand	Drainage material
$C^*$	20	20
$K_d$	12000	12000
$m^*$	0.372	0.372
$\alpha_p$	-0.95	-0.95
$I_s$	2	2
$B_g$	220	220
$C_t$	1.6	1.6
$e_{min}$	0.68	0.62
$e_{max}$	1.00	0.81
$Dr$ (in per one)	various	0.60
$M_p$	0.65	0.65
$M_{tf}$	$M_p / (13.75 \cdot (Dr - 0.40))$	0.17
$k' (m/s)$	$4.3 \cdot 10^{-4}$	$4.0 \cdot 10^{-2}$
$\gamma_s (kN/m^3)$	26.56	26.17

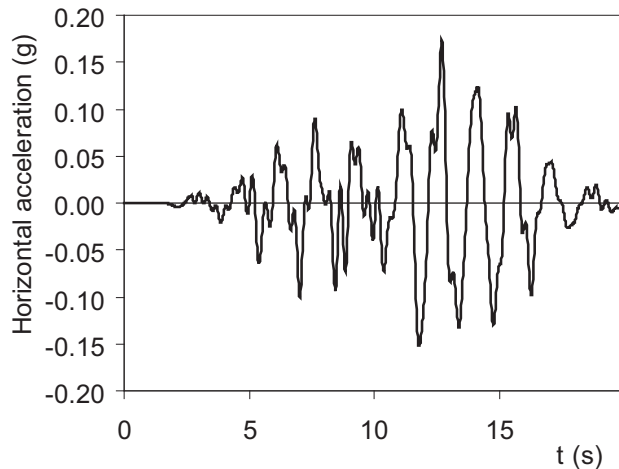


Figure 29. Input accelerogram in the analysed tests (after (17))

In all cases, the model gave fairly good results for the evolution of the pore water pressure inside the geometry, in both stages of generation and dissipation (consolidation). The computations in terms of accelerations fitted a bit worse to the experimental results, in part due to the high dependence of the response on the used time integration scheme and its parameters. In terms of displacements, the numerical model qualitatively determines the shape of the deformed geometry, but in this case the computations are not very accurate.

Figure 30 gives, as an example, the comparison of physical and numerical model results of pore water pressure evolution, and acceleration spectra for the case in which the dyke was made of dense Fraser River sand, at several locations of the geometry, as depicted in Fig.28. The detailed comparison can be checked in (32).

### 3.5.2. Optimal Design of Road Embankments at Seismic Sites

Numerical tools like the ones described above may help to engineers on designing geostructures, aiming to avoid as much as possible their breakage due liquefaction. An example is the design of road embankments at seismic sites. These geostructures very usually undergo a failure consisting of the pavement breakage due to liquefaction of the granular layer beneath (Fig.21). Longitudinal fissures, parallel to the road axis, but not in the centre of the road, appear often.

The numerical model validated above, formulated in terms of  $u-w$ , has been applied to a standard road embankment cross section (Fig.31), trying to numerically identify this typical failure, and to provide a design criteria to overcome this phenomenon at seismic sites. The accelerogram given in Fig.29 was applied as horizontal input motion at the numerical model. The involved soils were characterized by the model parameters given in Table 3.

In terms of excess pore water pressure, the numerical model gives the results which are summarized in Fig.32. After 10 seconds of earthquake, the maximum degree of liquefaction ( $r_u = \Delta p_w / \sigma'_{v0}$ ) occurs just beneath the road pavement, at two points symmetrically located and displaced from the road axis, which fits to field evidences of these failures

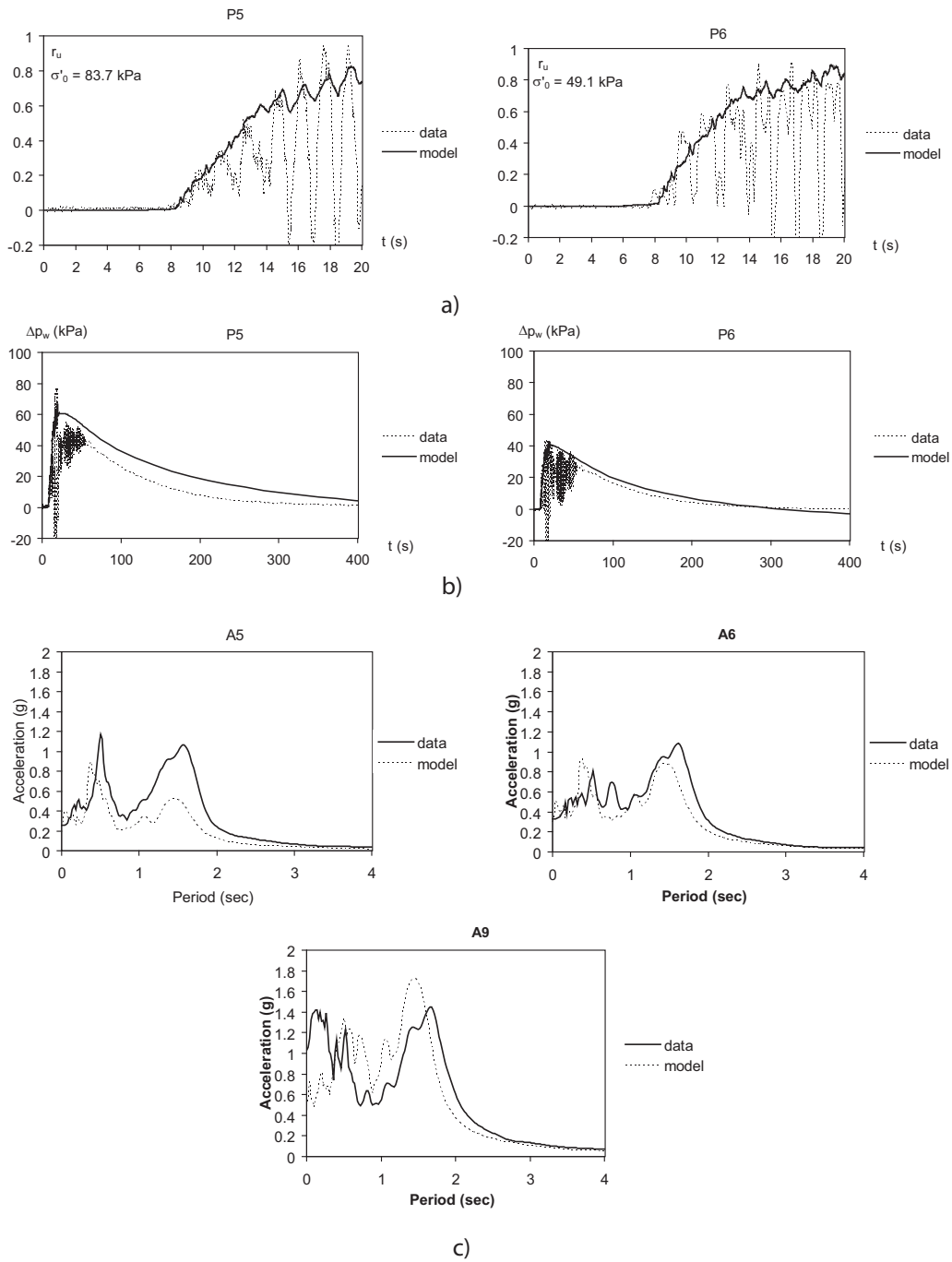


Figure 30. Experimental centrifuge (10) test data vs. numerical results at the dyke zone of: a) normalized pore water pressures ( $r_u = \Delta p_w / \sigma'_{v0}$ ) at generation stage, b) excess pore water pressures at generation and dissipation stages, and c) horizontal acceleration spectra at the transducers located inside the dyke.

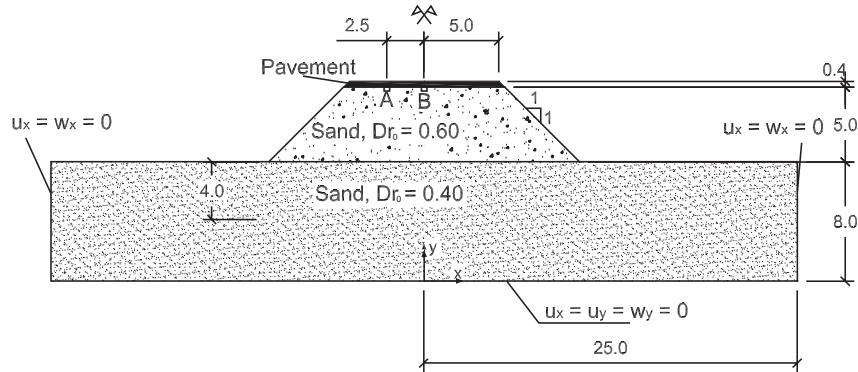


Figure 31. Cross section of the analysed road embankment (dimensions in meters), materials, and boundary conditions.

( $r_u = 1$  means liquefaction, since  $\Delta p_w$  equals  $\sigma'_{v0}$ , and then  $\sigma' = \sigma'_{v0} - \Delta p_w = 0$ ). If the pavement does not resist this pressure of water beneath and breaks, a slope slide may occur following the surfaces sketched at the cross section in Fig.32.

Several corrected geometries, including dense sand and / or drainage material at several embankment locations, were studied. Between all the analysed cases, the optimal was the one consisting of locating a drainage material layer just below the pavement (Fig.33). Figure 34 gives the results of the numerical model in terms of degree of liquefaction,  $r_u$ , of this corrective measure at 10 seconds of the same seismic loading. It is worth to point out that the maximum values of  $r_u$  are smaller in this case and less concentrated, and they do not occur just below the pavement. Drainage improves a lot in the whole geometry, avoiding the embankment failure due to liquefaction. Other corrective measures and the results given by the numerical model can be checked in (31).

### 3.5.3. Numerical Modelling of the Lower San Fernando Dam Failure

In spite of the high number of analyses made after the failure of the Lower San Fernando dam in 1971, the mechanisms of the upstream sand fill slide are not completely clear nowadays. Since the inspection of the seismographs recorded at the dam, it seems to be clear that the failure took place not during the earthquake, but several minutes later.

The above described numerical model (30), formulated in terms of  $u - w$ , has been applied to a simplified cross section of the dam, sketched in Fig.35, where the saturation line and the materials forming the dam are also depicted. Above the saturation line, the materials are considered completely dry, where the material suffers densification without development of excess pore water pressure. Since the accelerographs located at the dam were damaged during the earthquake, the real accelerogram is not available. For simulation purposes, the free-field horizontal accelerogram recorded at the neighbor Pacoima dam (254, CDMG Station 279), scaled to 0.6g, has been adopted as input motion of the model (Fig.36). The purpose of this study was to qualitatively clarify the failure of the dam. An exhaustive calibration of the numerical model was not carried out; instead, typical parameters for each material were used. The values for the sandy soil correspond to Fraser River

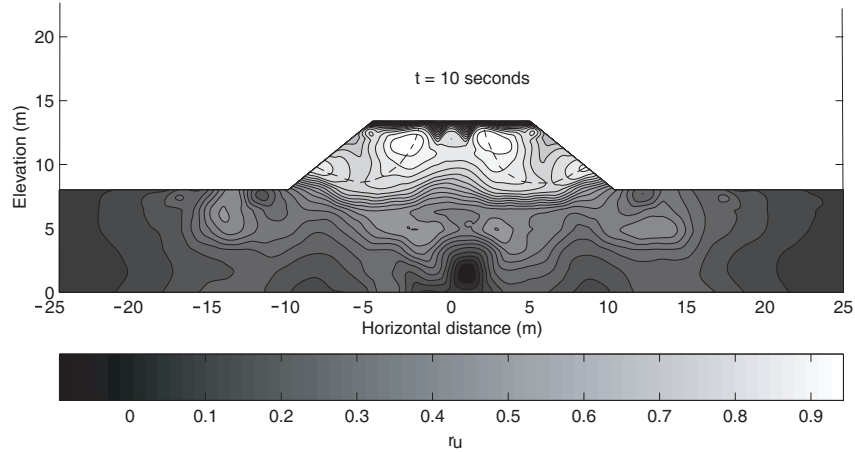


Figure 32. Degree of liquefaction,  $r_u = \Delta p_w / \sigma'_{v0}$ , of the road embankment at  $t=10$  seconds.

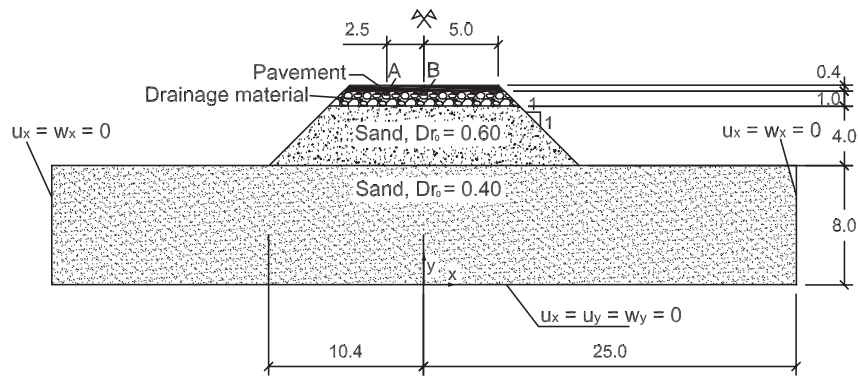


Figure 33. Geometry, materials and boundary conditions of the optimal corrective measure.

sand, with the parameters  $\alpha_p$  taken as  $-0.99$  in order to stabilize the solution in time, and then, to obtain the upper boundary solution (the maximum values of the excess pore water pressure). The used parameters are given in Table 4.

The results of the computation, in terms of degree of liquefaction,  $r_u$ , are given in Fig.37. These results show that, at the end of the earthquake, there is a point at the slope surface with a degree higher than 1 (liquefied), and most of the upstream sand fill had liquefied ( $r_u > 0.9$ , almost 1). However, the numerical computation yields that the residual strength of the soils was enough for preventing the breakage at this moment. Two minutes after the end of the earthquake, to critical points, with negative values of  $r_u$ , appeared. These negative values can be interpreted in the  $u - w$  coupled formulation as preferred pore water dissipation points. The exit of pore water under pressure could have triggered the slope slide several minutes after the end of the earthquake. A complete analysis of this case study, and its comparison to the field observations and other authors' calculations are given

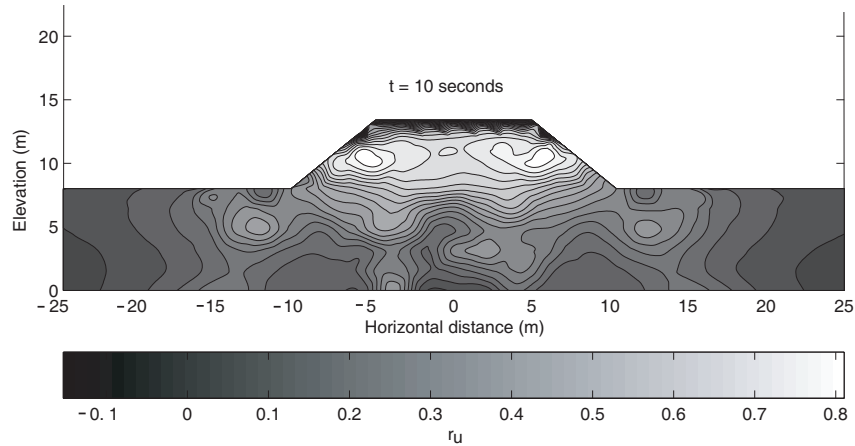


Figure 34. Degree of liquefaction,  $r_u$ , in the corrective measure of road embankment after 10 seconds of earthquake loading.

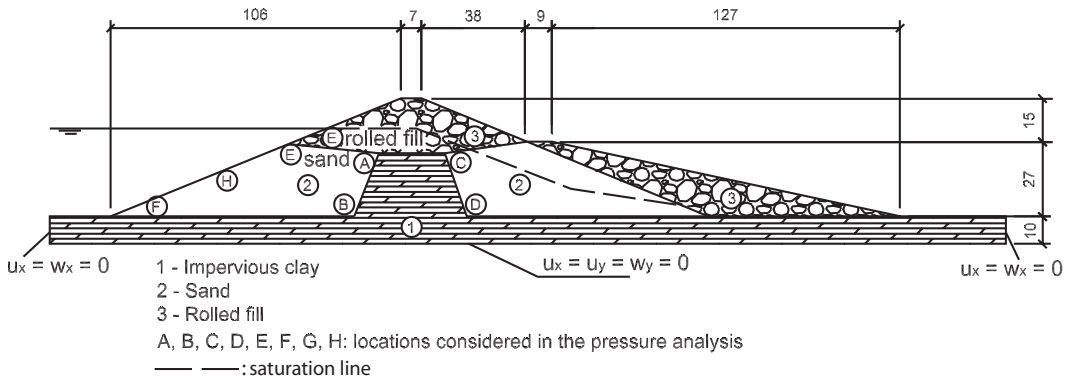


Figure 35. Geometrical model of the Lower San Fernando dam. Dimensions (in meters), materials and boundary conditions.

in detail in (9).

## Conclusion

This chapter presents field observations of densification and liquefaction cases, after what a summary of advances constitutive laws, formulations of Biot's equations and several examples of computation of both phenomena are provided. The main conclusions can be summarized as follows:

- From the analysis of field evidences it is worth noting that both densification and liquefaction may lead high strains and surface settlements, which may produce failure of foundations and slope slides to occur, and therefore, a risk for human lives and

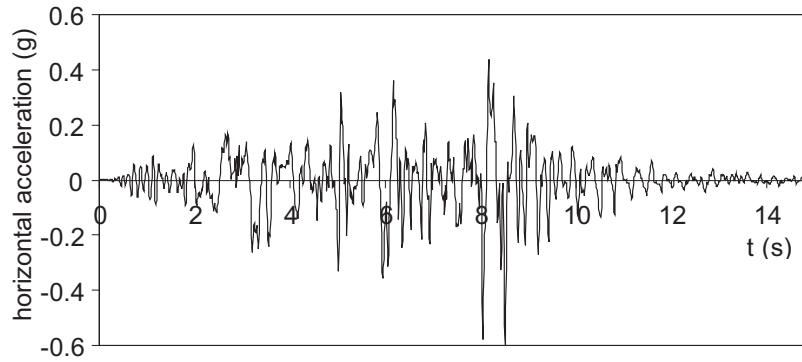


Figure 36. Horizontal accelerogram at the Pacoima dam (254, CDMG Station 279), San Fernando earthquake (February 9, 1971), scaled to  $|a_{max}| = 0.6g$ . (Courtesy of the National Information Service for Earthquake Engineering, EERC, University of California, Berkeley).

**Table 4. Soil model parameters of the soils involved in the model of the Lower San Fernando dam (30)**

Parameter	Sand	Impervious soil	Rolled fill
$C^*$	20	0	0
$K_d$	12000	1	12000
$m^*$	0.372	0.372	0.372
$\alpha_p$	-0.99	-0.99	-0.99
$I_s$	2	2	2
$B_g$	220	170	220
$C_t$	1.6	1.0	1.6
$e_{min}$	0.68	0.50	0.62
$e_{max}$	1.00	1.00	0.81
$Dr$ (in per one)	0.60	0.64	0.40
$M_p$	0.65	1.20	0.65
$M_{tf}$	0.17	0.28	0.65
$k' (m/s)$	$4.3 \cdot 10^{-4}$	$0.5 \cdot 10^{-8}$	$4.0 \cdot 10^{-2}$
$\gamma_s (kN/m^3)$	26.56	26.17	26.17

material resources to be spent in repairing infrastructures at seismic sites.

- Constitutive models capable to represent the soil behaviour under static or monotonic loadings, usually lack of accuracy when dynamic sand behaviour is to be modelled. Advanced models, including hardening and softening, non associative flow rules, and fatigue considerations, are required for representing this kind of phenomena.
- Biot's equations formulated in terms of displacements of both solid and fluid phases

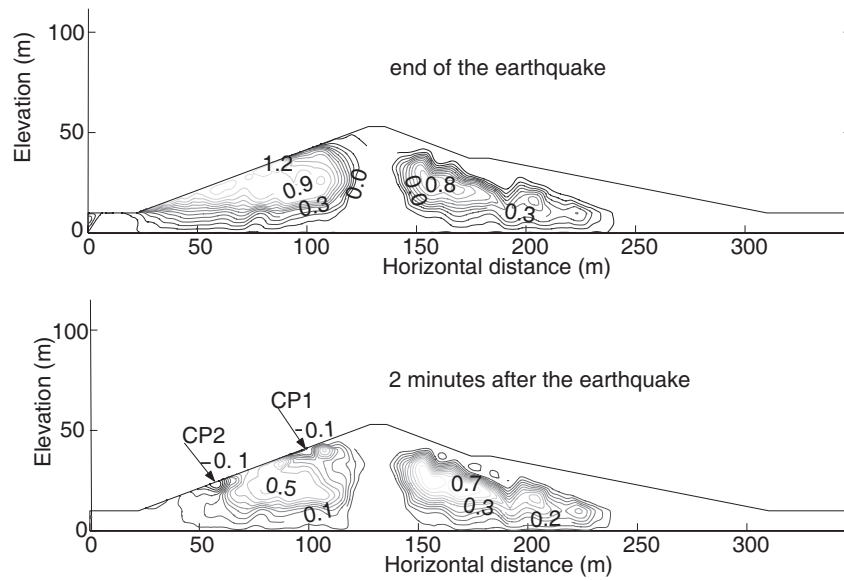


Figure 37. Numerical modelling of the Lower San Fernando dam during the San Fernando earthquake (1971). Degree of liquefaction,  $r_u$ , at the end of the earthquake and two minutes later.

are less efficient from the time of computation point of view (specially in 3-D models), but are more accurate when the permeability is high and/or the input loading acceleration is also high.

- For the case of densification, models based on the endochronic theory successfully represent the sand behaviour. These laws can be implemented in finite element based codes.
- For the case of liquefaction, again endochronic models, which represent the physical process of this phenomenon, are a very useful tool for modelling purposes. These laws, implemented in coupled codes formulated in  $u - w$ , can help to geotechnical engineers on designing geotechnical structures resistant to liquefaction, and avoid risk related to this process.

## References

- [1] Alarcón-Guzmán, A., Leonards, G.A., Chameau, J.L. *J. Geotechn. Engrg.* 1988, 114, 1089-1109.
- [2] Anderson, G.F. *An earthquake hazard study of a dune sand site in San Francisco, California. Thesis presented in partial fulfillment of the requirements for the degree of Master of Science*; San Jose State College: San Jose, CA, 1969.
- [3] Arulmoli, K.; Muraleetharan, K.K.; Hossain, M.M.; Fruth, L.S. *VELACS Laboratory*

- Testing Program, Soil Data Report*; The Earth Technology Corporation: Irvine, CA, Report to the National Science Foundation, Washington D.C. 1992.
- [4] Bazant, Z.P.; Krizek, R.J. *J. Engrg. Mech. Div.* 1975, 101, 317-332.
- [5] Bazant, Z.P.; Krizek, R.J. *J. Engrg. Mech. Div.* 1976, 102, 225-238.
- [6] Biot, M.A. *J. Acoust. Soc. Amer.* 1953, 28, 161-178.
- [7] Blázquez, R.; Krizek, R.J.; Bazant, Z.P. *J. Geotech. Engrg. Div.* 1980, 106, 785-801.
- [8] Blázquez, R.; López-Querol, S. *Soil Dyn. Earthq. Engrg.* 2006, 26, 888-898.
- [9] Blázquez, R.; López-Querol, S. *J. Geotechn. Env. Engrg.* 2007, 133, 1144-1153.
- [10] Byrne, P. (2003). Earthquake Induced Damage Mitigation from Soil Liquefaction. <http://www.civil.ubc.ca/liquefaction/>
- [11] Byrne, P.M.; Park, S.S.; Beaty, M.; Sharp, M.; Gonzalez, L.; Abdoun, T. *Can. Geotechn. J.* 2004, 41, 193-211.
- [12] Castro, G. *Liquefaction of sands*; Harvards Soil Mechanics Series N 81, Harvard University: Cambridge, MA, 1969.
- [13] Castro, G. *J. Geotechn. Engrg. Div. ASCE.* 1975, 101, 551-569.
- [14] Castro, G. *J. Geotechn. Engrg. Div. ASCE.* 1977, 103, 501-516.
- [15] Castro, G.; Poulos, S. J.; Leathers, F.D. *J. Geotechn. Engrg.* 1985, 111, 1093-1107.
- [16] Castro, G.; Seed, R. B.; Keller, T. O.; Seed, H. B. *J. Geotechn. Engrg.* 1992, 118, 406-427.
- [17] C-CORE. *Earthquake induced damage mitigation from soil liquefaction. Data report-centrifuge test CT2.* Contract report prepared for University of British Columbia. C-CORE report R-04-029-145. 2004.
- [18] Cuéllar, V. *Rearrangement measure theory applied to dynamic behavior of sand. Ph.D. dissertation*; Civil Engineering Department, Northwestern University: Evanston, IL, 1974.
- [19] Dafalias, Y.F.; Popov, E.P. *Act. Mech.* 1975, 21, 173-192.
- [20] Drnevich, V.P. *Effect of strain history on the dynamic properties of the sand. PhD dissertation*; Department of Civil Engineering, University of Kentucky: Lexington, KE, 1967.
- [21] Elgamal, A.; Yang, Z.; Parra, E.; Ragheb, A. *Intern. J. Plast.* 2003, 19, 883-905.
- [22] Finn, W.D.L.; Byrne, P.M. *Can. Geotechn. J.* 1976, 13, 355-363.
- [23] Gajo, A.; Saetta, A.; Vitaliani, R. *Int. J. Num. Meth. Engrg.* 1994, 37, 1231-1247.

- [24] González de Vallejo, L.; Tsige, M.; Cabrera, L. *Engrg. Geol.* 2005, 76, 179-190.
- [25] Greenfield, B.J.; Misiaszek, E.T. In *Proceedings, International Symposium on Wave Propagation and Dynamic Properties of Earth Materials*; University of New Mexico: Albuquerque, NM, Vol.1, pp 787-795.
- [26] Gu, W. H.; Morgenstern, N. R.; Robertson, P. K. *J. Geotechn. Engrg.* 1993, 119, 333-349.
- [27] Ishihara, K.; Tatsuoka, F.; Yasuda, S. *Soils Found.* 1975, 15, 29-44.
- [28] Khoei, A. R.; Azami, A. R.; Haeri, S. M. *Comp. Geotechn.* 2004, 31, 385-410.
- [29] Ko, H.Y.; Scott, R.F. *J. Soil Mech. Found. Div.* 1967, 93, 137-156.
- [30] López-Querol, S.; Blázquez, R. *Int. J. Num. Anal. Meth. Geom.* 2006, 30, 413-439.
- [31] López-Querol, S.; Blázquez, R. *Can. Geotech. J.* 2006, 43, 889-902.
- [32] López-Querol, S.; Blázquez, R. *Soil Dyn. Earthq. Engrg.* 2007, 27, 920-937.
- [33] Martin, G.R.; Finn, W.D.L.; Seed, H.B. *J. Geotechn. Engrg. Div., ASCE.* 1975, 101, 423-438.
- [34] Mira, P.; Pastor, M.; Li, T.; Liu, X. *Comp. Appl. Mech. Engrg.* 2003, 192, 4257-4277.
- [35] Olson, S.M. *Liquefaction analysis of level and sloping ground using field case histories and penetration resistance, PhD Thesis*; University of Illinois at Urbana-Champaign: Urbana, IL (<http://pgi-tp.ce.uiuc.edu/olsonwebfiles/olsonweb/index.htm>), 2001.
- [36] Olson, S. M.; Stark, T. D. *Can. Geotech. J.* 2002, 39, 329-347.
- [37] Papadimitriou, A.G.; Bouckovalas, G.D.; Dafalias, Y.F. *J. Geotechn. Geoenv. Eng.* 2001, 127, 973-983.
- [38] Papadimitriou, A.G., Bouckovalas, G.D. *Soil Dyn. Earthq. Engrg.* 2002, 22, 191-204.
- [39] Park, S.S.; Byrne, P. In *International Conference on Cyclic Behaviour of Soils and Liquefaction*, Bochum, 2004; pp 571-580.
- [40] Pastor, M.; Zienkiewicz, O.C.; Chan, A.H.C. *Int. J. Num. Anal. Meth. Geom.* 1990, 14, 151-190.
- [41] Pradel, D. *J. Geotechn. Geoenv. Engrg.* 1998, 124, 364-368.
- [42] Przewlocki, J.; Knabe, W. *Int. J. Num. Anal. Meth. Geom.* 1978, 19, 813-821.
- [43] Pyke, R.; Seed, H.B.; Chan, C.K. *J. Geotechn. Engrg. Div., ASCE.* 1975, 101, 379-398.
- [44] Qadimi, A.; Coop, M.R. *Geotechnique.* 2007, 57, 739-750.

- [45] Seed, H. B.; Lee, K. L. *J. Soil Mech. Found. Div., ASCE*. 1966, 92, 105-134.
- [46] Seed, H.B.; Silver, M.L. *J. Soil Mech. Found. Div., ASCE*. 1972, 98, 381-396.
- [47] Seed, H. B.; Lee, K. L.; Idriss, I. M.; Makdisi, F. I. *Analysis of the slides in the San Fernando dams during the earthquake on Feb. 9, 1971*; Earthquake Engineering Research Center, University of California: Berkeley, CA, 1973.
- [48] Seed, H. B. *Géotechnique*. 1979, 98, 213-263.
- [49] Seed, H. B.; Seed, R. B.; Harder, L. F.; Jong, H. L. *Re-evaluation for the Lower San Fernando dam, Report 2, Examination of the post-earthquake slide of February 9, 1971*; Contract Report GL-89-2, Department of the Army, US Army Corps of Engineers: Washington, DC, 1989.
- [50] Shiomi, T.; Tsukuni, S.; Zienkiewicz, O.C. In *Proceedings of the First Biot Conference on Poromechanics*, Thimus et al.; Balkema: Louvain la Neuve, BE, 1998; Vol. 1, pp 505-510.
- [51] Silver, M.; Seed, H.B. *J. Soil Mech. Found Div., ASCE*. 1971, 97, 1171-1182.
- [52] Terzaghi, K. *Erdbaumechanik*; Franz Dauticke, Viena, 1925.
- [53] Tokimatsu, K.; Seed, H.B. *J. Geotechn. Engrg.* 1987, 113, 861-878.
- [54] Valanis, K.C. *Arch. Mechan.* 1971, 23, 517-555.
- [55] Vierung, G. In *Proceedings, 5th International Conference on Soil Mechanics and Foundation Engineering*; Paris, FR, 1961; Vol. 1, pp 547-552.
- [56] Vincens, E.; Labbé, P.; Cambou, B. *Int. J. Num. Anal. Meth. Geom.* 1978, 27, 669-683.
- [57] Wijewickreme, D.; Sriskandakumar, S.; Byrne, P. *Can. Geotechn. J.* 2005, 42, 550-561.
- [58] Yang, Z.; Elgamal, A. *J. Engrg. Mech.* 2002, 128, 720-729.
- [59] Yang, Z.; Elgamal, A.; Parra, E. *J. Geotechn. Geoenv. Engrg.* 2003, 129, 1119-1127.
- [60] Youd, T.L. *J. Soil Mech. Found. Div., ASCE*. 1972, 98, 709-725.
- [61] Youd, T.L.; Idriss, I.M.; Andrus, R.D.; Arango, I.; Castro, G.; Christian, J.T.; Dobry, R.; Finn, W.D.L.; Harder, L.F.; Hynes, M.E.; Ishihara, K.; Koester, J.P.; Liao, S.S.C.; Marcuson, W.F.; Martin, G.R.; Mitchell, J.K.; Moriwaki, Y.; Power, M.S.; Robertson, P.K.; Seed, R.B.; Stokoe, K.H. *J. Geotechn. Geoenv. Engrg.* 2001, 127, 817-833.
- [62] Zienkiewicz, O.C.; Chang, C.T.; Hilton, E. *Int. J. Num. Anal. Meth. Geom.* 1978, 2, 381-404.
- [63] Zienkiewicz, O. C.; Y. M. *Dam Engrg.* 1991, 2, 307-322.
- [64] Zienkiewicz, O.C.; Chan, A.H.C.; Pastor, M.; Schrefler, B.A.; Shiomi, T. *Computational geomechanics with special reference to earthquake engineering*, John Wiley & Sons Ltd: England, 2000.

*Chapter 9*

## THE USE OF DISSIPATED ENERGY AT MODELING OF CYCLIC LOADED SATURATED SOILS

*S. Lenart*<sup>\*</sup>

Slovenian National Building and Civil Engineering Institute (ZAG), Slovenia

### Abstract

The energy concept for the analysis of densification and liquefaction of cohesionless soils was first introduced by Nemat-Nasser and Shokooch (1979). It is based on the idea that during deformation of these soils under dynamic loads, part of the energy is dissipated into the soil. This dissipated energy per unit volume is represented by the area of the hysteric strain-stress loop and could be determined experimentally. It considers both the amplitude of shear strain and the number of cycles, combining both the effects of stress and strain. Using the Palmgren-Miner cumulative damage hypothesis, the effect of random motions of an earthquake or other random dynamic load can be taken into account by dissipated energy use.

The main advantage of using the dissipated energy was found in the case of saturated soils. The relation between dissipated energy and the residual excess pore water pressure generated in saturated soils during dynamic loading is already well known. Recent studies have shown that similar relations exist also in the case of temporary excess pore pressures.

Besides relations between dissipated energy and pore pressure changes in saturated cyclic loaded soils, the paper highlights also the relation between dissipated energy and softening of soil during cyclic loading. Softening of soil during cyclic loading, so-called short-term flow, makes a perceivable impact on strain progression. After a few cycles of loading, soil starts to exhibit very low stiffness at the beginning of a load cycle and it strengthens later. It is obvious that strain developed during this short-term flow presents the main share of a total strain developed during cyclic loading, and it leads therefore to the deformation behavior of a soil. The duration of this phenomenon and stiffness of soil during this phase is in question.

It has been found that the duration of the softening phase, as well as shear modulus of soil during this phase are both related to residual pore pressure ratio. A simple constitutive model, especially suitable for a cyclic mobility modeling, was developed based on an energy approach. Its main part presents a new pore pressure generation model and findings related to short-term flow and dissipated energy.

---

\* E-mail address: stanislav.lenart@zag.si

## Introduction

Mechanical behavior of cyclically loaded soils can be quite complex. Geotechnical engineers are challenged by the need to characterize the most important aspects of cyclic loaded soil behavior as accurate as possible and in the same time to do it in the most simple way as possible. The problem even accelerates in the case when cyclic loaded soil loses its strength and dramatic deformations occur. The case is mostly observed when saturated loose cohesionless soils are involved.

Large deformation, even flow failure and excess pore pressures are hallmarks for liquefaction related phenomena. The term “liquefaction” is used to describe a number of different, though related phenomena. When saturated cohesionless soils are subjected to rapid loading, e.g. earthquake loading or other kinds of cyclic/dynamic loading, conditions might be understood as an undrained loading condition due to the inability of pore water to drain in a very short time period. A cohesionless soil subjected to cyclic loading has a tendency to densify. As pores between soil grains are filled with water, which can not drain sufficiently, the generation of excess pore pressure occurs. Kramer (1996) reports about two main groups of liquefaction phenomena that results from this process: flow liquefaction and cyclic mobility.

Flow liquefaction occurs when the shear strength of a soil in its liquefied state is smaller than the static shear stress required for equilibrium of a soil mass. Liquefied stress state in that case is presented by initial effective confining pressure decreased for an excess pore pressure. The effective stress conditions leading to flow liquefaction occurrence can be described most easily in stress path space. The response of five saturated cohesionless

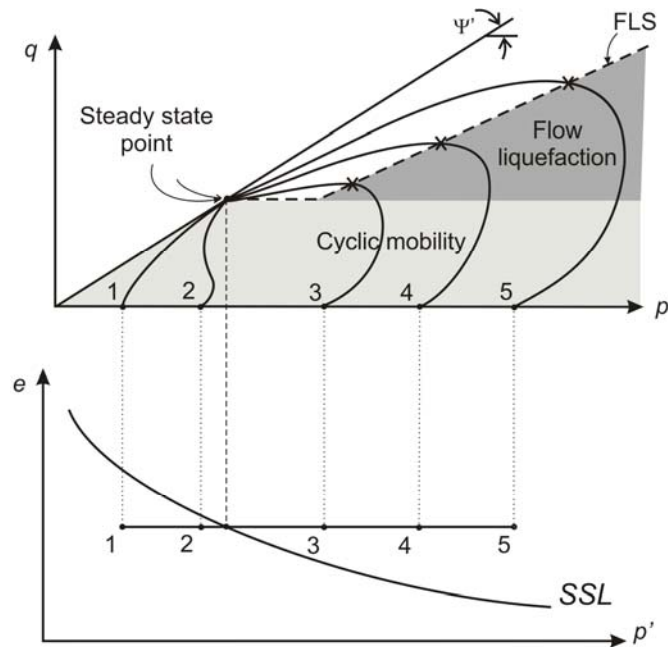


Figure 1. Initial conditions susceptible to either flow liquefaction or cyclic mobility (adapted from Kramer, 1996).

specimens isotropically consolidated to the same void ratio and different effective confining pressures, in undrained stress-controlled triaxial compression is shown in Figure 1 (adapted from Kramer, 1996). Regarding the initial states of specimens according to the steady state line, specimens 1 and 2 exhibit dilative behavior upon shearing starts, while specimens 3, 4 and 5 exhibit contractive behavior, which is necessary for flow liquefaction. The flow liquefaction is initiated at the peak of stress path in the case of the latter three specimens. The locus of points describing the effective stress conditions at the initiation of flow liquefaction, is a straight line (Kramer, 1996; Vaid and Chern, 1983) called flow liquefaction surface (FLS). All the specimens reach the same steady state point as they have the same void ratio. The FLS is truncated at the level of steady state point as flow liquefaction cannot occur if stresses are below this point. The FLS marks therefore the boundary between soil states at which either flow liquefaction or cyclic mobility can occur.

### Cyclic Mobility

While flow liquefaction produces large deformations actually driven by static shear stresses, deformations due to the cyclic mobility are developed incrementally during cyclic loading. Normally cyclic mobility deformations are not the flowing type and thus damages might be smaller, but still severe.

Deformations produced by cyclic mobility are driven by cyclic and static shear stresses. Cyclic mobility can occur during cyclic loading of saturated soil when the static shear stress is smaller than the steady-state shear strength. Initial states susceptible to cyclic mobility are shown in Figure 1. Depending on the range of static and cyclic shear stresses, in comparison with steady-state shear strength, different combinations of initial and cyclic loading condition can produce cyclic mobility (Kramer, 1996). In all cases, sufficient excess pore pressure has to be generated to move the stress path from its initial position in direction to failure envelope (Figure 2).

Generation of excess pore pressure is generally caused by cyclic loading. If cyclic stress is large enough, steady-state strength might be exceeded during cyclic loading. If this happens near the FLS, effective stress path can touch the FLS. Momentary instability can occur therefore, leading to significant strain development. If static shear stress is smaller than the steady-state strength, strain generally ceases when shear stress returns to the values below the steady-state strength.

If steady-state strength is not exceeded during cyclic loading, effective stress path approaches the so-called phase transformation surface (Ishihara, 1985). Phase transformation surface (PTS) presents a kind of boundary between dilative and contractive behavior of soil. Above the PTS a dilative tendency increases effective confinement (and consequently the shear strength), while below PTS soil exhibits a contractive behavior and thus tendency to generate excess pore pressure. Youd (1977) described clearly the rearrangements of soil grains happening in cyclic loaded soil when stress path approaches and crosses the PTS from one or the other side. Significant shear strain may develop without appreciable shear stress in moment of crossing the PTS (Figure 3). This, almost flowing behavior of soil when stress path meets the PTS causes serious problems in numerical modeling of cyclic mobility phenomena (Elgamal et al, 2003). Possible approach to define this highly yielded segment of

stress-strain response of soil as a finite phase by the use of dissipated energy is shown later in this paper.

When cyclic stresses are bigger than static shear stresses, stress reversal occurs. Thus each load cycle includes compressional and extensional loading. An excess pore pressure generated during cyclic loading causes movement of stress path in direction to zero effective stress (origin of  $q$ - $p$  graph). This state is called initial liquefaction (Seed and Lee, 1966). When stress path reaches it, only further oscillations along the compression and extension loading portions of the drained failure surface is possible due to continuation of cyclic or monotonic loading (Kramer, 1996).

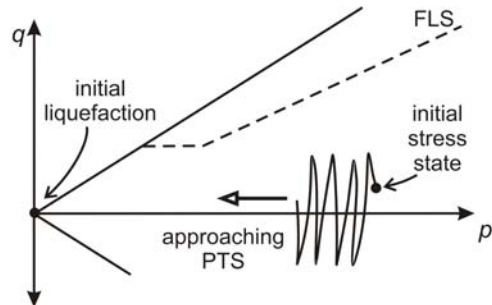


Figure 2. Generation of excess pore pressure due to the cyclic loading cause movement of stress path from its initial position in direction to failure envelope.

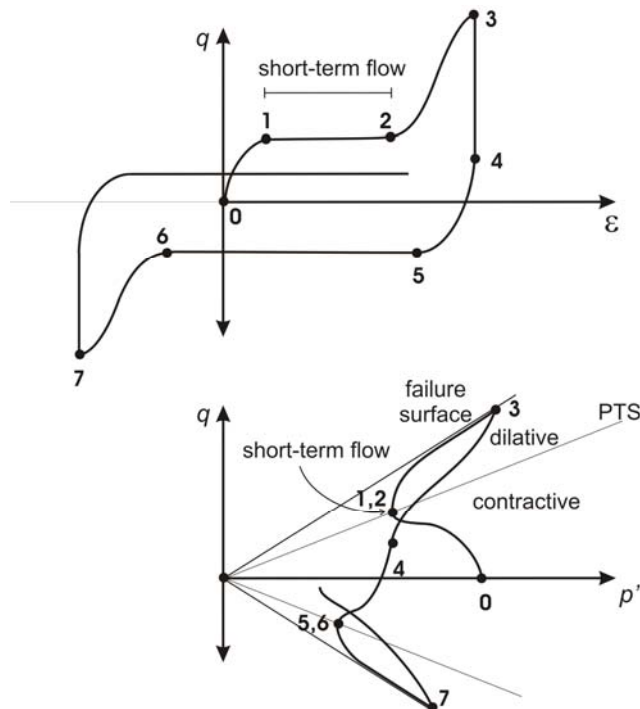


Figure 3. A typical stress path of cyclically loaded soil and shear-strain relationship when it crosses the phase transformation surface (adapted from Elgamal et al, 2003).

## Cumulative Damage Hypothesis

Figure 2 shows movement of stress path from its initial position due to changes of shear stresses (caused by cyclic loading) and due to the effective confining pressure decreasing. The latter happen due to the excess pore pressure generation. An excess pore pressure generation therefore actually leads the stress path movements and thus soil strength and stiffness changes. It is therefore of main importance for modeling of cyclic loaded soil to be able to define the function of pore pressure changes.

Pore water pressure changes in saturated soils are caused by soil structure changes (grain rearrangements). Pore pressure increases when soil contracts and decreases when it dilates. Changes from contractive to dilative behavior and opposite happen when stress path crosses the PTS. Initial effective stress states are generally located in contractive zone in cases of soils susceptible to liquefaction or cyclic mobility. That means that stress path moves during cyclic loading from initial point to the right, approaches the failure surface. Cyclic loading causes irrecoverable contraction of soil skeleton and thus the permanent (in case of undrained loading conditions) generation of excess pore pressure. It is necessary therefore to estimate the relationship between input of cyclic loading and irrecoverable deformation that it causes on one side, and excess pore pressure on the other side.

The problem itself was much interested by several researchers in the 1960s and 1970s in the evaluation of initiation of liquefaction perspective. Two main approaches: cyclic stress and cyclic strain approach were developed. They are based on experimental evidence that densification of dry soil structure and thus generation of excess pore pressure in saturated soil can be controlled either by cyclic stresses or cyclic strains. The main problem of these two approaches is irregularity of cyclic load (e.g. earthquakes, traffic loads, wind etc.). Comparison of a natural induced cyclic/dynamic loading with laboratory resistance requires conversion of an irregular time history to an equivalent series of uniform stress or uniform strain cycles. A random cyclic loading needs to be converted to an equivalently damaging uniform cyclic load.

Similar approach called cumulative damage hypothesis was proposed by Palmgren (1924) and further developed by Miner (1945) for metal fatigue analyses purpose. Seed and co-authors (1975) adopted hypothesis, with slight modifications, to compute number of equivalent cycles for random cyclic loading. The equivalent cycles concept was revised several times in last decades, while recently a procedure to computing number of equivalent cycles by equating dissipated energy of random and uniform cyclic loading was proposed (Green and Terri, 2005).

## Energy Approach to Liquefaction Risk Evaluation

There exists a need to convert an irregular cyclic loading to an equivalent damaging quantity, which would enables to evaluate a stress path movement from its initial position approaching the phase transformation surface and failure envelope. Process of liquefaction initiation seems a typical problem where the stress path movement before liquefaction occurrence needs to be evaluated. Having in mind the cumulative damage hypothesis, the use of energy in evaluation procedure is quite a logical step.

The energy released during earthquakes has been quantified for a long time by seismologists. They have even established simple correlations between released energy and common seismological parameters like magnitude of an earthquake (Gutenberg and Richter, 1956). To evaluate liquefaction risk by using energy means to find out the energy needed for the buildup of pore water pressure equal to the confining pressure. Large data sets involving liquefaction are needed to define properly such relationship. Kuribayashi and Tatsuoka (1975) presented maximum distance from an actual earthquake to a site at which liquefaction was observed to have occurred. They proposed the expression

$$\log R_{\max} = -3.6 + 0.77 \cdot M, \quad \text{Eq. 1}$$

where  $R_{\max}$  is distance measured in km and  $M$  is Richter magnitude. Data for the expression derived from Japanese earthquakes only. Similar expressions were introduced also for non-Japanese earthquakes (Youd, 1977). Based on the Gutenberg-Richter energy relation, Davis and Berrill (1982) proposed an attenuation model that assumes the rate of a magnitude of the energy decrease with a distance from site to the center of energy release. The model accounts energy dissipation due to the geometrical spreading and due to material damping. They also assumed that the increase in pore pressure is a linear function of dissipated energy. Proposed model has been revised several times (Berrill and Davis, 1985; Law et al, 1990). To avoid uncertainties regarding the energy attenuation on the way from source to the site, Trifunac (1995) proposed different expressions to compute the energy,  $E$  of the earthquake motions at the site. One of them (Eq.2) enables to compute energy of the earthquake motions at the site from the peak ground velocity at the site,  $v_{\max}$  the small strain shear modulus,  $G_{\max}$  and the duration of strong ground motion at the site,  $t$ .  $\sigma'_{vo}$  presents the initial effective vertical stress at selected depth. Based on the selection of the minimum distances to liquefiable sites and energy of the earthquake motions estimation, a threshold energy, which initiates the liquefaction, was suggested recently (Trifunac and Todorovska, 2004).

$$E = \frac{v_{\max} \cdot G_{\max} \cdot t}{\sigma'_{vo}} \quad \text{Eq. 2}$$

Integrating the acceleration time histories (Arias, 1970) Arias intensity was suggested as a quantitative measure for earthquake shaking intensity at the site. Arias intensity was explained (Kayen and Mitchell, 1977) as a sum of the two component energy per unit weight stored in a population of undamped linear oscillators evenly distributed in frequency at the end of earthquake. Arias intensity is unfortunately inherent dependent on frequency of the ground motion (Green and Mitchell, 2003), thus its use in liquefaction evaluation process is limited.

As a stress path movement is leaded by pore pressure changes, it of main importance to consider Nemat-Nasser and Shokooch (1979) study which shows theoretical relationship between the dissipated energy in laboratory samples and generated excess pore pressure. Figueroa et al. (1994) established experimentally relationship between the dissipated energy density and onset of liquefaction. Several other energy-based liquefaction evaluation procedures developed from laboratory data were described later. Besides empirical relations derived from laboratory tests, some researchers (Law et al, 1990; Davis and Berrill, 1998)

showed also that it is possible to obtain the dissipated energy density for the site data, where energy was released by an earthquake and dissipated in a soil layer. Dissipated energy density  $W$  is generally expressed in time  $t$  as

$$W(t) = \frac{1}{\sigma'_0} \int_0^t \sigma_{ij} d\varepsilon_{ij}, \quad \text{Eq. 3}$$

where  $\sigma_{ij}$  and  $\varepsilon_{ij}$  denotes stress and incremental strain tensors, respectively,  $t$  is a time in which total dissipated energy is in question.

### Mechanism of Dissipated Energy

Based upon the energy approach, Nemat-Nasser and Shokooh (1979) developed a mathematical model that explains densification of dry cohesionless soil and excess pore pressure generation of saturated cohesionless soil during cyclic loading. The theory is based on threefold physical observation (Figuroa et al, 1994). First, a certain amount of dissipated energy density  $\delta W$  is needed to change the void ratio of drained soil from  $e$  to  $e+\delta e$ . Second, this required amount of energy increases as the void ratio approaches the minimum void ratio  $e_{min}$ . And the third observation is the tendency to increase the pore pressure instead of decrease of void ratio if soil is saturated and undrained. The increase of pore pressure causes a decrease of intergranular forces and soil stiffness and thus incremental energy  $\delta W$  decreases with increasing pore water pressure. The latter finding about relationship between incremental dissipated energy and stiffness of a soil led to the idea that the dissipated energy required for pore water pressure changes during cyclic loading is related to dissipated energy per unit volume calculated from the hysteresis loops. This might be confirmed also by observations of Martin et al (1975) showing the relation between soil stiffness and pore water pressure changes. Therefore dissipated energy is defined as the area bounded by hysteresis loops of the stress-strain curve in case of results from laboratory cyclic loaded tests (Figure 4). Different expression were defined (Green, 2001) for computing dissipated energy from particular laboratory test results. In case of cyclic triaxial test the dissipated energy per unit volume of material  $\Delta W$  is determined using the trapezoidal rule to integrate Eq.3. A dimensionless dissipated energy ratio  $w$  is obtained when dissipated energy per unit volume of material  $\Delta W$  is divided by initial effective confining stress  $\sigma'_0$ . Indexes  $i$  and  $n$  in Eq.4 mean the increment number and total number of increments, respectively. Other symbols in Eq.4 are explained on Figure 4.

$$w(t) = \frac{1}{2 \cdot \sigma'_0} \sum_{i=1}^{n-1} (\sigma_{d,i+1} + \sigma_{d,i}) \cdot (\varepsilon_{a,i+1} - \varepsilon_{a,i}), \quad \text{Eq. 4}$$

Green (2001) proposed two dominant mechanisms of energy dissipation in saturated cohesionless cyclic loaded soils. First is frictional dissipation mechanism, where energy dissipates due to frictional sliding at grain to grain contact surfaces. The process happens even before gross sliding across the entire contact surface occurs, but the induced strain  $\gamma$  has to exceed the elastic threshold strain  $\gamma_{te}$  (Dobry et al, 1982; Vucetic, 1994). So far as the strain

is less than the volumetric threshold strain  $\gamma_{lv}$ , excess pore pressure cannot be generated. Second type of energy dissipation mechanism called viscous dissipation appears when the volumetric threshold strain is exceeded. Viscosity presents the force resisting to the relative movement of a water and soil grains. There are also some other mechanisms of energy dissipation, such as particle breakage. Their contributions are relatively insignificant in comparison with frictional and viscous mechanism.

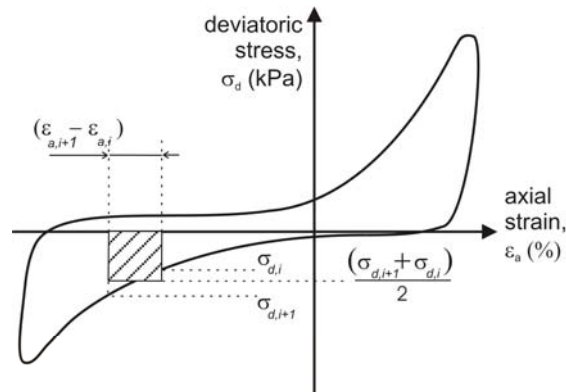


Figure 4. The dissipated energy per unit volume for a soil sample in cyclic triaxial loading.

Generally it is very difficult to divide contribution of these two mechanisms. By comparing the energy dissipated in dry and saturated samples Hall (1962) found out that the portion of energy dissipated by viscous mechanism increases as the strain amplitude decreases and the portion of energy dissipated by frictional mechanism increases with strain amplitude increase. Those findings are especially important because of the observations of Hardin (1965) showing that the quantity of energy dissipated by the frictional mechanism is independent of the frequency of loading, while the energy dissipated by viscous mechanism is proportional to the frequency of loading.

The contribution of viscous mechanism to total amount of dissipated energy is significant at small strain amplitude, but decreases as the strain amplitude increases. Large strain amplitudes are of our interest during cyclic mobility occurrence. It was shown that total dissipated energy at large strain amplitudes can be supposed mostly as a result of frictional mechanism (Whitman and Dobry, 1993). It is important for the use of dissipated energy in cyclic mobility modeling that therefore total amount of dissipated energy at large strain amplitude is relatively independent of frequency.

## Existing Energy-Based Pore Pressure Models

When the volumetric threshold strain is exceeded, an excess pore water pressure is generated in cyclic loaded saturated soil. Thus the effective stresses, which are of crucial importance for cyclic/dynamic loaded soil performance prediction, changes. One of the earliest approaches to dynamic effective stress analysis is an effective stress model for liquefaction by Finn et al (1977). They described the volumetric compaction and related pore water increases with shear strains depending on the stiffness and damping characteristics of a soil layer.

Furthermore, a single variable called damage parameter was introduced (Finn and Bhatia, 1981) for representing the pore water pressure generation data from constant stress or constant strain cyclic loading tests on saturated soils. One of the main advantages of the use of damage parameter is an existence of only one curve to describe all the test data at one relative density for the range of cyclic stresses or strains of interests. Data from constant stress or constant strain cyclic loading tests can be used directly to predict an excess pore water pressure generated by the irregular stress or strain histories. An evaluation of damage parameter is rather difficult job, including some not easy to understand variable transformations. But it shows the same principal idea as the dissipated energy approach.

Large range deformations occurring during cyclic loading of saturated soil are what we are concerned about when we try to capture the cyclic mobility or liquefaction into modeling procedure. As already explained, dissipated energy seems a proper modeling parameter, as it is not sensitive to loading rate or frequency. Besides that it considers both the amplitude of shear strain and the number of load cycles, combining the effect of stress and strain.

Green (2001) reviewed development of energy-based excess pore water pressure generation models. Nemat-Nasser and Shokooch (1979) established governing differential equations relating energy dissipation to the densification of dry samples and to the generation of excess pore water pressure  $\Delta u$  in saturated samples. A typical relation (Eq.5) was assumed by Mostaghel and Habibaghi (1979).

$$r_u = \frac{w}{e_0} \quad \text{Eq. 5}$$

$r_u$  denotes pore water pressure ratio ( $=\Delta u/\sigma'_0$ ) and  $e_0$  initial void ratio of soil.

Complementing the theoretical framework several researchers presented different numerical relations (Davis and Berrill, 1982; Simcock et al, 1983; Yamazaki et al, 1985; Law et al, 1990; Hsu, 1995; Liang, 1995; Figueroa et al, 1997; Green et al, 2000; Davis and Berrill, 2001). Presented expressions relate dissipated energy per unit volume of soil to the residual excess pore pressure, which is defined as the pore pressure in excess of hydrostatic conditions when the applied cyclic stress is zero. All of the expressions are empirical curve fit equations based on different laboratory results (mostly cyclic triaxial and hollow cylinder torsional shear tests) with different numbers of parameters. Most frequently used calibration parameters included in models are soil density, fabric and stress state. A typical general form derived from the proposed expressions could be written as

$$r_u = a \cdot w^b, \quad \text{Eq. 6}$$

where  $a$  and  $b$  are functions of soil type, relative density of soil, stress conditions, initial soil state parameters, etc. The pore pressure ratio used in the Eq.6 presents the pore pressure change caused by the rearrangements of soil particles and means the residual pore pressure change, which remains even when the load disappears. It is common to all of the proposed expressions that only residual pore pressure changes are taken into account. This is understandable as all of them were developed in bases of assessment of seismic induced liquefaction.

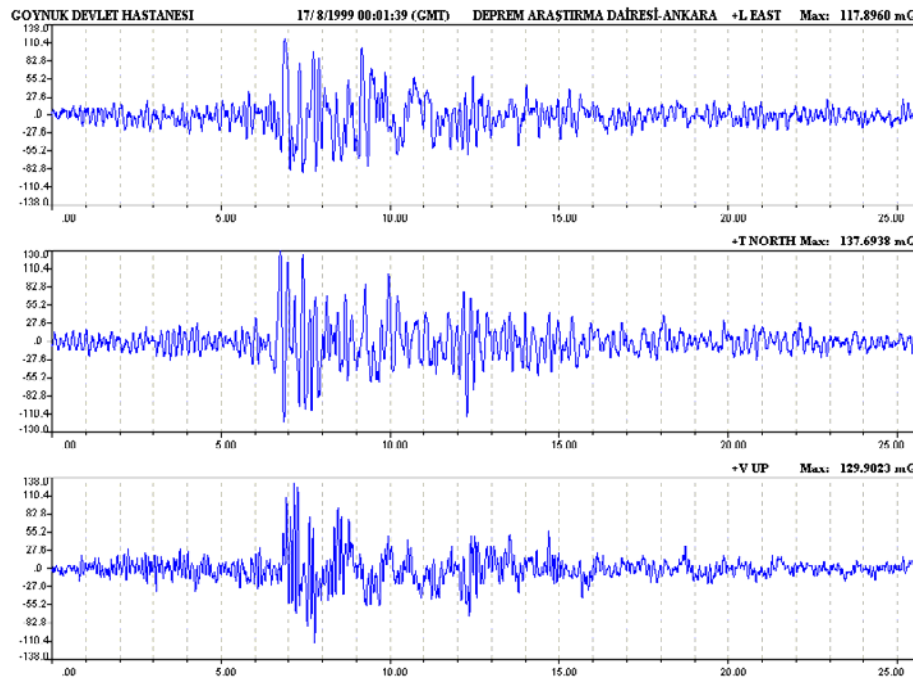


Figure 5. Acceleration Records of the August 17, 1999 00:02 7.4 Earthquake, Kocaeli, Turkey (TKYHP, 1999).

## The Effect of Pore Pressure Oscillations

It has been generally assumed for a long time that under seismic loading only cyclic shear stresses are imposed on the soil element (Das, 1992). Actually horizontal loadings acting on the soil element during seismic ground motions are usually a little bit more stressed on, but vertical loading can not be completely neglected. A fault movements cause three orthogonal components of translation motion that are commonly measured (Kramer, 1996). The ratio between horizontal and vertical component depends upon the type of a fault movement as well of some other local site conditions. Figure 5 shows acceleration records taken at Göynük (Bolu) location during 7.4 M earthquake Gölçük-Kocaeli 1999 in Turkey (TKYHP, 1999). It can be seen from presented records that vertical component might even exceeds horizontal component sometimes.

Purely one dimensional stress conditions are very rare in reality. Besides shear stresses, normally normal stresses appear, too. There is no doubt about compression component in case of vertically cyclic loaded soil, which may derive from foundation vibrations, traffic load etc. This kind of cyclic loading can also causes large range deformations occurrence.

When saturated soil is subjected to such a cyclic loading acting in horizontal and vertical direction, pore water pressures changes are not only of residual type.

The existing energy-based pore pressure models described above relates the dissipated energy and permanent pore water pressure changes which happen due to the soil particles rearrangements. Under simultaneous cyclic loading in normal and shear strain modes the temporary pore water pressure changes occur besides residual one. The existing energy-based

pore pressure models for cyclic loaded saturated soils neglect the temporary pore water pressure changes. Temporary pore water pressure changes are caused by transmission of compressive stresses onto the pore water. As the compressive stress oscillates during the usual cyclic loading, the temporary pore water pressure oscillates noticeable during cyclic loading as well.

While pore water has no shear stiffness and can not be affected by the shear stresses, the situation in case of normal stresses is completely different. Normal stresses transmit from soil skeleton onto the pore water (Figure 6). Changes of normal stresses from compression to extension and back are observed as oscillations of pore water pressure.

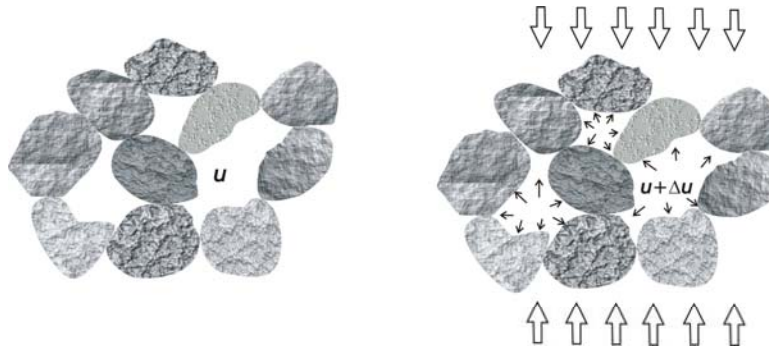


Figure 6. The transmission of compressive stresses onto the pore water.

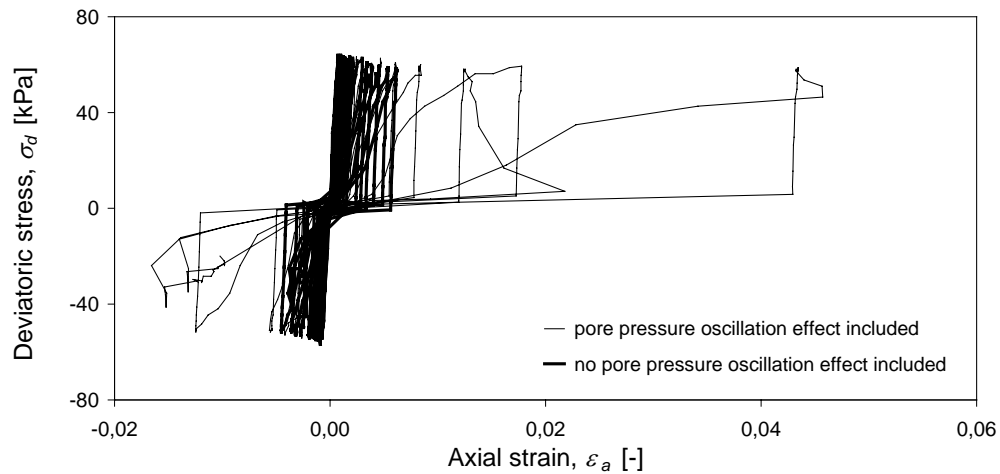


Figure 7. Strain development during a cyclic loading with pore pressure oscillation effect taken into account and without it.

A simple pore pressure model can be incorporated into nonlinear cyclic model (Finn et al, 1977; Osinov, 2003). Such models usually concern the soil deformed in one mode only. For example, simple shear mode is quite commonly used to describe deformation mode of soil deposits under seismic load. Their use is much less complicated than a use of tensorial models. A simple nonlinear cyclic model was used (Lenart, 2007) for a typical strain progression calculation in soil element. A record of real pore pressure changes in cyclic

loaded soil and the same record with pore water pressure oscillations subtracted from the original one were used as an input for calculations. The effect of pore water pressure oscillations upon the strain progression during the vertical cyclic loading of a saturated soil is demonstrated on Figure 7. The use of pore pressure models with and without the oscillation effect taken into account were compared in numerical modeling. As it can be understood from description of the nature of temporary pore pressure changes occurrence in saturated soil cyclic loaded in compression, the extreme pore pressure values occur at the same time as the extreme load does. This means that the material stiffness is the lowest at the moment of the greatest load. The pore pressure oscillations effect was found therefore to be large.

## New Proposed Pore Pressure Model

The basic idea of the new proposed pore pressure model is in dividing of an excess pore water pressure generated during cyclic loading into two parts: the temporary pore pressure change and the residual pore pressure change. The model proposes that the pore pressure ratio,  $r_u$  (Eq. 7) consist of its residual  $r_{u,r}$  and temporary  $r_{u,t}$  part. Both two parts are defined by equations (Eq. 8) and (Eq. 9).

$$r_u = r_{u,r} + r_{u,t} \quad \text{Eq. 7}$$

$$r_{u,r} = \frac{\Delta u}{\sigma'_0} \quad \text{Eq. 8}$$

$$r_{u,t} = F(t) \cdot \frac{\Delta \Delta u}{\sigma'_0} \quad \text{Eq. 9}$$

$\Delta u$  means an excess pore water pressure generated in the mean point of hysteresis loop at conditions when the applied cyclic stress is zero. Actually it is the residual pore water pressure, which we talked about above.  $\Delta \Delta u$  is an extreme pore pressure change in a loading cycle.  $F(t)$  is a time function of compressive stresses acting upon the soil element.

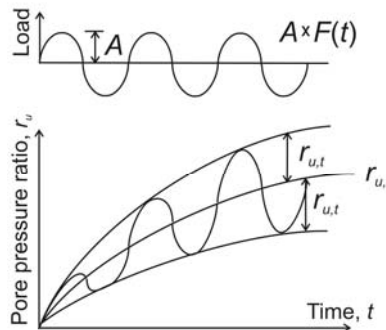


Figure 8. The total pore pressure ratio consist of the residual and temporary part.

The energy-based pore pressure models review shows that the modeling of residual pore water pressure change is based upon the relation to dissipated energy. Eq. 6 presents a typical general form for this kind of relation used by most of researchers. It was proposed that the temporary pore pressure changes due to the loading and unloading are function of dissipated energy as well. The difference between their maximum values during one loading cycle of uniform cyclic loading was neglected. The contribution of residual and temporary part of pore pressure ratio to the total pore pressure change is shown on Figure 8.

It was decided to relate both two parts of pore pressure ratio to a dissipated energy ratio. Author tried to find out linear relation between the proper function of dissipated energy ratio  $G(w)$  and residual and temporary part of pore pressure ratio respectively. Using the least square method, the best agreement between proposed relationship (Eq. 6) and empirical results was found if a dissipated energy ratio was raised to a power of one tenth of a mathematical constant  $e$  (base of the natural logarithm,  $e=2.71828 \dots$ ). Using a power function  $G(w)$  like presented in Eq. 10, relations between function of dissipated energy ratio and two kinds of pore pressure ratios was transformed into a linear one. Their slopes give parameters  $k_r$  and  $k_t$ , where  $r$  and  $t$  means residual and temporary changes, respectively. Typical results are shown on Figure 9.

$$G(w) = (w)^{e/10} \tag{Eq. 10}$$

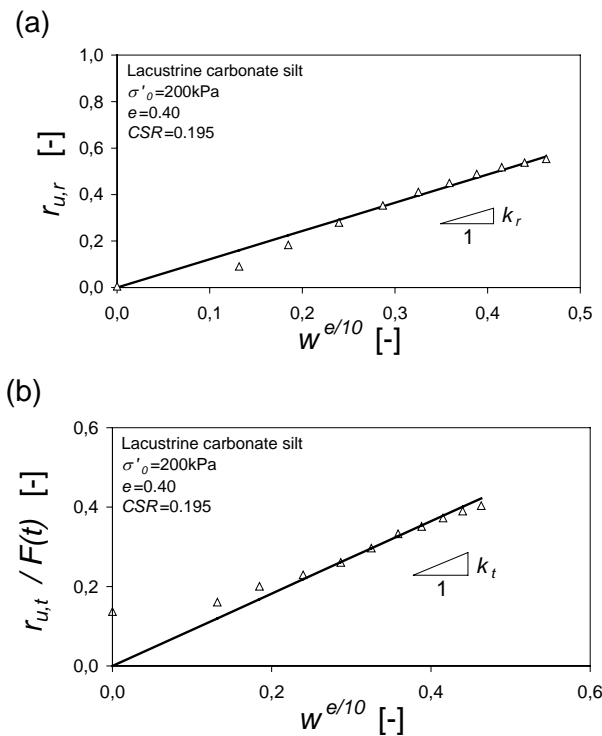


Figure 9. After transformation of dissipated energy ratio by function  $G(w)$  residual  $k_r$  (a) and temporary  $k_t$  (b) pore pressure parameters are evaluated (Lacustrine carbonate silt; Lenart, 2006a).

Knowing the time function  $F(t)$  of a normal component of dynamic loading to which soil is subjected, one can write the equation for evaluating the pore pressure ratio,  $r_u$  (Eq. 11). As it is based on dissipated energy per unit volume, it is independent of loading frequency or rate impacts in case of strain range typical for cyclic mobility or liquefaction.

$$r_u = (w)^{\%10} \cdot [k_r + k_t F(t)] \quad \text{Eq. 11}$$

Proposed pore pressure model differs from all other known energy-based pore pressure models mostly due to its temporary pore pressure component. When the subjects of modeling are mostly pore pressure changes, caused by shear mode loadings, the existing models do well their job. The main difference occurs when dynamic load acting in normal direction is present. Figure 10 presents results of an experiment compared to modeling of an excess pore water pressure generation. Saturated soil sample tested in cyclic triaxial apparatus was dynamic loaded by irregular seismic load recorded during Petrovac earthquake in Montenegro 1979 (Bubnov, 1980). Generated pore water pressure was measured during an experiment. Results were compared to the results of two different energy-based pore pressure models. First one is the new proposed pore pressure model with residual and temporary component. The other is recently presented energy-based pore pressure model (Green et al. 2000) covering only residual part of generated excess pore water pressure. The impact of temporary pore water pressure change upon the whole pore water pressure change happened during dynamic loading of saturated soil can be easily seen from the results below.

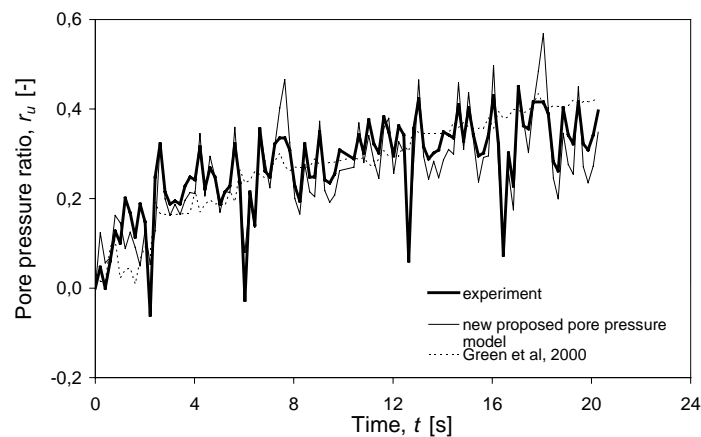


Figure 10. Measured and calculated pore pressure ratio.

## Dissipated Energy as a Modeling Parameter

Modeling of cyclic loaded saturated soils can be done in general by two types of models: true tensorial models and nonlinear cyclic models, if the empirical relations and diverse observational methods are excluded. Models from the first group establish a tensorial strain-stress relationship and are in principle applicable to arbitrary strain or loading path. They are necessary for two- and three- dimensional boundary value problems (Zienkiewicz et al,

1999). The main disadvantage of true tensorial models are their complexity and the way of calibration. Instead of their complexity, the parameters needed in those models are usually calibrated only against one-dimensional load mode. Nonlinear cyclic models incorporate less parameters than tensorial models. Their calibration is based upon the same type of deformation as in the problem to be solved (Osinov, 2003; Liyanapathirana and Poulos, 2002).

A pore pressure model presented above is supposed to be used in the second group of models for nonlinear effective stress analysis (Finn et al, 1977). It is an applicable tool to evaluate an exact position of saturated soil stress path during cyclic loading. It enables to take into account the progressive degradation of stiffness and strength of the soil in effective stress analysis for the dynamic response of saturated soils.

Irrespective of the approach to analysis, deficiency of all type of models appears when dealing with phases of sudden soil softening and significant regain in soil stiffness during cyclic loading at large deformations shown on Figure 11. Phenomenon of cyclic mobility is described at the beginning of this paper. Large deformations limited somehow with soil hardening occur when stress path is crossing the PTS. Several computational models have been developed for simulation of cyclic loaded saturated soil, specially the dilatancy effects following the flowing phase during the cyclic mobility. The flow and hardening rules presented by Elgamal et al (2003), based on the original framework of Prevost (1985) in which a multi-surface approach is adopted for cyclic hysteretic response, seems most promising at the moment. The contractive, perfectly plastic, and dilative phases (Figure 3) are incorporated by newly developed flow and hardening rules. The flow phase is directly controlled by the strain accumulation.

Recent study (Lenart, 2006a) shows that the highly yielded segment, when the stress path of cyclic loaded soil is crossing PTS, is limited by the amount of dissipated energy. The finding is explained more in details in continued paragraph. It has been used in simple 1D nonlinear cyclic model also presented below.

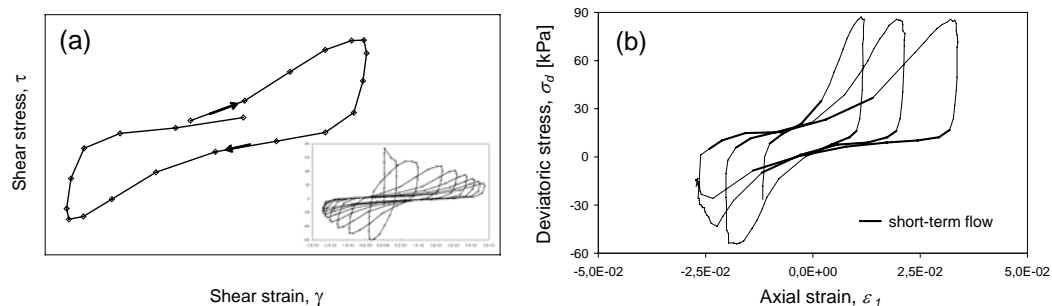


Figure 11. Typical hysteretic loop of the soil under cyclic loading (a) and marked short-term flow phase (b) (Lenart, 2008).

## Energy Dissipated during Flow Phase

Numerical versatility is one of the main challenges in the process of cyclic mobility modeling. Highly yielded segment develops when stress path crosses the PTS. The short-term

flow that occur during softening phase in cyclic loaded soils, causes uncertainties about deformation behavior of cyclic loaded saturated cohesionless soil. Two main questions arise when stress path meets the PTS – what is a remaining stiffness of the soil in softening phase and how large deformation can soil undertake before transformation from contractive to dilative phase (from softening to hardening)? As said, strain accumulation criteria might be used (Elgamal et al., 2003, Yang et al., 2003) to answer those questions when using general plasticity models.

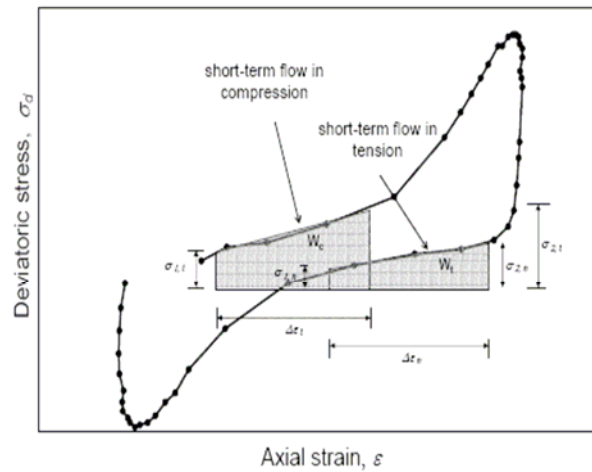


Figure 12. Evaluation of energy dissipated during short-term flow.

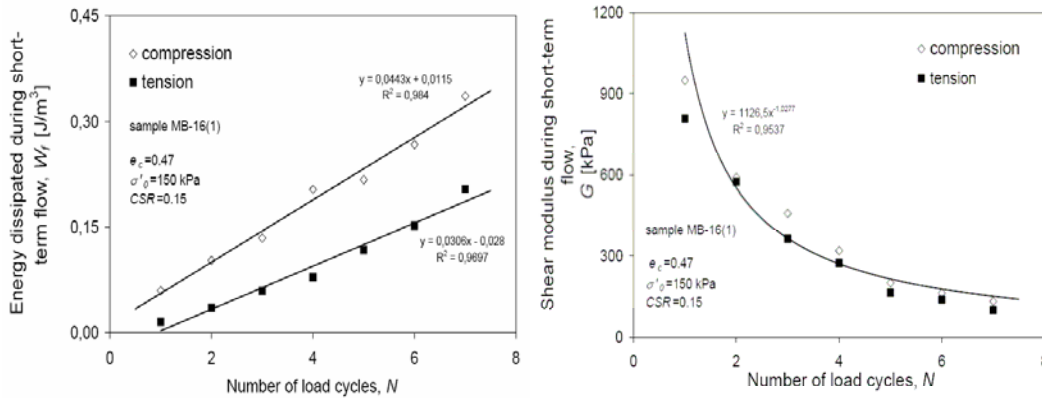


Figure 13. Typical impact of loading direction upon the dissipated energy and soil stiffness during short-term flow.

Trying to avoid complex equations describing plastic flow, dissipated energy was used as a parameter for soil behavior at short-term flow during cyclic mobility. A dissipated energy approach seems good solution due to the strain and stress combination. During soil particles movements, which lead to the soil skeleton contraction, a part of an energy, which is introduced to the soil through cyclic loading, is dissipated by the viscous and frictional mechanism. At large strain range, which is also the case of a short-term flow during cyclic mobility process, the frictional mechanism is expected to dominate. Thus the total amount of

dissipated energy can be approximated by the energy dissipated through the frictional mechanism. In spite of different evaluation of energy dissipated during short-term flow, it can be adopt that it is independent of frequency and loading rate. Figure 12 presents how to evaluate the energy, which dissipates during short-term flow in one loading cycle (Lenart, 2008). In each loading cycle a softening phase in compression and tension is defined. Short-term flow of each softening phase in stress-strain cycle is approximated by a single line. The area below this line presents dissipated energy. It is calculated as

$$W_{t(c)} = \frac{\sigma_{1,t(c)} + \sigma_{2,t(c)}}{2} \cdot \Delta\varepsilon_{t(c)}, \tag{Eq. 12}$$

where indexes  $t$  and  $c$  mean tension and compression respectively.  $\sigma$  and  $\varepsilon$  are stress and strain as marked on Figure 12. Separate energy dissipation for tension and for compression can be evaluated.

It is obvious that the energy dissipated during short-term flow increases with the number of load cycles. Similar the stiffness of material during softening phase decreases as the number of cycles increases. Author (Lenart, 2008) studied both two phenomena and found out that data of dissipated energy during short-term flow in one single load cycle is related linearly to the number of load cycles for a separate direction of loading. It has been found out that a short-term flow within one single load cycle is not identical when compression and when tension load is applied. Different amount of energy is dissipated in each case (Figure 13a) probably due to the cyclic test type, while loading direction does not affects the stiffness of soil during short-term flow (Figure 13b).

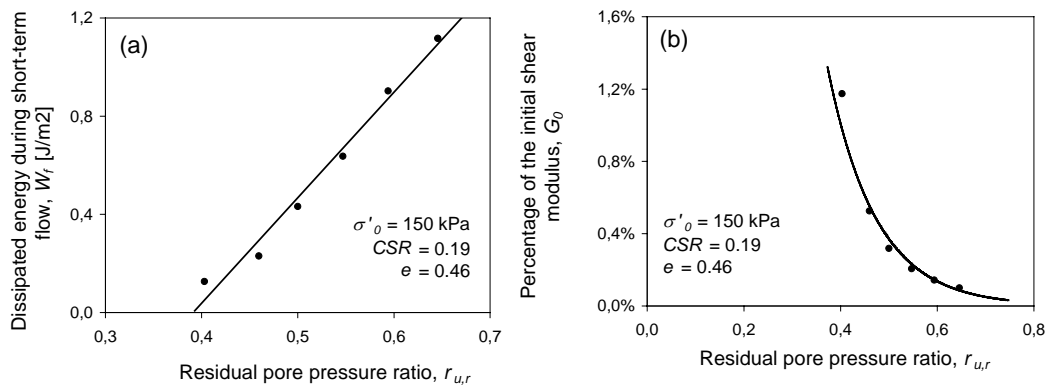


Figure 14. Typical relation between residual pore pressure ratio and energy dissipated during short-term flow phase (a) and shear modulus of soil during short-term flow phase (b).

For practical purpose, energy dissipated during compression can be added up to the energy dissipated during extension. Instead to the number of load cycles, which is not useful for irregular loadings, a sum is compared to the residual pore water pressure ratio  $r_{u,r}$  (Figure 14a). Residual pore water pressure is an exceeded pore pressure, which remains in soil even when the applied cyclic stress is zero. Similar, also the soil stiffness is compared to the same quantity (Figure 14b). Equations (Eq.13) and (Eq.14) are used to describe the relations.

$$W_f = n \cdot r_{u,r} - c \quad \text{Eq. 13}$$

$$G_f = a \cdot r_{u,r}^{-b} \quad \text{Eq. 14}$$

$a$ ,  $b$ ,  $c$  and  $n$  presents experimentally defined parameters. While others parameters are out of our interests at this place, ratio between parameters  $n$  and  $c$  is important for cyclic mobility modeling. It presents the residual pore pressure ratio at which soil softening due to cyclic mobility effects starts. It has been found out that ratio  $n/c$  is affected only by cyclic stress ratio  $CSR$ . Residual pore pressure ratio, at the “flow start” point, increases as  $CSR$  decreases (Figure 15). An impact of void ratio and initial confining pressure is not clear.

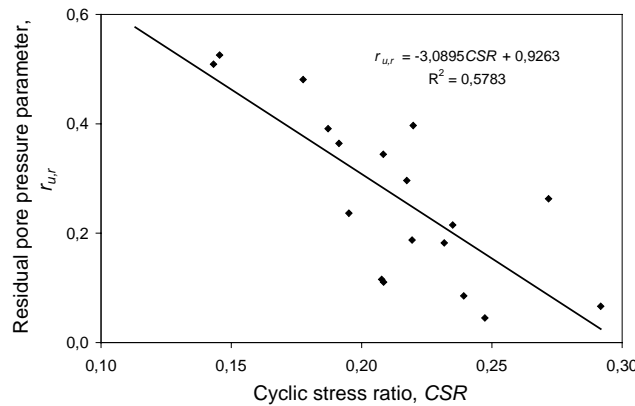


Figure 15. The impact of  $CSR$  upon the residual pore pressure ratio  $r_{u,r}$  when stress path meets the PTS for the first time.

## Experimental Program

Basic research laboratory test program was performed with a view to study the residual and temporary pore pressure parameters as well as energy dissipation during short-term flow phase within cyclic mobility occurrence. Cyclic triaxial system at the Laboratory of soil mechanics, University of Maribor, was used. Reconstituted samples of lacustrine carbonate silt from Stože landslide (Lenart, 2006b) and of silty sand from Sava valley in Boštanj (Vilhar and Lenart, 2007) were used in the experimental part of the study. Both two types of material originate from Slovenia and were involved in larger geotechnical projects with dynamic loaded soils (earthquake, railway load). Samples were prepared by means of wet tamping at specific moisture content and densities similar to those occurring naturally. Some physical properties of tested material are shown in Table 1. Their grain size distribution curves are presented in Figure 16. The tested specimens were solid cylinders, 7.0 cm in diameter and 14.0 cm in height.

Experimental work consisted of 65 cyclic triaxial tests performed on material from Stože landslide and 18 cyclic triaxial tests performed on material from Boštanj. All specimens were isotropically consolidated to effective confining pressure ranged from 50 to 200 kPa and cyclic loaded in undrained conditions afterwards. Uniform sine waves with frequency of 1 or

2 Hz separately and irregular time history adopted from Petrovac earthquake 1979 (Bubnov, 1980) were used for loading in axial direction.

**Table 1. Basic physical properties of tested materials**

		Lacustrine carbonate silt from Stože landslide	Silty sand from Sava valley in Boštanj
Dry unit weight	$\gamma_d$ (kN/m <sup>3</sup> )	18.0 – 20.0	15.7 – 16.5
Water content	$w$ (%)	7.0 – 13.0	17.8 – 23.8
Particle specific gravity	$\gamma_s$ (-)	2.83	2.69 – 2.75
Void ratio	$e$ (-)	0.33 – 0.49	0.63 – 0.72
Angle of internal friction	$\varphi$ (o)	33.7	30 – 35
Cohesion	$c$ (kPa)	0	0 - 10

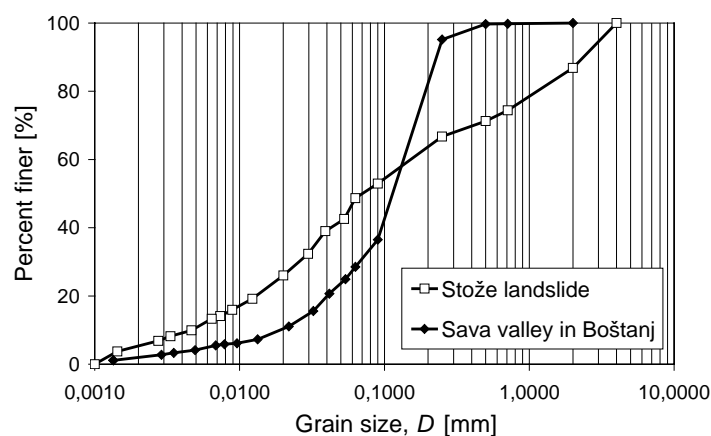


Figure 16. Gradation curves of tested materials.

### Pore Pressure Parameters

The impact of void ratio  $e$ , and cyclic stress ratio  $CSR$  upon the residual  $k_r$  and temporary  $k_t$  pore pressure parameters were empirically studied by the experimental program defined above. Data points were fitted together using the least-squares regression method. Following relationships were determined respectively:

- for lacustrine carbonate silt from Stože landslide

$$k_r = 5.28 \cdot e - 9.87 \cdot CSR + 0.87, \quad \text{Eq. 15}$$

$$k_t = 4.61 \cdot e + 6.13 \cdot CSR - 2.36 \quad \text{Eq. 16}$$

- for silty sand from Boštanj

$$k_r = 16.95 \cdot e - 0.007 \cdot CSR - 9.67, \quad \text{Eq. 17}$$

$$k_t = 11.77 \cdot e + 7.41 \cdot CSR - 8.71. \quad \text{Eq. 18}$$

The impact ratios of single parameters in Eq. 15-18 differ and they depend upon the soil being tested. Anyway, some common characteristics can be realized:

- Pore pressure parameters  $k_r$  and  $k_t$  increase as a void ratio of soil is increasing.
- Residual pore pressure parameter  $k_r$  decreases with an increasing cyclic stress ratio  $CSR$ .
- Temporary pore pressure parameter  $k_t$  increases with an increasing cyclic stress ratio  $CSR$ .

With other words, an excess pore pressure generation is stronger when cyclic loaded saturated soil is looser. Similarly, pore pressure oscillates stronger in loose soil as compressive stresses are easier transmitted to water in pores. On the other hand an increase of loading, e.i. an increase of cyclic stress ratio, causes a decrease of an excess pore pressure generation and an increase of pore pressure oscillation.

### Energy Dissipated during Short-Term Flow

During triaxial cyclic testings void ratio  $e$ , initial effective stress  $\sigma'_0$  and cyclic stress ratio  $CSR$  were changed to find out their impact upon the amount of dissipated energy and soil stiffness during short-term flow (Lenart, 2008). Figure 17 to Figure 19 show the results. It can be seen from Figure 17 that the void ratio does not effects dissipated energy noticeable, while stiffness of soil during flowing phase surprisingly increases if the void ratio increases. The amount of dissipated energy increases if cyclic stress ratio increases (Figure 18a) or if initial effective stress increases (Figure 19a). On the other hand, when  $CSR$  (Figure 18b) or  $\sigma'_0$  (Figure 19b) increases, stiffness of soil during short-term flow decreases.

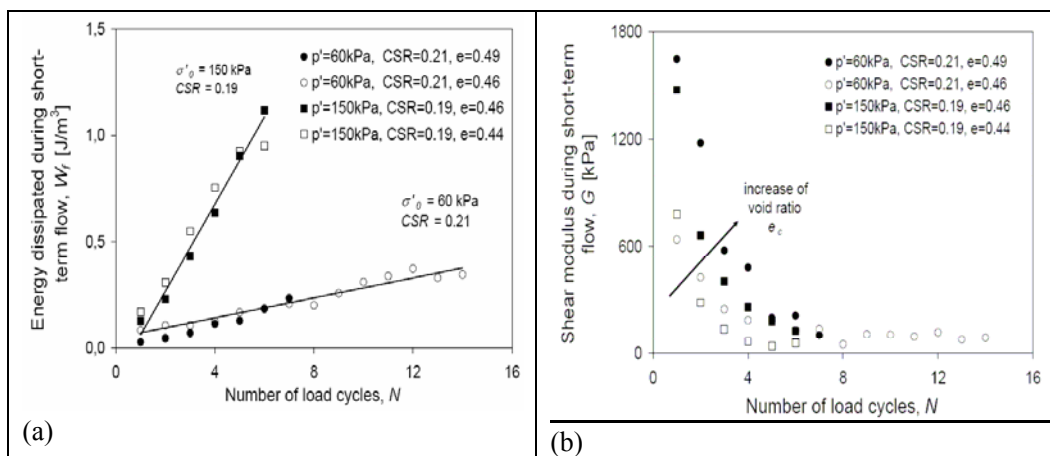


Figure 17. The effect of void ratio upon the dissipated energy (a) and soil stiffness (b) during short-term flow (Lenart, 2008).

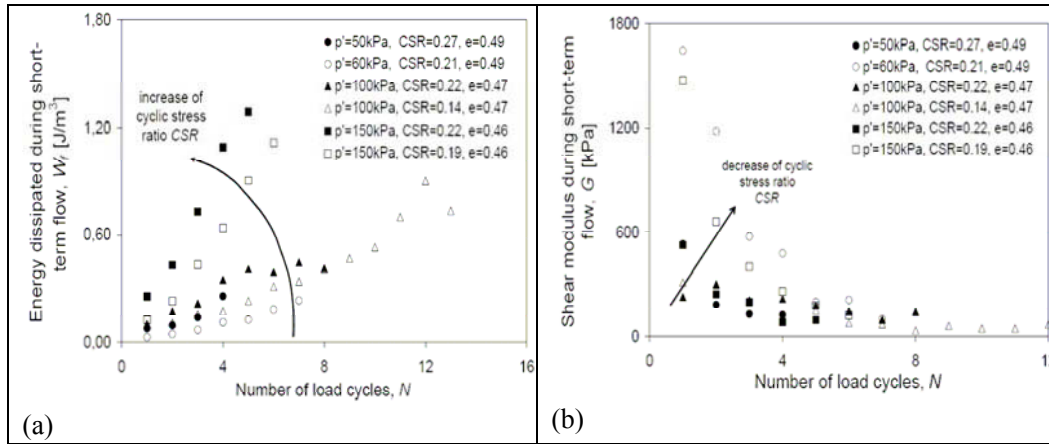


Figure 18. The effect of cyclic stress ratio upon the dissipated energy (a) and soil stiffness (b) during short-term flow (Lenart, 2008).

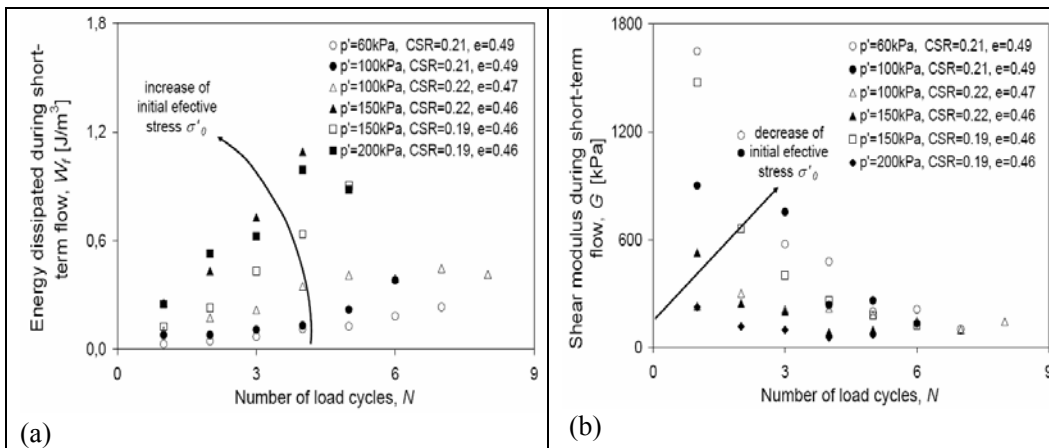


Figure 19. The effect of initial effective stress upon the dissipated energy (a) and soil stiffness (b) during short-term flow (Lenart, 2008).

Only 19 different tests were analyzed so far with a purpose to define impacts described in this paragraph. Some more results should be included to obtain more reliable conclusions.

### Modeling of Cyclic Triaxial Tests

Based on the presented pore pressure model and findings concerned with short-term flow during cyclic mobility, a simple 1D model for saturated soils, cyclic loaded in normal mode was established (Lenart, 2007). Its main goal is to find out the efficiency of dissipated energy use in modeling process. Some fundamental observations from experimental work were used.

After completion of a short-term flow phase, which occurs when stress path is crossing the PTS, soil starts to strengthen again. The shear modulus increases again up to the value from before of the flowing phase. The relation between dissipated energy and soil stiffness has been defined for a case of tested soil. The shape of a curve obtained in this way (Figure

20) is very similar to the well known shape of the relation between strain and stiffness. The advantage of the energy-stiffness curve is that it is less sensitive to the strain changes and it includes both stress and strain histories of a material relating them to the stiffness properties.

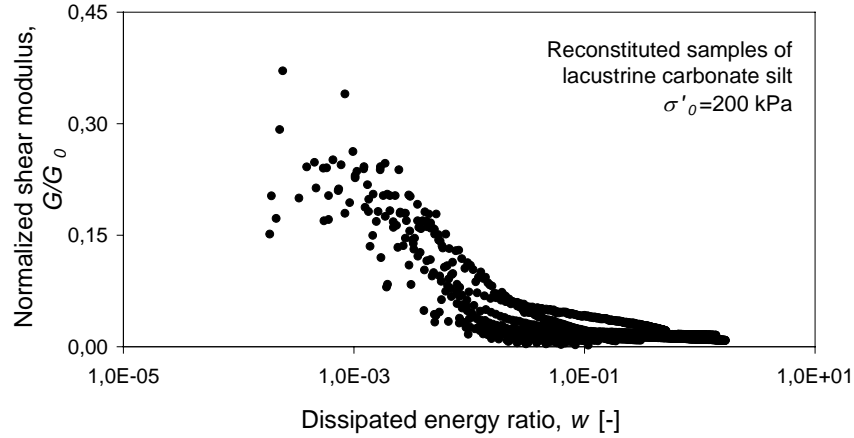


Figure 20. Typical shear modulus degradation curve when dissipated energy is used.

A simple numerical model of a vertically cyclically loaded soil body was used to model a series of cyclic triaxial tests (Lenart and Logar, 2006). The dynamic response of a soil sample loaded vertically by cyclic load was proposed to be one-dimensional. A concentrated mass connected by a nonlinear spring and a viscous damper to a base was vertically loaded by a known loading function of time,  $F(t)$ . The differential equation of motion is well known differential equation (Eq.19), where  $m$  means the mass of the oscillated body,  $k$  is the stiffness of a spring and  $c$  presents the damping of a viscous damper.

$$m\ddot{y} + c\dot{y} + ky = F(t) \quad \text{Eq. 19}$$

The soil stiffness defined by dissipated energy (Figure 20) was used in the model for a loading history before short-term flow appearance. During the short-term flow phase the stiffness of a soil was defined by relation defined in Eq.14. Soil starts to strengthen when short-term flow is finished. It has been assumed in the model that the stiffness of soil during strengthening and unloading is equal to the average stiffness from the last loading cycle. The soil stiffness during the cyclic loading defined above reflects hysteretic behavior of soil. The viscous damping of a system used in numerical model was calculated as 25% of critical damping  $C_{crit}$  (Eq.20; Liyanapathirana and Poulos, 2002).  $G_0$  means initial shear modulus of soil and  $\rho$  is a density of soil. Viscous damping was used only during the unloading phase, while viscous damping during loading was neglected. The whole process during cyclic loading, soil transformation from normal state into the flowing phase and back, is governed by the pore pressure changes, specially the residual pore pressure changes, as defined in the first part of this paper.

$$C_{crit} = 2\sqrt{G_0 \cdot \rho} \quad \text{Eq. 20}$$

Model was verified on results obtained by cyclic triaxial tests. Above defined pore pressure model and relations obtained by studying of a short-term flow during cyclic mobility were used in it. Their contributions seem the most important to the obtained results. Comparison of calculated and measured values of pore pressure, stress states, displacements, strains and stresses are shown for one typical test (Figure 21).

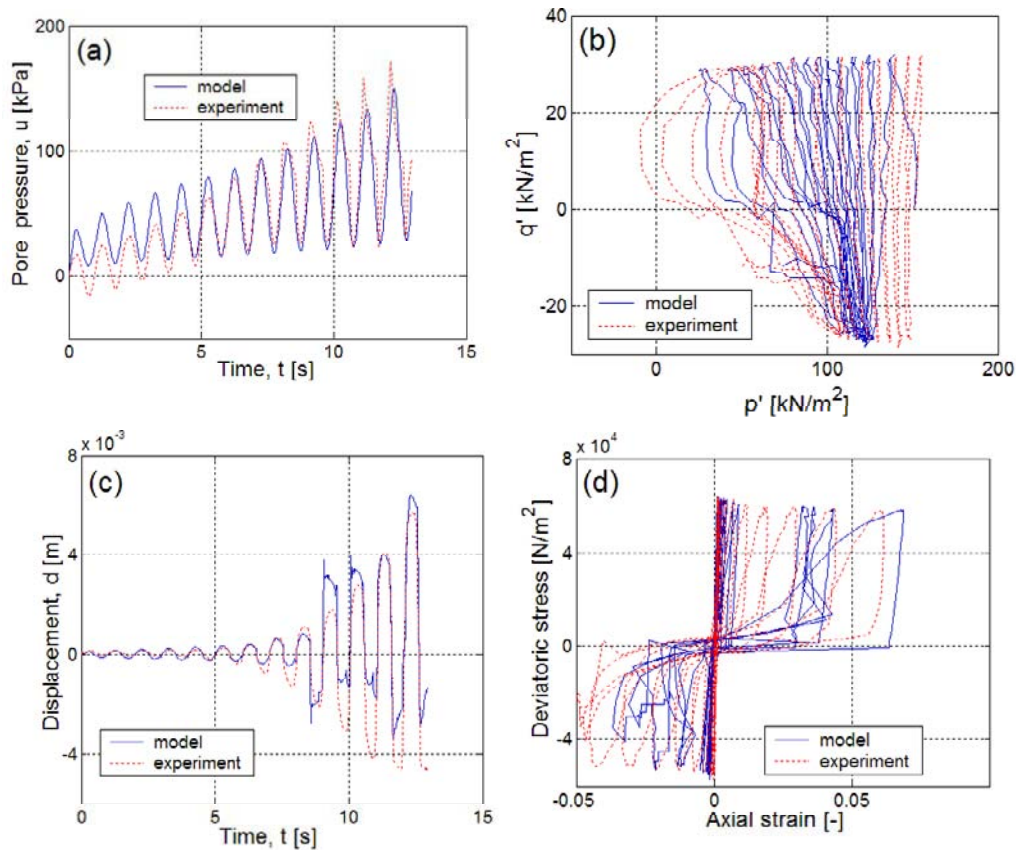


Figure 21. Typical simulation of a pore pressure (a), stress states (b), displacements (c) and stress-strain relation (d) for cyclic triaxial test of a reconstituted sample of lacustrine carbonate silt (Lenart, 2007).

## Conclusion

The loss of strength or stiffness of ground due to the generation of excess pore water pressure is one of the main characteristics of cyclic loaded saturated soil behavior. When the static shear stress is smaller than the steady-state shear strength, cyclic mobility occurs in such saturated soil during cyclic loading. The deformation behavior of two kinds of soil from Slovenia: lacustrine carbonate silt from Stože landslide and silty sand from Sava valley in Boštanj, has been studied in this work.

The results of cyclic triaxial tests were used to define the model describing pore pressure changes in cyclic loaded cohesionless saturated soils. The pore pressure change was divided

into two parts: the temporary pore pressure change and the residual pore pressure change. Temporary changes in pore pressure are due to the transmission of compressive stresses onto the pore water, whereas residual pore pressure changes are caused by volumetric changes and the rearrangement of soil particles due to these changes. Both parts (temporary and residual) of the pore pressure changes were evaluated with respect to the energy dissipated during the cyclic loading of the soil. Such an approach is independent of the rate and frequency of the loading in the large strain range, which is characteristic for cyclic mobility phenomena, too. It is therefore possible to describe pore pressure changes as a function of the dissipated energy for any kind of loading.

A new energy-based pore pressure model is presented which includes both parts of the pore pressure changes. It is possible to determine fairly exactly the pore pressure changes during cyclic loading using the concept of dissipated energy based on only two parameters and a known function of the loading. The effect of the void ratio and the cyclic stress ratio upon the two model parameters has been studied in more detail. The advantages of the proposed pore pressure model have been observed mainly in the case of soils which are cyclically loaded in compression, where the pore pressure oscillates noticeably during the loading. The effect of pore pressure oscillations upon strain progression during the vertical cyclic loading of a saturated soil has been demonstrated. It was found to be large, because extreme pore pressure values occur at the same time as the extreme load. This means that the material stiffness is the lowest at the moment when the load is the greatest. This is not taken into account in other existing pore pressure models.

A complete stress-strain relation for cyclically loaded saturated soils, based on the proposed pore pressure model is also presented. Special attention was focussed on short-term flow during cyclic mobility. The flowing phase occurs when stress path is crossing the PTS and is limited with soil hardening at the end of the phase. It has been found out that the limited amount of energy is dissipated during short-term flow, before hardening occurs. The fact that this kind of dissipated energy is also related to the residual pore pressure was used in modelling of cyclic loaded saturated soils. Some experimental cases were numerically analyzed. Good agreement was obtained between the results of the numerical analysis and the results of the laboratory tests measurements.

### **Acknowledgements**

The author wishes to thank the Laboratory of soil mechanics and Prof. B. Žlender of the Faculty of Civil Engineering, University of Maribor, Slovenia, who kindly made their testing equipment available for the research. The valuable help of G. Vilhar of the National Building and Civil Engineering Institute (ZAG) was much appreciated. The financial support of the Ministry of Higher Education, Science and Technology, Slovenia is gratefully acknowledged.

### **References**

- Arias, A. (1970). A Measure of Earthquake Intensity, *Seismic Design for Nuclear Power Plants* (R.J. Hansen ed.), The MIT Press, Cambridge, MA, 438-483

- Berrill, J.B. and Davis, R.O. (1985). Energy dissipation and seismic liquefaction of sands: Revised model, *Soils and Foundations*, Vol.25, No.2, 106-118
- Bubnov, S. (1980). Earthquake in Montenegro 15th of April 1979, *Savetovanje iskustva i uslovi za projektovanje i gradjenje posle zemljotresa u SR Crnoj Gori*, Savez gradjevinskih inženjera i tehničara SR Srbije, Njivice, 1-22 (in serb.)
- Das, B.M. (1992). *Principles of soil dynamics*. PWS-KENT Publishing Company, Boston, Massachusetts, 397-459
- Davis, R.O. in Berrill, J.B. (1982). Energy dissipation and seismic liquefaction in sands, *Earthquake Engineering and Structural Dynamics*, Vol. 10, 59-68
- Davis, R.O. and Berrill, J.B. (1998). Site-specific prediction of liquefaction, *Geotechnique*, **48**, No. 2, 289-293
- Davis, R.O. in Berrill, J.B. (2001). Pore Pressure and Dissipated Energy in Earthquakes – Field Verification, *Journal of Geotechnical and Geoenvironmental Engineering*, Vol. 127, No. 3, 269-274
- Liang, L. (1995). *Development of an Energy Method for Evaluating the Liquefaction Potential of a Soil Deposit*, PhD Dissertation, Case Western Reserve University
- Figuroa, J.L., Saada, A.S., Kern, D. in Liang, L. (1997). Shear strength and shear modulus degradation models based on the dissipated unit energy, *Proc. 4th International Conference on Soil Mechanics and Foundation Engineering*, Hamburg, Germany, A.A. Balkema Publishers, Vol. 1, 291-294
- Figuroa, J.L., Saada, A.S., Liang, L., in Dahisaria, N.M. (1994). Evaluation of Soil Liquefaction by Energy Principles, *Journal of Geotechnical Engineering*, ASCE, Vol. 120, No. 9, 1554-1569
- Finn, W.D.L. in Bhatia, S.K. (1981). Prediction of Seismic Porewater Pressures, *Proceedings 10th ICSMFE*, Vol. 3, 201-206
- Dobry, R., Ladd, R.S., Yokel, F.Y., Chung, R.M. in Powell, D. (1982). *Prediction of pore water pressure buildup and liquefaction of sands during earthquakes by cyclic strain method*, NBS Building Science Series 138, National Bureau of Standards, Gaithersburg, Maryland
- Elgamal, A., Yang, Z., Parra, E., in Ragheb, A. (2003). Modeling of Cyclic Mobility in Saturated Cohesionless Soils, *Int. J. Plasticity*, **19**, 883-905
- Figuroa, J.L., Saada, A.S., Liang, L., in Dahisaria, N.M. (1994). Evaluation of Soil Liquefaction by Energy Principles, *Journal of Geotechnical Engineering*, ASCE, Vol. 120, No. 9, 1554-1569
- Finn, W.D.L., Lee, K.W. in Martin, G.R. (1977). An Effective Stress Model for Liquefaction, *Journal of the Geotechnical Engineering Division*, ASCE, Vol. 103, No. GT6, 517-533
- Green, R.A., Mitchell, J.K. in Polito, C.P. (2000). An Energy-Based Excess Pore Pressure Generation Model for Cohesionless Soils, *Proc.: Developments in Theoretical Geomechanics – The John Booker Memorial Symposium* (D.W. Smith in J.P. Carter, ur.), Sydney, Australia, A.A. Balkema Publishers, 383-390
- Green, R.A. (2001). *Energy-Based Evaluation and Remediation of Liquefiable Soils*, Ph.D Thesis, Virginia Polytechnic Institute and State University, Blacksburg, Virginia
- Green, R.A. and Mitchell, J.K. (2003). A closer look at Arias intensity-based liquefaction evaluation procedures, *2003 Pacific Conference on Earthquake Engineering*, Paper No. 94

- Green, R.A. in Terri, G.A. (2005). Number of Equivalent Cycles Concept for Liquefaction Evaluations – Revisited, *Journal of Geotechnical and Geoenvironmental Engineering*, Vol. 131, No.4, 477-488
- Gutenberg, B. and Richter, C.F. (1956). Magnitude and Energy of Earthquakes, *Ann. Geofis.*, **9**, 1-15
- Hall, J.R. (1962). *Effects of amplitude on Damping and Wave Propagation in Granular Materials*, PhD Thesis, (F.E.Richart, Advisor), University of Florida
- Hardin, B.O. (1965). The Nature of Damping in Sands, *Journal of the Soil Mechanics and Foundations Division*, Vol. 91, SM1, 63-97
- Hsu, H.-L. (1995). Study on the relationship between shear work and pore pressure for saturated sand in undrained test, *Proc.: First Int. Conf. on Earthquake Geotechnical Engineering*, Vol. 1, A.A. Balkema Publishers, Rotterdam, Netherlands, 301-307
- Ishihara, K. (1985). Stability of natural deposits during earthquakes, *Proceedings, 11th International Conference on Soil Mechanics and Foundation Engineering*, San Francisco, Vol. 1, 321-376
- Kayen, R.E. in Mitchell, J.K. (1997). Assessment of Liquefaction Potential During Earthquakes by Arias Intensity, *Journal of Geotechnical and Geoenvironmental Engineering*, Vol. 123, No. 12, 1162-1174
- Kramer, S.L. (1996). *Geotechnical Earthquake Engineering*, Publ. Prentice Hall, 348-422
- Kuribayashi, E. and Tatsuoka, F. (1975). Brief review of liquefaction during earthquakes in Japan, *Soils and Foundations*, **15**, No. 4, 81
- Law, K.T., Cao, Y.L. in He, G.N. (1990). An energy approach for assessing seismic liquefaction potential, *Can. Geotech. J.*, **27**, 320-329
- Lenart, S. (2006a). *Numerical model for pore pressure change evaluation in soils with high liquefaction potential*, PhD Thesis, University of Ljubljana
- Lenart, S. (2006b). Deformation characteristics of lacustrine carbonate silt in the Julian Alps, *Soil Dynamics and Earthquake Engineering*, **26**, 131-142
- Lenart, S. (2007). Modeling of cyclic mobility – an energy approach, *Proc.4th International Conference on Earthquake Geotechnical Engineering*, Paper No. **1317**
- Lenart, S. (2008). The use of dissipated energy in cyclic mobility modeling, *12th Int. conf. of Int. Assoc. for Computer Methods and Advances in Geomechanics* (accepted)
- Lenart, S. and Logar, J. (2006). Numerical modelling of vertically loaded saturated soil, *XIII. Danube-European Conference on Geotechnical Engineering*, **83-88**
- Liyanapathirana, D.S. in Poulos, H. G. (2002). Numerical simulation of soil liquefaction due to earthquake loading, *Soil Dynamics and Earthquake Engineering*, **22**, 511-523
- Martin, G.R., Finn, L.W.D. in Seed, H.B. (1975). Fundamentals of Liquefaction under Cyclic Loading, *Jour. Geotechn. Eng. Div.*, ASCE, GT5, pp. 423-438
- Miner (1945) – vzeto iz Green 2005
- Miner, M.A. (1945). Cumulative damage in fatigue, *Trans. ASME* **67**, A159-A164
- Nemat-Nasser, S. in Shokoh, A. (1979). A unified approach to densification and liquefaction of cohesionless sand in cyclic shearing, *Can. Geotech. J.*, **16**(4), 659-678
- Osinov, V.A. (2003). Cyclic shearing and liquefaction of soil under irregular loading: an incremental model for the dynamic earthquake-induced deformation, *Soil Dynamics and Earthquake Engineering*, **23**, 535-548
- Palmgren, A. (1924). Die lebensdauer von kugella geru, *ZVDI*, **68**(14), 339-341 (in ger.)

- Prevost, J.H. (1985). A simple plasticity theory for frictional cohesionless soils, *Soil Dynamics and Earthquake Engineering*, **4**(1), 9-17
- Seed, H.B. in Lee, K.L. (1966). Liquefaction of saturated sands during cyclic loading, *J. Soil Mech. Found. Div.*, ASCE 92, SM6, 105-134
- Seed, H.B., Idriss, I.M., Makdisi, F. in Banerjee, N. (1975). Representation of irregular stress time histories by equivalent uniform stress series in liquefaction analysis, *Rep. No. EERC 75-29*, Earthquake Engineering Research Center, Univ. of California, Berkeley
- Simcock, K.J., Davis, R.O., Berrill, J.B. in Mullenger, G. (1983). Cyclic Triaxial Tests with Continuous Measurement of Dissipated Energy, *Geotechnical Testing Journal*, **6**(1), 35-39
- TKYHP. (1999). Acceleration Records of the August 17, 1999 00:02 7.4 Earthquake, Kocaeli, General Directorate of Disaster Affairs, Earthquake Research Department, *Turkey National Strong Ground Motion Program* (<http://angora.deprem.gov.tr/indexen.htm>)
- Trifunac, M.D. (1995). Empirical criteria for liquefaction in sands via standard penetration tests and seismic wave energy, *Soil Dynamics and Earthquake Engineering*, Vol. 14, 419-426
- Trifunac, M.D. and Todorovska, M.I. (2004). Maximum distance and minimum energy to initiate liquefaction in water saturated sands, *Soil Dynamics and Earthquake Engineering*, **24**, 89-101
- Vaid, Y.P. and Chern, J.C. (1983) Effect of static shear on resistance of liquefaction, *Soils and Foundations*, Vol. 23, No. 1, 47-60
- Vilhar, G. and Lenart, S. (2007). Dynamic and static liquefaction potential of a silty sand from Boštanj, Slovenia, *Proc.4th International Conference on Earthquake Geotechnical Engineering*, Paper No. **1318**
- Vucetic, M. (1994). Cyclic threshold shear strain in soils, *Journal of Geotechnical Engineering*, ASCE, Vol.120, No.12, 2208-2228
- Yamazaki, F.I., Towhata, I. in Ishihara, K. (1985). Numerical model for liquefaction problem under multidirectional shearing on horizontal plane, *Proc. 5th Int. Conf. on Numerical Methods in Geomechanics*, Vol. 1, Nagoya, Japan, 399-406
- Yang, Z. in Elgamal, A. (2003). Application of unconstrained optimization and sensitivity analysis to calibration of a soil constitutive model, *Int. J. for Numerical and Analytical Methods in Geomechanics*, **27**(15), 1277-1297
- Youd, T.L. (1977). Packing Changes and Liquefaction Susceptibility, *Journal of the Geotechnical Engineering Division*, ASCE, Vol. 103, GT8, 918-923
- Youd, T.L. (1977). Discussion, *Soils and Foundations*, **17**, No. 1, 82
- Zienkiewicz, O.C., Chan, A.H.C., Pastor, M., Schrefler, B.A. in Shiomi, T. (1999). *Computational geomechanics with special reference to earthquake engineering*, John Wiley & Sons, Chichester, England



*Chapter 10*

## **SIMPLIFIED MODAL RESPONSE HISTORY ANALYSIS FOR ASYMMETRIC-PLAN STRUCTURES**

*Jui-Liang Lin<sup>1,\*</sup> and Keh-Chyuan Tsai<sup>2,\*</sup>*

<sup>1</sup>Associate Research Fellow, National Center for Research on Earthquake Engineering,  
Taipei, Taiwan, R.O.C.

<sup>2</sup>Professor of Civil Engineering, National Taiwan University, and Director of National  
Center for Research on Earthquake Engineering, Taipei, Taiwan, R.O.C.

### **Abstract**

The modal equation of motion is the foundation of structural dynamics, which plays a key role in earthquake engineering computations. Each modal equation of motion has a corresponding single-degree-of-freedom (SDOF) modal system. Thus, the modal equation of motion and the corresponding SDOF modal system are regarded as the most basic elements synthesizing the motion of the original multiple-degree-of-freedom (MDOF) structure. Modal response history analyses are widely used in structural dynamic analyses due to the efficiency in calculation and the clarity in conception. Although the vibration modes are only meaningful for elastic structures, the inelastic SDOF modal systems have also been developed based on the pushover curve representing the relationship of roof translation versus base shear for the original MDOF structure. The stated inelastic SDOF modal systems are widely applied to earthquake engineering. One of such applications is using inelastic response spectra to estimate the seismic demands of original MDOF structures. In recent years, the modal response history analyses considering the effects of higher vibration modes were proposed to approximately estimate the seismic responses of inelastic MDOF structures. However, there are three relationships of two roof translations versus two base shears and one roof rotation versus one base torque simultaneously available for two-way asymmetric-plan buildings subjected to seismic loads. Moreover, the pushover curves representing the stated three relationships in acceleration-displacement response spectra (ADRS) format are bifurcated after the original MDOF structure becomes inelastic. Thus, it is unable to use the conventional SDOF modal system to simultaneously simulate the stated three force-deformation relationships for inelastic asymmetric-plan structures. This research decomposed the SDOF modal equation of motion into a set of three coupled equations of motion for two-way asymmetric-plan structures. The mentioned set of three coupled equations of motion is called

---

\* E-mail address: jllin@ncree.org.tw, kctsai@ncree.org.tw. (Corresponding author)

as three-degree-of-freedom (3DOF) modal equation of motion. The 3DOF modal system corresponding to each 3DOF modal equation of motion was constructed. The elastic properties of the 3DOF modal system are exactly obtained from the corresponding 3DOF modal equation of motion. The inelastic properties of the 3DOF modal system are determined from the properties of the mentioned three pushover curves of the original MDOF structure. It is verified that the modal response history analyses by using the proposed 3DOF modal systems for two-way asymmetric-plan inelastic building systems are more satisfactory than those by using conventional SDOF modal systems. It is also validated that the proposed 3DOF modal equations of motion are advantageous to the modal response history analyses for non-proportionally damped two-way asymmetric-plan elastic building systems.

## Introduction

Under the earthquake loads, asymmetric-plan buildings with irregular distributions of mass or stiffness are likely to undergo torsional responses coupled with the translational vibrations. This type of structures is likely to suffer more severe displacement demands at the corner elements under earthquake ground motions. It has been found that this is one of the key factors that have caused many buildings to collapse in recent earthquakes around the world. The seismic analysis of one-way asymmetric buildings has been studied by many researchers [Myslimaj and Tso 2002; Chopra and Goel 2004; Lin and Tsai 2007a]. However, the most general case for asymmetric-plan buildings under horizontal earthquake loads is the two-way asymmetric-plan type under bi-directional seismic ground motions. Due to the complicated coupling effects between one rotational and two translational inelastic vibrations, it is difficult to analyze the seismic behaviors of such buildings by using simple approaches. Not only the translational time histories at center of mass, but also the rotational time history is required to compute the corner responses. Hence, except the time-consuming nonlinear response time history analysis, there seems to be very few simplified methods, which can effectively obtain the approximate response time histories of the noted buildings. Chopra and Goel (2004) have indicated that simultaneous action of two horizontal components of ground motion and structural plans unsymmetric about both axes remained unsolved and required further investigations.

The inelastic response of one-storey system with one axis of asymmetry subjected to bi-directional base motion was studied by Riddell and Santa-Maria (1999). The authors concluded that the effect of the bi-directional ground motion for the ratio of peak deformations under bi-directional and uni-directional excitation is significant for the flexible-side element of buildings with short period of vibration. Hernandez and Lopez (2000) pointed out that the simultaneous action of two horizontal seismic components should be considered in the analysis of one-way and two-way asymmetric plans in order to avoid incursions in the inelastic range. Cruz and Cominetti (2000) investigated the validity of the design practice based on a uni-directional seismic analysis. These researchers all concluded that if the purpose of the analysis is to know the level of damage to which the columns of a structure are exposed, or the elastic or inelastic torsional behavior of building excited by seismic ground movements, the evaluation should be carried out considering the bi-directional earthquake. In order to develop the simplified methodology for the assessment of asymmetric-plan buildings under bi-axial excitation, an extensive parametric study has been performed on one-storey [Peruš and Fajfar 2005] and multi-storey [Marušić and Fajfar 2005] prototype buildings. All of the noted research has provided great contributions to advance the understanding and

methodologies in dealing with the analysis of two-way asymmetric-plan buildings under bi-directional seismic ground motions.

In order to reduce the excessive deformations on the edge of asymmetric-plan buildings, adding fluid viscous dampers (FVD) to asymmetric-plan building systems has been verified to be one of the effective approaches [Goel 1998; Goel 2000; Lin and Chopra 2001]. Although the research on the dynamic responses of non-proportionally damped symmetric-plan structures was conducted at a much earlier time [Moh *et al.* 1965; Itoh 1973; Roesset *et al.* 1973], the study of non-proportionally damped asymmetric-plan structures was performed much later [Goel 1998; Goel 2000; Lin and Chopra 2001; Lin and Tsai 2007b]. According to the literature review [Goel 2001], the analysis methods of non-proportionally damped systems were grouped into four categories and the corresponding shortcomings are briefly stated as follows. The first approach is to directly integrate the equation of motion of the original MDOF structure. The stated approach is numerically inefficient for structural systems with a lot of degrees of freedom. Clough and Mojtahedi (1976) proposed to directly integrate the truncated set of the coupled modal equations of motion, which is more efficient than dealing with the whole set of equation of motion of the original structural system. The second approach is the mode superposition method using complex mode shapes [Igusa *et al.* 1984; Veletsos and Ventura 1986; Goel 2000] which results in doubling the size of the eigenvalue problems and difficulties associated with the use of complex numbers in the dynamic response analysis. The third approach is the hybrid time-domain procedure [Ibrahimbegovic and Wilson 1989; Ibrahimbegovic *et al.* 1990; Claret and Venancio-Filho 1991], which iteratively solves the coupled modal equations of motion in time domain. However, this method cannot be implemented on most commercially available structural analysis programs. Spectral method for random vibration analysis of the non-proportionally damped structures has also been developed [Jangid and Datta 1993]. The last approach, also the most common and simplest approach, is to simply neglect the off-diagonal elements of the transformed damping matrix which is appealing to the engineering practice because it enables the use of the traditional modal analysis methods. Warburton and Soni (1977) studied the accuracy of the last approach. They proposed a condition involving the natural frequencies and the elements of the transformed damping matrix. If the noted condition is fulfilled, the response calculation errors would be limited to a specific range.

Goel (2001) investigated the effects of neglecting the off-diagonal terms of the transformed damping matrix on the seismic responses of non-proportionally damped one-way asymmetric systems. The specific aim of that study was to identify the range of system parameters for which this simplification can be used without introducing significant errors in the seismic responses of the asymmetric-plan systems. Goel (2001) concluded that the aforementioned approximation method is suitable for use over a wide range of parameters. The error parameter, defined by Warburton and Soni (1977), becomes excessive when the value of the normalized supplemental damping eccentricity  $\bar{e}_{sd}$  is close to -0.5. This conclusion indicates that the stated approximation method should not be used for asymmetric-plan systems with a large normalized supplemental damping eccentricity.

It was noted that the modal coordinates derived from two roof translations and roof rotation for inelastic two-way asymmetric-plan buildings are not equal to each other (Lin and Tsai 2008a). Lin and Tsai (2008a) further pointed out that the three pushover curves representing the relationships of two roof translations versus base shears and roof rotation

versus base torque in ADRS format are bifurcated when the original building becomes inelastic. Thus, the 3DOF modal system corresponding to the 3DOF modal equation of motion was derived to simultaneously simulate the stated three pushover curves (Lin and Tsai 2008a). The 3DOF modal system was also mathematically proofed to be identical to the conventional SDOF modal system for elastic two-way asymmetric-plan systems. It was found that the damping matrix of the 3DOF modal equation of motion keeps the properties of the damping for the original MDOF system (Lin and Tsai 2008b). Thus, the 3DOF modal equations of motion were advantageous to the modal response history analysis for asymmetric-plan systems with supplemental damping (Lin and Tsai 2008b).

## Three-Degree-of-Freedom Modal System

### Extension of UMRHA Procedure to Buildings under Bi-directional Ground Motions

The uncoupled modal response history analysis (UMRHA) for uni-axial asymmetric-plan structures [Chopra and Goel 2004] was briefly summarized by Lin and Tsai (2007a). The UMRHA procedure for two-way asymmetric buildings under bi-directional seismic ground motions are extended as follows:

The equation of motion for a typical two-way asymmetric-plan  $N$ -storey building under bi-directional seismic ground motions with each floor simulated as a rigid diaphragm is

$$\begin{aligned} \mathbf{M}\ddot{\mathbf{u}} + \mathbf{C}\dot{\mathbf{u}} + \mathbf{K}\mathbf{u} &= \mathbf{p}_{eff}(t) = -\mathbf{M}\mathbf{u}_x\ddot{u}_{gx}(t) - \mathbf{M}\mathbf{u}_z\ddot{u}_{gz}(t) \\ &= -\sum_{n=1}^{3N} \mathbf{s}_{xn}\ddot{u}_{gx}(t) - \sum_{n=1}^{3N} \mathbf{s}_{zn}\ddot{u}_{gz}(t) = -\sum_{n=1}^{3N} \Gamma_{xn}\mathbf{M}\boldsymbol{\phi}_n\ddot{u}_{gx}(t) - \sum_{n=1}^{3N} \Gamma_{zn}\mathbf{M}\boldsymbol{\phi}_n\ddot{u}_{gz}(t) \\ &= -\sum_{n=1}^{3N} (\Gamma_{xn}\ddot{u}_{gx} + \Gamma_{zn}\ddot{u}_{gz})\mathbf{M}\boldsymbol{\phi}_n \end{aligned} \quad (1)$$

The displacement vector  $\mathbf{u}$ , mode shape  $\boldsymbol{\phi}_n$ , mass matrix  $\mathbf{M}$ , damping matrix  $\mathbf{C}$  and stiffness matrix  $\mathbf{K}$  are

$$\begin{aligned} \mathbf{u} &= \begin{bmatrix} \mathbf{u}_x \\ \mathbf{u}_z \\ \mathbf{u}_\theta \end{bmatrix}_{3N \times 1}, \quad \boldsymbol{\phi}_n = \begin{bmatrix} \boldsymbol{\phi}_{xn} \\ \boldsymbol{\phi}_{zn} \\ \boldsymbol{\phi}_{\theta n} \end{bmatrix}_{3N \times 3N} \\ \mathbf{M} &= \begin{bmatrix} \mathbf{m}_x & \mathbf{0} & \mathbf{0} \\ \mathbf{0} & \mathbf{m}_z & \mathbf{0} \\ \mathbf{0} & \mathbf{0} & \mathbf{I}_0 \end{bmatrix}_{3N \times 3N}, \quad \mathbf{C} = \begin{bmatrix} \mathbf{c}_{xx} & \mathbf{c}_{xz} & \mathbf{c}_{x\theta} \\ \mathbf{c}_{zx} & \mathbf{c}_{zz} & \mathbf{c}_{z\theta} \\ \mathbf{c}_{\theta x} & \mathbf{c}_{\theta z} & \mathbf{c}_{\theta\theta} \end{bmatrix}_{3N \times 3N}, \quad \mathbf{K} = \begin{bmatrix} \mathbf{k}_{xx} & \mathbf{k}_{xz} & \mathbf{k}_{x\theta} \\ \mathbf{k}_{zx} & \mathbf{k}_{zz} & \mathbf{k}_{z\theta} \\ \mathbf{k}_{\theta x} & \mathbf{k}_{\theta z} & \mathbf{k}_{\theta\theta} \end{bmatrix}_{3N \times 3N} \end{aligned} \quad (2)$$

The influence vector  $\mathbf{u}_x$  and  $\mathbf{u}_z$  are equal to  $[\mathbf{1}^T \mathbf{0}^T \mathbf{0}^T]^T$  and  $[\mathbf{0}^T \mathbf{1}^T \mathbf{0}^T]^T$ , respectively, where  $\mathbf{1}$  and  $\mathbf{0}$  are  $N \times 1$  column vectors with all elements equal to one and zero, respectively. The  $\mathbf{m}_x$ ,  $\mathbf{m}_z$  and  $\mathbf{I}_0$  are the  $N \times N$  X-directional mass matrix, Z-directional mass matrix and the

mass moment of inertia matrix, respectively. The vector  $\mathbf{s}_{xn}$  and  $\mathbf{s}_{zn}$  are the  $n$ -th modal inertia force distribution in X- and Z-direction, respectively, equal to

$$\mathbf{s}_{xn} = \Gamma_{xn} \mathbf{M} \boldsymbol{\varphi}_n, \quad \mathbf{s}_{zn} = \Gamma_{zn} \mathbf{M} \boldsymbol{\varphi}_n \quad (3)$$

The  $\Gamma_{xn}$  and  $\Gamma_{zn}$  are the  $n$ -th modal participating factor in X- and Z-direction, respectively, equal to

$$\Gamma_{xn} = \frac{\boldsymbol{\varphi}_n^T \mathbf{M} \mathbf{u}_x}{\boldsymbol{\varphi}_n^T \mathbf{M} \boldsymbol{\varphi}_n}, \quad \Gamma_{zn} = \frac{\boldsymbol{\varphi}_n^T \mathbf{M} \mathbf{u}_z}{\boldsymbol{\varphi}_n^T \mathbf{M} \boldsymbol{\varphi}_n} \quad (4)$$

In an elastic state, the displacement vector,  $\mathbf{u}$ , can be assembled by the modal coordinate,  $D_n$ , as follows:

$$\mathbf{u}(t) = \sum_{n=1}^{3N} \mathbf{u}_n(t) = \sum_{n=1}^{3N} \boldsymbol{\varphi}_n D_n(t) \quad (5)$$

where  $\mathbf{u}_n$  is the  $n$ -th modal displacement response equal to  $\boldsymbol{\varphi}_n D_n$ . Since  $\Gamma_{xn}$  and  $\Gamma_{zn}$  are usually unequal to each other, they can not be eliminated on both sides of Equation (1) by using accustomed definition,  $\mathbf{u}_n = \boldsymbol{\varphi}_n Y_n = \boldsymbol{\varphi}_n \Gamma_n D_n$ . Therefore, the modal participating factors are included into  $D_n$  as shown in Equation (5). Equation (1) can be decomposed into  $3N$  equations, each equation representing a SDOF modal equation of motion, as follows:

$$\ddot{D}_n + 2\xi_n \omega_n \dot{D}_n + \omega_n^2 D_n = -\Gamma_{xn} \ddot{u}_{gx}(t) - \Gamma_{zn} \ddot{u}_{gz}(t), \quad n = 1 \sim 3N \quad (6)$$

Comparing Equation (6) with Equation (1), the  $n$ -th modal inertia force distribution,  $\mathbf{s}_n$ , is redefined as:

$$\mathbf{s}_n = \mathbf{M} \boldsymbol{\varphi}_n \quad (7)$$

With the definition of  $\mathbf{u}_n$  shown in Equation (5), Equation (6) shows that the  $n$ -th vibration mode is excited by the synthetic ground motion (SGM),  $\Gamma_{xn} \ddot{u}_{gx}(t) + \Gamma_{zn} \ddot{u}_{gz}(t)$ . Thus, the bi-directional ground accelerations can be simultaneously incorporated into the SGM for the modal response history analysis. Chopra and Goel (2004) assumed that only the  $n$ -th modal displacement response  $\mathbf{u}_n$  of inelastic MDOF structures is excited under the exertion of the  $n$ -th modal inertia force distribution  $\mathbf{s}_n$ . Hence,

$$\mathbf{u}_n(t) = \sum_{r=1}^{3N} \boldsymbol{\varphi}_r D_r(t) \approx \boldsymbol{\varphi}_n D_n(t) \quad (8)$$

This approximation is reasonable only because the excitation is the  $n$ -th mode contribution to the total excitation  $\mathbf{p}_{eff}(t)$ . It would not be valid for an excitation with lateral

force distribution different from  $\mathbf{s}_n$ . In other words, it expects that the  $n$ -th vibration mode shall be dominant even for inelastic systems. Therefore, even for structures deformed into an inelastic state, Equation (1) can still be decomposed into modal equations of motion:

$$\ddot{D}_n + 2\xi_n \omega_n \dot{D}_n + F_n = -\Gamma_{xn} \ddot{u}_{gx}(t) - \Gamma_{zn} \ddot{u}_{gz}(t), \quad n = 1 \sim 3N \quad (9)$$

where  $F_n$  is the  $n$ -th modal restoring force. The pushover analysis using the  $n$ -th modal inertia force distribution  $\mathbf{s}_n$  applied to the original MDOF building is carried out. By converting the relationship of roof translation and base shear into acceleration-displacement response spectra (ADRS) format, the relationship of force  $F_n$  and deformation  $D_n$  is determined. The modal response history  $D_n(t)$  is obtained by using step-by-step integration of Equation (9). The total displacement history  $\mathbf{u}(t)$  are obtained by using Equation (5), which is exactly accurate only for linearly elastic systems.

There are very few simplified methods for the seismic analysis of two-way asymmetric-plan buildings under simultaneous action of two horizontal components of ground motion. The bi-directional seismic ground motion considered in this study is more realistic than the single direction excitations. In order to simultaneously consider the two components of the ground motion, the SGM,  $\Gamma_{xn} \ddot{u}_{gx}(t) + \Gamma_{zn} \ddot{u}_{gz}(t)$ , for the  $n$ -th vibration mode is developed. Thus, the UMRHA method has been successfully extended to the two-way asymmetric-plan buildings subjected to two horizontal components of ground motion.

It is obvious that if a modal system acquires more rational modal force-deformation relationships, it would improve the accuracy of the analytical results obtained by using UMRHA. For two-way asymmetric buildings, each pushover analysis with the  $n$ -th modal inertia force distribution results in three pushover curves corresponding to the two lateral directions, X and Z, and one rotational direction, Y. It would be natural to use one of the translational, X (or Z), pushover curves to represent the SDOF modal system in which the X (or Z) component of displacements is dominant [Chopra and Goel 2004]. However, the dominant component of motion may be changed when the building system becomes inelastic. In addition, if the dominant motion of the vibration mode is rotation, then considering lateral motion, either X or Z, seems to be not reasonable. In order to solve the stated issue, the 3DOF modal system simultaneously simulating the stated three pushover curves is developed in the following sections of this study.

### **Bifurcating Characteristics of Pushover Curves for Asymmetric-Plan Structures**

In this study, the asymmetric-plan building systems asymmetric about both plan axes and subjected to bi-directional seismic ground motions are considered. The direction of gravity is opposite to the direction of the Y-axis. When the asymmetric-plan building system is pushed by the  $n$ -th modal inertial force distribution,  $\mathbf{s}_n$ , there are three pushover curves available. The three pushover curves represent the relationships of two base shears versus two roof translations at center of mass (CM) and base torque versus roof rotation. Let

$$D_{xn} = \frac{u_{xn,r}}{\phi_{xn,r}}, \quad D_{zn} = \frac{u_{zn,r}}{\phi_{zn,r}}, \quad D_{\theta n} = \frac{u_{\theta n,r}}{\phi_{\theta n,r}} \quad (10)$$

where subscript  $r$  stands for the roof component of displacement vector or mode shape in a specific direction ( $x$ ,  $z$  or  $\theta$ ) and subscript  $n$  stands for the  $n$ -th vibration mode. With Equation (10), the  $n$ -th modal displacement response can be defined as follows:

$$\mathbf{u}_n(t) = \begin{bmatrix} \boldsymbol{\varphi}_{xn} D_{xn}(t) \\ \boldsymbol{\varphi}_{zn} D_{zn}(t) \\ \boldsymbol{\varphi}_{\theta n} D_{\theta n}(t) \end{bmatrix}_{3N \times 1} = \begin{bmatrix} \boldsymbol{\varphi}_{xn} & \mathbf{0} & \mathbf{0} \\ \mathbf{0} & \boldsymbol{\varphi}_{zn} & \mathbf{0} \\ \mathbf{0} & \mathbf{0} & \boldsymbol{\varphi}_{\theta n} \end{bmatrix}_{3N \times 3} \begin{bmatrix} D_{xn}(t) \\ D_{zn}(t) \\ D_{\theta n}(t) \end{bmatrix}_{3 \times 1} \quad (11)$$

where  $D_{xn}$ ,  $D_{zn}$  and  $D_{\theta n}$  are called the  $n$ -th modal translations and modal rotation, respectively. Due to  $D_{xn}=D_{zn}=D_{\theta n}=D_n$  for proportionally-damped elastic systems, Equation (11) is equal to  $\mathbf{u}_n(t)=\boldsymbol{\varphi}_n D_n(t)$ , which is shown in Equation (5). The typical relationship of  $D_{xn}$ ,  $D_{zn}$  and  $D_{\theta n}$  for an asymmetric-plan building pushed by using the  $n$ -th modal inertia force distribution is depicted in Figure 1(a). The thick line shown in Figure 1(a) represents the real relationship of  $D_{xn}$ ,  $D_{zn}$  and  $D_{\theta n}$ , which deviates from the thin line representing  $D_{xn}=D_{zn}=D_{\theta n}$ . Because the translational and rotational deformations are not proportional in an inelastic state,  $D_{xn}$ ,  $D_{zn}$  and  $D_{\theta n}$  are no longer equal to each other when the  $n$ -th “vibration mode” of the original building system becomes inelastic. This clearly suggests that the conventional SDOF modal systems are not able to simultaneously represent the three inelastic modal responses,  $D_{xn}$ ,  $D_{zn}$  and  $D_{\theta n}$ , of asymmetric-plan structures. It can be further inferred that the seismic demands of asymmetric-plan buildings estimated by using the conventional SDOF modal systems lack the consideration of translation-rotation interaction. Thus, it is necessary to develop a new type of modal systems whose force-deformation relationships are able to simultaneously represent the stated three modal behaviors of the original asymmetric-plan system. The base torque,  $T_{bn}$ , induced by the modal inertia force distribution  $\mathbf{s}_n$  applied to the original building structure is

$$\begin{aligned} T_{bn} &= \sum_{i=1}^N T_{in} = \sum_{i=2N+1}^{3N} \sum_{j=1}^{3N} k_{ij} u_{n,j} = \sum_{i=1}^N \begin{bmatrix} \mathbf{k}_{\alpha x} & \mathbf{k}_{\alpha z} & \mathbf{k}_{\alpha \theta} \\ \mathbf{k}_{\beta x} & \mathbf{k}_{\beta z} & \mathbf{k}_{\beta \theta} \\ \mathbf{k}_{\gamma x} & \mathbf{k}_{\gamma z} & \mathbf{k}_{\gamma \theta} \end{bmatrix}_i \begin{bmatrix} \boldsymbol{\varphi}_{xn} D_{xn} \\ \boldsymbol{\varphi}_{zn} D_{zn} \\ \boldsymbol{\varphi}_{\theta n} D_{\theta n} \end{bmatrix} = \sum_{i=1}^N \omega_{\theta n}^2 I_{0i} \phi_{\theta ni} D_{\theta n} \\ &= \sum_{i=1}^N I_{0i} \phi_{\theta ni} A_{\theta n} = \left( \boldsymbol{\varphi}_n^T \mathbf{M} \begin{bmatrix} \mathbf{0} \\ \mathbf{0} \\ \mathbf{1} \end{bmatrix} \right) A_{\theta n} = \frac{\boldsymbol{\varphi}_n^T \mathbf{M} \begin{bmatrix} \mathbf{0} \\ \mathbf{0} \\ \mathbf{1} \end{bmatrix}}{\boldsymbol{\varphi}_n^T \mathbf{M} \boldsymbol{\varphi}_n} \boldsymbol{\varphi}_n^T \mathbf{M} \boldsymbol{\varphi}_n A_{\theta n} = \Gamma_{\theta n} M_n A_{\theta n} \end{aligned} \quad (12)$$

where  $T_{in}$  is the  $i$ -th storey torque. Similarly, the two base shears,  $V_{bxn}$  and  $V_{bzn}$ , induced by the  $n$ -th modal inertia force distribution  $\mathbf{s}_n$  applied to the original building structure are

$$V_{bxn} = \Gamma_{xn} M_n A_{xn}, \quad V_{bzn} = \Gamma_{zn} M_n A_{zn} \quad (13)$$

Thus,

$$A_{xn} = \frac{V_{bxn}}{\Gamma_{xn} M_n}, \quad A_{zn} = \frac{V_{bzn}}{\Gamma_{zn} M_n}, \quad A_{\theta n} = \frac{T_{bn}}{\Gamma_{\theta n} M_n} \quad (14)$$

where

$$\begin{aligned} \Gamma_{xn} &= \frac{\boldsymbol{\varphi}_n^T \mathbf{M} \mathbf{u}_x}{\boldsymbol{\varphi}_n^T \mathbf{M} \boldsymbol{\varphi}_n}, \quad \Gamma_{zn} = \frac{\boldsymbol{\varphi}_n^T \mathbf{M} \mathbf{u}_z}{\boldsymbol{\varphi}_n^T \mathbf{M} \boldsymbol{\varphi}_n}, \quad \Gamma_{\theta n} = \frac{\boldsymbol{\varphi}_n^T \mathbf{M} \mathbf{u}_\theta}{\boldsymbol{\varphi}_n^T \mathbf{M} \boldsymbol{\varphi}_n} \\ A_{xn} &= \omega_{xn}^2 D_{xn}, \quad A_{zn} = \omega_{zn}^2 D_{zn}, \quad A_{\theta n} = \omega_{\theta n}^2 D_{\theta n} \\ M_n &= \boldsymbol{\varphi}_n^T \mathbf{M} \boldsymbol{\varphi}_n, \quad \mathbf{u}_\theta = [\mathbf{0}^T \quad \mathbf{0}^T \quad \mathbf{1}^T]^T \end{aligned} \quad (15)$$

On the other hand, in the pushover procedure wherein the inertia force distribution is gradually increased to  $\lambda \mathbf{s}_n$ ,  $\lambda$  being a scaling factor, until the target displacement at a specified degree of freedom is reached. Hence, the base shears and base torque of the original MDOF building subjected to force  $\lambda \mathbf{s}_n$  are

$$V_{bxn} = [\mathbf{1}^T \quad \mathbf{0}^T \quad \mathbf{0}^T] \lambda \mathbf{s}_n = [\mathbf{1}^T \quad \mathbf{0}^T \quad \mathbf{0}^T] \lambda \mathbf{M} \boldsymbol{\varphi}_n = \lambda \mathbf{1}^T \mathbf{m}_x \boldsymbol{\varphi}_{xn} \quad (16)$$

$$V_{bzn} = [\mathbf{0}^T \quad \mathbf{1}^T \quad \mathbf{0}^T] \lambda \mathbf{s}_n = [\mathbf{0}^T \quad \mathbf{1}^T \quad \mathbf{0}^T] \lambda \mathbf{M} \boldsymbol{\varphi}_n = \lambda \mathbf{1}^T \mathbf{m}_z \boldsymbol{\varphi}_{zn} \quad (17)$$

$$T_{bn} = [\mathbf{0}^T \quad \mathbf{0}^T \quad \mathbf{1}^T] \lambda \mathbf{s}_n = [\mathbf{0}^T \quad \mathbf{0}^T \quad \mathbf{1}^T] \lambda \mathbf{M} \boldsymbol{\varphi}_n = \lambda \mathbf{1}^T \mathbf{I}_\theta \boldsymbol{\varphi}_{\theta n} \quad (18)$$

Substituting Equations (16) to (18) into Equation (14), it can be found that  $A_{xn} = A_{zn} = A_{\theta n} = \lambda$ . Let  $A_{xn} = A_{zn} = A_{\theta n} = A_n$ . Consequently, the relationships of two base shears versus roof translations and base torque versus roof rotation for asymmetric-plan buildings subjected to the  $n$ -th modal inertia force distribution shall be represented by three curves. By using Equations (10) and (14), the stated three curves in ADRS format are  $A_n$  versus  $D_{xn}$ ,  $A_n$  versus  $D_{zn}$  and  $A_n$  versus  $D_{\theta n}$ .

### Elastic Properties of 3DOF Modal Systems

A simple 3DOF structure with an eccentrically located lumped mass is depicted in Figure 1(b). The force-deformation relationships of this simple 3DOF structure are expected to represent those of the  $n$ -th vibration mode of a two-way asymmetric-plan MDOF building system. Thus, this simple 3DOF structure is called as the  $n$ -th 3DOF modal system in this study. The beam of the 3DOF modal system is rigid, the length projected on X-Y plane and Z-Y plane are equal to  $e_x$  and  $e_z$ , respectively. The beam is connected to the column by a Y-directional rotational spring whose stiffness is equal to  $k_\theta$ . The column of the 3DOF modal

system is rigid, the length equal to one and connected with the ground by two rotational springs. The stiffness of these two rotational springs at the column base are  $k_x$  and  $k_z$ . The rotational spring with stiffness  $k_z$  is in alignment with the X-axis. There is an angle  $\beta$  between the Z-axis and the other rotational spring with stiffness  $k_x$ . Since the stiffness sub-matrices  $\mathbf{k}_{xz}$  and  $\mathbf{k}_{zx}$  shown in Equation (2) are not necessarily equal to  $\mathbf{0}$ , the purpose of the stated angle  $\beta$  is to correlate the X- and Z-translational displacements with the Z- and X-axial shear forces, respectively. It is shown in the following derivation that the angle  $\beta$  would be equal to zero, i.e. the direction of the rotational spring with stiffness  $k_x$  would be in alignment with the Z-axis, if  $\mathbf{k}_{xz}$  and  $\mathbf{k}_{zx}$  are equal to  $\mathbf{0}$ . The masses,  $m_x$ ,  $m_z$ , and mass moment of inertia,  $I$ , are concentrated at the end of the beam as shown in Figure 1(b). The degrees of freedom of the 3DOF modal system defined at the lumped mass are the X- and Z-translation and Y-rotation, denoted as  $\tilde{D}_x$ ,  $\tilde{D}_z$  and  $\tilde{D}_\theta$ , respectively. The displacement vector, mass matrix and stiffness matrix of the 3DOF modal system are

$$\tilde{\mathbf{D}} = \begin{bmatrix} \tilde{D}_x \\ \tilde{D}_z \\ \tilde{D}_\theta \end{bmatrix}_{3 \times 1}, \quad \tilde{\mathbf{M}} = \begin{bmatrix} m_x & 0 & 0 \\ 0 & m_z & 0 \\ 0 & 0 & I \end{bmatrix}_{3 \times 3} \quad (19)$$

$$\tilde{\mathbf{K}} = \begin{bmatrix} k_x C^2 & & & \text{symm.} \\ k_x SC & & k_z + k_x S^2 & \\ -e_z k_x C^2 + e_x k_x SC & -e_z k_x SC + e_x (k_z + k_x S^2) & k_\theta + e_x^2 k_z + (e_x S - e_z C)^2 k_x & \end{bmatrix}_{3 \times 3} \quad (20)$$

where  $C = \cos\beta$  and  $S = \sin\beta$ . If  $\beta$  is approximate to zero, i.e. the rotational spring with stiffness equal to  $k_x$  almost aligns the Z-axis, the stiffness matrix of the 3DOF modal system is simplified as

$$\tilde{\mathbf{K}} = \begin{bmatrix} k_x & 0 & -e_z k_x \\ 0 & k_z & e_x k_z \\ -e_z k_x & e_x k_z & k_\theta + e_x^2 k_z + e_z^2 k_x \end{bmatrix}_{3 \times 3} \quad (21)$$

The tilt symbols above characters represent the physical quantities belonged to the 3DOF modal system. With Equations (1), (5) and (8), the equation of motion for the original MDOF system subjected to the  $n$ -th modal inertia force distribution  $\mathbf{s}_n$  multiplied by the SGM,  $\Gamma_{xn} \ddot{u}_{gx} + \Gamma_{zn} \ddot{u}_{gz}$ , is

$$\mathbf{M} \ddot{\mathbf{u}}_n + \mathbf{C} \dot{\mathbf{u}}_n + \mathbf{K} \mathbf{u}_n = -(\Gamma_{xn} \ddot{u}_{gx} + \Gamma_{zn} \ddot{u}_{gz}) \mathbf{s}_n = -(\Gamma_{xn} \ddot{u}_{gx} + \Gamma_{zn} \ddot{u}_{gz}) \mathbf{M} \boldsymbol{\phi}_n \quad (22)$$

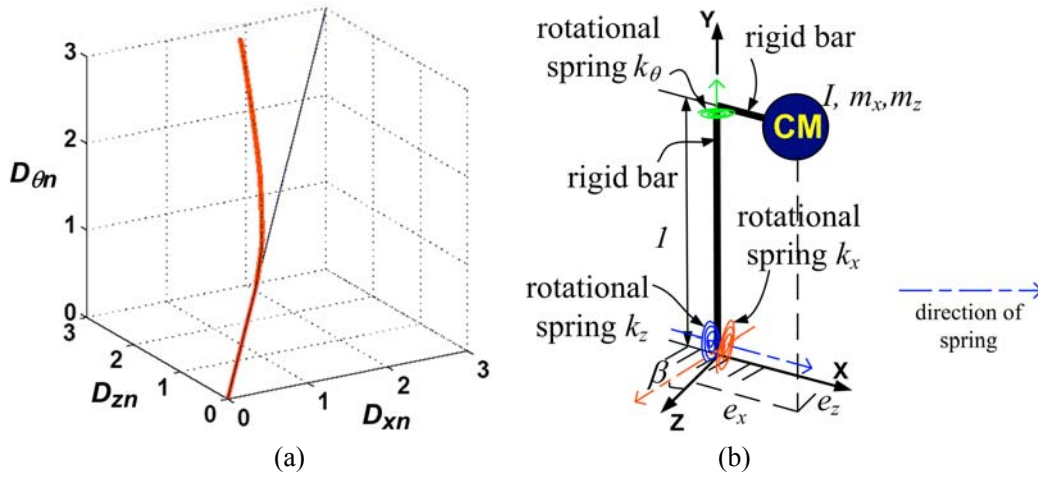


Figure 1. (a) Typical  $D_{xn}$ ,  $D_{zn}$  vs.  $D_{\theta n}$  curve; and (b) the  $n$ -th 3DOF modal system.

Substitute Equation (11) into Equation (22) and pre-multiply both sides of Equation (22)

by  $\begin{bmatrix} \Phi_{xn} & \mathbf{0} & \mathbf{0} \\ \mathbf{0} & \Phi_{zn} & \mathbf{0} \\ \mathbf{0} & \mathbf{0} & \Phi_{\theta n} \end{bmatrix}_{3N \times 3}^T$ . It results in

$$\mathbf{M}_n \ddot{\mathbf{D}}_n + \mathbf{C}_n \dot{\mathbf{D}}_n + \mathbf{K}_n \mathbf{D}_n = -\mathbf{M}_n \mathbf{1} (\Gamma_{xn} \ddot{u}_{gx} + \Gamma_{zn} \ddot{u}_{gz}) \quad (23)$$

where

$$\mathbf{D}_n = \begin{bmatrix} D_{xn} \\ D_{zn} \\ D_{\theta n} \end{bmatrix}_{3 \times 1}, \quad \mathbf{M}_n = \begin{bmatrix} \Phi_{xn}^T \mathbf{m}_x \Phi_{xn} & 0 & 0 \\ 0 & \Phi_{zn}^T \mathbf{m}_z \Phi_{zn} & 0 \\ 0 & 0 & \Phi_{\theta n}^T \mathbf{I}_0 \Phi_{\theta n} \end{bmatrix}_{3 \times 3}, \quad \mathbf{1} = \begin{bmatrix} 1 \\ 1 \\ 1 \end{bmatrix}_{3 \times 3} \quad (24)$$

$$\mathbf{C}_n = \begin{bmatrix} \Phi_{xn}^T \mathbf{c}_{xx} \Phi_{xn} & \Phi_{xn}^T \mathbf{c}_{xz} \Phi_{zn} & \Phi_{xn}^T \mathbf{c}_{x\theta} \Phi_{\theta n} \\ \Phi_{zn}^T \mathbf{c}_{zx} \Phi_{xn} & \Phi_{zn}^T \mathbf{c}_{zz} \Phi_{zn} & \Phi_{zn}^T \mathbf{c}_{z\theta} \Phi_{\theta n} \\ \Phi_{\theta n}^T \mathbf{c}_{\theta x} \Phi_{xn} & \Phi_{\theta n}^T \mathbf{c}_{\theta z} \Phi_{zn} & \Phi_{\theta n}^T \mathbf{c}_{\theta\theta} \Phi_{\theta n} \end{bmatrix}_{3 \times 3}, \quad \mathbf{K}_n = \begin{bmatrix} \Phi_{xn}^T \mathbf{k}_{xx} \Phi_{xn} & \Phi_{xn}^T \mathbf{k}_{xz} \Phi_{zn} & \Phi_{xn}^T \mathbf{k}_{x\theta} \Phi_{\theta n} \\ \Phi_{zn}^T \mathbf{k}_{zx} \Phi_{xn} & \Phi_{zn}^T \mathbf{k}_{zz} \Phi_{zn} & \Phi_{zn}^T \mathbf{k}_{z\theta} \Phi_{\theta n} \\ \Phi_{\theta n}^T \mathbf{k}_{\theta x} \Phi_{xn} & \Phi_{\theta n}^T \mathbf{k}_{\theta z} \Phi_{zn} & \Phi_{\theta n}^T \mathbf{k}_{\theta\theta} \Phi_{\theta n} \end{bmatrix}_{3 \times 3}$$

Equation (23) is a set of three coupled equations of motion denoted as the 3DOF modal equation of motion. Comparing Equations (19) and (20) with Equation (24) correspondingly, let

$$\tilde{\mathbf{D}} = \mathbf{D}_n, \quad \tilde{\mathbf{M}} = \mathbf{M}_n, \quad \tilde{\mathbf{K}} = \mathbf{K}_n \quad (25)$$

Thus, the elastic properties of the  $n$ -th 3DOF modal system can be completely determined as follows:

$$\begin{aligned}
 m_x &= \boldsymbol{\varphi}_{xn}^T \mathbf{m}_x \boldsymbol{\varphi}_{xn}, \quad m_z = \boldsymbol{\varphi}_{zn}^T \mathbf{m}_z \boldsymbol{\varphi}_{zn}, \quad I = \boldsymbol{\varphi}_{\theta n}^T \mathbf{I}_0 \boldsymbol{\varphi}_{\theta n} \\
 \beta &= \tan^{-1} \left( \frac{\boldsymbol{\varphi}_{zn}^T \mathbf{k}_{zx} \boldsymbol{\varphi}_{xn}}{\boldsymbol{\varphi}_{xn}^T \mathbf{k}_{xx} \boldsymbol{\varphi}_{xn}} \right), \quad k_x = \frac{\boldsymbol{\varphi}_{xn}^T \mathbf{k}_{xx} \boldsymbol{\varphi}_{xn}}{C^2}, \quad k_z = \boldsymbol{\varphi}_{zn}^T \mathbf{k}_{zz} \boldsymbol{\varphi}_{zn} - k_x S^2 \\
 \begin{bmatrix} e_x \\ e_z \end{bmatrix} &= \begin{bmatrix} k_x SC & -k_x C^2 \\ k_z + k_x S^2 & -k_x SC \end{bmatrix}^{-1} \begin{bmatrix} \boldsymbol{\varphi}_{xn}^T \mathbf{k}_{x\theta} \boldsymbol{\varphi}_{\theta n} \\ \boldsymbol{\varphi}_{zn}^T \mathbf{k}_{z\theta} \boldsymbol{\varphi}_{\theta n} \end{bmatrix}, \quad k_\theta = \boldsymbol{\varphi}_{\theta n}^T \mathbf{k}_{\theta\theta} \boldsymbol{\varphi}_{\theta n} - e_x^2 k_z - (e_x S - e_z C)^2 k_x
 \end{aligned} \tag{26}$$

Equation (26) shows that the angle  $\beta$  is resulted from the stiffness sub-matrix  $\mathbf{k}_{zx}$ . In general, when the principal axes of all columns are arranged in alignment with the global axes, the elements of sub-matrix  $\mathbf{k}_{zx}$  will be small compared with other elements of the stiffness matrix  $\mathbf{K}$ . Hence, it shows that the value of angle  $\beta$  will be small in most cases. If  $\beta$  is approximate to zero, the stiffness of rotational springs and eccentricities shown in Equation (26) could be further simplified as

$$\begin{aligned}
 k_x &= \boldsymbol{\varphi}_{xn}^T \mathbf{k}_{xx} \boldsymbol{\varphi}_{xn}, \quad k_z = \boldsymbol{\varphi}_{zn}^T \mathbf{k}_{zz} \boldsymbol{\varphi}_{zn}, \quad k_\theta = \boldsymbol{\varphi}_{\theta n}^T \mathbf{k}_{\theta\theta} \boldsymbol{\varphi}_{\theta n} - \frac{(\boldsymbol{\varphi}_{zn}^T \mathbf{k}_{z\theta} \boldsymbol{\varphi}_{\theta n})^2}{\boldsymbol{\varphi}_{zn}^T \mathbf{k}_{zz} \boldsymbol{\varphi}_{zn}} - \frac{(\boldsymbol{\varphi}_{xn}^T \mathbf{k}_{x\theta} \boldsymbol{\varphi}_{\theta n})^2}{\boldsymbol{\varphi}_{xn}^T \mathbf{k}_{xx} \boldsymbol{\varphi}_{xn}} \\
 e_x &= \frac{\boldsymbol{\varphi}_{zn}^T \mathbf{k}_{z\theta} \boldsymbol{\varphi}_{\theta n}}{\boldsymbol{\varphi}_{zn}^T \mathbf{k}_{zz} \boldsymbol{\varphi}_{zn}}, \quad e_z = \frac{-\boldsymbol{\varphi}_{xn}^T \mathbf{k}_{x\theta} \boldsymbol{\varphi}_{\theta n}}{\boldsymbol{\varphi}_{xn}^T \mathbf{k}_{xx} \boldsymbol{\varphi}_{xn}}
 \end{aligned} \tag{27}$$

It should be noted that the influence vector shown in Equation (24) indicates that the synthetic ground acceleration is simultaneously applied to the three degrees of freedom of the 3DOF modal system. One of the key points for constructing the 3DOF modal system lies in finding the angle  $\beta$ . The angle  $\beta$  takes the coupling term of the  $3 \times 3$  modal stiffness matrix, i.e.  $\boldsymbol{\varphi}_{xn}^T \mathbf{k}_{zx} \boldsymbol{\varphi}_{zn}$ , into account. When the stated angle equals to zero degree, it implies that there is no coupling in the two modal translations.

The equation of motion for the original MDOF building system describes the motion at the CM on each floor. The translational motion at the CM for an asymmetric-plan building consists of two parts. One is the translation at the center of rigidity (CR) and the other one is the rotation of the rigid floor diaphragm. The 3DOF modal system corresponding to the 3DOF modal equation of motion explicitly considers the rotational motion contributing to the total translations at the lumped mass of the modal system. In the appendix, it proves that one of the three vibration modes of the 3DOF modal system, denoted as active sub-mode, is identical to the vibration mode of the SDOF modal system and the other two, denoted as spurious sub-modes, are trivial, i.e. no contribution to the dynamic response of the elastic 3DOF modal system. Thus, the 3DOF modal system does not violate the fundamental principle of structural dynamics.

### Inelastic Properties of 3DOF Modal Systems

In an inelastic state, Equation (23) becomes

$$\mathbf{M}_n \ddot{\mathbf{D}}_n + \mathbf{C}_n \dot{\mathbf{D}}_n + \mathbf{R}_n = -\mathbf{M}_n \mathbf{1} (\Gamma_{xn} \ddot{u}_{gx} + \Gamma_{zn} \ddot{u}_{gz}) \quad (28)$$

where the restoring force,  $\mathbf{R}_n$ , is a  $3 \times 1$  column vector. By idealizing the three  $n$ -th modal pushover curves of the original MDOF system as three bi-linear curves, the corresponding three post-yielding stiffness ratios ( $\alpha_x$ ,  $\alpha_z$  and  $\alpha_\theta$ ) and three yielding forces ( $A_{xny}$ ,  $A_{zny}$  and  $A_{\theta ny}$ ) can be obtained. The six unknown inelastic parameters of the three bi-linear rotational springs used in the 3DOF modal system are determined accordingly. These six unknown parameters include the post-yielding stiffness of the rotational springs,  $k'_x$ ,  $k'_z$  and  $k'_\theta$ , and the yielding moments of the rotational springs,  $M_{yx}$  and  $M_{yz}$  and  $M_{y\theta}$ .

From the derivation shown in the appendix, the mode shape of the active sub-mode,  $\tilde{\boldsymbol{\Phi}}_a$ , is equal to  $[1 \ 1 \ 1]^T$ . Thus, the modal inertia force distribution of the active sub-mode,  $\mathbf{s}_a$ , is

$$\mathbf{s}_a = \tilde{\mathbf{M}} \tilde{\boldsymbol{\Phi}}_a = \begin{bmatrix} m_x \\ m_z \\ I \end{bmatrix}_{3 \times 1} \quad (29)$$

The displacements and forces of the 3DOF modal system subjected to  $\mathbf{s}_a$  presented in ADRS format are

$$\begin{aligned} \frac{\tilde{D}_x}{\tilde{\boldsymbol{\Phi}}_{ax}} &= \tilde{D}_x, & \frac{\tilde{D}_z}{\tilde{\boldsymbol{\Phi}}_{az}} &= \tilde{D}_z, & \frac{\tilde{D}_\theta}{\tilde{\boldsymbol{\Phi}}_{a\theta}} &= \tilde{D}_\theta \\ \frac{\tilde{V}_x}{\tilde{\boldsymbol{\Phi}}_{ax} m_x} &= \frac{\tilde{V}_z}{\tilde{\boldsymbol{\Phi}}_{az} m_z} = \frac{\tilde{T}}{\tilde{\boldsymbol{\Phi}}_{a\theta} I} = \frac{\tilde{V}_x}{m_x} = \frac{\tilde{V}_z}{m_z} = \frac{\tilde{T}}{I} = \tilde{A} \end{aligned} \quad (30)$$

where  $\tilde{V}_x$ ,  $\tilde{V}_z$  and  $\tilde{T}$  are the base shears and base torque of the 3DOF modal system subjected to  $\mathbf{s}_a$ . It should be noted that the base torque  $\tilde{T}$  is calculated on the projection point of the lumped mass on the X-Z plane. When all the rotational springs are elastic, the incremental displacements of the 3DOF modal system subjected to incremental  $\mathbf{s}_a$  are

$$\begin{bmatrix} \Delta \tilde{D}_x \\ \Delta \tilde{D}_z \\ \Delta \tilde{D}_\theta \end{bmatrix}_{3 \times 1} = \tilde{\mathbf{K}}^{-1} \Delta \mathbf{s}_a \quad (31)$$



The concept of “vibration mode” originated from elastic systems is only an approximation for inelastic systems. This so-called vibration mode of inelastic systems is time-variant which could change from time to time during the inelastic vibration. The “modal” response history analysis of inelastic systems is only an approximation approach. There are three pushover curves simultaneously available for each inelastic “vibration mode” of an asymmetric-plan building. The bifurcation of each “modal” pushover curves in an inelastic state is due to the non-proportional deformations of roof translations and roof rotation. The 3DOF modal system explicitly presenting rotational motion is able to simultaneously simulate the noted three pushover curves. It is natural and reasonable to have the 3DOF modal system represent the inelastic “vibration mode” of a two-way asymmetric-plan building in which three bifurcated pushover curves exist. There would be a dilemma encountered in choosing only one of the stated three pushover curves to represent the “vibration mode” of inelastic asymmetric-plan systems, especially when the vibration mode is rotational dominant or highly coupled in the three directions. The proposed 3DOF modal system is able to avoid the mentioned dilemma and realistically takes the translation-rotation interaction into consideration.

### Characteristics of the Damping Matrix for 3DOF Modal Systems

The modal damping matrix,  $\mathbf{C}_n$ , given in Equation (24) is equal to

$$\mathbf{C}_n = \begin{bmatrix} \boldsymbol{\varphi}_{xn} & \mathbf{0} & \mathbf{0} \\ \mathbf{0} & \boldsymbol{\varphi}_{zn} & \mathbf{0} \\ \mathbf{0} & \mathbf{0} & \boldsymbol{\varphi}_{\theta n} \end{bmatrix}^T \mathbf{C} \begin{bmatrix} \boldsymbol{\varphi}_{xn} & \mathbf{0} & \mathbf{0} \\ \mathbf{0} & \boldsymbol{\varphi}_{zn} & \mathbf{0} \\ \mathbf{0} & \mathbf{0} & \boldsymbol{\varphi}_{\theta n} \end{bmatrix} \quad (38)$$

If the original MDOF building is a proportionally damped system, i.e.

$$\mathbf{C} = \begin{bmatrix} \mathbf{c}_{xx} & \mathbf{c}_{xz} & \mathbf{c}_{x\theta} \\ \mathbf{c}_{zx} & \mathbf{c}_{zz} & \mathbf{c}_{z\theta} \\ \mathbf{c}_{\theta x} & \mathbf{c}_{\theta z} & \mathbf{c}_{\theta\theta} \end{bmatrix}_{3N \times 3N} = \alpha \mathbf{M} + \beta \mathbf{K} \quad (39)$$

the modal damping matrix would be

$$\mathbf{C}_n = \begin{bmatrix} \boldsymbol{\varphi}_{xn} & \mathbf{0} & \mathbf{0} \\ \mathbf{0} & \boldsymbol{\varphi}_{zn} & \mathbf{0} \\ \mathbf{0} & \mathbf{0} & \boldsymbol{\varphi}_{\theta n} \end{bmatrix}^T_{3N \times 3N} (\alpha \mathbf{M} + \beta \mathbf{K}) \begin{bmatrix} \boldsymbol{\varphi}_{xn} & \mathbf{0} & \mathbf{0} \\ \mathbf{0} & \boldsymbol{\varphi}_{zn} & \mathbf{0} \\ \mathbf{0} & \mathbf{0} & \boldsymbol{\varphi}_{\theta n} \end{bmatrix}_{3N \times 3N} = \alpha \mathbf{M}_n + \beta \mathbf{K}_n \quad (40)$$

Therefore, if the original MDOF building is a non-proportionally damped system, i.e.

$$\mathbf{C} \neq \alpha \mathbf{M} + \beta \mathbf{K} \quad (41)$$

the modal damping matrix would also be non-proportional, i.e.

$$\mathbf{C}_n \neq \alpha \mathbf{M}_n + \beta \mathbf{K}_n \quad (42)$$

It indicates that a non-proportionally damped two-way asymmetric-plan system will result in  $3N$  non-proportionally damped 3DOF modal equations of motion, which are able to take the out-of-phase motions between the modal translations and the modal rotation into account. Thus, the 3DOF modal equations of motion are more appropriate to be used in the modal response history analysis of non-proportionally damped asymmetric-plan structures than the SDOF modal equations of motion. The 3DOF modal equations of motion possess the non-proportionally damped property at the expense of increasing two DOFs in the modal coordinate. The proposed 3DOF modal equations of motion still can be easily computed by commercially available structural analysis programs. On the other hand, the proposed method keeps the clarity and the simplicity of the modal response history analysis in calculating the seismic responses of structures.

## Numerical Validation

There are three numerical examples to verify the proposed methodology. The first example is a proportionally damped three-storey asymmetric-plan building becoming inelastic under seismic excitations. The second and the third examples are a non-proportionally damped one-storey and three-storey asymmetric-plan building, respectively. These two non-proportionally damped buildings with fluid viscous dampers remain elastic under small seismic ground motions.

### Example One— Selected Structural System, Ground Motion and Basic Assumptions

The dimension of the prototype two-way asymmetric three-storey building is 4.5m long, 3m wide and 3@3m tall. Each floor is simulated as a rigid diaphragm. The property of the material is A36 steel. The elastic-hardening materials are applied on all members in the analysis. The member sizes of columns, beams and braces are H200×200×12×12, H200×150×6×9 and 2L90×90×10, respectively. The CM is intentionally placed with large eccentricity with respect to the center of floor plane. The mass and mass moment of inertia of each floor are equal to 9450 kg and 63030 kg·m<sup>2</sup>, respectively. Proportional damping with the damping ratios of the first and second vibration modes equal to 2% are used in the analysis. The building is shown in Figures 2(a) and 2(b). The vibration period and dominant motion for each vibration mode of this asymmetric-plan building are listed in Table 1. The seismic ground motion records considered in this verification are the sine wave with period equal to one second (Figures 2(c) and 2(d)) and the NS and EW components of 1940 El Centro earthquake (Figures 2(e) and 2(f)). The sine wave with peak ground acceleration (PGA) equal to 0.8g and 0.5g applied along the X- and Z-axis, respectively. The NS and EW components of 1940 El Centro earthquake are scaled to PGA equal to 0.8g and 0.49g, respectively, and

applied along the X- and Z-axis, respectively. The analytical results obtained by using proposed method, denoted as 3MA, are compared with benchmark solutions obtained by using nonlinear response history analysis (RHA) of the whole prototype structure. All the analysis were carried out by using PISA3D computer program [Tsai and Lin 2003] which is able to input ground acceleration records in translational as well as rotational directions.

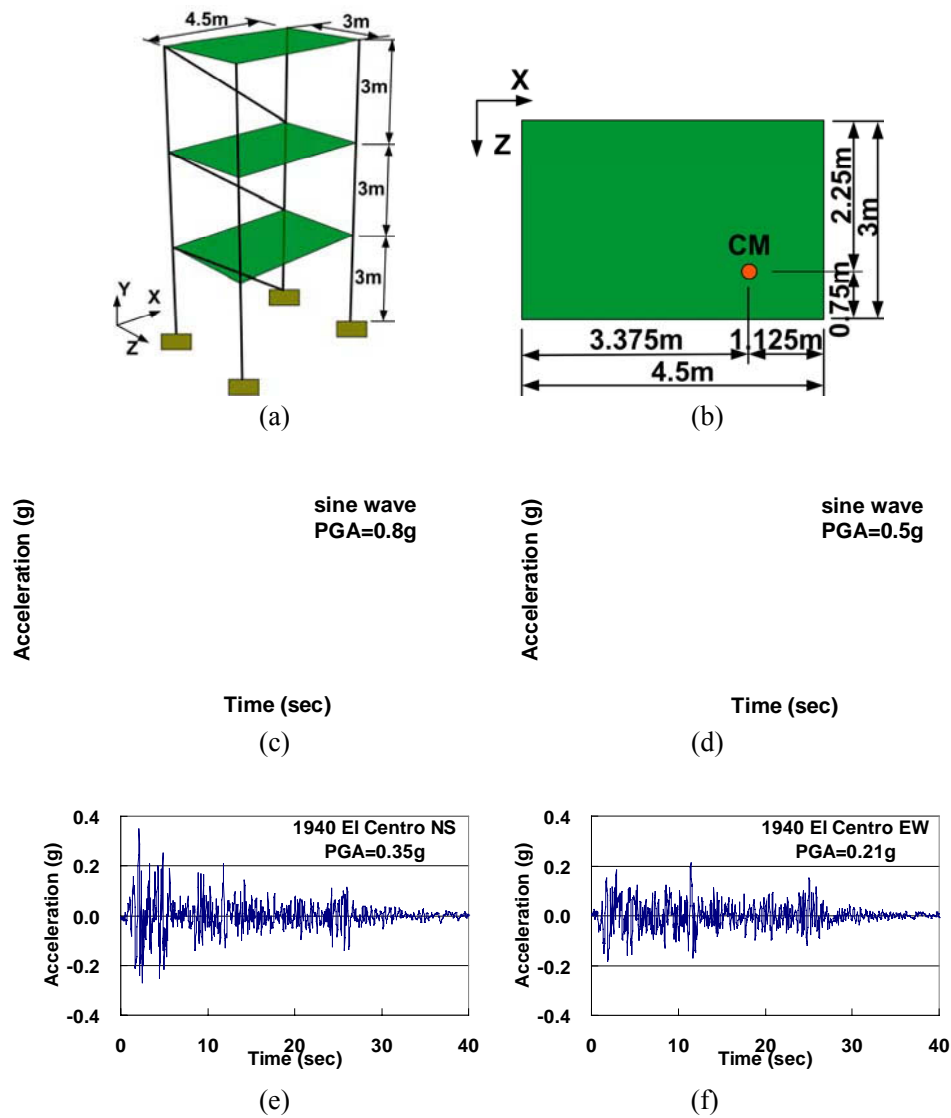


Figure 2. (a) The prototype building; (b) floor plane; (c) sine wave applied in X-direction; (d) sine wave applied in Z-direction; (e) 1940 El Centro earthquake NS component; and (f) 1940 El Centro earthquake EW component.

**Table 1. Properties of each vibration mode of prototype building**

Mode No.	1	2	3	4	5	6	7	8	9	
Period (s)	0.829	0.543	0.246	0.159	0.135	0.127	0.085	0.043	0.027	
$\phi_{x1}$	0.043	0.030	-0.119	-0.082	-0.139	0.054	-0.088	0.173	0.149	
$\phi_{x2}$	0.102	0.071	-0.091	-0.058	0.105	0.148	0.082	0.099	-0.171	
$\phi_{x3}$	0.142	0.100	0.104	0.072	-0.069	0.179	-0.025	-0.132	0.071	
$\phi_{z1}$	-0.043	0.061	0.116	-0.176	0.125	0.021	-0.200	-0.006	-0.006	
$\phi_{z2}$	-0.103	0.151	0.091	-0.143	-0.107	-0.018	0.178	-0.001	0.006	
$\phi_{z3}$	-0.144	0.215	-0.098	0.152	0.041	0.000	-0.068	0.003	-0.002	
$\phi_{\theta1}$	0.019	0.012	-0.052	-0.033	-0.053	-0.028	-0.033	-0.063	-0.054	
$\phi_{\theta2}$	0.044	0.029	-0.040	-0.025	0.058	-0.041	0.029	-0.035	0.062	
$\phi_{\theta3}$	0.061	0.040	0.044	0.026	-0.012	-0.069	-0.014	0.047	-0.025	
Dominant Motion	R	Z	R	Z	X	X	Z	X	X	
$\frac{\Gamma_n^2 M_n}{\sum_{i=1}^9 \Gamma_i^2 M_i}$ (%)	X	25.83	12.79	3.53	1.47	3.34	45.77	0.29	6.25	0.73
	Z	26.32	57.51	3.77	8.81	1.06	0.00	2.53	0.01	0.00
	R	32.33	13.69	4.87	2.31	0.14	39.94	0.67	5.37	0.68

### Summary of Analytical Results for Example One

The step-by-step procedures of the proposed method are summarized for the aforementioned analytical example:

1. Compute the elastic properties of the building, including the vibration periods of mode, the mode shapes and the modal participation masses. The elastic properties of the example building are shown in Table 1. It shows that the accumulation of the modal participation mass up to the 6th vibration mode is over 90% in all three directions. Therefore, only the 1st to the 6th mode will be considered in this analytical example.
2. Apply Equation (4), compute the synthetic ground motions,  $\Gamma_{xn}\ddot{u}_{gx}(t)+\Gamma_{zn}\ddot{u}_{gz}(t)$ , for each vibration mode.
3. Apply Equation (26), compute the elastic properties for each 3DOF modal systems. The properties of 3DOF modal systems for the 1st to the 6th vibration mode are shown in Table 2. The detailed analytical results of the sub-modal properties for each 3DOF modal system are listed in Table 3. The minor numerical errors of the values given in Table 3 are resulted from the analytical round-off error of the rigid column and the rigid beam simulated in the computer model. It is noted in Table 2 that the values of angle  $\beta$  are small since the principal axes of columns are parallel to the X-axis and Z-axis. From Table 3, it is confirmed that the vibration period of the active sub-mode for each 3DOF modal system is equal to that of the corresponding vibration mode of the original building. The mode shapes of the active sub-modes are all equal to  $[1 \ 1 \ 1]^T$ . The modal participation mass,  $\tilde{\Gamma}^2 \tilde{M}$ , of the active and the spurious sub-mode is equal to one and zero, respectively.

**Table 2. Properties of modal systems (1)**

Mode No.	$\beta$ (rad.)	$m_x$	$m_z$	$I$	$k_x$	$k_z$	$k_\theta$	$e_x$	$e_z$
1	0.00448	0.306	0.312	0.382	424.9	34.6	47.5	-0.483	0.961
2	-0.00976	0.151	0.687	0.162	209.1	76.1	20.2	0.212	0.892
3	-0.00014	0.314	0.295	0.390	3912.4	386.0	545.3	-0.501	0.948
4	0.00018	0.144	0.704	0.152	1778.8	920.2	213.1	0.202	0.873
5	-0.00117	0.332	0.271	0.397	9337.7	1239.3	1838.4	-0.522	0.922
6	-0.00039	0.538	0.007	0.455	824.0	29.5	337.3	-0.411	-0.596

**Table 3. Properties of modal systems (2)**

		1st sub-mode	2nd sub-mode	3rd sub-mode
Mode 1	$\tilde{T}$ (s)	0.830	0.542	0.126
	$\tilde{\Phi}^T$	[1.000 1.000 0.998]	[-0.698 1.482 -0.657]	[-1.336 -0.024 1.091]
	$\tilde{\Gamma}^2 \tilde{M}$	0.997	0	0
	Note	active	spurious	spurious
Mode 2	$\tilde{T}$ (s)	0.829	0.542	0.126
	$\tilde{\Phi}^T$	[-1.426 0.676 -1.531]	[0.994 0.999 1.011]	[-1.900 0.015 1.678]
	$\tilde{\Gamma}^2 \tilde{M}$	0	1	0
	Note	spurious	active	spurious
Mode 3	$\tilde{T}$ (s)	0.246	0.159	0.042
	$\tilde{\Phi}^T$	[-1.000 -1.000 -1.000]	[0.677 -1.544 0.624]	[1.312 0.034 -1.083]
	$\tilde{\Gamma}^2 \tilde{M}$	1	0	0
	Note	active	spurious	spurious
Mode 4	$\tilde{T}$ (s)	0.246	0.159	0.042
	$\tilde{\Phi}^T$	[1.477 -0.648 1.602]	[-1.001 -1.000 -1.000]	[1.941 -0.022 -1.734]
	$\tilde{\Gamma}^2 \tilde{M}$	0	1	0
	Note	spurious	active	spurious
Mode 5	$\tilde{T}$ (s)	0.135	0.086	0.028
	$\tilde{\Phi}^T$	[-1.000 -0.999 -1.001]	[0.654 -1.638 0.573]	[-1.260 -0.057 1.091]
	$\tilde{\Gamma}^2 \tilde{M}$	1	0	0
	Note	active	spurious	spurious
Mode 6	$\tilde{T}$ (s)	0.292	0.127	0.096
	$\tilde{\Phi}^T$	[0.926 -0.501 -1.086]	[1.000 0.961 1.000]	[-0.042 11.99 -0.126]
	$\tilde{\Gamma}^2 \tilde{M}$	0	0.999	0
	Note	spurious	active	spurious

4. Apply Equations (10) and (14), compute pushover curves by applying the  $n$ -th modal inertia force distribution  $\mathbf{s}_n$  defined in Equation (7) to the original MDOF building. The components of  $\mathbf{s}_n$  vectors for the first three modes are given in

Table 4. In order to accurately represent the modal force-deformation relationships for each modal system, one-cycle push-pull is used instead of the conventional pushover. The one-cycle push-pull curves for the first three vibration modes are shown in thin lines in Figure 3. It demonstrates that the three hysteretic loops of each vibration mode of the original MDOF building are bifurcated after the vibration mode becomes inelastic.

**Table 4. The components of  $s_n$  vectors for the first three vibration modes**

	$x1$	$x2$	$x3$	$z1$	$z2$	$z3$	$\theta1$	$\theta2$	$\theta3$
$s_1$	-0.403	-0.960	-1.343	0.402	0.969	1.361	-1.167	-2.780	-3.872
$s_2$	0.287	0.675	0.942	0.581	1.426	2.031	0.758	1.809	2.521
$s_3$	1.128	0.857	-0.982	-1.096	-0.860	0.922	3.264	2.521	-2.755

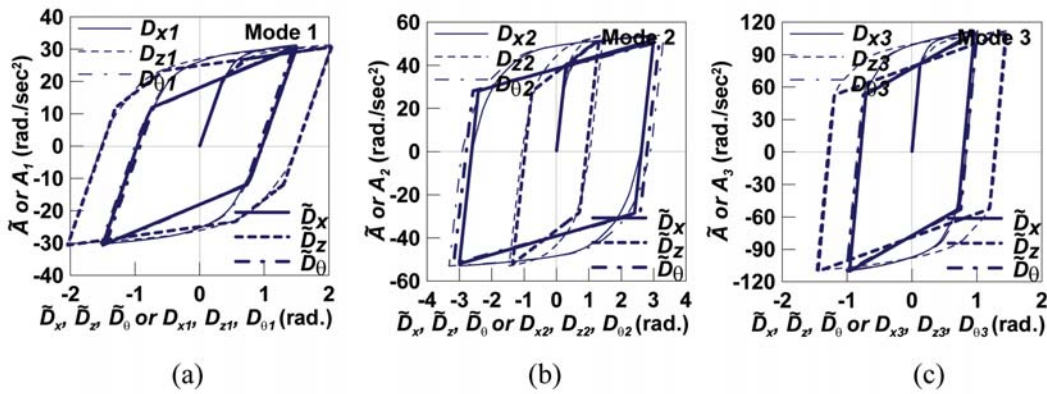


Figure 3. Force and deformation relationships of prototype building and 3DOF modal systems: (a) 1st mode; (b) 2nd mode; and (c) 3rd mode.

- Idealize the pushover curves obtained from step 4 as bilinear curves. Apply Equations (34) to (37), compute the inelastic properties for each 3DOF modal system.
- Apply Equation (30), conduct the one-cycle push-pull analysis by applying  $s_a$  defined in Equation (29) to each 3DOF modal system. Verify the consistency of the one-cycle push-pull curves of the 3DOF modal systems and those of the original building. The one-cycle push-pull curves for the first three 3DOF modal systems are shown in thick lines in Figure 3. It shows that the bifurcating characteristic of each vibration mode can be well simulated by the corresponding 3DOF modal system. Therefore, this confirms that the translation-rotation interaction can be taken into account by using the 3DOF modal systems in dynamic modal analyses.
- Apply Equations (23) and (11), conduct the response history analysis for each 3DOF modal system. In this study, instead of conducting an inelastic response history analysis immediately, an elastic response history analysis is carried out first. This is to illustrate the accuracy of the 3MA for the example building subjected to the low intensity ground accelerations and remained in the elastic

range. The two sine wave ground accelerations shown in Figures 2(c) and 2(d) are both scaled down to  $\text{PGA}=0.01\text{g}$  for the elastic response history analysis. The analytical roof deformations are shown in Figure 4. It confirms that the 3MA is identical to the conventional elastic modal response history analysis. The time history analysis of the 3DOF modal systems subjected to the sine waves ( $\text{PGA}=0.8\text{g}$  and  $0.5\text{g}$ ) and El Centro earthquakes ( $\text{PGA}=0.8\text{g}$  and  $0.49\text{g}$ ) are subsequently carried out (Figure 5). It is evident in Figures 5(a), 5(b), 5(d) and 5(e) that the three curves are no longer identical. It is concluded that the responses of the 1st and 2nd 3DOF modal systems have become inelastic under the noted ground motions. Since the 3rd 3DOF modal system is essentially elastic, the three vibrating components of the modal system, i.e.  $\tilde{D}_x$ ,  $\tilde{D}_z$  and  $\tilde{D}_\theta$ , are equal to each other as evidenced in Figures 5(c) and 5(f). The rest of the modal systems, i.e. the fourth to the sixth vibration mode, all remain elastic (not shown). Therefore, only the force-deformation relationships and responses histories for the 1st to the 3rd vibration modes of the prototype building and the corresponding 3DOF modal systems are shown in Figures 3 and 5.

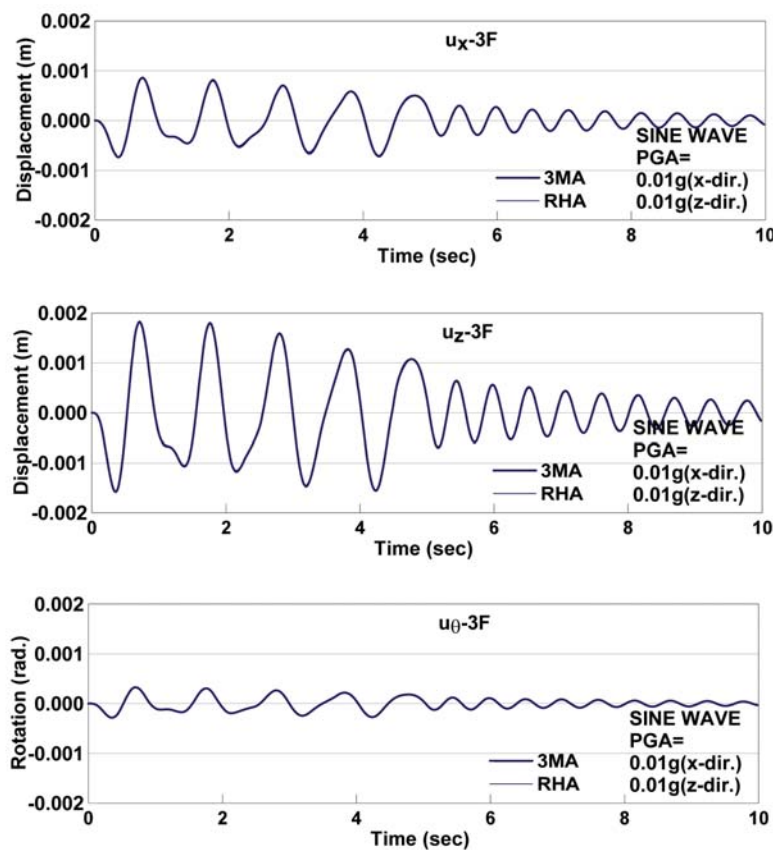


Figure 4. Elastic response histories of prototype building obtained by using 3MA and RHA: (a) roof X-directional translation; (b) roof Z-directional translation; and (c) roof rotation.

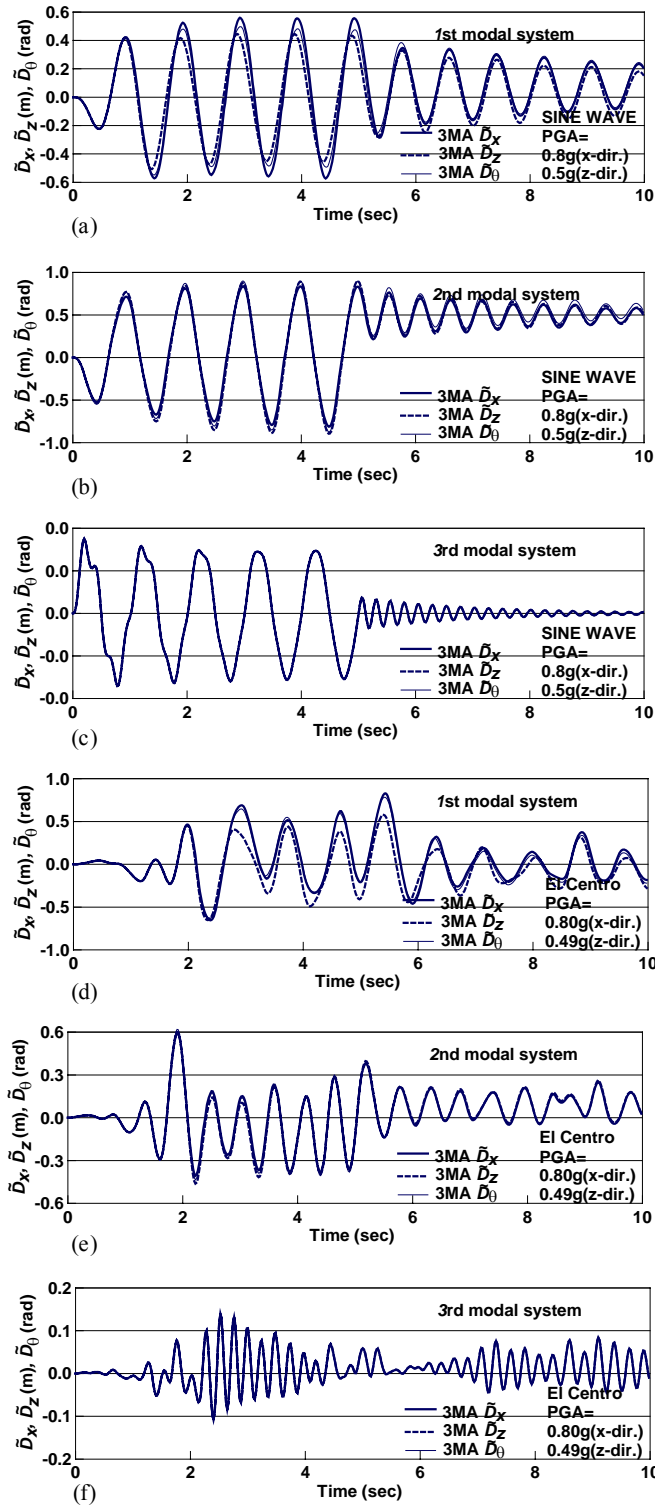


Figure 5. Response time histories of 3DOF modal system: (a) 1st mode; (b) 2nd mode; (c) 3rd mode under sine wave; (d) 1st mode; (e) 2nd mode; and (f) 3rd mode under El Centro earthquake.

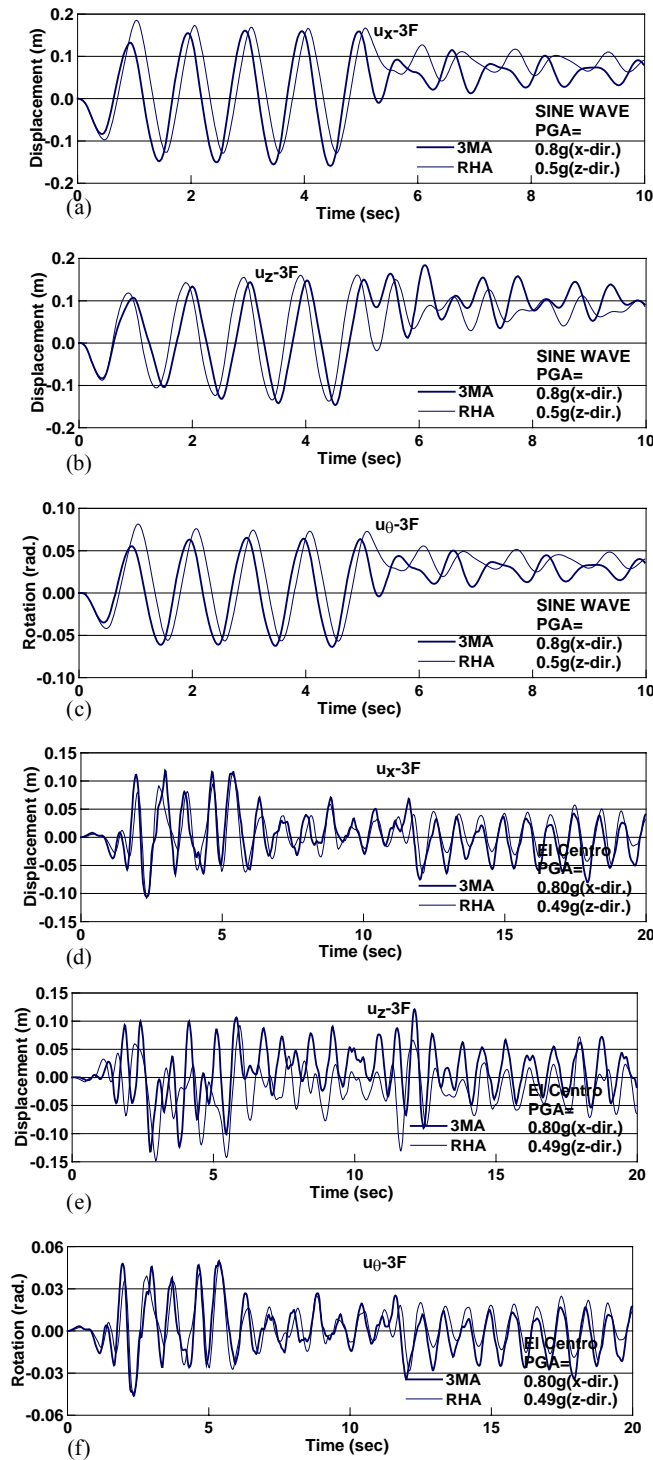


Figure 6. Response time histories of prototype building obtained by 3MA and RHA(a) roof X-directional translation; (b) roof Z-directional translation; (c) roof rotation under sine wave; (d) roof X-directional translation;(e) roof Z-directional translation;(f) roof rotation under El Centro earthquake.

8. Apply Equations (5), the response history of the original MDOF building is obtained using the arithmetic summation of the modal response histories. The translational and rotational displacements at CM on the roof of the original building subjected to the sine waves and El Centro earthquakes obtained by using proposed method compared with benchmark solutions are shown in Figures 6. From Figures 6(a) to 6(f), it is confirmed that the proposed method can satisfactorily estimate the peak responses and residual displacements. Except the response history of Z-directional translation shown in Figure 6(e) is somewhat offset from the benchmark solutions.

The further analysis (not shown in this study) shows that the error of the maximum response is increased as the intensity of the input ground motion increased. The further analysis also shows that the error of the maximum response is increased as the major component of ground motion applied to the weak direction of the building. However, since the frequency contents of earthquakes and the corresponding nonlinear characteristics of the structures (shifting of vibration frequency) could vary from earthquake to earthquake, the effects of the earthquake intensity on the accuracy of the proposed method should be investigated based on the statistics for a set of buildings excited by an ensemble of ground motions. Since uncoupled modal response history analysis appears not limited for the analysis of buildings with irregular elevation or weak-column strong-beam mechanism, the proposed method should have no such restriction either.

### Examples Two and Three— Selected Structural System, Ground Motion and Basic Assumptions

The one-storey and the three-storey asymmetric-plan buildings with viscous dampers shown in Figure 7 are analyzed by three methods including the direct integration of the equation of motion, simple approximation method and the proposed method. The mentioned simple approximation method is the SDOF modal response history analysis by neglecting the off-diagonal elements of the transformed damping matrix. The results obtained by using the direct integration of the equation of motion are regarded as the benchmark solutions in this study. All of the beams and columns of the noted prototype buildings are symmetric making the CR coincident with the geometric center of each floor. The CM is eccentrically located as shown in Figure 7. The left and the upper sides of CR, shown in Figure 7(c), are denoted as the stiff sides. The sides opposite to the stiff sides are denoted as flexible sides. It is seen in this research that the analytical errors resulted from the use of the simple approximation method are great when the center of supplemental damping (CSD) is on the stiff sides of each floor. Thus, the viscous dampers are purposely placed on the stiff sides in order to intensify the demonstration of the accuracy of the analytical results obtained by using the proposed method. According to the investigation of the errors in responses of the one-storey one-way asymmetric-plan buildings [Goel 2001], the errors introduced by simple approximation method are over 20% when the normalized supplemental damping eccentricity,  $\bar{e}_{sd} = e_{sd}/a$ , is equal to -0.5. The values of  $e_{sd}$  and  $a$  represent the distance from CM to CSD and the plane dimension of the building perpendicular to the seismic ground motion, respectively. The CM

is eccentrically located making the values of normalized supplemental damping eccentricities in two horizontal directions both equal to -0.75. Therefore, choosing  $\bar{e}_{sd} = -0.75$  is large enough to verify the effectiveness of the proposed method. The damping coefficients of dampers,  $C_x$  and  $C_z$ , along the X-axis and Z-axis are calculated as:

$$C_x = 2m_x \omega_x \xi_{sdx}, \quad C_z = 2m_z \omega_z \xi_{sdz} \quad (43)$$

where  $\xi_{sdx}$  and  $\xi_{sdz}$  are the supplemental damping ratios along the X- and Z-axis, respectively.  $\omega_x$  and  $\omega_z$  are the circular vibration frequencies of the first X- and Z-translational dominant vibration modes, respectively. The supplemental damping ratios,  $\xi_{sdx}$  and  $\xi_{sdz}$ , used in these two prototype buildings are both equal to 30%. The properties of these two buildings are shown in Table 5 to Table 8. The units used in these tables are  $kN$ ,  $m$  and  $second$ . That is, the units of values shown in those tables are:  $kN \times sec^2/m$  for  $\mathbf{m}_x$  and  $\mathbf{m}_z$ ;  $kN \times sec^2 \times m$  for  $\mathbf{I}_0$ ;  $kN \times sec/m$  for  $\mathbf{c}_{xx}$ ,  $\mathbf{c}_{zz}$  and  $\mathbf{c}_{xz}$ ;  $kN \times sec$  for  $\mathbf{c}_{x\theta}$ ,  $\mathbf{c}_{z\theta}$ ;  $kN \times sec \times m$  for  $\mathbf{c}_{\theta\theta}$ ;  $kN/m$  for  $\mathbf{k}_{xx}$ ,  $\mathbf{k}_{zz}$  and  $\mathbf{k}_{xz}$ ;  $kN$  for  $\mathbf{k}_{x\theta}$ ,  $\mathbf{k}_{z\theta}$ ;  $kN \times m$  for  $\mathbf{k}_{\theta\theta}$ . The  $n$ -th column vector of the matrix  $\Phi$  shown in Table 6 and Table 8 is the  $n$ -th undamped mode shape,  $\phi_n$ , of the original MDOF building. The upper, middle and lower  $3 \times 1$  sub-column vectors of  $\phi_n$  are the  $\phi_{xn}$ ,  $\phi_{zn}$  and  $\phi_{\theta n}$ , respectively. For example, the vectors  $\phi_{xn}$ ,  $\phi_{zn}$  and  $\phi_{\theta n}$  of the first vibration mode of the three-storey building

are equal to  $\begin{bmatrix} 0.2458 \\ 0.1819 \\ 0.0804 \end{bmatrix}$ ,  $\begin{bmatrix} -0.0493 \\ -0.0351 \\ -0.0145 \end{bmatrix}$  and  $\begin{bmatrix} 0.0227 \\ 0.0163 \\ 0.0068 \end{bmatrix}$ , respectively. The matrices  $\Phi$  shown in

Table 6 and Table 8 have been normalized which make  $\Phi^T \mathbf{M} \Phi$  equal to identity matrices. The  $n$ -th diagonal elements of matrices  $\Phi^T \mathbf{C} \Phi$  and  $\Lambda^{1/2}$  shown in Table 6 and Table 8 are the values of  $2\omega_n \xi_n$  and  $\omega_n$ , respectively. The noted values are used in the  $n$ -th SDOF modal equation of motion shown in Equation (6). The floors are simulated as rigid diaphragms. The Rayleigh damping is assumed as the inherent damping of the two prototype buildings. The damping ratios of the first and the third vibration mode of the two prototype buildings are specified as 2%. The ground acceleration records used in this study are the NS and EW components of 1940 El Centro earthquake shown in Figures 2(e) and 2(f), respectively. The noted NS and EW components of ground acceleration records are scaled down and applied along the Z- and X-axis, respectively. The PGA of NS/EW components are equal to 0.14g/0.086g and 0.1g/0.061g for the one-storey and the three-storey building, respectively. The two buildings both remain elastic under the excitation of the noted ground motions.

**Table 5. The properties of the one-storey building.**

M			C						K		
			C <sub>0</sub>			C <sub>sd</sub>					
9.45		<i>symm.</i>	10.355		<i>symm.</i>	161.48		<i>symm.</i>	8638.4		<i>symm.</i>
0	9.45		-0.002	8.053		0	114.32		-3.226	4599	
0	0	23.03	-3.704	2.947	43.688	-363.3	385.84	2119.7	-6501	5171.3	53437

**Table 6. The undamped eigenvectors,  $\Phi$ , eigenvalues,  $\Lambda$ , and the transformed damping matrix of the one-storey building.**

$\Phi = \begin{bmatrix} \phi_{x1} & \phi_{x2} & \phi_{x3} \\ \phi_{z1} & \phi_{z2} & \phi_{z3} \\ \phi_{\theta1} & \phi_{\theta2} & \phi_{\theta3} \end{bmatrix}$			$\Lambda^{1/2} = \begin{bmatrix} \omega_1 & 0 & 0 \\ 0 & \omega_2 & 0 \\ 0 & 0 & \omega_3 \end{bmatrix}$			$\Phi^T C \Phi$		
0.06163	0.30769	-0.08573	20.163	0	0	3.9103		<i>symm.</i>
-0.31137	0.07734	0.05375	0	28.48	0	-5.5397	13.956	
0.04562	0.04604	0.19804	0	0	50.035	-9.4736	1.7029	107.21

**Table 7. The properties of the three-storey building.**

<b>M</b>	9.45								
	0	9.45						<i>symm.</i>	
	0	0	9.45						
	0	0	0	9.45					
	0	0	0	0	9.45				
	0	0	0	0	0	9.45			
	0	0	0	0	0	0	23.03		
	0	0	0	0	0	0	0	23.03	
<b>C<sub>0</sub></b>	7.000								
	-6.375	15.264						<i>symm.</i>	
	1.581	-8.742	17.69						
	0.002	-0.0024	0.00023	12.524					
	-0.0026	0.0034	-0.0014	-14.81	34.203				
	0.00035	-0.0015	0.0028	5.1035	-23.64	43.591			
	-3.749	4.777	-1.1904	11.821	-16.638	5.753	86.01		
	4.776	-9.951	6.5615	-16.639	36.23	-26.628	-111.93	246.34	
-1.191	6.562	-11.768	5.753	-26.628	46.826	36.694	-174.3	312.28	
<b>C<sub>sd</sub></b>	123.17								
	-123.17	246.34						<i>symm.</i>	
	0	-123.17	246.34						
	0	0	0	159.26					
	0	0	0	-159.26	318.52				
	0	0	0	0	-159.26	318.52			
	-277.13	277.13	0	537.51	-537.51	0	2437.6		
	277.13	-554.26	277.13	-537.51	1075	-537.51	-2437.6	4875.3	
0	277.13	-554.26	0	-537.51	1075	0	-2437.6	4875.3	
<b>K</b>	3336.3								
	-4248.1	8843						<i>symm.</i>	
	1053.6	-5825.5	10460						
	1.4011	-1.6114	0.1541	7017.1					
	-1.7432	2.2805	-0.9119	-9869.1	21463				
	0.2328	-1.0125	1.8681	3400.9	-15753	27720			
	-2498	3183.1	-793.28	7876.9	-11087	3833.6	54078		
	3182.9	-6631.3	4372.4	-11088	24143	-17744	-74587	160920	
-793.58	4372.8	-7842.2	3834	-17745	31203	24452	-116120	204860	



**Table 8. Continued**

$\Phi^T C \Phi$	1.945								
	-1.396	1.851					<i>symm.</i>		
	-2.146	-0.944	26.653						
	-0.895	0.833	1.934	14.964					
	-0.625	0.840	-0.536	10.530	11.784				
	0.615	-0.493	-1.124	1.901	1.973	33.321			
	0.482	-0.449	-0.364	0.431	1.518	21.311	24.043		
	0.731	1.168	-15.906	-18.004	4.924	-3.347	5.926	198.47	
	-0.718	-0.331	9.418	-0.846	2.727	-37.435	8.518	35.461	407.41

### Summary of Analytical Results for Examples Two and Three

The analytical results obtained by using direct integration of the equation of motion, the simple approximation method and the proposed method are denoted as RHA, SMA and 3MA, respectively, in this paper. RHA stands for response history analysis; SMA stands for modal response history analysis by using SDOF modal equations of motion; 3MA stands for modal response history analysis by using 3DOF modal equations of motion. The  $3 \times 3$   $\mathbf{M}_n$ ,  $\mathbf{C}_n$  and  $\mathbf{K}_n$  matrices, defined in Equations (23) and (24), of the first three vibration modes for the one-storey building are shown in Table 9. The sum of the nine elements of matrix  $\mathbf{M}_n$  is equal to one. The sum of the nine elements of matrix  $\mathbf{C}_n$  and  $\mathbf{K}_n$  are equal to the values of the  $n$ -th diagonal element of the matrix  $\Phi^T C \Phi$  and  $\Lambda$ , respectively, shown in Table 6. The modal translations,  $D_{xn}$  and  $D_{zn}$ , and the modal rotation,  $D_{\theta n}$ , of the elastic one-storey building calculated by using 3MA are no longer equal to each other as shown in Figure 8. It is caused by the non-proportional damping effect. The total responses of this non-proportionally damped building obtained by using 3MA and SMA compared with those obtained by using RHA are shown in Figures 9(a) and 9(b), respectively. Figure 9(a) shows that the analytical results obtained by using 3MA are almost the same as those obtained by using RHA. Figure 9(b) shows that the responses obtained by using SMA are obviously deviated from the benchmark solutions. The errors of the peak X- and Z- translational and Y-rotational responses obtained by using SMA are equal to 19.5%, 0.04% and 31.9%, respectively.

**Table 9. The modal matrices,  $\mathbf{M}_n$ ,  $\mathbf{C}_n$  and  $\mathbf{K}_n$  of the one-storey building.**

$n$ th mode	$\mathbf{M}_n$			$\mathbf{C}_n$			$\mathbf{K}_n$		
1st	0.036		<i>symm.</i>	0.653		<i>symm.</i>	32.806		<i>symm.</i>
	0	0.916		0.000	11.864		0.062	445.870	
	0	0	0.048	-1.032	-5.523	4.503	-18.278	-73.462	111.230
2nd	0.895		<i>symm.</i>	16.268		<i>symm.</i>	817.820		<i>symm.</i>
	0	0.057		0.000	0.732		-0.077	27.507	
	0	0	0.049	-5.200	1.384	4.586	-92.096	18.414	113.280
3rd	0.069		<i>symm.</i>	1.263		<i>symm.</i>	63.490		<i>symm.</i>
	0	0.027		0.000	0.354		0.015	13.287	
	0	0	0.903	6.232	4.139	84.849	110.370	55.048	2095.800

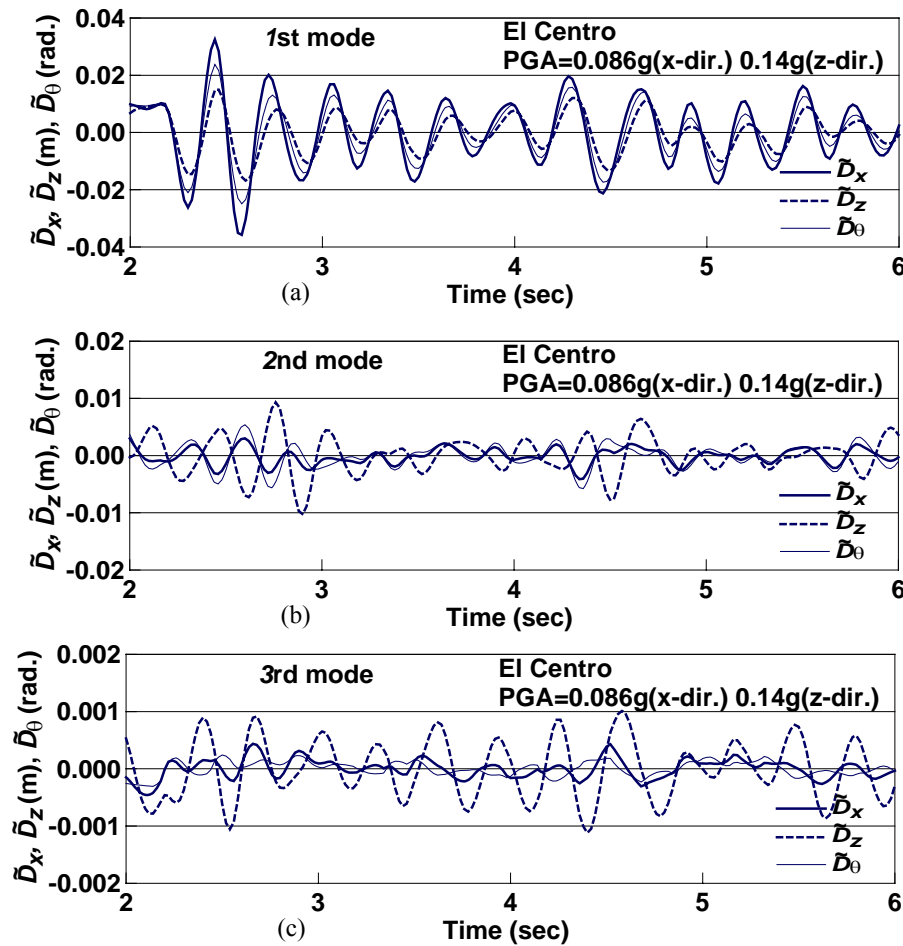


Figure 8. The (a) 1st (b) 2nd (c) 3rd modal responses of the one-storey building obtained by using 3MA.

The  $3 \times 3$   $\mathbf{M}_n$ ,  $\mathbf{C}_n$  and  $\mathbf{K}_n$  matrices of the nine vibration modes of the three-storey building are shown in Table 10. The sum of the nine elements of matrix  $\mathbf{M}_n$  is equal to one. Again, the sum of the nine elements of matrix  $\mathbf{C}_n$  and  $\mathbf{K}_n$  are equal to the values of the  $n$ -th diagonal element of the matrix  $\Phi^T \mathbf{C} \Phi$  and  $\Lambda$ , respectively, shown in Table 8. The first three modal responses of the three-storey building obtained by using 3MA are shown in Figure 10. The modal translations and modal rotation are not equal to each other. It reflects the non-proportional damping effect. The total responses of this non-proportionally damped three-storey building obtained by using 3MA and SMA compared with those obtained by using RHA, are shown in Figures 11 and 12, respectively. Figure 11 shows that the analytical results obtained by using 3MA are almost the same as those obtained by RHA. Figure 12 shows that the responses obtained by using SMA are obviously deviated from the benchmark solutions. The errors of the peak X- and Z-translational and Y-rotational responses on the roof are 0.6%, 18.2% and 28.9%, respectively. Moreover, the phases of response histories obtained by using SMA are quite different from those obtained by using RHA. The roof responses of the three-storey building obtained by using 3MA and SMA are also shown in

Figure 13, but only consider the first three vibration modes. In this example, three vibration modes are sufficient to obtain accurate results. Thus, this shows that it is not necessary to incorporate the entire  $3N$  modes (9 modes in this example) in the proposed method. It appears that the proposed method has been inherited the advantage of the modal response history analysis, only the first few modes are required for an earthquake response analysis.

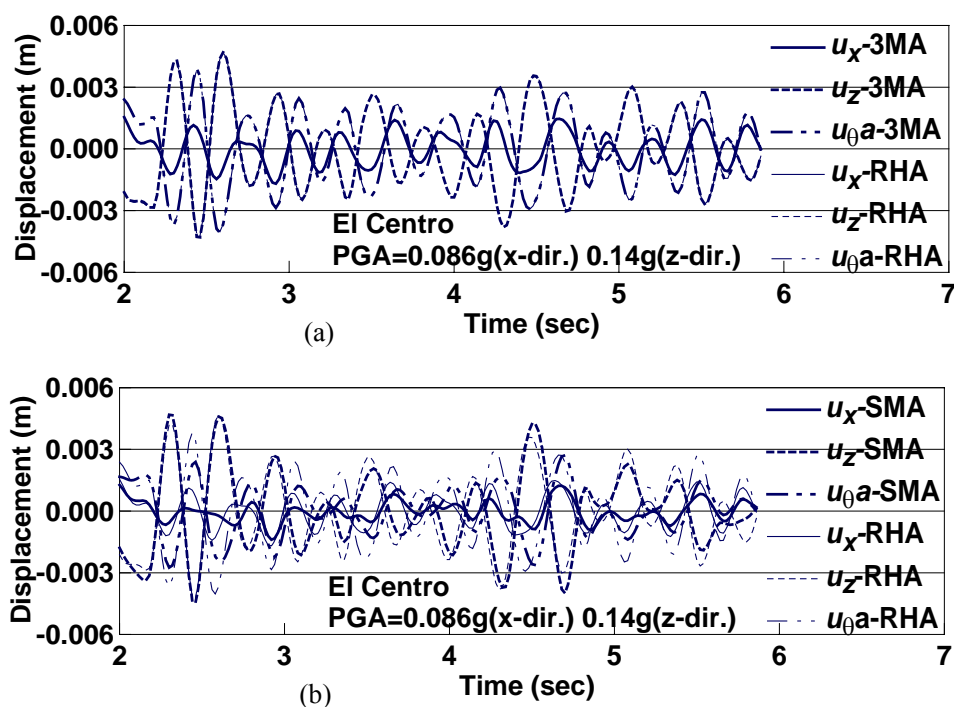


Figure 9. The total responses of the one-storey building obtained by using (a) 3MA and RHA (b) SMA and RHA.

Table 10. The modal matrices,  $M_n$ ,  $C_n$  and  $K_n$  of the three-storey building.

Nth mode	$M_n$			$C_n$			$K_n$		
1 <sup>st</sup>	0.944		<i>symm.</i>	2.847		<i>symm.</i>	53.141		<i>symm.</i>
	0	0.0366		0.000	0.147		0.000	3.997	
	0	0	0.0190	-0.538	-0.210	0.447	-3.625	-2.078	6.702
2 <sup>nd</sup>	0.0492		<i>symm.</i>	0.146		<i>symm.</i>	2.776		<i>symm.</i>
	0	0.8845		0.000	3.564		0.000	96.594	
	0	0	0.0663	0.226	-1.935	1.561	1.534	-19.056	23.336
3 <sup>rd</sup>	0.0078		<i>symm.</i>	0.040		<i>symm.</i>	1.167		<i>symm.</i>
	0	0.0789		0.000	0.327		0.000	8.654	
	0	0	0.9133	0.209	2.175	21.519	1.788	21.084	321.340
4 <sup>th</sup>	0.962		<i>symm.</i>	20.829		<i>symm.</i>	566.540		<i>symm.</i>
	0	0.0225		0.000	0.654		-0.031	29.146	
	0	0	0.0153	-3.412	-1.030	2.364	-32.593	-16.632	57.737

Table 10. Continued

nth mode	$M_n$			$C_n$			$K_n$		
5th	0.0316		<i>symm.</i>	0.674		<i>symm.</i>	18.886		<i>symm.</i>
	0	0.8930		0.000	25.887		0.034	1158.500	
	0	0	0.0753	1.440	-15.45	13.251	13.547	-241.700	305.500
6th	0.9773		<i>symm.</i>	43.742		<i>symm.</i>	1710.800		<i>symm.</i>
	0	0.0130		0.000	0.757		-0.040	57.833	
	0	0	0.0098	-6.034	-1.325	3.539	-82.185	-36.189	134.670
7th	0.0186		<i>symm.</i>	0.828		<i>symm.</i>	32.491		<i>symm.</i>
	0	0.8961		0.000	54.589		0.048	4068.600	
	0	0	0.0853	2.401	-33.02	29.863	33.127	-899.990	1168.400
8th	0.0053		<i>symm.</i>	0.127		<i>symm.</i>	3.418		<i>symm.</i>
	0	0.0850		0.000	2.403		-0.004	113.400	
	0	0	0.9097	2.155	16.108	159.41	19.769	257.730	3695.600
9th	0.0037		<i>symm.</i>	0.165		<i>symm.</i>	6.471		<i>symm.</i>
	0	0.0904		0.000	5.495		-0.007	410.430	
	0	0	0.9059	3.554	34.691	325.260	48.638	936.840	12517.000

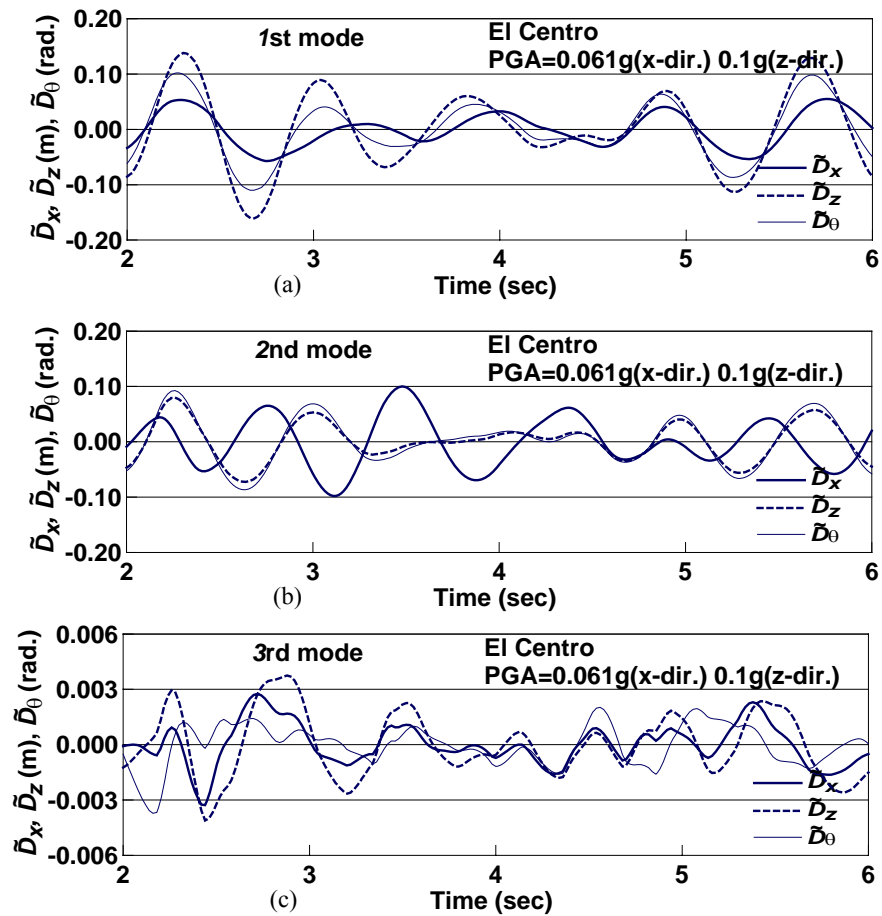


Figure 10. The (a) 1st (b) 2nd (c) 3rd modal response of three-storey building obtained by using 3MA.

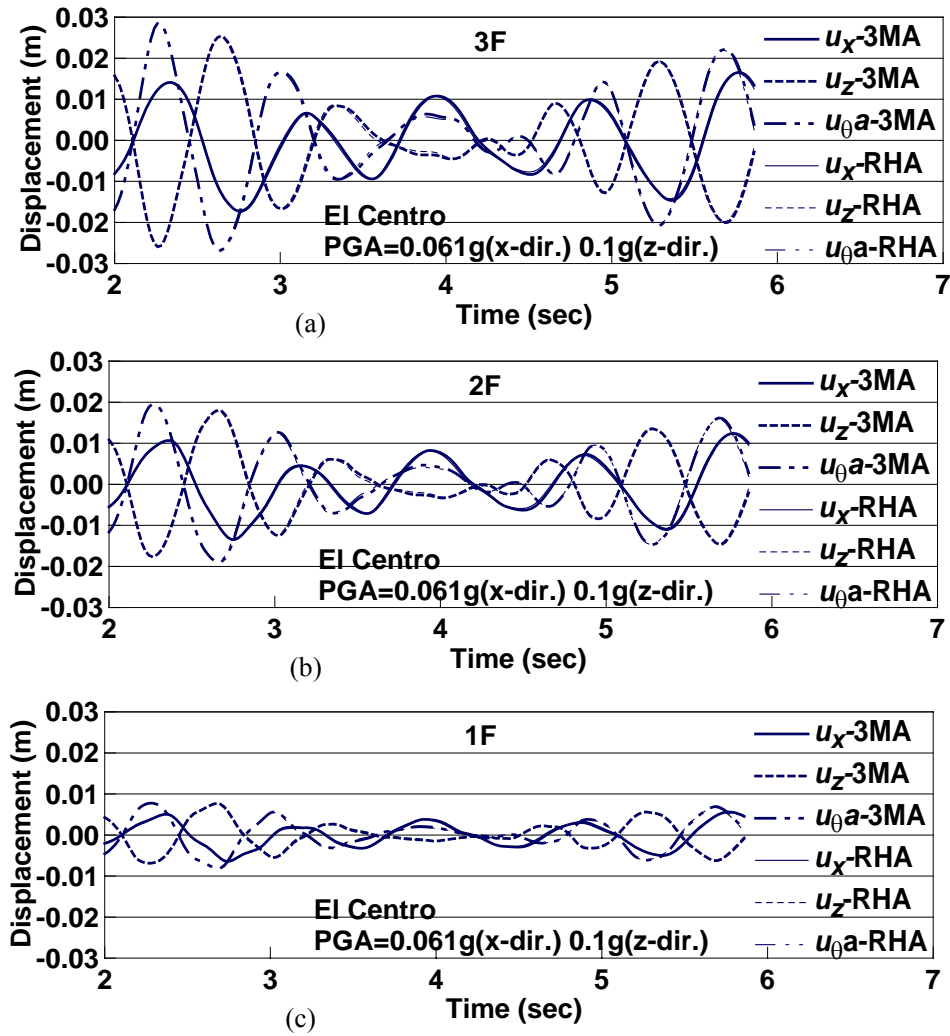


Figure 11. The total translational and rotational responses at the (a) 3rd (b) 2nd (c) 1st floor obtained by using 3MA and RHA.

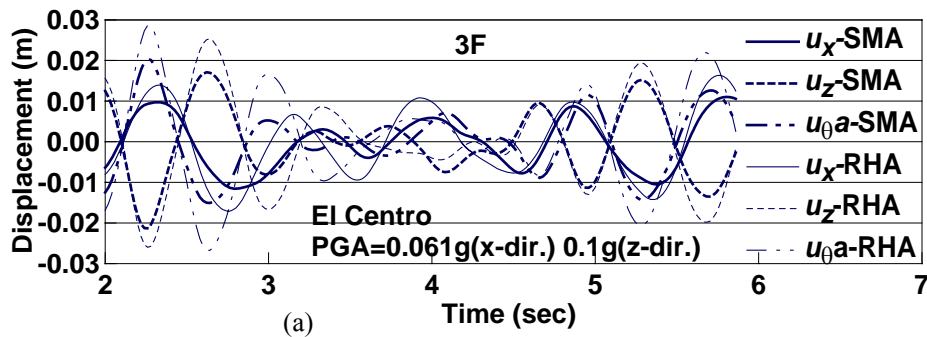


Figure 12. Continued on next page.

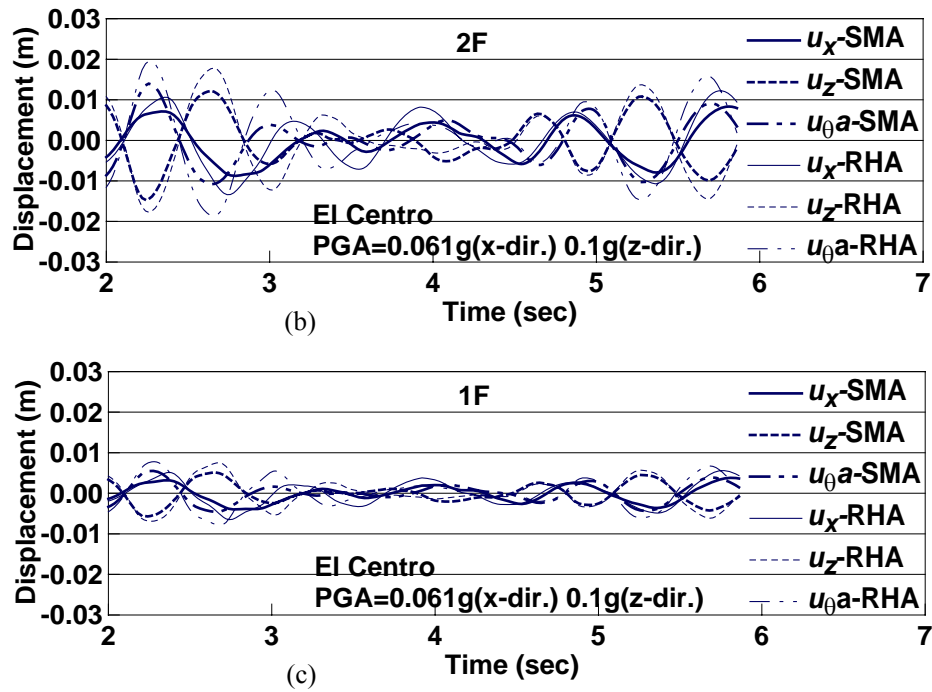


Figure 12. The total translational and rotational responses at the (a) 3rd (b) 2nd (c) 1st floor obtained by using SMA and RHA.

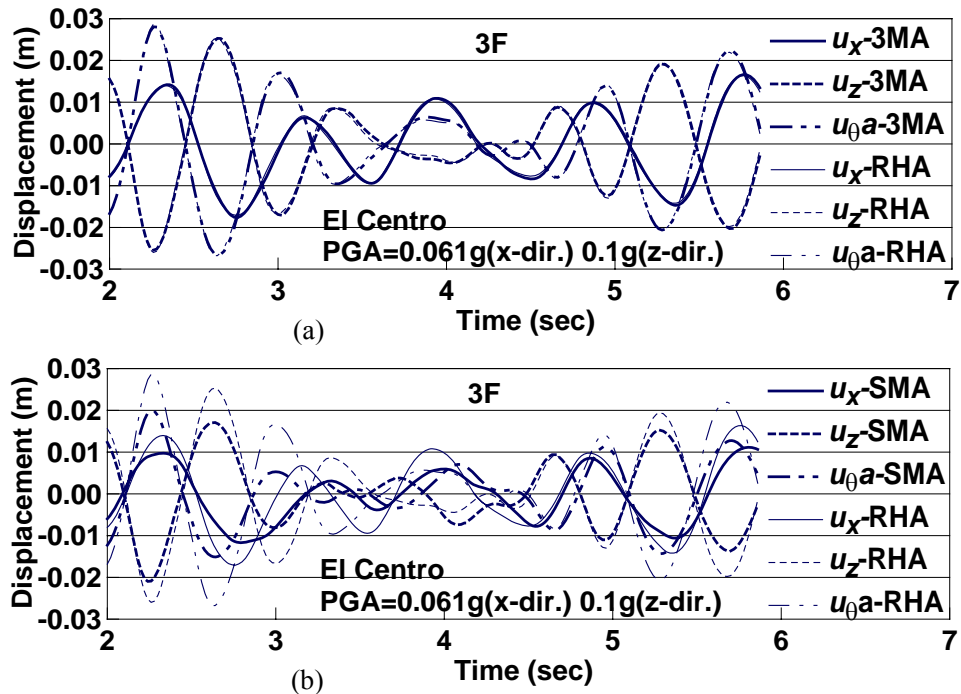


Figure 13. The total translational and rotational responses, only considering the first three vibration modes, obtained by using (a) 3MA and RHA (b) SMA and RHA.

From the verification of these two examples, it shows that the 3DOF modal equations of motion possessing the non-proportional damping characteristic are more appropriate for the modal response history analysis of non-proportionally damped asymmetric-plan buildings. Since the errors of the translational and the rotational responses simultaneously occurred at CM, it may amplify the errors of the translational responses at corners and deteriorate the applicability of the simple approximation method to asymmetric-plan buildings. The proposed method provides a better alternative to deal with this kind of structures.

## Conclusion

The bifurcation of pushover curves for asymmetric-plan structures subjected to the modal inertia force distribution  $s_n$  are noticed. Hence, the application of conventional SDOF modal systems is insufficient to assess the inelastic modal behaviors, which are used to approximately estimate the inelastic seismic demands of asymmetric-plan structures. The 3DOF modal equations of motion for two-way asymmetric-plan buildings were constructed. Each 3DOF modal equation of motion has a corresponding 3DOF modal system. The 3DOF modal system is consistent with the SDOF modal system in an elastic state and is capable of simulating the mentioned bifurcating characteristic in an inelastic state. The proposed 3MA approach is able to take the non-proportionality and interaction of the modal translations and the modal rotation into consideration. Moreover, the two-directional ground motions are simultaneously considered in the proposed method. It appears that the proposed method is reasonable and general for the seismic assessment of the asymmetric-plan building systems subjected to bi-directional seismic ground motions. The effectiveness of the 3DOF modal system is verified by comparing the seismic responses obtained by using 3MA and RHA.

The proposed 3DOF modal equation of motion is also advantageous to the modal response history analysis of non-proportionally damped asymmetric-plan elastic systems. The mentioned advantage is due to the proportionalities of the damping matrices in the 3DOF modal equations of motion dependent upon that of the damping matrix of the original MDOF system. It makes the modal translations and modal rotation to be different from each other for a non-proportionally damped elastic structure. The 3DOF modal equations of motion are more realistic in simulating the modal behaviors of non-proportionally damped structures than the SDOF modal equations of motion. The accuracy of modal response history analysis by using the 3DOF modal equations of motion was verified shown in two numerical examples. The proposed method is very simple and efficient. Thus, it is more appealing to be used in practical engineering.

## Acknowledgement

This research is sponsored by the National Science Council, Republic of China, under Grant NSC 95-2221-E-002-317-MY2. This financial support is gratefully acknowledged. The cooperation of B.Z. Lin and Y.J. Yu, the authors of PISA3D computer program, making the analytical tool available, is particularly appreciated.

## Appendix

### Verification of 3DOF Modal Systems

Letting the seismic force and damping equal to zero, Equation (22) can be written as:

$$(\mathbf{K} - \omega_n^2 \mathbf{M}) \mathbf{u}_n = \mathbf{0} \quad (\text{A1})$$

By substituting Equation (5) for  $\mathbf{u}_n$  and pre-multiplied by  $\boldsymbol{\varphi}_n^T$ , Equation (A1) can be written as:

$$\begin{bmatrix} \boldsymbol{\varphi}_{xn} \\ \boldsymbol{\varphi}_{zn} \\ \boldsymbol{\varphi}_{\theta n} \end{bmatrix}^T (\mathbf{K} - \omega_n^2 \mathbf{M}) \begin{bmatrix} \boldsymbol{\varphi}_{xn} \\ \boldsymbol{\varphi}_{zn} \\ \boldsymbol{\varphi}_{\theta n} \end{bmatrix} D_n = 0 \quad (\text{A2})$$

Therefore,

$$\begin{aligned} & \begin{bmatrix} \boldsymbol{\varphi}_{xn} \\ \boldsymbol{\varphi}_{zn} \\ \boldsymbol{\varphi}_{\theta n} \end{bmatrix}^T (\mathbf{K} - \omega_n^2 \mathbf{M}) \begin{bmatrix} \boldsymbol{\varphi}_{xn} \\ \boldsymbol{\varphi}_{zn} \\ \boldsymbol{\varphi}_{\theta n} \end{bmatrix} \\ &= \begin{bmatrix} \boldsymbol{\varphi}_{xn} \\ \boldsymbol{\varphi}_{zn} \\ \boldsymbol{\varphi}_{\theta n} \end{bmatrix}^T \left( \begin{bmatrix} \mathbf{k}_{xx} & \mathbf{k}_{xz} & \mathbf{k}_{x\theta} \\ \mathbf{k}_{zx} & \mathbf{k}_{zz} & \mathbf{k}_{z\theta} \\ \mathbf{k}_{\theta x} & \mathbf{k}_{\theta z} & \mathbf{k}_{\theta\theta} \end{bmatrix} - \omega_n^2 \begin{bmatrix} \mathbf{m}_x & \mathbf{0} & \mathbf{0} \\ \mathbf{0} & \mathbf{m}_z & \mathbf{0} \\ \mathbf{0} & \mathbf{0} & \mathbf{I}_0 \end{bmatrix} \right) \begin{bmatrix} \boldsymbol{\varphi}_{xn} \\ \boldsymbol{\varphi}_{zn} \\ \boldsymbol{\varphi}_{\theta n} \end{bmatrix} \quad (\text{A3a}) \\ &= \boldsymbol{\varphi}_{xn}^T (\mathbf{k}_{xx} - \omega_n^2 \mathbf{m}_x) \boldsymbol{\varphi}_{xn} + \boldsymbol{\varphi}_{zn}^T \mathbf{k}_{xz} \boldsymbol{\varphi}_{xn} + \boldsymbol{\varphi}_{\theta n}^T \mathbf{k}_{\theta x} \boldsymbol{\varphi}_{xn} \\ &+ \boldsymbol{\varphi}_{xn}^T \mathbf{k}_{xz} \boldsymbol{\varphi}_{zn} + \boldsymbol{\varphi}_{zn}^T (\mathbf{k}_{zz} - \omega_n^2 \mathbf{m}_z) \boldsymbol{\varphi}_{zn} + \boldsymbol{\varphi}_{\theta n}^T \mathbf{k}_{z\theta} \boldsymbol{\varphi}_{zn} \\ &+ \boldsymbol{\varphi}_{xn}^T \mathbf{k}_{\theta x} \boldsymbol{\varphi}_{\theta n} + \boldsymbol{\varphi}_{zn}^T \mathbf{k}_{\theta z} \boldsymbol{\varphi}_{\theta n} + \boldsymbol{\varphi}_{\theta n}^T (\mathbf{k}_{\theta\theta} - \omega_n^2 \mathbf{I}_0) \boldsymbol{\varphi}_{\theta n} \\ &= A(\omega_n^2) + B(\omega_n^2) + C(\omega_n^2) = 0 \end{aligned}$$

where

$$A(\omega_n^2) = \boldsymbol{\varphi}_{xn}^T (\mathbf{k}_{xx} - \omega_n^2 \mathbf{m}_x) \boldsymbol{\varphi}_{xn} + \boldsymbol{\varphi}_{zn}^T \mathbf{k}_{xz} \boldsymbol{\varphi}_{xn} + \boldsymbol{\varphi}_{\theta n}^T \mathbf{k}_{\theta x} \boldsymbol{\varphi}_{xn} \quad (\text{A3b})$$

$$B(\omega_n^2) = \boldsymbol{\varphi}_{xn}^T \mathbf{k}_{xz} \boldsymbol{\varphi}_{zn} + \boldsymbol{\varphi}_{zn}^T (\mathbf{k}_{zz} - \omega_n^2 \mathbf{m}_z) \boldsymbol{\varphi}_{zn} + \boldsymbol{\varphi}_{\theta n}^T \mathbf{k}_{z\theta} \boldsymbol{\varphi}_{zn} \quad (\text{A3c})$$

$$C(\omega_n^2) = \boldsymbol{\varphi}_{xn}^T \mathbf{k}_{\theta x} \boldsymbol{\varphi}_{\theta n} + \boldsymbol{\varphi}_{zn}^T \mathbf{k}_{\theta z} \boldsymbol{\varphi}_{\theta n} + \boldsymbol{\varphi}_{\theta n}^T (\mathbf{k}_{\theta\theta} - \omega_n^2 \mathbf{I}_0) \boldsymbol{\varphi}_{\theta n} \quad (\text{A3d})$$

Similarly, by substituting Equation (11) for  $\mathbf{u}_n$  and pre-multiplied by  $\begin{bmatrix} \boldsymbol{\varphi}_{xn} & \mathbf{0} & \mathbf{0} \\ \mathbf{0} & \boldsymbol{\varphi}_{zn} & \mathbf{0} \\ \mathbf{0} & \mathbf{0} & \boldsymbol{\varphi}_{\theta n} \end{bmatrix}^T$ ,

Equation (A1) can be written as follows:

$$\begin{aligned} & \begin{bmatrix} \boldsymbol{\varphi}_{xn} & \mathbf{0} & \mathbf{0} \\ \mathbf{0} & \boldsymbol{\varphi}_{zn} & \mathbf{0} \\ \mathbf{0} & \mathbf{0} & \boldsymbol{\varphi}_{\theta n} \end{bmatrix}^T (\mathbf{K} - \omega^2 \mathbf{M}) \begin{bmatrix} \boldsymbol{\varphi}_{xn} D_{xn} \\ \boldsymbol{\varphi}_{zn} D_{zn} \\ \boldsymbol{\varphi}_{\theta n} D_{\theta n} \end{bmatrix} \\ & = \begin{bmatrix} \boldsymbol{\varphi}_{xn} & \mathbf{0} & \mathbf{0} \\ \mathbf{0} & \boldsymbol{\varphi}_{zn} & \mathbf{0} \\ \mathbf{0} & \mathbf{0} & \boldsymbol{\varphi}_{\theta n} \end{bmatrix}^T (\mathbf{K} - \omega^2 \mathbf{M}) \begin{bmatrix} \boldsymbol{\varphi}_{xn} & \mathbf{0} & \mathbf{0} \\ \mathbf{0} & \boldsymbol{\varphi}_{zn} & \mathbf{0} \\ \mathbf{0} & \mathbf{0} & \boldsymbol{\varphi}_{\theta n} \end{bmatrix} \begin{bmatrix} D_{xn} \\ D_{zn} \\ D_{\theta n} \end{bmatrix} = \mathbf{0} \end{aligned} \quad (\text{A4})$$

Therefore,

$$\begin{aligned} & \det \left( \begin{bmatrix} \boldsymbol{\varphi}_{xn}^T (\mathbf{k}_{xx} - \omega^2 \mathbf{m}_x) \boldsymbol{\varphi}_{xn} & \boldsymbol{\varphi}_{xn}^T \mathbf{k}_{xz} \boldsymbol{\varphi}_{zn} & \boldsymbol{\varphi}_{xn}^T \mathbf{k}_{x\theta} \boldsymbol{\varphi}_{\theta n} \\ \boldsymbol{\varphi}_{zn}^T \mathbf{k}_{zx} \boldsymbol{\varphi}_{xn} & \boldsymbol{\varphi}_{zn}^T (\mathbf{k}_{zz} - \omega^2 \mathbf{m}_z) \boldsymbol{\varphi}_{zn} & \boldsymbol{\varphi}_{zn}^T \mathbf{k}_{z\theta} \boldsymbol{\varphi}_{\theta n} \\ \boldsymbol{\varphi}_{\theta n}^T \mathbf{k}_{\theta x} \boldsymbol{\varphi}_{xn} & \boldsymbol{\varphi}_{\theta n}^T \mathbf{k}_{\theta z} \boldsymbol{\varphi}_{zn} & \boldsymbol{\varphi}_{\theta n}^T (\mathbf{k}_{\theta\theta} - \omega^2 \mathbf{I}_0) \boldsymbol{\varphi}_{\theta n} \end{bmatrix} \right) \\ & = \det \left( \begin{bmatrix} A - \hat{k}_{xz} - \hat{k}_{x\theta} & \hat{k}_{xz} & \hat{k}_{x\theta} \\ \hat{k}_{zx} & B - \hat{k}_{zx} - \hat{k}_{z\theta} & \hat{k}_{z\theta} \\ \hat{k}_{\theta x} & \hat{k}_{\theta z} & C - \hat{k}_{\theta x} - \hat{k}_{\theta z} \end{bmatrix} \right) \\ & = ABC - AC(\hat{k}_{zx} + \hat{k}_{z\theta}) - BC(\hat{k}_{xz} + \hat{k}_{x\theta}) - AB(\hat{k}_{\theta x} + \hat{k}_{\theta z}) \\ & + (A + B + C)(\hat{k}_{xz} \hat{k}_{\theta x} + \hat{k}_{z\theta} \hat{k}_{\theta x} + \hat{k}_{xz} \hat{k}_{\theta z}) = 0 \end{aligned} \quad (\text{A5})$$

where

$$\begin{aligned} \hat{k}_{xx} &= \boldsymbol{\varphi}_{xn}^T \mathbf{k}_{xx} \boldsymbol{\varphi}_{xn} & \hat{k}_{zz} &= \boldsymbol{\varphi}_{zn}^T \mathbf{k}_{zz} \boldsymbol{\varphi}_{zn} & \hat{k}_{\theta\theta} &= \boldsymbol{\varphi}_{\theta n}^T \mathbf{k}_{\theta\theta} \boldsymbol{\varphi}_{\theta n} \\ \hat{k}_{xz} &= \boldsymbol{\varphi}_{xn}^T \mathbf{k}_{xz} \boldsymbol{\varphi}_{zn} & \hat{k}_{x\theta} &= \boldsymbol{\varphi}_{xn}^T \mathbf{k}_{x\theta} \boldsymbol{\varphi}_{\theta n} & \hat{k}_{z\theta} &= \boldsymbol{\varphi}_{zn}^T \mathbf{k}_{z\theta} \boldsymbol{\varphi}_{\theta n} \end{aligned} \quad (\text{A6})$$

When  $\omega^2 = \omega_n^2$ , it can be obtained from Equations (A3a)-(A3d) and (A5) that  $A(\omega_n^2) = B(\omega_n^2) = C(\omega_n^2) = 0$ . Hence,  $D_{xn} : D_{zn} : D_{\theta n} = 1 : 1 : 1$ . That is to say, the 3DOF modal system has an active sub-mode with square of circular frequency  $\omega_a^2$  equal to  $\omega_n^2$  and its corresponding mode shape  $\tilde{\boldsymbol{\varphi}}_a$  is equal to  $[1 \ 1 \ 1]^T$ .

The square of circular frequency  $\omega_a^2$  can be obtained from Equations (19), (25), (A6) and  $\tilde{\boldsymbol{\varphi}}_a$  as follows:

$$\begin{aligned} \tilde{\boldsymbol{\varphi}}_a^T (\tilde{\mathbf{K}} - \omega_a^2 \tilde{\mathbf{M}}) \tilde{\boldsymbol{\varphi}}_a &= 0 \\ \text{then } \begin{bmatrix} 1 \\ 1 \\ 1 \end{bmatrix}^T \begin{bmatrix} \hat{k}_{xx} - \omega_a^2 m_x & \hat{k}_{xz} & \hat{k}_{x\theta} \\ \hat{k}_{xz} & \hat{k}_{zz} - \omega_a^2 m_z & \hat{k}_{z\theta} \\ \hat{k}_{x\theta} & \hat{k}_{z\theta} & \hat{k}_{\theta\theta} - \omega_a^2 I \end{bmatrix} \begin{bmatrix} 1 \\ 1 \\ 1 \end{bmatrix} &= 0 \quad (\text{A7}) \\ \text{set } m_x + m_z + I &= 1 \\ \text{then } \omega_a^2 &= \hat{k}_{xx} + \hat{k}_{zz} + \hat{k}_{\theta\theta} + 2(\hat{k}_{xz} + \hat{k}_{x\theta} + \hat{k}_{z\theta}) \end{aligned}$$

From the viewpoint of energy, it can be proved that the two spurious sub-modes have no contribution on the elastic response of a 3DOF modal system. The proof is as follows:

The square of circular frequencies and mode shapes of spurious sub-modes of a 3DOF modal system are denoted as  $\omega_{s1}^2, \omega_{s2}^2$  and  $\tilde{\boldsymbol{\varphi}}_{s1}, \tilde{\boldsymbol{\varphi}}_{s2}$ , respectively. The virtual work done by the  $n$ -th modal inertia force distribution multiplied by the  $n$ -th synthetic ground motion, i.e.  $-(\Gamma_{xn}\ddot{u}_{gx} + \Gamma_{zn}\ddot{u}_{gz})\mathbf{s}_n$ , on the original MDOF building is:

$$-\boldsymbol{\delta}\mathbf{u}_n^T (\Gamma_{xn}\ddot{u}_{gx} + \Gamma_{zn}\ddot{u}_{gz})\mathbf{s}_n = \boldsymbol{\delta}\mathbf{u}_n^T (\mathbf{M}\ddot{\mathbf{u}}_n + \mathbf{C}\dot{\mathbf{u}}_n + \mathbf{K}\mathbf{u}_n) \quad (\text{A8})$$

where  $\boldsymbol{\delta}\mathbf{u}_n$  is the virtual displacement. Substitute  $\mathbf{u}_n = \boldsymbol{\varphi}_n D_n$  into Equation (A8) and it can be obtained that

$$-(\Gamma_{xn}\ddot{u}_{gx} + \Gamma_{zn}\ddot{u}_{gz})M_n \delta D_n = (M_n \ddot{D}_n + C_n \dot{D}_n + K_n D_n) \delta D_n \quad (\text{A9})$$

Moreover, denote  $(M_n \ddot{D}_n + C_n \dot{D}_n + K_n D_n) \delta D_n = \delta E_n$ , which represents the virtual work done by the  $n$ -th modal inertia force distribution multiplied by the  $n$ -th synthetic ground motion. Similarly, substitute Equation (11) into Equation (A8) and it can be obtained that

$$-(\Gamma_{xn}\ddot{u}_{gx} + \Gamma_{zn}\ddot{u}_{gz})(m_x \delta D_{xn} + m_z \delta D_{zn} + I \delta D_{\theta n}) = \delta \mathbf{D}_n^T (\tilde{\mathbf{M}}\ddot{\mathbf{D}}_n + \tilde{\mathbf{C}}\dot{\mathbf{D}}_n + \tilde{\mathbf{K}}\mathbf{D}_n) \quad (\text{A10})$$

where  $\mathbf{D}_n = [D_{xn} \ D_{zn} \ D_{\theta n}]^T$ . Due to  $D_{xn} = D_{zn} = D_{\theta n} = D_n$  for elastic building systems, the left-hand side of Equation (A10) becomes as:

$$\begin{aligned} &-(\Gamma_{xn}\ddot{u}_{gx} + \Gamma_{zn}\ddot{u}_{gz})(m_x + m_z + I) \delta D_n \\ &= -(\Gamma_{xn}\ddot{u}_{gx} + \Gamma_{zn}\ddot{u}_{gz}) (\boldsymbol{\varphi}_{xn}^T \mathbf{m}_x \boldsymbol{\varphi}_{xn} + \boldsymbol{\varphi}_{zn}^T \mathbf{m}_z \boldsymbol{\varphi}_{zn} + \boldsymbol{\varphi}_{\theta n}^T \mathbf{I} \boldsymbol{\varphi}_{\theta n}) \delta D_n \quad (\text{A11}) \\ &= -(\Gamma_{xn}\ddot{u}_{gx} + \Gamma_{zn}\ddot{u}_{gz}) M_n \delta D_n \end{aligned}$$

which is same as the left-hand side of Equation (A9). Therefore, the right-hand side of Equation (A10) should be equal to that of Equation (A9), i.e.

$$\delta \mathbf{D}_n^T (\tilde{\mathbf{M}} \ddot{\mathbf{D}}_n + \tilde{\mathbf{C}} \dot{\mathbf{D}}_n + \tilde{\mathbf{K}} \mathbf{D}_n) = \delta E_n \quad (\text{A12})$$

The displacement vector of a 3DOF modal system can be expressed as:

$$\tilde{\mathbf{D}} = \mathbf{D}_n = \begin{bmatrix} D_{xn} \\ D_{zn} \\ D_{\theta n} \end{bmatrix} = \tilde{\boldsymbol{\varphi}}_a q_a + \tilde{\boldsymbol{\varphi}}_{s1} q_{s1} + \tilde{\boldsymbol{\varphi}}_{s2} q_{s2} \quad (\text{A13})$$

where  $q_a$ ,  $q_{s1}$ ,  $q_{s2}$ , are the modal coordinates of active sub-mode, the first spurious sub-mode and the second spurious sub-mode, respectively. Substituting Equation (A13) into the right-hand side of Equation (A10) and using the orthogonal properties of mode shapes, it can be obtained that

$$\delta \mathbf{D}_n^T (\tilde{\mathbf{M}} \ddot{\mathbf{D}}_n + \tilde{\mathbf{C}} \dot{\mathbf{D}}_n + \tilde{\mathbf{K}} \mathbf{D}_n) = \delta E_a + \delta E_{s1} + \delta E_{s2} \quad (\text{A14a})$$

where

$$\delta E_a = \tilde{\boldsymbol{\varphi}}_a^T (\tilde{\mathbf{M}} \ddot{\boldsymbol{\varphi}}_a \ddot{q}_a + \tilde{\mathbf{C}} \tilde{\boldsymbol{\varphi}}_a \dot{q}_a + \tilde{\mathbf{K}} \tilde{\boldsymbol{\varphi}}_a q_a) \delta q_a \quad (\text{A14b})$$

$$\delta E_{s1} = \tilde{\boldsymbol{\varphi}}_{s1}^T (\tilde{\mathbf{M}} \ddot{\boldsymbol{\varphi}}_{s1} \ddot{q}_{s1} + \tilde{\mathbf{C}} \tilde{\boldsymbol{\varphi}}_{s1} \dot{q}_{s1} + \tilde{\mathbf{K}} \tilde{\boldsymbol{\varphi}}_{s1} q_{s1}) \delta q_{s1} \quad (\text{A14c})$$

$$\delta E_{s2} = \tilde{\boldsymbol{\varphi}}_{s2}^T (\tilde{\mathbf{M}} \ddot{\boldsymbol{\varphi}}_{s2} \ddot{q}_{s2} + \tilde{\mathbf{C}} \tilde{\boldsymbol{\varphi}}_{s2} \dot{q}_{s2} + \tilde{\mathbf{K}} \tilde{\boldsymbol{\varphi}}_{s2} q_{s2}) \delta q_{s2} \quad (\text{A14d})$$

From Equations (A12) and (A14a), it can be obtained that

$$\delta E_n = \delta E_a + \delta E_{s1} + \delta E_{s2} \quad (\text{A15})$$

Since the circular frequency  $\omega_a^2$  and the mode shape  $\tilde{\boldsymbol{\varphi}}_a$  of the active sub-mode is equal to  $\omega_n^2$  and  $[1 \ 1 \ 1]^T$ , respectively, the virtual work done by the active sub-mode,  $\delta E_a$ , is equal to  $\delta E_n$ . Therefore, from Equation (A15), the virtual work done by the two spurious sub-modes,  $\delta E_{s1}$  and  $\delta E_{s2}$ , should be equal to zero. Thus, it can be concluded that the two spurious sub-modes have no contribution on the elastic responses of a 3DOF modal system.

Consequently, it is proved that the active sub-mode is same as the  $n$ -th mode of the original building and the spurious sub-modes has no contribution on the elastic modal response. This confirms that the 3DOF modal system derived from Equations (19) to (27) does not violate the fundamental theory of structural dynamics for elastic systems.

## References

- [1] Lin, J.L. & Tsai, K.C. (2007a). Simplified seismic analysis of asymmetric building systems. *Earthquake Engineering and Structural Dynamics*, **36**, 459-479.
- [2] Chopra, A.K. & Goel, R.K. (2004). A modal pushover analysis procedure to estimate seismic demands for unsymmetric-plan buildings. *Earthquake Engineering and Structural Dynamics*, **33**, 903-927.
- [3] Myslimaj, B. & Tso, W.K. (2002). A strength distribution criterion for minimizing torsional response of asymmetric wall-type systems. *Earthquake Engineering and Structural Dynamics*, **31**, 99-120.
- [4] Riddell, R. & Santa-Maria, H. (1999). Inelastic response of one-storey asymmetric-plan systems subjected to bi-directional earthquake motions. *Earthquake Engineering and Structural Dynamics*, **28**, 273-285.
- [5] Hernández, J.J. & López, O.A. (2000). Influence of bidirectional seismic motion on the response of asymmetric buildings. *Proceedings of 12<sup>th</sup> World Conference on Earthquake Engineering*, Auckland, New Zealand, 2000.
- [6] Cruz, E.F. & Cominetti, S. (2000). Three-dimensional buildings subjected to bi-directional earthquakes. Validity of analysis considering uni-directional earthquakes. *Proceedings of 12<sup>th</sup> World Conference on Earthquake Engineering*, Auckland, New Zealand, 2000.
- [7] Peruš, I. & Fajfar, P. (2005). On the Inelastic Torsional Response of Single-Storey Structures under Bi-axial Excitation. *Earthquake Engineering and Structural Dynamics*, **34**, 931-941.
- [8] Marušić, D. & Fajfar, P. (2005). On the inelastic seismic response of asymmetric buildings under bi-axial excitation. *Earthquake Engineering and Structural Dynamics*, **34**, 943-963.
- [9] Tsai, K.C. & Lin, B.Z. (2003). User manual for the platform and visualization of inelastic structural analysis of 3D systems PISA3D and VISA3D. *Report No. CEER/R92-04*, Center for Earthquake Engineering Research, National Taiwan University.
- [10] Goel, R.K. (1998). Effects of supplemental viscous damping on seismic response of asymmetric-plan systems. *Earthquake Engineering and Structural Dynamics*, **27**, 125-141.
- [11] Goel, R.K. (2000). Seismic behavior of asymmetric buildings with supplemental damping. *Earthquake Engineering and Structural Dynamics*, **29**, 461-480.
- [12] Lin, W.H. & Chopra, A.K. (2001). Understanding and predicting effects of supplemental viscous damping on seismic response of asymmetric one-storey systems. *Earthquake Engineering and Structural Dynamics*, **30**, 1475-1494.
- [13] Lin, J.L. & Tsai, K.C. (2007b). Simplified seismic analysis of one-way asymmetric elastic systems with supplemental damping. *Earthquake Engineering and Structural Dynamics*, **36**, 783-800.
- [14] Moh, Z.L., Goldberg, J.E. & Bogdanoff, J.L. (1965). On modal distribution of damping. *West Virginia University Bulletin, Engineering Experimental Station Technical Bulletin*, No **74**.

- 
- [15] Itoh, T. (1973). Damped vibration mode superposition method for dynamic response analysis. *Earthquake Engineering and Structural Dynamics*, **2**, 47-57.
- [16] Rosset, J., Whitman R.V. & Dobry R. (1973). Modal analysis for structures with foundation interaction. *Journal of Structural Division, ASCE*, **99**, 399-416.
- [17] Goel, R.K. (2001). Simplified analysis of asymmetric structures with supplemental damping. *Earthquake Engineering and Structural Dynamics*, **30**, 1399-1416.
- [18] Clough, R.W. & Mojtahedi, S. (1976). Earthquake response analysis considering non-proportional damping. *Earthquake Engineering and Structural Dynamics*, **4**, 489-496.
- [19] Igusa, T, Der Kiureghian, A. & Sackman, J.L. (1984). Modal decomposition method for stationary response of non-classically damped systems. *Earthquake Engineering and Structural Dynamics*, **12**, 121-136.
- [20] Veletsos, A.S. & Ventura, C.E. (1986). Modal analysis of non-classically damped linear systems. *Earthquake Engineering and Structural Dynamics*, **14**, 217-243.
- [21] Ibrahimbegovic, A. & Wilson, E.L. (1989). Simple numerical algorithms for the mode superposition analysis of linear structural systems with non-proportional damping. *Computers and Structures*, **33**, 523-531.
- [22] Ibrahimbegovic, A., Chen, H.C., Wilson, E.L. & Taylor, R.L. (1990). Ritz method for dynamic analysis of large discrete linear systems with non-proportional damping. *Earthquake Engineering and Structural Dynamics*, **19**, 877-889.
- [23] Claret, A.M. & Venancio-Filho, F. (1991). A modal superposition pseudo-force method for dynamic analysis of structural systems with non-proportional damping. *Earthquake Engineering and Structural Dynamics*, **20**, 303-315.
- [24] Jangid, R.S. & Datta, T.K. (1993). Spectral analysis of systems with non-classical damping using classical mode superposition technique. *Earthquake Engineering and Structural Dynamics*, **22**, 723-735.
- [25] Warburton, G.B. & Soni, S.R. (1977). Error in response calculations for non-classically damped structures. *Earthquake Engineering and Structural Dynamics*, **5**, 365-376.
- [26] Lin, J.L. & Tsai, K.C. (2008a). Seismic analysis of two-way asymmetric building systems under bi-directional seismic ground motions. *Earthquake Engineering and Structural Dynamics*, **37**, 305-328.
- [27] Lin, J.L. & Tsai, K.C. (2008b). Seismic analysis of non-proportionally damped two-way asymmetric elastic buildings under bi-directional seismic ground motions. *Journal of Earthquake Engineering*, (in press).



# INDEX

## A

A $\beta$ , 357  
absorption, 71, 78  
accounting, 78  
accuracy, 6, 8, 26, 27, 31, 32, 34, 39, 98, 195, 230, 276, 280, 290, 325, 328, 341, 345, 355  
ACI, 251, 252, 253  
ad hoc, 230  
adequate housing, 82  
advocacy, 82  
age, 177, 180, 183, 187, 198, 203  
aid, 158  
air, 68, 71, 79, 136, 153  
air pollution, 71  
air quality, 136, 153  
algorithm, 36, 211  
alloys, 221, 222, 223, 251, 252, 253, 254  
alluvial, 183, 200, 203  
Alps, 320  
alternative, 64, 69, 160, 221, 355  
amplitude, xi, 3, 7, 12, 13, 70, 75, 91, 98, 99, 108, 115, 159, 161, 164, 169, 170, 171, 173, 174, 177, 178, 179, 182, 183, 185, 186, 187, 189, 190, 192, 203, 204, 206, 211, 218, 225, 226, 238, 258, 260, 261, 262, 265, 273, 295, 302, 303, 320  
analysts, 166  
analytical models, ix, 155  
analytical tools, 161  
Andes, 51  
animals, 68  
appendix, 333, 334  
application, 22, 52, 63, 68, 79, 83, 105, 132, 133, 164, 212, 213, 215, 216, 217, 220, 224, 228, 230, 234, 237, 251, 254, 266, 281, 355  
arithmetic, 345  
Army, 294  
ART, 255  
artificial, 7, 133, 136, 152, 153, 160  
asphalt, 72, 272  
Assam, 266, 268

assessment, ix, x, 51, 92, 121, 132, 155, 156, 158, 161, 179, 205, 210, 211, 212, 218, 221, 239, 252, 303, 324, 355  
assumptions, 26, 98, 101, 159  
asymmetry, 324  
Athens, 17, 51  
atmospheric pressure, 25  
attacks, 67, 68  
attention, 136, 220, 224, 318  
automotive, 71  
autoregressive model, 133  
averaging, 5, 8

## B

bacteria, 68  
ballast, 117  
bandwidth, 70, 168  
Bayesian, ix, 135, 136, 142, 145, 151, 152, 153  
beams, 77, 101, 114, 244, 245, 246, 251, 337, 345  
behavior, xi, 48, 52, 91, 92, 97, 106, 217, 221, 222, 223, 224, 226, 230, 231, 232, 233, 234, 236, 237, 239, 240, 241, 244, 248, 250, 251, 252, 253, 254, 292, 295, 296, 297, 299, 310, 316, 317, 324, 360  
bell, 252  
benchmark, 338, 345, 349, 350  
bifurcation, 336, 355  
biological, 68  
Biot's equations, 256, 282, 289, 290  
black, 68, 71, 181  
blocks, vii, 17, 18, 20, 21, 22, 23, 41, 50, 71, 190, 239  
boils, 266, 267, 268, 270  
bonds, 67  
boundary conditions, 5, 6, 7, 284, 287, 288, 289  
boundary value problem, 308  
bounds, 142, 173  
BRB, 220, 221  
breakdown, 82  
buildings, x, xii, 58, 66, 67, 78, 82, 83, 84, 85, 86, 87, 156, 157, 166, 219, 221, 241, 243, 245, 246, 248, 250, 252, 253, 254, 267, 269, 323, 324, 325, 326, 328, 329, 330, 337, 345, 346, 348, 355, 360, 361

burning, 71

## C

- calibration, 162, 211, 276, 281, 287, 303, 309, 321  
 California, 51, 52, 74, 75, 84, 86, 131, 152, 158, 213, 214, 215, 217, 247, 251, 253, 257, 267, 268, 269, 270, 271, 272, 273, 290, 291, 294, 321  
 Canada, 212, 216  
 candidates, 137, 142  
 capacity, 56, 77, 90, 220, 221, 226, 229, 236, 239, 240, 246, 256, 257, 277  
 carbon, 68  
 carbonates, 177, 183  
 case study, 41, 113, 115, 120, 121, 126, 130, 213, 214, 217, 270  
 cast, 209  
 CBF, 220, 221, 239, 241, 242, 243, 250, 251  
 C-C, 292  
 chain scission, 67, 68  
 channels, 162, 190  
 Chávez, 159, 161, 213, 215  
 chemical, 68, 69, 183, 223  
 chemical composition, 223  
 chemical industry, 183  
 chemical properties, 69  
 chemicals, 67, 68, 69  
 Chile, 58, 74, 75, 76, 83  
 China, viii, ix, 55, 56, 58, 84, 85, 87, 89, 90, 91, 114, 115, 117, 120, 121, 124, 126, 130, 131, 132, 135, 136, 137, 140, 142, 145, 151, 152, 153, 355  
 Chinese, 128, 152  
 chloride, 69  
 civil engineering, 72, 103, 136, 220, 223, 230  
 civil structures, 220  
 classes, 124, 136, 137, 139, 142, 145, 146, 147, 151  
 classical, 160, 361  
 classification, 24, 81, 136, 141  
 classified, 141  
 clay, 27, 28, 29, 34, 48, 49, 141, 171, 187, 198, 200, 202  
 clays, 26, 27  
 codes, 18, 22, 161, 195, 209, 255, 276, 291  
 cohesion, 79  
 cohesiveness, 78  
 collaboration, 82  
 column vectors, 326, 346  
 community, 57, 71, 82  
 compaction, 72, 79, 256, 263, 302  
 complementary, 71, 221, 239  
 complex numbers, 325  
 complexity, viii, x, 135, 152, 219, 221, 237, 250, 309  
 components, 21, 71, 75, 78, 80, 98, 100, 113, 116, 140, 159, 160, 161, 163, 166, 167, 168, 169, 170, 171, 172, 173, 174, 177, 178, 179, 234, 260, 282, 283, 304, 324, 328, 337, 340, 341, 342, 346  
 composite, 85  
 composition, 187, 191, 194  
 comprehension, viii, 89, 101, 109  
 compressibility, 72, 79, 282  
 compression, 79, 104, 220, 241, 257, 273, 274, 282, 297, 298, 304, 305, 306, 311, 318  
 computation, vii, 3, 4, 6, 7, 8, 101, 232, 263, 288, 289, 291  
 computer, 18, 34, 35, 39, 72, 73, 84, 97, 113, 131, 161, 162, 195, 217, 338, 339, 355  
 computers, 115  
 computers, 51, 115, 133, 361  
 computing, 164, 210, 299, 301  
 concentration, 8, 68, 248  
 conception, xi, 323  
 concrete, 6, 48, 71, 83, 220, 231, 251, 252, 253, 256, 272  
 conduction, 235  
 configuration, 3, 6, 18, 34, 35, 36, 39, 40, 42, 45, 46, 47, 50, 73, 78, 99, 187, 239, 240, 241, 265, 273  
 confinement, 66, 297  
 conjugate gradient method, 8  
 consolidation, 24, 25, 28, 29, 30, 66, 285  
 construction, 3, 5, 56, 63, 66, 68, 79, 82, 90, 114, 121, 158, 211  
 construction materials, 66  
 consultants, 41  
 consumption, 72  
 contamination, 80  
 continuity, 282  
 contracts, 299  
 control, vii, 71, 128, 162, 220, 221, 251, 252, 253, 254, 258  
 controlled, 130, 179, 224, 240, 257, 260, 261, 297, 299, 309  
 convection, 235  
 convective, 282  
 convergence, 113  
 conversion, 159, 162, 299  
 cooling, 236  
 copper, 230  
 correlation, 27, 143, 169, 190, 191, 193, 194, 211, 280  
 correlation coefficient, 143, 191  
 correlations, 277, 300  
 corrosion, 223, 239  
 cosine, 163  
 cost-effective, 58  
 costs, ix, 56, 58, 155, 210  
 countermeasures, 256  
 coupling, 91, 92, 114, 115, 118, 119, 120, 121, 164, 324, 333  
 coverage, 163  
 covering, 58, 308  
 Cp, 235  
 CRC, 83  
 creep, 66, 83, 84, 85, 104, 105  
 critical points, 288  
 critical state, 25, 26, 273, 274, 276  
 critical temperature, 236  
 critical value, 42  
 cross-sectional, 39, 245

crust, 159  
 CSR, 277, 278, 279, 307, 311, 312, 313, 314  
 cultural, 220, 251  
 cycles, xi, 60, 177, 220, 224, 225, 226, 229, 236,  
 257, 258, 259, 260, 261, 262, 263, 264, 265, 273,  
 276, 295, 299, 303, 311  
 cycling, 253

## D

damping, x, 7, 9, 40, 48, 49, 58, 71, 72, 73, 79, 93,  
 96, 100, 102, 103, 109, 110, 111, 125, 162, 206,  
 208, 209, 219, 220, 221, 222, 223, 239, 241, 250,  
 251, 252, 254, 300, 302, 316, 325, 326, 336, 337,  
 345, 346, 347, 348, 349, 350, 355, 356, 360, 361  
 danger, 92  
 data processing, 212  
 data set, 156, 206, 207, 300  
 database, ix, 135, 137, 140, 141, 151, 211  
 DBD, 241, 245, 248  
 death, 57, 82, 156  
 decay, 195  
 decomposition, 361  
 decoupling, viii, 55, 56, 81  
 defects, 66  
 deficiency, 309  
 definition, 19, 141, 279, 327  
 deformability, 272  
 deformation, xi, xii, 8, 13, 20, 22, 35, 36, 39, 40, 42,  
 46, 47, 56, 58, 80, 92, 101, 104, 109, 221, 222,  
 224, 225, 230, 234, 239, 243, 246, 295, 296, 299,  
 305, 309, 310, 317, 320, 323, 328, 329, 330, 341,  
 342  
 degradation, vii, 17, 18, 22, 48, 49, 50, 67, 68, 72,  
 73, 106, 220, 224, 225, 241, 309, 316, 319  
 degradation mechanism, 67  
 degree, xi, xii, 41, 68, 78, 92, 97, 237, 253, 277, 285,  
 287, 288, 291, 323, 324, 330, 333  
 degrees of freedom, viii, 89, 91, 98, 283, 325, 331,  
 333  
 delays, 102, 124  
 demand, 243, 250  
 demographic, 156  
 density, ix, 41, 67, 69, 72, 78, 79, 91, 107, 137, 156,  
 163, 195, 235, 256, 257, 258, 261, 262, 264, 273,  
 276, 300, 303, 316  
 deposits, 6, 63, 78, 160, 163, 180, 183, 187, 195,  
 200, 215, 305, 320  
 detection, 136  
 developing countries, 55, 57, 58, 82, 84, 86  
 developing nations, 85  
 deviation, 136, 191  
 diaphragm, 326, 333, 337  
 differentiation, 27  
 dilation, 25, 26, 273, 280, 281  
 disaster, 90  
 discomfort, 106  
 discontinuity, 211  
 discordance, 194

discretization, 4  
 dislocation, 106  
 distribution, 7, 141, 142, 143, 169, 183, 185, 186,  
 187, 190, 191, 209, 211, 245, 249, 312, 327, 328,  
 329, 330, 331, 334, 340, 355, 358, 360  
 divergence, 192  
 division, 159, 188  
 DOI, 132, 133  
 downhole, 215, 217  
 drainage, 67, 256, 284, 287  
 drinking, 80  
 drinking water, 80  
 dry, x, 18, 39, 40, 105, 255, 256, 258, 259, 260, 261,  
 272, 287, 299, 301, 302, 303  
 ductility, 77, 82, 85, 220, 221, 223, 237, 239, 241,  
 243, 244, 248, 250  
 dumping, 5  
 durability, 71  
 duration, xi, 42, 175, 177, 181, 250, 295, 300  
 dynamic loads, xi, 60, 295

## E

earth, 52, 270, 272  
 Earth Science, 212, 273  
 Eastern Europe, 86  
 ecology, 80  
 economic, 81  
 economy, 82  
 Education, 133, 318  
 efficacy, 220  
 Egypt, 58  
 eigenvalue, 101, 325  
 eigenvalues, 347, 348  
 elastic deformation, 98  
 elasticity, 6, 72, 232  
 elongation, 66  
 endothermic, 228, 235  
 energy, vii, viii, x, xi, 55, 58, 59, 71, 77, 78, 80, 92,  
 219, 220, 221, 223, 224, 226, 228, 229, 231, 234,  
 235, 236, 237, 239, 240, 245, 250, 251, 295, 298,  
 299, 300, 301, 302, 303, 304, 307, 308, 309, 310,  
 311, 312, 314, 315, 316, 318, 319, 320, 321, 358  
 energy density, 301  
 energy recovery, 71  
 energy transfer, 77  
 engineering, vii, viii, xi, 3, 4, 5, 6, 8, 51, 52, 57, 58,  
 71, 72, 79, 81, 82, 83, 90, 105, 128, 135, 136, 152,  
 157, 161, 215, 216, 253, 254, 276, 294, 321, 323,  
 325, 355  
 enthusiasm, 212  
 envelope, 297, 298, 299  
 environment, 6, 8, 82, 213, 229, 235  
 environmental, 71, 80, 90, 239  
 environmental effects, 71  
 environmental issues, 80  
 Environmental Protection Agency, 86  
 equating, 299

equilibrium, 19, 22, 34, 35, 36, 99, 103, 229, 282, 296  
 equipment, 162, 276, 318  
 erosion, 190  
 estimating, viii, 27, 36, 38, 72, 135, 152, 158, 160, 194, 209, 213, 217  
 Europe, 85, 207, 212  
 European, 51, 52, 53, 71, 83, 161, 251, 253, 320  
 European Commission, 51, 52, 71, 83  
 evidence, 77, 78, 79, 85, 138, 142, 183, 266, 267, 270, 275, 299  
 evolution, 108, 235, 236, 274, 280, 285  
 excitation, 36, 39, 40, 60, 61, 62, 91, 92, 94, 95, 104, 106, 115, 116, 118, 125, 126, 128, 133, 174, 324, 327, 346, 360  
 exertion, 327  
 exothermic, 228, 235  
 expansions, 153  
 experimental condition, 212  
 explosions, x, 156, 174, 175  
 exposure, 66, 209  
 extrapolation, 195, 211

## F

fabric, 303  
 facies, 198  
 failure, 21, 22, 34, 64, 66, 67, 68, 82, 246, 251, 256, 270, 272, 274, 276, 277, 278, 279, 281, 285, 287, 289, 296, 297, 298, 299  
 FAS, 70, 75, 76, 78  
 fatalities, 40, 55  
 fatigue, x, 219, 223, 224, 239, 253, 290, 299, 320  
 faults, 156, 157, 162, 180, 182, 183, 190, 203, 204, 205, 211  
 Federal Emergency Management Agency (FEMA), 252  
 FEM, 4, 7, 49, 50, 101  
 financial support, 318, 355  
 finite element method, 4, 14, 101, 283  
 fireproof, 71  
 floating, 98, 99, 267  
 flow, xi, 68, 180, 241, 283, 290, 295, 296, 297, 309, 310, 311, 312, 314, 315, 316, 317, 318  
 fluid, x, 255, 256, 273, 274, 275, 280, 282, 283, 290, 325, 337  
 flushing, 214  
 fossil, 266  
 Fourier, 7, 8, 12, 13, 70, 75, 159, 163, 164, 167, 168, 169, 170, 171, 172, 173, 174, 178, 211  
 fracture, 136, 153  
 free energy, 234  
 free radical, 68  
 freedom, xi, xii, 91, 97, 237, 253, 323, 324, 330  
 freedoms, 122  
 friction, x, 24, 25, 26, 34, 35, 41, 42, 44, 57, 59, 60, 61, 63, 65, 104, 105, 219, 221, 239, 240, 241, 246, 247, 248, 249, 250, 251, 254, 313  
 fuel, 71

fulfillment, 291  
 function values, 97  
 fungi, 68

## G

garbage, 86  
 gas, 183  
 gauge, 106  
 generation, xi, 22, 23, 24, 26, 27, 229, 235, 253, 285, 286, 295, 296, 299, 301, 303, 308, 314, 317  
 geology, 158, 162, 167, 180, 195, 213, 214  
 geomembranes, 84, 85, 87  
 geophysical, ix, 155, 195, 205, 208, 210, 211  
 Germany, 90, 214, 216, 251, 319  
 Global Positioning System, 162  
 GPS, 162  
 grading, 258  
 gradings, 258, 272  
 grain, 23, 24, 51, 272, 299, 301, 312  
 grains, 283, 296, 297, 302  
 graph, 259, 298  
 gravitational force, 63  
 gravity, 17, 18, 19, 20, 36, 39, 40, 46, 48, 50, 51, 52, 93, 276, 328  
 Greece, 17, 153, 175, 215  
 ground water, 80  
 groundwater, 80  
 grouping, 206  
 groups, 124, 193, 194, 296  
 Guangdong, 84, 137, 140, 141

## H

Haifa, 170, 171, 172, 173, 183, 184, 185, 186, 198, 199, 200, 202, 203, 204, 205, 206, 207  
 harmful, 78, 108  
 harmful effects, 78  
 hazards, ix, 156  
 HDPE, 60, 65, 69  
 head, 82  
 health, 80, 153  
 heat, 228, 229, 235  
 heat loss, 229, 235  
 heat transfer, 235  
 heating, 228, 236  
 heavy metal, 68  
 heavy metals, 68  
 height, 6, 37, 39, 40, 46, 77, 114, 115, 117, 118, 119, 120, 166, 170, 242, 245, 249, 270, 312  
 Hessian matrix, 138  
 heterogeneous, 4, 270  
 high density polyethylene, 60  
 high risk, 212  
 high-frequency, 78, 213  
 high-speed, viii, 89, 90, 91, 97, 109, 114, 117, 121, 124, 128, 131, 132, 133  
 highways, 256  
 homogeneous, 191, 194

hospitals, 58  
 housing, 58, 86  
 human, 56, 81, 160, 289  
 hunting, 106, 107, 108, 109, 115  
 hybrid, 251, 253, 325  
 hypothesis, xi, 161, 295, 299  
 hysteresis, x, 219, 221, 222, 223, 224, 225, 226, 228, 229, 230, 231, 232, 233, 236, 237, 238, 239, 240, 244, 250, 301, 306  
 hysteresis loop, 221, 222, 224, 225, 229, 231, 236, 237, 238, 239, 240, 250, 301, 306

## I

ice, 69  
 identification, vii, 52, 133, 139, 142, 192, 277, 284  
 identity, 346  
 implementation, 57, 60, 83, 160, 161, 224, 230, 250  
 incompressible, 283  
 indices, 117, 118, 126, 127, 128, 237, 238, 243  
 industrial, 223  
 industrial application, 223  
 inelastic, xi, xii, 56, 221, 232, 234, 241, 245, 248, 323, 324, 325, 326, 327, 328, 329, 334, 335, 336, 337, 341, 342, 355, 360  
 inertia, 18, 35, 93, 327, 328, 329, 330, 331, 334, 337, 340, 355, 358  
 infiltration, 67  
 information sharing, 82  
 infrastructure, vii, 3, 4, 5, 6, 9, 11  
 inherited, 351  
 initial state, 273, 274, 297  
 initiation, 297, 299  
 injuries, 57  
 INS, 86  
 inspection, 287  
 instability, 36, 106, 210, 272, 297  
 instruments, 162, 164  
 integration, 7, 39, 91, 113, 125, 283, 285, 328, 345, 349  
 intensity, x, 79, 128, 129, 130, 161, 180, 187, 217, 219, 300, 319, 341, 345  
 interaction, viii, 4, 8, 65, 78, 85, 89, 91, 92, 97, 103, 104, 105, 111, 112, 131, 132, 133, 164, 166, 174, 178, 210, 282, 329, 336, 341, 355, 361  
 interaction effect, 8  
 interactions, 102, 104, 122, 133  
 interface, 6, 18, 19, 21, 22, 25, 36, 37, 39, 42, 45, 55, 56, 57, 58, 59, 60, 61, 62, 65, 80, 81, 85, 192  
 interference, 160  
 international, 57, 82, 83, 216  
 interpretation, 187, 204, 212  
 interval, 8, 141, 197, 198, 199, 201, 202  
 inventions, 81  
 inversion, 215  
 investigations, 60, 63, 73, 137  
 iron, 80  
 island, 153

isolation, vii, viii, 55, 56, 57, 58, 59, 60, 62, 63, 65, 66, 67, 68, 69, 70, 71, 73, 77, 78, 80, 81, 83, 84, 85, 86, 87, 252, 254  
 isotropic, 14, 273  
 iteration, 19, 39

## J

$J_c$ , 99  
 joints, 106, 221

## K

Kalman filter, 153  
 kinetics, 234, 235, 236  
 Kobe, 51, 84, 158, 214, 220, 270, 272

## L

L1, 106  
 L2, 106  
 Lagrangian, 51  
 lakes, 266  
 laminated, 57, 71, 80  
 land, 63, 68, 82, 90, 211  
 land tenure, 82  
 land use, 90, 211  
 landfill, 69, 71  
 large-scale, 4, 6  
 law, 19, 36, 234, 260, 264, 280, 282  
 laws, xi, 255, 262, 276, 279, 280, 289, 291  
 layering, 159  
 leaching, 80  
 lead, 79, 92, 130, 158, 163, 211, 231, 246, 289, 310  
 Lebanon, 156, 180  
 Levant, 180  
 life-cycle, 224  
 life-cycle cost, 224  
 likelihood, 80, 136, 137, 138, 142, 152  
 limitation, 226  
 limitations, 181, 213  
 linear, vii, viii, 6, 17, 18, 21, 34, 35, 40, 41, 48, 49, 50, 72, 73, 89, 92, 98, 104, 105, 138, 212, 220, 229, 231, 237, 243, 264, 300, 307, 334, 335, 361  
 linear function, 138, 300  
 linear systems, 361  
 liquefaction, x, xi, 51, 78, 79, 85, 255, 256, 264, 266, 267, 270, 272, 273, 274, 276, 277, 280, 285, 287, 288, 289, 291, 292, 295, 296, 297, 298, 299, 300, 302, 303, 308, 319, 320, 321  
 liquids, 183  
 literature, 34, 39, 68, 195, 260, 262, 266, 325  
 living conditions, 82  
 location, 8, 22, 28, 29, 36, 40, 41, 75, 161, 162, 177, 245, 272, 274, 277, 284, 304  
 locus, 297  
 logging, 195  
 long distance, 102  
 long period, 92, 160, 213, 216  
 long-term, 67

Los Angeles, 14, 214, 237, 247, 251, 270  
 loss of control, 108  
 losses, 156  
 low temperatures, 69  
 L-shaped, 86

## M

M1, 92, 94, 95, 96, 332, 334  
 Macao, 135  
 Macau, 135, 151, 153  
 Macedonia, 71  
 machines, 140  
 manganese, 80  
 mantle, 159  
 mapping, 153, 194  
 masonry, 220  
 material resources, x, 255, 290  
 mathematical, 4, 8, 234, 237, 250, 265, 301, 307  
 matrix, viii, 5, 7, 89, 95, 96, 99, 100, 102, 103, 110, 111, 112, 113, 131, 140, 282, 325, 326, 327, 331, 333, 336, 337, 345, 346, 347, 348, 349, 350, 355  
 measurement, 101, 136, 137, 139, 163, 194, 226, 237  
 measures, 66, 79, 287  
 mechanical, x, 69, 133, 219, 221, 224, 225, 226, 229, 230, 234, 235, 239, 240, 241, 255, 278  
 mechanical behavior, 225, 229, 230  
 mechanical energy, 229, 235  
 mechanical properties, x, 224, 226, 255  
 mechanical structure, 133  
 mechanics, 4, 104, 136, 312, 318  
 media, 4  
 median, 248, 249  
 Mediterranean, 176, 212  
 Megacities, 86  
 memory, x, 219, 221, 222, 251, 252, 253, 254  
 metals, 221, 250, 280  
 Mexico, 86, 158, 213, 215, 216, 217  
 Mexico City, 158, 216, 217  
 microstructure, 222  
 Middle East, 207  
 migration, 82  
 Miocene, 180, 183, 200, 202  
 mixing, 79  
 mobility, xi, 276, 280, 295, 296, 297, 299, 302, 303, 308, 309, 310, 312, 315, 317, 318, 320  
 modeling, x, xi, 5, 20, 70, 72, 98, 101, 109, 136, 137, 139, 151, 162, 169, 192, 193, 194, 211, 217, 219, 221, 253, 295, 297, 299, 302, 303, 306, 307, 308, 309, 312, 315, 320  
 models, x, 11, 22, 25, 49, 62, 91, 114, 132, 136, 153, 158, 162, 170, 198, 205, 206, 207, 208, 219, 221, 230, 233, 234, 237, 238, 239, 250, 251, 256, 262, 263, 276, 277, 279, 280, 284, 290, 291, 303, 304, 305, 306, 307, 308, 309, 310, 318, 319  
 modules, 164  
 modulus, xi, 40, 49, 72, 73, 231, 232, 234, 263, 280, 281, 295, 300, 311, 315, 316, 319  
 moisture, 312

moisture content, 312  
 molecular weight, 60  
 Monte-Carlo simulation, ix, 155  
 Montenegro, 308, 319  
 movement, vii, 17, 18, 19, 22, 36, 50, 56, 64, 77, 98, 99, 102, 103, 104, 107, 108, 109, 202, 298, 299, 300, 302, 304  
 MTS, 223, 240  
 multivariate, 133

## N

National Bureau of Standards, 319  
 National Science Foundation, 292  
 natural, ix, x, 8, 58, 71, 77, 78, 84, 86, 90, 116, 122, 124, 135, 138, 162, 166, 179, 215, 216, 255, 299, 307, 320, 325, 328, 336  
 Nb, 109, 111, 113  
 neglect, 305, 325  
 network, 163  
 neural network, 136, 152, 153  
 neural networks, 136, 152, 153  
 Nevada, 215, 276  
 nickel (Ni), 20, 21, 22, 223, 253  
 nitrogen, 71  
 nitrogen oxides, 71  
 nodes, vii, 17, 18, 21, 34, 39, 42, 50, 101, 112, 265  
 noise, ix, x, 135, 136, 137, 139, 151, 155, 156, 158, 160, 161, 162, 163, 164, 165, 166, 167, 168, 169, 170, 173, 174, 176, 179, 180, 181, 187, 194, 205, 210, 211, 212, 213, 214, 215, 216, 218  
 nonlinear, ix, x, 72, 78, 104, 105, 131, 155, 158, 214, 219, 220, 221, 237, 243, 244, 245, 249, 250, 251, 305, 308, 309, 316, 324, 338, 345  
 non-linear, 8, 161  
 non-uniform, 34, 41, 92, 102, 104, 121, 130, 131, 133, 143  
 non-uniformity, 102, 104  
 North America, 152, 206, 213  
 Northridge Earthquake, 64  
 NSC, 355  
 numerical analysis, 6, 318  
 numerical computations, 4, 279  
 numerical tool, 264

## O

observations, x, 156, 158, 162, 163, 166, 179, 193, 195, 206, 209, 215, 224, 265, 288, 289, 301, 302, 315  
 ocean waves, 181  
 OCR, 28  
 one dimension, 304  
 operator, 282  
 optimization, 211, 321  
 organic solvent, 69  
 orientation, 162  
 orthogonality, 101  
 oscillation, 226, 236, 305, 306, 314

oscillations, 298, 305, 306, 318  
 oxidation, 67, 68  
 oxygen, 68

## P

Pacific, 319  
 parallel simulation, 14  
 parameter, 24, 26, 27, 73, 74, 76, 133, 138, 139, 140, 141, 142, 147, 151, 196, 210, 221, 239, 264, 281, 303, 310, 312, 314, 325  
 parameter estimation, 140  
 particles, x, 23, 255  
 passive, x, 78, 86, 219, 220, 251, 252  
 pendulum, 57  
 performance, x, 6, 66, 67, 69, 83, 84, 132, 219, 220, 221, 223, 239, 241, 243, 245, 248, 250, 251, 258, 277, 278, 302  
 periodic, 106  
 permeability, 72, 282, 283, 291  
 Perth, 214  
 perturbation, 4  
 PGA, 136, 137, 138, 139, 140, 141, 142, 143, 144, 145, 146, 147, 148, 337, 338, 342, 343, 344, 346, 350, 351, 352, 353, 354  
 pH, 69  
 phase transformation, 221, 228, 234, 235, 274, 275, 276, 277, 278, 279, 281, 297, 298, 299  
 philosophy, 78  
 physical properties, 85, 313  
 physics, xi, 142, 255  
 pigments, 68  
 pipelines, 183  
 planar, 242  
 planning, 52, 53, 211, 215  
 plastic, 23, 25, 48, 49, 50, 79, 224, 246, 258, 278, 279, 280, 309, 310  
 plastic deformation, 224, 246, 279  
 plastic strain, 278, 279  
 plasticity, 48, 49, 53, 86, 278, 280, 310, 321  
 plausibility, ix, 135, 137, 138, 139, 142, 145, 146, 148, 151  
 Pleistocene, 171, 180, 187, 202  
 Pliocene, 171, 187, 198, 202  
 pollutant, 183  
 pollution, 90  
 polyethylene, 69  
 polymer, 66, 67, 68  
 polymer structure, 67, 68  
 polymers, 66, 69  
 polynomial, ix, 135  
 polypropylene, 60, 68, 85  
 population, ix, 55, 68, 155, 156, 210, 300  
 pore, x, xi, 18, 21, 22, 23, 24, 25, 26, 27, 31, 34, 35, 40, 42, 44, 50, 78, 255, 256, 273, 274, 275, 277, 278, 279, 280, 282, 283, 285, 286, 287, 288, 295, 296, 297, 298, 299, 300, 301, 302, 303, 304, 305, 306, 307, 308, 309, 311, 312, 313, 314, 315, 316, 317, 318, 319, 320

pores, 296, 314  
 power, 91, 107, 115, 123, 124, 162, 307  
 prediction, viii, ix, 4, 17, 19, 26, 40, 50, 135, 136, 137, 139, 140, 141, 142, 144, 145, 147, 148, 150, 151, 206, 209, 213, 231, 302, 319  
 prediction models, 137  
 preference, 145  
 pressure, x, xi, 18, 22, 24, 25, 26, 27, 32, 33, 34, 35, 42, 44, 66, 67, 78, 85, 255, 256, 273, 274, 275, 277, 278, 279, 280, 281, 282, 283, 284, 285, 287, 288, 295, 296, 297, 298, 299, 300, 301, 302, 303, 304, 305, 306, 307, 308, 309, 311, 312, 313, 314, 315, 316, 317, 318, 319, 320  
 prevention, 251  
 probability, 79, 90, 137, 138, 209, 213  
 procedures, 51, 79, 84, 237, 241, 245, 252, 300, 319, 339  
 program, x, 34, 35, 39, 59, 72, 73, 84, 161, 164, 217, 219, 223, 312, 313, 338, 355  
 progressive, 309  
 promote, 82, 105  
 propagation, viii, 3, 4, 89, 131, 160  
 property, x, 6, 71, 130, 219, 230, 234, 337  
 proportionality, 355  
 proposition, 25  
 protection, 58, 59, 71, 72, 82, 87, 220, 254  
 protocol, 240  
 protocols, 80  
 prototype, x, 205, 219, 246, 247, 284, 324, 337, 338, 339, 341, 342, 344, 345, 346  
 PSD, 123, 124  
 pseudo, 103, 112, 361  
 PTFE, 60  
 public, 58, 80  
 public health, 80  
 public housing, 58  
 PVC, 65, 69

## R

radical, 68  
 radius, 6, 90  
 rail, viii, 89, 104, 105, 106, 107, 109, 111, 112, 113, 115, 117, 118, 119, 120, 126, 127, 128, 130, 131  
 railway track, 92  
 rain, 90, 91, 124, 132, 164  
 random, xi, 106, 108, 115, 132, 136, 206, 261, 295, 299, 325  
 range, 27, 69, 75, 77, 78, 109, 130, 141, 142, 158, 167, 169, 170, 176, 177, 179, 187, 195, 198, 202, 223, 234, 237, 243, 256, 259, 283, 297, 303, 304, 308, 310, 318, 324, 325, 342  
 rationality, 4  
 raw material, 69  
 Rayleigh, 7, 125, 346  
 reality, 62, 83, 279, 304  
 recovery, 71, 221, 222, 232  
 recurrence, 213  
 recycling, 71, 86

- reduction, x, 58, 62, 66, 70, 71, 76, 77, 78, 166, 236, 237, 247, 250, 255
- regional, ix, 156, 158, 174, 176, 182, 183, 191, 195, 209
- regression, 136, 152, 206, 211, 244, 313
- regression analysis, 152
- regression equation, 136
- regression method, 313
- regulations, 252
- rehabilitation, 220, 252
- reinforcement, 85
- relationship, xi, 24, 26, 104, 106, 112, 119, 129, 190, 191, 211, 216, 223, 229, 230, 231, 232, 234, 245, 250, 258, 274, 280, 298, 299, 300, 301, 307, 308, 320, 323, 328, 329
- relationships, viii, xi, xii, 24, 26, 27, 49, 85, 89, 131, 152, 194, 209, 313, 323, 325, 328, 329, 330, 341, 342
- relaxation, 66, 84
- reliability, 153, 160, 162, 163, 164, 210, 212, 216
- repair, x, 56, 220, 224, 246, 251
- research, viii, xii, 3, 51, 55, 56, 58, 59, 63, 66, 72, 81, 82, 89, 91, 92, 131, 136, 251, 256, 257, 262, 273, 274, 276, 277, 312, 318, 323, 324, 325, 345, 355
- researchers, 91, 104, 166, 220, 224, 233, 257, 274, 299, 300, 303, 307, 324
- reservoir, 270
- residential, 40, 58, 69, 165, 166
- residential buildings, 40
- resistance, vii, 17, 18, 19, 21, 22, 23, 34, 35, 36, 40, 41, 42, 50, 65, 66, 68, 69, 80, 220, 223, 239, 253, 293, 299, 321
- resistivity, 193
- resolution, vii, 3, 4, 195, 214
- resources, viii, 55, 58, 82
- response time, 116, 324
- restoration, 220
- returns, 297
- reusability, 224, 239, 247
- rigidity, 333
- risk, 92, 156, 160, 183, 187, 220, 289, 291, 300
- risks, 57, 81, 276
- Ritz method, 361
- RMS, 76
- roads, 256, 272
- robustness, 69, 73, 74, 137, 139, 142, 147, 151, 239
- rocky, 66
- rolling, 79, 91, 98, 99, 104, 105, 107, 132
- room temperature, 223, 229
- root-mean-square, 75, 79
- rotations, 122
- rubber, 55, 57, 58, 69, 70, 71, 72, 73, 78, 80, 81, 82, 83, 84, 85, 86
- rural population, 82
- safety, viii, 34, 57, 89, 90, 91, 92, 106, 108, 109, 114, 117, 121, 126, 128, 129, 130, 131, 132, 224, 243
- salts, 68
- sample, 24, 28, 29, 30, 260, 261, 273, 274, 275, 277, 302, 308, 316, 317
- sand, 27, 41, 52, 56, 63, 64, 65, 69, 70, 72, 75, 76, 77, 79, 83, 85, 198, 201, 202, 208, 256, 257, 258, 259, 260, 261, 262, 263, 264, 265, 266, 267, 268, 270, 272, 273, 274, 276, 278, 280, 281, 282, 284, 285, 287, 288, 290, 291, 292, 312, 313, 317, 320, 321
- saturation, x, 41, 255, 287, 289
- scaling, 83, 137, 276, 330
- scanning electron microscopy, 68
- scatter, x, 156, 166, 191, 194, 210, 211
- scattering, 162
- science, 136, 152
- scrap, 58, 71, 72, 80
- searching, 38, 105
- sediment, 160, 161, 172, 187, 190, 191, 193, 194, 211, 214, 215, 216, 218
- sediments, viii, 55, 58, 81, 83, 156, 161, 163, 171, 173, 177, 179, 183, 187, 190, 191, 195, 198, 202, 203, 204, 211, 213, 214, 216, 217
- selecting, 164, 166, 210
- SEM, 68
- sensitivity, ix, 135, 162, 163, 321
- sensors, 162, 174
- sentences, 82
- separation, 22, 23, 42, 133
- series, x, 35, 69, 73, 104, 163, 190, 209, 219, 223, 299, 316, 321
- settlements, 256, 257, 261, 263, 266, 289
- Shanghai, viii, 89, 90, 121, 131, 132, 152
- shape, x, 19, 26, 36, 37, 39, 63, 64, 101, 113, 123, 167, 168, 171, 179, 190, 192, 193, 206, 211, 219, 220, 221, 222, 224, 226, 236, 245, 250, 251, 252, 253, 254, 285, 315, 316, 326, 329, 334, 346, 357, 359
- shape memory alloys, 220, 250, 251, 252, 253
- shape-memory, 251, 252, 254
- shear, xi, 23, 24, 25, 26, 27, 28, 29, 30, 31, 32, 33, 34, 40, 41, 42, 48, 49, 53, 57, 59, 62, 65, 71, 72, 77, 78, 79, 80, 141, 163, 177, 195, 206, 214, 243, 244, 245, 246, 257, 258, 259, 260, 261, 262, 263, 264, 273, 274, 276, 277, 278, 279, 280, 281, 284, 295, 296, 297, 298, 299, 300, 302, 303, 304, 305, 308, 311, 315, 316, 317, 319, 320, 321, 323, 328, 331
- shear strength, 24, 27, 30, 72, 78, 79, 296, 297, 317
- shock, 208
- short period, 324
- short-term, xi, 295, 309, 310, 311, 312, 314, 315, 316, 317, 318
- sign, 101, 112, 235, 280
- signals, 162, 163, 173, 179, 209, 216

<b>S</b>
----------

SAC, 247, 253

- simulation, vii, x, 3, 4, 6, 7, 8, 14, 39, 52, 133, 210, 213, 219, 231, 232, 233, 236, 237, 250, 287, 309, 317, 320
- simulations, 4, 35, 69, 73, 77, 78, 114, 124, 210, 237
- sine, 92, 162, 312, 337, 338, 342, 343, 344, 345
- sine wave, 92, 312, 337, 338, 342, 343, 344, 345
- singular, 4
- sites, ix, xi, 41, 68, 69, 84, 155, 157, 158, 159, 160, 161, 162, 163, 166, 167, 169, 170, 171, 172, 173, 176, 181, 182, 184, 188, 193, 194, 195, 203, 205, 206, 208, 209, 210, 211, 213, 215, 217, 255, 285, 290, 300
- skeleton, x, 255, 256, 266, 299, 305, 310
- Slovenia, 295, 312, 317, 318, 321
- SMA, x, 219, 220, 221, 222, 223, 224, 230, 231, 232, 233, 234, 235, 237, 239, 241, 243, 244, 245, 246, 250, 253, 254, 349, 350, 351, 353, 354
- SME, 253
- smoke, 71
- smoothing, 163
- smoothness, 90
- SNS, 163
- society, 136
- software, 48, 121
- soil particles, 66, 71, 79, 303, 304, 310, 318
- solid phase, 222, 224, 246, 282
- solutions, 338, 345, 349, 350
- spatial, ix, 3, 4, 5, 92, 97, 101, 156, 163, 187, 190, 209, 211
- specialists, 161
- specific gravity, 313
- specific heat, 229, 235
- spectra, ix, x, xi, xii, 8, 75, 77, 83, 152, 155, 156, 159, 160, 162, 163, 164, 166, 167, 168, 169, 170, 171, 172, 173, 174, 178, 179, 191, 206, 208, 209, 210, 211, 213, 217, 241, 244, 285, 286, 323, 328
- spectral analysis, 164, 169
- spectral component, 171, 172
- spectrum, ix, 7, 12, 13, 70, 78, 123, 124, 155, 159, 160, 163, 166, 168, 169, 170, 206, 208, 209, 217, 242, 244
- speed, 24, 25, 28, 90, 91, 92, 93, 97, 98, 106, 108, 114, 115, 118, 119, 121, 125, 126, 127, 128, 129, 130, 131, 132, 232
- springs, 62, 97, 98, 100, 331, 333, 334, 335
- SPT, 263, 277
- stability, vii, x, 17, 18, 20, 21, 22, 35, 41, 50, 52, 90, 106, 114, 133, 156, 166, 167, 210, 211, 232, 272
- stabilization, 71, 283
- stabilize, 226, 288
- stages, 24, 26, 27, 233, 285, 286
- standard deviation, 142, 148, 166, 172, 173, 176, 179, 237
- standards, 80, 90
- statistics, 345
- steady state, 274, 297
- steel, 62, 86, 133, 220, 221, 222, 231, 239, 245, 247, 250, 253, 260, 337
- steel plate, 260
- stiffness, x, xi, 5, 25, 48, 64, 78, 80, 85, 96, 99, 100, 102, 109, 110, 111, 116, 141, 224, 228, 231, 233, 246, 255, 256, 257, 295, 299, 301, 302, 305, 306, 309, 310, 311, 314, 315, 316, 317, 318, 324, 326, 330, 331, 333, 334, 335
- stochastic, 5, 15, 152, 155, 209, 210, 211, 213, 217
- stockpile, 71, 72
- strain, xi, 4, 22, 25, 27, 40, 48, 49, 66, 72, 85, 161, 222, 223, 224, 226, 227, 228, 229, 230, 231, 232, 234, 236, 238, 241, 244, 245, 246, 250, 253, 254, 257, 258, 259, 260, 261, 262, 263, 264, 282, 292, 295, 297, 298, 299, 300, 301, 302, 303, 304, 305, 306, 308, 309, 310, 311, 316, 317, 318, 319, 321
- strains, 52, 64, 66, 72, 78, 224, 236, 256, 258, 260, 261, 263, 272, 276, 280, 282, 289, 299, 302, 303, 317
- strategies, 220
- strength, vii, viii, 17, 18, 22, 24, 25, 26, 27, 28, 29, 34, 35, 40, 41, 42, 46, 48, 50, 57, 66, 71, 79, 85, 220, 237, 239, 241, 244, 245, 288, 296, 297, 299, 309, 317, 319, 360
- stress-strain curves, 224, 230, 231, 233
- stretching, 90, 102
- substances, 80
- suburban, 160
- suffering, 256, 274
- sulphur, 71
- sunlight, 67, 68
- superimpose, 203
- superposition, 91, 94, 101, 239, 325, 361
- supplemental, vii, 325, 326, 345, 346, 360, 361
- supply, 162
- surface layer, 4, 161
- surface roughness, 106
- survival, 253
- sustainability, 71
- symbols, 38, 140, 301, 331
- synthetic, viii, ix, 55, 58, 59, 60, 63, 64, 65, 66, 67, 68, 87, 155, 210, 327, 333, 339, 358
- system analysis, 104, 115
- systematic, ix, 156, 158, 178, 212
- systems, xi, xii, 58, 59, 77, 80, 81, 84, 91, 102, 131, 132, 153, 220, 221, 231, 237, 239, 241, 250, 251, 252, 253, 254, 323, 324, 325, 326, 328, 329, 336, 339, 340, 341, 342, 355, 358, 359, 360, 361

<b>T</b>
----------

- technology, viii, 55, 58
- teeth, 68
- temperature, x, 66, 67, 69, 219, 221, 222, 223, 226, 228, 229, 230, 233, 234, 235, 236, 237, 238, 239, 250
- tensile, 66, 85, 221, 253
- tensile strength, 85
- tensile stress, 66
- tension, 220, 233, 241, 311
- territory, 180
- test data, 231, 233, 236, 286, 303

TGV, 90, 97  
 theoretical, 104, 114, 173, 300, 303  
 theory, viii, 4, 8, 23, 25, 69, 89, 92, 104, 105, 263, 273, 280, 291, 292, 301, 321, 359  
 thermal, 69, 221, 226, 235  
 thermal expansion, 69  
 thermo-mechanical, 233, 234, 236, 237, 239, 250  
 Thessaloniki, 215  
 threat, 55  
 three-dimensional, vii, 3  
 threshold, 128, 300, 301, 302, 321  
 Ti, 20, 244, 253  
 time increment, 7, 35, 36, 39  
 time series, 131, 133  
 timing, 162  
 tires, 71, 86  
 titanium, 223  
 Tokyo, 3, 132, 133  
 tolerance, 72  
 tolls, 82  
 topographic, 41, 42  
 torque, xii, 323, 326, 328, 329, 330, 334  
 traffic, 90, 91, 166, 299, 304  
 training, 223, 224, 225, 241  
 trajectory, 41  
 transducer, 253  
 transfer, x, 57, 69, 70, 80, 156, 159, 192, 194, 195, 196, 197, 198, 199, 200, 201, 204, 205, 206, 211, 220, 241  
 transformation, 22, 34, 163, 222, 223, 224, 225, 226, 228, 229, 230, 231, 234, 235, 236, 244, 246, 250, 274, 297, 307, 310, 316  
 transformations, 303  
 transition, 232, 233, 235  
 translation, xi, 304, 323, 328, 329, 331, 333, 336, 341, 342, 344, 345  
 translational, 122, 324, 328, 331, 333, 338, 345, 346, 349, 350, 353, 354, 355  
 transmission, 59, 305, 318  
 transparent, 7  
 transportation, 90  
 traveling waves, 130  
 trend, viii, x, 62, 77, 89, 90, 104, 182, 190, 236, 255, 256  
 Turkey, 52, 74, 75, 76, 132, 158, 175, 216, 304, 321  
 two-dimensional, 4, 14, 70, 73, 282  
 two-way, xii, 323, 324, 325, 326, 328, 330, 336, 337, 355, 361

## U

U.S. Geological Survey, 152  
 ultraviolet, 66, 67, 68  
 uncertainty, ix, 72, 135, 140, 142, 146, 147, 151  
 uniaxial tension, 226  
 uniform, ix, 34, 48, 92, 102, 108, 120, 121, 125, 130, 138, 141, 142, 155, 217, 299, 307, 321  
 United Nations, 58, 82

United Nations Industrial Development Organization, 58  
 United States, 58, 71, 80, 85, 86  
 updating, 136  
 urban, ix, 82, 155, 156, 157, 160, 163, 166, 183, 187, 205, 206, 210, 211, 214, 215  
 urban areas, ix, 82, 155, 156, 160, 163, 166, 183, 187, 205, 206, 210  
 urban population, 82  
 urbanization, 82  
 US Army Corps of Engineers, 254, 294  
 USEPA, 71, 86  
 Utah, 29

## V

validation, 240, 276  
 validity, 6, 159, 324  
 values, 7, 24, 26, 27, 31, 32, 35, 36, 40, 42, 48, 49, 72, 73, 76, 113, 125, 127, 139, 141, 142, 144, 145, 147, 148, 151, 181, 187, 190, 191, 195, 198, 209, 229, 233, 237, 243, 250, 258, 262, 264, 265, 281, 283, 287, 288, 297, 306, 307, 317, 318, 339, 345, 346, 349, 350  
 variability, ix, 155, 162, 163, 179, 183, 191, 210  
 variable, 18, 51, 121, 136, 234, 262, 303  
 variables, 73, 136, 234  
 variance, 140  
 variation, 5, 41, 42, 49, 60, 163, 226, 228, 229, 235, 237, 238, 250, 280  
 vector, 5, 8, 95, 96, 100, 103, 104, 111, 112, 113, 138, 139, 140, 142, 282, 283, 326, 327, 329, 331, 333, 334, 346, 359  
 vehicles, viii, 71, 89, 91, 92, 97, 98, 99, 102, 104, 106, 107, 108, 109, 110, 111, 115, 117, 118, 125, 126, 127, 128, 130, 131, 132  
 velocity, 7, 18, 21, 35, 42, 44, 48, 49, 60, 78, 93, 99, 102, 103, 105, 125, 127, 128, 130, 141, 152, 158, 159, 162, 163, 170, 171, 173, 183, 187, 190, 191, 194, 195, 198, 200, 202, 203, 204, 206, 211, 215, 300  
 versatility, 309  
 vibration, xi, 71, 91, 92, 93, 97, 98, 99, 101, 102, 106, 108, 109, 116, 122, 123, 131, 165, 176, 177, 178, 190, 211, 238, 253, 257, 262, 265, 323, 324, 325, 327, 328, 329, 330, 333, 336, 337, 339, 341, 342, 345, 346, 349, 350, 351, 354, 361  
 victims, 81  
 viscoelastic materials, 66  
 visualization, 360  
 voids, 68, 79  
 volumetric changes, 318  
 vulnerability, 81, 82

## W

Washington, 82, 83, 85, 215, 216, 252, 292, 294  
 waste, 68, 71, 82, 83, 84  
 waste products, 82

water, x, xi, 23, 34, 40, 41, 48, 67, 78, 255, 270, 277, 278, 279, 282, 283, 285, 286, 287, 288, 295, 296, 299, 300, 301, 302, 303, 304, 305, 306, 307, 308, 311, 314, 317, 318, 319, 321  
water table, 34, 40, 41, 48  
wave propagation, vii, viii, 3, 4, 6, 14, 89  
wavelengths, 106, 124  
weathered, 202  
weathering, 141  
web, 101  
wells, 198, 199  
West Indies, 215  
wet, 261, 312  
wind, 100, 164, 174, 299  
windows, x, 156, 163, 164, 166, 170, 210  
wires, x, 219, 223, 224, 225, 226, 227, 228, 229, 230, 231, 232, 233, 234, 236, 239, 240, 241, 243, 244, 245, 246, 250, 252, 253, 254

witnesses, 256

**X**

X-axis, 331, 339, 346

**Y**

Y-axis, 328

yield, 158, 161, 179, 203, 210, 221, 224, 237, 245, 246, 279, 280

**Z**

Zone 1, 187, 206

Zone 2, 187

Zone 3, 187